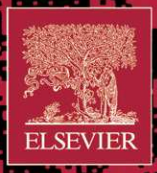

RECRYSTALLIZATION
and
Related Annealing Phenomena

Second Edition

F.J. Humphreys
and
M. Hatherly

RECRYSTALLIZATION
AND RELATED ANNEALING PHENOMENA

SECOND EDITION

Elsevier Internet Homepage: http://www.elsevier.com

Consult the Elsevier homepage for full catalogue information on all books, journals and electronic products and services.

Titles of Related Interest

Books

BEVER
Encyclopedia of Materials Science and Engineering
8-Volume Set

BLOOR, BROOK, FLEMING & MAHAJAN
The Encyclopedia of Advanced Materials
4-Volume Set

CAHN
Encyclopedia of Materials Science and Engineering
Supplementary Volumes 1, 2 & 3

CAHN
The Coming of Materials

Related Journals

Free specimen copy gladly sent on request. Elsevier Ltd, The Boulevard, Langford Lane, Kidlington, Oxford, OX5 1GB, UK

Acta Metallurgica et Materialia

Calphad

Journal of Physics and Chemistry of Solids

Materials Research Bulletin

Progress in Crystal Growth and Characterization of Materials

Scripta Metallurgica et Materialia

Materials Science and Engineering-A

Journal of Alloys & Compounds

Reference Work

The Encyclopedia of Materials: Science and Technology

To Contact the Publisher

Elsevier welcomes enquiries concerning publishing proposals: books, journal special issues, conference proceedings, etc. All formats and media can be considered. Should you have a publishing proposal you wish to discuss, please contact, without obligation, the publisher responsible for Elsevier's Materials Science publishing programme:

David Sleeman
Publishing Editor
Elsevier Ltd
The Boulevard, Langford Lane
Kidlington, Oxford
OX5 1GB, UK

Phone: +44 1865 843178
Fax: +44 1865 843920
E-mail: d.sleeman@elsevier.com

General enquiries, including placing orders, should be directed to Elsevier's Regional Sales Offices – please access the Elsevier homepage for full contact details (homepage details at the top of this page).

RECRYSTALLIZATION
AND RELATED ANNEALING PHENOMENA

SECOND EDITION

by

F.J. HUMPHREYS

University of Manchester Institute of Science and Technology, UK

and

M. HATHERLY

University of New South Wales, Australia

2004

ELSEVIER

Amsterdam Boston Heidelberg London New York Oxford
Paris San Diego San Francisco Singapore Sydney Tokyo

ELSEVIER Ltd
The Boulevard, Langford Lane
Kidlington, Oxford OX5 1GB, UK

First edition: 1995
Second impression (of first edition): 2002
Second edition: 2004

Library of Congress Cataloging in Publication Data
A catalog record from the Library of Congress has been applied for.

British Library Cataloguing in Publication Data
A catalogue record from the British Library has been applied for.

ISBN: 0 08 041884 8 (Cased version of First Edition)
ISBN: 0 08 042685 9 (Flexi version of First Edition)
ISBN: 0 08 044164 5 (Cased version of Second Edition)

♾ The paper used in this publication meets the requirements of ANSI/NISO Z39.48-1992 (Permanence of Paper).
Printed in The Netherlands.

CONTENTS

CHAPTER 14
CONTINUOUS RECRYSTALLIZATION DURING AND AFTER LARGE STRAIN DEFORMATION 451

CHAPTER 15
CONTROL OF RECRYSTALLIZATION 469

ThisPageIntentionallyLeftBlank

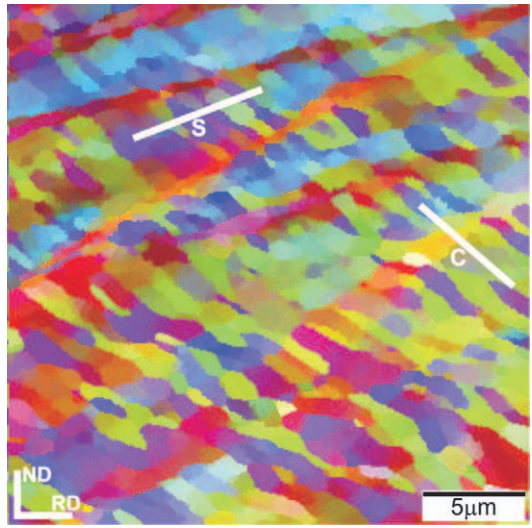

Fig. 2.12(b). See p. 33.

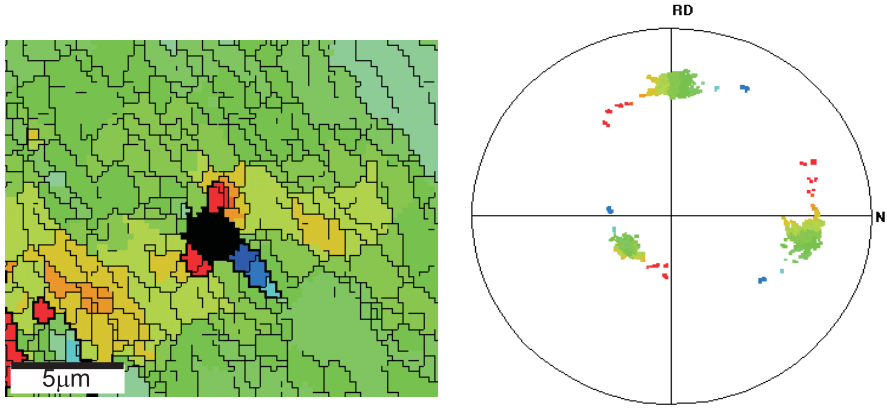

(a) (b)

Fig. 2.38. See p. 64.

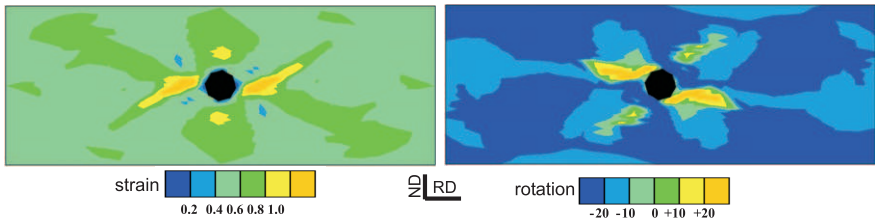

(a) (b)

Fig. 2.39. See p. 64.

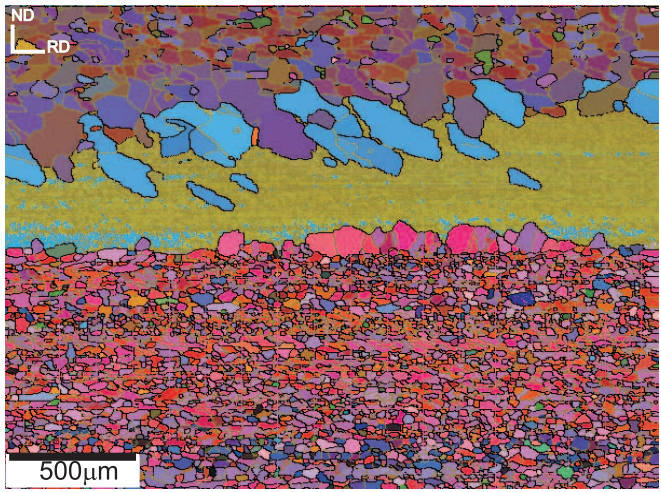

Fig. 7.15. See p. 240.

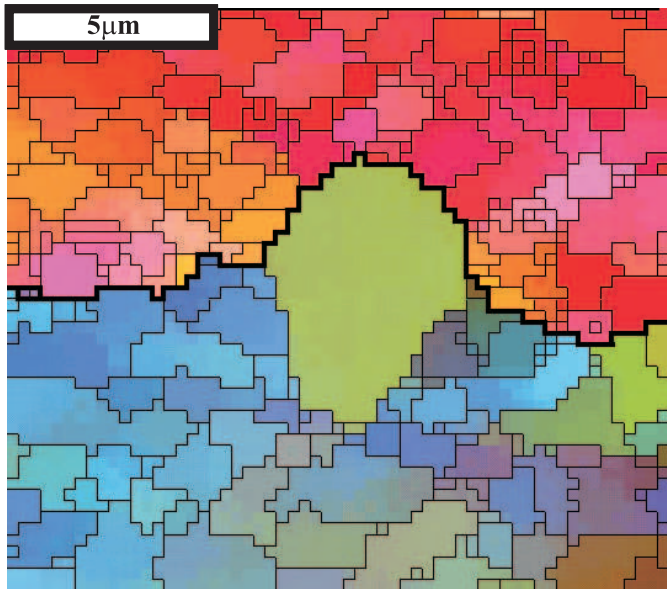

Fig. 7.31. See p. 257.

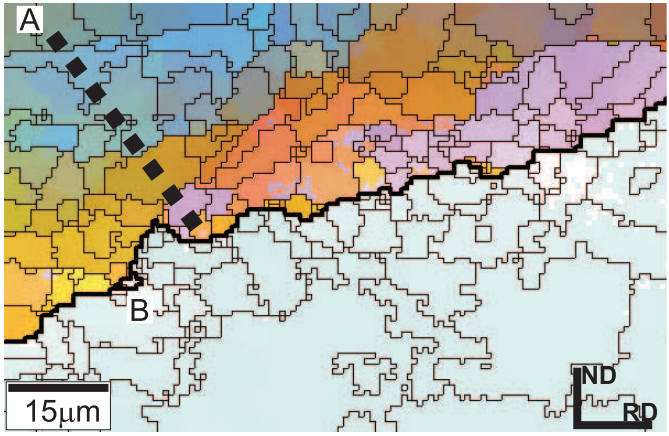

Fig. 13.22(a). See p. 440.

ThisPageIntentionallyLeftBlank

SYMBOLS

The following notation is generally used in the text. The subscripts i or n indicate the use of letters or numbers for particular symbols. On rare occasions where the letters or symbols are used for other purposes, this is specifically stated.

b	Burgers vector of a dislocation
c,c_n,C,C_n,K_n	These denote 'local' constants which are defined in the text
d	Diameter of second-phase particle
D	Grain or subgrain diameter
D_i	Diffusivity (s = bulk diffusion, b = boundary diffusion, c = core diffusion)
F_v	Volume fraction of second-phase particles
G	Shear modulus
E_i	Energy. e.g. stored energy of deformation E_D
k	Boltzmann constant
M	Boundary mobility
N_v	Number of grains or second-phase particles per unit volume
N_s	Number of particles per unit area
P or P_i	Pressure on a boundary
Q or Q_i	Activation energy, (for diffusion:- s = bulk, b = boundary, c = core)
R	Grain or subgrain radius
s	Shear strain
t	Time
T, T_m	Temperature, melting temperature (K)
v	Velocity of dislocation or boundary
V	Volume
α,β	Constants
γ	Energy of an interface or boundary
γ_{SFE}, γ_{RSFE}	Stacking fault energy, reduced stacking fault energy
γ_b	Energy of a high angle boundary
γ_s	Energy of a low angle boundary
ε	True strain
$\dot{\varepsilon}$	True strain rate

θ	Misorientation across a boundary
λ	Interparticle spacing (defined in equation A2.13)
ν	Poisson ratio
ν_0	Atomic vibrational frequency
ρ	Dislocation density
Σn	Coincidence grain boundaries. 1/n is the fraction of sites common to both grains
σ	True stress
τ	Shear stress
Φ, φ_1, φ_2	Euler angles (defined in appendix 1)
Ω	Orientation gradient

ABBREVIATIONS

ARB	Accumulative roll bonding
CA	Cellular automata
CPFEM	Crystal plasticity finite element modelling
CLS	Cahn, Lücke, Stüwe (theory of solute drag)
CSL	Coincidence site lattice
DDW	Dense dislocation wall
EBSD	Electron backscatter diffraction
ECAE	Equal channel angular extrusion
ECD	Equivalent circle diameter
FE	Finite element (modelling)
FEGSEM	Field emission gun scanning electron microscope
GBCD	Grain boundary character distribution
GBE	Grain boundary engineering
GNB	Geometrically necessary boundary
HAGB	High angle grain boundary
HSLA	High strength low alloy (steel)
HVEM	High voltage transmission electron microscope
IDB	Incidental dislocation boundary

IF	Interstitial free (steel)
JMAK	Johnson–Mehl–Avrami–Kolmogorov kinetic model
LAGB	Low angle grain boundary
MD	Molecular dynamics
MLI	Mean linear intercept
ND, RD, TD	Normal, rolling and transverse directions in a rolled product
ODF	Orientation distribution function
PSN	Particle stimulated nucleation of recrystallization
SEM	Scanning electron microscope
SFE	Stacking fault energy
SIBM	Strain induced boundary migration
SMG	Sub-micron-grained (alloy)
SPF	Superplastic forming
TEM	Transmission electron microscope

PREFACE TO THE FIRST EDITION

Recrystallization and the related annealing phenomena which occur during the thermomechanical processing of materials have long been recognised as being both of technological importance and scientific interest. These phenomena are known to occur in all types of crystalline materials; they occur during the natural geological deformation of rocks and minerals, and during the processing of technical ceramics. However, the phenomena have been most widely studied in metals, and as this is the only class of material for which a coherent body of work is available, this book inevitably concentrates on metallic materials. Although there is a vast body of literature going back 150 years, and a large collection of reviews which are detailed in chapter 1, there have only been two monographs published in recent times on the subject of recrystallization, the latest nearly 20 years ago. Since that time, considerable advances have been made, both in our understanding of the subject and in the techniques available to the researcher.

Metallurgical research in this field is mainly driven by the requirements of industry, and currently, a major need is for quantitative, physically-based models which can be applied to metal-forming processes so as to control, improve and optimise the microstructure and texture of the finished products. Such models require a more detailed understanding of both the deformation and annealing processes than we have at present. The development of the underlying science to a level sufficient for the construction of the required models from first principles provides a goal for perhaps the next 10 to 20 years.

The book was written to provide a treatment of the subject for researchers or students who need a more detailed coverage than is found in textbooks on physical metallurgy, and a more coherent treatment than will be found in the many conference proceedings. We have chosen to emphasise the scientific principles and physical insight underlying annealing rather than produce a comprehensive bibliography or handbook.

Unfortunately the generic term annealing is used widely to describe two metallurgical processes. Both have a common result in that a hardened material is made softer, but the mechanisms involved are quite different. In one case, associated with the heat treatment of ferrous materials, the softening process involves the $\gamma \rightarrow \alpha$ phase transformation. In the second case, which is the one relevant to this book, the softening is a direct result of the loss via recovery and recrystallization, of the dislocations introduced by work hardening.

It is not easy to write a book on recrystallization, because although it is a clearly defined subject, many aspects are not well understood and the experimental evidence is often poor and conflicting. It would have been desirable to quantify all aspects of the

phenomena and to derive the theories from first principles. However, this is not yet possible, and the reader will find within this book a mixture of relatively sound theory, reasonable assumptions and conjecture. There are two main reasons for our lack of progress. First, we cannot expect to understand recovery and recrystallization in depth unless we understand the nature of the deformed state which is the precursor, and that is still a distant goal. Second, although some annealing processes, such as recovery and grain growth are reasonably homogeneous, others, such as recrystallization and abnormal grain growth are heterogeneous, relying on local instabilities and evoking parallels with apparently chaotic events such as weather.

It must be recognised that we are writing about a live and evolving subject. Very little is finished and the book should therefore be seen as a snapshot of the subject at this particular time as seen by two scientists who are undoubtedly biased in various ways. We hope that when a second edition of this volume is produced in perhaps 10 years time, or a new treatment is attempted, many aspects of the subject will have become clearer.

Recovery and recrystallization depend on the nature of the deformed state and involve the formation, removal and movement of grain boundaries. For these reasons we have included treatments of the deformed state in chapter 2, and the nature of grain boundaries in chapter 3. These are both large topics which merit complete books in themselves, and we have not attempted a comprehensive coverage but have merely aimed to provide what we regard as essential background information in order to make the volume reasonably self-contained. Chapter 4 is concerned with the migration and mobility of grain boundaries, and this contains some background information.

The main topics of the book – recovery, recrystallization and grain growth are covered in chapters 5 to 11 and include specific chapters on ordered materials, two-phase alloys and annealing textures. In order to illustrate some of the applications of the principles discussed in the book we have selected a very few technologically important case studies in chapter 12. The final chapter outlines the ways in which computer simulation and modelling are being applied to annealing phenomena, and in the appendix we provide an introduction to the measurement and representation of textures for the benefit of readers who are not specialists in this area.

John Humphreys
Manchester Materials Science Centre
University of Manchester Institute of Science and Technology
U.K.

Max Hatherly
School of Materials
University of New South Wales
Australia

August 1994

The need to reprint the book has provided an opportunity for us to correct some of the errors and to carry out minor modifications to the text.

May 1996

PREFACE TO THE SECOND EDITION

This second edition has a similar philosophy and format to the first, although developments in the subject have necessitated some significant changes. Recrystallization remains a very active research area, judging by the number of publications and conferences on this and related areas, and the continuing developments in many areas make it a difficult subject to capture. As in the preface to the first edition, we ask the reader to remember that this book presents a personal view of the subject, at a particular moment in time.

There have been two important changes in methods of investigating and analysing recrystallization since the first edition. The first is in the experimental determination of microstructure and texture, where the increase in the power and application of the Electron Backscatter Diffraction (EBSD) technique has provided data of a type which was previously unavailable, and many examples of its use are included in the book. The other change is in the increased amount of modelling and simulation of annealing processes which is now carried out.

In terms of the subject areas covered in the first edition of the book, there has been significant new activity in two areas of fundamental importance to the understanding of recrystallization; the characterisation of the deformed state, and the measurement of grain boundary properties. Some new areas have also opened up. In the first edition we briefly mentioned new research which indicated that deformation to very large strains might lead to microstructural stability on subsequent annealing. This has now become a major research area which is not only of scientific interest, but is also a potential method of producing strong alloys, and this is given detailed coverage in this edition. Developments in this and other areas have highlighted the difficulties of applying the traditional terminologies to new phenomena, and it is now considered necessary to subdivide recovery, recrystallization and grain growth into 'discontinuous' and 'continuous' variants.

Changes in the layout of the book include a separation of deformation microstructure (chapter 2) and deformation texture (chapter 3), introduction of a simple analytical model which embraces recovery, recrystallization and grain growth (chapter 10), a consideration of continuous recrystallization during and after large strain deformation (chapter 14), and a summary of the methods of measuring recrystallization (appendix 2).

Finally, access to video clips of some in-situ annealing experiments and simulations which may be of interest, is provided at the web site:- http://www.recrystallization.info

April 2003

John Humphreys
Max Hatherly

ThisPageIntentionallyLeftBlank

ACKNOWLEDGEMENTS

Figures have been reproduced with permission from the following sources:

The following figures are copied from *Acta Materialia* with the permission of Elsevier Science, P.O. Box 800, Oxford OX5 1DX: Figure 13.10 from Nes, E. and Marthinsen, K. (2002), Mats. Sci. and Eng. A322, 176. 'Origin of cube texture during hot rolling of commercial Al–Mn–Mg alloys', (figure 6). Figure 2.10 from Liu, Q., Juul Jensen, D. and Hansen, N. (1998), Acta mater. 46, 5819. 'Effect of grain orientation on deformation structure in cold rolled aluminium', (figure 2). Figure 16.6 from Upmanyu, M., Srolovitz, D.J., Shvindlerman, L.S. and Gottstein, G. (1999), Acta Mater. 47, 3901. 'Misorientation/dependence of intrinsic boundary mobility', (figure 2). Figure 4.19 from Goukon, N., Yamada, T and Kajihara, M. (2000), Acta Mater. 48, 2837. 'Boundary energies of Σ11 [110] asymmetric tilt boundaries', (figure 2). Figure 5.2 from Winning, M. Gottstein, G and Shvindlerman, L.S. (2001), Acta Mater. 49, 211. 'Stress induced grain boundary motion', (figures 12 and 13). Figure 5.33 from Protasova, S.G., Gottstein, G. Sursaeva, V.G. and Shvindlerman, L.S. (2001), Acta mater. 49, 2519. 'Triple junction motion in aluminium tricrystals', (figure 5). Figure 2.33 from Duckham, A., Knutsen, R.D. and Engler, O. (2001), Acta Mater. 49, 2739. 'Influence of deformation variables on the formation of shear bands in Al–1Mg', (figure 3). The following figures are copied from *Scripta Materialia* with the permission of Elsevier Science, P.O. Box 800, Oxford OX5 IDX: Figure 5.12 from Molodov, D.A., Czubayko, U., Gottstein, G. and Shvindlerman, L.S. (1995), Scripta Metall. Mater. 32, 529. 'Mobility of $<111>$ tilt grain boundaries...', (figures 4 and 5). Figure 4.3 from Hutchinson, W.B., Ryde, L., Bate, P.S. and Bacroix, B. (1996), Scripta Mater. 35, 579. ''On the description of misorientations...', (figure 4). Figure 12.7 from Engler, O. (2001b), Scripta Mater. 44, 299. 'An EBSD local texture study on the nucleation of recrystallization...', (figure 1). Figure 4.7 from Yang, C.-C., Rollett, A.D., and Mullins, W.W. (2001). Scripta Materialia, 44, 2735. 'Measuring relative grain boundary energies...', (figure 4).

The following figures are copied from *Materials Science and Engineering*, with the permission of Elsevier Science, P.O. Box 800, Oxford OX5 IDX: Figure 2.5 from Hughes, D.A. (2001), Mats. Sci. Eng. A319, 46. 'Microstructure evolution, slip patterns...', (figure 4). Figure 2.3b from Nes, E. and Marthinsen, K. (2002), Mats. Sci. and Eng. A322, 176. 'Modelling the evolution in microstructure and properties...', (figure 6). Figure 6.27 from Haslam, A.J., Phillpot, S.R., Wolf, D., Moldovan, D. and Gleiter, H. (2001), Mats. Sci. Eng. A318, 293. 'Mechanisms of grain growth in nanocrystalline fcc metals...', (figure 4). Figure 15.3 from Engler, O. and Hirsch, J.

(2002), Mats. Sci. Eng. A336, 249. 'Texture control by thermomechanical processing. . .', (figure 10).

The following figure is copied from *Intermetallics*, with the permission of Elsevier Science, P.O. Box 800, Oxford OX5 IDX: Figure 8.7 from Huang, Y.D. and Froyen L. (2002), Intermetallics, 10, 473. 'Recovery, recrystallization and grain growth. . .', (figure 5).

The following figures are copied from *Materials Science and Technology* with the permission of Maney Publishing, 1 Carlton House Terrace, London SW1Y 5DB: Figure 3.3 from Hirsch, J. (1990b), Mats. Sci. and Tech. 6, 1048. 'Correlation of deformation texture and microstructure', (figure 3). Figure 15.15 from Hayes, J.S., Keyte, R. and Prangnell, P.B. (2000), Mats. Sci. and Tech. 16, 1259. 'Effect of grain size on tensile behaviour of a submicron-grained Al–3wt%Mg alloy', (figure 6).

The following figure is copied from *Materials Science Forum*, with the permission of Trans Tech Publications Ltd. Brandrain 6, CH-8707, Ueticon-Zuerich, Switzerland: Figure 3.15 from Benum, S., Engler, O. and Nes, E. (1994), Mats. Sci. Forum, 157–162, 913.

In the first edition of this book we acknowledged a great debt to those with whom we had discussed and argued over the subjects covered by this book over a period of very many years. During the writing of the book we had particularly useful discussions and correspondence with Brian Duggan, Bevis Hutchinson and Erik Nes. A large number of others helped by providing advice, material and in many other ways. They include Sreeramamurthy Ankem, Mahmoud Ardakani, Christine Carmichael, Michael Ferry, Brian Gleeson, Gunther Gottstein, Brigitte Hammer, Alan Humphreys, Peter Krauklis, Lasar Shvindlerman, Tony Malin, Paul Munroe, Nigel Owen, Phil Prangnell, Fred Scott, Karen Vernon-Parry and David Willis.

A significant amount of the new research which has contributed to the second edition of the book has been carried out in Manchester, and the strong support of the Engineering and Physical Sciences Research Council and Alcan International is gratefully acknowledged. The help, advice and support of Pete Bate has been particularly valuable, and the Manchester Light Alloy Processing Group, including Philip Prangnell, Norman Ridley, Hedieh Jazaeri, Peter Hurley, Yan Huang, Andrew Clarke, Martin Ashton, Ian Brough, and Matthew Jones, and their provision of data and figures has made a major contribution to this edition. During the preparation of the second edition, critical comments and suggestions from Michael Ferry and Robert Moon of the University of New South Wales have been extremely valuable.

Finally, and as in the first edition, we must acknowledge the patience and understanding shown by our wives Anna and Lorna during the writing of the book.

Chapter 1

INTRODUCTION

1.1 THE ANNEALING OF A DEFORMED MATERIAL

1.1.1 Outline and terminology

The free energy of a crystalline material is raised during deformation by the presence of dislocations and interfaces, and a material containing these defects is thermodynamically unstable. Although thermodynamics would suggest that the defects should spontaneously disappear, in practice the necessary atomistic mechanisms are often very slow at low homologous temperatures, with the result that unstable defect structures are retained after deformation (fig. 1.1a).

If the material is subsequently heated to a high temperature (**annealed**), thermally activated processes such as solid state diffusion provide mechanisms whereby the defects may be removed or alternatively arranged in configurations of lower energy.

The defects may be introduced in a variety of ways. However, in this book we will mainly be concerned with **those defects, and in particular dislocations, which are introduced during plastic deformation.** The point defects introduced during deformation anneal out at low temperatures and generally have little effect on the mechanical properties of the material. In considering only materials which have undergone substantial plastic deformation, we necessarily limit the range of materials with which we will be concerned. Metals are the only major class of crystalline material to undergo substantial plastic deformation at low homologous temperatures, and much of this book will be concerned with the annealing of deformed metals. However, at high temperatures, many minerals and ceramics readily deform plastically, and the

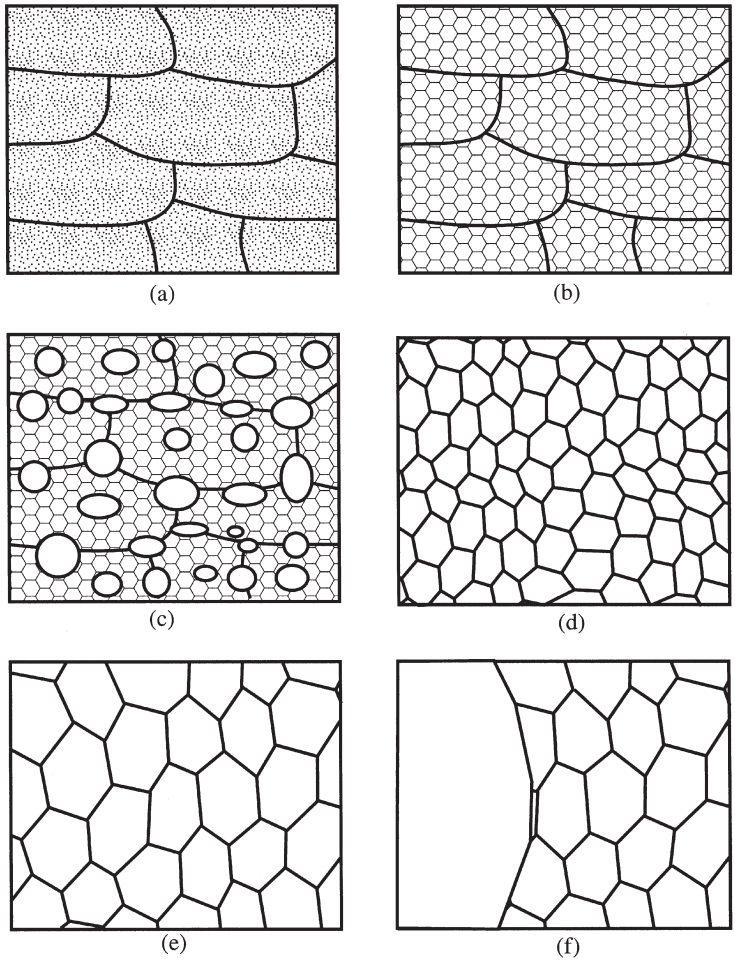

Fig. 1.1. Schematic diagram of the main annealing processes; (a) Deformed state, (b) Recovered, (c) Partially recrystallized, (d) Fully recrystallized, (e) Grain growth and (f) Abnormal grain growth.

annealing of these is of great interest. In addition, some annealing processes such as **grain growth** are relevant to cast or vapour deposited materials as well as to deformed materials.

On annealing a cold worked metal at an elevated temperature, the microstructure and also the properties may be partially restored to their original values by **recovery** in which annihilation and rearrangement of the dislocations occurs. The microstructural changes during recovery are relatively homogeneous and do not usually affect the boundaries between the deformed grains; these changes in microstructure are shown schematically in figure 1.1b. Similar recovery processes may also occur during deformation,

particularly at high temperatures, and this **dynamic recovery** plays an important role in the **creep** and **hot working** of materials.

Recovery generally involves only a partial restoration of properties because the dislocation structure is not completely removed, but reaches a metastable state (fig. 1.1b). A further restoration process called **recrystallization** may occur in which new dislocation-free grains are formed within the deformed or recovered structure (fig. 1.1c). These then grow and consume the old grains, resulting in a new grain structure with a low dislocation density, (fig. 1.1d). Recrystallization may take place during deformation at elevated temperatures and this is then termed **dynamic recrystallization.**

Although recrystallization removes the dislocations, the material still contains grain boundaries, which are thermodynamically unstable. Further annealing may result in **grain growth,** in which the smaller grains are eliminated, the larger grains grow, and the grain boundaries assume a lower energy configuration (fig. 1.1e). In certain circumstances this **normal grain growth** may give way to the selective growth of a few large grains (fig. 1.1f), a process known as **abnormal grain growth or secondary recrystallization.**

Recent research has shown that borderlines between the various annealing phenomena are often unclear, and it is known that recovery, recrystallization and grain growth may occur in two ways. They occur heterogeneously throughout the material, such that they may be formally described in terms of **nucleation** and **growth** stages, and in this case they are described as **discontinuous** processes. Alternatively, they may occur uniformly, such that the microstructures evolve gradually with no identifiable nucleation and growth stages. In this case, the prefix **continuous** is used to categorise the phenomena. It should be emphasised that this is a phenomenological categorisation which does not imply the operation of any particular micromechanism. The 'continuous' phenomena include recovery by subgrain growth, continuous recrystallization and normal grain growth and the 'discontinuous' phenomena include discontinuous subgrain growth, primary recrystallization and abnormal grain growth. Therefore, as shown in table 1.1 there are at least **six** static annealing phenomena which need to be considered.

Although these processes are analysed separately in later chapters, there are circumstances when they can be considered within a unified framework, as discussed in chapter 10. This has the merit of not only emphasising the common features of the

Table 1.1
Examples of static annealing phenomena.

	Recovery	Recrystallization	Grain growth
Continuous	Subgrain growth	Continuous recrystallization	Normal grain growth
Discontinuous	Discontinuous subgrain growth	Primary recrystallization	Abnormal grain growth

various processes, but, in breaking down the conventional distinctions between the various annealing phenomena, allows also for the emergence of new phenomena which may not conveniently fit into the traditional categories.

1.1.2 The importance of annealing

Many metallic materials are produced initially as large castings which are then further processed in the solid state by forging, rolling, extrusion etc., to an intermediate or final product. These procedures, which may be carried out hot or cold, and which may involve intermediate anneals, are collectively termed **thermomechanical processing.** Recovery, recrystallization and grain growth are core elements of this processing.

To a large extent the mechanical properties and behaviour of a metal depend on the dislocation content and structure, the size of the grains and the orientation or **texture** of the grains. Of these, the dislocation content and structure are the most important. The mechanical properties depend primarily on the number of dislocations introduced during cold working and their distribution. As this increases from $\sim 10^{11}$ m^{-2}, typical of the annealed state, to $\sim 10^{16}$ m^{-2}, typical of heavily deformed metals, the yield strength is increased by up to 5–6 times and the ductility decreased. If the strain hardened material is subsequently heated to $\sim T_m/3$ dislocation loss and rearrangement occur and this is manifested by a decrease in strength and increased ductility. There is an enormous literature on the magnitude of these changes and any adequate treatment is beyond the scope of this book. For details of these the reader is referred to the appropriate volumes of **Metals Handbook.**

The grain size and texture after annealing are determined mainly by the recrystallization process, and there are numerous examples of the need to control grain size. For example, a small grain size increases the strength of a steel and may also make it tougher. However, a large grain size may be required in order to reduce creep rates in a nickel-based superalloy for use at high temperatures. Superplastic forming, in which alloys are deformed to large strains at low stresses, is becoming an important technological process for the shaping of advanced materials. Great ingenuity must be exercised in producing the required fine grain size and preventing its growth during high temperature deformation. The control of texture is vital for the successful cold forming of metals, a particularly important example being the deep drawing of aluminium or steel to produce beverage cans.

1.2 HISTORICAL PERSPECTIVE

1.2.1 The early development of the subject

Although the art of metalworking including the procedures of deformation and heating has been practised for thousands of years, it is only comparatively recently that some understanding has been gained of the structural changes which accompany these processes. The early history of the annealing of deformed metals has been chronicled very elegantly by Beck (1963), and it is clear that the pace of scientific understanding

was largely dictated by the development of techniques for materials characterisation. It should be noted that this constraint still applies.

1.2.1.1 Crystallinity and crystallization

In 1829, the French physicist Felix Savart found that specimens from cast ingots of various metals exhibited acoustic anisotropy, and concluded that cast ingots consisted of crystals of different orientations. He also found that although the anisotropy was changed by plastic deformation and subsequent annealing, heating alone produced no change. This is the first recorded evidence for a structural change occurring during the annealing of a cold worked metal.

In the mid 19th century, the concept of the crystallization of metals was extensively discussed, and it was widely thought that plastic deformation rendered metals amorphous. This belief arose from the inability to observe grain structures in the deformed metals using visual inspection. On reheating the deformed metal however, the grain structure could sometimes be seen (Percy 1864, Kalischer 1881), and this was then interpreted as **crystallization** of the metal from its amorphous state.

The introduction of metallographic techniques by Sorby, culminating in his paper of 1887 took the subject a step forward. He was able to study the elongated grains in deformed iron and note that on heating, a new equiaxed grain structure was produced, a process which he termed **recrystallization.** Furthermore, Sorby recognised that the distorted grains must be unstable, and that recrystallization allowed a return to a stable condition. Despite Sorby's work, the idea that cold worked metals were amorphous persisted for some years and was not finally abandoned until the Bakerian lecture by Ewing and Rosenhain in 1900 in which it was clearly shown that plastic deformation took place by slip or twinning, and that in both of these processes the crystal structure was preserved.

1.2.1.2 Recrystallization and grain growth

Although recrystallization had been identified by the beginning of the 20th century, recrystallization and grain growth had not clearly been distinguished as separate processes. The outstanding work by Carpenter and Elam (1920) and Altherthum (1922) established that stored energy provided the driving force for recrystallization, and grain boundary energy that for grain growth. This is shown by the terminology for these processes used by Altherthum – Bearbeitungsrekristallisation (cold-work recrystallization) and Oberflächenrekristallisation (surface tension recrystallization).

In 1898 Stead had proposed that grain growth occurred by grain rotation and coalescence, and although Ewing and Rosenhain presented convincing evidence that the mechanism was one of boundary migration, Stead's idea was periodically revived until the work of Carpenter and Elam finally settled the matter in favour of boundary migration.

1.2.1.3 Parameters affecting recrystallization

By around 1920, many of the parameters which affected the recrystallization process and the resultant microstructure had been identified.

Kinetics – The relationship of the recrystallization temperature to the melting temperature had been noted by Ewing and Rosenhain (1900), and Humfrey (1902) showed that the rate of recrystallization increased with an increase in annealing temperature.

Strain – Sauveur (1912) found that there was a critical strain for recrystallization, and a relationship between grain size and prior strain was reported by Charpy (1910). Carpenter and Elam (1920) later quantified both of these effects.

Grain growth – In a very early paper on the control of microstructure during annealing, Jeffries (1916) showed that **abnormal grain growth** in thoriated tungsten was promoted in specimens in which normal grain growth had been inhibited.

Further developments in the understanding of recrystallization were not possible without a more detailed knowledge of the deformed state. This was provided by the development of the dislocation theory in 1934, and a notable early review of the subject following the advent of the dislocation theory is that of Burgers (1941).

From about this period it becomes difficult to distinguish the papers of historical interest from the early key papers which are still relevant to current thinking, and the latter are cited as appropriate within the various chapters of this book. However, it may be helpful to the reader to have a source list of books, reviews and conferences on the subject from the past 50 years, and this is given below.

1.2.2 Some key literature (1952–2003)

Monographs on Recrystallization

Byrne, J.G. (1965), **Recovery, Recrystallization and Grain Growth.** McMillan, New York.

Cotterill, P. and Mould, P.R. (1976), **Recrystallization and Grain Growth in Metals.** Surrey Univ. Press, London.

Novikov, V. (1997), **Grain Growth and Control of Microstructure and Texture in Polycrystalline Materials.** CRC Press, Boca Raton.

Multi-author, edited compilations on Recrystallization

Himmel, L. (ed.), (1963), **Recovery and Recrystallization of Metals.** Interscience, New York.

Margolin, H. (ed.), (1966), **Recrystallization, Grain growth and Textures.** ASM, Ohio, USA.

Haessner, F. (ed.), (1978), **Recrystallization of Metallic Materials.** Dr. Riederer-Verlag, G.m.b.H Stuttgart.

Review articles and books containing chapters on Recrystallization

Burke, J.E. and Turnbull, D. (1952), **Recrystallization and Grain Growth.** Progress in Metal Phys., 3, 220.

Beck, P.A. (1954), **Annealing of Cold-worked Metals.** Adv. Phys., 3, 245.

Leslie, W.C., Michalak, J.T. and Aul, F.W. (1963), **The annealing of cold-worked iron.** In: **Iron and its Dilute Solid Solutions.** (eds.) Spencer and Werner. Interscience. New York. 119.

Christian, J.W. (2002), **The Theory of Transformations in Metals and Alloys.** 2nd edition, Pergamon, Oxford.

Jonas, J.J., Sellars, C.M. and Tegart, W.J. McG. (1969), **Strength and Structure Under Hot Working conditions.** Met. Revs., 130, 1.

Martin, J.W. and Doherty, R.D. (1976), **The Stability of Microstructure in Metals.** Cambridge University Press.

Cahn, R.W. (1996), in **Physical Metallurgy.** (eds.) Cahn and Haasen. 4th edition. North-Holland, Amsterdam.

Hutchinson, W.B. (1984), **Development and Control of Annealing Textures in Low-Carbon Steels.** Int. Met. Rev., 29, 25.

Honeycombe, R.W.K. (1985), **The Plastic Deformation of Metals.** Edward Arnold.

Humphreys, F.J. (1991), **Recrystallization and Recovery.** In: **Processing of Metals and Alloys.** (ed.) R.W. Cahn. VCH. Germany. 371.

Doherty, R.D., Hughes, D.A., Humphreys, F.J., Jonas, J.J., Juul Jensen, D., Kassner, M.E., King, W.E., McNelly, T.R., McQueen, H.J. and Rollett, A.D. (1997), **Current issues in recrystallization: a review.** Mats. Sci. & Eng., A238, 219.

Proceedings of International Conferences

International Recrystallization Conference Series (1990–1999)

Chandra, T. (ed.), (1991), **Recrystallization'90.** TMS, Warrendale, USA.

Fuentes, M. and Gil Sevillano, J. (eds.), (1992), **Recrystallization'92.** Trans. Tech. Pubs. Switzerland.

McNelley, T.R. (ed.), (1997), **Recrystallization and Related Annealing Phenomena – Rex'96.**

Sakai, T. and Suzuki, H.G. (1999), **Recrystallization and Related Phenomena – Rex'99.** Japan Inst. Metal.

International Grain Growth Conferences (1991–1998)

Abbruzzese, G. and Brozzo, P. (eds.), (1991). **Grain Growth in Polycrystalline Materials.** Trans. Tech. Publications, Switzerland.

Grain Growth in Polycrystals II, Kitabyushu Japan, (1995).

Weiland, H., Adams, B.L. and Rollett, A.D. (eds.), (1998), **Grain Growth in Polycrystals III.** TMS.

International Conferences on Recrystallization and Grain Growth
A combination of the former ***Recrystallization*** and ***Grain Growth*** series of International conferences, which will be held every three years.

Gottstein, G. and Molodov, D.A. (eds.), (2001). **First International Conference on Recrystallization and Grain Growth - Rex&GG.** Springer-Verlag, Berlin.

Second International Conference on Recrystallization and Grain Growth - Rex&GGII. (2004), Annecy, France.

International Texture Conference (ICOTOM) Series
Conferences are held every 3 years.
The 13th Conference was held in Seoul, Korea in 2002.
The 14th Conference will be held in Levven, Belgium in 2005.

International Risø Symposia
Held annually in Risø, Denmark, the proceedings in 1980, 1983, 1986, 1991, 1995 and 2000 are of particular relevance.

International Thermomechanical Processing Conferences (Thermec)
General coverage of all aspects of thermomechanical processing. Proceedings published by TMS.

Thermec'97, Wollongong, Australia.

Thermec'2000, Las Vegas, USA.

Thermec'2003, Madrid, Spain.

Other International Conferences
Recrystallization in the Control of Microstructure. Institute of Metals, London. Keynote papers published in Metal Science J., 8. (1974).

Recrystallization in the Development of Microstructure. Leeds. Institute of Metals, London. Published in Metal Science, 13. (1979).

Microstructure and Mechanical Processing. Cambridge. Institute of Materials, London. Keynote papers published in Materials Science and Tech., 6. (1990).

Fundamental of Recrystallization. Zeltingen, Germany. A number of short papers from this meeting are published in Scripta Metall. Mater., 27, (1992).

Thermomechanical Processing - TMP^2, Stockholm, ASM, (1996).

Deformation Processing of Metals, London. Published in Phil. Trans. Royal Soc., 1441–1729, (1999).

Thermomechanical Processing: Mechanics, Microstructure and Control, University of Sheffield, Palmiere, Mahfouf and Pinna (eds.) BBR Solutions, (2003).

1.3 FORCES, PRESSURES AND UNITS

The annealing processes discussed in this book mainly involve the migration of internal boundaries within the material. These boundaries move in response to thermodynamic driving forces, and specific quantitative relationships will be discussed in the appropriate chapter. It is however useful at this stage to set out some of the terminology used and also to compare the energy changes which occur during the various annealing processes with those which drive phase transformations.

1.3.1 Pressure on a boundary

The processes of recovery, recrystallization and grain growth are all driven by the defect content of the material. Consider a small part of the microstructure of a single-phase crystalline material as shown in figure 1.2, which consists of two regions **A** and **B** separated by a boundary at position **x.** Let us assume that the two regions contain different defect concentrations and that the free energies of these regions per unit volume are G^A and G^B respectively.

The boundary will move if the Gibbs free energy of the system is thereby lowered, and if an area **a** of the boundary moves a distance **dx**, then the change in free energy of the system is

$$\mathbf{dG} = \mathbf{dx}(G^A - G^B)\mathbf{a} \tag{1.1}$$

The **force, F,** on the boundary is given by **dG/dx,** and the **pressure, P,** on the boundary, is given by **F/a,** and thus

$$\mathbf{P} = -\frac{1}{\mathbf{a}}\frac{\mathbf{dG}}{\mathbf{dx}} = G^A - G^B = \Delta G \tag{1.2}$$

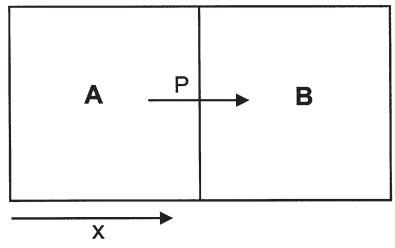

Fig. 1.2. The pressure on a boundary.

If ΔG in equation 1.2 is given in units of Jm^{-3}, then the pressure on the boundary (**P**) is in Nm^{-2}. There is some confusion in the literature regarding terminology, and the terms **force on a boundary** and **pressure on a boundary** are both used for the parameter which we have defined above by **P.** As **P** has units of Nm^{-2} which are those of pressure, there is some logic in using the term **pressure,** and we will adopt this terminology.

1.3.2 Units and the magnitude of the driving pressure

Although we will be discussing the forces and pressures acting on boundaries in some detail in later chapters, it is useful at this stage to examine, with examples, some of the forces involved in annealing. This will serve to demonstrate the **units** used in the book and also to give some idea of the relative magnitudes of the forces involved in annealing. A good discussion of forces arising from a variety of sources is given by Stüwe (1978).

Recrystallization – driving pressure due to stored dislocations
The driving force for recrystallization arises from the elimination of the dislocations introduced during deformation. The stored energy due to a dislocation density ρ is $\sim 0.5\ \rho Gb^2$, where **G** is the shear modulus and **b** the Burgers vector of the dislocations. A dislocation density of 10^{15}–10^{16} m^{-2}, which is typical of the cold worked state in copper ($G = 4.2 \times 10^{10}$ Nm^{-2}, $\mathbf{b} = 0.26$ nm) therefore represents a stored energy of $\sim 2 \times 10^6$–2×10^7 Jm^{-3} ($\sim$10–100 J/mol) and gives rise to a driving pressure for recrystallization of $\sim$ **2–20 MPa.**

Recovery and grain growth – driving pressure due to boundary energy
Recovery by subgrain coarsening and grain growth following recrystallization are both driven by the elimination of boundary area. If the boundary energy is γ **per unit area** and the boundaries form a three-dimensional network of spacing D, then the driving pressure for growth is given approximately as $3\gamma/D$. If the energy of a low angle grain boundary (γ_s) is 0.2 Jm^{-2}, and that for a high angle boundary (γ_b) is 0.5 Jm^{-2}, we find that $\mathbf{P} \sim$ **0.6 MPa** for the growth of 1 μm subgrains during recovery, and that $\mathbf{P} \sim \mathbf{10^{-2}}$ **MPa** for the growth of 100 μm grains.

Comparison with the driving forces for phase transformations
It is of interest to compare the energy changes which occur during annealing, as discussed above, with those which occur during phase transformations. For example a typical value of the latent heat of fusion for a metal is $\sim$**10 kJ/mol** and that for a solid state transformation is $\sim$**1 kJ/mol.** We therefore see that the energies involved in annealing of a cold worked metal are very much smaller than those for phase transformations.

Chapter 2

THE DEFORMED STATE

2.1 INTRODUCTION

The emphasis in this and the following chapter is quite different to that of the remaining chapters of the book. The most significant of the many changes associated with recrystallization and other annealing phenomena is the decrease in the density of dislocations. In this chapter we are concerned with dislocation **accumulation** rather than dislocation **loss** and with the increases in stored energy that are a result of deformation. The dislocations provide the driving force for the annealing phenomena dealt with in the remaining chapters.

A comparison of the present chapter with those dealing with annealing will reveal discrepancies between our current knowledge of the deformed state and our requirements for the understanding of annealing. For example, we currently have an incomplete understanding of the rates of dislocation accumulation during deformation and of the large-scale deformation heterogeneities which are important in nucleating recrystallization, and this impedes the formulation of quantitative models of recrystallization. On the other hand, we now have a great deal of information about the formation of boundaries during deformation, but have not yet formulated annealing theories which adequately take these into account. Such discrepancies provide useful pointers to areas which require further research.

During deformation the microstructure of a metal changes in several ways. First, and most obvious, the grains change their shape and there is a surprisingly large increase in the total grain boundary area. The new grain boundary area has to be created during

deformation and this is done by the incorporation of some of the dislocations that are continuously created during the deformation process. A second obvious feature, particularly at the electron microscope level, is the appearance of an internal structure within the grains. This too, results from the accumulation of dislocations. Except for the small contribution of any vacancies and interstitials that may have survived, the sum of the energy of all of the dislocations and new interfaces represents the stored energy of deformation. There is one other consequence of deformation that is relevant to the study of annealing processes. During deformation the orientations of single crystals and of the individual grains of a polycrystalline metal change relative to the direction(s) of the applied stress(es). These changes are not random and involve rotations which are directly related to the crystallography of the deformation. As a consequence the grains acquire a preferred orientation, or **texture,** which becomes stronger as deformation proceeds, and this is considered in chapter 3.

Every stage of the annealing process involves loss of some of the stored energy and a corresponding change in microstructure. The release of stored energy provides the driving force for recovery and recrystallization, but it is the nature of the microstructure that controls the development and growth of the nuclei that will become recrystallized grains and also their orientation. If these changes are to be understood it is essential that we begin by examining the nature of the deformed state, the generation of microstructure and particularly the development of inhomogeneities in that microstructure. Unfortunately our knowledge of these matters is still imperfect and Cottrell's assessment of the situation some 50 years ago is still valid.

Few problems of crystal plasticity have proved more challenging than work hardening. It is a spectacular effect, for example enabling the yield strength of pure copper and aluminium crystals to be raised a hundredfold. Also, it occupies a central place in the subject, being related both to the nature of the slip process and to processes such as ***recrystallization*** *and creep. It was the first problem to be attempted by the dislocation theory of slip and may well prove the last to be solved.*

A.H. Cottrell (1953)

2.2 THE STORED ENERGY OF COLD WORK

2.2.1 Origin of the stored energy

Most of the work expended in deforming a metal is given out as heat and only a very small amount (~1%) remains as energy stored in the material. This stored energy, which provides the source for all the property changes that are typical of deformed metals, is derived from the point defects and dislocations that are generated during deformation. However, the mobility of vacancies and interstitials is so high that except in the special case of deformation at very low temperatures, point defects do not contribute significantly to the stored energy of deformation. In the common case of deformation at ambient temperatures almost all of the stored energy is derived from the accumulation of dislocations and the essential difference between the deformed and the annealed states lies in the dislocation content and arrangement. Because of this, discussion of the

significance of the deformation microstructure during recovery and recrystallization must be based on the density, distribution and arrangement of dislocations.

The increase in dislocation density is due to the continued trapping of newly created mobile dislocations by existing dislocations and their incorporation into the various microstructural features that are characteristic of the deformed state. One of the simplest of these is the grain shape. During deformation, the grains of a polycrystalline metal change their shape in a manner that corresponds to the macroscopic shape change. As a result there is an increase in grain boundary area. Consider the case of a cube-shaped grain during rolling. After 50% reduction the surface area of this grain is increased by ~16%; after 90% reduction the increase is 270% and after 99% reduction it is 3267%. The retention of contiguity requires that this new grain boundary area be continuously created during deformation and this is done by the incorporation of some of the dislocations generated during deformation.

The energy associated with this increase in area represents a significant part of the stored energy of cold working and obviously it will be greater for small grain sizes and large strains. Gil Sevillano et al. (1980) have considered the case of a severely compressed metal ($\varepsilon = 5$, i.e. reduction in thickness ~99.3%), with grain size 10 μm and cubic grains. It was assumed that the grain boundary energy remained constant at 0.7 Jm^{-2}. The energy stored in the grain boundaries under these conditions was predicted to be ~10^6 Jm^{-3}, i.e. ~71 J/mol for copper.

The rate of increase of grain boundary area per unit volume depends very much on the mode of deformation. The grains of a rolled sheet become laths, those of a drawn wire become needles and those of a compressed specimen are disc shaped. Figure 2.1 shows the calculated increase as a function of strain for several deformation modes. This increase in boundary area is an important factor in promoting continuous recrystallization after large strain deformation as discussed in chapter 14.

A second significant feature of the deformation microstructure is the appearance of an internal structure within the grains. This may take several forms but all of these involve the creation of boundaries of some sort. Many of the newly created dislocations are subsequently located in these internal boundaries. A further source of dislocations and, therefore of stored energy is associated with the presence in the metal of second-phase particles that may deform less readily or not at all. This incompatibility results in the formation of additional dislocations as discussed in §2.9.2.

In a typical lightly-deformed metal the stored energy is about 10^5 Jm^{-3}. This is a surprisingly low value. It represents only about 0.1% of the latent heat of fusion (~13 kJ/mol for the solidification of copper) and is very much smaller than the energy changes associated with phase transformations (0.92 kJ/mol for the α–γ transformation in iron). As a consequence of this, any phase transformations that may occur at the annealing temperature, e.g. precipitation of a second phase or an ordering reaction, may have a profound effect on the recrystallization behaviour. Nevertheless this small amount of stored energy is the source of all the strengthening that occurs during deformation and its loss leads to all of the property changes that occur during annealing.

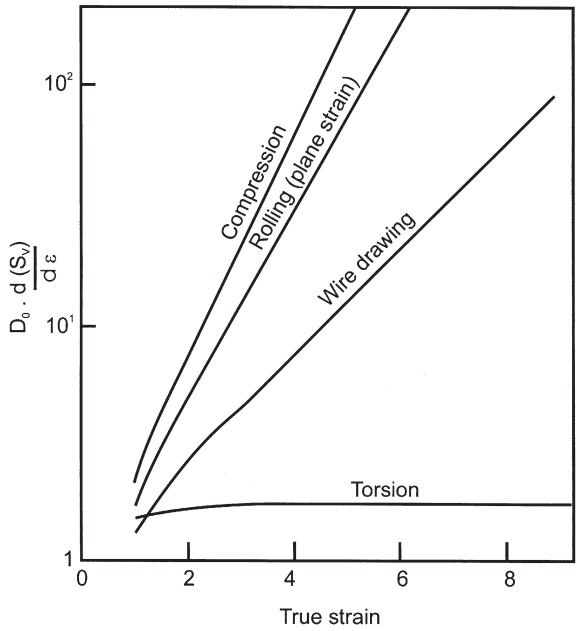

Fig. 2.1. Rate of growth of grain boundary area per unit volume (S_V) for different modes of deformation assuming an initial cubic grain of size D_0, (after Gil Sevillano et al. 1980).

The increase in dislocation density during deformation arises from both the trapping of existing dislocations and the generation of new dislocations. During deformation, the dislocations (of Burgers vector b) move an average distance L, and the **dislocation density (ρ)** is related to the true strain (ε) by

$$\varepsilon = \rho bL \tag{2.1}$$

The value to be attributed to L and its variation with strain are responsible for much of the uncertainty in current theories of work hardening. In some cases it is possible to define limiting values, e.g. grain size or interparticle spacing. Consideration of these has given rise to what Ashby (1970) has called **geometrically stored** and **statistically necessary** dislocations. Further consideration of the work hardening of metals is however, outside the scope of this volume.

2.2.2 Measurements of overall stored energy

The determination of stored energy is not easy. It may be measured directly by calorimetry or X-ray diffraction or determined indirectly from the change in some physical or mechanical property of the material. A summary of these techniques is given in appendix 2.

2.2.2.1 Calorimetry

A good account of the results of the extensive early calorimetric measurements can be found in Bever et al. (1973). However the magnitude of the energy change involved is so low that even the best calorimetric methods require great attention to detail. The values obtained depend on such factors as composition (particularly impurity levels), grain size, and the extent and temperature of deformation. A brief summary follows:

- Stored energy increases with strain. Typical values for copper deformed in tension at room temperature are shown in figure 9.6a.
- Variations in redundant work may produce large differences in the energy stored if the method of deformation is changed. In the case of copper, values of 3.2–5.7 J/mol for tensile deformation should be compared to 3.8–8.3 J/mol for comparable compression and ~95 J/mol for wire drawing.
- At low and medium strain levels ($\varepsilon < 0.5$) more energy is stored in fine grained material than in coarse grained. At high strain levels the energy stored is usually found to be independent of grain size, although Ryde et al. (1990) have reported a higher stored energy in copper with a coarse grain size.

The development of differential scanning calorimeters (e.g. Schmidt 1989, Haessner 1990) resulted in a renewed interest in the calorimetric measurement of stored energy, and these authors examined the energy release from several metals after deformation by torsion at −196°C. Their results are shown in figure 2.2. The low temperature peaks are associated with the loss of point defects and can be ignored for our purpose but the high temperature peaks are due to dislocation loss and recrystallization. Analysis of the

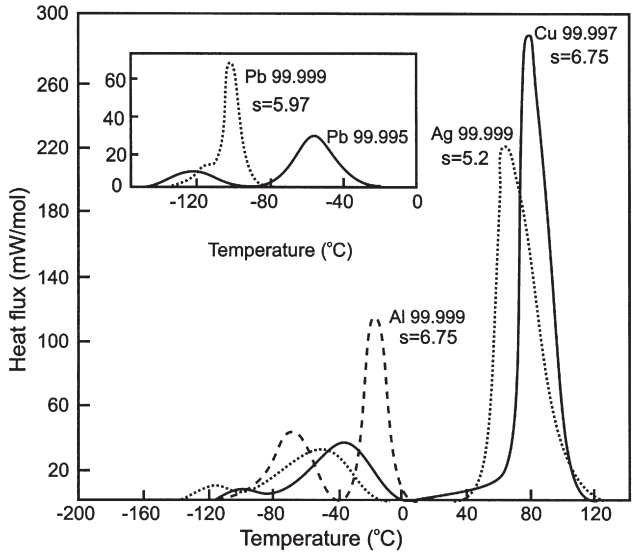

Fig. 2.2. Calorimetric readings during heating of aluminium, lead, copper and silver specimens deformed in torsion at −196°C to several different values of surface shear strain (**s**), (unpublished results of J. Schmidt, quoted by Haessner 1990).

Table 2.1
Recrystallization data for metals deformed at 77K, (Schmidt 1989).

	Al 99.999at%	Pb 99.999at%	Cu 99.997at%	Ag 99.999at%
Reduced stacking fault energy (γ_{SFE}/Gb) ($\times$1000)	26	15	4.7	2.6
Shear strain	6.75	5.97	6.75	5.2
Stored energy, J/mol	69.6	21.5	216	220
Expended energy, J/mol	3151	1400	5592	4914
E(stored)/E(expended)	0.022	0.015	0.039	0.045
Dislocation density*, m^{-2}	3.1×10^{15}	1.7×10^{15}	10×10^{15}	8.7×10^{15}

*Calculated from $[E_{stored})/Gb^2]$.

recrystallization peaks, produced the results shown in table 2.1; the magnitude of the stored energy ranges from 21.5 to 220 J/mol.

The values of stored energy for lead and aluminium are very much lower than those for copper and silver and are a direct consequence of the differences in **stacking fault energy (γ_{SFE})**. The stacking fault energy, which is related to the atomic bonding in the material, determines the extent to which unit dislocations dissociate into partial dislocations. Such dissociation, which is promoted by a low value of γ_{SFE}, hinders the climb and cross slip of dislocations, which are the basic mechanisms responsible for recovery. Dislocation theory therefore predicts that high values of γ_{SFE} should promote dynamic dislocation recovery and table 2.1 shows that γ_{SFE} for the two groups is consistent with this expectation. Attention is also drawn to the small fraction of the energy expended during deformation which is stored in the materials.

2.2.2.2 X-ray line broadening

A measure of the stored energy of a deformed metal can also be found from analysis of X-ray line broadening. This technique measures only the inhomogeneous lattice strain energy, and the difference between this and the calorimetric results provides a striking indication of the significance of the dislocation content to stored energy. The X-ray values are typically of the order of 8–80 J/mol for heavily cold worked metals in which the calorimetric value is 250–800 J/mol. The use of high intensity synchrotron X-ray sources gives more accurate results than conventional sources and more readily enables the determination of local dislocation densities as a function of grain orientation as discussed below.

2.2.3 Relationship between stored energy and microstructure

The annealing behaviour of a deformed metal is dependent not only on the overall stored energy, but more importantly on its spatial distribution. On a local scale,

inhomogeneity of stored energy will affect the nucleation of recrystallization, and larger-scale heterogeneity will influence the growth of the new grains. In order to predict the annealing behaviour, it is therefore important to determine the distribution of the defects resulting from deformation.

In this section, for the purpose of relating the microstructure and stored energy, we will assume a very simple model in which the microstructure of a polycrystal consists, in addition to the high angle grain boundaries, of only the following two components, although it will be shown in §2.4, that this is an oversimplification of the situation.

- **Cells or subgrains,** which are typically equiaxed micron-sized volumes bounded by dislocation walls. These walls are either tangled (cells) or are well-ordered low angle boundaries (subgrains). Examples of cell structures are seen in figures 2.9a and b.
- **Dislocations,** other than those which comprise the cell/subgrain boundaries.

Information about the nature and distribution of these components may be obtained experimentally using a wide variety of experimental methods, including transmission electron microscopy (TEM), X-ray diffraction, scanning electron microscopy (SEM) and electron backscatter diffraction (EBSD), as outlined in appendix 2.

2.2.3.1 Stored energy and dislocation density

In materials in which the dislocation density is low, the dislocation content may be measured directly by transmission electron microscopy. However, the density of dislocations in even moderately deformed metals is such that they cannot be counted accurately, and inhomogeneous distribution of the dislocations, for example into a cell structure, makes measurement even more difficult. An estimate of the dislocation density may also be obtained from the mechanical properties of the material. For example, a relationship between flow stress (σ) and dislocation density of the form

$$\sigma = c_1 G b \rho^{1/2} \tag{2.2}$$

where c_1 is a constant of the order of 0.5 and G is the shear modulus, has been shown to hold for a wide variety of materials (e.g. McElroy and Szkopiak 1972).

If the energy of the dislocation core is neglected and if isotropic elasticity is assumed, the energy (E_{dis}) per unit length of dislocation line is given approximately by

$$E_{dis} = \frac{G\, b^2\, f(\nu)}{4\pi} \ln\left(\frac{R}{R_0}\right) \tag{2.3}$$

where:

R is the upper cut-off radius (usually taken to be the separation of dislocations, $\rho^{-1/2}$),
R_0 is the inner cut-off radius (usually taken as between b and 5b),
$f(\nu)$ is a function of Poisson's ratio (ν), which, for an average population of edge and screw dislocations is $\sim(1 - \nu/2)/(1 - \nu)$.

For a dislocation density ρ the stored energy is then

$$E_D = \rho E_{dis} \tag{2.4}$$

Although this relationship is appropriate if the dislocations are arranged in such a way that the stress fields of other dislocations are screened, the energies of the dislocations present in real materials are not wholly represented by such simple considerations. Dislocations in even moderately worked metals are kinked and jogged and are found in pile-ups and in intricate tangles. Dislocation theory shows that the energy of a dislocation depends on its **environment** and is for example highest in a pile-up and lowest when in a cell or subgrain wall.

In most cases where only very approximate values of dislocation energy are needed, equation 2.3 can be simplified to

$$E_{dis} = c_2 G b^2 \tag{2.5}$$

where c_2 is a constant of $\sim$0.5.

The stored energy is then given as

$$E_D = c_2 \rho G b^2 \tag{2.6}$$

The rate of storage of dislocations in the microstructure with increasing strain, is not easy to predict theoretically, and the problems in formulating models of microstructural evolution, have been reviewed by Nes (1998). If we neglect the dislocations which have created new high angle boundary (§2.2.1), the total dislocation density (ρ_{tot}) comprises those dislocations which are stored in the form of cell/subgrain boundaries (ρ_b), and those which are within the cells or subgrains (ρ_i).

Measurements of the total dislocation density in aluminium (Zehetbauer 1993), copper (Zehetbauer and Seumer 1993) and iron (Schafler et al. 1997), show that ρ_{tot} increases rapidly up to a true strain of $\sim$0.5, and thereafter increases linearly with strain, as shown in figure 2.3a. However, at larger strains, an increasing proportion of dislocations is stored in the form of cell/subgrain boundaries, and TEM measurements show that in aluminium, ρ_i increases little at strains larger than 0.3 as shown in figure 2.3b.

2.2.3.2 Stored energy and cell/subgrain structure

If the deformation microstructure consists of well-defined, equiaxed **subgrains** (§2.4.1), the stored energy may be estimated from the subgrain diameter (D) and the specific energy (γ_s) of the low angle grain boundaries which comprise the subgrain walls. The area of low angle boundary per unit volume is $\sim$3/D and hence the energy per unit volume (E_D) is given approximately by

$$E_D \approx \frac{3\gamma_s}{D} \approx \frac{\alpha \gamma_s}{R} \tag{2.7}$$

where α is a constant of $\sim$1.5.

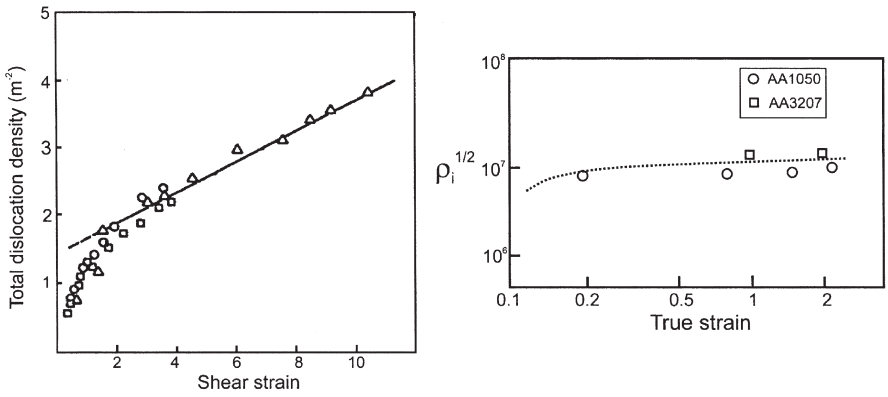

(a) (b)

Fig. 2.3 Dislocation densities in deformed metals. (a) The total dislocation density (ρ_{tot}) in deformed copper, (Zehetbauer and Seumer 1993). (b) The density of free dislocations (ρ_i) in aluminium, (Nes and Marthinsen, 2002).

As discussed in §4.3, the boundary energy (γ_s) is directly related to the misorientation (θ) across the boundary (equations 4.5 or 4.6) and therefore equation 2.7 may be expressed in terms of the parameters D and θ, both of which may be measured experimentally, as:

$$E_D = \frac{3\gamma_s\theta}{D\theta_m}\left(1 - \ln\frac{\theta}{\theta_m}\right) \approx \frac{K\theta}{D} \tag{2.8}$$

where θ_m is defined with equation 4.6 and K is a constant.

Although the use of equation 2.8 may be justified for boundaries in which the dislocation content and spacing are close to their equilibrium values, its application to less organised dislocation boundaries, such as those of cells, is unlikely to be accurate.

The cell/subgrain size – For metals deformed at room temperature, the cell/subgrain size decreases with increasing strain. Gil Sevillano et al. (1980) found that a wide range of metals exhibited a similar behaviour, which was independent of the mode of deformation, as shown in figure 2.4, and this trend has been confirmed by most later work. Nes (1998) has pointed out that above a strain of ~1, the cell sizes shown in figure 2.4 are inversely proportional to the strain.

The cell/subgrain misorientation – The variation of the orientation change across cell or subgrain boundaries with strain has not been as extensively investigated as that of the scale of the substructure. Much of the work has been carried out by diffraction in the TEM. In many cases a comparatively small number of misorientation measurements have been made, and it is unfortunate that few papers give any indication of the statistical

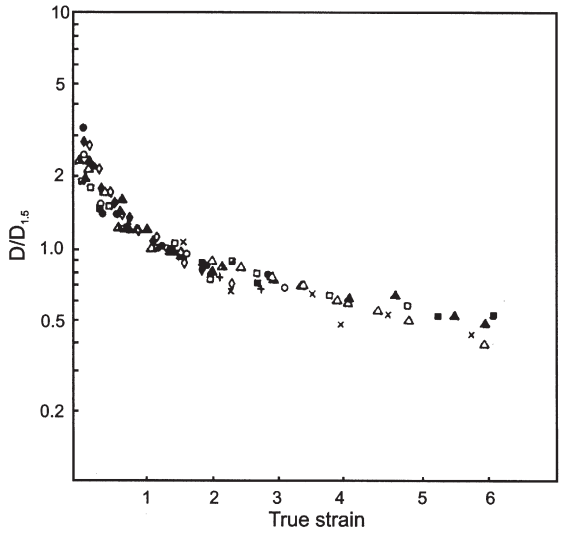

Fig. 2.4. Average cell size as a function of strain for Al, Cu, Fe, Ni, Cr, Nb, (from data assembled by Gil Sevillano et al. (1980) from different authors). The cell size is expressed as a fraction of $D_{1.5}$, the cell size at a strain of 1.5. Values of $D_{1.5}$ are Al ~ 0.5 μm, Cu ~ 0.3 μm, Ni ~ 0.3 μm, Fe ~ 0.3 μm, Cr ~ 0.4 μm, Nb ~ 0.2 μm.

significance of the data. EBSD measurements (appendix 2.6.1) provide data of much better statistical significance, but it is only recently that high resolution EBSD, with the capability of adequately resolving the deformed microstructures, has become available.

In their review, Gil Sevillano et al. (1980) found that the mean cell/subgrain misorientations increased with strain. However, results for aluminium alloys, summarised by Nes (1998) indicated that the misorientation saturated at ~2–3° at strains of ~1. This is contradicted by the TEM results on aluminium (Liu and Hansen 1995) and nickel (Hughes and Hansen 2000) shown in figure 2.5a and by the EBSD measurements of Hurley and Humphreys (2003) (fig. 2.5b), all of which show misorientations increasing with strain, and do not include misorientations associated with large scale deformation bands. The misorientations associated with more specific types of cell/subgrain boundary will be discussed in §2.4.2.

Orientation gradients – The mean subgrain misorientation is only one of the parameters describing the variation of orientation within a grain. Of particular importance for the **nucleation** of recrystallization (§7.6) are the **long range orientation gradients** in the material. In many cases it is found that although the nearest-neighbour misorientations are low, there may be significant orientation gradients within a grain, and the orientation gradient, $\Omega = d\theta/dx$, can be defined as the rate of accumulation of misorientation across some region of the microstructure (Ørsund et al. 1989). However, because of the complexity of deformed microstructures, such a concept is generally only

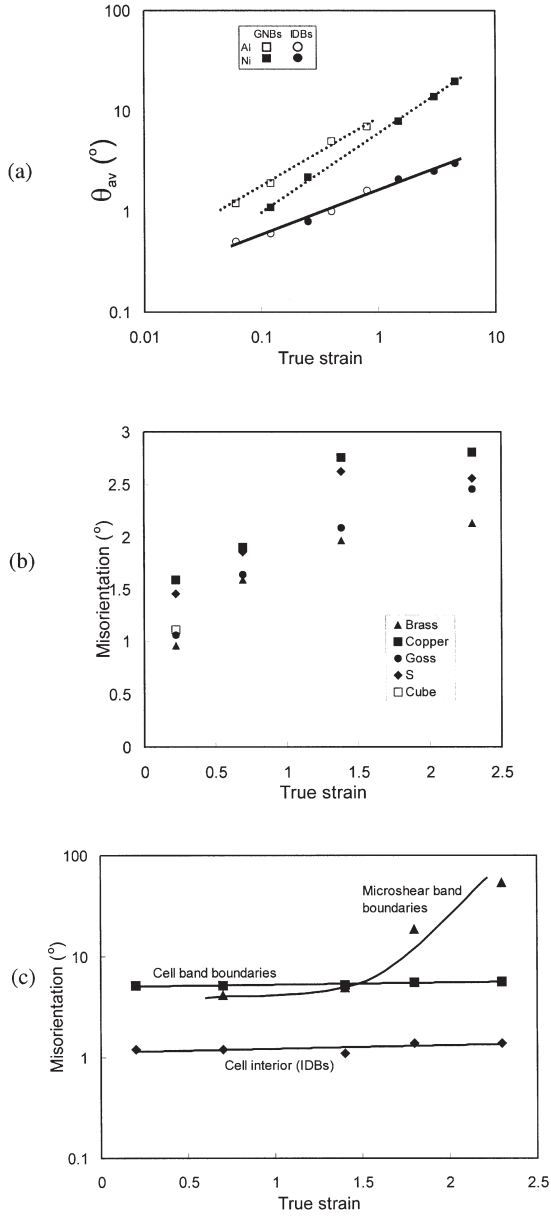

Fig. 2.5. The effect of strain on boundary misorientations in aluminium. (a) The misorientation of incidental dislocation boundaries (IDBs) and geometrically necessary boundaries (GNBs) in aluminium and nickel, (Hughes 2001). (b) The effect of grain orientation on cell misorientations in Al–0.1%Mg, (Hurley and Humphreys 2003). (c) The effect of strain on the mean misorientations of cell, cell-band and microshear-band boundaries in Al–0.1%Mg, (data from Hurley and Humphreys (2003).

useful when applied to specific microstructural features such as the regions adjacent to second-phase particles (§2.9.3) or transition bands (§2.7.3).

2.2.3.3 Orientation dependence of stored energy

It has been found experimentally that both the cell/subgrain size and the misorientation may be dependent on the grain orientation, and therefore, from equation 2.7, we expect the stored energy to vary in the different **texture components** of the material. As will be discussed later, this may have important implications for the recrystallization behaviour. The pioneering work in this area was a study of 70% cold rolled iron by Dillamore et al. (1972). At this level of rolling the microstructure consists mainly of a cell-type structure and it was found that the cell size and the misorientation between neighbouring cells were orientation dependent (fig. 2.6). For the $\{hkl\}<110>$ components of the rolling texture, small cells and large misorientations were associated with rolling plane orientations near {110}, while larger cells and small misorientations occurred for {001} orientations. From equation 2.8 it is seen that if the dislocations are concentrated mainly in cell or subgrain walls then the stored energy should be greatest for small cells and large misorientations, and Dillamore et al. concluded that

$$E_{110} > E_{111} > E_{112} > E_{100}$$

This result has proved to be very useful in providing understanding of the recrystallization textures found in low carbon steels. Every and Hatherly (1974), using the X-ray line broadening method found, in a 70% rolled, killed steel, a similar orientation dependence of the stored energy to that calculated by Dillamore et al. (1972), and their data are included in figure 2.7 which shows results from several

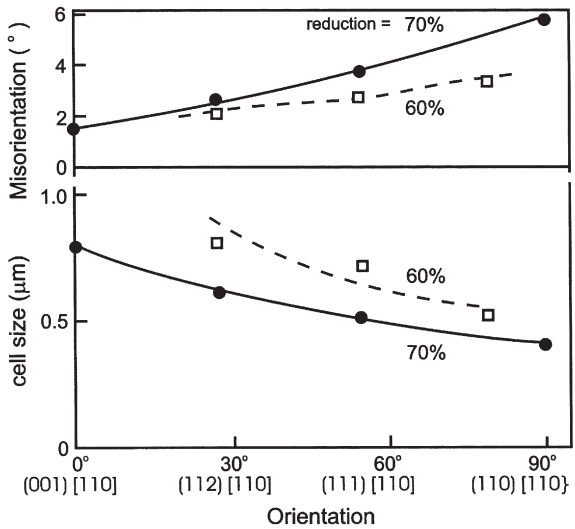

Fig. 2.6. Variation of cell size and cell boundary misorientation in rolled iron as a function of local orientation, (after Dillamore et al. 1972).

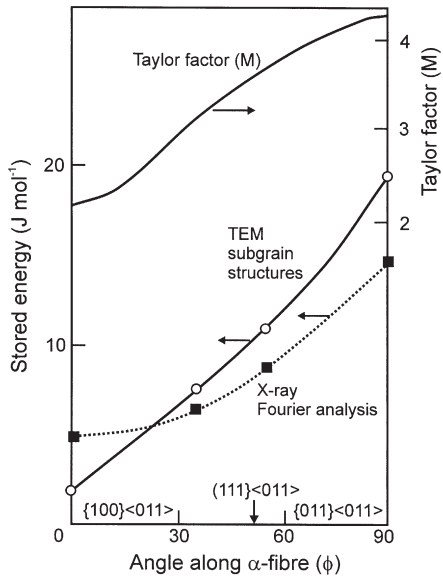

Fig. 2.7. Stored energies of deformation for different orientations in the α-fibre of cold-rolled iron and steel. TEM results from Dillamore et al. (1967) and X-ray Fourier analysis from Every and Hatherly (1974). Also shown is the variation of the Taylor factor (M), (Hutchinson 1999).

investigations of the effects of local orientation on stored energy in rolled iron and low carbon steel. These workers also examined the microstructures of their specimens and found that the predominant, high energy components ($\{110\}<uvw>$ and $\{111\}<uvw>$) consisted of cells elongated in both the transverse and rolling directions. These cells were 0.15–0.20 μm thick, 2–3 times longer, and had orientations within 10° of a $<110>$ zone between {110} and {111}. The other, low energy components ($\{211\}<uvw>$ and $\{100\}<uvw>$) were associated with larger equiaxed cell structures of diameter 0.30–0.45 μm, and orientations lying in zones within 30° of {100}. Similar results were obtained by Willis and Hatherly (1978) from an interstitial-free (IF) steel, and recent neutron diffraction (Rajmohan et al. 1997) and synchrotron diffraction measurements (Borbely and Driver 2001) of stored energy are also in agreement with the earlier results. The effect of grain orientation on stored energy in iron and steel is well summarised in figure 2.7 (Hutchinson 1999), where it is seen to correlate with the Taylor factor (§3.7.1.2). If it is assumed that the total amount of slip activity in a grain is dependent on the Taylor factor, then such a correlation is to be expected.

There is less information on the effect of grain orientation on cells or subgrains in aluminium deformed at ambient temperatures. However, Hurley and Humphreys (2003) have recently found that although the subgrain size shows little orientation dependence, the mean subgrain misorientations show an orientation dependence as seen in figure 2.5b. Such a dependence is consistent with the trends found during high temperature deformation and shown in table 13.1.

2.2.3.4 Modelling the stored energy

Models for the increase in stored energy with strain have been reviewed by Nes (1998). The model of Nes and colleagues (Nes 1998, Nes and Marthinsen 2002) simplifies microstructure to three parameters, the cell size, the dislocation density within the cells, and the thickness of the cell walls, a parameter which decreases with increasing strain, as cells tend to become subgrains. Although such models have been developed primarily to account for the work hardening of metals, they are potentially useful for modelling the driving pressure for recrystallization.

2.3 CRYSTAL PLASTICITY

2.3.1 Slip and twinning

In cubic metals the two basic methods of deformation are **slip** and **twinning** and the most significant material parameter with respect to the choice of method is the value of the **stacking fault energy** (γ_{SFE}). In metals with a low value of γ_{SFE}, the difficulty of cross-slip reduces the ability of the material to change its shape during plastic deformation by slip alone, and therefore deformation twinning may occur.

The planes and directions of both processes are a function of the crystal structure and tables 2.2 and 2.3 show these data for cubic metals. As shown by table 2.2 the crystallography of slip in fcc metals is simple. In most cases slip takes place on the most densely packed planes and in the most densely packed directions. Together these factors define the slip system, $\{111\}<110>$. It has been known for many years however, that

Table 2.2
Crystallography of slip in cubic metals.

Structure	Slip system	
	Plane	Direction
fcc	{111}	<110>
bcc	{110}	<111>
	{112}	<111>
	{123}	<111>

Table 2.3
Crystallography of twinning in cubic metals.

Structure	Twinning shear	Twinning plane	Twinning direction
fcc	0.707	{111}	<112>
bcc	0.707	{112}	<111>

other systems sometimes operate at high temperatures and particularly in metals with high values of $\gamma_{SFE,}$ the systems observed involving slip on {100}, {110}, {112} and {122} planes (Hazif et al. 1973). More recently, the operation of such **non-octahedral slip** in aluminium at high deformation temperatures, which is inferred from surface slip markings (Maurice and Driver 1993), has been shown to influence the development of microstructures and textures (§13.2.4). Unusual, low-temperature slip has also been reported on {111}, {110} and {122} planes and Yeung (1990) has observed slip on a number of non-octahedral planes in the low stacking fault energy alloy 70:30 brass at high values of strain. For summaries of recent work in this area the reader is referred to the papers of Bacroix and Jonas (1988), Yeung (1990) and Maurice and Driver (1993).

In bcc metals slip occurs in the close packed $<111>$ directions but the slip plane may be any of the planes {110}, {112} or {123}; each of these planes contains the close packed slip direction, $<111>$. The choice of slip plane is influenced by the temperature of deformation. At temperatures below $T_m/4$ {112} slip occurs; between $T_m/4$ and $T_m/2$ {110} slip is favoured and at temperatures above $T_m/2$ {123} is preferred. At room temperature iron slips on all three planes in a common $<111>$ direction and the term pencil glide is used to describe the nature of the slip process in this case. One consequence of such slip is the wavy nature of the slip lines seen on pre-polished surfaces of deformed specimens.

In general, bcc metals deform by slip, as do fcc metals with medium to high values of γ_{SFE} such as copper ($\sim$80 mJm^{-2}) and aluminium ($\sim$170 mJm^{-2}). In metals with low values of γ_{SFE} such as silver or in alloys like 70:30 brass and austenitic stainless steels with γ_{SFE} $\sim$20 mJm^{-2}, the dislocations dissociate to form stacking faults, and twinning is the preferred mode of deformation. The tendency to deform by twinning is increased if the deformation temperature is lowered or the strain rate increased.

In polycrystalline hexagonal metals deformation begins by slip but, because of the lack of sufficient slip systems to accommodate the imposed strain, slip is soon accompanied by twinning as an important deformation mode.

2.3.2 Deformation of polycrystals

The actual planes and directions associated with slip and twinning correspond to the system with the greatest resolved shear stress and are differently oriented from grain to grain in polycrystalline metals. In general, slip or twinning processes initiated in one grain are confined to that grain and can readily be distinguished from those occurring in neighbouring grains. It should not be thought however, that deformation is homogeneous in any grain of the aggregate. When a single crystal specimen is deformed it is usually free to change its shape subject only to the need to comply with any external constraints (e.g. grip alignment in a simple tension test). This freedom does not exist for the individual grains of an aggregate which are subjected to the constraints exercised by every one of several neighbours each of which is deforming in a unique manner. It will be obvious that contiguity must be maintained if deformation is to continue and it is a direct consequence of this need that the deformation processes will

Table 2.4
Stacking fault energy of metals, (Murr 1975).

Metal	γ_{SFE} (mJm^{-2})	Metal	γ_{SFE} (mJm^{-2})
Aluminium	166	Zinc	140
Copper	78	Magnesium	125
Silver	22	91Cu:9Si	5
Gold	45	Zirconium	240
Nickel	128	304 Stainless steel	21
Cobalt (fcc)	15	70Cu:30Zn	20

be different in various parts of any particular grain, leading to the development of **microstructural inhomogeneity.**

The imposed deformation strain and the constraints between neighbouring grains affect the choice and number of the operating slip systems, and with respect to the subject of this book, there are two important consequences of this slip activity:

- The slip processes and their variation both within and between grains, largely determine the **deformation microstructures,** discussed in this chapter.
- The changes in orientation which are a consequence of the crystal plasticity, determine the **deformation textures,** discussed in chapter 3.

Theories and models of crystal plasticity – have been developed for many years. Although these can now provide good predictions of the development of deformation textures (§3.7), they have not been very successful in modelling the development of the complex microstructures discussed later in this chapter. This is largely due to the scale of the problem. The microstructures are generally too large and complex to be accounted for by dislocation theory, but are on too small a scale to be successfully modelled by finite element (FE) methods. Although crystal plasticity has been successfully incorporated into FE models (Sarma and Dawson 1996, Bate 1999, Dawson et al. 2002), and can predict some aspects of large-scale deformation heterogeneity, significant improvements need to be made before these models can account for the formation of deformation heterogeneities in sufficient detail to assist in the understanding of the nucleation of recrystallization.

It is because of their primary relevance to the formation of deformation textures that we have opted to discuss the various **theories of crystal plasticity** in chapter 3.

2.4 CUBIC METALS WHICH DEFORM BY SLIP

Metals of high or moderate stacking fault energy such as aluminium alloys, α-iron, nickel and copper deform by slip. In most cases the deformation is heterogeneous, and because crystals generally change orientation during deformation, as discussed

in chapter 3, regions of different orientation develop within the original grains. This **grain subdivision** or **fragmentation,** has been recognised for many years, but it is only recently that many aspects of the resulting microstructures have become reasonably clear. It is now known that there is a wide range of length scales, from nanometres to millimetres, at which the microstructure is subdivided during deformation, and we will first consider the various microstructural features which constitute this scale-based hierarchy, before discussing the ways in which the microstructures evolve with strain. It should be recognised that despite a very large body of literature on this subject in the past 20 years, many aspects remain unclear.

Much recent work has shown that many deformed metals develop rather similar types of microstructures, and that these change in a similar way with increasing strain. If the relationships between some of these microstructural features were to obey simple laws, it would be easier to model microstructural development, and because of this, there has been significant interest in examining **similitude** and **scaling** of deformation microstructure.

An inverse relationship between cell size (D) and strain (ε), which can be scaled to fit most metals has already been noted in §2.2.3.2. An inverse relationship between the cell size (D) and the square root of dislocation density inside the cells (ρ_i) is often found during high temperature deformation (equation 13.9), and a similar relationship has also been found after low temperature deformation of copper and iron (Staker and Holt 1972). However, it has been shown that in aluminium, this relationship breaks down for $\varepsilon > 0.3$, when ρ_i tends to saturate (Nes and Saeter 1995, Nes 1998).

Similitude in the development of boundary separations, misorientations and misorientation distributions with strain has also been reported for deformation-induced boundaries (see §2.4.1), and is reviewed by Hughes (2002).

2.4.1 The microstructural hierarchy

In this section we summarise the main features of the microstructures in deformed metals of medium and high stacking fault energy, and it is convenient to classify the microstructures according to the scale of the heterogeneity as shown schematically in figure 2.8, for a sample deformed in plane strain compression. Further details of these features and their formation during deformation are discussed in subsequent sections.

Dislocations – Dislocations may exist as tangles or other rather random structures (fig. 2.8a), particularly after low strains, as discussed in §2.2.3. In metals which do not form cells, such diffuse arrangements of dislocations are found even after large strains as discussed in §2.4.3.

Cells and subgrains – In many metals, the majority of the dislocations produced on deformation form the boundaries of cells or subgrains (fig. 2.8b), which are the smallest volume elements in the deformed microstructure. Their character and dimensions were discussed in §2.2.3, and TEM micrographs of cells in deformed copper are shown in figures 2.9a and b. Some cell walls may be aligned or have different misorientations, and this enables further sub-classification of these features as discussed in §2.4.2.

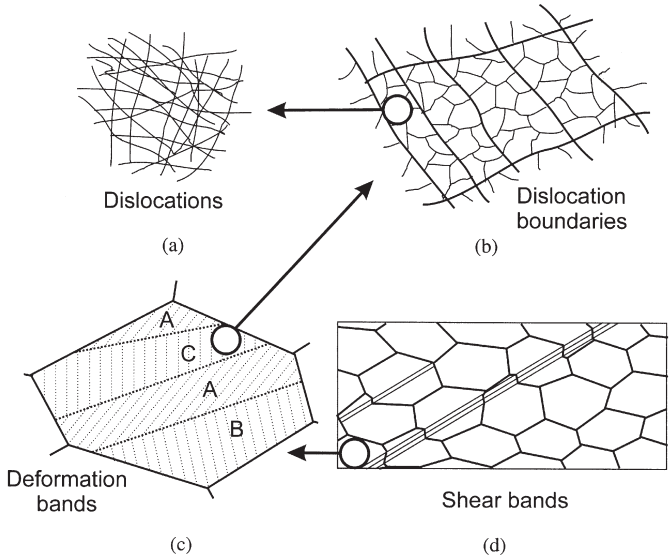

Fig. 2.8. The hierarchy of microstructure in a polycrystalline metal deforming by slip. The various features are shown at increasing scale: (a) Dislocations, (b) Dislocation boundaries, (c) Deformation and transition bands within a grain, (d) Specimen and grain-scale shear bands.

Deformation and transition bands – It is often found that individual grains within the sample, particularly in coarse-grained materials, subdivide on a large scale during deformation (fig 2.8c) into regions of different orientation, as a consequence of either inhomogeneous stresses transmitted by neighbouring grains or the intrinsic instability of the grain during plastic deformation. The resulting **deformation bands** deform on different slip systems and may develop widely divergent orientations. The narrow regions between the deformation bands, which may be either diffuse or sharp, are termed **transition bands.** Examples of deformation bands in α-brass and aluminium are shown in figures 2.9c and d.

Shear bands – Figure 2.8d shows a polycrystalline sample in which intense shear has occurred on planes inclined to the rolling plane. These shear bands, which are non-crystallographic in nature, may pass through several grains, and even extend through the specimen. They are a result of plastic instability, and can be thought of as the rolling equivalent of the 'necking' which occurs in a tensile test. Examples are seen in figures 2.9e and f.

2.4.2 The evolution of deformation microstructure in cell-forming metals

Many aspects of the formation of the larger-scale features of the microstructure, such as deformation bands and shear bands are common to most metals, and will be discussed

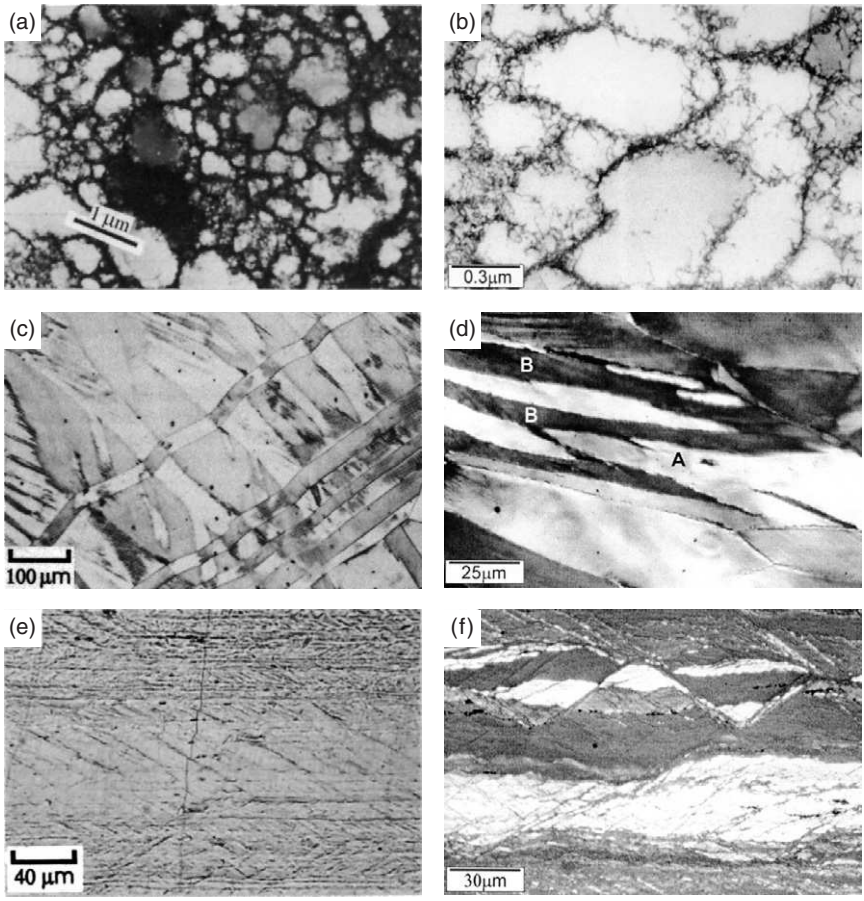

Fig. 2.9. Various features of deformed microstructures; (a) Cell structure in 25% cold rolled copper (micron bar shown), (b) Details of cell structure, (c) 70:30 brass compressed 12%, showing deformation bands, (d) Deformation bands (B) in a grain (A) in Al–1%Mg, (e) Shear bands developed by light rolling on pre-polished, and lightly scratched, surface of 83% cold rolled copper, (Malin and Hatherly 1979), (f) Shear bands in Al–Zn–Mg alloy cold rolled 90%, (courtesy of W.B. Hutchinson).

in §2.7 and §2.8 respectively. In this section we consider only the evolution of the microstructure at the cell/subgrain level shown in figure 2.8b.

During the past 20 years, there has been a surprising amount of interest in the detailed characterisation of the cell and subgrain structures formed during the deformation of fcc metals, particularly aluminium and nickel, at ambient temperatures. Much of this research stems from the group at Risø, led by Hansen. Recent discussions of this research include Hughes and Hansen (1997), Hansen and Juul Jensen (1999) and Hughes (2001).

2.4.2.1 Small strainzs ($\varepsilon < 0.3$)
Random distributions of dislocations are rarely observed in cell-forming metals. Although the slip process tends to produce high densities of dislocations on the active slip planes, energy considerations (e.g. Kuhlmann-Wilsdorf 1989) promote relaxation into boundaries by dynamic and/or static recovery. The balance between these two processes, which is affected by the nature of the material and the deformation temperature, determines the degree to which the deformed microstructure exhibits crystallographic alignment and whether the boundaries are diffuse (cells) or sharp (subgrains).

Cell formation – As shown schematically in figure 2.8b and in the TEM micrograph of figure 2.10, we can distinguish between at least two types of cell or subgrain boundary. There are **small (0.5–1 μm), approximately equiaxed cells separated by small ($\sim 1^\circ$) misorientations.** The size, shape and misorientation of these cells does not change very much during deformation (figs 2.4 and 2.5) and it is therefore thought that these cell boundaries are **transient** features of the microstructure, being the result of a dynamic balance between dislocation annihilation and trapping. The overall cell sizes shown in figure 2.4 include all low angle boundaries. However, if the various types of boundary are measured separately, the cell size in aluminium is found to initially decrease with increasing strain (ε) to ~ 0.5 μm, but to remain almost constant at $\varepsilon > 0.5$ (Hughes 2001, Hurley and Humphreys 2003). The term **incidental dislocation boundaries (IDBs)** has been used to describe such boundaries (Kuhlmann-Wilsdorf and Hansen 1991), which are then distinguished from the higher angle, and often aligned, **geometrically necessary boundaries (GNBs)** which are discussed below. However, although we will make some use of this terminology in referring to the published literature, we do not find this a helpful classification.

We consider that it is the **transient** or **persistent** nature of boundaries which is most important in microstructural evolution, and that this characteristic differentiates these *transient* cell boundaries from other *persistent* deformation-induced boundaries, and from *persistent* features such as microshear or transition bands.

Cell blocks and cell bands – In both aluminium and nickel, the cells may occur in blocks as shown schematically in figure 2.8b (Bay et al. 1992). It is thought that the slip activity is similar within individual blocks, but differs between the blocks. In this way, each cell block can deform relatively homogeneously on less than the five slip systems required by plasticity theory (Taylor 1938) (§3.7.1.2), and the overall strain is then accomplished by the variation of slip activity between the blocks. A TEM micrograph and accompanying sketch, showing a typical arrangement of cell blocks is shown in figure 2.10. As seen in figure 2.10, the cell blocks are elongated, and a little more than one cell in width. This is typical of most deformed microstructures in aluminium, and these features are often better described as **cell bands.**

The cell blocks or bands are bounded by longer, aligned boundaries, which have been termed **dense dislocation walls** (DDWs), **microbands,** or **cell-band walls.** These are of higher misorientation angle than the boundaries within the cell blocks (Liu and Hansen 1995, Hughes and Hansen 2000, Hughes 2001, Hurley and Humphreys 2003), as shown in figures 2.5a and c. The misorientations across alternate cell-band walls tend to oscillate about a mean, with no substantial long range orientation gradient.

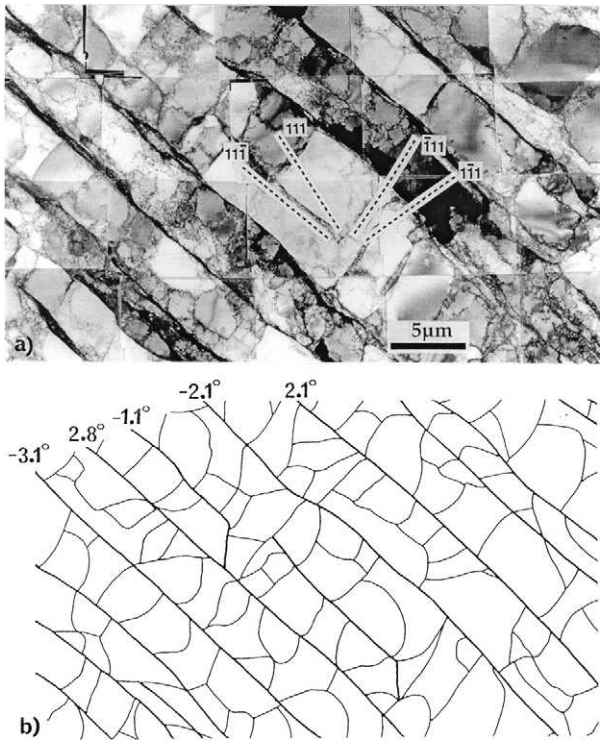

Fig. 2.10. TEM micrograph (a) of cell block structure in 10% cold rolled aluminium (ND-RD plane) and sketch (b) of the area showing the misorientations across the cell block boundaries (heavy lines), (Liu et al. 1998).

These boundaries have been termed **geometrically necessary boundaries (GNBs)** (Kuhlmann-Wilsdorf and Hansen 1991), because they accommodate the misorientations between blocks of material of different orientation. However, this term is misleading because even the small cells of low misorientation discussed above are also *geometrically necessary* at a smaller scale. If this were not so, these cell boundaries would disappear on annealing, whereas they recover to form well-organised low angle subgrain boundaries as seen in figure 6.13.

If the cell-band boundaries (GNBs) are distinguished from the cell boundaries (IDBs), as shown in figure 2.5a, it is seen that the cell-band boundary misorientations increase substantially with increasing strain. However, if the cell-band boundaries are further distinguished from **microshear-band** boundaries (another class of aligned boundary which appear at larger strains and are discussed in §2.4.2.2), their misorientations appear to remain relatively constant in aluminium, as seen in figure 2.5c.

The alignment of the boundaries – In a sample deformed in plane strain compression, the long microband or cell-band boundaries are aligned approximately parallel to the transverse direction and at an angle of 25–40° to the rolling plane. In most grains only

one strong set of microbands is seen, but in some cases two are formed. These are the planes of high shear stress, and are similar to those on which shear bands form (§2.8). In some cases the alignment in fcc metals deformed by rolling is close to {111} slip planes and in other cases it is not (e.g. Liu et al. 1998, Hansen and Juul Jensen 1999, Hurley and Humphreys 2003). However, the detailed analysis of Hurley et al. (2003) has established that the alignment in cold rolled polycrystalline aluminium is related to the deformation geometry and that any crystallographic alignment is coincidental. However, some evidence of crystallographic alignment of the boundaries has been found for samples deformed in tension (Winther et al. 2000), and these authors have shown that the nature of the alignment is influenced by the grain orientation. The alignment is clearly linked to strong slip activity, and is presumably also influenced by dynamic recovery. In polycrystals deformed at elevated temperatures where similar aligned bands form, there is no indication that the alignment is crystallographic (§13.2.3).

The microstructures discussed above have been investigated most extensively in aluminium and nickel, but rather similar structures have been reported in copper and iron. In copper rolled to low strains, the microstructure consists mainly of cells, but long, thin plate-like microbands 0.1 to 0.3 μm thick, initially aligned on {111} planes are seen (Bourelier and Le Héricy 1963, Malin and Hatherly 1979, Hatherly 1980) as shown in figure 2.11a. These appear to be similar to the crystallographically aligned microbands discussed above. Because there is much less dynamic recovery in copper than in aluminium, it is to be expected that more alignment of dislocations on active {111} slip planes will be retained in copper.

2.4.2.2 Moderate strains ($0.3 < \varepsilon < 1$)

At larger strains, the aligned cell-band structures of figure 2.10 are often intersected by thin shear bands within the grains (Hughes and Hansen 1993, Rosen et al. 1995), examples of which are shown in figure 2.12. Because these shear the elongated cell-bands into an '**S**' shape, they have been termed 'S-bands'. However, as this may cause some confusion with bands of material of the 'S-orientation', we prefer to use the term **microshear** bands. If the boundaries and not the dislocations are of primary interest, there are many benefits of using high resolution EBSD rather than TEM to investigate the deformed microstructures in aluminium (Hurley and Humphreys

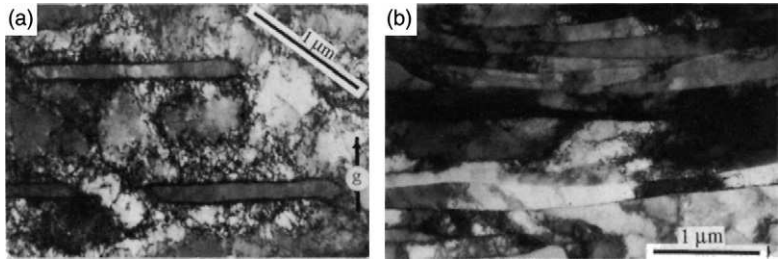

Fig. 2.11. TEM micrographs cold rolled copper. (a) Microbands in 18% rolled material, (b) Microbands in 98% rolled material. The specimen plane is ND-RD, and a 1 μm bar parallel to RD is shown, (Malin and Hatherly 1979).

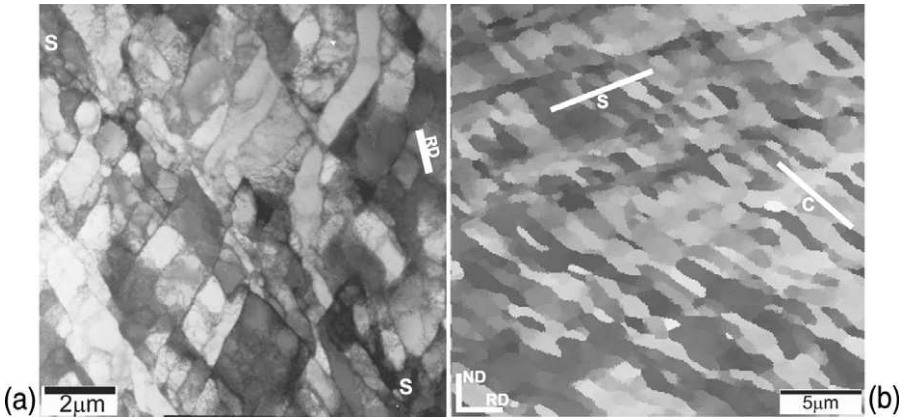

Fig. 2.12. Microstructure in ND-RD plane of Al-0.1%Mg, cold-rolled 50%, showing the interaction of the microshear bands and aligned cell bands. (a) TEM micrograph, showing microshear band **S-S** shearing the cell bands. (b) EBSD map in which the colours represent orientations, showing the cell bands (C) and microshear bands (S). The regions within the microshear bands are seen to have similar orientations, (Hurley and Humphreys 2003). (See colour plate section for fig. 2.12b).

2002, 2003), because much larger areas can be examined and quantitatively analysed. Figure 2.12b shows microshear boundaries intersecting the cell-bands in aluminium. The microshear bands are typically 1–2 μm thick and contain cells of a similar size and misorientation to the cell-bands. With increasing strain, the regions within these microshear bands become progressively misoriented from the cell-bands as shown in figure 2.5c, indicating that the shearing remains operative. The microshear bands seen in aluminium appear to be very similar to those reported for copper (Malin and Hatherly 1979).

2.4.2.3 Large strains ($\varepsilon > 1$)

With increasing strain, the microshear bands and the cell-bands become more closely aligned with the rolling plane, and at $\varepsilon > 2$ the various bands cannot be clearly identified, and at this stage, the microshear band walls have become high angle boundaries as seen in figure 2.5c. The rolled microstructures then consist almost entirely of long lamellar boundaries, many of them high angle, aligned parallel to the rolling plane, as shown in figure 2.11b. Rather similar structures of this type are found in aluminium, nickel, copper and iron, and in the latter, there is evidence (Every and Hatherly 1974) that the extent of formation of the lamellar boundary structures is dependent on orientation.

Because the annealing behaviour of alloys deformed to very large strains (>3) may be significantly different from that of materials deformed to lower strains, we give some further consideration to large strain deformation in §14.3.

2.4.2.4 Summary

We have highlighted three microstructural features – cells, cell-bands (microbands), and microshear (S) bands, and the effect of strain on the misorientations across these boundaries in aluminium is shown in figure 2.5c. Additional information about the way in which the microstructure evolves may be obtained by examining the effect of strain on the alignment of these boundaries with the rolling plane as shown for aluminium in figure 2.13.

Cells – The cell size, shape and boundary misorientation changes little with strain, which is consistent with these boundaries being **transient** features of the microstructure.

Cell-band walls – The misorientations of the cell-band (microband) walls changes very little with strain, and for $\varepsilon < 1.5$, figure 2.13 shows that there is little change in their alignment with the rolling plane. The significance of this may be seen by comparison with the change of alignment which would be found for rigid body rotation of passive features in the microstructure. These two factors suggest that at moderate strains the cell-bands or microbands are also **transient** microstructural features which may migrate or re-form during the deformation, up to $\varepsilon \sim 1.5$. Above this strain, the bands undergo rigid body rotation, suggesting that they are no longer active, and have become **persistent** microstructural features.

Microshear bands – In microshear (S) bands the misorientations across the walls increase with increasing strain (fig. 2.5c), and the walls are seen from figure 2.13 to rotate at a rate consistent with a rigid body. This suggests that once formed, these features are permanent features of the microstructure, although the shear within them, and the misorientations across them, increase with strain. This observation is consistent with the earlier observations of Malin and Hatherly (1979) on similar bands in copper.

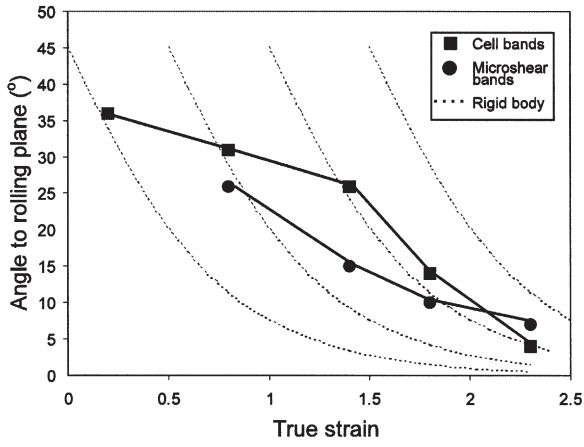

Fig. 2.13. The effect of strain on the alignment of cell and microshear bands with the rolling plane in rolled Al-0.1%Mg. Rigid body rotations are shown for comparison, (after Hurley and Humphreys 2003).

Much of the early work on the characterisation of deformed microstructures was carried out on copper and iron, whereas the extensive work of recent years has concentrated on aluminium and nickel. As discussed above, rather similar features have been identified in all these materials, but detailed and quantitative comparisons between these materials have not yet been made.

2.4.3 Non-cell-forming metals

The addition of 3–5% of magnesium to aluminium in solid solution, hinders dynamic recovery and prevents the formation of dislocation cell structures and many of the other dislocation boundaries discussed in the previous section (Korbel et al. 1986, Hughes 1993, Drury and Humphreys 1996, Kuhlmann-Wilsdorf 2000). Many of the dislocations were found to be arranged in a diffuse geometric pattern along {111} slip planes that defined a so-called **Taylor lattice** (Kuhlmann-Wilsdorf 1989). Adjacent Taylor lattice regions were misoriented by 0.5–1°, and separated by diffuse boundaries **(domain boundaries).** Crystallographically associated microbands, rather similar to those found in copper (fig. 2.11a) were found to develop from these on {111} planes (Korbel et al. 1986, Hughes 1993). As the strain increases, the microbands broaden and cross grain boundaries to become shear bands.

2.5 CUBIC METALS WHICH DEFORM BY SLIP AND TWINNING

In materials with low values of stacking fault energy (silver, austenitic stainless steels, many copper-rich alloys, etc.) a dislocation cell structure does not form and the dislocations dissociate to form planar arrays of stacking faults on the slip planes (fig. 2.14a). At a comparatively early stage of deformation, thin bands of very fine deformation twins then develop.

2.5.1 Deformation twinning

Twinning is a major deformation mode in fcc metals with $\gamma_{SFE} < 25$ mJm^{-2} and in all cph metals. It may also occur in fcc metals with high values of γ_{SFE} and in bcc metals if deformation occurs at low temperatures or high strain rates. In all cases the extent of twinning is orientation dependent.

Manifestations of twinning can be seen on polished surfaces, in etched specimens and in the electron microscope. The well known **strain markings** (fig. 2.14b) have been shown by Duggan et al. (1978b) to consist of very fine deformation twins (fig. 2.14c). These features develop freely on the {111} planes of many fcc alloys of copper and in 18:8 stainless steel. In 70:30 brass, the strain markings appear first near the grain boundaries and in compressed specimens are present on more than one system at strains less than 0.1 (Samuels 1954). They are profuse in most grains at $\varepsilon \sim 0.8$. The width of the markings is determined primarily by γ_{SFE} and the deformation temperature (Hatherly 1959) and as these increase, the markings and the constituent twins become wider (cf. figs. 2.14b and 2.15a). Because of these factors, twinning is a prominent feature of the microstructure of copper after deformation at low temperatures (fig. 2.15b).

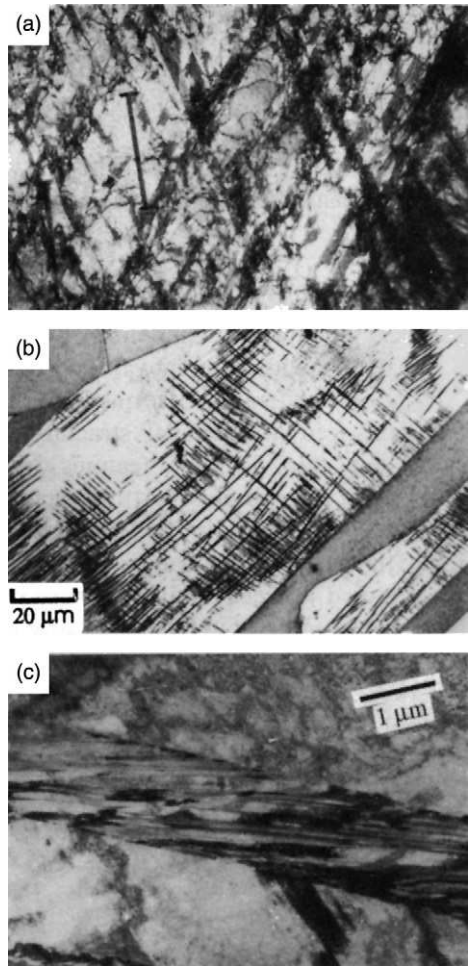

Fig. 2.14. (a) Stacking faults in 15% cold rolled, copper-13at.% aluminium alloy, (Malin 1978), (b) Strain markings in 70:30 brass after 14% compression, (c) deformation twins in 30% cold rolled 70:30 brass, (Duggan et al. 1978b). (All electron micrographs are taken from RD-ND sections, and show 1 μm marker parallel to RD.)

The significance of γ_{SFE} in determining the deformation mode and therefore the nature of the microstructure is apparent in the electron microscope (Duggan et al. 1978b, Wakefield and Hatherly 1981). In low γ_{SFE} materials, the dislocations are dissociated into partials and planar arrays of stacking faults occur (fig. 2.14a). As the strain increases the dislocation content of the faulted structure rises rapidly and bands of very fine twins appear. The size of the twins and their frequency depend particularly on γ_{SFE} and in the following discussion the values given apply to rolled 70:30 brass. The first

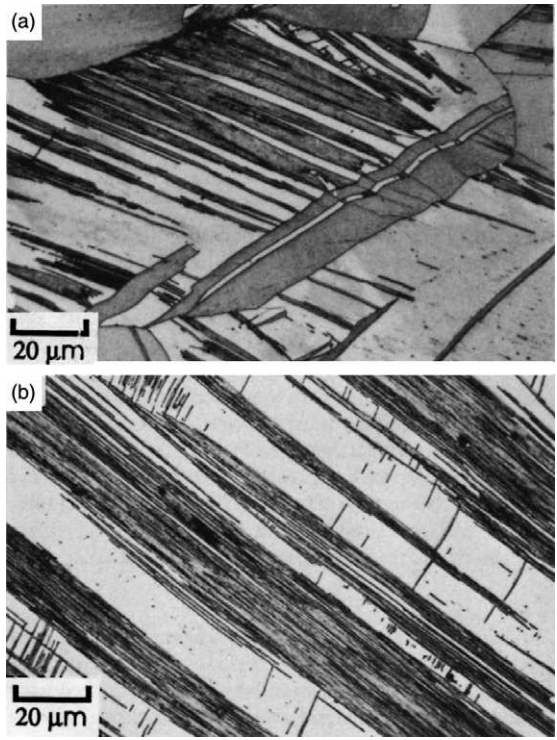

Fig. 2.15. Strain markings in deformed copper and brass showing effects of stacking fault energy and deformation temperature: (a) 90:10 brass compressed 32% at room temperature; (b) (100)[001] single crystal of copper, rolled 60% at −196°C, (Hatherly and Malin 1979).

twins appear at $\varepsilon \sim 0.05$ and clustering into bands follows almost immediately. The twins are extremely fine, with thickness in the range 0.2–0.3 nm, and the twin-parent repeat distance within the bands ranges from 0.5 to 3 nm. These dimensions do not appear to change during deformation but the volume of twinned material increases gradually to about 25%. As rolling proceeds the twins are rotated, as rigid body features, into alignment with the rolling plane and in some grains and deformation bands this process is complete at $\varepsilon \sim 0.8$–1.0 (fig 2.16). The overall twin aligning process continues with further strain and is almost perfect at $\varepsilon \sim 2$.

2.5.2 The effect of stacking fault energy

The effect of stacking fault energy on these structures is very marked. In the very low γ_{SFE} ($\sim$3 mJm^{-2}) alloy Cu–8.8at% Si, Malin et al. (1982a) reported faulting and twinning on all four {111} planes during rolling to $\varepsilon = 0.4$ (fig. 2.17). In such a structure the gradual alignment of a set of deformation twins with the rolling plane is clearly impossible and in the absence of an alternative deformation mode, shear band

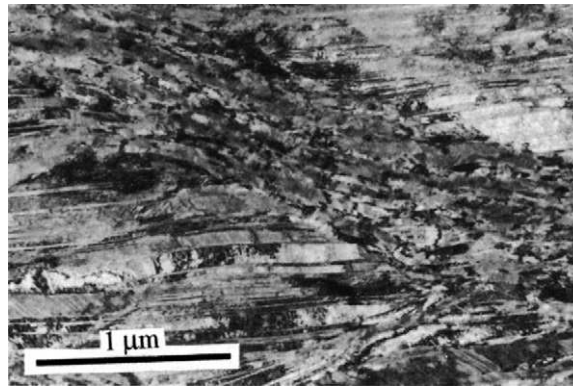

Fig. 2.16. Aligned deformation twins in 50% cold rolled 70:30 brass and inclined shear band, (Duggan et al. 1978b). TD-plane section, (1 μm marker parallel to RD).

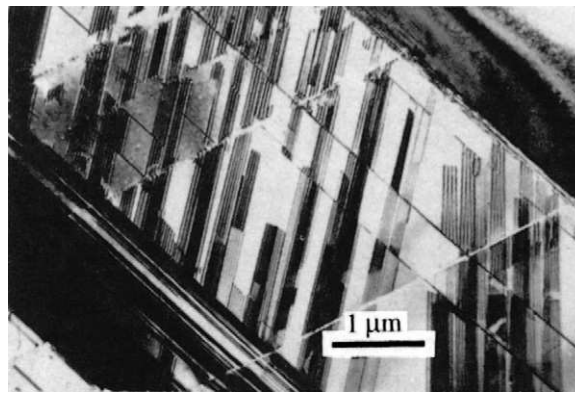

Fig. 2.17. Stacking faults and fine deformation twins in rolled copper-8.8at.%Si, (Hatherly and Malin 1979). TD plane section, (1 μm marker parallel to RD).

formation begins at $\varepsilon = 0.4$–0.5. This alloy cracks along macroscopic shear bands at quite low strains ($\varepsilon \sim 1.2$). In alloys with intermediate values of γ_{SFE}, e.g. 90:10 brass and some stainless steels, the microstructure is determined additionally by the local orientation (Wakefield and Hatherly 1981). In some grains (or deformation bands) the orientation favours twinning and in others slip. The resulting microstructure consists of volumes containing cells and microbands adjacent to volumes showing deformation twins. In some grains where the orientation is appropriate, both slip and twinning occur and as the orientation changes so too does the deformation mode. Twinning is the preferred deformation mode during rolling in regions oriented at $\{112\}<111>$ and $\{100\}<001>$ but twinning is not observed in regions oriented at $\{110\}<001>$ or $\{110\}<112>$. For a discussion of the relationship between orientation and twinning in fcc metals see Köhlhoff et al. (1988a).

2.6 CLOSE PACKED HEXAGONAL (CPH) METALS

As with other metals the deformation of polycrystalline cph metals begins with slip, but the symmetry of the lattice and the availability of slip systems are less than with cubic metals. Under these conditions slip cannot continue as the only deformation mode and twinning becomes significant at quite low strains ($\varepsilon < 0.2$). The most obvious feature of the microstructure of deformed cph metals is the rapid development of a profuse array of large, broad, lenticular deformation twins (fig. 2.18). The twins originate usually as long, thin lamellae at low strain levels, but broaden rapidly. Twins are broader in cph metals than in cubic metals because of the smaller value of the twinning shear. Despite their profusion in the microstructure the contribution of twinning to the overall deformation at medium to high strain levels is usually small. The reason for this lies in the limited magnitude of the twinning shear. As twinning ceases, deformation by slip occurs in the newly developed twins and the whole process is repeated. Tables 2.5 and 2.6 give details of the crystallography of the most frequent slip and twinning systems in cph metals.

Unlike slip, twinning occurs in only one direction, and the crystallography is such that elongation is generated in one direction and contraction in others. Inspection of table 2.6 shows that one twinning system is common to all of the cph metals, viz. $\{10\bar{1}2\} < \bar{1}011 >$. If the c/a ratio is >1.633 (the ideal value), as in zinc and cadmium, twinning occurs only on this system but if c/a is <1.633 more than one system may operate. The strain produced by the twinning shear depends on the twinning system and the value of c/a. For $\{10\bar{1}2\} < \bar{1}011 >$ twinning the strain is greatest for low values of c/a but if other twinning systems are possible these will lead to larger strains. The sense of the shape change also depends on the perfection of packing. For the value $c/a = \sqrt{3} = 1.732$ no twinning is possible but for $c/a < 1.733$ the sense of the shape

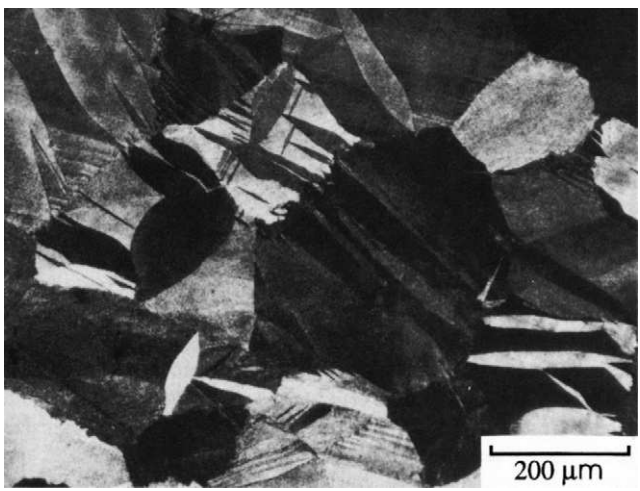

Fig. 2.18. Deformation twins in polycrystalline magnesium deformed 8% in compression at 260°C, (Ion et al. 1982).

Table 2.5
Slip systems in cph metals at room temperature, (Grewen 1973).

Metal	c/a	Slip system	
		Predominant	Seldom
Cd	1.89	$\{0001\} < 11\bar{2}0 >$	$\{11\bar{2}2\} < 11\bar{2}3 >$
Zn	1.88		
Co, Mg	1.62	$\{0001\} < 11\bar{2}0 >$	$\{10\bar{1}0\} < 11\bar{2}0 >$
Zr	1.59	$\{0001\} < 11\bar{2}0 >$	$\{10\bar{1}0\} < 11\bar{2}0 >$
Ti	1.59	$\{10\bar{1}0\} < 11\bar{2}0 >$	$\{0001\} < 11\bar{2}0 >$

Table 2.6
Twinning systems in cph metals, (Grewen 1973).

Metal	c/a	Twinning shear	Twinning element	
			Plane	Direction
Cd	1.89	0.17		
Zn	1.88	0.14	$\{10\bar{1}2\}$	$< \bar{1}011 >$
Co	1.62	0.13		
Mg	1.62	0.13	$\{10\bar{1}2\}$	$< \bar{1}011 >$
Zr,Ti	1.59	0.167	$\{10\bar{1}2\}$	$< \bar{1}011 >$

change is opposite to that for $c/a > 1.732$. In practice this means that twinning should occur only if directions that are shortened by twinning lie in the appropriate directions during processing, e.g. radially during wire drawing.

It will be seen that for metals with c/a greater than ideal, basal slip is favoured while prismatic slip is preferred for those with c/a less than ideal. In general dislocations are confined to the closely packed basal plane and do not move freely from it. There have been only a few detailed examinations of the deformation microstructure in any of these metals and it is difficult to draw general conclusions.

In rolled titanium (c/a < ideal) deformation twinning is found in all grains at a very early stage (Blicharski et al. 1979). The twins are broad and lenticular and usually form on two or more systems. Because of the small twinning shear, further deformation requires the formation of smaller twins between and within those first formed, but eventually this is no longer possible and fresh twins do not form at moderate strain levels ($\varepsilon \sim 0.75$). At high strain levels the twins undergo a rigid body rotation into alignment with the rolling plane so as to produce a microstructure of thin elongated bands. Shear bands begin to

form at $\varepsilon \sim 2.8$ in this aligned structure but considerable ductility still remains at much higher strain levels.

The microstructure of deformed zinc is interesting. The c/a ratio is high and so too is γ_{SFE} ($\sim$140 mJm^{-2}), but the melting point is low and room temperature deformation occurs at $\sim 0.4T_m$. Large twins are seen in every grain of polycrystalline zinc after very light rolling ($\varepsilon = 0.07$) but no further twins develop as rolling continues to $\varepsilon = 0.2$ and slip is the preferred deformation mode in this strain range (Malin et al. 1982b). Shear band formation begins in the strain range $0.2 < \varepsilon < 0.5$ but the shear bands are detected only by the presence of bands of very small recrystallized grains that outline their positions. It seems clear that recrystallization follows shearing closely in this low melting point metal. The new strain-free grains deform by slip and twinning and deformation continues in this way to high strain levels. These changes are easily recognized in the deformation textures and will be referred to in chapter 3.

2.7 DEFORMATION BANDS

As discussed in §2.4.1 and shown in figures 2.8 and 2.9c and 2.9d, the coarsest form of grain subdivision is the formation of deformation bands, and because these are easily identified by optical microscopy, they have been recognized for a long time. Major attention was first focused on them by Barrett (1939) who argued that inhomogeneities of this type contributed to the inability to predict the strain hardening behaviour and the orientation changes taking place during deformation. Following Barrett the term **deformation band** is used to describe a volume of approximately constant orientation, that is significantly different to the orientation(s) present elsewhere in that grain. Kuhlmann-Wilsdorf et al. (1999) have presented an extensive review of the early work on deformation bands and on the conditions under which they form.

2.7.1 The nature of deformation bands

The different features are illustrated schematically in figure 2.8c which shows a region B, which has a different orientation to that in the grain proper A. The region at the edge of the deformation band where the orientation changes from B to A may have a finite width, in which case it is called a **transition band.** However, in some cases the orientation change is sharp, and this is then a **deformation-induced grain boundary.** In many cases deformation bands occur with approximately parallel sides and involve a double orientation change A to C and then C to A. A deformation band of this special type is called a **kink band** following the nomenclature of Orowan (1942). The micrograph of figure 2.9c shows a complex microstructure of kink bands and deformation bands in α-brass, and figure 2.9d shows deformation bands in an Al–Mg alloy. The development of deformation bands is an inevitable consequence of the deformation of polycrystals (and also of constrained single crystals), and the details of the microstructure are determined by the crystallographic nature of the deformation process.

2.7.2 The formation of deformation bands

The nature and formation of deformation banding has been extensively studied in recent years because of its relevance to the generation of deformation textures. Chin (1969) identified two types of deformation bands. One of these originates in the ambiguity associated with the selection of the operative slip systems. In many cases the imposed strain can be accommodated by more than one set of slip systems and the different sets lead to rotations in different senses. In the second type, different regions of a grain may experience different strains if the work done within the bands is less than that required for homogeneous deformation and if the bands can be arranged so that the net strain matches the overall deformation. This latter is similar to the reasoning used to explain the formation of cell blocks (§2.4.1). In their model of rolling texture development, Lee et al. (1993) examined the second of these cases and showed theoretically that as few as two independent slip systems may suffice to accommodate the shape change. Their work is consistent with the relaxed constraints models of plasticity discussed in §3.7.1. Kuhlmann–Wilsdorf (1999) has recently discussed the formation of deformation bands in terms of her low energy dislocation model.

2.7.3 Transition bands

A transition band develops when neighbouring volumes of a grain deform on different slip systems and rotate to different end orientations. In its most usual form the transition band consists of a cluster of long narrow cells or subgrains with a cumulative misorientation from one side of the cluster to the other. It is sometimes found, particularly in aluminium alloys (Hjelen et al. 1991), that the width of the transition band is reduced to only one or two units but the large orientation change across the band is retained.

Dillamore and Katoh (1974) considered the case of axisymmetric compression of iron and showed that the rotation paths for various orientations followed those shown in figure 2.19a. For orientation gradients that straddle the line joining [110] and [411] a very sharp transition band develops as part of the gradient rotates towards [100] and part towards [111]. The more general case is shown at A. For the gradient B–B′ both extremities rotate towards [111] and the heterogeneity is gradually lost. For a gradient C–C′ the extremes follow different paths and misorientation persists in a diminished form. Figure 2.19b shows that the experimentally determined fibre texture after 88% compression is in good agreement with the model used. Dillamore and Katoh also considered the special case of the formation of a transition band in heavily rolled copper having the orientation $\{100\}<001>$ at its centre. The implications of the Dillamore–Katoh model for the generation of the cube texture during recrystallization are discussed in chapter 12.

2.7.4 The conditions under which deformation bands form

The details of transition band formation depend strongly on the grain orientation, as discussed above. However, the occurrence of deformation bands is dependent on the microstructure and deformation conditions.

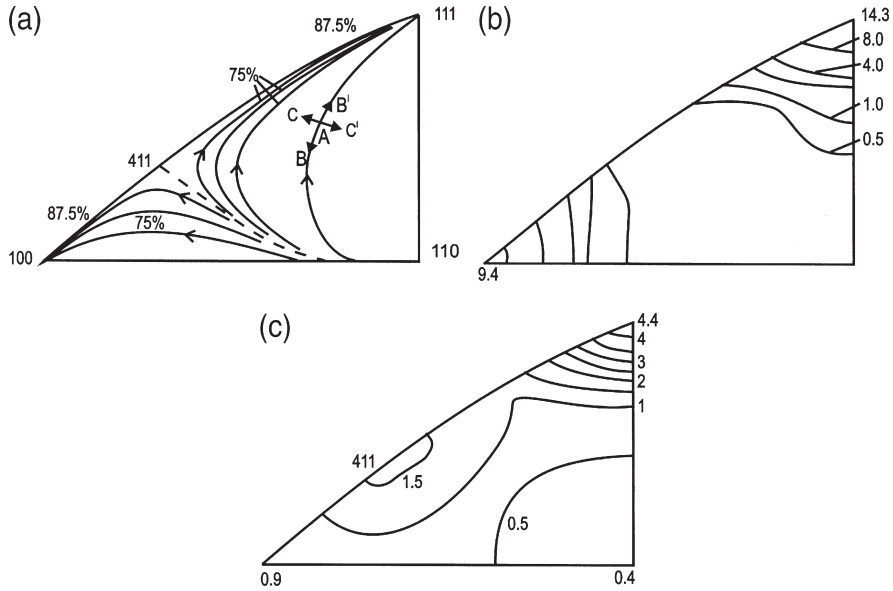

Fig. 2.19. Texture development in axially compressed iron. (a) Predicted rotations from three different initial orientations after 70% and 88% reduction in thickness, (b) Deformation texture after 88% compression, (c) Recrystallization texture of (b) material, (after Dillamore et al. 1974).

The **grain orientation** is an important factor in determining whether or not a grain will deform relatively homogeneously or fragment by deformation banding, as may be seen from figure 2.19. For example, the $\{110\}<001>$ Goss orientation in fcc materials is very stable under condition of plane strain deformation (§3.7.1.4), and single crystals (Ferry and Humphreys 1996a), and large-grained polycrystals (Somerday and Humphreys 2003b) can undergo extensive deformation without the development of large-scale heterogeneities, as seen in figure 7.15.

The **initial grain size** is of particular importance, and deformation banding occurs much more readily in coarse grained metals, as reviewed by e.g. Kuhlmann–Wilsdorf (1999), Humphreys et al. (1999). Lee and Duggan (1993) measured a decrease in the numbers of deformation bands per grain in copper with decreasing grain size, and Humphreys et al. (1999) concluded that in aluminium, deformation banding did not occur in material with a grain size less than ~20 μm. Lee et al. (1993) using an energy criterion, predicted that the number of deformation bands per grain should be proportional to the square root of the grain size.

There is extensive evidence that deformation banding **decreases at higher temperatures** (see e.g. Kuhlmann–Wilsdorf et al. 1999). This effect is discussed in §13.2, and may be seen in figure 13.6.

2.8 SHEAR BANDS

Shear bands, which occur in many metals and alloys, were described in detail by Adcock (1922), but until the work of Brown (1972) on aluminium and Mathur and Backofen (1973) on iron, were largely forgotten. These bands correspond to narrow regions of intense shear that occur independently of the grain structure and independently also of normal crystallographic considerations. In rolled material they occur at $\sim 35^\circ$ to the rolling plane and parallel to the transverse direction (figures 2.8d, 2.9e and 2.9f). Note the offsets at the scratch in figure 2.9e which show the shear associated with the bands.

2.8.1 Metals of medium or high stacking fault energy

At high strain levels, $\varepsilon > 1.2$ for copper, shear bands form in colonies in each of which only one set of parallel bands develops (fig. 2.9e). The colonies are usually several grains thick and the bands in alternate colonies are in opposite senses, so that a herringbone pattern develops (Malin and Hatherly 1979). Any grain boundaries in the colony are crossed without deviation. The structure of a shear band is clearly resolved in figure 2.20a; the aligned microbands of the rolled iron have been swept into the shear band and local elongation and thinning have contributed to the shear strain. The distinct lattice curvature of figure 2.20a is characteristic of a shear band that has been associated with only light to moderate shearing, and the similarity to the microshear (S) bands in deformed aluminium (figure 2.12a) can be seen. A typical microstructure formed at large strains is shown in figure 2.20b. The shear in bands of this type is large, and values as high as 6 have been reported, although 2–3 is a more usual value. At still higher levels of strain, larger shear bands develop which cross a rolled sheet from one surface to the other and when eventually a uniform population of these bands exists, failure occurs along them.

2.8.2 Metals of low stacking fault energy

The shear band morphology in materials with low values of γ_{SFE} is quite different to that found in metals which do not develop deformation twins (Hatherly 1982, Hatherly and Malin 1984). In rolled 70:30 brass, isolated shear bands are first seen at $\varepsilon \sim 0.8$ and specifically in regions where twin alignment with the rolling plane is already well established (fig. 2.16; Duggan et al. 1978b), and soon afterwards ($\varepsilon \sim 1$) two families of shear bands are seen in many regions. The bands form initially at approximately $\pm 35^\circ$ to the rolling plane and divide the sheet into rhomboidal prisms with long axes parallel to TD. The twin alignment within the prisms is nearly perfect and most theories of shear band formation are based on the supposition that continued deformation by either slip or twinning is no longer viable in such an aligned structure. As shown in figure 2.21, the bands themselves consist of an array of very small 'crystallites' (volumes of almost perfect lattice) which are usually elongated in the direction of shear with aspect ratios in the range of 2:1–3:1. Typical shear bands in 70:30 brass range in thickness from 0.1–1 μm and the individual crystallites vary in width from 0.02–0.1 μm.

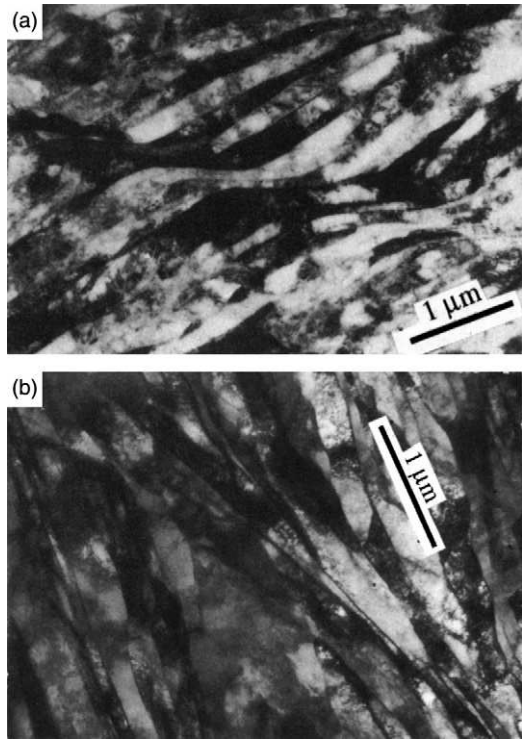

Fig. 2.20. Shear bands in metals deforming by slip. (a) Shear band in 85% cold rolled iron (Willis 1982). (b) Shear band in 97% cold rolled copper, (Malin and Hatherly 1979). (ND-RD plane; 1 μm marker parallel to RD).

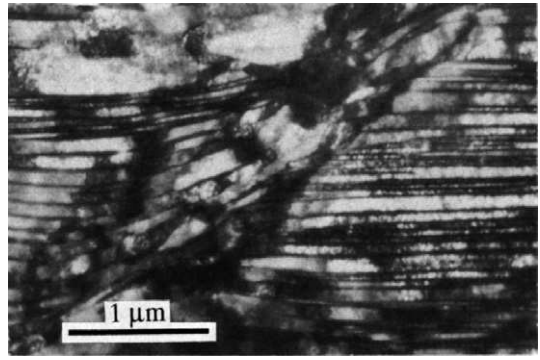

Fig. 2.21. Internal crystallite structure in a shear band in a (110)[111] copper single crystal, cold rolled 65% at 77°K, which has deformed by twinning, (Köhlhoff et al. 1988a). (ND-RD section with 1 μm marker parallel to RD).

The orientations of the crystallites are particularly interesting. Their volume in heavily deformed metals is such that they should make a significant contribution to the rolling texture, and shear bands are a major nucleation site for recrystallized grains. Duggan et al. (1978a) reported large ($>20^\circ$) orientation differences between neighbouring crystallites in 70:30 brass that were not cumulative. An overall preference was detected for rolling plane orientations near {110} and a substantial population was found near $\{110\}<001>$. This orientation is a major component of the shear texture in fcc metals.

The shear associated with individual bands is high with average values of 3–4 often reported but shears as high as 10 are sometimes found (Duggan et al. 1978b). The importance of shear band formation as a deformation process is strikingly illustrated by figure 2.22. A longitudinal section from a specimen of 50% cold rolled, 70:30 brass, was polished and then lightly scratched at right angles to the rolling direction. The figure shows the development of shear bands during a subsequent rolling of 10% reduction and the magnitude of the shear strain. The number of shear bands increases rapidly with strain and in the range $0.8 < \varepsilon < 2.6$ shear band formation appears to be the major deformation mode and at the latter level of strain only minor amounts of twinned material remain. As in the case of high γ_{SFE} materials, further deformation leads to the formation of large through-thickness shear bands and eventually fracture occurs along these.

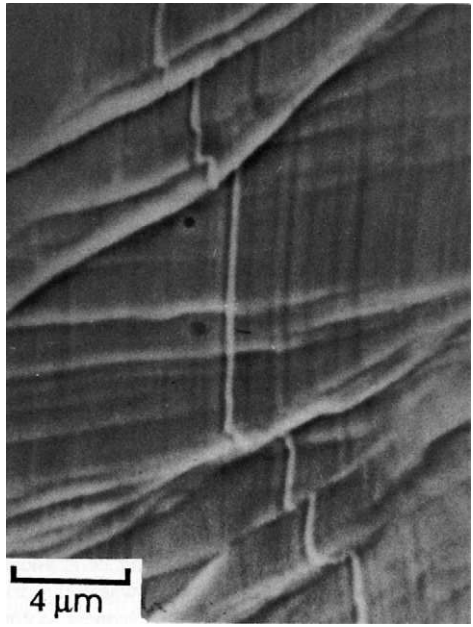

Fig. 2.22. 70:30 Brass specimen initially rolled 50%, then polished and lightly scratched normal to rolling direction before further rolling of 10% reduction (TD-plane section). Note the magnitude of the shear, (Duggan et al. 1978b).

2.8.3 The formation of shear bands

A shear band is a form of plastic instability and in plane strain deformation (or rolling) the condition for instability is

$$\frac{1}{\sigma}\frac{d\sigma}{d\varepsilon} < 0 \tag{2.9}$$

Dillamore and colleagues (Dillamore 1978a, Dillamore et al. 1979), have written this condition as

$$\frac{1}{\sigma}\frac{d\sigma}{d\varepsilon} = \frac{n}{\varepsilon} + \frac{m}{\dot{\varepsilon}} + \frac{1+n+m}{M_T}\frac{dM_T}{d\varepsilon} - \frac{m}{\rho}\frac{d\sigma}{d\varepsilon} < 0 \tag{2.10}$$

where n and m are the usual strain hardening and strain rate exponents, ρ the dislocation density, and M_T the Taylor factor (defined as Σ_S/ε, where Σ_S is the total shear strain on all active slip systems, and ε is the normal strain).

Of the various terms in the equation, that in ε is always positive, that in $\dot{\varepsilon}$ is usually positive and that ρ is negative. It follows that if instability is to occur at medium to high strain levels, and in the absence of strain rate effects, it must be because the term in M_T becomes negative through a negative value of $dM_T/d\varepsilon$. This latter expression corresponds to geometric softening, in that instability is favoured if it causes a lattice rotation into a geometrically softer condition. $dM_T/d\varepsilon$ can be calculated from $dM_T/d\theta$ (the rate of change of hardness with orientation) and $d\theta/d\varepsilon$ (the rate of change of orientation with strain). Dillamore et al. (1979) have shown that this factor is both negative and a minimum close to $\pm 35^\circ$ for typical rolled metals with well developed textures.

2.8.4 The conditions for shear banding

The 'copper type' shear bands discussed in §2.8.1 occur in a variety of metals, and their occurrence depends on a number of factors.

Grain size – Several authors including Ridha and Hutchinson (1984) and Korbel et al. (1986) have shown that the tendency for shear banding increased with increasing grain size.

Orientation – The effect of orientation on shear banding has been demonstrated by Morii et al. (1985) in single crystals of Al–Mg.

Solute – The addition of manganese to copper, which does not affect the stacking fault energy, leads to the formation of extensive shear banding (Engler 2000) and magnesium promotes shear banding in aluminium (Duckham et al. 2001).

Deformation temperature – Several authors have demonstrated that shear banding becomes less common at high temperatures. The combined effects of deformation temperature and strain on the tendency for shear banding in Al–1%Mg are well summarised in figure 2.23 from the work of Duckham et al. (2001).

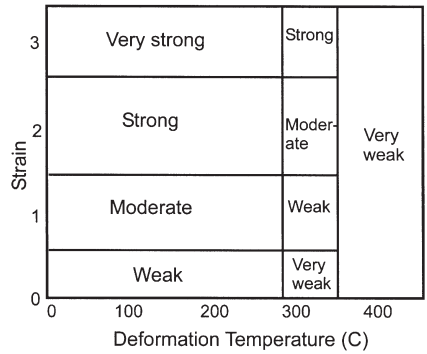

Fig. 2.23. The tendency for shear band formation in Al–1%Mg as a function of strain and deformation temperature, (Duckham et al. 2001).

2.9 THE MICROSTRUCTURES OF DEFORMED TWO-PHASE ALLOYS

Most industrial alloys contain more than one phase, the microstructure comprising a matrix phase and dispersed second-phase particles. If these particles are present during deformation, they will affect the microstructure, and this in turn may affect the subsequent annealing behaviour. The most important aspects of the deformation structures in two-phase alloys in this respect are:

- **The effect of the particles on the overall dislocation density.** This may increase the driving pressure for recrystallization.
- **The effect of the particles on the inhomogeneity of deformation in the matrix.** This may affect the availability and viability of the sites for recrystallization.
- **The nature of the deformation structure in the vicinity of the particles.** This determines whether or not particle-stimulated nucleation of recrystallization (PSN) will be possible.

During deformation of an alloy containing second-phase particles, the dislocations will bow around the particles as shown in figure 2.24. An analysis of the situation in terms of elementary dislocation theory follows. For particles of radius r and spacing λ along the dislocation line, the force exerted on each particle (F) is given by:

$$F = \tau b \lambda \tag{2.11}$$

where τ is the applied stress.

If the strength of the particle is less than F, then the particle deforms, otherwise the dislocation reaches the semicircular configuration of figure 2.24b, when the applied stress is given by

$$\tau_0 = \frac{Gb}{\lambda} \tag{2.12}$$

which is the well known **Orowan stress.**

The dislocation then proceeds to encircle the particle, leaving an **Orowan loop** as shown in figure 2.24c. A micrograph of such loops in a nickel alloy is shown in figure 2.25. Because of its line tension, an Orowan loop exerts a shear stress on the particle which is given approximately by

$$\tau = \frac{Gb}{2r} \tag{2.13}$$

If the particle is strong enough to withstand this stress, it does not deform and the net result of the passage of a matrix dislocation is the generation of extra dislocation in the

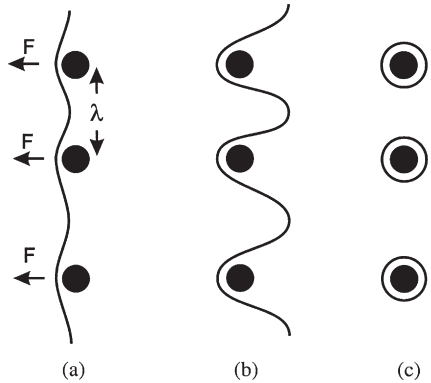

Fig. 2.24. The formation of Orowan loops at second-phase particles.

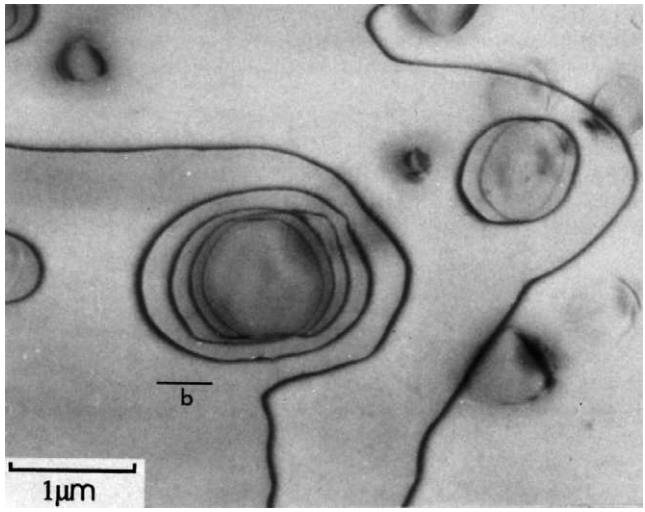

Fig. 2.25. Orowan loops at Ni_3Si particles in a Ni–6%Si single crystal, (Humphreys and Ramaswami 1973).

form of the Orowan loop, at the particle. If the particle deforms either before or after the Orowan configuration is reached, no extra dislocations are generated at the particle.

Detailed discussion of the factors affecting the strength of particles is beyond the scope of this volume, and the reader is referred to the reviews of Martin (1980), Brown (1985), Humphreys (1985) and Ardell (1985) for further details. However it is important to realise that the subsequent deformation behaviour and hence **the density and arrangement of dislocations in the deformed material is dependent on whether or not the particles deform.**

2.9.1 Dislocation distribution in alloys containing deformable particles

If the particle of figure 2.26a deforms as shown in figure 2.26b, then its size on the slip plane is effectively reduced by the Burgers vector b of the dislocation. As a smaller particle is normally weaker than a larger particle, the slip plane is softened and subsequent dislocations will tend to move on the same plane, thus concentrating slip into bands as shown in figure 2.26d. This is illustrated in the micrograph of figure 2.27, where shear offsets of ~0.1 μm indicate the passage of several hundred dislocations on the same plane.

The slip distribution in alloys containing small particles has been discussed by Hornbogen and Lütjering (1975) and by Martin (1980) as follows.

The yield stress of a crystal containing deformable particles is often given by an equation of the form

$$\tau = CF_V^{1/2}d^{1/2} \tag{2.14}$$

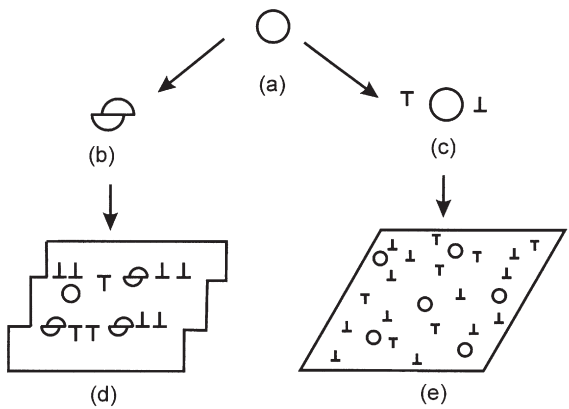

Fig. 2.26. The effect of particle strength on the distribution of slip. A deforming particle (b) leads to slip concentration (d). A non-deforming particle (c) results in more homogeneous slip (e).

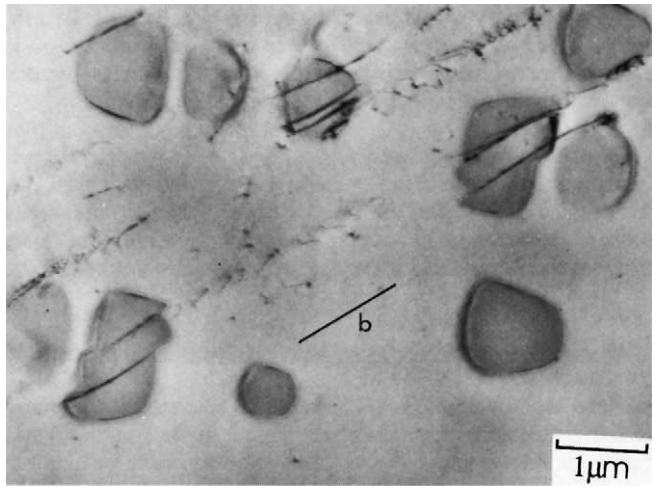

Fig. 2.27. Deformed Ni_3Si particles in a Ni–6%Si single crystal, (Humphreys and Ramaswami 1973).

where C is a constant dependent upon the particular hardening mechanism which is operative (e.g. coherency strains). If n dislocations shear a particle, the diameter of the particle will be reduced by nb. The stress for further deformation then becomes

$$\tau = C F_V^{1/2}(d - nb)^{1/2} = C F_V^{1/2} d^{1/2} \left(1 - \frac{nb}{d}\right)^{1/2} \tag{2.15}$$

Thus the slip plane is softened, so that further slip tends to occur on that plane. This is in contrast to the case of non-deformable particles, where the dislocation debris left by previous dislocations (e.g. the Orowan loops of fig. 2.25) makes it more difficult for slip to occur on the same plane, thus tending to make slip relatively homogeneous (fig. 2.26e).

The amount by which a slip plane is weakened by the passage of a dislocation is the parameter $d\tau/dn$, and differentiation of equation 2.15 gives

$$\frac{d\tau}{dn} = \frac{-bCF_V^{1/2}}{2d^{1/2}} \left(1 - \frac{nb}{d}\right)^{-1/2} \tag{2.16}$$

We thus see that the tendency for coarse slip is increased by small particles, a large volume fraction and a large value of C.

There are many recorded examples of particle shearing leading to slip concentration. This is of particular concern in the design of high strength precipitation hardened alloys, in which the slip concentration may adversely affect the fracture toughness and the fatigue behaviour (e.g. Polmear 1995). An example of this is found in binary Al–Li alloys

in which precipitates of the ordered δ' phase are formed. These particles deform during deformation, leading to extensive shear localisation (Sanders and Starke 1982).

As the shape and size of the particles changes during deformation, so the slip distribution may also be a function of strain. Kamma and Hornbogen (1976) found that small platelike particles of Fe_3C in steel deformed, leading to the formation of shear bands. However, at high strains, the bands broadened, and the slip became homogeneous. Nourbakhsh and Nutting (1980) showed that in overaged Al–Cu alloys containing large plates of θ', the deformation was initially inhomogeneous as the θ' plates deformed. At strains above 1, the plates disintegrated to give small spherical particles and as found by Kamma and Hornbogen, a more homogeneous slip distribution resulted. The same authors also found that in the underaged alloy, the small GP zones which resulted in slip concentration at lower strains, were dissolved at strains of 5 and the deformation behaviour of the alloy then became similar to that of the solid solution.

We therefore conclude that the slip distribution in alloys containing deformable particles is complex and may alter with strain as changes in the particle size and shape are induced by the deformation.

2.9.2 Dislocation distribution in alloys containing non-deformable particles

2.9.2.1 Dislocation density

If a deforming matrix contains non-deformable particles, then, as was first shown by Ashby (1966, 1970) there is a strain incompatibility between the two phases as shown in figure 2.28. In figure 2.28a, a spherical particle of radius r is contained within an undeformed matrix. On deformation by a shear strain s, then, as shown in figure 2.28b, a deformable particle will comply with the imposed strain. However, if the particle does not deform, then as shown in figure 2.28c, there is a local strain incompatibility. This can be accommodated by the generation of dislocations at the particle-matrix interface and also, if the interface is weak, by the formation of voids. A more detailed consideration of the dislocation generation near the particle is given in §2.9.3. However, the length of dislocation generated is not very sensitive to the details of the mechanism, and it is readily shown that the incompatibility may be accommodated approximately by the generation of n circular prismatic dislocation loops of Burgers vector b and radius r, where

$$s = \frac{nb}{2r} \tag{2.17}$$

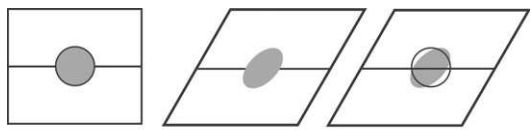

Fig. 2.28. The incompatibility between a deforming matrix and a non-deforming particle. (a) undeformed, (b) deformed particle, (c) non-deformable particle.

The length of dislocation per particle, L, is thus

$$L = \frac{4\pi r^2 s}{b} \tag{2.18}$$

and the dislocation density (ρ_G) due to this effect is $N_V L$. Taking N_V as given by equation A2.11, then

$$\rho_G = \frac{3F_V s}{rb} \tag{2.19}$$

These have been termed the **geometrically necessary** dislocations by Ashby.

The total density of dislocations generated in the material will be approximately $\rho_G + \rho_s$, where ρ_s is the density of dislocations which would be generated in the single-phase matrix (see §2.2). However, because dislocations will be lost by recovery during or after the deformation, this is an upper limit. Figure 2.29 shows the estimated density of dislocations ($\rho_G + \rho_s$) generated for a matrix of grain size 100 μm (equations 2.1 and 2.19), as a function of strain and particle content, neglecting the effects of dynamic recovery.

Although there is little quantitative data, there is evidence that in particle-containing single crystals or polycrystals deformed to **small strains,** the dislocation density is much greater than in single-phase materials of similar composition. For single crystals of copper, oriented for single slip, and containing alumina particles, Humphreys and Hirsch (1976) found that the dislocation density was close to that predicted by equation 2.19. However, analysis of the data of Lewis and Martin (1963) on copper polycrystals containing oxide particles shows that the dislocation densities at tensile strains of 0.08 are very much lower than those predicted. There is little data available for large strains, where the situation is often complicated by dynamic recovery and the formation of dislocation boundaries rather than free dislocations.

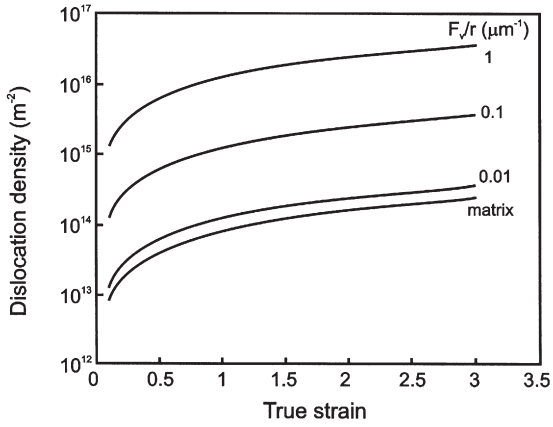

Fig. 2.29. Predicted dislocation densities in particle-containing alloys.

There are comparatively few direct measurements of the stored energy of particle-containing alloys. Adam and Wolfenden (1978) found the stored energy of an Al-Mg-Si alloy deformed to a strain of 0.1 to be some ten times that of pure aluminium. Measurements of stored energy in particle-containing copper alloys by Baker and Martin 1983a (fig. 9.6a), show an increase in stored energy with strain which is in approximate agreement with equation 2.19 at low strains, with some indication that the stored energy saturates at strains larger than ~1. Other measurements of the stored energy of dispersion hardened copper alloys deformed to large strains (Bahk and Ashby 1975, Chin and Grant 1967) indicate that the stored energy in these alloys is not significantly greater than for pure copper.

As the dislocation density is generally found to be directly related to the flow stress (equation 2.2), some indication of the change in dislocation content with strain may often be inferred from the stress-strain behaviour. From such experiments, there is considerable evidence that the work hardening in two-phase alloys, which is initially high, frequently falls to that of a comparable single-phase alloy after strains of ~0.05 in copper (Lewis and Martin 1963), in steels (Anand and Gurland 1976), and in aluminium alloys (Lloyd and Kenny 1980).

In summary, it is apparent that the large increase in dislocation density predicted by equation 2.19 and figure 2.29, for alloys containing small non-deformable particles are only obtained for very small strains, and that at the larger strains which are usually of importance for recrystallizing materials, dynamic recovery may reduce the dislocation density to a value little larger than that for a single-phase alloy.

2.9.2.2 Cell and subgrain structures

It has often been reported that particles affect the dislocation cell structures formed on deformation. As discussed in §2.2.3, cell and subgrain structures are products of dynamic recovery and will therefore be greatly influenced by any parameters which affect the generation or the recovery of dislocations.

A dispersion of small non-deformable second-phase particles results in dislocation generation (§2.9.2.1) and also affects dynamic recovery by impeding the movement of dislocations. Dislocations will only pass strong particles if the local stress exceeds that given by equation 2.12. Therefore although dislocations will be free to move in the regions between particles, they will tend to be held up at particles. In a similar manner, the particles will pin cell or subgrain boundaries (§4.6). Recovery processes which occur on a scale **smaller** than the interparticle spacing (λ) will therefore be relatively unaffected by the particles, but recovery processes involving rearrangement of dislocations on a scale **larger** than the interparticle spacing will be hindered. The interparticle spacing may therefore be expected to affect the size and misorientation of the dislocation cells or subgrains. The cell size (D) is typically 0.5–1 μm in many metals and decreases with increasing strain (fig. 2.4). If $\lambda < D$ we would expect the cell structure to be affected by the particles. However, if $\lambda > D$, the particles would be expected to have little effect on cell formation.

The cell size – Observations of cell formation in dispersion strengthened copper with very small interparticle spacing ($\lambda \sim 0.1$ μm) (Lewis and Martin 1963 and

Brimhall et al. 1966) indicate that compared with copper, the dislocation cells are more diffuse, form at larger strains, and have a size related to the interparticle spacing. However, in oxide-containing aluminium (Hansen and Bay 1972) and copper (Baker and Martin 1983b), where the interparticle spacing is 0.3 to 0.4 μm, the cell size was not found to significantly differ from that of the pure matrix. In a study of the effect of strain on the substructure of two-phase aluminium alloys, Lloyd and Kenny (1980) found that at low strains the cell size was related to the interparticle spacing, but at larger strains, the cell size was reduced and was almost independent of particle size as shown in figure 2.30. Recent EBSD measurements shown in table 2.7 also indicate that the cell sizes in particle-containing and particle-free alloys are similar.

The cell misorientation – Early electron diffraction experiments on copper (e.g. Brimhall et al. 1966) indicated that the lattice misorientation between cells in alloys with a small interparticle spacing, was less than in the single-phase matrix. However, later work on copper (e.g. Baker and Martin 1983b) and aluminium (Hansen and Bay 1972), in which the interparticle spacings were larger, found the misorientations to be similar to those of single-phase alloys.

Results of a recent EBSD investigation of aluminium and copper alloys, both of which have been shown to contain sufficient particles to prevent recrystallization, are shown in table 2.7. For both aluminium and copper, the particles do not significantly affect the cell size. However, in both cases the cell misorientations are greatly reduced by the particles, and it is significant that the **long range orientation gradients,** which were measured as the extreme (uncorrelated) misorientations within a 10 μm x 10 μm area, were also shown to be much smaller in the particle-containing materials. These give general confirmation of the earlier results which showed that **where the interparticle spacing is similar to the cell size, there is a corresponding homogenisation of the deformation microstructure.**

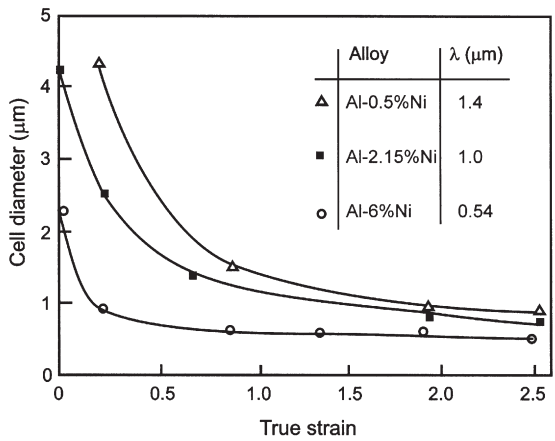

Fig. 2.30. The cell size as a function of strain in Al–Ni alloys, (after Lloyd and Kenny 1980).

Table 2.7
The effects of small, non-deformable, second-phase particles on local and long range misorientations in copper and aluminium, determined by EBSD. (Al–Si samples from Humphreys and Brough (1997), Cu–Al_2O_3 samples from Humphreys and Ardakani (1996)).

Alloy	Particle			Subgrain		Orientation spread (°) in 10×10 μm
	d (μm)	$\mathbf{F_V}$	λ (μm)	Size (μm)	Mis'n (°)	
Al–0.1Mg	—	—	—	0.9	2.1	12
Al–0.8Si	0.10	8×10^{-3}	0.80	1.1	1.4	7
Cu (5n)	—	—	—	0.35	1.5	21
Cu–Al_2O_3	0.05	7×10^{-3}	0.43	0.32	0.9	9

2.9.2.3 Larger scale deformation heterogeneities

There is less evidence as to the effect of non-deformable particles on larger scale heterogeneities in the deformation structure such as **deformation bands** or **shear bands.** During the deformation of single-phase alloys, a grain may, in addition to changing orientation, deform inhomogeneously and divide into regions of different orientation as shown in figures 2.31a and b (cf. fig. 2.8c), and Habiby and Humphreys (1993) found evidence that large (>1 μm) silicon particles could act as nucleation sites for such deformation bands in aluminium. Humphreys and Ardakani (1994) found that during the deformation in plane-strain compression of aluminium crystals of the unstable (001)[110] orientation, the crystal split into two orientations which rotated towards the stable 'copper' orientations (112)[11$\bar{1}$] and ($\bar{1}\bar{1}$2)[111], as shown schematically in figure 2.31b. Large non-deforming particles, by modifying the plastic deformation close to the particle caused a small portion of crystal to rotate in the 'wrong' sense (fig. 2.31c), thus nucleating a small deformation band within one of the components which had the orientation of the other component. Ferry and Humphreys (1996b) found a similar effect in particle-containing crystals of the $\{011\}<100>$ Goss orientation.

It is probable that large inclusions may be responsible for **nucleating** deformation bands by such a mechanism in many commercial alloys. However there is no indication (Habiby and Humphreys 1993) that sub-micron sized particles have any significant effect on the **scale** of deformation band formation in aluminium.

Particles may also affect the formation of **shear bands** which, as discussed in §2.8 are often the result of a low rate of work hardening. This is frequently found for alloys containing deformable second-phase particles (§2.9.1), and a number of investigations have reported the formation of shear bands in such alloys (e.g. Kamma and Hornbogen 1976, Sanders and Starke 1982, Lücke and Engler 1990). In alloys containing large volume fractions of non-deformable particles, the initially high work hardening rate is not maintained to high strains and therefore these materials may also be prone to the formation of shear bands. Examples of this have been noted for Al-Mg-Si alloys (Liu and Doherty 1986) and for aluminium matrix particulate composites (Humphreys et al. 1990).

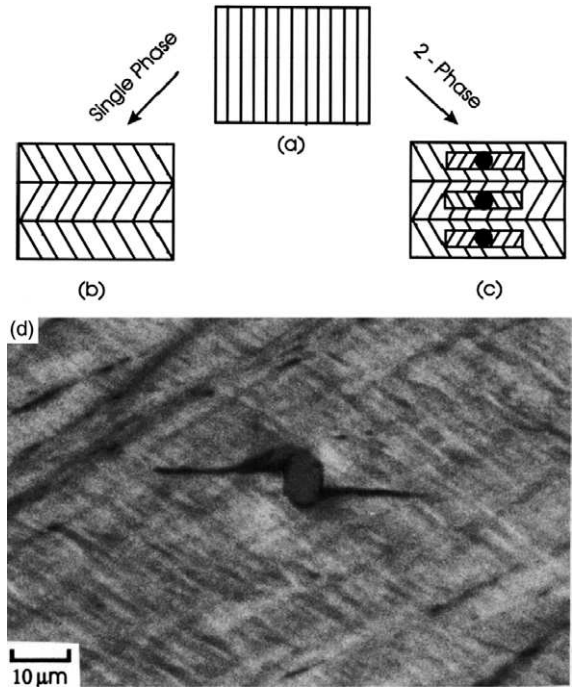

Fig. 2.31. The nucleation of deformation bands at particles. (a) Undeformed crystal of unstable orientation, (b) Formation of deformation bands in the deformed single-phase crystal, (c) Formation of small deformation bands at particles, (d) Optical micrograph showing deformation zone associated with a 10 µm particle in an Al–Si crystal of the same orientation, (Humphreys and Ardakani 1994).

2.9.3 Dislocation structures at individual particles

We have seen that second-phase particles affect the density and distribution of dislocations in the matrix, and that this may influence the driving force for recrystallization. In addition, we need to consider the accumulation of dislocations in the vicinity of large particles as this may lead to these regions becoming sites for recrystallization nucleation.

As discussed in §2.9.2, if the particles are strong enough to resist the passage of dislocations, then Orowan loops may be formed, and the stress on a particle from a single Orowan loop is given by equation 2.13. During continued deformation, more loops will form and the resulting stress will rapidly rise to a level where, if the particle does not deform, there will be local plastic flow or **plastic relaxation** in the matrix to relieve these stresses. Because of the high stresses associated with them, Orowan loops are very unstable and are rarely observed. The nature of this plastic

relaxation has been extensively studied for single crystals deformed to low strains, and to a much lesser extent in single crystals or polycrystals deformed to large strains. We are primarily interested here in those aspects of the deformation structures which are relevant to recrystallization, and for further details of the dislocation mechanisms the reader is referred to the reviews of Brown (1985) and Humphreys (1985).

For small particles and low strains, plastic relaxation generally involves the generation of prismatic dislocation loops, which are of lower energy than Orowan loops. These may be prismatic loops of the same Burgers vector as the gliding dislocations (primary prismatic loops) or alternatively, secondary prismatic loops of a different Burgers vector may be generated. In deformed single crystals, rows of primary prismatic loops aligned with the particles are found as seen in figure 2.32. In polycrystals, although aligned rows of loops are not generally observed, there is evidence that prismatic loops are formed at the particles.

At larger strains and larger particles, more complex dislocation structures are formed, and these are often associated with local lattice rotations close to the particles (fig 2.33), and such regions are commonly termed **particle deformation zones.** The form and distribution of such dislocation structures at particles are primarily functions of the strain and the particle size, although other factors such as shape, interface strength and matrix are known to be important (see e.g. Humphreys 1985). The effect of strain and particle size on the relaxation mechanisms in aluminium single crystals is summarised in figure 2.34. The transition from the dislocation structures such as figure 2.32 which are considered as non-rotational or 'laminar plastic flow' to the particle deformation zones such as in figure 2.33, which can be considered to involve 'rotational plastic flow', is difficult to predict theoretically as it is on a scale which is midway between dislocation and continuum mechanics. Brown (1997), using a dislocation plasticity model, has

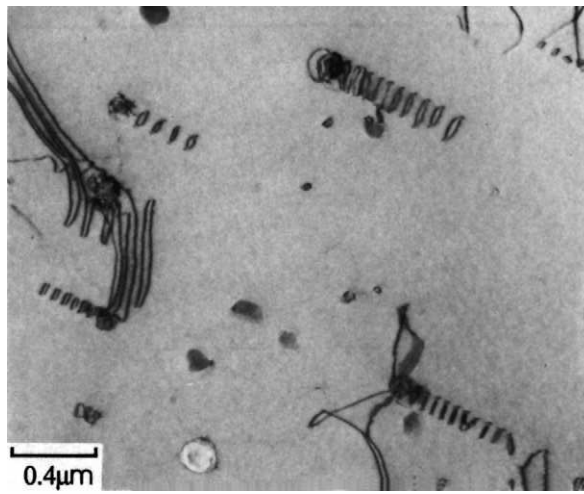

Fig. 2.32. Primary prismatic loops at Al_2O_3 particles in an α-brass crystal, (Humphreys 1985).

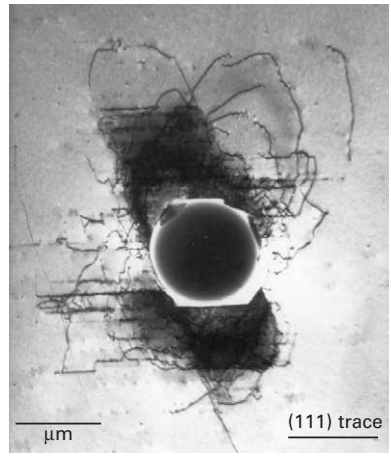

Fig. 2.33. Deformation zones at a silica particle above and below the primary slip plane, (111), in a deformed α-brass crystal. The primary Burgers vector is normal to the page, (Humphreys and Stewart 1972).

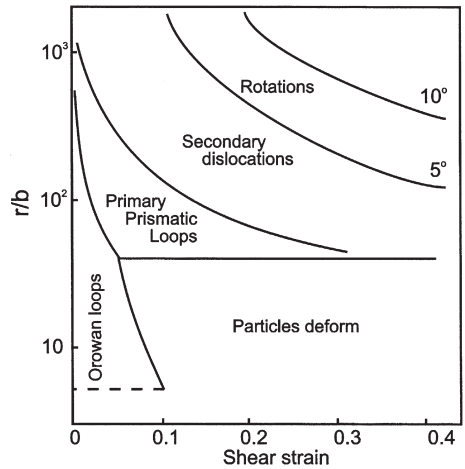

Fig. 2.34. Deformation mechanisms at particles in aluminium as a function of strain and normalised particle radius, (after Humphreys 1979a).

suggested that the transition at a particle of diameter d may occur at a shear strain (s) given by

$$s = \left(\frac{b}{d}\right)^3 \left(\frac{\sqrt{2}\alpha G}{\sigma_f}\right)^2 \tag{2.20}$$

where α is a constant of $\sim$0.5 and σ_f is the friction stress in the matrix.

The deformation zones formed at large particles are of particular interest as they are the source of particle stimulated nucleation of recrystallization (PSN) and may therefore have a strong influence on the grain size and texture after recrystallization.

2.9.4 Deformation zones at particles

Most of the detailed measurements of deformation zones at particles have been made on particle-containing single crystals oriented for single slip, and deformed in tension, although some information about the orientations within the deformation zones has been obtained from single crystals deformed in plane strain compression, and from deformed polycrystals.

2.9.4.1 Single crystals deformed in tension

In particle-containing single crystals of copper and aluminium, oriented for single slip, and deformed in tension (Humphreys 1979a) found that for particles of diameter less than 0.1 μm, deformation zones with local lattice rotations were not formed, and in such cases it was assumed that plastic relaxation occurred by the generation of prismatic loops as discussed above.

At larger particles, local lattice rotations were found to occur about the $<112>$ roller axis perpendicular to both the primary Burgers vector and the primary slip plane normal. The maximum rotation (θ_{max}) which was found to be close to the particle-matrix interface, and to decrease with distance (x) from the particle as shown in figure 2.35, dropped to a level indistinguishable from that of the matrix at distances of the order of the particle diameter ($x \sim d$). The data were found to fit an empirical

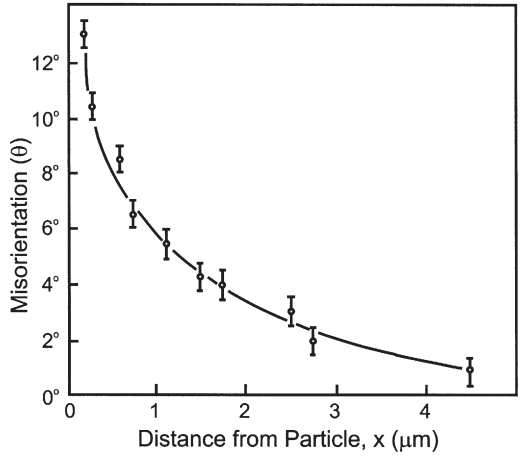

Fig. 2.35. Lattice misorientation at a 3 μm silicon particle in a deformed aluminium crystal as a function of distance from the interface, (Humphreys 1979a).

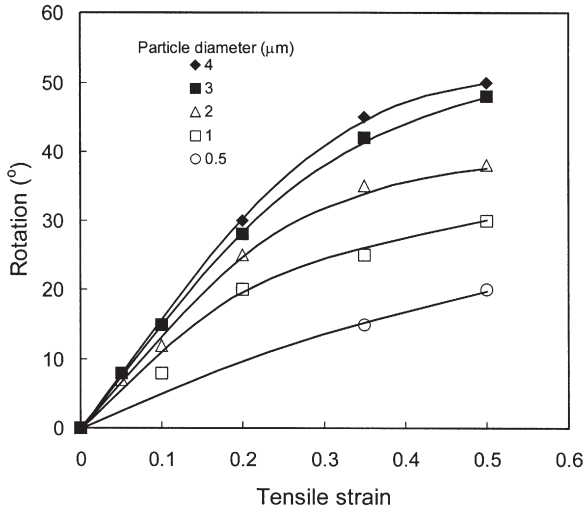

Fig. 2.36. The mean maximum misorientation at particles as a function of strain and particles size, (data from Humphreys 1979a).

equation of the form

$$\tan\theta = \tan\theta_{max}\exp\left(-\frac{c_1 x}{d}\right) \tag{2.21}$$

where c_1 is a constant equal to 1.8.

For particles of diameter greater than ~2.5 μm, θ_{max} was found to be a function only of the shear strain, s, (fig 2.36), indicating that lattice rotations were the only relaxation mechanism. The relationship between θ_{max} and s was of the form

$$\theta_{max} = c_2 \tan^{-1} s \tag{2.22}$$

where c_2 is a constant of the order of unity.

For particles in the size range 0.1 to ~2.5 μm, the maximum misorientation was a function of both strain and particle size as shown in figure 2.36, indicating that plastic relaxation occurred both by the formation of prismatic loops and rotated deformation zones. For such particles, the maximum misorientation (θ'_{max}) was found to fit the empirical equation

$$\theta'_{max} = 0.8\,\theta_{max}(d - 0.1)^{0.2} \tag{2.23}$$

where d is the particle diameter expressed in microns.

For elongated particles, it was found that the maximum misorientation occurred at the ends of the particle.

The detailed shape of the deformation zones described above was not determined, although the rotated regions tend to lie above and below the primary slip plane as seen in figure 2.33. In order to discuss recrystallization of the deformation zones in §9.3, it is convenient to have a semi-quantitative model of the zones, in which we assume that the zone is an 'onion skin' structure of concentric spherical low angle boundaries (fig 9.12). The distribution of dislocations in the deformation zone is directly related to the orientation distribution as given by equation 2.21.

The orientation gradient, $d\theta/dx$, at a distance x from the surface of the particle is given by

$$\frac{d\theta}{dx} = -\frac{c_1 \tan\theta_{max} \cos^2\theta}{d} \exp\left(-\frac{c_1 x}{d}\right) \tag{2.24}$$

and the dislocation density ρ, at distance x, assuming the low angle boundaries to comprise square networks of dislocations, is

$$\rho = \frac{2c_1 \tan\theta_{max} \cos^2\theta}{bd} \exp\left(-\frac{c_1 cx}{d}\right) \tag{2.25}$$

2.9.4.2 Single crystals deformed by plane strain compression or rolling

The microstructures of particle-containing aluminium single crystals of the following orientations, deformed in channel die plane strain compression have been investigated: $\{001\}<110>$ (Humphreys and Ardakani 1994), $\{011\}<100>$ (Ferry and Humphreys 1996b), $\{011\}<01\bar{1}>$ (Ferry and Humphreys 1996c). These have shown the rotations within the particle deformation zone to be related to the operating slip systems. The rotation axes are usually close to the transverse direction (TD), or to a nearby $<112>$ axis (see fig. 9.16a). These results are in agreement with those of the previous section, confirming that the subgrain size was considerably smaller in the deformation zones, that larger misorientations were found at the edges of platelike particles, and that the deformation zone typically extended for a distance of one particle diameter from the particle surface. Later investigations of rolled particle-containing aluminium crystals (Engler et al. 1999, 2001) have produced similar results.

2.9.4.3 Deformed polycrystals

There is little quantitative data for deformation zones in polycrystals mainly because of the severe experimental difficulties inherent in such measurements. The deformation zone in a rolled alloy is generally found to be elongated in the rolling direction as shown schematically in figure 2.37. Regions of highly misoriented small subgrains of diameter <0.1 μm are found close to the particle, but further away, the subgrains are elongated and distorted by the presence of the particle (Humphreys 1977, Hansen and Bay 1981). An example of the microstructure adjacent to large particles after cold rolling to a strain of 3.9, is shown in figure 14.4.

Few systematic studies of misorientations have been made, and it is commonly reported that even after large strains, the misorientation between the matrix and the deformation zone is of the order of 30°–40°, (e.g. Gawne and Higgins 1969, Humphreys 1977, Herbst

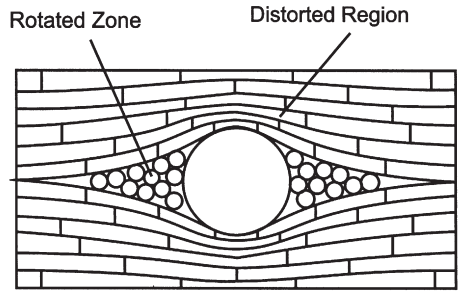

Fig. 2.37. A deformation zone in a rolled polycrystal, (after Porter and Humphreys 1979).

and Huber 1978, Bay and Hansen 1979, Liu et al. 1989). These misorientations were typically measured as **angle-axis pairs,** defined as the minimum angle of rotation (and the rotation axis) necessary to bring the crystals into register (§4.2). Because of the symmetry of cubic crystals, this is not necessarily the same as the **physical misorientation** which has occurred during deformation, and a mean misorientation of $\sim 40^\circ$ would be measured for **randomly** oriented crystals (§4.2). Therefore from such experimental measurements, we can only deduce that the physical misorientations are at least as large as the measured values, but because of the crystal symmetry they could be considerably larger.

A TEM microtexture technique in which the orientation spread within a small volume adjacent to a particle is measured (Humphreys 1983), has been used to investigate the misorientations within deformation zones at particles in polycrystalline aluminium deformed in uniaxial compression (Humphreys and Kalu 1990), and it was found that in many cases more than one deformation zone was formed per particle, and that the magnitude of the rotations increased with both strain and particle size. The recent development of High Resolution Electron Backscatter Diffraction (EBSD) has enabled the size, shape and orientation of deformation zones at particles in rolled polycrystals to be determined, and an example is shown in figure 2.38.

2.9.4.4 Modelling the deformation zone

The formation of a deformation zone at a micron-sized particle in a polycrystal during rolling is a process which occurs at a **scale which is difficult to model successfully.** The process is too complex to be analysed accurately in terms of individual dislocation reactions, whilst larger scale models such as finite element models have not been able to incorporate the subtle fine-scale size-dependent features of the deformation zones. Simple models based on dislocations and crystal plasticity have been proposed by Ashby (1966), Sandström (1980), Ørsund and Nes (1988), Humphreys and Kalu (1990) and Humphreys and Ardakani (1994). For the simplest case, of particles in a crystal deforming by single slip (§2.9.4.1), the best approach is currently the dislocation plasticity model of Brown (1997), which predicts that the misorientation in the deformation zone (θ) decreases with distance (x) from the particle of diameter d as

$$\tan\theta = -\frac{\tan(s)}{2}\ln\left(\frac{d}{x}\right) \tag{2.26}$$

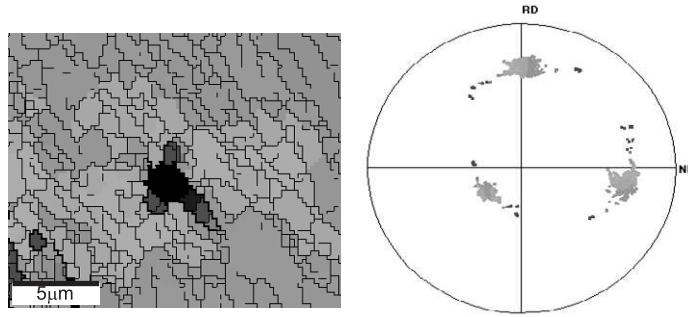

Fig. 2.38. EBSD measurement of misorientations at a 3 μm particle in an aluminium alloy (AA1200), cold rolled 75%. (a) EBSD map showing highly misoriented regions adjacent to the particle. (b) 100 pole figure of the area. The colours used for both map and pole figure represent rotations about the transverse direction (TD), blue in one direction and red in the other, with the matrix orientation green, (courtesy of A.P. Clarke). (See colour plate section).

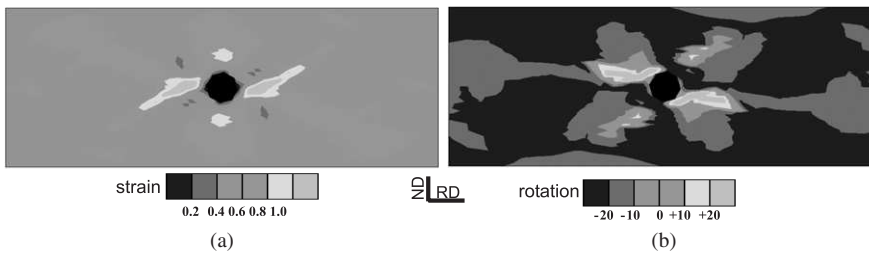

Fig. 2.39. Results of 2-D CPFEM simulation of plane strain deformation of a particle-containing $\{001\} < 110 >$ crystal deformed to a strain of 0.5 in plane strain compression. (a) von Mises effective strain, (b) crystal rotation about the constrained direction, in degrees (TD), (Humphreys and Bate 2002). (See colour plate section).

which gives a reasonable fit to the experimental data of Humphreys (1979a), as does the empirical equation 2.21. However, none of these models make a realistic attempt to predict the shape of the deformation zone.

For more complex situations, such as single crystals or polycrystals deformed in plane strain compression, some success has been achieved by incorporating **crystal plasticity into finite element models (CPFEM)** (Bate 1999). Figures 2.39a and b show the strain and orientation distributions predicted for a crystal of aluminium of initial orientation $\{001\} < 110 >$ deformed to a strain of 0.5, which was the case examined experimentally by Humphreys and Ardakani (1994). There is a good general agreement between the model (fig. 2.39b) and experiment (shown in fig. 2.31c), with the two 'plumes' of material near the particle rotating in the opposite sense to the matrix, toward the complementary 'copper' orientation.

The main drawback of such models is their **lack of a length scale,** i.e., the particles could be of any size, whereas in reality, it is known that there is a strong size effect for smaller particles as shown in figures 2.34 and 2.36. Gradient plasticity has been incorporated into finite element models in order to introduce a length scale (Fleck and Hutchinson 1994, Bassani 2001). However, incorporation of gradient plasticity into the CPFEM modelling of deformation at particles as described above, has been shown to have only a small effect on the results (Humphreys and Bate 2002), and has not predicted the reduction in the extent or magnitude of the deformation zones for small particles, which is found experimentally.

ThisPageIntentionallyLeftBlank

Chapter 3

DEFORMATION TEXTURES

3.1 INTRODUCTION

Many mechanical and physical properties of crystals are anisotropic, and therefore the properties of a polycrystalline aggregate will depend on whether the individual grains or subgrains, which comprise the sample, are randomly oriented or tend to have some preferred crystallographic orientation. The sum of the crystallographic orientations of the crystallites within a polycrystalline aggregate is known as the **texture** of the material. Conventionally, the texture and microstructure of a material have been considered separately. However, as techniques to determine the orientations of microstructure on a local scale (**microtexture**) have been developed as discussed in Appendix 1, the distinction between microstructure and texture has become somewhat blurred, and the orientation and dimensional parameters of the microstructure are often considered together. Nevertheless, because textures require special methods of representation (Appendix 1), it is useful to consider the orientation changes that take place during deformation separately from the microstructural development which was discussed in chapter 2.

The orientation changes that take place during deformation are not random. They are a consequence of the fact that deformation occurs on the most favourably oriented slip or twinning systems and it follows that the deformed metal acquires a preferred orientation or texture. If the metal is subsequently recrystallized, nucleation occurs preferentially in association with specific features of the microstructure, i.e. with regions of particular orientation. The ability of the nucleus to grow may also be influenced by the orientations of adjacent regions in the microstructure. Together these features,

nucleation and growth, ensure that a texture also develops in the recrystallized metal. Such textures are called **recrystallization textures** to distinguish them from the related but quite different **deformation textures** from which they develop. In this chapter we are concerned only with deformation textures and their relationship to microstructure, and recrystallization textures are considered separately in chapter 12. A detailed account of the voluminous, early literature relating to textures of both types is to be found in the text of Wassermann and Grewen (1962) and the review of Dillamore and Roberts (1965). More recent accounts are to be found in the reports of a regular series of international conferences (§1.2.2).

The representation of crystallographic textures is complex. Until recently the standard method of representing textures was by means of **pole figures** (see, for example Barrett and Massalski 1980, Hatherly and Hutchinson 1979, Randle and Engler 2000). Nowadays there is increasing use of **orientation distribution functions (ODFs)** which give a more complete description of the texture. For those unfamiliar with texture analysis, details of the various methods of texture acquisition and representation are given in Appendix 1.

3.2 DEFORMATION TEXTURES IN FACE-CENTRED CUBIC (FCC) METALS

Most of the texture data available in the literature and almost all of the ODF data refers to rolled materials. For this reason the brief account that follows is concerned mainly with rolling textures. The deformation textures of fcc metals are determined primarily by the stacking fault energy (γ_{SFE}). At one extreme, exemplified by aluminium with γ_{SFE} $\sim$170 mJm^{-2} and copper with γ_{SFE} $\sim$80 mJm^{-2}, slip is the deformation mode and the rolling textures, after large reductions, are very similar to that of figure 3.1a. At the other extreme, metals and alloys of low stacking fault energy ($\gamma_{SFE} < 25$ mJm^{-2}), such as 70:30 brass, austenitic stainless steel or silver, develop a quite different texture, which is similar to that of figure 3.1b. The term **texture transition** is widely used to describe the changes that occur over the intermediate range of γ_{SFE}. It is customary to refer to the textures of metals with high values of γ_{SFE} as **pure metal textures** to distinguish them from the **alloy type textures** characteristic of materials with low values of γ_{SFE}.

3.2.1 Pure metal texture

The 100 and 111 pole figures for 95% cold rolled aluminium are shown in figure 3.2 (Grewen and Huber 1978); it is to be noted that the pole figures for rolled copper (fig. 3.1a) are almost identical. Superimposed on the pole figure of figure 3.2 are the ideal orientations, $\{112\}<111>$, $\{110\}<112>$, $\{123\}<412>$, that are commonly used to describe the texture. Nowadays the last of these has been largely replaced by the slightly different orientation $\{123\}<634>$. A number of the common texture components have acquired the simple names and symbols given in table 3.1 which also gives details of the Euler angles of the main texture components of rolled fcc metals in the first subspace.

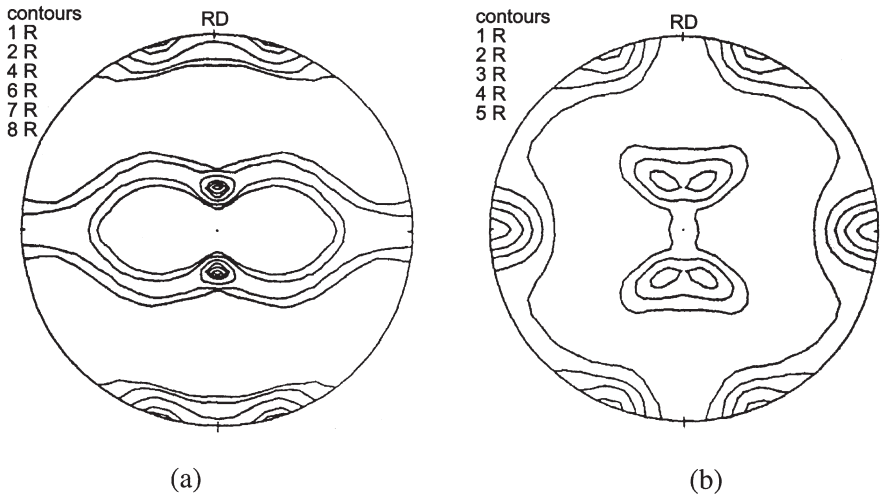

Fig. 3.1. 111 Pole figures of 95% cold rolled fcc metals; (a) copper; (b) 70:30 brass, (Hirsch and Lücke 1988a).

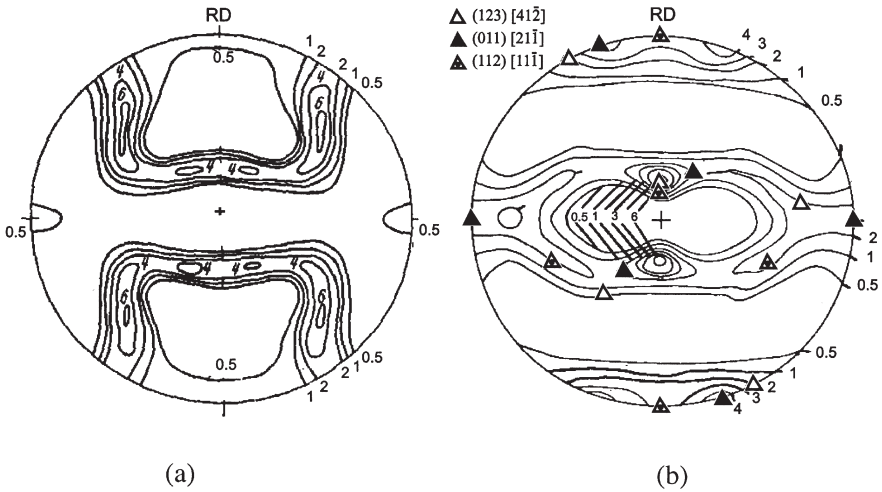

Fig. 3.2. Pole figures of 95% cold rolled aluminium; (a) 100 pole figure; (b) 111 pole figure showing positions of several ideal orientations, (Grewen and Huber 1978).

Examination of figure 3.2 shows that no combination of these orientations corresponds to **all** of the high intensity regions and therefore a description of the texture in terms of these ideal components is inadequate. More information is given by describing the texture as a spread of orientations from $\{112\}<111>$ through $\{123\}<412>$ to $\{110\}<112>$ but such a description does not specify the crystallographic nature of the orientations within the spread.

Table 3.1
Texture components in rolled fcc metals (1st subspace).

Component, symbol	{hkl}	< uvw >	φ_1	Φ	φ_2
Copper, C	112	111	90	35	45
S	123	634	59	37	63
Goss, G	011	100	0	45	90
Brass, B	011	211	35	45	90
Dillamore, D	4,4,11	11,11,8	90	27	45
Cube	001	100	0	0	0

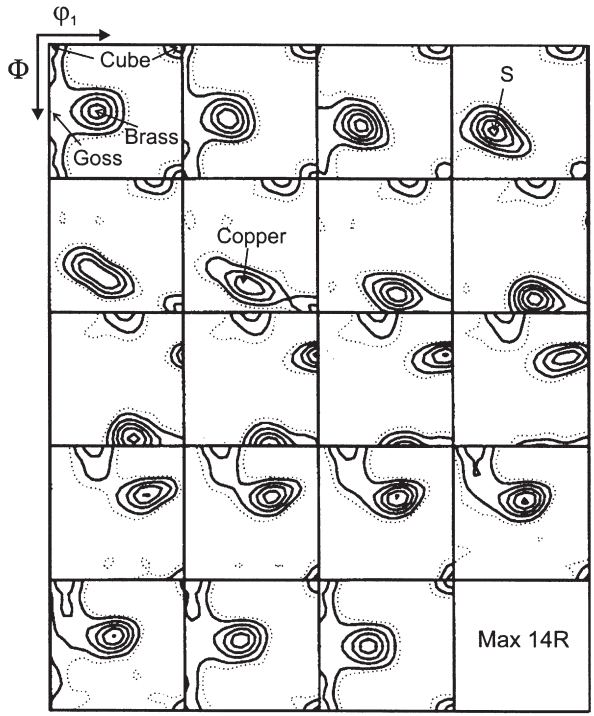

Fig. 3.3. ODF of 90% cold rolled aluminium. The positions of some important orientations are indicated, (Hirsch 1990b).

A better description of the texture is provided by the ODF as shown for 95% cold rolled aluminium in figure 3.3. The first, and most important observation is that the texture is now represented by a continuous **tube** of orientations which runs from {110} < 112 > (B) at $\Phi = 45°$, $\varphi_2 = 90°$, $\varphi_1 = 35°$ through {123} < 634 > (S) at $\Phi = 37°$, $\varphi_2 = 63°$, $\varphi_1 = 59°$ to {112} < 111 > (C) at $\Phi = 35°$, $\varphi_2 = 45°$, $\varphi_1 = 90°$. A schematic representation of the tube is given in figure 3.4 where one of the two branches has been omitted for the sake of

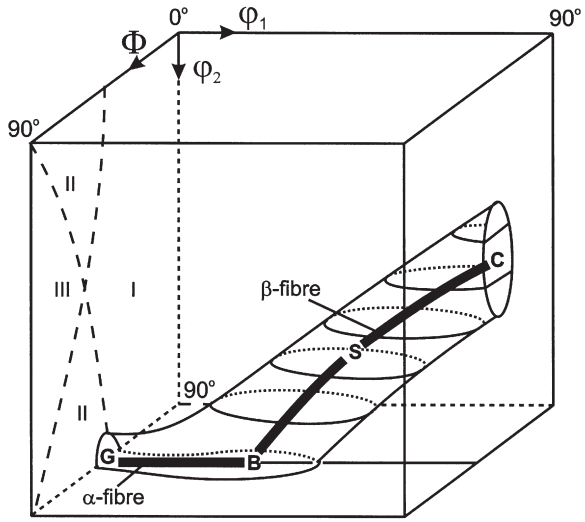

Fig. 3.4. Schematic representation of the fcc rolling texture in the first subspace of three dimensional Euler angle space, (after Hirsch and Lücke 1988a).

clarity. The omitted branch is that observed in the sections $\varphi_2 = 0$–$45°$. The tube shown in figure 3.4 can also be described in terms of its axis or skeleton line. By convention the axis of the tube shown is called the β-fibre and many recent studies of rolled fcc metals report data only in the form of orientation density along this fibre (Hirsch and Lücke 1988a). A second fibre, the α-fibre can be seen in figure 3.4 where it extends from $\{110\} < 001 >$ (G) at $\Phi = 45°$, $\varphi_2 = 90°$, $\varphi_1 = 0°$ to $\{110\} < 112 >$ (B) at $\Phi = 45°$, $\varphi_2 = 90°$, $\varphi_1 = 35°$.

Figure 3.5 shows the orientation density values along the α and β-fibres for rolled copper. For low reductions the variation of intensity along the fibres is small with values of 2–4 times random (xR). The homogeneity along the fibres deteriorates as rolling continues and this occurs first in the α-fibre. By 95% reduction the α tube has almost disappeared from the texture but the β tube is still prominent. If further rolling occurs, deterioration of the β tube begins and pronounced peaks develop. In particular the S component strengthens to become the major component of heavily rolled copper or aluminium. Hirsch and Lücke (1988a) discuss these results in great detail in their analysis of texture development in rolled fcc metals. The essential points are that at low strains the textures are best described by relatively homogeneous orientation tubes, whereas at high strains these degenerate into peaks corresponding to the texture components of table 3.1.

The ODF can also be used to describe the texture quantitatively in terms of a small number of major components. In this technique the volume fractions, M_i, of the selected components are calculated for the appropriate volumes of ODF space. The derived values for 95% cold rolled copper, whose ODF is similar to that of figure 3.3 are given in table 3.2.

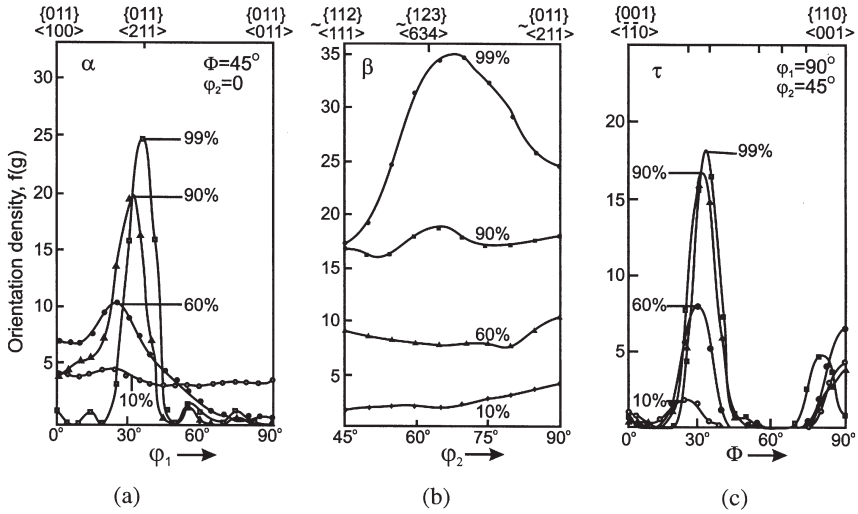

Fig. 3.5. Orientation densities f(g) along the major fibres in 95% cold rolled copper; (a) α-fibre; (b) β-fibre; (c) τ-fibre, (Hirsch and Lücke 1988a).

Table 3.2
Volume percentages of major orientations in 95% cold-rolled copper (Hirsch and Lücke 1988a).

Component	M_i	Component	M_i, %
Copper, C	27	Brass, B	8
S	38	B/S, {168} < 211 >	18
Goss, G	3	Other	6

3.2.2 Alloy texture

The pole figure of figure 3.1b and the ODF of figure 3.6 show that metals with low values of γ_{SFE} develop sharp {110} < 112 > textures. By comparison with metals with high values of γ_{SFE} the α-fibre is much more prominent in the alloy texture (see the $\varphi_2 = 0°$ section at $\Phi = 45°$ and $\varphi_1 = 0$–$35°$). Also present in the alloy texture are two further fibres referred to as the γ and τ-fibres (Hirsch and Lücke 1988a). The τ-fibre is a significant feature of the texture of materials with intermediate values of γ_{SFE} ($\sim$40 mJm^{-2}). All four fibres associated with rolled fcc metals are shown in figure 3.7. The γ-fibre corresponds to volume elements with {111} planes parallel to the rolling plane, i.e. to the aligned deformation twins in the microstructure (see fig. 2.21) and extends from {111} < 112 > at $\Phi = 55°$, $\varphi_2 = 45°$, $\varphi_1 = 30/90°$ to {111} < 110 > at $\Phi = 55°$, $\varphi_2 = 45°$, $\varphi_1 = 0/60°$. The τ-fibre corresponds to orientations having a < 110 > direction parallel to TD and extends along the line $\varphi_1 = 90°$, in the $\varphi_2 = 45°$ section from the {112} < 111 >, C, orientation to the {110} < 001 >, G, orientation at $\Phi = 35°$ and 90° respectively.

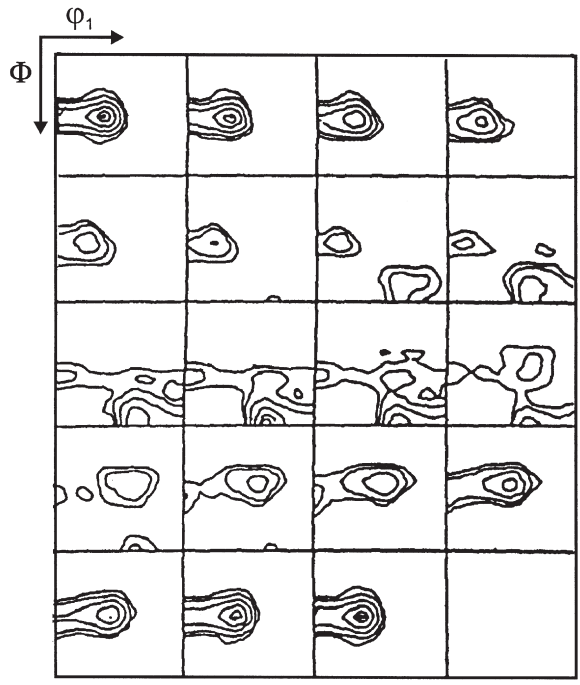

Fig. 3.6. ODF of 95% cold rolled 70:30 brass, (Hirsch and Lücke 1988a).

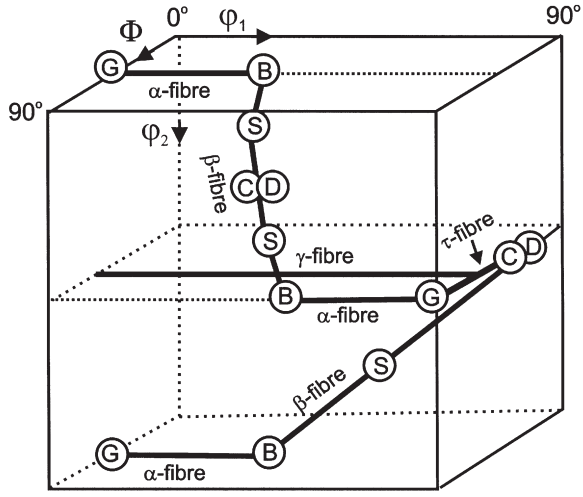

Fig. 3.7. Plots of important fibres in fcc materials, (Hirsch and Lücke 1988b).

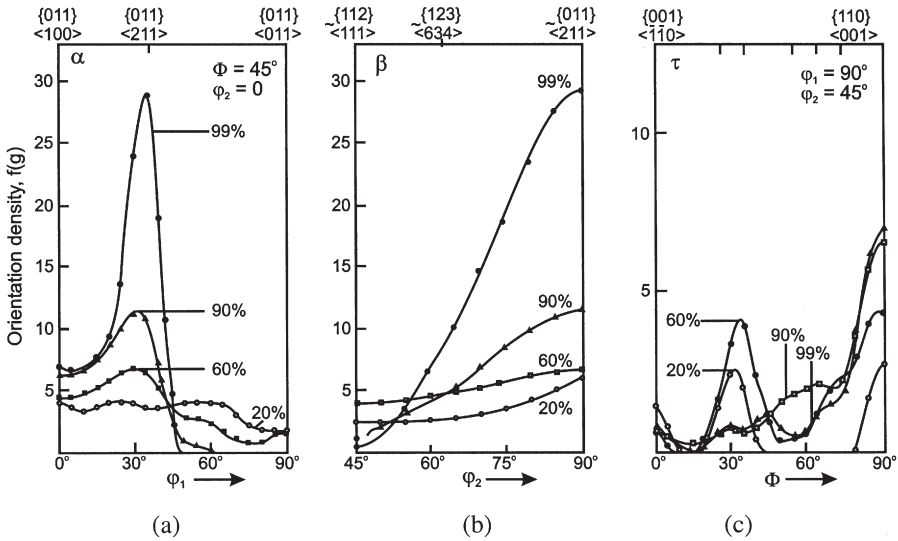

Fig. 3.8. Orientation densities f(g) along the major fibres in 70:30 brass, cold rolled to various reductions; (a) α-fibre; (b) β-fibre; (c) τ-fibre, (Hirsch and Lücke 1988a).

Figure 3.8 shows the intensity of the α, β and τ-fibres for cold rolled 70:30 brass. It may be seen that as deformation proceeds,

- the α tube is retained with the Goss component remaining strong,
- the Brass component strengthens steadily with rolling,
- both the Copper and S components become less significant.

Although the 'alloy' textures discussed above were found in fcc materials of low stacking fault energy, there is good evidence that similar textures occur in alloys of copper and aluminium which do not have low stacking fault energies. Engler (2000) has shown that the addition of manganese to copper, which does not affect the stacking fault energy, leads to a very similar transition in the rolling texture to that discussed above. High strength, age-hardenable aluminium alloys, particularly Al–Li alloys, also develop strong $\{110\}<112>$ rolling textures (Bowen 1990, Lücke and Engler 1990), which are quite different from those of other aluminium alloys, and an example of this is seen in figure 3.16. The reasons for such a texture transition are discussed in §3.7.3.

3.3 DEFORMATION TEXTURES IN BODY-CENTRED CUBIC (BCC) METALS

The deformation textures of bcc metals and alloys are generally more complex than those of fcc metals and despite the overwhelming importance of the steel industry they have been less extensively investigated, much of the research coming from the groups of Hutchinson and Lücke (see, e.g. the reviews of Hutchinson 1984, Raabe and Lücke 1994,

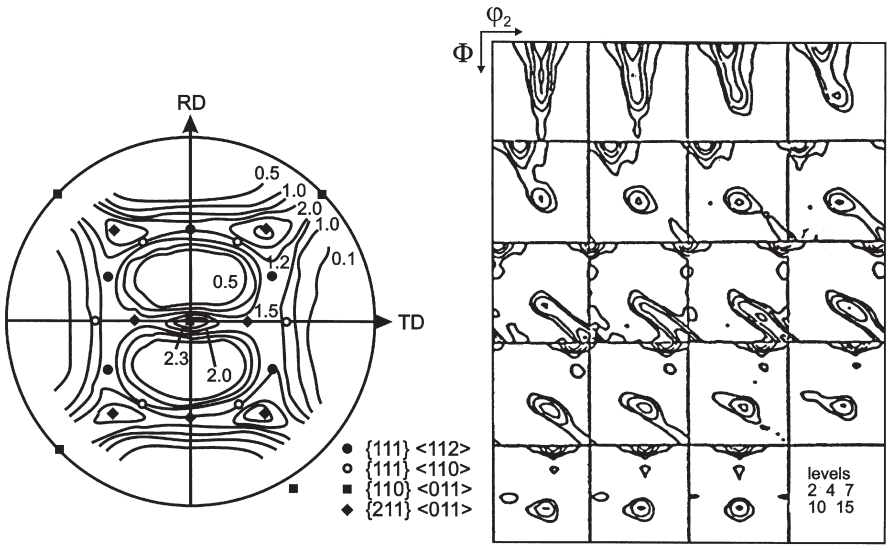

(a) (b)

Fig. 3.9. Rolling texture of 90% cold rolled low carbon steel; (a) 200 pole figure (Hutchinson 1984); (b) ODF (Lücke and Hölscher 1991).

Hutchinson and Ryde 1997). The rolling texture of iron and low carbon steel is largely independent of composition and processing variables and even such major microstructural inhomogeneities as shear bands have little effect. A typical 200 pole figure is shown in figure 3.9a, where the positions of four prominent orientations are highlighted:- $\{111\}<112>$, $\{110\}<011>$, $\{211\}<011>$ and $\{111\}<110>$. Table 3.3 gives the Miller indices and Euler angles of the important bcc rolling texture components.

An ODF from a 90% cold rolled low carbon steel is shown in figure 3.9. The nature of the bcc rolling texture is such that the data are sometimes best displayed by sections at constant values of ϕ_1 rather than ϕ_2 as for fcc metals, and this is done in figure 3.9b. However, in many cases the important information can be portrayed by a single section at $\phi_2 = 45^\circ$ (see table 3.3), and most authors now prefer to discuss the textures of bcc steels solely in terms of this section.

An ODF section at $\phi_2 = 45^\circ$ for a cold rolled interstitial-free (IF) steel is shown in figure 3.10a, and the location of important texture components are shown in figure 3.10b. It may be seen that the main components lie in two bands forming a letter **L**. The upright band represents a partial fibre texture with the $<110>$ fibre axis parallel to the rolling direction, and spreads from $(001)[1\bar{1}0]$ to approximately $(111)[1\bar{1}0]$ as the angle Φ varies from 0^o to $\sim 55^o$. This fibre, which includes the components $\{001\}<110>$, $\{211\}<011>$ and $\{111\}<011>$ is usually known as the **α-fibre**. The horizontal band occurs at $\Phi \sim 55^o$ and spreads through all values of ϕ_1. This **γ-fibre** can be described as a complete fibre texture with $<111>$ parallel to the sheet normal. Reference to figure

Table 3.3
Texture components in rolled bcc metals.

{hkl}	< uvw >	φ_1	Φ	ϕ_2
001	110	45	0	0
211	011	51	66	63
111	011	60	55	45
111	112	90	55	45
11,11,8	4,4,11	90	63	45
110	110	0	90	45

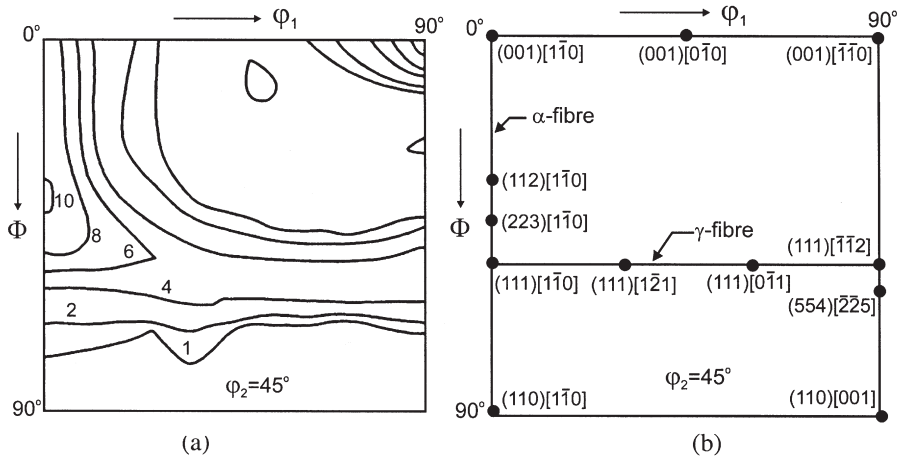

Fig. 3.10. $\phi_2 = 45^{\circ}$ section of ODF for cold rolled IF steel; (a) experimental data, (b) location of important texture components, (Hutchinson and Ryde 1997).

3.10b shows that it contains the two pairs of equivalent orientations (111)[1$\bar{1}$0], (111)[1$\bar{2}$1], (111)[0$\bar{1}$1] and (111)[$\bar{1}\bar{1}$2].

The orientation density along the α-fibre (fig. 3.11) increases fairly uniformly with strain up to ~70% reduction but with further rolling {112} < 110 > and {111} < 110 > become more prominent. The γ-fibre is relatively uniform at reductions up to 80% but thereafter the {111} < 110 > component strengthens.

3.4 DEFORMATION TEXTURES IN CLOSE PACKED HEXAGONAL (CPH) METALS

The information available for cph metals is rather limited, and reviews of the results of experiments and modelling are given by Philippe (1994) and Kocks et al. (1998). It is to

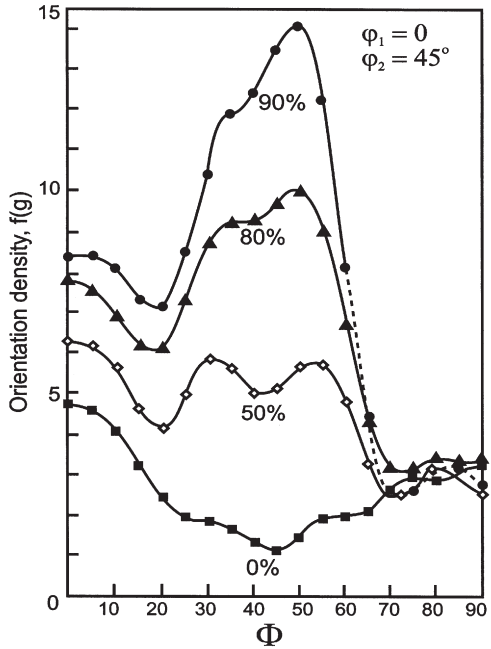

Fig. 3.11. Development of rolling texture in cold rolled, low carbon steel as shown by orientation density along the α-fibre, (von Schlippenbach and Lücke 1984).

be expected from the data given in table 2.5 that the rolling texture will be influenced by the c/a ratio and the particular slip systems that operate (Grewen 1973).

For metals with c/a close to the ideal value of 1.633 the rolling texture has a strong $\{0001\}<1100>$ component which is a direct consequence of the favoured basal plane slip (fig. 3.12a). In zinc and cadmium which have higher c/a ratios the basal planes are tilted some 20–30° about the transverse direction (fig. 3.12b). Such a texture is predictable if basal slip is combined with twinning as shown by the microstructure of deformed cph metals. For the remaining metals with c/a less than ideal, the basal planes are again rotated out of the rolling plane but this time the rotation axis is parallel to RD rather than TD and the tilt angle is 30–40° (fig. 3.12c); the rotation axis is $<1010>$. Several recent investigations using ODF analysis have confirmed the earlier pole figure analyses (Philippe 1994).

In the case of titanium, for example, the major components of the texture after 90% reduction are $\{1214\}<1010>$, $\{1212\}<1010>$ and $\{1210\}<1010>$ all of which have the $<1010>$ RD alignment (Inoue and Inakazu 1988). The first and most important of these can be seen at $\Phi = 37°$, $\varphi_1 = 0°$, $\varphi_2 = 0°$ in figure 3.13. This component develops only at reductions greater than ~50%, and at this level of deformation twinning becomes a major deformation mode. It should be noted that the symmetry of cph metals is such that only values of φ_2 in the range 0–60° need to be shown in the ODF.

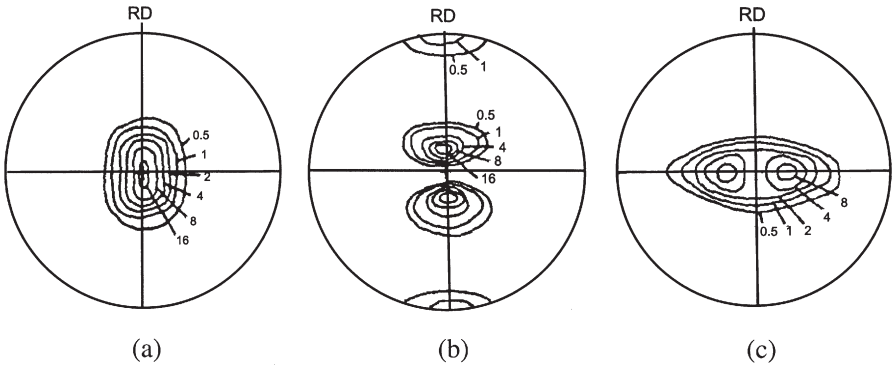

Fig. 3.12. Rolling textures (0002 pole figures) of cold rolled cph metals: (a) magnesium, c/a ideal; (b) zinc, c/a high; (c) titanium c/a low, (Hatherly and Hutchinson 1979).

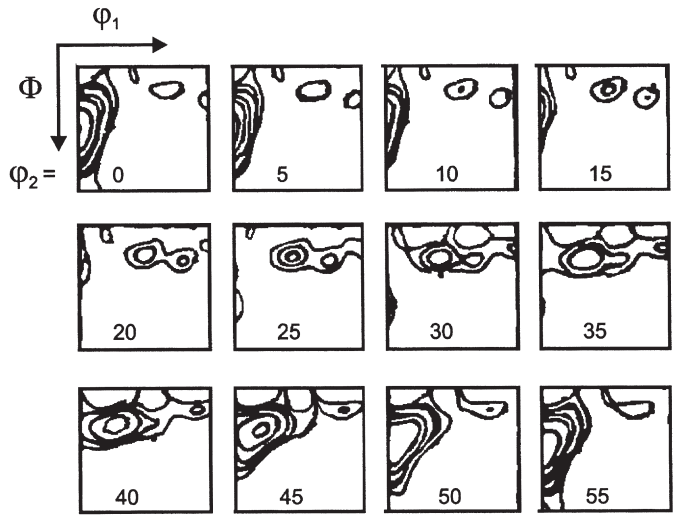

Fig. 3.13. Rolling texture of 90% cold rolled titanium, (Nauer-Gerhardt and Bunge 1988).

3.5 FIBRE TEXTURES

The deformation textures of materials deformed by uniaxial processes such as tension, wire drawing, extrusion etc., are invariably fibre textures and the results are most commonly expressed as inverse pole figures. For fcc metals the texture is described simply as a double fibre texture with $<111>$ and $<100>$ parallel to the axis as shown in figure 3.14. The relative proportions of each are determined primarily by γ_{SFE} and vary from very small amounts of the $<100>$ component in metals like aluminium (γ_{SFE}

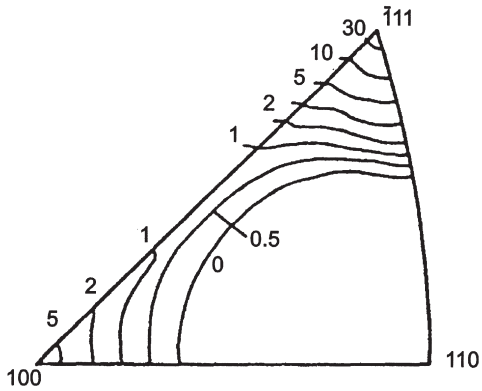

Fig. 3.14. Inverse pole figure for cold drawn aluminium wire, (Hatherly and Hutchinson 1979).

high) to nearly 100% in materials with low values of γ_{SFE} like silver (Schmidt and Wassermann 1927). For bcc metals the fibre axis is always $<110>$ and in cph metals the preferred axis is $<1010>$. Compression textures are somewhat different and almost opposite to those just described. For fcc metals a $<110>$ texture is most frequently reported but in some low γ_{SFE} materials $<111>$ components also form. Most bcc metals develop textures containing mixed $<100>$ and $<111>$ components as shown in figure 2.19b. For a more detailed account of this subject the reader is referred to Barrett and Massalski (1980).

3.6 FACTORS WHICH INFLUENCE TEXTURE DEVELOPMENT

In the previous sections, we have discussed the nature of the textures formed during the deformation of metals. The strength of the textures and the balance between the various texture components will depend on the texture of the starting material, and we will not discuss this further, except to state that very few undeformed metals, either cast or recrystallized have random textures. The strength of the deformation textures increase with deformation as the grains align themselves according to crystal plasticity considerations, and the effect of rolling reduction in fcc and bcc alloys is seen in figures 3.5, 3.8 and 3.11. In addition to strain, there are a number of factors which may affect the deformation texture, and these are briefly considered below.

3.6.1 Rolling geometry and friction

Most analyses of the textures developed on rolling, assume that plane strain conditions apply and that the texture develops uniformly through the thickness of the material. However, this is rarely true in practice, and through-thickness variations are commonly found (e.g. Dillamore and Roberts 1965). The two most important parameters are the

rolling geometry and the friction. Within the roll gap there is a neutral plane in which the relative velocity of the sample and rolls changes direction. Shears of opposite sense are imposed on the deforming material on either side of the neutral plane, and thus material near the sample surface undergoes shear in both directions (redundant shear). The texture gradients though the sheet are greatest for small diameter rolls, small reductions per pass, and for thick sheet.

The texture heterogeneity becomes more pronounced under conditions of high friction. The surface shear textures developed in fcc metals include $\{001\}<110>$ and $\{111\}<110>$ components, and figure 3.15 from the work of Benum et al. (1994), shows the strong $\{001\}<110>$ texture developed near the surface of an aluminium alloy cold rolled without lubricant. With well lubricated rolls, the texture near the surface was similar to the typical rolling texture shown in figure 3.3.

Through-thickness variations in texture are also influenced by the properties of the material, and are particularly severe in high strength aluminium alloys (Bowen 1990), and figure 3.16 shows the variation of texture through the thickness of rolled Al–Li (AA8090) plate.

3.6.2 Deformation temperature

The temperature of deformation may influence the development of texture and, as many industrial rolling operations are carried out warm or hot, this is an important

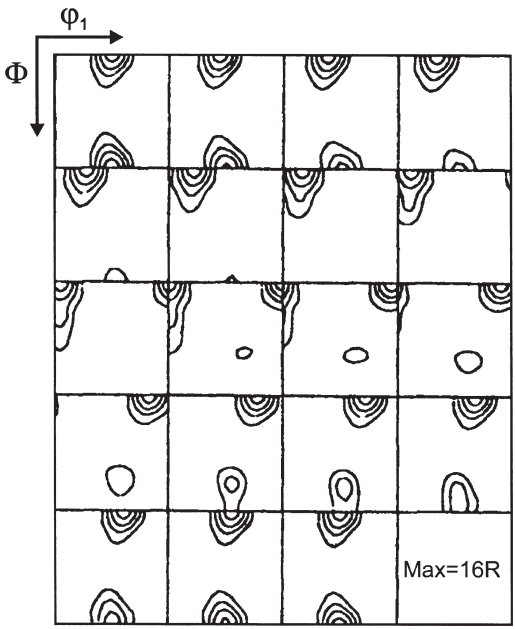

Fig. 3.15. Formation of a shear texture near the surface of an Al–Mn alloy (AA3003), cold rolled with no lubricant, (Benum et al. 1994).

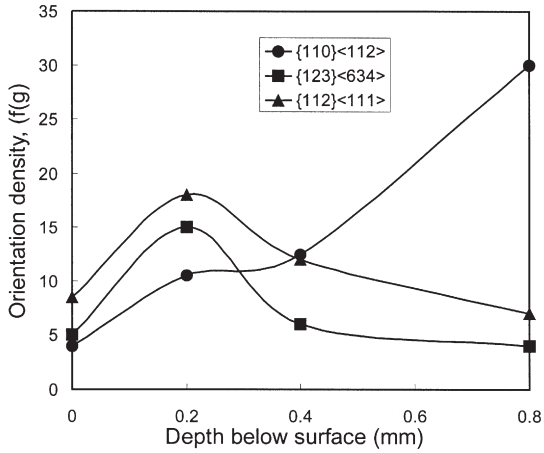

Fig. 3.16. The through-thickness variation of texture in rolled Al–Li (AA8090) 1.6 mm sheet, (Bowen 1990).

parameter. Factors which may alter the texture during rolling at elevated temperatures include an increased rate of dynamic recovery, an increase in the homogeneity of deformation or the operation of different slip systems (Bacroix and Jonas 1988).

In copper, (Hatherly et al. 1986), and aluminium (Bate and Oscarsson 1990) an increase in the Brass texture component is found at elevated temperatures. The increased stability of the Cube texture in aluminium during high temperature deformation is of particular importance and is discussed in §13.2.4.

In ferrite, the presence of interstitial elements has been found to have a strong effect on texture formation during warm rolling. Barnett and Jonas (1997) showed that the interstitials provided a viscous drag on dislocations, resulting in a positive strain rate sensitivity, whereas in interstitial-free (IF) steels, where the interstitial atoms are combined in stable particles (TiN, TiC), this behaviour is not shown. In figure 3.17 the effect of temperature on the strain-rate sensitivity index (**m**) is shown for steels with and without interstitial carbon, and compared with the texture sharpness. For the IF steels, **m** is close to zero at all temperatures, and there is little change in the strength of the texture with temperature. However, the low-carbon steel has a regime of weakened texture around 300°C when **m** is negative, but a much stronger texture above 400°C where **m** is markedly positive. The positive strain rate sensitivity leads to more homogeneous deformation (Barnett 1998), which, in agreement with plasticity models (Hutchinson 1999), results in a sharpened texture.

3.6.3 Grain size

There is disagreement in the early literature as to whether or not grain size has an influence on the deformation texture. Some of this discrepancy has been resolved by the work of Hansen et al. (1985), who found that in aluminium, the textures after rolling

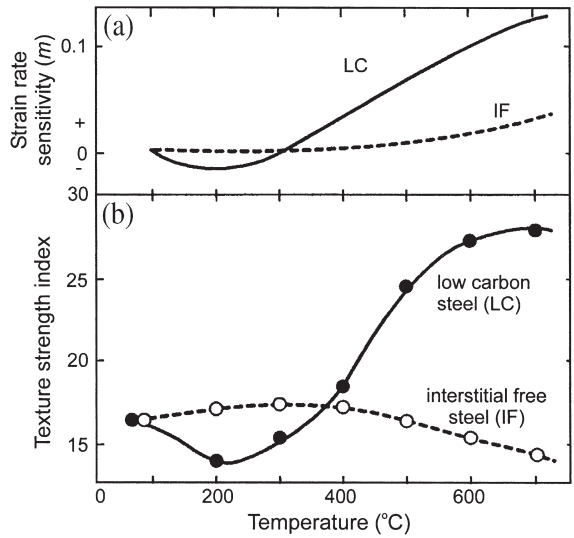

Fig. 3.17. The effect of ferrite rolling temperature for interstitial free (IF) and low-carbon (LC) steels on (a) Strain rate sensitivity index (m), (b) Strength of the deformation texture, (Barnett and Jonas 1997).

reductions larger than 90% were almost unaffected by the initial grain size. However, at intermediate strains, textures developed more slowly in coarse-grained material. It is likely that this effect is caused by the tendency of large-grained material to deform inhomogeneously via deformation banding as discussed in §2.7. Lee and Duggan (1993) have modelled the effect of deformation banding on texture formation and shown that it is expected to retard texture development.

3.6.4 Shear banding

The formation of shear bands (§2.8) may change the deformation texture. In fcc metals of medium to high stacking fault energy, shear bands may occur when there is extensive solid solution hardening, e.g. Al–Mg (Duckham et al. 2001), Cu–Mn (Engler 2000) or if the material contains deformable second-phase particles (Lücke and Engler 1990). Shear bands tend to cause rotation of the material about the transverse direction, and this may lead to changes in intensity of the texture and an intensity redistribution along the β-fibre. In particular, the Copper component is weakened and the Brass and Goss components strengthened by shear banding.

3.6.5 Second-phase particles

The effect of second-phase particles on the deformation texture depends on the size, volume fraction and strength of the particles. A dispersion of small deformable particles generally leads to an increased yield strength but little work hardening (§2.9.1), and in

this situation it is likely that shear banding will occur, with the effect on texture discussed above (Lücke and Engler 1990).

Large (> 1 μm) non-deformable particles are associated with a zone of lattice rotation (§2.9.4), and in these regions the formation of the normal deformation texture is disrupted (§2.9.4). The volume of this zone is comparable to that of the particle, and therefore for conventional alloys, in which the particle volume fraction is typically less than ~0.05, the overall effect on the deformation texture is small. However, in particulate metal matrix composites, which have up to 30% by volume of particles, the volume of the particle deformation zones is significant, and the deformation textures may be very weak (Bowen and Humphreys 1991).

3.7 THEORIES OF DEFORMATION TEXTURE DEVELOPMENT

There have been many attempts to predict the evolution of textures during deformation, based on theories of polycrystalline plasticity. This is a very large and active research field which we cannot attempt to cover in detail, and will only briefly outline some of the approaches. For a clear account of the underlying basic principles, the reader is referred to Reid (1973), and reviews of the application of polycrystalline plasticity theory to texture development are given by Gil Sevillano (1980) and Kocks et al. (1998).

The early theories of polycrystalline plasticity were based on a macroscopic approach in which the grains in a sample deformed in response to the imposed strain according to some overall principles. More recent models have taken account of the interactions between individual grains.

3.7.1 Macroscopic models

3.7.1.1 The Sachs theory

In the earliest of the theories, the lower bound or **Sachs** model (Sachs 1928), it is assumed that each grain deforms independently of its neighbours and on the slip system that has the greatest resolved shear stress, i.e. in precisely the manner of an unconstrained single crystal of the same orientation.

In these circumstances a crystal (grain) deforms on the most highly stressed slip system, and an fcc crystal deformed in uniaxial tension will, for example, rotate until a $<112>$ direction is parallel to the tensile axis, and will rotate towards $<110>$ in compression (see Reid 1973). If sheet rolling is approximated to a biaxial stress state with compression in the normal direction, and tension in the rolling direction, then an unconstrained crystal will rotate to a stable $\{011\}<211>$ orientation (the Brass orientation).

3.7.1.2 The Taylor theory

In the alternative, upper bound or **full constraints** model of **Taylor** (1938) it is assumed that all grains undergo the same shape change, i.e. that of the overall polycrystalline specimen. The strain tensor is always symmetrical and together with the constant volume requirement for plasticity gives five independent strain components. To match

these exactly requires five independent shears, i.e. homogeneous slip on five independent slip systems. In cubic crystals there are a large number of ways of choosing five particular slip systems from all those available (384 combinations in fcc), and Taylor assumed that the combination of slip systems selected for a grain during an increment of deformation was that which achieved the required strain with the minimum internal work. The alternative but equivalent '**maximum work principle**' of Bishop and Hill (1951), suggested that the state of stress required to cause a given increment of strain is the one that maximises the work done on the material by the applied stress.

The stresses required to activate a slip system are expressed by the orientation or **Taylor factor (M)** which is defined as τ_C/σ, where σ is the external stress and τ_C is critical resolved shear stress on each of the slip systems activated. Grains with a low value of **M** are thus favourably oriented for deformation.

On the Taylor model, a bcc grain deforming by $\{110\}<111>$ slip in uniaxial tension is predicted to rotate towards $<110>$ (fig. 2.19a), whereas an fcc crystal will rotate towards either the $<111>$ or $<100>$ orientation depending on the starting orientation. (Note that the predicted strain path is the same as that shown for bcc in figure 2.19a, but with the arrows reversed.)

3.7.1.3 Relaxed constraints models

A later development was the formulation of the so-called **relaxed constraints models** to account for the deformation of non-equiaxed grains (Honeff and Mecking 1978, Kocks and Canova 1981, Hirsch and Lücke 1988b). This term is used in order to distinguish such models, which allow the operation of less than five independent slip systems, from the full constraints model of Taylor and the zero constraints model of Sachs. Like these the relaxed constraints models assume that slip is homogeneous within a grain and that any effects of individual location within the microstructure can be ignored, i.e. all grains of the same orientation behave similarly. It is then assumed that during rolling some shear is permitted in the planes defined by ND-RD (fig. 3.18b), ND-TD (fig. 3.18c) and RD-TD (fig. 3.18d) either separately or in combination. It will be clear from figure 3.18

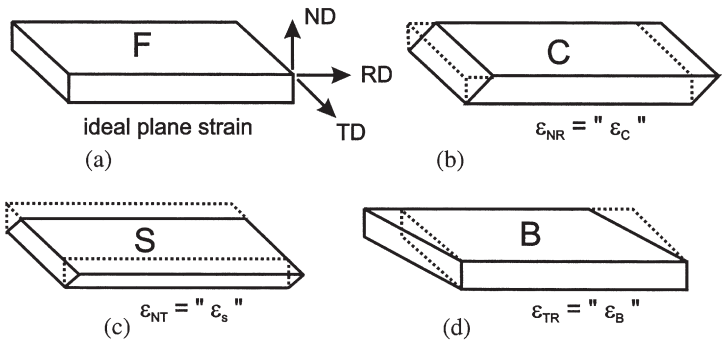

Fig. 3.18. The changes resulting from the deformation of an originally cubic grain under conditions of (a) full constraints, and (b)–(d) relaxed constraints as defined in the text, (after Hirsch and Lücke 1988b).

that the first two of these are possible at reasonably high strains, because any incompatibility between neighbouring grains must be decreasing as the ratio of grain thickness to length or width decreases. The situation is quite different for RD-TD relaxation where the incompatibility between flat grains increases rapidly with strain. The various relaxations lead to different grain shapes and consequently the models are also referred to as lath (ND-RD relaxation) or pancake (combined ND-RD/ND-TD relaxation) type models.

3.7.1.4 Predicting the rolling texture

During plastic deformation, grain orientations change according to the selection of slip systems and the amount of slip occurring on each. Although the orientations of most grains will alter significantly during deformation, some will not, and others will change only slowly. The behaviour depends on both the crystal structure and the geometry of the deformation process. **Stable** orientations are defined as those which stay constant and towards which all neighbouring orientations move during deformation. **Metastable** orientations are those from which orientations move away, but where the rate of orientation change may be very small. These orientations, which are listed in tables 3.1 and 3.3, will therefore dominate the deformation textures. The models discussed in §3.7.1.2 and §3.7.1.3 may be used to make detailed predictions about the formation of deformation textures, and the following summary, for fcc materials, is based on the review by Hirsch and Lücke (1988b).

- The full constraints Taylor model (fig. 3.18a) predicts a stable end orientation of $\{4,4,11\}<11,11,8>$, sometimes referred to as the Dillamore orientation. The stability of other orientations can be accounted for on the basis of the relaxed constraints models discussed in §3.7.1.3.
- If some shear is allowed in the ND-RD plane (fig. 3.18b), then the $\{112\}<111>$, or **Copper** orientation is the predicted stable end orientation.
- If only the ND-TD shear is allowed (fig. 3.18c), the $\{4,4,11\}<11,11,8>$, **Dillamore** orientation and the $\{123\}<634>$, **S** orientation develop.
- If both ND-RD and ND-TD shears occur, i.e. free shear in the rolling plane, then both **Copper** and **S** textures, with a spread along the β-fibre are predicted, which is close to the texture found experimentally for copper and aluminium (figs. 3.3 and 3.5).
- If TD-RD shear is allowed (fig. 3.18d), the texture changes significantly and a strong $\{011\}<211>$, **brass** component, together with other α-fibre components scattered as far as the $\{011\}<100>$ **Goss** texture is predicted, which is close to the observed texture of brass seen in figure 3.6.
- The occurrence of other peaks in the deformation texture, particularly for highly symmetrical **metastable** orientations such as $\{011\}<100>$, **Goss** or $\{001\}<100>$, **Cube**, is due to the fact that although they are unstable, except at the exact ideal orientation, flow away from them is slow, and therefore they persist, often until very large strains.

3.7.1.5 Comparison with experiment

Neither the Sachs nor Taylor theories fully explains the changes taking place during deformation, but there is general agreement that the Taylor model is better.

There is considerable evidence that, particularly in large-grained specimens, the slip behaviour in the centre of a grain is different from that near the grain boundaries (e.g. Hirth 1972). In the boundary regions where the constraint of neighbouring grains is greatest, more slip systems are active than in the centres of the grains, which are less influenced by the boundaries. Therefore in the boundary regions the plasticity approaches Taylor type behaviour, and in the grain centres it may approach Sachs type behaviour (Kocks and Canova 1981, Leffers 1981). An important consequence of such differences in slip activity across a grain is that the different parts of the grain inevitably rotate to different orientations during the deformation and thus deformation bands develop within a grain (§2.7).

The agreement between the experimental textures and those predicted by the Taylor model is quite good for fcc metals with medium to high values of γ_{SFE} and for bcc metals, i.e. for metals that deform by slip. However, theory predicts textures that develop more rapidly and are sharper than those observed in practice. In the case of metals with low values of γ_{SFE} the Taylor model is much less satisfactory and a Sachs type model gives better results (Leffers 1981). In both cases the lack of accuracy has its origin mainly in the failure of the simple theories to recognise the heterogeneities of deformation (§2.4) which contribute so significantly to the microstructure. The texture predictions of the relaxed constraints theories give improved results for high deformations. The incorporation of grain size inhomogeneities such as deformation bands into models of texture development is relatively straightforward (Lee et al. 1993), as these inhomogeneities are directly related to the local crystal plasticity as discussed above.

3.7.2 Recent Models

In attempting to make better predictions of the nature and rate of formation of deformation textures, more recent models abandon the assumption of homogeneous strain, and use a variety of methods to predict textures. Some of these models are listed below.

Self-consistent models. These use a mean field approach in which the deformation of each crystallite is considered individually within the surroundings of a homogeneous matrix (Molinari et al. 1987).

Grain neighbour interaction models. The LAMEL model (Van Houtte et al. 1999) starts from the Taylor model and considers the deformation of pairs of grains.

Crystal plasticity finite element models. These models (e.g. Kalidindi et al. 1992) use finite element methods, but include constitutive crystal plasticity equations. They can take account not only of nearest neighbour grain interactions, but also long-range interactions. However, they are very computer intensive.

3.7.3 The texture transition

One of the earliest attempts to incorporate microstructural heterogeneity was that of Wassermann (1963) who suggested that the texture transition in fcc metals could be

rationalised if the rolling textures of all fcc metals were considered to be similar at low reductions (up to 50%) and to consist of a spread from $\{112\}<111>$ (C) to $\{011\}<211>$ (B). Wassermann argued that in metals of low stacking fault energy, and at larger strains, twinning occurred preferentially in crystals of the former orientation, which were thereby rotated to $\{552\}<115>$. Normal slip would then result in the development of the observed $\{110\}<001>$ orientation. However, this hypothesis has been negated by subsequent TEM observations which show that the twins produced are extremely fine (fig. 2.14) and bear no relationship to the bulk macroscopic features envisaged by Wassermann.

There have been many subsequent attempts to explain the texture transition. Hutchinson et al. (1979) recognized that the very fine twinned structures seen in metals like 70:30 brass were incompatible with Wassermann's concept of bulk twinning and proposed a five-stage pattern of texture development that was more consistent with microstructure:

(i) 0–50% reduction: rotations due to slip produce a copper type texture in both copper and brass
(ii) 40–60% reduction: fine twinning occurs in brass in suitably oriented grains, especially near $\{112\}<111>$
(iii) 50–80% reduction: in twinned volumes slip is restricted to planes parallel to the twin boundaries leading to overshooting and the formation of $\{111\}<uvw>$ components by coupled rotation
(iv) 60–95% reduction: increasing volume of shear bands destroys the $\{111\}<uvw>$ orientations, inhibits components formed by homogeneous deformation and contributes additional components including $\{110\}<001>$
(v) Above 85% reduction: deformation becomes homogeneous leading to sharpening of the stable $\{110\}<112>$ texture.

Later work has cast some doubt on the similarity of the copper and brass textures in the range 0–50% reduction. While the extensive ODF work of Hirsch and Lücke (1988a) supports this view Leffers and Juul Jensen (1988) have shown that the development of the $\{112\}<111>$ component is different in copper and brass (15% Zn) and detailed work by Gryzliecki et al. (1988) on a copper–germanium alloy (8.8% Ge) supports this result. As shown earlier, twinning is certainly present in many of the grains of 70:30 brass at 50% reduction and some texture difference should be expected. There is also a difficulty with the orientation changes occurring in the range 50-80% reduction where the orientation $\{110\}<112>$ has not been considered significant. The more recent studies just mentioned have shown that this component is already developing at an early stage and Lee et al. (1993) have argued that this can be accounted for by progressive deformation banding. The subsequent rapid development of $\{110\}<112>$ at high strains is attributed by Chung et al. (1988) to a homogeneous shear deformation of the fine crystallites formed by shear banding.

More recent work has considered the relationships between texture evolution and deformation mode. El-Danaf et al. (2000) have examined copper and 70:30 brass after deformation by simple and plane strain compression, and by shear. A texture transition occurred at a true strain level of $\sim$0.5 in both compression modes, but not in simple shear at any strain level up to 1.62. Twinning was observed in brass specimens after all three deformation modes. The authors concluded that the onset of the transition is

connected with the rate of strain hardening and the onset of micro-scale, shear banding rather than with twinning and point out that, although twinning leads to increased strain hardening, the more significant factor is the onset of strain localisation and subsequent shear band formation.

The work of Engler (2000) on copper–manganese alloys is particularly relevant to discussion of the transition. In these alloys, the stacking fault energy remains relatively unchanged in the range 0–12 at.% Mn but on rolling a strong texture transition was observed. The rolling textures of 4, 8 and 12% Mn alloys were similar to those found in rolled copper–zinc alloys containing 5, 10 and 30% Zn respectively. Figure 3.19 from this work should be compared with figure 3.8b. Contrary to the work of El-Danaf et al. (2000) a texture transition was not observed after deformation in simple compression. Only limited metallography was reported, but shear band development, similar to that found in copper (fig. 2.9e), was observed at high strain levels in alloys containing 4 and 8% Mn; the frequency of shear banding was less than in the comparable copper–zinc alloys. No evidence of twinning was reported and none would be expected in these alloys. The experimental results were supported by calculations based on a modified Taylor model that takes into consideration material parameters such as work hardening rate and flow stress.

These results cast serious doubt on explanations of the transition based on deformation by twinning and subsequent, extensive shear band formation. Engler proposed that the transition is due to an increase in yield strength, which promotes shear band formation thereby leading to the development of a strong brass component in the texture rather than the copper component, and to the reported existence of short range order in the copper–manganese system (Pfeiler 1988), which would favour planar slip and hence shear band formation and the development of the brass component. The most

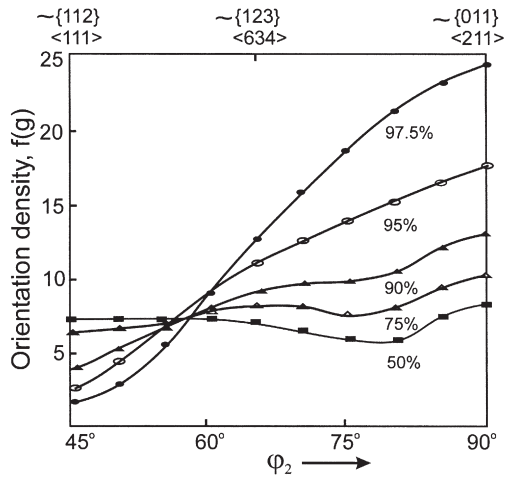

Fig. 3.19. The β-fibre intensity in Cu-8%Mn, cold rolled to various reductions, showing the development of a strong $\{011\}<211>$ texture component, (after Engler, 2000).

significant result, however, is the failure to observe a texture transition after deformation in uniaxial compression. If this is due to a yield stress effect, it would suggest that the transition may be associated only with deformation by plane strain compression and rolling.

Although, as discussed above, the texture transition was first reported in fcc **alloys of low stacking fault energy,** and interpreted in terms of the onset of deformation twinning, it is now known that in addition to these materials, a similar transition occurs in **copper–manganese alloys** as discussed above, and there is also similar texture transition which occurs in **age-hardened aluminium alloys** (§3.2.2), in which planar slip is promoted by the deformable second-phase particles (§2.9.1). **The available evidence therefore suggests that the texture transition in fcc alloys is primarily a result of the onset of planar slip and shear banding.**

ThisPageIntentionallyLeftBlank

Chapter 4

THE STRUCTURE AND ENERGY OF GRAIN BOUNDARIES

4.1 INTRODUCTION

The majority of the book is concerned with the ways in which boundaries separating regions of different crystallographic orientation are formed or are rearranged on annealing either during or after deformation. In this chapter we will introduce some aspects of the structure and properties of these boundaries and in chapter 5 we discuss the migration and the mobility of boundaries. We will concentrate on those aspects of grain boundaries which are most relevant to recovery, recrystallization and grain growth and will not attempt to give a full coverage of the subject. Further information on grain boundaries may be found in the books by Hirth and Lothe (1968), Bollmann (1970), Gleiter and Chalmers (1972), Chadwick and Smith (1976), Balluffi (1980), Wolf and Yip (1992), Sutton and Balluffi (1995) and Gottstein and Shvindlerman (1999).

If we consider a grain boundary such as that shown in figure 4.1, the overall geometry of the boundary is defined by the orientation of the boundary plane AB with respect to one of the two crystals (two degrees of freedom) and by the smallest rotation (θ) required to make the two crystals coincident (three degrees of freedom). There are thus **five macroscopic degrees of freedom** which define the geometry of the boundary. In addition to this, the boundary structure is dependent on three **microscopic degrees of freedom,** which are the rigid body translations parallel and perpendicular to the boundary. The

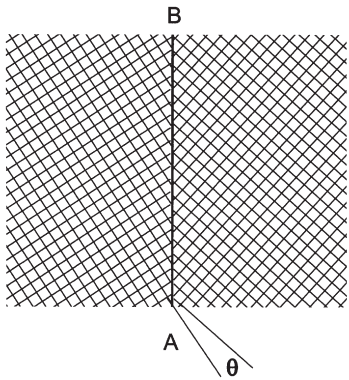

Fig. 4.1. A grain boundary between two crystals misoriented by an angle θ about an axis normal to the page.

structure of the boundary depends also on the local displacements at the atomic level and is influenced by external variables such as temperature and pressure, and internal parameters such as bonding, composition and defect structure. As many of the properties of a grain boundary are dependent on its structure, a knowledge of boundary structure is a necessary prerequisite to understanding its behaviour. Although there has been extensive experimental and theoretical work in this area over the past few decades, there is still a great deal of uncertainty about the structure and properties of boundaries. Most of this work has been carried out for **static boundaries** and there is even more uncertainty over the structure, energy and properties of the **migrating boundaries** which will be important during annealing. In addition, most of the experimental measurements have been made close to the melting temperature. We must therefore recognise that our ability to understand the phenomena of recovery, recrystallization and grain growth may well be limited by our lack of knowledge of the boundaries themselves.

It is convenient to divide grain boundaries into those whose misorientation is greater than a certain angle – **high angle grain boundaries (HAGB),** and those whose misorientation is less than this angle – **low angle grain boundaries (LAGB).** The angle at which the transition from low to high angle boundaries occurs is typically taken as **between 10° and 15°** and is to some extent dependent on what properties of the boundary are of interest. As a very general guide, low angle boundaries are those which can be considered to be composed of arrays of dislocations and whose structure and properties vary as a function of misorientation, whilst high angle boundaries are those whose structure and properties are not generally dependent on the misorientation. However, as discussed below, there are 'special' high angle boundaries which do have characteristic structures and properties, and therefore a crude division of boundaries into these two broad categories must be used with caution.

4.2 THE ORIENTATION RELATIONSHIP BETWEEN GRAINS

As discussed above, there are five macroscopic degrees of freedom needed to define a boundary. However, it is difficult to determine the orientation of the boundary plane

experimentally (§A2.6.3), and in many cases, we neglect it and consider only the three parameters which define the orientation between the two grains adjacent to a boundary. **It should however be recognised that the use of such an incomplete description of a boundary may cause problems in the interpretation of boundary behaviour.**

The relative orientation of two cubic crystals is formally described by the rotation of one crystal which brings it into the same orientation as the other crystal. This may be defined by the rotation matrix

$$R = \begin{bmatrix} a_{11} & a_{12} & a_{13} \\ a_{21} & a_{22} & a_{23} \\ a_{31} & a_{32} & a_{33} \end{bmatrix} \tag{4.1}$$

where a_{ij} are column vectors of direction cosines between the cartesian axes. The sums of the squares of each row and of each column are unity, the dot products between column vectors are zero, so only three independent parameters are involved. The rotation angle (θ) is given by

$$2\cos\theta + 1 = a_{11} + a_{22} + a_{33} \tag{4.2}$$

and the direction of the rotation axis **[uvw]** is given by

$$[(a_{32} - a_{23}), (a_{13} - a_{31}), (a_{21} - a_{12})]. \tag{4.3}$$

In cubic materials, because of the symmetry, the relative orientations of two grains can be described in **24** different ways. In the absence of any special symmetry, it is conventional to describe the rotation by the angle/axis pair associated with the **smallest** misorientation angle, and this is sometimes called the **disorientation.** The range of θ which can occur is therefore limited, and Mackenzie (1958) has shown that the maximum value of θ is 45° for $<100>$, 60° for $<111>$, 60.72° for $<110>$ and a maximum of 62.8° for $<1,1,\sqrt{2}-1>$. For a polycrystal containing grains of random orientation, the distribution of θ is as shown in figure 4.2, with a mean of 40°.

It should be emphasised that the misorientation distribution shown in figure 4.2 will only occur for a random grain assembly, and that a non-random distribution of orientations (i.e. a crystallographic texture) such as is normally found after thermomechanical processing, will alter the misorientation distribution. Examples of this are found in strongly textured material where the large volume of similarly oriented grains results in a large number of low/medium angle boundaries (e.g. figs. 14.3a, and A2.1), and in materials containing large numbers of special boundaries (i.e. the coincidence site boundaries discussed in §4.4.1) as shown in figure 11.8.

Figure 4.2 shows the distribution of misorientation angles regardless of the misorientation axes. However, if proximity to a specific misorientation axis is specified, the distribution may be markedly altered. For example figure 4.3 shows the distribution of misorientation angles predicted for a randomly oriented grain assembly in which only the axes closest to $<110>$ are considered. The curve now shows two peaks, and as demonstrated by Hutchinson et al. (1996), experimental observation of such peaks may

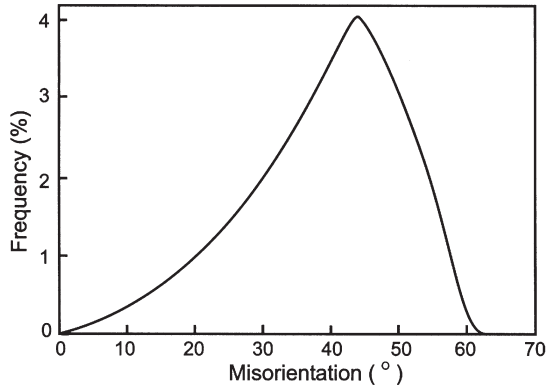

Fig. 4.2. The misorientation distribution for a randomly oriented assembly of grains.

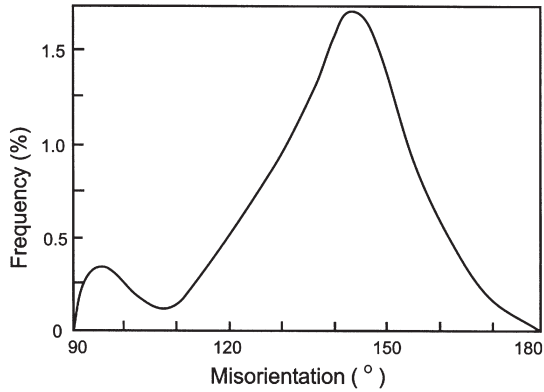

Fig. 4.3. The distribution of misorientation angles for a randomly oriented assembly of grains, for rotation axes closest to $<110>$, (after Hutchinson et al. 1996).

be wrongly interpreted as evidence of a predominance of boundaries with special orientation relationships.

As discussed in appendix 2, the technique of electron backscatter diffraction (EBSD), allows misorientation distributions of the type shown in figure 4.2, sometimes known as **Mackenzie plots,** to be readily obtained. As shown in figure A2.1, such plots provide an excellent 'fingerprint' of the microstructure, and are likely to become extensively used in the future.

The **angle/axis** notation described above is commonly used to express misorientations. However, there are several other ways of expressing the orientation relationship, including Euler angles (**misorientation distribution functions**) and **Rodrigues-Frank space.** The use of these methods for describing absolute orientations is outlined in appendix 1 and will not be further considered here.

4.3 LOW ANGLE GRAIN BOUNDARIES

A low angle boundary or sub-boundary can be represented by an array of dislocations (Burgers 1940, Read and Shockley 1950). The simplest such boundary is the symmetrical **tilt boundary,** shown schematically in figure 4.4 in which the lattices on either side of the boundary are related by a misorientation about an axis which lies in the plane of the boundary. The boundary consists of a wall of parallel edge dislocation aligned perpendicular to the slip plane. Such boundaries were first revealed as arrays of etch pits on the surface of crystals, but are now more commonly observed by transmission electron microscopy.

4.3.1 Tilt boundaries

If the spacing of the dislocations of Burgers vector **b** in the boundary is **h**, then the crystals on either side of the boundary are misoriented by a small angle θ, where

$$\theta \approx \frac{b}{h}. \tag{4.4}$$

The energy of such a boundary γ_s, is given (Read and Shockley 1950) as:

$$\gamma_s = \gamma_0 \theta(A - \ln\theta) \tag{4.5}$$

where $\gamma_0 = Gb/4\pi(1-v)$, $A = 1 + \ln(b/2\pi r_0)$ and r_0 is the radius of the dislocation core, usually taken as between b and 5b.

According to this equation, the energy of a tilt boundary increases with increasing misorientation (decreasing **h**) as shown in figure 4.5. Combining equations 4.4 and 4.5 we note that as θ increases, the energy **per dislocation** decreases as shown in figure 4.5, showing that a material will achieve a lower energy if the same number of dislocations are arranged in fewer, but higher angle boundaries. As shown in figure 4.6, the theory is in good agreement with experimental measurements for small values of θ, although it is

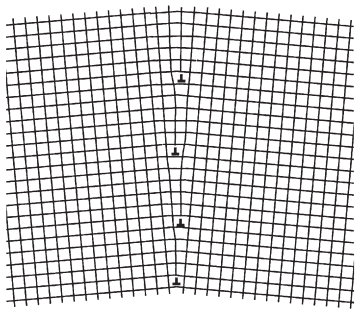

Fig. 4.4. A symmetrical tilt boundary.

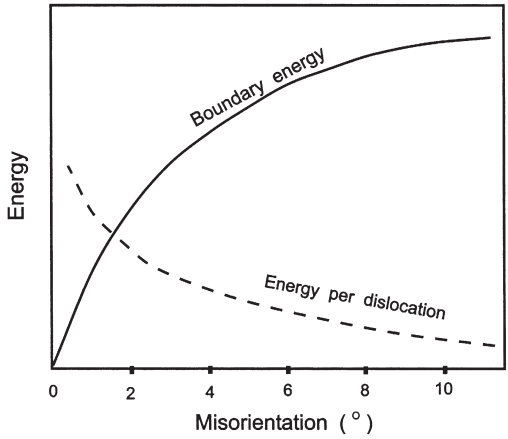

Fig. 4.5. The energy of a tilt boundary and the energy per dislocation as a function of the crystal misorientation.

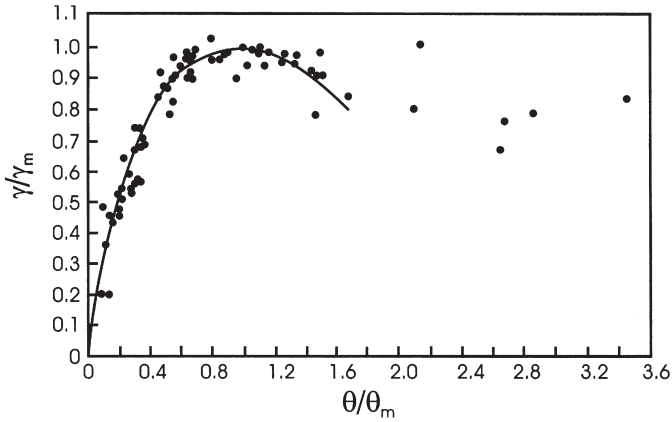

Fig. 4.6. The measured (symbols) and calculated (solid line) energy of low angle tilt boundaries as a function of misorientation, for various metals, (after Read 1953).

unreasonable to use this dislocation model for large misorientations, because when θ exceeds $\sim 15^\circ$, the dislocation cores will overlap, the dislocations lose their identity and the simple dislocation theory on which equation 4.5 is based becomes inappropriate.

It is often convenient (Read 1953) to use equation 4.5 in a form where the boundary energy (γ_s) and misorientation (θ) are normalised with respect to the values of these parameters (γ_m and θ_m) when the boundary becomes a high angle boundary (i.e. $\theta \sim 15^\circ$).

$$\gamma = \gamma_m \frac{\theta}{\theta_m}\left(1 - \ln\frac{\theta}{\theta_m}\right) \tag{4.6}$$

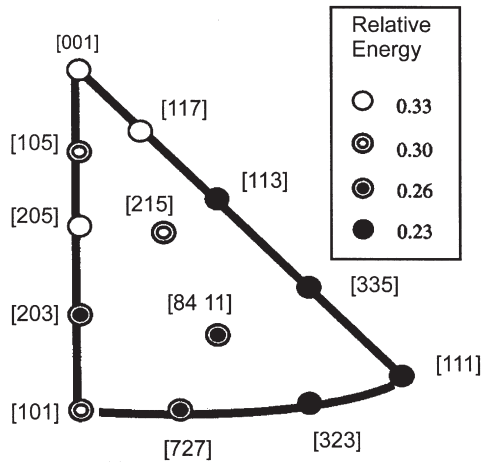

Fig. 4.7. The variation of the energy of low angle grain boundaries with misorientation axis, (after Yang et al. 2001).

Although the Read-Shockley relationship is widely used, there have been very few experimental measurements of the energy of low angle boundaries. However, detailed measurements of triple junction geometry and crystallography in polycrystalline aluminium foils, accompanied by statistical analysis have recently been used to determine boundary energies by Yang et al. (2001). The results show good agreement with the Read–Shockley relationship (equation 4.6). These authors also found a small dependence of the energy of low angle boundaries on the misorientation axis as shown in figure 4.7, with axes close to $<100>$ having the highest energy and those close to $<111>$ the lowest.

4.3.2 Other low angle boundaries

In the more general case, dislocations of two or more Burgers vectors react to form two-dimensional networks whose character depends on the types of dislocation involved. For example a **twist** boundary, which is a boundary separating crystals related by a misorientation about an axis lying perpendicular to the boundary plane, may be formed by two sets of screw dislocations. If the Burgers vectors of the two sets of dislocations are orthogonal then the dislocations do not react strongly and the boundary consists of a square network of dislocations (fig. 4.8a,c). However, if the Burgers vectors are such that the two sets of dislocations react to form dislocations of a third Burgers vector as shown in figure 4.8b,d then a hexagonal network may be formed. If **h** is the spacing of the dislocations in the network the misorientation (θ) is given approximately by equation 4.4. The exact shape of the dislocation network will depend on the angle that the boundary plane makes with the crystals. Further details of the reactions involved in forming low angle grain boundaries may be found in textbooks on dislocation theory (e.g. Friedel 1964, Hirth and Lothe 1982, Hull and Bacon 2001).

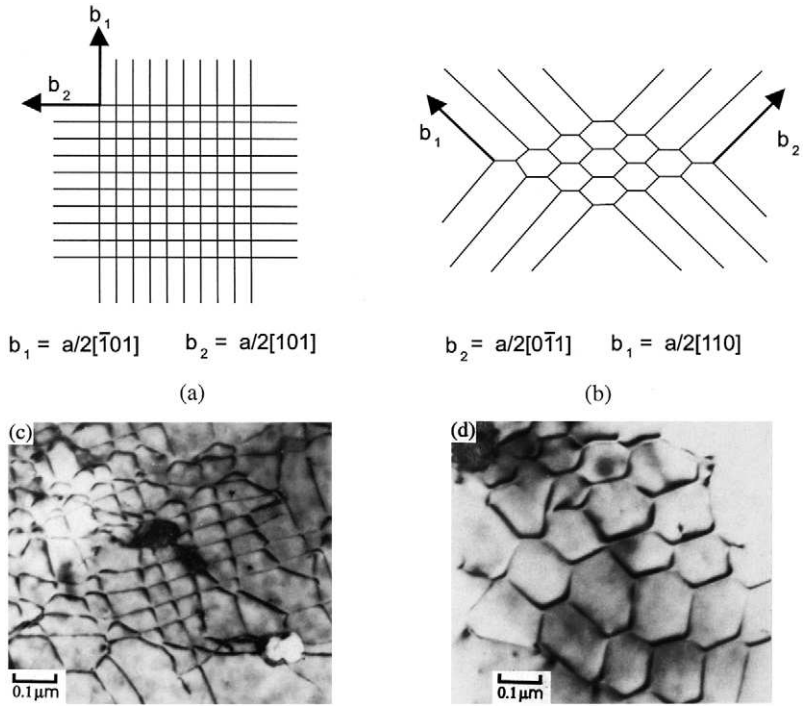

Fig. 4.8. The formation of low angle twist boundaries from dislocation arrays. (a) A square network formed from screw dislocations of orthogonal Burgers vector, (b) A hexagonal network formed by screw dislocations with 120° Burgers vectors, (c) TEM micrograph of a square twist boundary in copper, (Humphreys and Martin 1968), (d) TEM micrograph of a hexagonal twist boundary in copper, (Humphreys and Martin 1968).

4.4 HIGH ANGLE GRAIN BOUNDARIES

Although the structure of low angle grain boundaries is reasonably well understood, much less is known about the structure of high angle grain boundaries. Early theories suggested that the grain boundary consisted of a thin 'amorphous layer' (§1.2.1), but it is now known that these boundaries consist of regions of good and bad matching between the two grains. The concept of the **coincidence site lattice (CSL)** (Kronberg and Wilson 1949), and extensive computer modelling, together with atomic resolution microscopy have in recent years considerably advanced the subject.

4.4.1 The coincidence site lattice

Consider two interpenetrating crystal lattices and translate them so as to bring a lattice point of each into coincidence, as in figure 4.9. If other points in the two lattices coincide

Table 4.1
Rotation axes and angles for coincidence site lattices of Σ < 31.

Σ	θ°_{min}	Axis	Frequency %
1	0	Any	2.28
3	60	< 111 >	1.76
5	36.87	< 100 >	1.23
7	38.21	< 111 >	0.99
9	38.94	< 110 >	1.02
11	50.48	< 110 >	0.75
13a	22.62	< 100 >	0.29
13b	27.80	< 111 >	0.39
15	48.19	< 210 >	0.94
17a	28.07	< 100 >	0.20
17b	61.93	< 221 >	0.39
19a	26.53	< 110 >	0.33
19b	46.83	< 111 >	0.22
21a	21.79	< 111 >	0.19
21b	44.40	< 211 >	0.57
23	40.45	< 311 >	0.50
25a	16.25	< 100 >	0.11
25b	51.68	< 331 >	0.44
27a	31.58	< 110 >	0.20
27b	35.42	< 210 >	0.39
29a	43.61	< 100 >	0.09
29b	46.39	< 221 >	0.35

Data from Mykura 1980. Column 4, lists the frequencies of the occurrence of the boundaries predicted for a random grain assemble (Pan and Adams 1994), using the Brandon criterion.

(the solid circles in fig. 4.9), then these points form the coincident site lattice. The reciprocal of the ratio of CSL sites to lattice sites is denoted by **Σ.** For example in figure 4.9, Σ is seen to be 5. In the general case where there is no simple orientation relationship between the grains, Σ is large and the boundary, which has no special properties, is often referred to as a **random boundary.** However, for certain orientation relationships for which there is a good fit between the grains, Σ is small and this may confer some special properties on the boundary. Good examples of this are the coherent twin (Σ3) boundary shown in figure 4.10, low angle grain boundaries (Σ1), and the high mobility Σ7 boundaries in fcc materials which are discussed in §5.3.2.

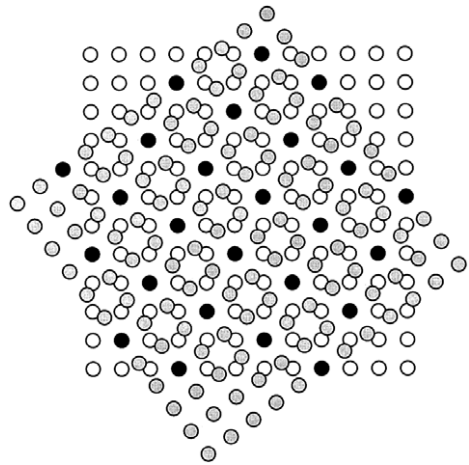

Fig. 4.9. A coincident site lattice (Σ5) formed from two simple cubic lattices rotated by 36.9° about an <001> axis. Filled circles denote sites common to both lattices.

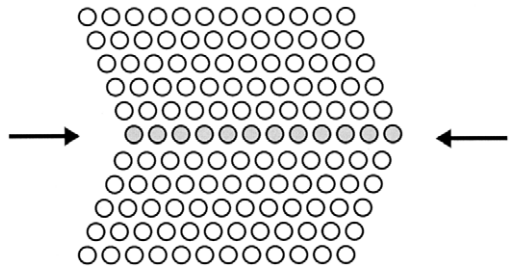

Fig. 4.10. A coherent twin (Σ3) boundary.

The concept of **Grain Boundary Engineering,** in which the properties of the material are improved by processing the material so as to maximise the number of CSL or 'special' boundaries has been developed in recent years (Watanabe 1984), and is discussed in more detail in §11.3.2.3.

Further details of the geometry of CSL boundaries and extensive tables of CSL relationships may be found in Brandon et al. (1964), Grimmer et al. (1974), Mykura (1980) and Warrington (1980). Table 4.1 shows the relationship between Σ and the angle/axis rotation for boundaries up to and including Σ29.

4.4.2 The structure of high angle boundaries

The atomic structure at the grain boundary is determined by relaxation of the atoms, which is dependent on the nature of the atomic bonding forces, and there has been

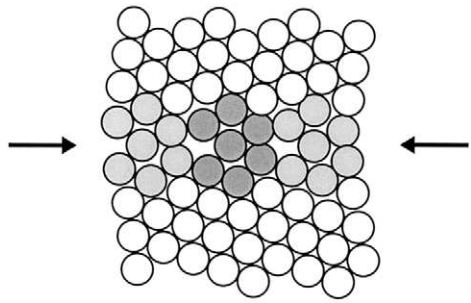

Fig. 4.11. The repeating structural units in a special grain boundary, (after Gleiter 1971).

extensive computer simulation of these structures (e.g. Gleiter 1971, Weins 1972, Vitek et al. 1980, Balluffi 1982, Wolf and Merkle 1992). It is predicted that a high degree of atomic-level coherency is maintained across the boundary and that regular, well defined **structural units** are formed. In the boundary of figure 4.11, the repeating structural units are shaded.

The CSL is a geometric relationship and any deviation from the exact coincidence relationship discussed above will destroy the CSL. However, even in this situation the boundary structure can be maintained by introducing **grain boundary dislocations** which can locally accommodate the mismatch in much the same way as dislocations preserve the lattice in low angle ($\Sigma 1$) grain boundaries. The Burgers vector of the boundary dislocations can be much smaller than a lattice vector. It is also predicted (King and Smith 1980) that some grain boundary dislocations are associated with **steps** in the boundary. These boundary defects are of importance in the mobility of boundaries and are discussed further in §5.4.1.3.

The structure of grain boundaries has been extensively investigated by high resolution electron microscopy and other techniques (e.g. Gronski 1980, Pond 1980, Sass and Bristowe 1980, Krakow and Smith 1987, Seidman 1992, Wolf and Merkle 1992). The experimental observations have broadly confirmed the computer calculations and show that although the CSL is generally lost during the atomic relaxation at the boundaries, the periodicity of the boundary structure is retained by a network of grain boundary dislocations.

A CSL boundary which deviates from the exact relationship by an angle $\Delta\theta$ but in which the structure is maintained by an array of grain boundary dislocations may still possess the special properties appropriate to the CSL boundary, and it is therefore useful to define $\Delta\theta$. As $\Delta\theta$ increases, the spacing of the boundary dislocations decreases (equation 4.4) and the limiting value of $\Delta\theta$ will be reached when the dislocation cores overlap. The angular deviation limit will be related to the periodicity of the boundary, and is often taken as the **Brandon criterion** (Brandon 1966).

$$\Delta\theta \leq 15\Sigma^{-1/2} \tag{4.7}$$

Observations of discrete grain boundary dislocations and measurements of the properties of special boundaries (see e.g. Palumbo and Aust 1992, Randle 1996) suggest that this criterion is too lax and that a better limit is

$$\Delta\theta \leq 15\Sigma^{-5/6}. \tag{4.8}$$

4.4.3 The energy of high angle boundaries

On the basis of the structural models outlined above, it might be expected that the energy of the boundary would be a minimum for an exact coincidence relationship and that it would increase as the orientation deviated from this, due to the energy of the network of accommodating boundary dislocations. However, the correlation between the **geometry** and the **energy** of a boundary is more complicated than this

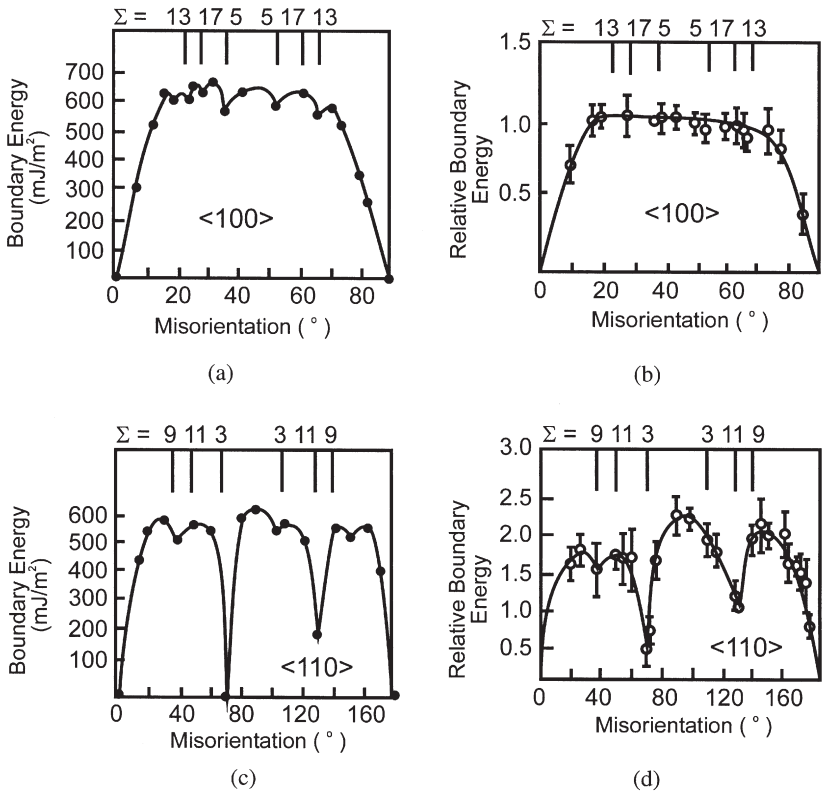

Fig. 4.12. The computed (a) and (c) and measured (b) and (d) energies at 650°C for symmetrical <100> and <110> tilt boundaries in aluminium, (Hasson and Goux 1971).

(Goodhew 1980) as is illustrated by figure 4.12 which shows a comparison of the measured and calculated energies of symmetrical tilt boundaries in aluminium. It can be seen that low energy cusps are found only for the $\Sigma 3$ (coherent twin) and $\Sigma 11$ boundaries and that the predicted cusps for $\Sigma 5$ and $\Sigma 9$ are not detected. However, more recent measurements of boundary energies in high purity metals (e.g. Miura et al. 1990, Palumbo and Aust 1990) have found evidence for more low energy special boundaries than were found in earlier work.

The experimental measurements of boundary energy have been reviewed by Palumbo and Aust (1992). It is suggested that the lack of low energy cusps may in some cases be due to an insensitivity in the measurement technique and in other cases be due to small amounts of impurity. There is evidence that the energy and presumably the structure of high angle boundaries is affected by impurity segregation. Measurements of boundary energy in Ag–Au and Cu–Pb (Gleiter 1970a, Sauter et al. 1977) suggest that with increasing segregation, the energy of special grain boundaries tends towards that of random boundaries as shown schematically in figure 4.13, and more recent experiments (Palumbo and Aust 1992) have confirmed this trend.

Sutton and Balluffi (1987) concluded from a survey of the experimental measurements that there is no simple relationship between the energy of a boundary and the overall **geometry** of the boundary as defined by the macroscopic degrees of freedom, and that parameters such as a low value of Σ were not necessarily indicative of a low energy. It is likely that the boundary energy is determined primarily by the **microscopic** structure of the boundary and that atomic bonding plays an important role. Computer simulations (Smith et al. 1980, Wolf and Merkle 1992) suggest that the local **volume expansion** or **free volume** associated with a boundary is important, and the latter authors predict a linear relationship between boundary energy and volume expansion.

Some caution is however needed in interpreting the experimental measurements of boundary energy and applying these to the annealing processes considered later in this

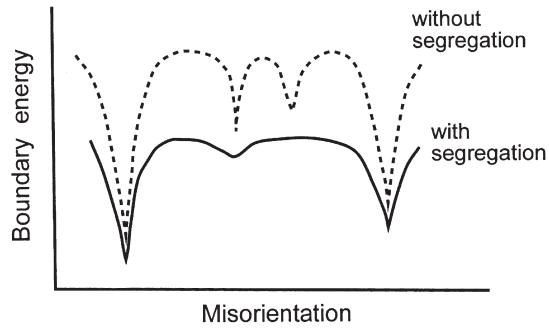

Fig. 4.13. Schematic diagram showing the changes in the energy versus misorientation relationship due to solute atoms, with and without segregation at the boundaries, (Sauter et al. 1977).

Table 4.2
Measured grain boundary energies (mJm^{-2}) (Data from Murr 1975).

Material	High angle grain boundary energy	Coherent twin boundary energy	Incoherent twin boundary energy
Ag	375	8	126
Al	324	75	—
Au	378	15	—
Cu	625	24	498
Cu–30 wt% Zn	595	14	—
Fe (γ)	756	—	—
Fe–3 wt% Si	617	—	—
Stainless steel (304)	835	19	209
Ni	866	43	—
Sn	164	—	—
Zn	340	—	—

book, because such measurements are normally made at very high homologous temperatures in order for equilibrium to be achieved. There is evidence both from experiments (Gleiter and Chalmers 1972, Goodhew 1980, Shvindlerman and Straumal 1985, Rabkin et al. 1991, Sutton and Balluffi 1995, Gottstein and Shvindlerman 1999), and molecular dynamic simulations (Wolf 2001) that some special boundaries may exhibit a **phase transition** at very high temperatures, and that this may involve either a transformation to a different ordered structure or to a liquid-like structure. Such transitions will have significant effects on the boundary energies and on other properties such as diffusion and mobility, as is further discussed in §5.3.1.

It is to be expected that the structure and hence the energy of a special boundary will be dependent on the actual plane of the boundary, as demonstrated by Lojkowski et al. (1988). As shown in table 4.2, the energy of the $\Sigma 3$ coherent twin boundary is much smaller than that of the non-coherent boundary.

4.5 THE TOPOLOGY OF BOUNDARIES AND GRAINS

In addition to the structure and properties of individual grain boundaries we need to be aware of the arrangements of boundaries within a material. As boundaries are non-equilibrium defects, a single-phase material is in its most thermodynamically stable state when all boundaries are removed. This is not often achieved and much of this book is devoted to a discussion of the processes by which high and low angle boundaries are eliminated or rearranged into metastable configurations. In this section we consider the nature of these metastable arrangements of boundaries.

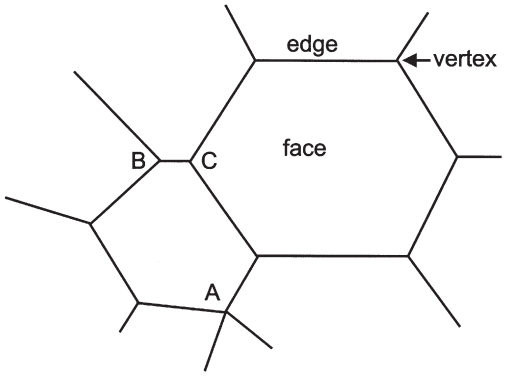

Fig. 4.14. A 2-D section of a grain structure. The 4-rayed vertex at **A** will tend to decompose into two 3-rayed vertices such as **B** and **C**.

C.S. Smith set out the topological requirements of space-filling and the role of boundary tensions in his classic paper of 1952 and these have been reviewed by Atkinson (1988). In both 2-D and 3-D, the microstructure consists of **vertices** joined by **edges** or **sides** which surround **faces** as shown schematically in figure 4.14. In the 3-D case, the faces surround **cells** or **grains.** The cells, faces, edges and vertices of any cellular structure obey the conservation law of equation 4.9, known as **Euler's equation,** provided that the face or cell at infinity is not counted.

$$\begin{aligned} F - E + V &= 1 \text{ (2-D plane)} \\ -C + F - E + V &= 1 \text{ (3-D Euclidean space)} \end{aligned} \tag{4.9}$$

where **C** is the number of cells, **E** edges, **F** faces and **V** vertices.

The number of edges joined to a given vertex is its coordination number **z.** For topologically stable structures, $z = 3$ in 2-D and $z = 4$ in 3-D. Thus in 2-D, a 4-rayed vertex such as that shown at A in figure 4.14 will be unstable and will decompose to two 3-rayed vertices such as B and C.

4.5.1 Two-dimensional microstructures

In a two-dimensional microstructure, the material will be divided into grains or subgrains separated by boundaries and, if boundaries are mobile, a local mechanical equilibrium will be established at the vertices of grains. Consider the three grains 1, 2 and 3 shown in figure 4.15. The boundaries have specific energies γ_{12}, γ_{13}, and γ_{23}, and at equilibrium these energies are equivalent to boundary tensions per unit length. For the three boundaries of figure 4.15 the stable condition is

$$\frac{\gamma_{12}}{\sin\alpha_3} = \frac{\gamma_{13}}{\sin\alpha_2} = \frac{\gamma_{23}}{\sin\alpha_1} \tag{4.10}$$

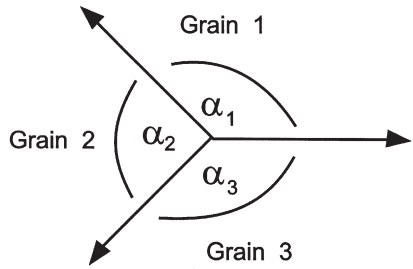

Fig. 4.15. The forces at a boundary triple point.

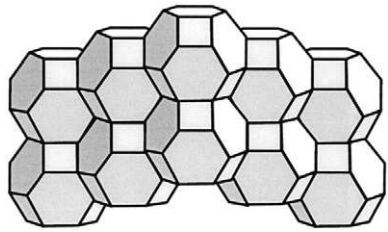

Fig. 4.16. Body centred cubic packing of truncated octahedra, (after Smith 1952).

If all boundaries have the same energy, then equation 4.10 shows that the three grains will meet at angles of 120°. In this situation an array of equal sized hexagonal grains would be stable. Whatever the actual arrangement of the grains in a two-dimensional microstructure, it follows from equation 4.9 that if $z = 3$, the mean number of sides per grain or cell is 6.

4.5.2 Three-dimensional microstructures

It has been shown (Smith 1952) that there is no three-dimensional plane-faced polyhedron which, when repeated, can simultaneously completely fill space and balance the boundary tensions. Truncated octahedra stacked in a bcc arrangement as shown in figure 4.16 come close, filling the space but not having the correct angles to balance the boundary forces. The **Kelvin tetrakaidecahedron,** figure 4.17, which has doubly curved boundary surfaces satisfies both conditions.

Polycrystalline materials are usually examined on a random planar section and therefore sectioning effects will mean that the angles measured on the microstructure will not necessarily be the true boundary angles. However, in microstructures of well annealed single-phase materials, the sectioned grains often approximate to hexagons, and it has been shown (Smith 1948) that the distribution of measured angles is Gaussian, peaking at the true angle. Figure 4.18 shows some measurements for high angle grain

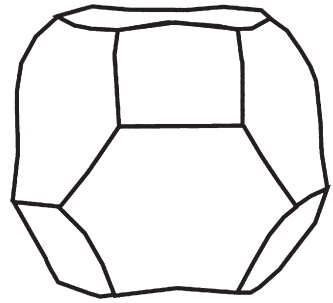

Fig. 4.17. The Kelvin tetrakaidecahedron.

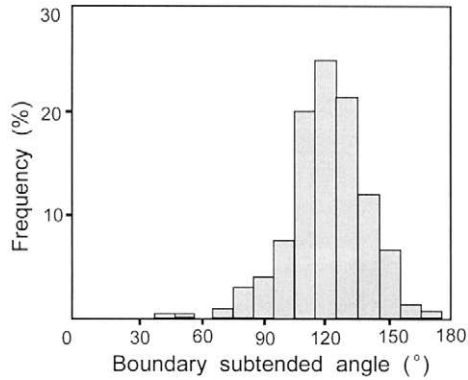

Fig. 4.18. The frequency of grain boundary angles for high energy boundaries in α-brass, (after Smith 1948).

boundaries in annealed α-brass. It may be seen that the data peak at 120° which is the equilibrium angle.

If, as is usually the case, the boundary energies are not equal, the regular geometric structures discussed above will not be stable. An example of this is the microstructure of recrystallized α-brass, shown in figure 7.36, which contains both normal or 'random' high angle boundaries and low energy $\Sigma 3$ coherent twins. The lower energy of the twin boundaries is apparent from the angles, little larger than 90° which they make with the random high angle boundaries at **A.** This should be compared with the angles at the triple point **B** involving only high energy boundaries. For similar reasons, low angle grain boundaries whose energies are strongly dependent on misorientation (fig. 4.6) are rarely arranged at 120° to each other as seen in the recovered microstructure shown in figure 6.21.

The instability resulting from the interaction between the space-filling requirements and the boundary tensions, provides the driving pressure for the growth of subgrains and grains which are discussed in later chapters.

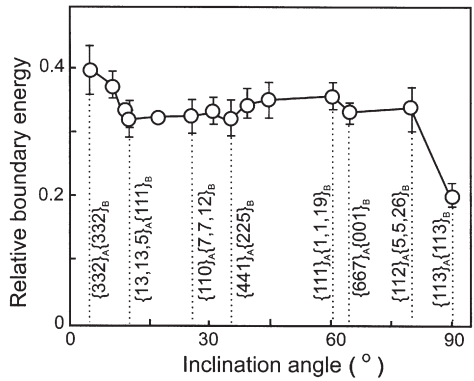

Fig. 4.19. The relative boundary energy for asymmetric [110] Σ11 tilt boundaries in copper, as a function of boundary inclination, (after Goukon et al. 2000).

4.5.3 Grain boundary facets

The example of Σ3 twin boundaries discussed above and shown in figure 7.36, is an extreme example of grain boundaries developing facets. Faceting of grain boundaries has long been known to occur in many metals (see e.g. Sutton and Balluffi 1995, Gottstein and Shvindlerman 1999). In order for a boundary to be facetted spontaneously, the decrease in the total boundary energy must overcome the increase in the total boundary area. Faceting is therefore only likely to occur under conditions when the boundary energy depends strongly on the boundary plane, and the most common situation is for low energy CSL boundaries. It is found that the faceting behaviour of a particular boundary may be strongly dependent on the impurity level (Ference and Balluffi 1988), and on the temperature (Hsieh and Balluffi 1989). Figure 4.19 shows the effect of boundary inclination angle on the relative energies of asymmetric Σ11 {110] boundaries in copper (Goukon et al. 2000) and this has been found to correlate well with the faceting behaviour. Faceting of the boundaries of recrystallizing grains is also sometimes observed (§5.3.2.2), and an example is seen in figure 5.16.

4.5.4 Boundary connectivity

The importance of non-random distribution of grain **orientations** or texture is widely recognised and discussed in detail in chapters 3 and 12. However, it has also been suggested that the non-random spatial distribution of grain **misorientations** may also be important, particularly for CSL boundaries. If such boundaries have values of properties such as strength or diffusivity which are markedly different from the other boundaries, then clustering effects and their linking or **connectivity** may have an influence on the chemical, physical or mechanical properties of the material (Watanabe 1994), and such effects are an important consideration in **grain boundary engineering** (§11.3.2.3).

4.5.5 Triple junctions

Although in this chapter we are mainly concerned with the properties of the grain faces or boundaries, there is evidence that the properties of the vertices or **triple junctions** may play a role in microstructural evolution and have an influence on grain growth and this is considered in §5.5.

4.6 THE INTERACTION OF SECOND-PHASE PARTICLES WITH BOUNDARIES

A dispersion of particles will exert a retarding force or pressure on a low angle or high angle grain boundary and this may have a profound effect on the processes of recovery, recrystallization and grain growth. The effect is known as **Zener drag** after the original analysis by Zener which was published by Smith (1948). The magnitude of this interaction depends the nature of the particle and interface, and the shape, size, spacing and volume fraction of the particles. The definitions of the parameters of a second phase distribution are given in appendix 2.8.

4.6.1 The drag force exerted by a single particle

4.6.1.1 General considerations

Let us consider first, the interaction of a boundary of specific energy γ with a spherical particle of radius **r** which has an incoherent interface.

If the boundary meets the particle at an angle β as shown in figure 4.20 then the restraining force on the boundary is:

$$F = 2\pi r\gamma \cos\beta \sin\beta \tag{4.11}$$

The maximum restraining effect (F_S) is obtained when $\beta = 45°$, when

$$F_S = \pi r\gamma \tag{4.12}$$

As discussed by Nes et al. (1985), there have been many different derivations of this force, but the result is usually similar to the above. It should be noted that when a boundary intersects a particle, the particle effectively removes a region of boundary

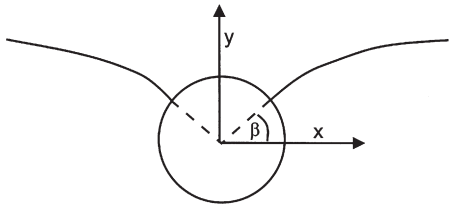

Fig. 4.20. The interaction between a grain boundary and a spherical particle.

equal to the intersection area and thus the energy of the system is lowered, and boundaries are therefore **attracted** to particles.

Equation 4.12 predicts that the pinning force exerted by a particle should be proportional to the grain boundary energy (γ). Therefore we expect the pinning due to low angle boundaries and low energy Σ boundaries to be less than for 'random' high angle boundaries. There is surprisingly little evidence of this, although Humphreys and Ardakani (1996) showed that in copper, the pinning pressure on boundaries close to $40^\circ < 111 >$ ($\Sigma 7$) was some 10% smaller than for other high angle boundaries.

4.6.1.2 The effect of particle shape

The particle shape, if not spherical, will have some effect on the pinning force (Ryum et al. 1983, Nes et al. 1985). The latter authors considered the interaction of a boundary with an ellipsoidal particle as shown in figure 4.21. Their treatment assumes that the grain boundary meets the particle at an angle of 90° and that the particle makes a planar hole in the boundary. They calculated the drag force for the two extreme cases shown in figure 4.21, and showed that the maximum forces were

Case 1
$$F_1 = F_S\left(\frac{2}{(1+e)\,e^{1/3}}\right) \tag{4.13}$$

Case 2 for $e \geq 1$
$$F_2 = F_S\left(\frac{1+2.14e}{\pi\, e^{1/2}}\right) \tag{4.14}$$

Case 2 for $e \leq 1$
$$F_2 = F_S\, e^{0.47} \tag{4.15}$$

where **e** is the eccentricity of the ellipsoidal particle. When $\mathbf{e} = 1$ then the particle is a sphere, and F_S is the drag from a spherical particle of the same volume. Figure 4.22 shows how F_1 and F_2 vary with aspect ratio for a particle of constant volume. It can be seen that the pinning force is only significantly larger than that of a spherical particle

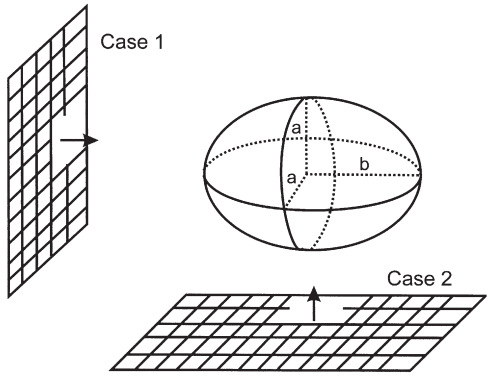

Fig. 4.21. The interaction of boundaries with an ellipsoidal particle, (after Nes et al. 1985).

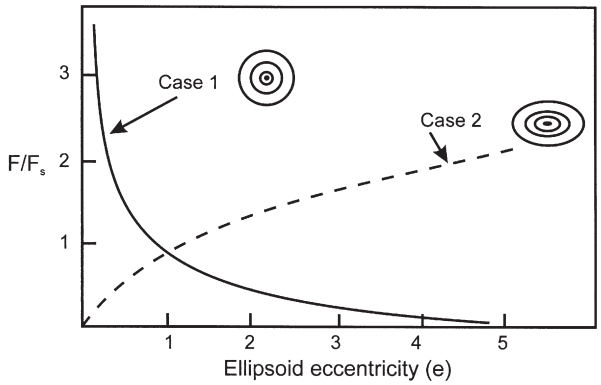

Fig. 4.22. The drag force as a function of particle aspect ratio for the two cases illustrated in figure 4.21, (after Nes et al. 1985).

for the case of thin plates meeting the boundary face-on and long needles meeting the boundary edge-on.

Ringer et al. (1989) have analysed the interaction of a boundary with cubic particles. The strength of the interaction depends upon the orientation of the cube relative to the boundary and in the extreme case, when the cube side is parallel to the boundary, the drag force is almost twice that of a sphere of the same volume. However, as this is a special case, it is unlikely to be a very significant factor in practice.

4.6.1.3 Coherent particles

If a high angle grain boundary moves past a coherent particle then the particle will generally lose coherence during the passage of the boundary. As the energy of the incoherent interface is greater than that of the original coherent interface, energy is required to cause this transformation, and this energy must be supplied by the moving boundary. Therefore, as first shown by Ashby et al. (1969), coherent particles will be more effective in pinning boundaries than will incoherent particles.

Following the analysis by Nes et al. (1985), if the grains are denoted 1 and 2 and the particle as 3, as in figure 4.23a, then there are now three different boundary energies γ_{12}, γ_{13} and γ_{23}. These boundaries meet at the particle surface, and if equilibrium is established then

$$\gamma_{23} = \gamma_{31} + \gamma_{12}\cos\alpha \tag{4.16}$$

and

$$\cos\alpha = \frac{\gamma_{23} - \gamma_{13}}{\gamma_{12}} \tag{4.17}$$

The drag force is then

$$F_C = 2\pi r\gamma\cos(\alpha - \theta)\cos\theta \tag{4.18}$$

F_C is a maximum when $\theta = \alpha/2$ and $\alpha = 0$, giving

$$F_C = 2\pi r\gamma \tag{4.19}$$

Thus coherent particles are twice as effective in pinning a grain boundary as incoherent particles of the same size.

The passage of a high angle boundary past a coherent particle, results in the particle losing coherency. As a small incoherent particle will be less stable (Gibbs-Thomson effect), there are a number of alternative interactions. For example the particle may **dissolve** during passage of the boundary and **re-precipitate** in a coherent orientation, it may **reorient** itself to a coherent orientation, or the boundary may **cut** through the particle (Doherty 1982).

Dissolution – There is experimental evidence that small coherent particles can be dissolved by a moving boundary. The problem has been discussed by Doherty (1982) and by Nes et al. (1985). The latter authors show that in these circumstances the pinning force due to a coherent particle is dependent not only on the particle size, but also on the concentration of the alloy. The pinning force is given by

$$F = \frac{2\pi AkTr^2}{3V}\ln\left(\frac{C_0}{C_{eq}}\right) - 2\pi\gamma' r \tag{4.20}$$

where A = Avogadro's number, k = Boltzmann's constant, V is the molar volume of the precipitate phase, C_0 is solute concentration, C_{eq} is the equilibrium concentration and γ' is the energy of the coherent interface.

Following dissolution, the particles may re-precipitate coherently behind the grain boundary or alternatively discontinuous precipitation may occur at the boundary.

Coherent particles on a stationary boundary – If there is insufficient driving force for a boundary to move past the coherent particles or to dissolve them then the particles will become incoherent along the boundary. As a consequence of this, the equilibrium shape of the particles on the boundary will alter as shown in figure 4.23b. The increase in radius of curvature of the particles on the boundary will then cause them to coarsen at the expense of the smaller spherical coherent particles, thus increasing the pinning of the boundary (Howell and Bee 1980).

Passage of boundary through coherent particles – In some circumstances the precipitate may be cut by the boundary and undergo the same orientation change as the grain surrounding it, as shown in figure 4.23c. This has been observed in nickel alloys containing the coherent γ' phase (Porter and Ralph 1981, Randle and Ralph 1986), and in aluminium alloys containing semi-coherent Al_3Sc particles (Jones and Humphreys 2001).

4.6.2 The drag pressure due to a distribution of particles

Having considered the pinning force from a single particle, we now need to calculate the restraining pressure on the boundary due to an array of particles. This is a complicated problem which has not yet been completely solved.

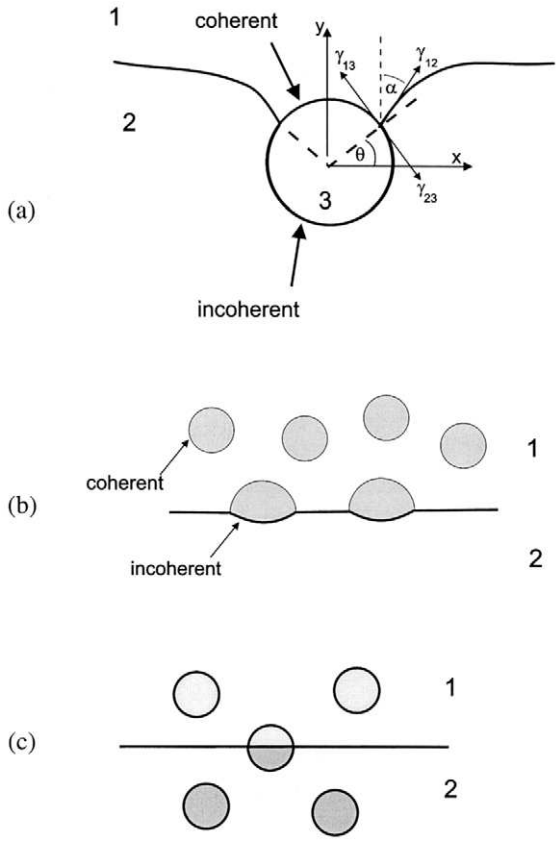

Fig. 4.23. The interaction between a coherent particle and a high angle grain boundary. (a) The boundary by-passes the particle; (b) The boundary halts at the particles; (c) The boundary cuts through the particle.

4.6.2.1 Drag from a random distribution of particles

For a volume fraction F_V of randomly distributed spherical particles of radius **r**, the number of particles per unit volume (N_V) is given (appendix 2.8) by

$$N_V = \frac{3\,F_V}{4\pi\,r^3} \tag{4.21}$$

If the boundary is planar, then particles within a distance **r** on either side of the boundary will intersect it. Therefore the number of particles intersecting unit area of the boundary is

$$N_S = 2rN_V = \frac{3F_V}{2\pi\,r^2} \tag{4.22}$$

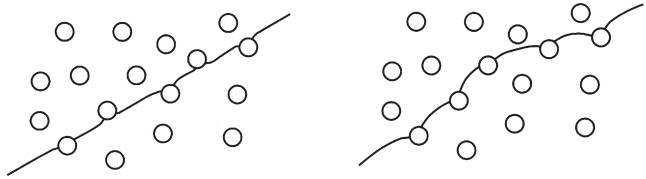

(a) (b)

Fig. 4.24. Interaction of particles with (a) a rigid planar boundary; (b) a flexible boundary.

The pinning pressure exerted by the particles on unit area of the boundary is given by

$$P_Z = N_S F_S \tag{4.23}$$

and hence from equations 4.12 and 4.22

$$P_Z = \frac{3F_V\gamma}{2r} \tag{4.24}$$

This type of relationship was first proposed by Zener (Smith 1948), although in the original paper because N_S was taken as r. N_V, the pinning pressure was half that of equation 4.21. P_Z as given by equation 4.24 is commonly known as the **Zener pinning pressure.**

It is clear that this calculation is not rigorous, because if the boundary is rigid as is assumed, then as many particles will be pushing the boundary one way as will be pulling it the other as shown in figure 4.24a, and the net pinning pressure will be nil. (This is a similar problem to that encountered in calculating the interaction of a dislocation with an array of solute atoms). Therefore the boundary must relax locally from a planar configuration, as shown in figure 4.24b, if pinning is to occur.

More rigorous calculations of the Zener drag have been attempted by many authors, and the reader is referred to the reviews by Nes et al. (1985), Hillert (1988) and Doherty et al. (1989) for further details. However, it is concluded that the more sophisticated calculations do not lead to relationships which differ significantly from equation 4.24, which remains widely used. Although some early computer simulations suggested that the Zener drag was not given correctly by equation 4.24, more recent simulations by Miodownic et al. (2000) have confirmed the Zener relationship (see also §11.4.2).

4.6.2.2 Effects of boundary-particle correlation

The assumption of a planar or near planar boundary as required to give the Zener pinning pressure of equation 4.24 will only be reasonable if the grain or subgrain size is very much larger than the interparticle spacing, as pointed out by Anand and Gurland (1975), Hellman and Hillert (1975), Hutchinson and Duggan (1978), Hillert (1988), and Hunderi and Ryum (1992a). If this is not the case, then we need to examine, albeit in a

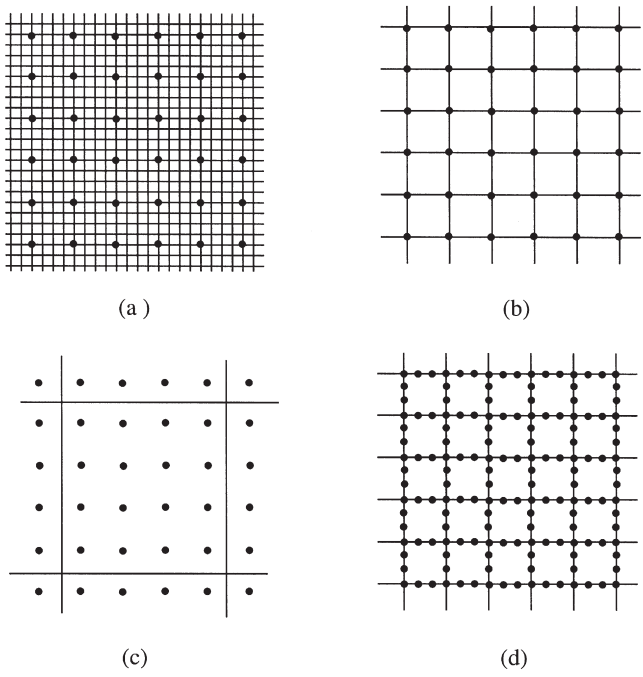

Fig. 4.25. Schematic diagram of the correlation between particles and boundaries as a function of grain size.

simplified way, the consequences. In figure 4.25 we identify four important cases. In figure 4.25a the grains are much smaller than the particle spacing, in figure 4.25b the particle spacing and grain size are similar, in figure 4.25c the grain size is much larger than the particle spacing and in figure 4.25d, the particles are inhomogeneously distributed so as to lie only on the boundaries. In all these cases there is a strong correlation between the particles and the boundaries, although an accurate assessment of the pinning force is difficult and is dependent on the details of the particle and grain (or subgrain) arrangement.

Consider the particles and boundaries which form the three-dimensional cubic arrays shown in figure 4.25. For case **a**, it is reasonable to assume that all the particles lie not only on boundaries, but at vertices in the grain structure, because in these positions the particles, by removing the maximum boundary area, minimise the energy of the system.

If the grain edge length is **D**, then the grain boundary area per unit volume is 3/D. The number of particles per unit area of boundary (N_A) is given by

$$N_A = \frac{\delta N_V D}{3} \tag{4.25}$$

where δ is a factor which depends on the positions of the particles in the boundaries. For particles on boundary faces, $\delta = 1$. For particles at the vertices as shown in figures 4.25

(a) and (b), $\delta = 3$ and hence, using equation 4.21

$$N_A = \frac{\delta N_V D}{3} = \frac{3DF_V}{4\pi r^3} \tag{4.26}$$

For incoherent spherical particles the pinning pressure on the boundary (P'_Z) will then be given by

$$P'_Z = F_S N_A = \frac{3DF_V\gamma}{4r^2} \tag{4.27}$$

This relationship will be valid for grain sizes up to and including that shown in figure 4.25b, in which the grain size and particle spacing are the same (D_C). In this situation, the spacing of the particles on the cubic lattice (L) is equal to D_C and is given by

$$L = D_C = N_V^{-1/3} = \left(\frac{4\pi r^3}{3F_V}\right)^{1/3} \tag{4.28}$$

at which point the pinning force reaches a maximum $P'_{Z\max}$ given by

$$P'_{Z\max} \approx \frac{1.2\gamma F_V^{2/3}}{r} \tag{4.29}$$

As the grain size increases beyond D_C, the number of particles per unit area of boundary (N_A) will decrease from that given by equation 4.26 and eventually reach N_S as given by equation 4.22. We can treat this transition from correlated to non-correlated boundary in the following approximate manner.

The number of boundary corners per unit volume in a material of grain size **D** is given approximately by $1/D^3$, and the fraction of particles lying on these potent pinning sites is therefore, for the condition $D \geq D_C$.

$$X = \frac{1}{N_V D^3} \tag{4.30}$$

When $D = D_C$ then from equation 4.28 we find $X = 1$. Thus as the grains grow, a diminishing fraction of particles is able to sit at the grain corners.

The number of corner-sited particles per unit area of boundary is then

$$N_C = XN_V D \tag{4.31}$$

The remaining particles will sit on grain boundaries or grain edges or lie within the grains. In this simple analysis we assume that the particles which are not sitting at grain corners are intersected at random by boundaries and therefore the number per unit area is

$$N_r = 2rN_V(1 - X) \tag{4.32}$$

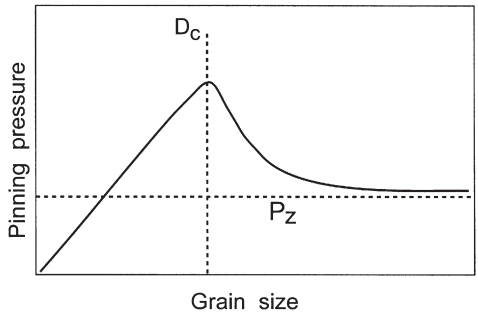

Fig. 4.26. The effect of grain size on the Zener pinning force for a given particle dispersion.

Thus the total number of particles per unit area of boundary is $N_c + N_r$ and, using equation 4.23, the pinning pressure is given by

$$P''_Z = \pi r \gamma [X N_V D + (1 - X) 2 N_V r] \tag{4.33}$$

or, when $D \geq D_C$

$$P''_Z = \pi r \gamma \left(\frac{1}{D_2} + (1 - \frac{1}{N_V D^3}) 2 N_V r \right) \tag{4.34}$$

In figure 4.26, we show the pinning pressure on the boundary as a function of the grain size. It can be seen that as the grain size increases, the pinning pressure rises according to equation 4.27, peaks when the grain size approaches D_C and eventually falls (equation 4.33) to the Zener pinning pressure as given by equation 4.24.

It should be noted that actual values of the peak pinning pressure discussed here are based on a very simple geometry and are not accurate. However, the principle that the pinning pressure varies in a manner similar to that shown in figure 4.26 is undoubtedly correct and has some important implications for recovery, recrystallization and grain growth of particle-containing materials which will be discussed in later chapters.

4.6.2.3 Drag from non-random particle distributions

In many alloys the particles may not be randomly distributed. Of particular importance is the situation in which the particles are concentrated in planar bands as shown in figure 4.27. This type of structure is often found in rolled products such as Al-killed steels, most commercial aluminium alloys, and products made by powder metallurgy. In many cases the individual particles are also rod or plate-like and aligned parallel to the rolling plane. Nes et al. (1985) have modelled the case shown in figure 4.27a and have calculated the grain aspect ratio following primary recrystallization.

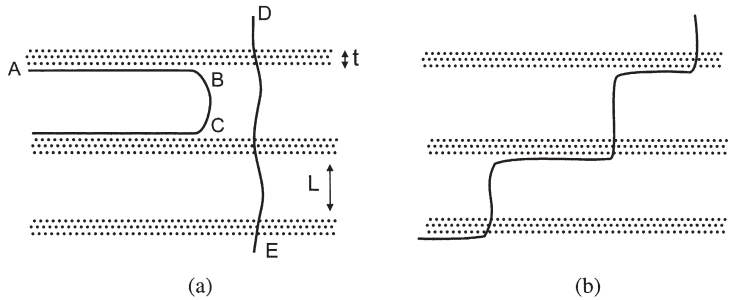

Fig. 4.27. The interaction of boundaries with planar arrays of particles. (a) The effect of boundary orientation on pinning; (b) Propagation of a boundary through planar arrays of particles, (after Nes et al. 1985).

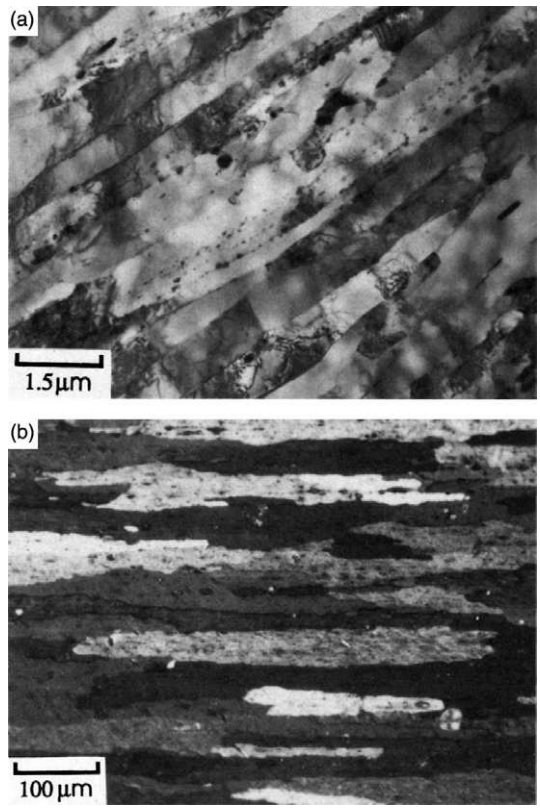

Fig. 4.28. (a) Transmission electron micrograph illustrating the pinning of low angle boundaries by planar arrays of small oxide particles in a rolled aluminium billet produced by powder metallurgy, (TD plane sections); (b) Optical micrograph of the same material after recrystallization showing an elongated grain structure, (Bowen et al. 1993).

Let us assume that spherical particles of radius **r** are aggregated in bands of thickness **t**, which are spaced a distance of **L** apart. A boundary AB lying parallel to the planar bands experiences a drag

$$P_{PZ} = \frac{P_Z L}{t} \tag{4.35}$$

where P_Z is the drag pressure if the particles are uniformly distributed as given by equation 4.23.

The drag on a boundary lying perpendicular to the bands depends strongly on the shape of the boundary. For example the curved boundary segment BC in figure 4.27a does not experience any pinning. However, if the boundary is long, e.g. segment DE, and if the driving pressure is uniformly distributed the average pinning pressure is P_Z. In either case, the pinning force is significantly greater in the direction normal to the bands and this anisotropy will be reflected in the shape of the grains or subgrains. Nes et al. (1985) have shown that the boundary is expected to propagate in a staggered manner as shown in figure 4.27b. Figure 4.28a is a transmission micrograph of a rolled powder metallurgy aluminium sheet product showing how bands of small oxide particles interact with the **low angle boundaries** and affect the shape of the subgrains during recovery, and figure 4.28b is an optical micrograph of the same material after recrystallization, which clearly shows how interaction of the aligned oxide particles with **high angle boundaries** results in an elongated grain structure after recrystallization.

Another important situation in which non-random particle distribution may occur is when the second-phase particles are precipitated onto pre-existing low or high angle boundaries (e.g. Hutchinson and Duggan 1978). In this case, as shown schematically in figure 4.25d, all (or most) of the particles lie on the boundaries. The effective number of particles per unit area of boundary is given approximately by equation 4.27 with δ in equation 4.26 equal to 1, and the pinning force (P_X) by

$$P_X = F_S N_A = \frac{\gamma D F_V}{4r^2} \tag{4.36}$$

ThisPageIntentionallyLeftBlank

Chapter 5

THE MOBILITY AND MIGRATION OF BOUNDARIES

5.1 INTRODUCTION

The structure and energy of grain boundaries were discussed in chapter 4. In this chapter we examine the models and mechanisms of boundary migration and in particular the mobilities of boundaries, in order to provide a foundation for the discussions of recovery, recrystallization and grain growth in later chapters. More detailed discussion of some of the issues raised in this chapter can be found in the recent books about boundaries and interfaces by Sutton and Balluffi (1995) and Gottstein and Shvindlerman (1999).

5.1.1 The role of grain boundary migration during annealing

The migration of low angle (LAGB) and high angle grain boundaries (HAGB) plays a central role in the annealing of cold worked metals. Low angle boundary migration occurs during recovery and during the nucleation of recrystallization, and high angle boundary migration occurs both during and after primary recrystallization.

Despite the importance of grain boundary migration during annealing, the details of the process are not well understood. This is mainly because boundary migration involves atomistic processes occurring rapidly, at high temperatures, and under conditions

which are far from equilibrium. It is therefore very difficult to study boundary migration experimentally or to deal with it theoretically. Although there is a wealth of experimental evidence accumulated over many years, in many cases results are contradictory and few clear patterns emerge. However, it is evident that even very small amounts of solute have an extremely large influence on the boundary mobility and it is therefore very difficult to determine the **intrinsic mobility** of a boundary. Although a great deal is now known about the structure of grain boundaries (chapter 4), and models for grain boundary migration based on boundary structure have been formulated, there is as yet little evidence of quantitative agreement between the models and the experimental results.

5.1.2 The micromechanisms of grain boundary migration

Low angle and high angle grain boundaries migrate by means of atomistic processes which occur in the vicinity of the boundary. In this section we briefly outline the various mechanisms which have been proposed, in order to prepare for the more detailed considerations which appear later in this chapter.

The mechanism of boundary migration depends on several parameters including the **boundary structure** which, in a given material, is a function of **misorientation** and **boundary plane**. It also depends on the experimental conditions, in particular the **temperature** and the nature and magnitude of the **forces** on the boundary, and it is also strongly influenced by point defects in the material such as **solutes** and **vacancies.**

It is well established that low angle grain boundaries migrate through the movement by **climb** and **glide** of the dislocations which comprise the boundary, and many aspects of LAGB migration may therefore be interpreted in terms of the theory of dislocations.

The basic process during the migration of high angle boundaries is the transfer of atoms to and from the grains which are adjacent to the boundary, and models based on such **thermally activated atomic jumps** constitute the earliest models of boundary migration. As discussed in §4.4.2, the structure of a grain boundary is related to its crystallography, and there is evidence that boundaries may migrate by movement of intrinsic boundary defects such as **ledges** or **steps** or **grain boundary dislocations.** In some cases boundary migration may involve **diffusionless shuffles,** which are processes involving the cooperative movement of groups of atoms (cf. diffusionless phase transformations). In certain circumstances combined **sliding and migration** of boundaries may also occur.

Because the atomic packing at grain boundaries is less dense than in the perfect crystal, grain boundaries are associated with a **free or excess volume** which depends on the crystallography of the boundary (§4.4.3). This leads to a strong interaction with solute atoms and to the formation of a **solute atmosphere** which, at low boundary velocities, moves with the boundary and impedes its migration. The range of boundary velocities is very large. For example, in the case of **grain growth** the boundary may move relatively slowly through almost perfect crystal. However, during **recrystallization** the boundary moves at a very high velocity (often much higher than during diffusion-controlled phase transformations). In this case, the boundary migrates into highly defective material, leaving perfect crystal behind it. The mechanism by which the boundary removes the defects during recrystallization is not known, but it is reasonable to suppose that the

boundary energies and structures may differ for the cases of grain growth and recrystallization.

5.1.3 The concept of grain boundary mobility

A grain boundary moves with a velocity (v) in response to the net pressure ($\mathbf{P} = \Sigma \mathbf{P_i}$) on the boundary (§1.3). It is generally assumed that the velocity is directly proportional to the pressure, the constant of proportionality being the **mobility (M)** of the boundary, and thus

$$v = MP \tag{5.1}$$

This type of relationship is predicted by reaction rate theory (§5.4.1) if the mobility is independent of the driving force and if $\mathbf{P} \ll \mathbf{kT}$, and should be independent of the details of the mechanism of boundary migration.

There are however proposed boundary migration mechanisms such as step or boundary dislocation controlled migration (Gleiter 1969b, Smith et al. 1980) where the mobility depends on the driving force, and under certain conditions it is then predicted that this relationship may not hold. If the boundary mobility is controlled by solute atoms then, as discussed in §5.4.2, the **retarding pressure due to solute drag** ($\mathbf{P_{sol}}$) may be a function of the boundary velocity. Although a complex relationship between **driving pressure** ($\mathbf{P_d}$) and velocity may be found (e.g. fig. 5.32), equation 5.1 may still be obeyed if **P** in equation 5.1 is replaced by ($\mathbf{P_d} - \mathbf{P_{sol}}$).

Surprisingly, there are comparatively few experimental measurements of the relationship between velocity and driving pressure. Results consistent with equation 5.1 have been obtained by Viswanathan and Bauer (1973) for copper and by Demianczuc and Aust (1975) for aluminium. More recently, Huang and Humphreys (1999a) have confirmed this relationship by in-situ SEM measurements of boundary mobility during the recrystallization of aluminium. Although Rath and Hu (1972) and Hu (1974) fitted their data for zone refined aluminium to a power law relationship $\mathbf{v} \propto \mathbf{P^n}$ with $n \gg 1$, Gottstein and Shvindlerman (1992) argued that the Rath and Hu experiments were strongly influenced by thermal grooving and by re-analysing their data and taking this into account, showed that they were consistent with equation 5.1. A re-examination of the early experimental results by Vandermeer and Hu (1994) has also concluded that they can be reconciled with equation 5.1.

The mobility of grain boundaries is temperature dependent and is usually found to obey an Arrhenius type relationship of the form

$$M = M_0 \exp\left(-\frac{Q}{RT}\right) \tag{5.2}$$

The slope of a plot of ln(M) or ln(v) (for constant **P**), against 1/T therefore yields a value of Q, the apparent activation energy which, as is further discussed below, may be related to the atom-scale thermally activated process which controls boundary migration.

However, this is not always the case, and great care should be taken in the interpretation of experimentally measured activation energies.

5.1.4 Measuring grain boundary mobilities

Our current knowledge of grain boundary mobility is very much limited by the lack of good experimental data. In addition to the problems arising from the effects of trace amounts of impurities on mobility (§5.3.3), the actual measurements are extremely difficult to make (appendix 2.7.2).

Measurements of boundary mobility are made by determining the velocity of a boundary in response to a well defined driving force. Experiments in which the velocity of a boundary is measured during recrystallization may be difficult to interpret, because the driving pressure which arises from the stored energy, and is typically 10–100 MPa, is not easy to measure accurately, varies throughout the microstructure and does not remain constant with time, decreasing as recovery proceeds. However, in a subgrain-forming material such as aluminium, subgrain sizes and misorientations in well-recovered materials can now be determined quite accurately by EBSD (Humphreys 2001) and therefore the driving pressure can be calculated from these parameters according to equation 2.8 (Huang and Humphreys 1999a). Many measurements of boundary mobility have been carried out on materials with a better characterised driving force, such as an as-cast substructure or by using bicrystals of carefully controlled geometry (e.g. Masteller and Bauer 1978, Gottstein and Shvindlerman 1999). In such experiments however the driving pressure is much lower (around 10^{-2} MPa), and it is not clear to what extent measurements of boundary mobility in materials with such low driving forces are directly applicable to migrating boundaries in recrystallizing material. In addition, there is evidence that moving boundaries interact with dislocations, and that defects affect boundary mobility (§5.3.4), indicating that there may be a real physical difference between boundary migration in deformed and undeformed material.

It should be noted that many of the measurements of boundary migration are conducted under conditions where the driving force is constant and the results are expressed as boundary velocities rather than mobilities (e.g. fig. 5.9). As equation 5.1 is expected to be obeyed, the mobility will be directly proportional to the velocity, and it is therefore reasonable to discuss such results in terms of boundary mobility even though this parameter has not actually been measured.

5.2 THE MOBILITY OF LOW ANGLE GRAIN BOUNDARIES

5.2.1 The migration of symmetrical tilt boundaries under stress

Although boundaries migrate during recovery, recrystallization and grain growth under driving pressures arising from defects or boundary curvature, it has long been known that symmetrical tilt boundaries, such as shown in figure 4.4 can move readily under the influence of stress (Washburn and Parker 1952, Li et al. 1953). The mobility of such

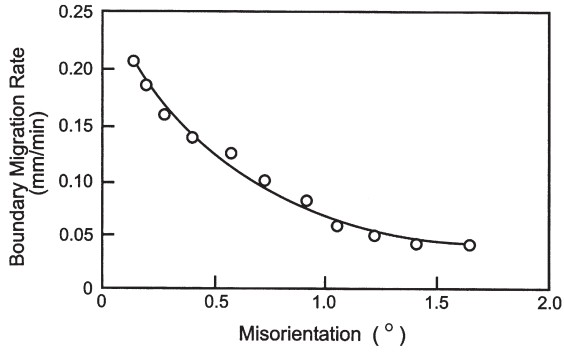

Fig. 5.1. The effect of misorientation on the mobility of symmetrical tilt boundaries in zinc at 350°C under a constant stress, (after Bainbridge et al. 1954).

boundaries has been shown to depend on both temperature and boundary misorientation, and the effect of misorientation on the migration under constant stress of symmetrical tilt boundaries in zinc is shown in figure 5.1. It may be seen that as the misorientation increases and the dislocations in the boundary become closer together (equation 4.4), the mobility decreases. It is presumed that the dominant mechanism during boundary migration is glide of the edge dislocations which comprise the boundary, although dislocation boundaries in real materials will be more complicated than that of figure 4.4, and their migration will require some dislocation climb.

Recent investigations of the migration of planar symmetrical $<111>$ and $<112>$ tilt boundaries in very high purity aluminium under the influence of small shear stresses (Winning et al. 2001) have revealed a number of interesting features. As shown in figure 5.2, there is a sharp transition in mobilities at misorientations (θ) of $\sim 14°$. The mobilities of the lower angle boundaries are found not to depend significantly on the boundary misorientation, although there is very limited data for $\theta < 10°$. The activation enthalpy for migration of the low angle boundaries is close to that for self diffusion, which is consistent with dislocation climb control, whilst that for high angle boundaries is lower, and close to that for boundary diffusion. The relative mobilities of high and low angle boundaries under stress therefore depends on temperature as shown in figure 5.2, where it is seen that at very high homologous temperatures, low angle boundaries move more rapidly than high angle boundaries. A comparison of boundary migration under stress with that driven by curvature (Winning et al. 2002), indicates that although the low angle boundary mobilities are similar, those for high angle boundaries may differ greatly and depend on the tilt axis.

There are two factors which need to be considered in applying the above results to recovery, recrystallization and grain growth of polycrystals.

If a boundary moves by dislocation glide under the influence of an applied stress, this implies that such movement must inevitably lead to a shape change. In unconstrained single crystals such as were used for these experiments, this may have little effect, but in a grain constrained within a polycrystal this will lead to the generation of internal

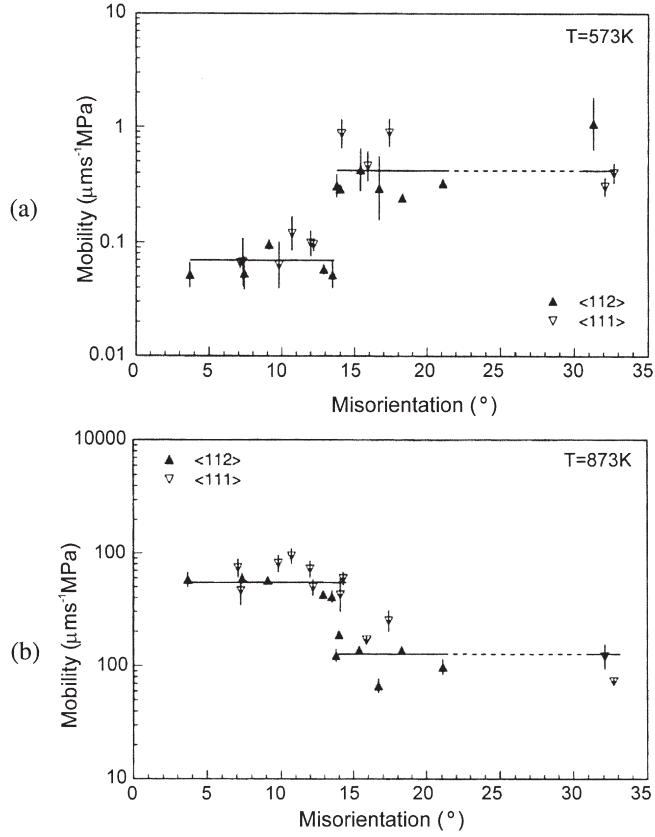

Fig. 5.2. Dependence of the grain boundary mobility on the misorientation angle for the motion of symmetrical planar $<112>$ and $<111>$ tilt boundaries in high purity aluminium, under the influence of stress. (a) 573K, (b) 873K, (Winning et al. 2001).

stresses which will oppose further boundary migration. A grain or subgrain microstructure contains many types of boundary, and the behaviour of symmetrical tilt boundaries may be untypical of the more general low angle boundaries found in a deformed and recovered metal (§6.4.2). Further work is therefore required on the behaviour of 'random low' and high angle boundaries under stress before the relevance of the above results to annealing processes in polycrystals can be established.

5.2.2 General low angle boundaries

5.2.2.1 Measurements of the mobility of low angle boundaries

It has long been recognised that the mobilities of general low angle boundaries are significantly lower than those of high angle boundaries. However, there are few systematic investigations of the mobility of such boundaries and of the effect of

misorientation. This is a major problem, because, as discussed in §6.5.3, a knowledge of the mobility of general low angle boundaries is a critical factor in developing an understanding of the annealing of deformed metals.

Early work which has shown that low and medium angle boundaries have a low mobility includes that of Tiedema et al. (1949) who found that recrystallized grains oriented within a few degrees of the matrix grew very slowly and were left as island grains, Graham and Cahn (1956) on aluminium, Rutter and Aust (1960) on lead, and Walter and Dunn (1960b) on iron. It should be emphasised that the references cited provide only a few largely qualitative observations and do not include a systematic investigation of the effect of misorientation on mobility.

Sun and Bauer (1970) and Viswanathan and Bauer (1973) used a bicrystal technique, in which the boundary energy provided the driving force for migration, to measure the mobility of high and low angle boundaries in NaCl and copper. Their results were reported as a mobility parameter K′ which is the product of the mobility M and the boundary energy γ. This parameter is similar to the **'reduced mobility',** which is often used in investigations of curvature driven grain growth.

$$K' = 2\gamma M \tag{5.3}$$

The results for sodium chloride are shown in figure 5.3 and for copper in figure 5.4. Both figures clearly show a large difference in mobility between low and high angle boundaries. From figure 5.4 it may be seen that K′ for the high angle boundaries in copper is some three orders of magnitude greater than that for low angle (2–5°) boundaries. As the boundary energy for 20° tilt boundaries in copper is only around four times that of 2° boundaries (Gjostein and Rhines 1959), the difference in mobility between high and low angle boundaries is therefore a factor of ~250. It is also seen that the activation energies for migration of the low angle boundaries are in both materials very much higher than for the high angle boundaries. In the case of copper, the value of ~200 kJ/mol for the low angle boundaries is close to that for self diffusion (table 5.1) and for NaCl, the value of 205 kJ/mol is close to that for the diffusion of Na^+ in NaCl.

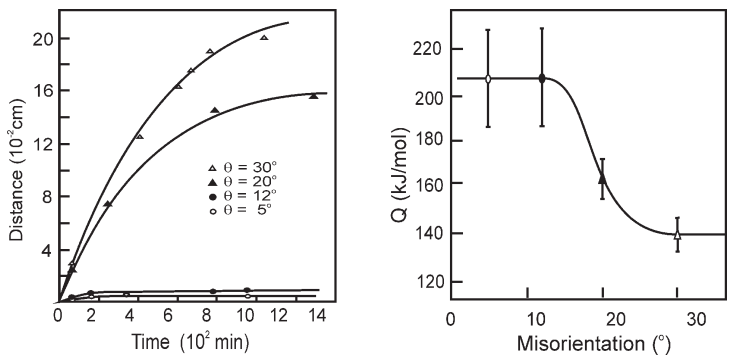

Fig. 5.3. a) Displacement of a curved boundary with time at 750°C in a NaCl bicrystal as a function of misorientation about a <100> axis. b) Activation energy for boundary migration, (after Sun and Bauer 1970).

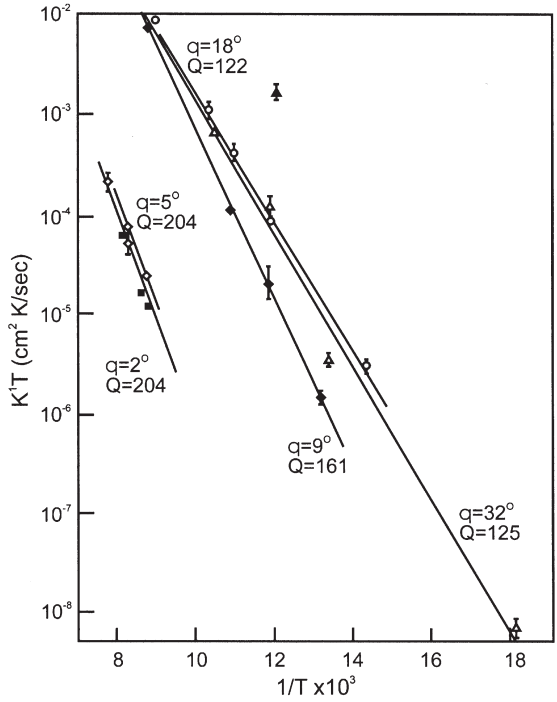

Fig. 5.4. Variation of boundary mobility parameter $\mathbf{K}'$ with temperature and misorientation for 99.999% copper. The activation energies (Q in kJ/mol) for each group of boundaries are also shown, (after Viswanathan & Bauer 1973).

Measurements on high purity zinc and aluminium bicrystals by Fridman et al. (1975) have confirmed that the mobility of medium angle boundaries increases with increasing misorientation as shown in figure 5.13. Figure 5.13c also confirms that the activation energy for LAGB migration is higher than that for HAGB migration, although the reported activation energies for migration of LAGBs appear to be considerably higher than those for self diffusion.

Several investigations of the mobilities of low angle boundaries in aluminium have recently been reported. Huang and Humphreys (2000) measured the growth rates of subgrains in deformed single $\{110\}<001>$ crystals of Al–0.05%Si. Crystals of this orientation are stable during plane strain compression and do not recrystallize, thereby allowing extensive subgrain growth to occur (§6.5.2). The mobilities of low angle boundaries of misorientations between 2.5–5.5° were calculated, and are shown in figure 5.5, where it is seen that the mobility increases by a factor of ~50 as the misorientation rises by ~3° in this range.

Investigation of cube-oriented crystals of the same material enabled the range of LAGB misorientations to be increased (Huang, Humphreys and Ferry 2000), and the combined effects of temperature and misorientation on mobility are shown in figure 5.6.

Table 5.1
Activation energies for self, core and boundary diffusion for a selection of materials.

Material	T_m (K)	G (GPa)	b (nm)	Q_S (kJ/mol)	Q_C (kJ/mol)	Q_B (kJ/mol)	γ_b (Jm^{-2})
Al	933	25.4	0.286	142	82	84	0.324a
Au	1336	27.6	0.288	164			0.38a
Cu	1356	42.1	0.256	197	117	104	0.625a
α-Fe	1810	69.2	0.248	239	174	174	0.79a
Γ-Fe	1810	81	0.258	270	159	159	0.76a
NaCl	1070	15	0.399	217 (Na^+)	155	155	0.5c
Pb	601	7.3	0.349	109	66	66	0.2b
Sn	505	17.2	0.302	140b		37b	0.16b
Zn	693	49.3	0.267	91.7	60.5	60.5	0.34a

Data are from Frost and Ashby (1982) unless otherwise indicated.
a) Murr (1975)
b) Friedel (1964)
c) Sun and Bauer (1970)

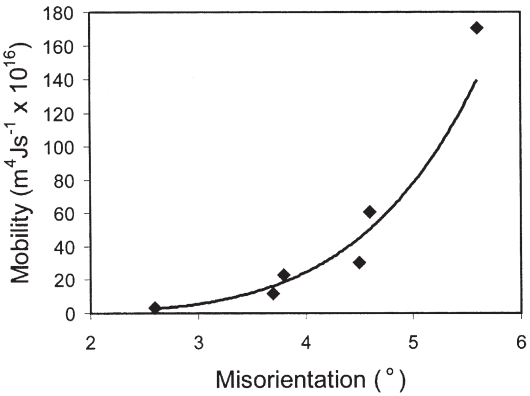

Fig. 5.5. The effect of misorientation on the mobility of low angle boundaries in Al–0.05%Si at 300°C, measured from subgrain growth in single crystals, (data from Huang and Humphreys 2000).

The activation energy for boundary migration was found to be a function of misorientation up to ~14°, above which it remained constant (fig. 5.7). The activation energies were all in the range 125–154 kJ/mol, consistent with values for the lattice diffusion of Si in Al, and suggesting that the boundary migration is controlled by lattice diffusion of a solute atmosphere (§5.4.2).

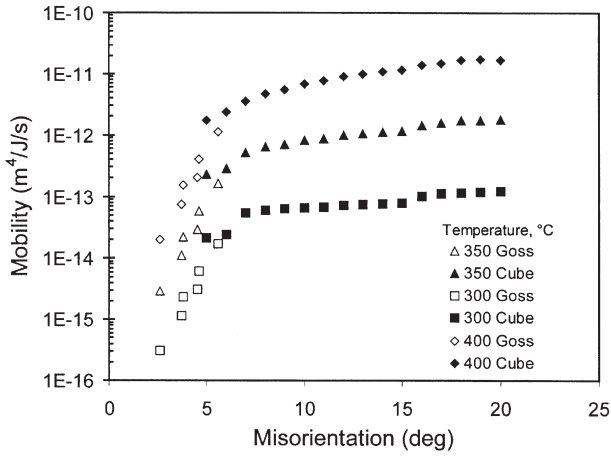

Fig. 5.6. The effect of misorientation and temperature on boundary mobility in Al–0.05%Si as a function of misorientation, measured from subgrain growth in crystals of Goss and Cube orientation, (Huang et al. 2000a).

Yang et al. (2001) determined the mobilities of low angle boundaries in 99.98% Al from detailed analysis of the geometry of triple junctions in thin foils. Their results are quite similar to those shown in figures 5.5 and 5.6.

The determination of boundary mobilities either by subgrain growth or from triple junction geometry is based on the premise that the microstructural evolution is controlled by the **mobility of the boundaries** and not the **triple junctions.** The circumstances under which triple junction mobility may be rate limiting are discussed in §5.5.

5.2.2.2 Mechanisms of low angle boundary migration

The mechanisms of low angle boundary migration are poorly understood, and the few systematic investigations of the mobilities of low angle boundaries discussed above, provide the following clues to the mechanisms of low angle boundary migration:

- Low angle boundaries migrate at a rate consistent with equation 5.1, showing that the mobility is a constant for a particular boundary during isothermal annealing.
- Low angle boundary migration is controlled by a bulk diffusion process.
- The boundary mobility increases significantly with increasing misorientation.

Nes (1995a) has discussed various possible rate controlling mechanisms, including thermally activated glide, cross-slip, climb and solute drag. Furu et al. (1995) have suggested that the subgrain growth kinetics which they measured in polycrystalline commercial aluminium alloys were most consistent with a process of thermally activated glide and solute drag. In such a situation the apparent activation energy for migration is dependent on subgrain size and will not remain constant during growth or for different microstructures. The experimental results discussed in §5.2.2.1 which show that the

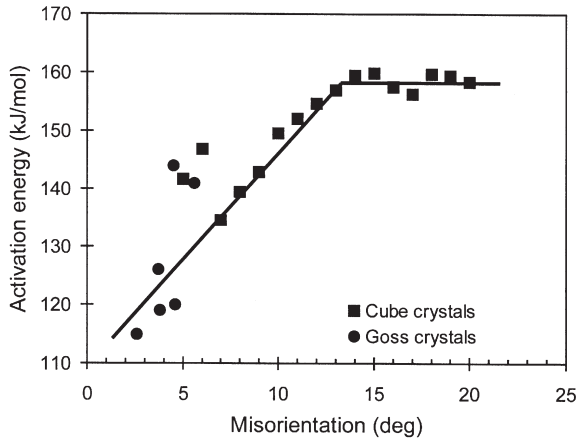

Fig. 5.7. The effect of misorientation on the activation energies for low angle boundary migration in Al–0.05%Si, measured from subgrain growth in single crystals, (Humphreys and Huang 2000).

activation energy remains constant for a range of subgrain sizes and boundary misorientations, are more consistent with earlier suggestions (e.g. Sandström 1977b) that the boundary movement occurs by climb of the dislocations comprising the boundary, at a rate controlled by the lattice diffusion of solute. Although it has been suggested (Ørsund and Nes 1989) that at low temperatures boundary migration may be controlled by dislocation pipe or core diffusion, there is currently no experimental evidence of this.

5.2.2.3 Theories of the mobility of low angle boundaries

As the energy and structure of low angle boundaries are sensitive to misorientation, the intrinsic boundary mobility is also expected to depend on these parameters. The migration of low angle boundaries in general requires climb of dislocations in the boundary and this is expected to be the rate determining process. The theory of the mobility of low angle grain boundaries has been discussed by Sandström (1977b) and Ørsund and Nes (1989), and these authors suggest that the mobility of low angle boundaries is given by

$$M = \frac{CD_s b}{kT} \tag{5.4}$$

where C is a constant of the order of unity and D_s is the coefficient of self diffusion.

An important factor discussed by Hirth and Lothe (1968), and not considered by the above investigators, is that there is no net flow of matter as the boundary moves and therefore the vacancy source-to-sink spacing is approximately equal to the dislocation spacing (**h**) in the boundary, which is related to the boundary misorientation (equation 4.4).

In view of the large orientation dependence of the boundary structure on misorientation (θ), the mobility of low angle boundaries is likely to show some dependence on θ, which is not found in equation 5.4, and the following approximate analysis (Humphreys and Hatherly 1995), which was based on discussions with E. Nes, and has some similarity to that presented by Furu et al. (1995), is suggested.

Consider a boundary bowing to a radius of curvature **R.** The pressure (**P**) on the boundary due to the curvature is given by

$$P = \frac{2\gamma_s}{R} \tag{5.5}$$

where γ_s is the boundary energy as given by equation 4.5. For small values of θ we use the approximation $\gamma_s \sim c_1 Gb\theta$, where c_1 is a small constant.

If we assume that equation 5.1 applies, the boundary velocity is given by

$$v_b = \frac{dR}{dt} = \frac{2M\gamma_s}{R} = \frac{2c_1 MGb\theta}{R} \tag{5.6}$$

Case A – Very low angle boundaries ($\theta \to 0$) We first consider the movement of boundaries in which the dislocations are spaced far apart. In this limiting situation we can assume that the behaviour of the individual dislocations in the boundary is dominant. An individual dislocation in the boundary is bowed to a radius of curvature **R** and the force on unit length of the dislocation is given approximately by

$$F = \frac{Gb^2}{2R} \tag{5.7}$$

For dislocation climb under conditions of negligible vacancy supersaturation, $Fb^2 \ll kT$ and the climb velocity (v_d) of a dislocation under the influence of a force **F** is given approximately (Friedel 1964, Hirth and Lothe 1968), as

$$v_d = D_s c_j \left(\frac{Fb}{kT}\right) \tag{5.8}$$

Where c_j is the concentration of jogs. Substituting for **F** as given by equation 5.7

$$v_d = \frac{D_s c_j Gb^3}{2kTR} \tag{5.9}$$

As the dislocations are assumed to be essentially independent in such a low angle boundary, the velocity of all the dislocations in the boundary is given by equation 5.9 and therefore $v_d = v_b$. Thus from equations 5.6 and 5.9

$$v_b = \frac{2c_1 MGb\theta}{R} = \frac{D_s c_j Gb^3}{2kTR} \tag{5.10}$$

and hence

$$M = \frac{D_s c_j b^2}{4 c_1 kT\theta} \tag{5.11}$$

i.e. in this limiting case:

- The dominant mechanism is climb of individual dislocations
- $v = M.P$ is expected to hold
- M is inversely proportional to θ

Case B – Boundaries where the dislocation cores overlap ($\theta > 15^\circ$–20°) In this situation we have effectively reached the case of a high angle boundary, and for a general boundary we can reasonably assume (§5.4.1.1)

- The dominant mechanism is atom jumps across the boundary
- $v = M.P$ is expected to hold
- M is independent of θ

Case C – The intermediate case This is probably the most important regime for the recovery of deformed polycrystals, but the most difficult to analyse.

C1 (medium angles) When the boundary angle is large and **h** is small, the movement of the boundary is probably dominated by atom transfer over a distance **h,** and the process is analogous to the diffusion of atoms through a membrane of thickness **h,** which would result in **M** being inversely proportional to **h,** i.e. $M \propto \theta$.

C2 (low to medium angles) This is a transition regime in which the dominant mechanism is not clear. There are two opposing factors.

- The decrease in mobility with increasing θ due to the factors discussed for case A will tend to decrease the mobility as θ increases.
- As θ increases, **h,** the vacancy source-to-sink distance decreases, and this, as discussed above, will increase the dislocation climb rate and hence the mobility.

It is expected that the second effect will eventually dominate as θ increases, leading to a minimum mobility at some small misorientation. The extent to which a theory based on the behaviour of individual dislocations can be applied is also unknown, because reactions at dislocation nodes may become a dominant factor (Hirth and Lothe 1968). In the absence of a specified mechanism, it is not known if the mobility is independent of driving force as is assumed by equation 5.1. On the basis of the above analysis, it is suggested that the variation of the mobility of a general low angle boundary with misorientation may be as shown in figure 5.8.

Comparison with experiment Measurements of the activation energies for LAGB migration or recovery generally indicate control by lattice diffusion as predicted by the model.

The heavy lines in figure 5.8 indicate regions for which there is significant experimental evidence as detailed below.

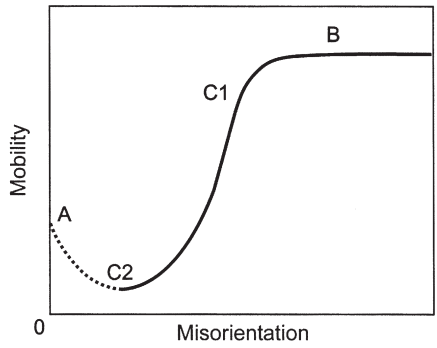

Fig. 5.8. Schematic diagram of the possible variation of the mobility of general low angle boundaries with misorientation. The letters correspond to cases discussed in the text.

REGION A. There are no recent experimental data for this region, but a decrease in mobility with increasing misorientation for $\theta < 1°$, for the special case of symmetrical tilt boundaries under stress, is shown in figure 5.1.

REGION B. There is reasonable evidence that the mobility of random HAGBs is high and independent of θ.

REGION C1. There is evidence. e.g. figures 5.3 to 5.6, that the mobility of boundaries in the range 5–20° increases with θ and saturates at about 14–20°. There is a change in the misorientation dependence of the activation energy for migration at ~14–15° (e.g. figs. 5.2, 5.6 and 5.7) which is consistent with a change in boundary structure, i.e. from a low angle to a high angle boundary.

REGION C2. For misorientations in the range 2–5°, there is evidence in aluminium, that the boundary mobilities increase rapidly with increasing θ (fig. 5.5). Mobilities in this range are typically 10–500 times lower than for a random high angle boundary.

In summary, it is quite clear that although considerable progress has been made in the past decade, further experimental and theoretical work is needed before our understanding of the mobilities of low angle grain boundaries can adequately provide a sound basis for the development of detailed models of annealing.

5.3 MEASUREMENTS OF THE MOBILITY OF HIGH ANGLE BOUNDARIES

5.3.1 The effect of temperature on grain boundary mobility in high purity metals

5.3.1.1 The activation energy for boundary migration

Measurements of the temperature dependence of boundary mobility are often analysed in terms of equation 5.2 to determine the activation energies (Q) and pre-exponential factors (M_0), in the expectation that the values of Q may provide information as to atomic-scale thermally activated processes which control boundary migration.

Table 5.2
The activation energy for migration of high angle grain boundaries in metals of high purity (Haessner and Hofmann 1978).

Material	Activation energy for migration (kJ/mol)	Pre-exponential factor (m/s)	Temperature range (K)	Experiment
Aluminium	63	2×10^4	273–350	Recrystallization
Aluminium	67	4.8×10^3	615–705	Capillary
Copper	121	7.5×10^6	405–485	Recrystallization
Copper	123	2.4	700–975	Capillary
Gold	80	5.8×10^{-1}	593–613	Recrystallization
Lead	25	1.1×10^{-2}	473–593	Striated structure
Tin	25	4.5×10^{-1}	425–500	Striated structure
Zinc[a]	63		525–625	Capillary

[a]Data from Kopetski et al. (1975)

Figure 5.4 is typical of data found for metals of very high purity, where the linear relationship between the logarithm of mobility and 1/T implies a single activation energy over the range of conditions investigated, and table 5.2 shows some experimental data for the mobility of high angle boundaries, obtained by several techniques in a variety of high purity metals. Comparison of the activation energies for boundary migration in table 5.2 with the activation energies for diffusion given in table 5.1 shows that the activation energy for boundary migration in high purity metals is often close to that for grain boundary diffusion, i.e. about half that for bulk diffusion.

5.3.1.2 Transition temperatures

In impure metals or alloys, as will be discussed in §5.3.3, the variation of mobility with temperature is more complicated than that of figure 5.3, with more than one apparent activation energy being found over a range of temperatures. However, even in high purity metals a change in mobility and activation energy is sometimes found at very high homologous temperatures. There are two likely explanations for this:

(a) Changes in boundary structure, in which coincidence site or ordered boundaries may become more disordered and therefore lose their special properties, may occur at elevated temperatures.

There is some evidence from experiments on high purity lead (Rutter and Aust 1965) and copper (Aust et al. 1963, Ferran et al. 1967) that the higher mobility of special boundaries is lost at high temperatures, and this has been interpreted in terms of a change in grain boundary character at high temperatures (see also §4.4.3). Maksimova et al. (1988) have measured a discontinuous change in mobility with increasing temperature for $\Sigma 17$, $28^\circ <001>$ boundaries in 99.9999% tin. Boundaries within $\sim 1^\circ$ of this were found to show a discontinuous **drop** in mobility with increasing temperature

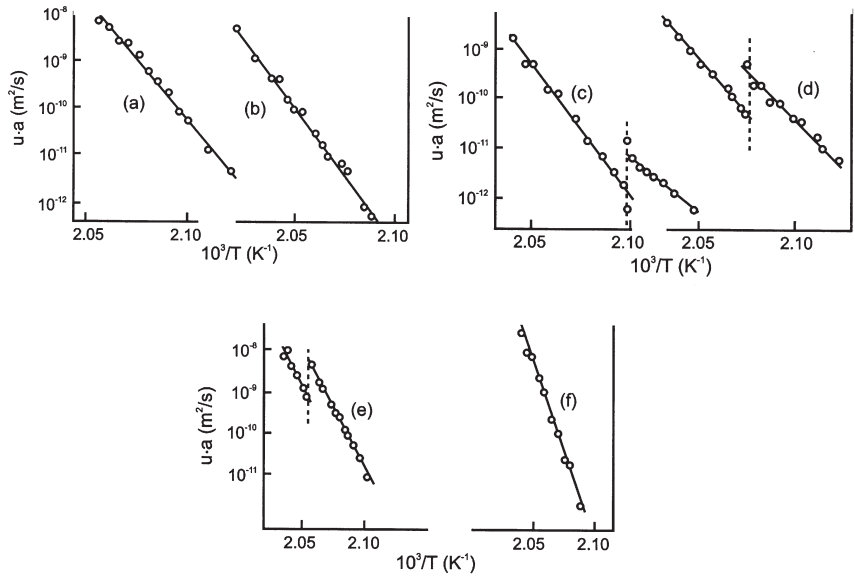

Fig. 5.9. Temperature dependence of the $<001>$ tilt boundary migration rate in tin, for constant driving force. The results show a discontinuous change in mobility for boundaries within ~1° of the 28°, Σ17 boundary. (a) 26.0°, (b) 26.5°, (c) 27°, (d) 27.7°, (e) 28.2°, (f) 29.5°, (after Maksimova et al. 1988).

at temperatures between 0.94 and 0.98 T_m as shown in figure 5.9, whereas boundaries misoriented by more than this amount from Σ17 did not show a transition. Boundaries in the higher temperature regime had a **higher** activation energy, and the authors claimed that this was due to the transition from a special boundary to a general boundary at high temperatures. Wolf and colleagues (e.g. Wolf 2001) have recently provided convincing evidence, using molecular dynamics modelling, of a reversible change in structure of special boundaries, to a disordered 'liquid-like' state at high temperature.

(b) The mechanism of boundary migration may change at high temperatures.

Other work has shown a discontinuous transition to a high temperature regime of higher boundary mobility and low activation energy for migration. Gleiter (1970c) has detected a discontinuous change in properties for $<100>$ tilt boundaries in high purity lead at temperatures in the range 0.7 to 0.8 T_m, the actual temperature depending on the crystallography of the boundary. The high temperature regime is characterised by a very low activation energy for migration (26 kJ/mol) whereas at the lower temperatures the activation energy is 58 kJ/mol which is close to that for boundary diffusion (table 5.1). In zinc, there have been reports of a transition to a very low activation energy of ~17 kJ/mol at $T > 0.91\ T_m$ (Gondi et al. 1992) which is comparable with that for liquid diffusion, and Kopetski et al. (1979) have found a sharp transition to a regime of zero activation energy for boundary mobility in zinc at temperatures above ~0.9 T_m as shown in figure 5.10. Although Gleiter (1970c) interpreted his results in terms of a

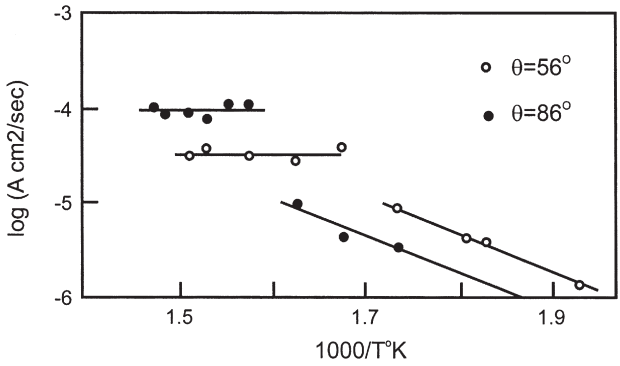

Fig. 5.10. Temperature dependence of the reduced mobility (A) of $<1120>$ tilt boundaries in zinc, for two values of misorientation, showing a transition to a high temperature regime of zero activation energy, (after Kopetski et al. 1979).

transition to a different boundary structure, there is a similarity between all three sets of measurements, and the last two have been interpreted in terms of a change in the mechanism of boundary migration from one controlled by diffusion to one involving cooperative atomic shuffles (§5.4.1.4). Further evidence for such transitions and discussion of the mechanisms can be found in Sutton and Balluffi (1995) and Gottstein and Shvindlerman (1999).

5.3.2 The effect of orientation on grain boundary migration in high purity metals

Because boundary migration involves diffusion processes in and across the boundary, it is to be expected that the structure of the boundary should affect its mobility. In order to define the relationship between two grains it is necessary to specify both the **orientation relationship between the grains** and the **orientation of the boundary plane** (§4.1). Although, as discussed below, there are some data on the effect of these parameters on grain boundary migration, the information is far from complete.

5.3.2.1 The orientation dependence of grain boundary mobility

There is extensive evidence that not only do high angle grain boundaries have a greater mobility than low angle boundaries (§5.2.2) but that the mobilities and activation energies for migration of high angle boundaries are dependent on orientation. Early work in this area includes that of Cook and Richards (1940) and Bowles and Boas (1948) who found rapid growth of certain orientations in copper, and Beck et al. (1950) who showed that in lightly rolled high purity aluminium, grains with a misorientation of $\sim 40^\circ$ about a $<111>$ axis exhibited the largest growth rate. Kronberg and Wilson (1949) who carried out recrystallization experiments on copper, found that grains related to the deformed matrix by a rotation of 22°–38° about a common $<111>$ axis, and by 19° about a $<100>$ axis grew most rapidly. They postulated that there was a relationship between the fast-growing orientations and boundary structure and that **special boundaries,** (later known as **Kronberg-Wilson boundaries),** which had a high

density of **coincidence sites** (§4.4.1) often exhibited fast rates of growth. One of the best known early investigations of the effect of misorientation on mobility is that by Liebmann et al. (1956) who measured the migration rate of $<111>$ tilt boundaries during the recrystallization of 99.8% aluminium crystals which had been lightly deformed. They found the mobility to be a maximum for a misorientation of $\sim 40^\circ$ about a $<111>$ axis, a result which has proved to be of great importance to the theory of recrystallization texture development in fcc metals (§12.3.2). Their results were obtained on lightly strained material in which the impurities were present as dispersed phases. In experiments on similar material in which the impurities were retained in solid solution, a high mobility of $40^\circ <111>$ boundaries was not observed (Green et al. 1959). However, at larger strains (e.g. 80% by rolling), high mobility of these boundaries was observed irrespective of microstructure, for a wide range of purity levels (from 99.97%–99.9999%) (Parthasarathi and Beck 1961, Gleiter and Chalmers 1972). Growth selection experiments on aluminium (Ibe and Lücke 1966) showed similar results, although such experiments must be interpreted with some caution as they do not directly yield boundary mobilities or velocities. Figure 5.11 shows the results of a more recent investigation of the effect of orientation on boundary mobility during the recrystallization of aluminium, in which the effects of both the misorientation angle and axis on mobility are shown. The very broad peak ($\pm 10^\circ$) of figure 5.11a is in agreement with the earlier, more limited results of Liebmann et al. (1956), and contrasts with the much sharper peaks ($\pm 0.2^\circ$) which are typically obtained from curvature-driven grain growth (e.g. fig. 5.12).

Although it is normally found in aluminium alloys that the only fast growing boundaries are those around $40^\circ <111>$, recent investigation of recrystallization in high purity aluminium have shown that at low temperatures ($<150^\circ$C), there is a transition to preferential growth of grains with a relationship of 28–38° about $<100>$ to the deformed matrix (Huang and Humphreys 1999b).

The existence of certain orientation relationships which are associated with a rapid growth rate is well established for a large number of metals (Gleiter and Chalmers 1972), and a summary of the early observations is given in table 5.3. The fact that a boundary has a large number of coincidence sites is not necessarily an indication that it has a high mobility and it is well known that the high angle boundary with the most coincidence sites, the $\Sigma 3$ twin boundary, has an extremely low mobility (Graham and Cahn 1956). It was shown in chapter 4 that although some low Σ boundaries have a low energy, this is not universally the case, and this is reinforced by the data in table 5.3 which show that high mobility has only been identified for a few values of Σ. As is discussed in §5.3.3, the orientation dependence of boundary migration is closely linked to solute effects, and therefore some care must be taken in interpreting the data of table 5.3.

Extensive measurements of boundary mobilities have been carried out by Shvindlerman and colleagues using curvature driven growth in high purity bicrystals of aluminium and other materials. Figure 5.12 shows data for the migration of $<111>$ tilt boundaries in very high purity aluminium and figure 5.13 shows the effects of both misorientation and purity for $<100>$ tilt boundaries in aluminium.

Such experiments enable the relationships between mobility and misorientation to be studied with great precision. It is seen from figure 5.12a that there are two distinct and narrow peaks, at 38.2° and 40.5°. Figures 5.12a and b show that the relative strength of

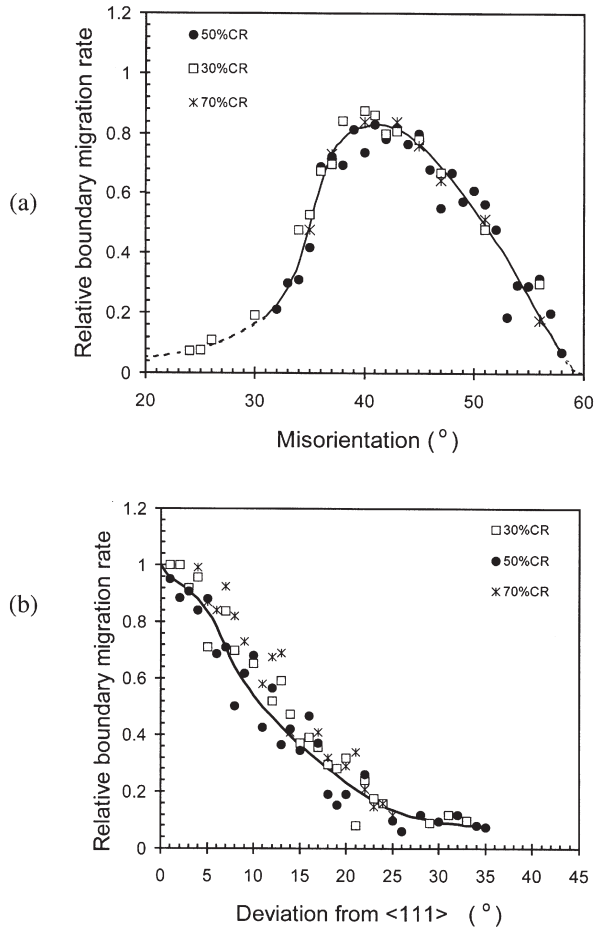

Fig. 5.11. The relative migration rates of recrystallizing grain boundaries as a function of (a) misorientation angle, for boundaries with axes within 10° of $<111>$, (b) deviation from a $<111>$ axis, for boundaries with misorientations between 30 and 50°, (Huang and Humphreys 1999a).

the peaks varies with temperature, and at low temperatures the 38.2° peak is important, whereas at higher temperatures the 40.5° peak dominates. The different temperature dependence of the mobilities of the two types of boundary are evident in figure 5.12b, and this is also expressed as a difference in activation energy as shown in figure 5.12c. The 38.2° $<111>$ boundary is the coincidence site boundary $\Sigma 7$, for which special properties might be expected. The reason for the shift at high temperatures to a peak at 40.5° is not clear, but may be associated with a transformation to a more random boundary structure (Molodov et al. 1995), or may be associated with impurities. In high purity materials, the effects of small amounts of impurity may have a very large influence on the activation energy for boundary mobility as seen in figure 5.13.

Table 5.3
Orientations for which rapid growth is commonly found.

Nearest coincidence relationship			Experimental relationship		Metal	Structure	Reference
Sigma	Rotation	Axis	Rotation	Axis			
Σ7	38.2	< 111 >	35–45	< 111 >	Al	fcc	Liebmann et al. (1956)
			38	< 111 >	Cu	fcc	Kronberg and Wilson (1949)
			36–42	< 111 >	Pb	fcc	Aust and Rutter (1959a)
Σ13a	22.6	< 100 >	23	< 100 >	Al	fcc	May and Erdmann (1959)
			19	< 100 >	Cu	fcc	Kronberg and Wilson (1949)
Σ13b	27.8	< 111 >	30	< 111 >	Cu	fcc	Beck (1954)
			30	< 111 >	Ag	fcc	Ibe and Lücke (1966)
			20–30	< 111 >	Nb	bcc	Stiegler et al. (1963)
Σ13	30	< 0001 >	30	< 0001 >	Zn	cph	Ibe and Lücke (1966)
			30	< 0001 >	Cd	cph	Ibe and Lücke (1966)
Σ17	28.1	< 100 >	26–28	< 100 >	Pb	fcc	Aust and Rutter (1959)
			30	< 100 >	Al	fcc	Fridman et al. (1975)
Σ19	26.5	< 110 >	27	< 110 >	Fe–Si	bcc	Ibe and Lücke (1966)

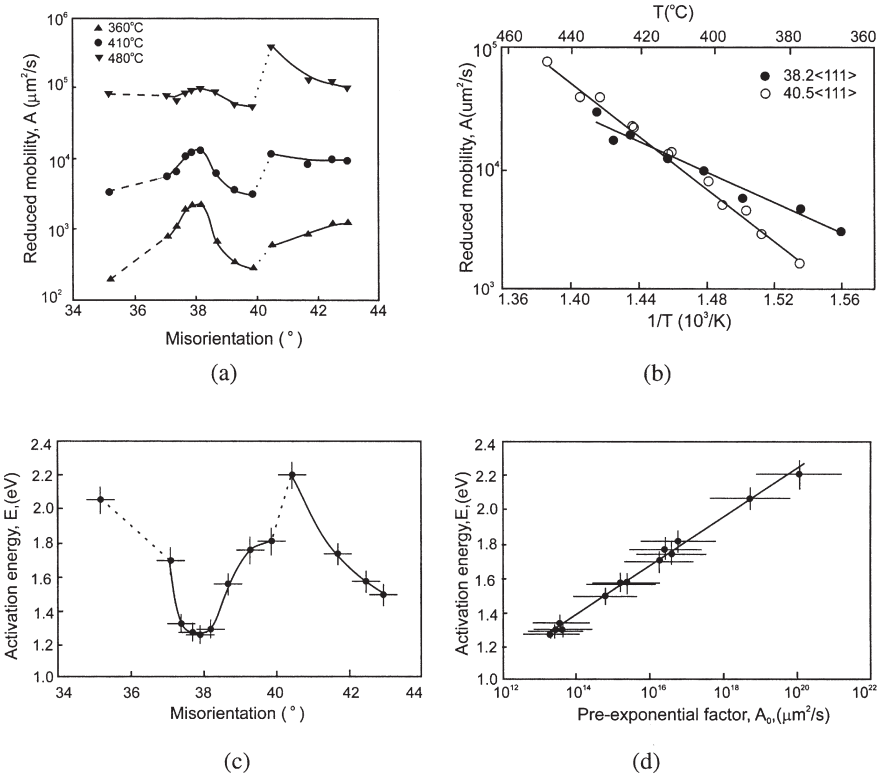

Fig. 5.12. The mobility of $<111>$ tilt boundaries in 99.999 at% Al determined by curvature-driven growth experiments. (a) The effect of temperature on the reduced mobility, (b) The temperature dependence of the reduced mobility of 38.2° and 40.5° $<111>$ tilt boundaries, (c) The activation energy for migration, (d) The relationship between activation energy and pre-exponential factor, (after Molodov et al. 1995).

It is often found that for a particular type of boundary, there is a relationship between changes of the activation energy (Q) and the pre-exponential factor (M_0) as the misorientation is varied, and this is known as the **'compensation effect'** (Molodov et al. 1995). The relationship is

$$Q = \alpha \ln(M_0) + \beta \tag{5.12}$$

where α and β are constants.

Figure 5.12d shows that the relationship between Q and M_0 for boundaries close to $\Sigma 7$ in high purity aluminium is in agreement with equation 5.12. Such a relationship means that in a plot of ln(M) against 1/T, as in figure 5.12b, the various straight lines intersect at a common point (the **compensation temperature**). Such a relationship implies a coupling between the enthalpies and entropies of activation (Molodov et al. 1995,

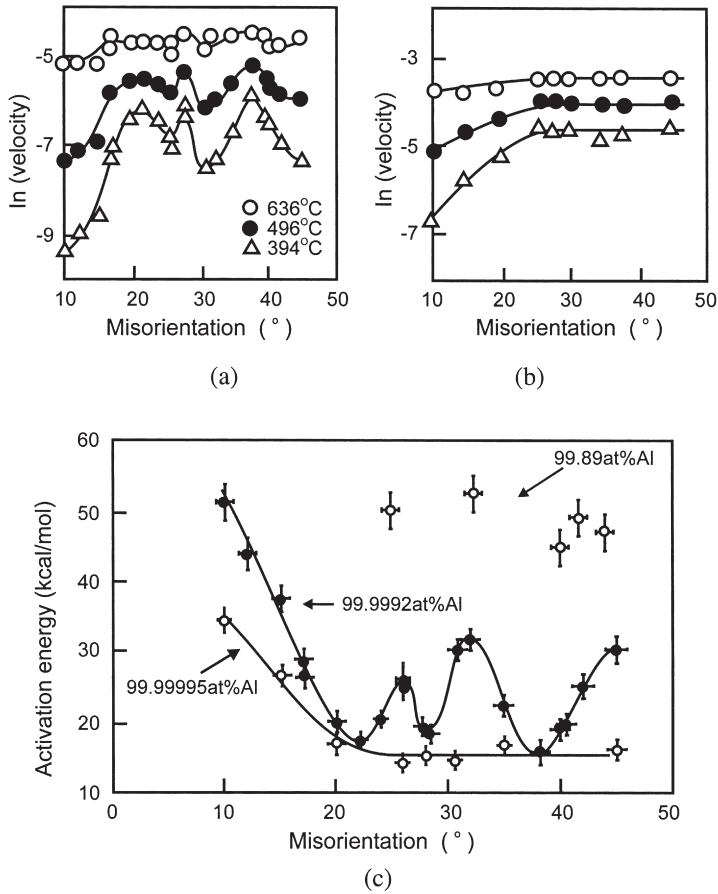

Fig. 5.13. The mobility of <100> tilt boundaries in aluminium. (a) The effect of temperature and misorientation on the mobility of boundaries in 99.9992 at% aluminium, (b) The effect of temperature and misorientation on the mobility of boundaries in 99.99995 at% aluminium, (c) The orientation dependence of the activation energy for migration in samples of different purity, (Fridman et al. 1975).

Sutton and Balluffi 1995). The relationship of equation 5.12 has also been found to hold for low angle grain boundaries ($\Sigma 1$) in aluminium (Huang et al. 2000a). This type of relationship only applies to boundaries of similar type. For example, molecular dynamic simulations predict that boundaries close to either $\Sigma 7$ or $\Sigma 13$ will produce relationships in accord with equation 5.12, but that the constants α and β will be different for the two cases (Upmanyu et al. 1999).

It should be noted that a compensation effect may also be found for other thermally activated grain boundary processes such as diffusion (Sutton and Balluffi 1995).

The orientation dependence of grain boundary migration has implications for the texture developed during recrystallization and grain growth (§12.3.2). In the case of primary recrystallization, it is impossible to define accurately, other than on a very local scale, the relationship between the growing grain and the deformed matrix, because any grain of the deformed material will contain a highly misoriented substructure (§2.4). Therefore caution must be exercised in the application of mobility-orientation relationships to recrystallizing material, and in particular in relating a high boundary mobility to a specific boundary structure. The boundary misorientation is normally defined by an axis/angle pair (§4.2) and there is abundant evidence that, as indicated by figure 5.11a and table 5.3, there is a significant spread of angles for which a high mobility is found. There is less information as to the importance of deviation from a $<111>$ axis, although figure 5.11b shows that this peak is also very broad.

5.3.2.2 The effect of boundary plane on mobility

It has long been known that for a particular misorientation, the boundary mobility may depend on the actual boundary plane (Gleiter and Chalmers 1972). An extreme example is the $\Sigma 3$ twin orientation in fcc metals where the coherent {111} plane boundary is very immobile, whereas the incoherent twin boundary has much greater mobility. It is noticeable that in many cases, grains with an orientation relationship for rapid growth show very anisotropic growth, and an early and very clear example of this is seen in the work of Kohara et al. (1958). For fcc metals the anisotropy is such that the faces parallel to the $<111>$ rotation axis (i.e. the twist boundaries) grow much more slowly than the tilt boundaries (Gottstein et al. 1978), and thus an unconstrained grain tends to become plate-shaped as seen in figure 5.14.

The mobility of 40° $<111>$ tilt boundaries during recrystallization has been found to be some ten times larger than that of the twist boundaries (Huang and Humphreys 2000), and it has also been shown (Huang and Humphreys 1999a) that the **mobilities of the 40° $<111>$ twist boundaries are similar to those of 'random' high angle boundaries.**

During the recrystallization of high purity aluminium at temperatures below $\sim 150^\circ C$, grains with an orientation relationship of $\sim 30^\circ$ about a $<100>$ direction to the matrix (close to $\Sigma 17$), may develop an approximately octahedral shape during recrystallization (figure 5.15) and this has been shown to be due to the growth being most rapid in $<100>$ directions (Huang and Humphreys 1999b). Growth is rapid in all the $<100>$ directions and not just in the direction parallel to the misorientation axis.

In all three of the cases discussed above, $\Sigma 3$, $\Sigma 7$ and $\Sigma 17$, the grains develop asymmetric shapes which are determined by the orientation relationships between the deformed matrix and the recrystallizing grain, and which are the result of anisotropic boundary mobilities.

A quite different example is the crystallographic faceting of recrystallizing grains. There is some evidence from x-ray topography (e.g. Gastaldi, Jourdan and Grange 1992, Sutton and Balluffi 1995) of faceting parallel to low index planes of the new grains during the later stages of recrystallization in pure aluminium, although this behaviour is not commonly observed in recrystallizing aluminium. However, a recent investigation of nickel alloys which had been internally oxidised (Humphreys 2000), has shown evidence of very strong faceting parallel to {100} planes of the recrystallizing grains as shown in

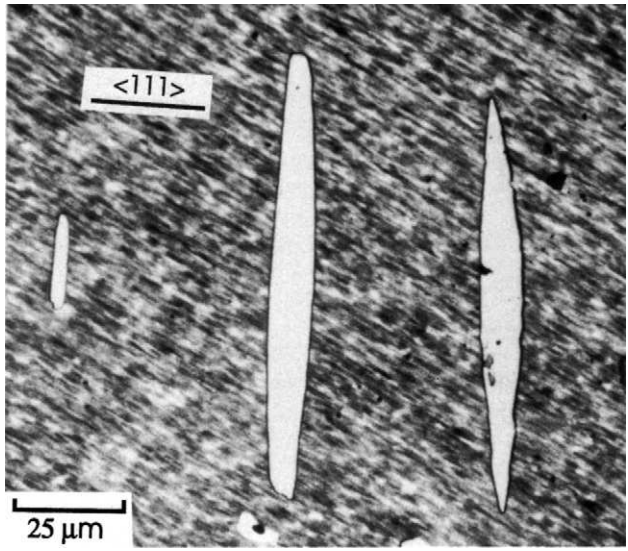

Fig. 5.14. Optical micrograph of lenticular grains, viewed edge-on in a recrystallizing single crystal of Al–0.05%Si. The grains are rotated by ~40° to the deformed matrix about the marked < 111 > axis, and the broad face of the plate is parallel to the rotation axis, (Ardakani and Humphreys 1994).

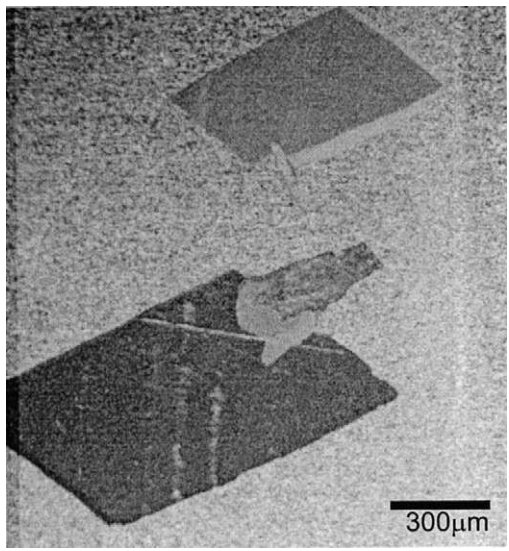

Fig. 5.15. SEM micrograph showing recrystallization in high purity aluminium at 50°C. The grains are misoriented by ~30° to the deformed matrix and grow preferentially in directions parallel to < 100 > of the recrystallizing grains, resulting in an approximately octahedral grain shape, (Huang and Humphreys 1999b).

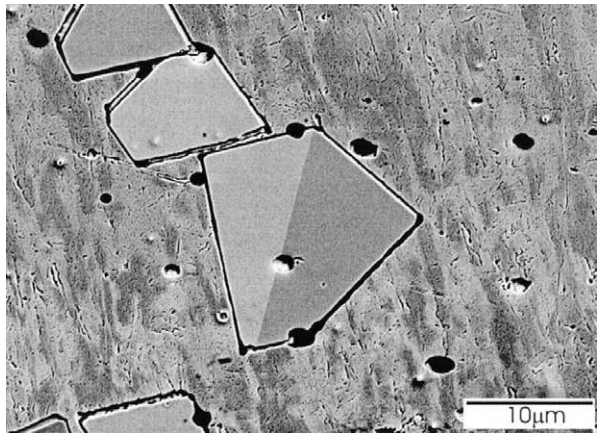

Fig. 5.16. SEM micrograph of recrystallization in a Ni-SiO_2 alloy at 600°C. The recrystallizing grains are faceted on their {100} planes, and the central grain is twinned, (Humphreys 2000).

figure 5.16. The facets are on the recrystallizing grain, and are not affected by the orientation relationship to the deformed matrix. The growth of the grains is therefore somewhat similar to the growth of crystals from the melt, i.e. crystallization rather than recrystallization. As the facets are not evident in the fully recrystallized material, such microstructures appear to be the result of facetted growth rather than anisotropic boundary energies. A reasonable interpretation of such growth behaviour is that the recrystallization is controlled by a ledge mechanism akin to that which occurs for crystal growth from the melt or during vapour deposition. Although it is not yet clear why such a mechanism should control recrystallization in this material, the recent report of similar faceting in electrodeposited nickel with sulphur impurities (Hibbard et al. 2002), suggests that it may be due to impurity segregation at the recrystallizing boundaries.

5.3.3 The influence of solutes on boundary mobility

Solute elements have an enormous effect on boundary migration and very small amounts of impurity may reduce the mobility by several orders of magnitude (Dimitrov et al. 1978) as shown in figure 5.17a. Because the effects of solute are so strong, particularly at low concentrations, it is very difficult to be confident that the mobilities measured in 'pure' metals and discussed in §5.3.1 and §5.3.2 actually represent the intrinsic behaviour of boundaries.

5.3.3.1 The effect of solute concentration

From figure 5.17 it may be seen that the relationship between mobility and solute content shows two distinct regimes separated by a transition region:-

(a) **At high solute concentrations the mobility is low and decreases with increasing solute concentration.** In this low mobility regime it is thought that an atmosphere of solute

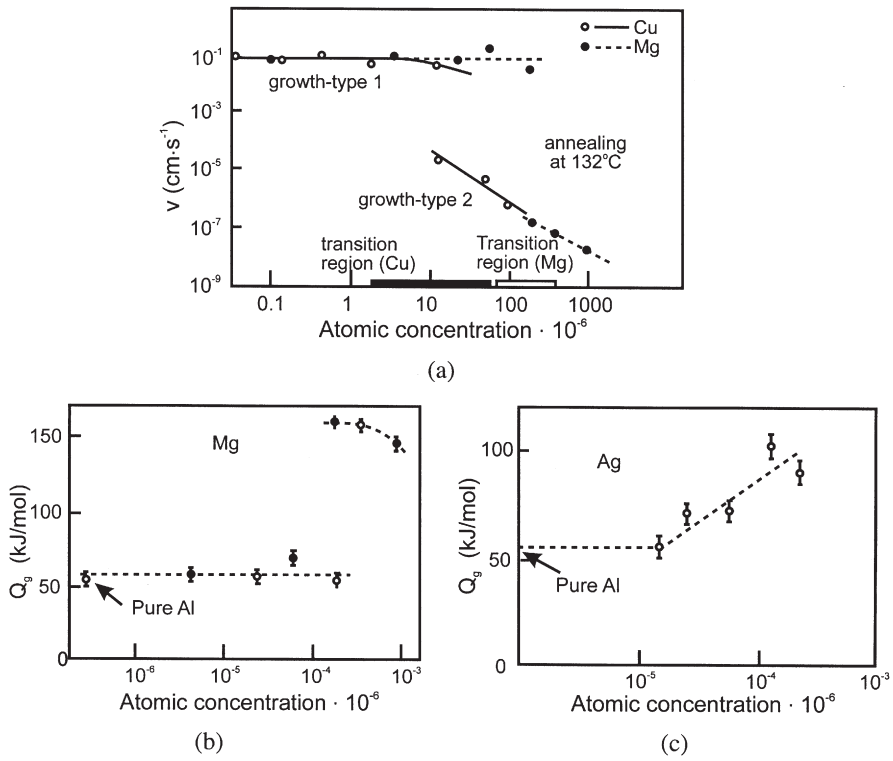

Fig. 5.17. The effect of impurities on the growth rate of new grains in deformed aluminium. (a) The effect of copper and magnesium additions on the growth rate, (b) The effect of magnesium on the activation energy for boundary migration, (c) The effect of silver on the activation energy for boundary migration, (after Frois and Dimitrov 1966).

atoms is associated with the boundary. The boundary velocity is then controlled by the rate of diffusion of the impurity atoms (§5.4.2). Gordon and Vandermeer (1966) have shown that for aluminium containing small amounts of copper, in the low mobility regime the boundary velocity at constant driving force is inversely proportional to the solute concentration as shown in figure 5.18.

(b) **At low solute concentrations the mobility is higher and solute has little influence on the mobility.** In this high mobility regime, the boundary mobility is little affected by solute and it is thought that the boundary has broken away from its solute atmosphere (§5.4.2).

For the cases of copper and magnesium in aluminium shown in figure 5.17a, there is a very sharp transition between the two regimes. However, similar experiments have shown more gradual transitions for silver (fig. 5.17c) or iron (Montariol 1963) in aluminium. In the same solvent, different solutes may, as shown in figure 5.17a affect

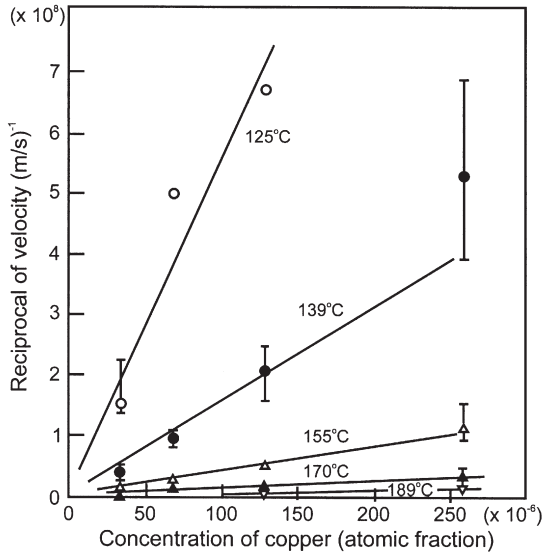

Fig. 5.18 The effect of copper on the migration rate of boundaries in aluminium, (after Gordon and Vandermeer 1966).

the critical concentration at which the transition occurs and, as is apparent in figure 5.17a may also reduce the mobility in the slow regime by different amounts.

The apparent activation energy for boundary migration is also a function of the solute content, exhibiting a transition at the critical solute content at which boundary breakaway occurs as shown in figures 5.17b and c. The details of the transition are different in both cases. For the magnesium solute (fig. 5.17b) the transition is abrupt, whereas for the silver solute (fig. 5.17c) it is gradual.

In most cases it is found that the activation energies at low solute concentrations are essentially solute independent and correspond to those found for materials of very high purity as shown in table 5.2. The apparent activation energy at higher solute concentrations is typically close to that for self diffusion or for diffusion of the solute in the solvent, and, as seen from figures 5.17b and c, may depend on solute concentration.

5.3.3.2 The effect of temperature

The combined effects of temperature and solutes on mobility are best seen from plots of the logarithm of mobility against 1/T. As shown in figure 5.19 for boundary mobility in Au with 20ppm Fe (Grunwald and Haessner 1970), such a plot may show both a change to a lower apparent activation energy and a sharp increase in mobility at a higher temperature. Similar results have been reported for lead (Aust 1969) and copper (Grewe et al. 1973). In most cases it is found that the activation energies at high temperatures

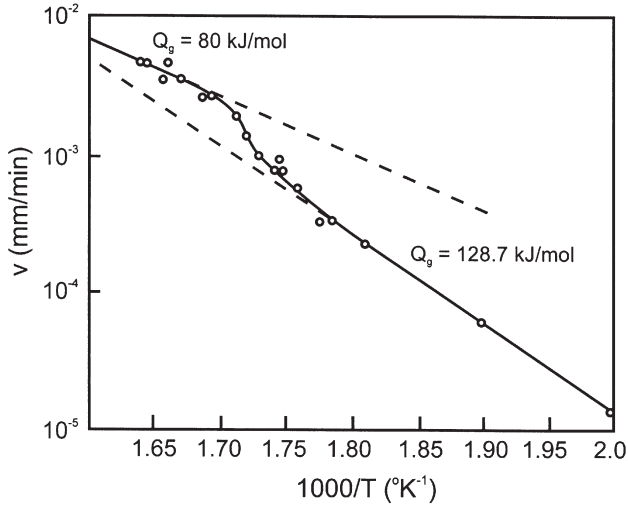

Fig. 5.19. The effect of temperature on the migration velocity of a 30° <111> tilt boundary in gold, (after Grunwald & Haessner 1970).

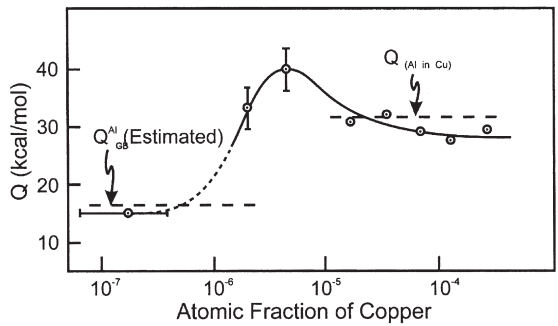

Fig. 5.20. The effect of copper additions on the activation energy for boundary migration in aluminium, (after Gordon and Vandermeer 1962).

correspond to those found for materials of very high purity and the activation energy at low temperature is typically close to that for self diffusion.

In many cases (Gordon & Vandermeer 1962, Fridman et al. 1975) a peak is found in the activation energy at the transition, as is shown in figure 5.20. The origin of this peak can be seen in figure 5.19, where during the transition, the slope of the line (i.e. apparent activation energy) increases. This is clearly an apparent activation energy due to a transition in the effect of solutes on the boundary and does not correspond to the activation energy of a physical mechanism.

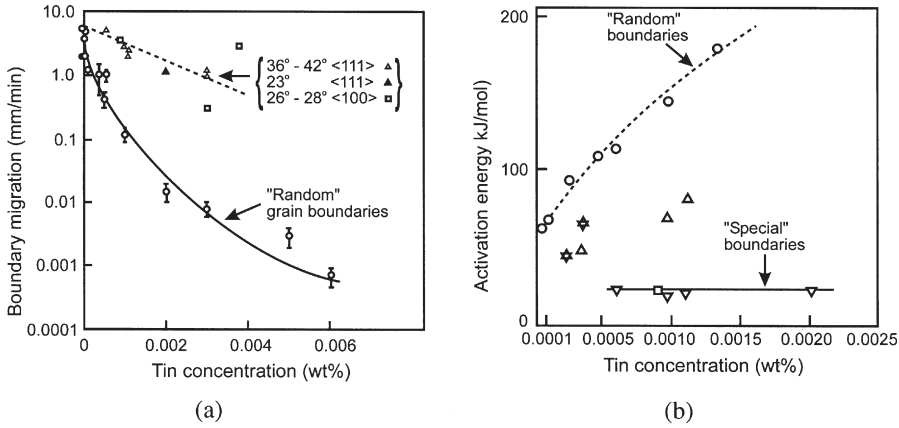

Fig. 5.21. (a) The rate of grain boundary migration at 30°C in zone-refined lead crystals doped with tin (after Aust and Rutter 1959a), (b) The effect of tin on the activation energy for the migration of random and special boundaries in lead, (after Aust and Rutter 1959b).

5.3.3.3 The effect of orientation

It has been known for a long time that the effects of solutes on boundary mobility are dependent on the crystallography of the boundary, and that **special boundaries,** i.e. those which are close to a coincidence relationship, are less susceptible to effects of solute than are **random boundaries** (Kronberg and Wilson 1949, Aust and Rutter 1959a,b). The well-known results obtained by Aust and Rutter on tin-doped lead are shown in figure 5.21. At low impurity concentrations the mobilities of the special and general boundaries are similar. As the impurity level is increased the mobility of the random boundaries is affected much more by the impurities. The combined effects of misorientation and solute have also been demonstrated for tilt boundaries in $<111>$ and $<100>$ rotated grains in aluminium, as shown in figures 5.12 and 5.13. For aluminium of 99.9992 at% purity, except at the highest temperature, the mobility fluctuates with misorientation, with maximum growth rates occurring near coincidence rotations (fig 5.13a). However as shown in figure 5.13b, for material of 99.99995 at% purity, the mobility is found to be almost independent of orientation for $\theta > 20°$. These results confirm those of Aust and Rutter (1959a,b) and indicate that:

The orientation dependence of grain boundary mobility (§5.3.2.1) arises primarily from an orientation dependence of solute segregation to the boundary rather than an intrinsic structure dependence of grain boundary mobility.

There is some evidence, such as that shown in figure 5.13c, that the orientation dependence of mobility disappears not only at high purities, but also at lower purity levels. Experiments on zinc (Sursaeva et al. 1976, Gottstein and Shvindlerman 1992), demonstrate a similar effect, which indicates that the window within which orientation dependence of mobility is found, may be determined by both the boundary structure and the purity level as shown schematically in figure 5.22.

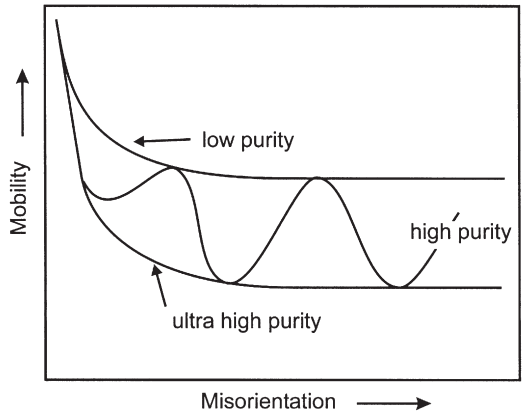

Fig. 5.22. Schematic diagram showing the dependence of the activation energy of grain boundary mobility for different purity levels, (after Gottstein and Shvindlerman 1992).

The evidence for the disappearance of the orientation dependence of boundary mobility at lower purities is not conclusive, and, as discussed by Haessner and Hoffmann (1978), the results of Fridman et al. (1975) for the lowest purity material in figure 5.13c contradict those of Demianczuc and Aust (1975) who found an orientation dependence of mobility in aluminium of similar purity. In addition, much of the evidence for the orientation dependence of mobility in aluminium (Liebmann et al. 1956, Yoshida et al. 1959) was obtained in material of much lower purity. The effect of solutes on the orientation dependence of migration warrants further investigation.

Gordon and Vandermeer (1966) and Gottstein and Shvindlerman (1992) speculate that with lower impurity levels than have yet been achieved, it is conceivable that random grain boundaries would move more easily than special boundaries because the lower energy of the special boundaries would provide a greater barrier to the transitory structure modification required when a boundary moves. However, this argument does not take account of the possibility discussed in §5.4.1 that special boundaries in high purity materials may move by a low energy mechanism involving atomic shuffles, a mechanism which would not be available to random boundaries.

5.3.3.4 The effects of temperature and orientation

There is evidence that in copper (Aust et al. 1963) and lead (Rutter and Aust 1965), the higher mobility of special boundaries in materials of moderate purity may disappear at high temperatures as shown in figure 5.23. This may be due to the evaporation of the solute atmosphere at boundaries at high temperatures (§5.4.2).

5.3.4 The effect of point defects on boundary mobility

The interaction of vacancies and other point defects with static high angle grain boundaries has been extensively investigated (e.g. Balluffi 1980), and it has been shown

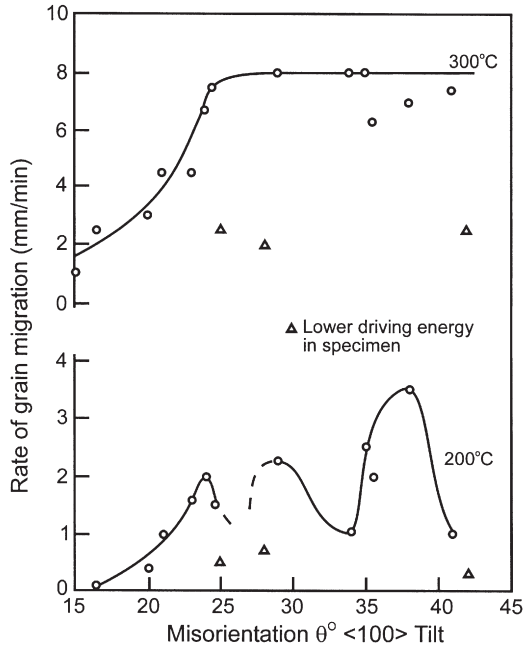

Fig. 5.23. The effect of temperature and orientation on the velocity of tilt boundaries in lead under a constant driving force, (after Rutter and Aust 1965).

that boundaries may act as sources and sinks for point defects and that point defects interact with grain boundary dislocations. The effect of point defects on a migrating boundary is less clear, although there is evidence (Hillert and Purdy 1978, Smidoda et al. 1978) that the diffusion coefficient of a moving boundary is several orders of magnitude larger than that of a stationary boundary.

5.3.4.1 The effect of vacancies on boundary mobility

The role of defects on boundary mobility has been extensively discussed e.g. Cahn (1983), Gleiter and Chalmers (1972), Haessner and Hofmann (1978). Although these reviewers are in general agreement that a vacancy flux or supersaturation enhances boundary mobility, the experimental evidence for this is not extensive. Evidence which indicates that vacancies enhance migration was obtained by Haessner and Holzer (1974), who showed that neutron irradiation increased the boundary velocity in recrystallizing copper single crystals as shown in figure 5.24. In this material the irradiation produces Frank vacancy loops, and although this increases the driving force for recrystallization, the authors claim that calorimetric measurements showed that this effect was negligible and that the vacancy loops increased the boundary mobility. Support for this is provided by the work of Atwater et al. (1988), who attributed increased grain growth rates in ion-bombarded thin films of gold, germanium and silicon to the effect of the point defects on boundary mobility.

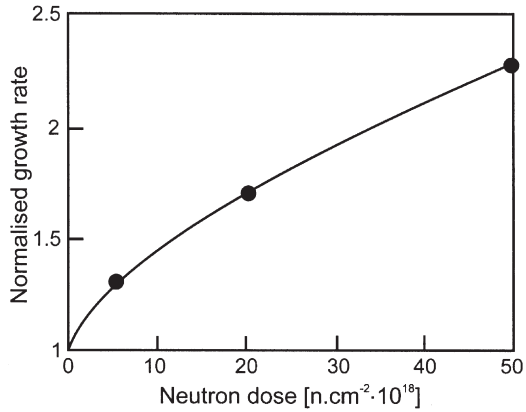

Fig. 5.24. The effect of neutron irradiation on the boundary migration rate in copper, (after Haessner and Holzer 1974).

Other indirect evidence indicating that vacancies affect boundary mobility comes from the sintering of copper wires, when the presence of pores on a boundary is found to increase its mobility (Alexander and Balluffi 1957), and from the sintering of alumina, when small pores are found to be consumed by slowly migrating boundaries (Coble and Burke 1963).

The basic concept that the vacancies swept up by a moving boundary will increase the free volume of the boundary and therefore aid atom movement across the boundary is plausible (Gordon and Vandermeer 1966), but has not been backed by rigorous theory. Such a model implies that the structure of static and moving boundaries will be different and also suggests that boundary structure and hence mobility may be dependent on boundary velocity. This problem is most likely to be resolved ultimately by dynamic computer simulations of boundary migration.

It may be difficult to separate the effects of vacancies on the boundary mobility and on the driving pressure for boundary migration. Estrin et al. (1999, 2000) have discussed the thermodynamic effects of vacancies during grain growth. During grain growth, the boundary area per unit volume decreases, and the consequent elimination of the excess free volume associated with the boundaries will lead to injection of vacancies into the grains. As this increases the energy of the grains, there will therefore be a reduction in the driving pressure for grain growth. This effect is only likely to be important for very fine-grained materials, but is predicted to have a significant influence on the stability of nanocrystalline materials against grain growth. This is a similar argument to that advanced for a solute-limited grain size (§11.4.2.5).

5.3.4.2 Generation of defects by moving boundaries

A moving boundary may act as a source of defects, and there is evidence (Gleiter 1980) that in material of low dislocation density, a higher dislocation density may be left behind a migrating boundary. This is attributed to the formation of dislocations by

growth accidents rather than to the emission of dislocations by stress relaxation at the boundary. Gleiter suggests that in a similar manner, growth accidents will lead to vacancies being left behind a moving boundary, and cites experimental evidence of a vacancy supersaturation behind moving boundaries in aluminium and nickel alloys.

5.3.5 The scope of experimental measurements

It should be emphasised that for a number of reasons we cannot confidently draw general conclusions about the mobility of high angle grain boundaries during recrystallization.

- It is extremely difficult to carry out reliable experimental investigations of boundary mobility.
- There are a large number of variables to be investigated including solvent, solute, concentration, misorientation, boundary plane, temperature and driving force, and therefore there have been few systematic investigations.
- The most detailed systematic investigations have been carried out by curvature driven grain growth, with driving pressures which are a significantly lower than those found in recrystallization, at very high temperatures, and on special boundaries.

5.4 THEORIES OF THE MOBILITY OF HIGH ANGLE GRAIN BOUNDARIES

In this section we examine the extent to which the migration of high angle boundaries in pure and solute-containing alloys can be accounted for theoretically. This subject is discussed in more detail in the recent books by Sutton and Balluffi (1995) and Gottstein and Shvindlerman (1999).

5.4.1 Theories of grain boundary migration in pure metals

A schematic diagram of a grain boundary is shown in figure 5.25a. Models of grain boundary migration are generally based on the assumption that atoms are continually detached from the grains (e.g. A and B) by thermal activation and move into the more disordered region of the boundary itself (e.g. C), which is shown exaggerated in figure 5.25a. The atoms are then re-attached to one of the grains. If the atom flux in both directions is equal then the boundary is static. However, if there is a driving force for migration then the flux will be greater in one direction. There are several proposed variants on this general model, the main variables being:

Single or group activation. Migration may occur either by the activation of single atoms or by the collective movement of a group of atoms.

The role of atoms in the boundary region. Atoms detached from a parent grain are either immediately reattached to a grain or may remain or move in the boundary region.

Preferential sites. If the crystallography of the boundary is taken into account then there may be preferential sites for detachment and attachment of atoms.

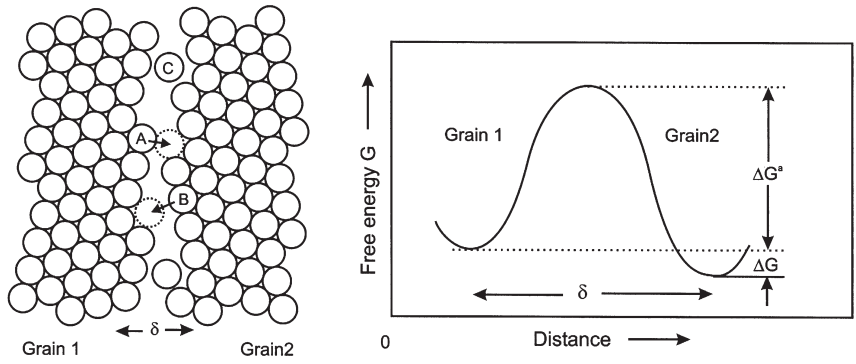

(a) (b)

Fig. 5.25. Grain boundary migration by means of atom jumps. (a) The mechanism of migration, (b) The free energy of an atom during a jump across the boundary.

5.4.1.1 Thermally activated boundary migration – early single-process models

The theory of boundary migration based on reaction rate theory, in which boundary movement is controlled by single atom movements, was proposed by Turnbull (1951), and in this section we use this type of approach to illustrate the nature of the problem. Consider the boundary of figure 5.25a, which is considered to have a thickness δ, moving to the left under the influence of a free energy difference of ΔG. In order for an atom to break away from its parent grain it must acquire, by thermal activation, an activation energy of ΔG^a as shown in figure 5.25b. If the frequency of atomic vibration is ν_0, then the number of times per second that the atom acquires this energy is $\nu_0 \exp(-\Delta G^a/kT)$. If there are **n** atoms per unit area of boundary which are suitable sites for a jump, then the number of jumps per second from a grain is $n\nu_0 \exp(-\Delta G^a/kT)$. However, they will not all be in favourable positions to jump, and therefore we include a grain boundary structure dependent factor A_J, which is the fraction of atoms able to jump. As not all atoms may find a suitable site for attachment to the other grain, then we introduce an accommodation factor A_A, which is the fraction of successful attachments. The effective flux of atoms from grain 1 to grain 2 will thus be

$$A_J A_A n \nu_0 \exp\left(-\frac{\Delta G^a}{kT}\right)$$

In the same manner, there will be a flux of atoms from grain 2 to grain 1, given by

$$A_J A_A n \nu_0 \exp\left(\frac{-\Delta G^a + \Delta G}{kT}\right)$$

There will therefore be a net flux from grain 1 to grain 2 of

$$J = A_J A_A n \nu_0 \exp\left(\frac{-\Delta G^a}{kT}\right)\left(1 - \exp\left(\frac{-\Delta G}{kT}\right)\right) \tag{5.13}$$

If the boundary velocity is v, and the interatomic spacing is b, then,

$$v = J\frac{b}{n} = A_J A_A \nu_0 b \exp\left(\frac{-\Delta G^a}{kT}\right)\left(1 - \exp\left(\frac{-\Delta G}{kT}\right)\right) \tag{5.14}$$

As the free energy changes during recrystallization are small, we may assume that $\Delta G \ll kT$ and expand $\exp(-\Delta G/kT)$ giving

$$v = A_J A_A \nu_0 b \exp\left(\frac{-\Delta G^a}{kT}\right)\left(\frac{\Delta G}{kT}\right) \tag{5.15}$$

As the driving pressure $P = \Delta G$ then

$$v = A_J A_A \nu_0 b \exp\left(\frac{-\Delta G^a}{kT}\right)\frac{P}{kT} \tag{5.16}$$

and substituting $\Delta G = \Delta H – T\Delta S$ then

$$v = A_J A_A \nu_0 b \exp\left(\frac{-\Delta H^a}{kT}\right)\exp\left(\frac{\Delta S}{k}\right)\frac{P}{kT} \tag{5.17}$$

Equation 5.17 is therefore identical in form to equation 5.1 with

$$M = \frac{A_J A_A \nu_0 b}{kT}\exp\left(\frac{-\Delta H^a}{kT}\right)\exp\left(\frac{\Delta S}{k}\right) \tag{5.18}$$

The model discussed above is very general and not specific enough to allow prediction of the parameters such as the activation energy (ΔH^a). For example, although the activated process is often identified with grain boundary diffusion, in this model the atoms move **across** the boundary rather than **within** it and the two processes are not necessarily identical. Also, a better defined basis for the parameters A_J and A_A needs to be developed. These problems, and the question of whether atoms migrate within the boundary region have been addressed more specifically in later theories which take account of the boundary structure and which attempt to relate the mobility to movements in grain boundary defects such as **steps** or **dislocations** as discussed below.

5.4.1.2 Early group-process theories

In the earliest group-process theory by Mott (1948), groups (islands) of atoms move from one grain into the boundary region and similar groups attach themselves to the other grain. Later developments of this type of model are reviewed by Gleiter and Chalmers (1972). The attractiveness of such models was that because groups of atoms were thermally activated, this required a much larger activation energy than that for a single atom (equation 5.18), which was at that time in accord with experimental observations. However, when it was later shown that such large activation energies were due to impurities (§5.3.3), and were not characteristic of boundaries in pure materials (table 5.2), attention switched to single-process theories. As discussed below, there is now some evidence that cooperative atomic movements are important in boundary

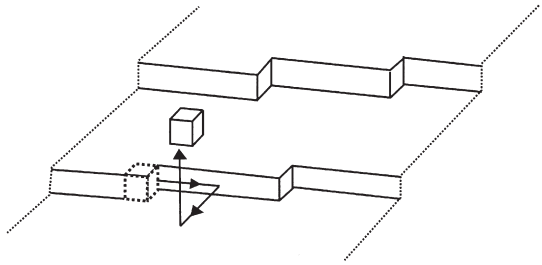

Fig. 5.26. The ledge mechanism of boundary migration. An atom is detached from a kink in the ledge, migrates along the ledge and into the boundary, (after Gleiter 1969b).

migration of pure materials and newer versions of group-process models are currently being developed.

5.4.1.3 Step models

An early attempt to incorporate the effects of boundary structure into a model for boundary mobility was made by Gleiter (1969b) who proposed a detailed atomistic model in which boundary migration occurred by the movement of steps or kinks in the boundary as shown in figure 5.26. Evidence for the existence of such steps had been found from transmission electron microscopy (Gleiter 1969a). The steps move by the addition or removal of atoms from the steps, and the atoms are assumed to diffuse for short distances within the grain boundary. This is an analogous process to that occurring during the growth of crystals from a vapour, and interface migration by ledge movement is a well established mechanism for the movement of interphase boundaries during phase transformations (Aaronson et al. 1962).

For driving pressures of the magnitude encountered during annealing, Gleiter calculates the boundary velocity to be

$$v = b\nu_0 \Psi \exp\left(\frac{\Delta G^a}{kT}\right)\frac{P}{kT} \tag{5.19}$$

This is similar to equation 5.15, but modified by a factor Ψ which is a function containing details of the step configuration in a boundary of thickness δ, and which is of the form

$$\Psi = \frac{c}{\delta}\left(1 + \frac{b}{\delta}\left(\frac{1}{f_1} - \frac{1}{f_2}\right)\right) \tag{5.20}$$

where **c** is a constant and f_1 and f_2 are functions of the step density on the crystals either side of the boundary. The mobility of the boundary is predicted to be dependent on both the misorientation and the boundary plane through the terms f_1 and f_2. For example for the case of crystals rotated about a $<111>$ axis in fcc metals, the ledge density and hence the mobility is predicted to be lowest for the {111} twist boundaries as is found in practice (§5.3.2.2).

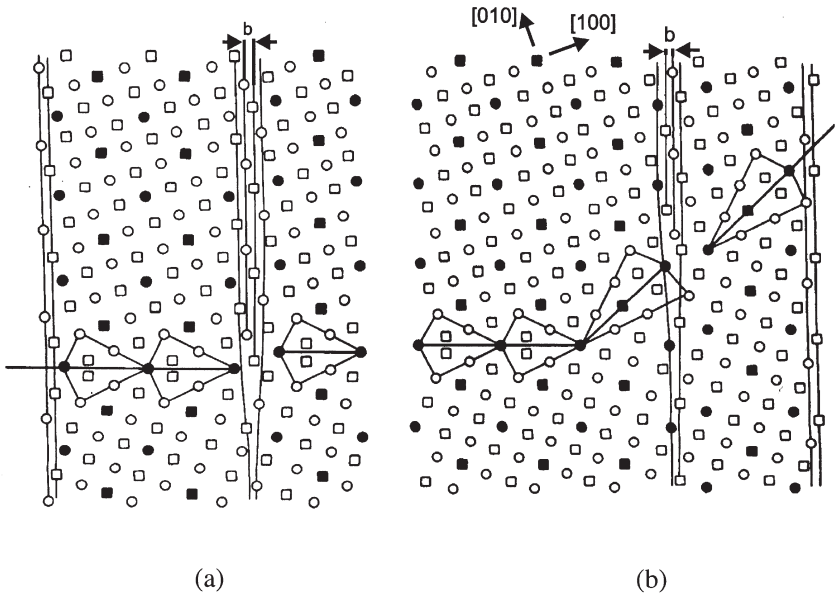

Fig. 5.27. Atomic arrangement of a Σ5 tilt boundary in an fcc lattice which contains dislocations with Burgers vectors (a) parallel to the boundary or (b) inclined to the boundary. In (a) the boundary dislocations can move by glide, whereas in (b) climb and glide are required. The open symbols represent the ABA... stacking sequence of the {001} planes and the filled symbols are coincidence sites, (Smith et al. 1980).

5.4.1.4 Boundary Defect Models

An improvement in the understanding of the defect structure of high angle grain boundaries, and recognition that steps and intrinsic boundary dislocations are common features, has led to experimental and theoretical investigations into the role of these defects in the processes of boundary migration. There is a very close relationship between boundary steps and boundary dislocations, and in general, boundary dislocations have steps in their cores (King and Smith 1980). The example shown in figure 5.27 is of a $1/10 < 310 >$ dislocation in a boundary close to Σ5 in an fcc material. The height of these steps depends on the Burgers vector of the dislocation, the boundary plane and the crystallography of the boundary. When such dislocations move, then the steps move and boundary migration inevitably occurs. There is extensive evidence that boundary dislocations move and multiply and that they retain their core structure at elevated temperatures (e.g. Dingley and Pond 1979, Rae 1981, Smith 1992).

In special cases, the dislocations can glide in the boundary plane and therefore athermal boundary migration is possible. A well known example of this is the case of $1/6 < 112 >$ twinning dislocations in fcc materials. These dislocations move by glide on the {111} planes and the twin plane advances by one {111} planar spacing for the passage of each dislocation. In the more general case, the dislocation cannot glide in the boundary and a combined glide/climb movement of the boundary dislocations is required.

If boundary movement is accomplished by the collective movement of a density ρ of boundary defects each moving at velocity **v** and having a step height **h,** then the boundary velocity (v_b) will be given (Smith 1992) by an expression of the form

$$v_b = h\rho v \tag{5.21}$$

Glide of boundary dislocations is of course associated with shear deformation and the process of boundary dislocation motion results in a combined migration and sliding of the boundary. Such a combined process has been modelled by Bishop et al. (1980) and has been observed in zinc bicrystals by Ando et al. (1990), and on near $\Sigma 5$ boundaries in gold bicrystals by Babcock and Balluffi (1989a), who found good correlation between the movement of boundary dislocations and the migration and sliding of a boundary under stress. It should however be noted that such dislocation motion results in a **shape change,** which if not relaxed can exert a back-stress such as to cancel out the driving pressure for boundary migration (Smith et al. 1980). This suggests that the behaviour of unconstrained bicrystals may be different from that of the constrained polycrystals which are of more general importance in recrystallization and grain growth (cf. §5.2.1).

Further experiments of Babcock and Balluffi (1989b) in which the boundaries migrated under the influence of capillary forces at high temperature showed quite different behaviour. The boundaries migrated in a jerky fashion and the movement of boundary dislocations was found to account only for a negligible part of the boundary migration, particularly for more general boundaries. Whether or not such jerky boundary migration is genuine or is an artefact of the experiment is not yet clear, although similar behaviour has been found by a number of workers. On the basis of their experiments and from computer simulations (Majid and Bristowe 1987) and Babcock and Balluffi (1989b) have interpreted these experiments in terms of **local cooperative shuffling** of atoms in a process similar to that proposed by Bauer and Lanxner (1986). This mechanism is shown schematically for a $\Sigma 5$ $<001>$ twist boundary in figure 5.28.

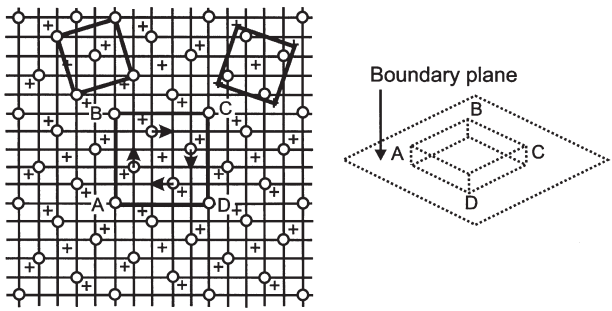

Fig. 5.28. Proposed mechanism of migration of $\Sigma 5$ [001] twist boundary by atomic shuffling. (a) View along [001] showing first planes of crystal 1 (O) and crystal 2 (+) facing the boundary. Vectors show the atomic shuffles of atoms in crystal 1 required to displace the boundary by a/2 and produce the square boundary ledge shown obliquely in (b), (after Babcock and Balluffi 1989b).

Babcock and Balluffi (1989b) argue that this is a more important mechanism of boundary migration than is the movement of boundary dislocations. However, the number of atoms which must move in a coordinated manner in such a shuffle is large for high order CSLs, and therefore this **type of mechanism is only likely to be effective in a highly ordered boundary and not in a general boundary.**

5.4.1.5 The status of boundary migration models

Theoretical and experimental work in recent years has largely concentrated on the behaviour of low Σ boundaries, and in particular on symmetrical tilt boundaries in materials of very high purity. As such simple boundaries are not typical of more general boundaries, this has probably led to an over-emphasis on the importance of boundary structure and defects in interpreting the migration of boundaries as was concluded by Smith (1992).

Although the movement of steps or boundary dislocations certainly occurs, and can explain some properties of some boundaries, the important process in the more general case appears to be the thermally activated transport of atoms across boundaries and the migration would seem to be controlled by the activation energy for this process. Apart from special cases, there is no good evidence that the sites of attachment and detachment have any significant effect.

It has long been recognised that in general boundaries the **local excess volume or porosity** of the boundary is a very important parameter which may determine not only the energy of the boundary (§4.4.2), but also the migration behaviour (Seeger and Haasen 1956, Gordon and Vandermeer 1966), and that except for low Σ boundaries, this is likely to be more important than the atomistic details of the boundary structure. The concept of excess boundary volume can explain a number of important factors which are related to the boundary crystallography, including the higher mobility of tilt boundaries than twist boundaries (§5.3.2.2) and the relative effect of solutes on general and special boundaries (§5.3.3).

5.4.2 Theories of grain boundary migration in solid solutions

Most theories of the effects of solutes on boundary mobility are based on that proposed by Lücke and Detert (1957) for dilute solid solutions. The theory was further developed independently by Cahn (1962) and by Lücke and Stüwe (1963), and later extended to include higher solute contents by Lücke and Stüwe (1971).

There are several other earlier theories which are reviewed by Lücke and Stüwe (1963), Gordon and Vandermeer (1966) and Gleiter and Chalmers (1972) and there have been several later models, notably those proposed by Bauer (1974) and by Hillert and Sundman (1976) and Hillert (1979) who extended the theory to include high solute contents. However, the **Cahn–Lücke–Stüwe (CLS)** model is still widely accepted as giving a good semi-quantitative account of the effects of solute on boundary migration, and this is the basis for the following discussion.

The CLS theory is based on the concept that atoms in the region of a boundary have a different energy (**U**) to those in the grain interior because of the different local atomic

environment. There is therefore a force (**dU/dx**) between the boundary and a solute atom which may be positive or negative, depending on the specific solute and solvent. The total force from the boundary on all solute atoms is **P = ΣdU/dx,** and an equal and opposite force is exerted by the solute atoms on the boundary. The result of this interaction is an excess or deficit of solute (an atmosphere) in the vicinity of the boundary, and the solute concentration (**c**) is given by

$$c = c_0 \exp\left(-\frac{U}{kT}\right) \tag{5.22}$$

where c_0 is the equilibrium solute concentration.

For a stationary boundary and a solute which is attracted to the boundary, the interaction energy (**U**), force (**F**), solute concentration (**c**) and diffusion coefficient (**D**) are shown in figure 5.29 as a function of distance (**x**) from the boundary.

The extent to which an element segregates to a stationary boundary is usually related to its solubility, and as a general rule the tendency for segregation increases as the solubility decreases as is shown in figure 5.30. It is therefore to be expected that the force exerted by solute atoms on a boundary, which is a function of the solute concentration in the boundary and solute diffusivity, will depend strongly on the specific solute and solvent combination.

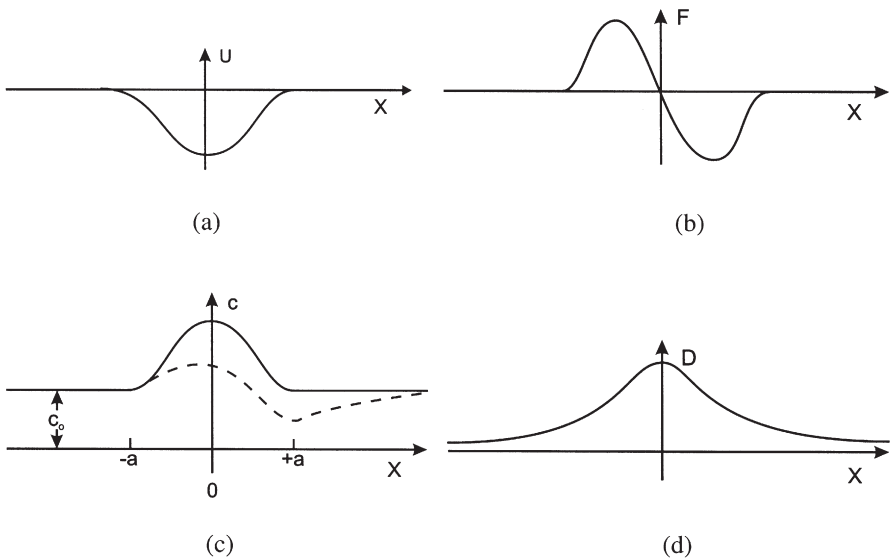

Fig. 5.29. Schematic diagrams of the interaction of solute with a boundary. (a) The potential U(x), (b) The interaction force F(x) between a solute atom and the boundary, (c) The resulting distribution of solute atoms for a stationary boundary (full line) and a boundary moving from left to right (dotted line), (d) Diffusivity in the boundary region D(x).

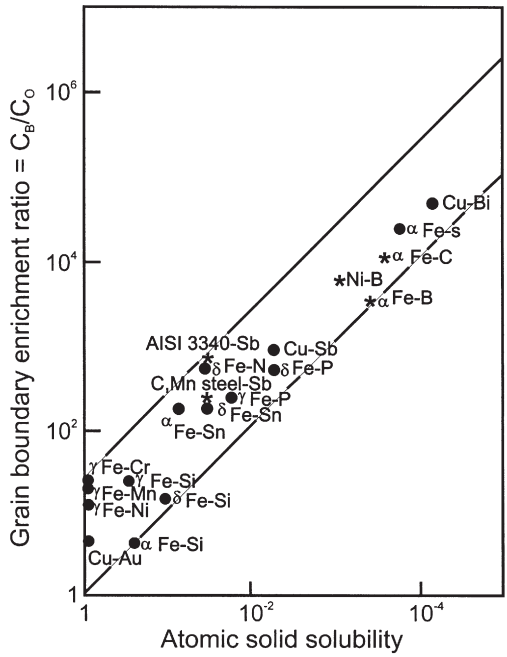

Fig. 5.30. Increasing grain boundary enrichment with decreasing solid solubility in a range of systems, (after Hondros and Seah 1977).

If moving boundaries have a larger free volume than stationary boundaries (§5.3.4), then it is to be expected that solubility in a moving boundary will be greater than in a static boundary. There is some indirect evidence for this from a study of Pb–Au alloys by Simpson et al. (1970) who found that precipitation occurred at grain boundaries in specimens undergoing grain growth which were quenched and aged, whereas this effect was not found in material with stationary boundaries.

5.4.2.1 Low boundary velocities

For a moving boundary, the solute profile becomes asymmetric as shown in figure 5.29c such that the centre of gravity of the distribution lags behind the boundary.

For the case illustrated in figure 5.29c, where the boundary is moving from left to right, there is therefore a net force due to the solute, dragging the boundary to the left. As the boundary velocity increases, the solute lags further behind the boundary.

The relationship between the driving pressure (**P**) and boundary velocity (**v**) at low velocities is found to be

$$P = \frac{v}{M} + \alpha c_0 v \tag{5.23}$$

where M is the mobility of the boundary in the absence of solute, and α is a constant which depends on the details of the model.

It may be seen from equation 5.23 that the velocity is predicted to be inversely proportional to the solute concentration (c_0). The apparent activation energy for boundary migration will be the mean value for solute diffusion in the boundary region, which will depend both on the value of U and the assumed U-x and D-x profiles (fig. 5.29). Hillert (1979) has shown that the choice of these parameters has a large effect on the results. For example, the CLS model assumed a wedge shaped energy-well rather than that shown in figure 5.29a, and it also assumed that diffusivity is constant throughout the material. It should be emphasised that this theory is limited to dilute solid solutions ($c_0 < 0.1\%$). Hillert (1979) calculated the boundary mobility using a model which allows the boundary diffusivity to differ from that of the bulk and found that the maximum value of the solute drag was much smaller than predicted by equation 5.23 if an increased boundary diffusivity was assumed.

5.4.2.2 High boundary velocities

The relationship between boundary velocity and driving pressure at intermediate velocities is very difficult to calculate as it depends critically on the details and parameters of the model. However a limiting case is reached at high boundary velocities when the solute atoms can no longer keep up with the boundary, which then breaks away from its atmosphere. In this case

$$P = \frac{v}{M} + \frac{c_0}{\alpha' v} \tag{5.24}$$

where α' is a constant.

It is estimated that the first term is dominant and therefore the solute atoms have only a small effect. The mobility and activation energy are then expected to be similar to the intrinsic values for a boundary in a pure metal (§5.3.1).

Equations 5.23 and 5.24 are combined by Cahn (1962) and Lücke and Stüwe (1963) to give

$$P = \frac{v}{M} + \frac{\alpha c_0 v}{1 + \alpha\alpha' v^2} \tag{5.25}$$

5.4.2.3 Predictions of the model

This model predicts that the retarding force due to solute drag varies with boundary velocity, reaching a maximum value as shown in figure 5.31. This figure also shows that the solute drag becomes less effective at high temperatures, and this is because under these conditions the solute concentration near the grain boundary decreases in accord with equation 5.22, so that the atmosphere effectively evaporates.

Although, for the reasons discussed above, it is difficult to fully quantify the CLS model, it is of interest to look at the qualitative predictions regarding the relationships

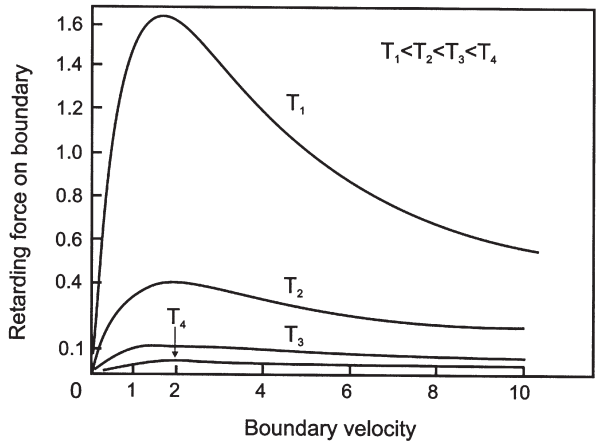

Fig. 5.31. The variation of solute drag force with boundary velocity and temperature, (after Lücke and Stüwe 1963).

between driving pressure, solute concentration and temperature and boundary velocity, as shown schematically in figure 5.32. In figure 5.32a the effect of three levels of solute content on the relationship between velocity and driving pressure is shown and compared with the behaviour of the pure material in which the velocity is proportional to the driving pressure (equation 5.1). It may be seen that for very low solute concentrations the curve is continuous, and deviates only slightly from that predicted for the pure material. However, for high solute concentrations, the curve is S-shaped and predicts a discontinuous change of velocity (dotted lines) from the lower branch (equation 5.23) and the upper branch (equation 5.19). In figure 5.32b, the boundary velocity is plotted as a function of temperature for the cases of low solute **A**, high solute **B** and no solute **C.** The slope of the plot of ln(v) vs 1/T may be interpreted in terms of an apparent activation energy. The straight lines **D** and **E** superimposed on **A** and **B,** represent the limiting cases for low velocity as given by equation 5.23.

5.4.2.4 Correlation of experiment and theory

Although the experimental data are very limited and the theories cannot as yet be fully quantified, it appears that many features of the experimental results can be qualitatively explained in terms of the CLS model.

- **At low velocities the velocity is inversely proportional to the solute concentration**

This result, which is predicted by equation 5.23, is consistent with the experimental results shown in figure 5.17.

- **At higher driving forces or lower solute concentrations, there is a transition to a high velocity regime in which the boundary velocity is independent of solute content**

This is clearly shown in the results of figures 5.17 and 5.19.

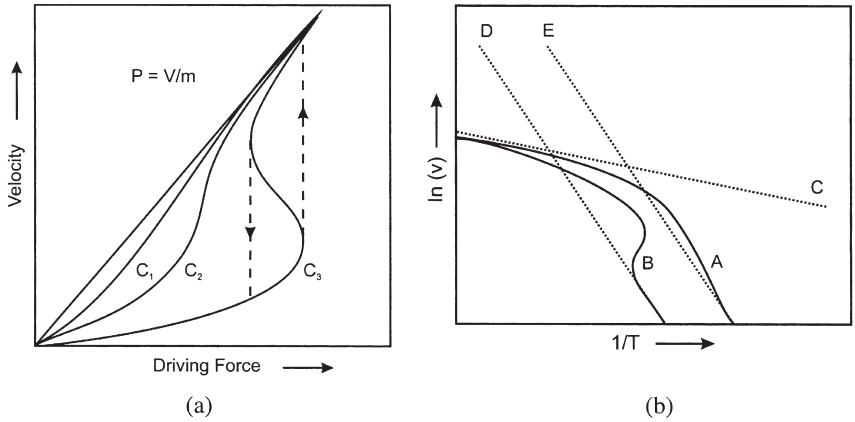

Fig. 5.32. (a) Predicted grain boundary velocity as a function of the driving force for different solute concentrations $c_3 > c_2 > c_1$, (b) Predicted grain boundary velocity as a function of temperature for low (curve A) and high (curve B) solute concentrations. Curve C represents the behaviour for the pure material and curves D and E the low velocity limiting case described by equation 5.23, (after Lücke and Stüwe 1963).

- **The apparent activation energy will decrease as the temperature increases**

This result, which is predicted by the model as shown in figure 5.32b, is in accord with many of the experimental results discussed in §5.3.3. The model predicts that at low boundary velocity, the mobility is controlled by solute diffusion and therefore an activation energy appropriate for this process is expected. Figure 5.32b predicts that in moving from the low to high velocity regimes, the apparent activation energy should exhibit a peak. The data shown in figures 5.17, 5.19 and 5.20 are consistent with this. In some cases, e.g. figure 5.17, the activation energy in the low velocity regime is a function of solute content. This may be due to the effect of solute on the boundary free volume and hence on the activation energy for solute diffusion. The model predicts (fig. 5.32b) that in the high velocity regime, the activation energy for boundary migration should be similar to that for high purity material. The experimental results show that this is often the case.

- **The nature of the transition depends on the solute concentration and driving force**

Figure 5.32b shows that the nature of the velocity transition with increasing temperature is predicted to be gradual for low solute concentrations and sharp for higher concentrations. There is evidence that both gradual (figs. 5.19 and 5.20) and discontinuous transitions (fig. 5.17) can occur, although a change in the nature of the transition as a function of solute content has not yet been demonstrated in a single investigation.

- **The effect of solute is less at higher temperatures**

Equation 5.22 shows that at higher temperatures the solute atmosphere will be much weaker. The results shown in figure 5.23 are in agreement with this.

5.4.2.5 Development of the theory

Although the CLS model appears to be in reasonable qualitative agreement with many of the experimental results, it is generally agreed that it cannot make realistic quantitative predictions. The CLS approach is based on the segregation of impurities to grain boundaries, and the activation energy for migration, is predicted to be dependent on the solute and solvent, but independent of the solute concentration. However, recent experiments have shown the activation energy to increase significantly with the addition of small solute concentrations to high purity aluminium, (Molodov et al. 1998), and these authors have suggested that this is due to an interaction between the solute atoms at the boundary. Taking this into account by applying the Bragg-Williams theory of regular solutions, they showed that the boundary migration enthalpy includes the enthalpy of impurity migration, the adsorption energy of solutes in the boundary and the energy of interaction between adsorbed atoms, and that the theory gives a better account of the experimental results.

There are a number of other factors which will need to be incorporated into quantitative theories of grain boundary migration in solute-containing alloys. These include **the effect of solutes on boundary structure, energy and diffusivity and the interaction of solutes and boundary crystallography.**

5.5 THE MIGRATION OF TRIPLE JUNCTIONS

5.5.1 Introduction

This chapter has been concerned with the migration and mobility of grain boundaries. However, in a 3-D polycrystal (or a subgrain structure), the grains are joined not only at boundaries, but also at **triple junction** lines (§4.5) and **quadruple junction** points. The triple junctions are defects which will have particular atomic structures and energies (Palumbo and Aust 1992, King 1999).

Galina et al. (1987) first suggested that triple junctions might have a finite mobility and that under some circumstances this, rather than the boundary mobility might limit the rate of growth of a grain assembly. It is postulated that by analogy with equation 5.1, the triple junction velocity ($\mathbf{v_{TJ}}$) is proportional to the driving pressure ($\mathbf{P_{TJ}}$) and the mobility ($\mathbf{M_{TJ}}$)

$$v_{TJ} = M_{TJ} P_{TJ} \tag{5.26}$$

The mobilities of the triple junctions can only be accurately measured experimentally for a very limited set of geometrical configurations and have been reported for 99.999% zinc (Czubayco et al. 1998), and 99.999% aluminium (Protasova et al. 2001) in tri-crystals containing symmetrical tilt boundaries.

It is found that the temperature dependence of boundary and triple junction mobilities is markedly different as shown in figure 5.33, with the activation energy for triple junction migration being approximately twice that for self diffusion.

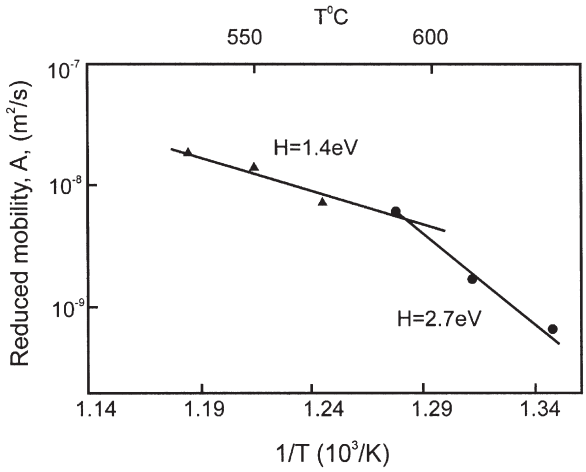

Fig. 5.33. Temperature dependence of triple junction (●) and grain boundary (▲) mobilities in 99.999%Al, (Protasova et al. 2001).

Molecular dynamic simulations (Upmanyu et al. 2002) and 2-D vertex models (Weygand et al. 1998a) are in general agreement with the limited experimental data, and it is significant that the molecular dynamic simulations indicate that the mobility of a triple junction depends also on its direction of motion.

5.5.2 The importance of triple junction mobility

Both experiments and simulations show that triple junction mobility is finite and may be sufficiently small to limit the rate of grain boundary migration. In such circumstances, the usual assumption that the rate of subgrain (§6.5) or grain (§11.1) growth is controlled by boundary mobility would be incorrect. The effects of finite triple junction mobility on the grain growth of a polycrystal have been examined theoretically (Gottstein et al. 2000) and by computer simulation (Weygand et al. 1999), and the main conclusions are that when triple junction drag is significant,

- The isothermal grain growth kinetics are similar to those for boundary control, i.e. $\mathbf{R} \propto \mathbf{t}^{1/2}$ (§11.1)
- The scaling behaviour for grain size distribution (§11.1.1) disappears
- The von Neumann-Mullins law (§11.1.5) is no longer valid

Because of the limited data available, it is difficult to ascertain the conditions under which triple junction drag will be a significant factor in grain growth, but it is expected that this will be for small grain sizes, low temperatures and near high symmetry misorientations. The simulations (Upmanu et al. 2002) suggest that triple junction drag may only be significant in materials of grain size up to ~50 interatomic spacing, and therefore important only for nanocrystalline materials. The large differences in the activation energies for boundary and triple junction migration

(figure 5.33) should enable the controlling mechanism to be identified from measurements of the temperature dependence of the grain growth kinetics of polycrystals.

Although there is currently little data available for materials of very small grain sizes, the measured activation energies for both grain growth and subgrain growth (5.2.2.1) are typically close to those for self diffusion, corresponding to control by boundary rather than triple junction migration. The grain growth kinetics of an Al–Mg alloy (fig. 14.12), measured over a large range of sizes, appear to be similar at both small ($< 0.5\,\mu m$) and large grain sizes (Hayes et al. 2002), suggesting that a common mechanism operates.

ThisPageIntentionallyLeftBlank

Chapter 6

RECOVERY AFTER DEFORMATION

6.1 INTRODUCTION

6.1.1 The occurrence of recovery

The term **recovery** refers to changes in a deformed material which occur prior to recrystallization, and which partially restore the properties to their values before deformation. It is now known that recovery is primarily due to changes in the dislocation structure of the material, and in discussing recovery it is most convenient to concentrate on the microstructural aspects.

Recovery is not confined to plastically deformed materials, and may occur in any crystal into which a non-equilibrium, high concentration of point or line defects has been introduced. Well known examples of this are materials which have been irradiated or which have been quenched from high temperatures. In these situations recovery will occur on subsequent annealing and this may restore the properties and microstructure completely to the original condition (e.g. Koehler et al. 1957, Baluffi et al. 1963). In this chapter we are concerned only with recovery which occurs on annealing after prior deformation.

Even in the case of deformed metals, point defects as well as dislocations will be formed during deformation. However, as most of the excess point defects will anneal out at low temperatures, this does not usually constitute a separately identifiable stage of the recovery of a cold worked metal and will not be considered further.

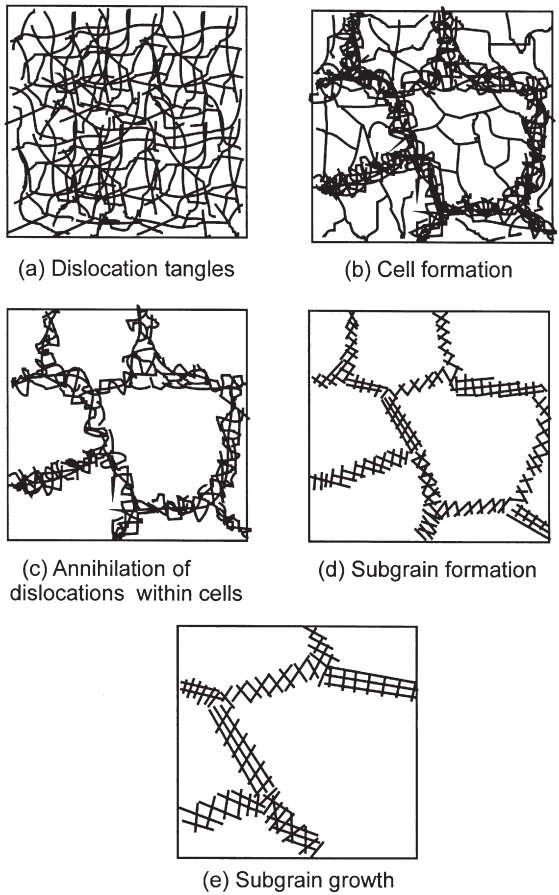

Fig. 6.1. Various stages in the recovery of a plastically deformed material.

Dislocation recovery is not a single microstructural change but a series of events which are schematically shown in figure 6.1, and a detailed discussion of these recovery processes is given in §6.3 to §6.5. Whether any or all of these occur during the annealing of a particular specimen will depend on a number of parameters, including the material, purity, strain, deformation temperature and annealing temperature. In many cases some of these stages will have occurred during the deformation as **dynamic recovery**. Although the recovery stages tend to occur in the order shown, there may be significant overlap between them.

Before considering the details of recovery, we should note that recovery and recrystallization are competing processes as both are driven by the stored energy of the deformed state (§2.2). Once recrystallization has occurred and the deformation substructure has been consumed, then clearly no further recovery can occur. The extent of recovery will therefore depend on the ease with which recrystallization occurs.

Conversely, because recovery lowers the driving force for recrystallization, a significant amount of prior recovery may in turn influence the nature and the kinetics of recrystallization. The division between recovery and recrystallization is sometimes difficult to define, because recovery mechanisms play an important role in nucleating recrystallization. Additionally, as will be discussed at the end of this chapter, there are circumstances in which there is no clear distinction between the two phenomena.

The extensive early work on the recovery of deformed metals has been reviewed by Beck (1954), Bever (1957) and Titchener and Bever (1958), but despite its obvious importance, recovery attracted little interest in later years. However, the current industrially driven move to produce quantitative physically-based models for annealing processes has resulted in renewed interest in recovery (e.g. Nes 1995a).

6.1.2 Properties affected by recovery

During recovery, the microstructural changes in a material are subtle and occur on a small scale. The microstructures as observed by optical microscopy do not usually reveal much change and for this reason, recovery is often measured indirectly by some bulk technique, for example by following the change in some physical or mechanical property.

Measurement of the changes in stored energy by calorimetry is the most direct method of following recovery because the stored energy is related to the number and configuration of the dislocations in the material (§2.2). In a classic series of experiments Clareborough and colleagues (Clareborough et al. 1955, 1956, 1963) studied the stored energy release in copper, nickel and aluminium. The development of high-sensitivity differential scanning calorimeters has, in recent years, led to their use to measure annealing phenomena, although as discussed in appendix 2.2.1, interpretation of the

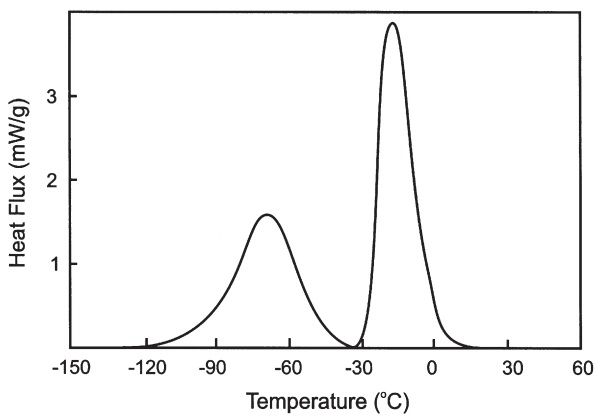

Fig. 6.2. The recovery of 99.999% Al deformed to a true strain of 6.91 at 77K as measured by differential scanning calorimetry, (Schmidt & Haessner 1990).

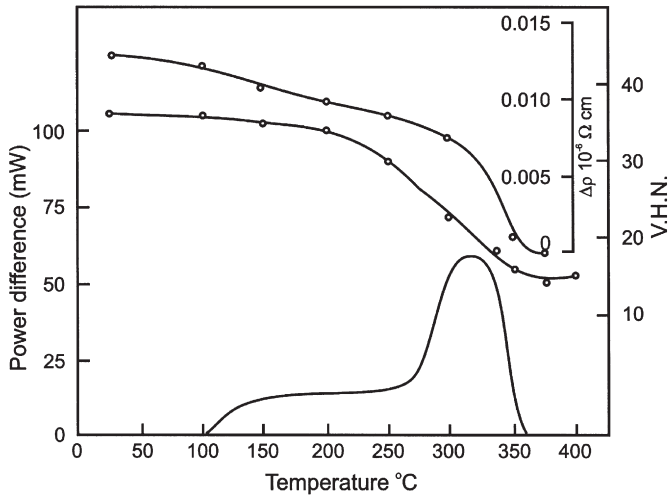

Fig. 6.3. The recovery of 99.998% Aluminium deformed 75% in compression, measured by calorimetry, electrical resistivity and hardness. Heating rate 6°C/min, (Clareborough et al. 1963).

results may not be straightforward. Figure 6.2 from the work of Schmidt and Haessner (1990), shows the annealing of high purity aluminium which was deformed at −196°C and maintained at that temperature until the calorimetry was performed. The peak at around −70°C is due to the recovery of point defects and that at ∼−20°C is due to recrystallization. A separate peak due to dislocation recovery is not detected. The 99.999% high purity aluminium recrystallizes at such a low temperature that either no significant dislocation recovery occurs prior to recrystallization, or else the peak is too close to that due to recrystallization to be detected. Figure 6.3 shows the heat evolved on annealing 99.998% aluminium after deformation at room temperature. In this case two stages are detected, the broad peak at 100–250°C corresponds to the heat evolved during dislocation recovery and the peak at 300°C to that evolved during recrystallization.

Several other physical properties which are altered during plastic deformation are subsequently modified by recovery, and these include density and electrical resistivity (fig. 6.3). It is however difficult to relate these quantitatively to the microstructural changes which occur during recovery, and as is the case for stored energy, these parameters are sensitive to any small amounts of phase transformation which may occur on annealing.

The microstructural changes which occur during recovery affect the mechanical properties, and therefore recovery is often measured by changes in the yield stress or hardness of the material (fig. 6.3), although these changes are often small. The mechanical properties of a recovered material are of great practical importance and their relationship to the microstructural changes has been extensively studied (§6.5.2.3).

6.2 EXPERIMENTAL MEASUREMENTS OF RECOVERY

6.2.1 The extent of recovery

6.2.1.1 The effect of strain

For polycrystalline metals, complete recovery can only occur if the material has been lightly deformed (Masing and Raffelsieper 1950, Michalak and Paxton 1961). However, single crystals of hexagonal close-packed metals such as zinc, which can be deformed to large strains on only one slip system, are able to completely recover their original microstructure and properties on annealing (Haase and Schmid 1925, Drouard et al. 1953). Single crystals of cubic metals if oriented for single slip and deformed in stage 1 of work hardening may also recover almost completely on annealing (Michalak and Paxton 1961). However, if the crystals are deformed into stages II or III of work hardening, then recrystallization may intervene before any significant amount of recovery has occurred (Humphreys and Martin 1968). This behaviour is explainable in terms of the annealing behaviour of the various types of dislocation structure produced during deformation (§6.3).

The fraction of the property change which may be recovered on annealing at a constant temperature is usually found to increase with strain (Leslie et al. 1963). However, this trend may be reversed in more highly strained materials, because of the earlier onset of recrystallization.

6.2.1.2 The effect of annealing temperature

The annealing curves of lightly deformed iron (fig. 6.4) and zinc (fig. 6.5) indicate that more complete recovery occurs at higher annealing temperatures.

6.2.1.3 The nature of the material

The nature of the material itself also determines the extent of recovery. One of the most important parameters is the **stacking fault energy** γ_{SFE}, which, by affecting the extent to which dislocations dissociate, determines the rate of dislocation climb and cross slip, which are the mechanisms which usually control the rate of recovery (§6.3). In metals of low stacking fault energy (table 2.4) such as copper, α-brass and austenitic stainless steel, climb is difficult, and little recovery of the dislocation structure normally occurs prior to recrystallization. However, in metals of high stacking fault energy such as aluminium and α-iron, climb is rapid, and significant recovery may occur as seen in figures 6.3 and 6.4. Solutes may influence recovery by their effect on the stacking fault energy (as discussed above), by pinning dislocations, or by affecting the concentration and mobility of vacancies. Solute pinning of dislocations will both inhibit dynamic recovery, resulting in a higher stored energy than for a solute-free material, and also inhibit static recovery. As the former will promote and the latter retard recovery, it is difficult to predict the net effect. For example, magnesium is known to pin dislocations in aluminium, and to retard dynamic recovery (§2.4.3), leading to a higher stored energy in Al–Mg alloys than pure aluminium. On subsequent annealing, even though Mg impedes the dislocations during recovery, the recovery in the Al–Mg alloys is rapid (Barioz et al. 1992), and may be faster than in pure aluminium (Perryman 1955). In a similar manner, small amounts of manganese pin the dislocations in iron

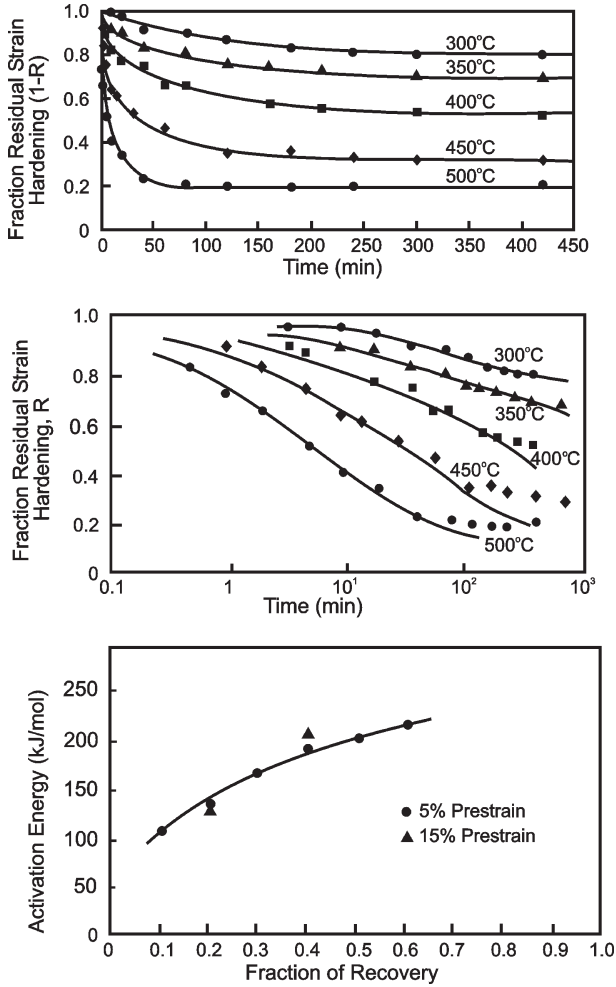

Fig. 6.4. Isothermal recovery of iron deformed 5% at 0°C. (a) Recovery of hardness as a function of time, (b) Logarithmic plot, (c) Change of activation energy during recovery, (Michalak and Paxton 1961).

(Leslie et al. 1963), and by inhibiting dynamic recovery and retaining a high dislocation content, promote subgrain formation on subsequent annealing.

6.2.2 Measurements of recovery kinetics

Experimentally, recovery is often measured by the changes in a single parameter, such as hardness, yield stress, resistivity or heat evolution. If the change of such a parameter from the annealed condition is $\mathbf{X_R}$, then the kinetics of recovery, $\mathbf{dX_R/dt}$ may be

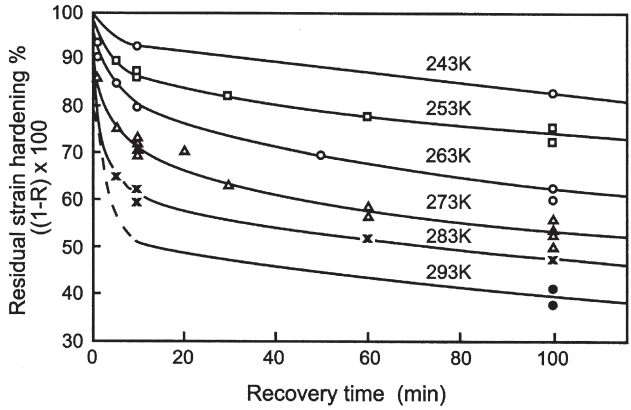

Fig. 6.5. Recovery in zinc crystals deformed to a shear strain of 0.08, (Drouard et al. 1953).

determined from experiment. It is often difficult to obtain a fundamental insight into recovery from such analyses, firstly because the relationship of the parameter $\mathbf{X_R}$ to the **microstructure** is usually very complex, and secondly because recovery may involve several concurrent or consecutive atomistic mechanisms (fig. 6.1) each with its own kinetics.

6.2.2.1 Empirical kinetic relationships

Experimental results have been analysed in terms of several different empirical relationships between $\mathbf{X_R}$ and **t**. The two most commonly reported isothermal relationships, which we will refer to as **types 1 and 2** are as follows:

Type 1 kinetics:

$$\frac{dX_R}{dt} = -\frac{c_1}{t} \tag{6.1}$$

which on integration gives

$$X_R = c_2 - c_1 \ln t \tag{6.2}$$

where c_1 and c_2 are constants.

It is clear that this form of relationship cannot be valid during the early stages of recovery ($t \to 0$) when $X_R \to X_0$ or at the end of recovery ($t \to \infty$) when $X_R \to 0$.

Type 2 kinetics:

$$\frac{dX_R}{dt} = -c_1 X_R^m \tag{6.3}$$

which on integration gives

$$X_R^{-(m-1)} - X_0^{-(m-1)} = (m-1)c_1 t \tag{6.4}$$

for $m > 1$, and

$$\ln(X_R) - \ln(X_0) = c_1 t \tag{6.5}$$

for $m = 1$.

6.2.2.2 Recovery of single crystals deformed in single slip

The kinetics of recovery of single crystals of zinc deformed at $-50°C$ in simple shear so that deformation occurred by shear on the basal plane were measured by Drouard et al. (1953) and are shown in figure 6.5. The extent of the recovery (**R**) was defined in terms of the yield stress of the recovered crystals (σ), the yield stress of the as-deformed crystal (σ_m) and the yield stress of the undeformed crystal (σ_0) as

$$R = \frac{(\sigma_m - \sigma)}{(\sigma_m - \sigma_0)} \tag{6.6}$$

The relationship between the amount of recovery, time and temperature was found, over a wide range of conditions to be

$$R = c_1 \ln t - \frac{Q}{kT} \tag{6.7}$$

These are **type 1** kinetics, and the activation energy (**Q**) was found to be 83.7 kJ/mol, which is close to the activation energy for self diffusion of zinc (table 5.1).

Other measurements of recovery in zinc crystals (Cottrell and Aytekin 1950) and aluminium crystals (Kuhlmann et al. 1949, Masing and Raffelsieper 1950) have also found a relation between $\mathbf{X_R}$ and time, of a form consistent with **type 1** kinetics.

An unusual type of recovery has been found in deformed dispersion-hardened single crystals of copper (Hirsch and Humphreys 1969, Gould et al. 1974). If these crystals are deformed to shear strains of up to ~0.15 at room temperature or below, then on annealing at room temperature, a large fraction of the work hardening recovers in a short time, as shown in figure 6.6. The activation energy for the process is found to be ~90 kJ/mol, which is less than half the activation energy for self diffusion in copper (table 5.1). This recovery effect has been attributed to the annealing out of the unstable high energy **Orowan loops** which form at the particles during deformation (§2.9.3), by a process of dislocation climb controlled by **pipe or core diffusion.** Although similar effects have been reported in particle-containing aluminium single crystals (Stewart and Martin 1975), this type of recovery has not been detected in particle-containing polycrystals, and may be a consequence of the simpler dislocation structures formed in deformed single crystals.

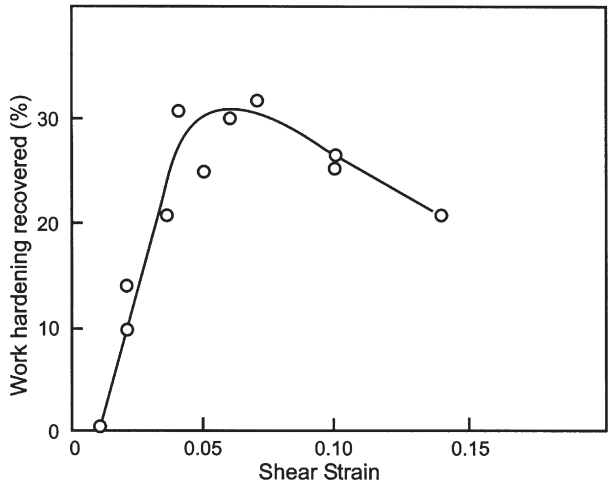

Fig. 6.6. The amount of work hardening which is recovered in 3hrs at room temperature in Cu–Al_2O_3 crystals oriented for single slip, and deformed at 77K, (Humphreys and Hirsch 1976).

6.2.2.3 Recovery kinetics of polycrystals

The recovery kinetics of iron in figure 6.4 are typical of metals in which extensive recovery occurs, and show that the rate of recovery is initially rapid and then decreases monotonically.

Type 1 kinetic relationships have frequently been found to describe recovery in polycrystals, and plots of fractional recovery against log(time) for iron are shown in figure 6.4b. However, it may be seen from this figure that a straight line corresponding to equation 6.2 is usually only found over part of the recovery range as would be expected from this type of relationship.

An activation energy for recovery may be obtained from the temperature dependence of the recovery rate at a particular stage of the recovery, using the usual Arrhenius relationship. In some cases the activation energy is found to rise as recovery proceeds. For example, Michalak and Paxton (1961) measuring the recovery kinetics of zone-refined iron deformed 5%, found that the activation energy rose from 91 kJ/mol at the start of recovery to ~220 kJ/mol (close to that for self diffusion in iron), when recovery was essentially complete as shown in figure 6.4c. Van Drunen and Saimoto (1971) measured the recovery kinetics of deformed $<100>$ copper crystals at various temperatures, and found kinetics of type 2 with $m = 2$, and an activation equal to that for self diffusion in copper.

An interpretation of the types of kinetics discussed above can only be obtained if the physical processes occurring during recovery are understood. In the following sections we will discuss three levels of recovery – **dislocation annihilation, dislocation rearrangement and subgrain growth,** and where possible relate these mechanisms to the recovery kinetics.

6.3 DISLOCATION MIGRATION AND ANNIHILATION DURING RECOVERY

During recovery the stored energy of the material is lowered by dislocation movement. There are two primary processes, these being the **annihilation of dislocations** and the **rearrangement of dislocations** into lower energy configurations. Both processes are achieved by glide, climb and cross-slip of dislocations. We do not intend to discuss the physics of dislocations in detail, and for further information the reader should consult a suitable reference such as Friedel (1964), Hirth and Lothe (1968) or Hull and Bacon (2001).

6.3.1 General considerations

A schematic diagram of a crystal containing an array of edge dislocations is shown in figure 6.7. The elastic stress fields of the dislocations interact and the resultant forces will depend on the Burgers vectors and relative positions of the dislocations. For example, dislocations of opposite sign on the same glide plane e.g. A and B, may annihilate by gliding towards each other. Such processes can occur even at low temperatures, lowering the dislocation density during deformation and leading to **dynamic recovery.** Dislocations of opposite Burgers vector on different glide planes, e.g. C and D, can annihilate by a combination of glide and climb. As climb requires thermal activation, this can only occur at high homologous temperatures. A similar configuration of screw dislocations would recover by the annihilation of dislocations by cross-slip. This would occur at low homologous temperatures in a material such as aluminium with a high stacking fault energy, but at higher temperatures for a material of lower stacking fault energy.

The crystal of figure 6.7 contains dislocations of only one type of Burgers vector and it contains equal numbers of dislocations of the two signs. Thus complete recovery by dislocation annihilation is possible. This corresponds to the case of crystals which have deformed by slip on only one system as discussed in §6.2.1.1.

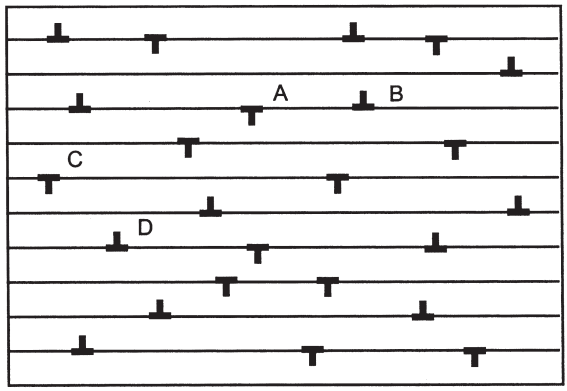

Fig. 6.7. Schematic diagram of a crystal containing edge dislocations.

6.3.2 The kinetics of dipole annihilation

Two parallel dislocations of opposite Burgers vector, such as C and D in figure 6.7 are known as a dislocation dipole. In a well known paper, Li (1966) discussed the kinetics of annihilation of dislocation dipoles of edge, screw or mixed character.

The attractive force (**F**) between two parallel screw dislocations of opposite sign, separated by a distance **x** is

$$F = \frac{G\,b^2}{2\pi x} \tag{6.8}$$

If the dislocation climb velocity is proportional to **F** (see equation 5.8), then the dipole separation will decrease as

$$\frac{dx}{dt} = -c_1 F \tag{6.9}$$

Combining equations 6.8 and 6.9 we obtain

$$\frac{dx}{dt} = \frac{c_2}{x} \tag{6.10}$$

Measurements of the life of screw dipoles in LiF (Li 1966) shown in figure 6.8 are in agreement with this relationship. Li also showed that the kinetics of annihilation of edge and mixed dipoles would be similar to those of equation 6.10.

In order to use this theory to calculate the recovery of a material containing a distribution of dipoles, it is necessary first to assume that the dipoles do not interact with each other, and second to know the initial distribution of dipole heights. Li (1966),

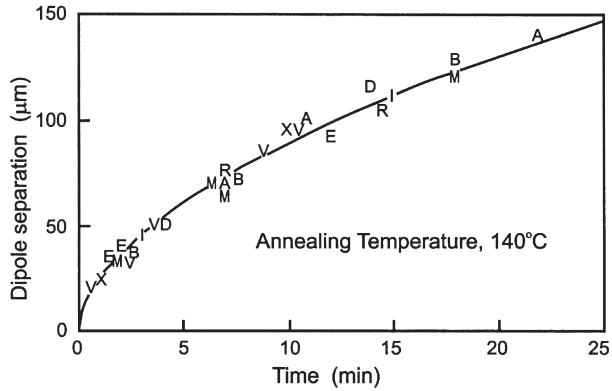

Fig. 6.8. Life of screw dislocation dipoles in LiF crystals, (Li 1966).

making assumptions about the dipole size distribution based on their mechanism of formation during deformation showed that

$$\frac{d\rho}{dt} = -c_1\rho^2 \tag{6.11}$$

or

$$\frac{1}{\rho} - \frac{1}{\rho_0} = c_1 t \tag{6.12}$$

where ρ_0 is the initial dislocation density. These kinetics are equivalent to those of equations 6.3 and 6.4 (**type 2 kinetics**) with **m = 2.**

Rates of change in dislocation density during recovery consistent with **type 2** kinetics have been found by Li (1966) for LiF (m = 2) and by Prinz et al. (1982) in copper and nickel (m = 3).

It is of interest to compare the kinetics of the annihilation of non-interacting dislocation dipoles with the kinetics predicted for a random array of parallel edge dislocations such as is shown schematically in figure 6.7 when both dipole and longer range interactions are considered. The elastic forces acting on a single edge dislocation due to a parallel dislocation of the same or opposite Burgers vector are known (see e.g. Hirth and Lothe 1968, Hull and Bacon 2001), and for an array such as shown in figure 6.7, the forces acting on any dislocation may be taken to be the sum of the forces due to the other dislocations. If the velocity of a dislocation is assumed to be proportional to the force acting on it (equation 5.8), an assumption which was shown to be valid for the dipoles discussed above, then the rearrangement of the dislocation array due to its internal forces may be computed. Starting with a computer-simulated array of 500 dislocations of each of the two opposite Burgers vectors, the microstructure evolves as shown in figure 6.9, and the kinetics are shown in figure 6.10. Although the rate of recovery is initially consistent with equation 6.11, it subsequently falls more rapidly with time and, as shown in figure 6.10b, is closer to a relationship of the form $\boldsymbol{\rho^{-1.5} \propto t}$. The reason for the slower recovery rate at longer times may be seen from examination of figure 6.9b. As annealing proceeds, the formation and annihilation of dislocation dipoles occurs, e.g. at **D.** However, in addition to this, the dislocations begin to form low energy tilt boundaries (**B**), and as these are reasonably stable structures, the rate of dislocation annihilation is now much slower. Therefore there are **two** recovery mechanisms operating simultaneously, **dislocation annihilation and rearrangement into stable configurations;** this illustrates well the difficulties in analysing recovery data in terms of a single recovery mechanism.

The simulation described above neglects the behaviour of screw dislocations and is therefore unlikely to accurately predict the annealing of a deformed material containing dislocations of one type of Burgers vector. However, it does indicate that in addition to dipole interactions, other longer range interactions may be important in determining the annealing kinetics, and this simulation is in general agreement with the in-situ HVEM annealing experiments of Prinz et al. (1982) which showed low angle boundary formation and dipole annihilation to occur concurrently.

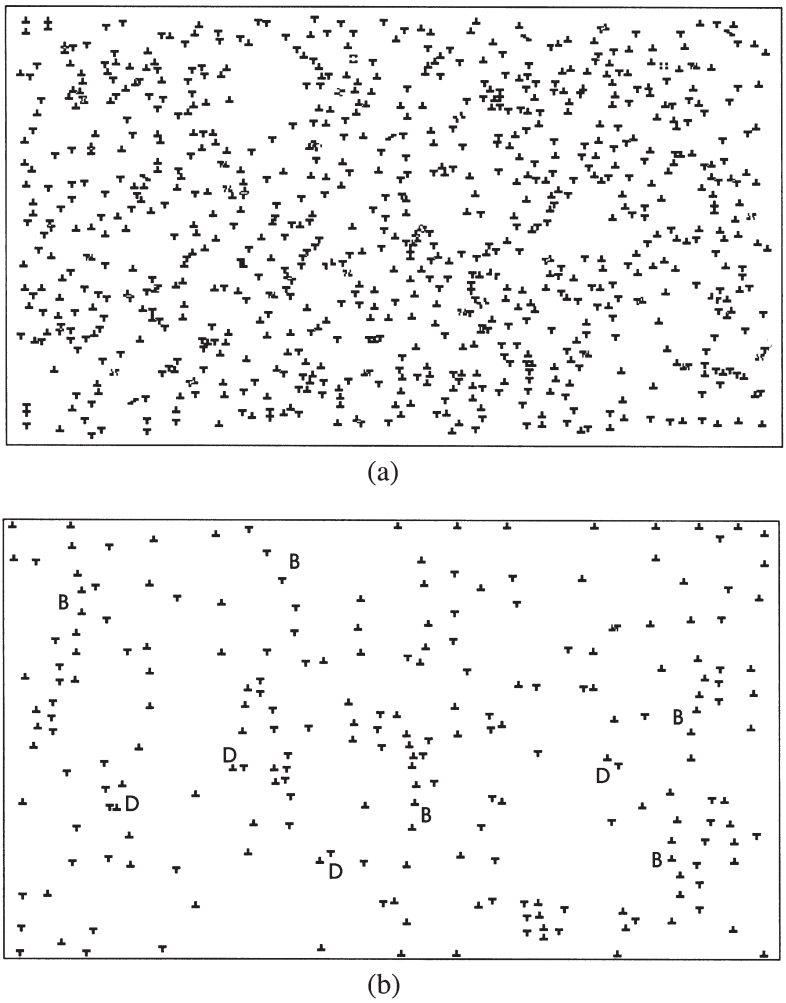

Fig. 6.9. Computer simulation of the annealing of edge dipoles (a) initial microstructure, (b) later stage of recovery showing the incipient formation of low angle boundaries.

6.3.3 Recovery kinetics of more complex dislocation structures

In the above section we considered only the recovery of simple dislocation arrays consisting of parallel dislocations of similar Burgers vector. In polycrystals and single crystals deformed on more than one slip system, the dislocation structures are much more complex, and Friedel (1964) has considered the recovery kinetics of general dislocation structures. It is not obvious which mechanism controls dislocation movement during recovery in various circumstances, as in addition to **dislocation**

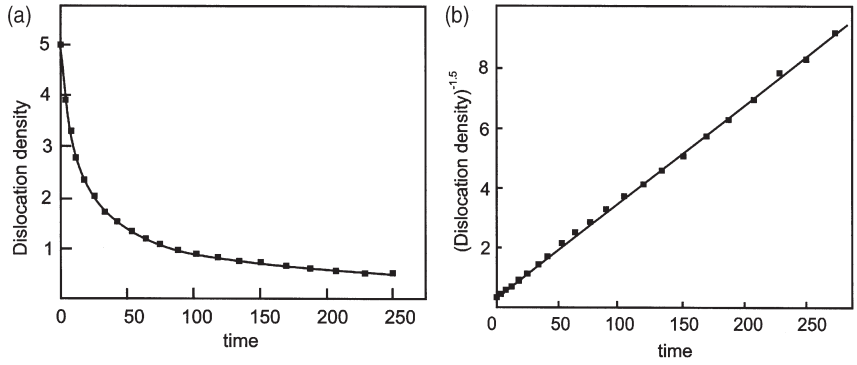

Fig. 6.10. Kinetics of recovery in the computer simulation of figure 6.9, (a) The variation of dislocation density (ρ) with time; (b) The variation of $\rho^{-1.5}$ with time.

climb by either **bulk** or **core** diffusion, there is also the possibility that the processes of **thermally activated glide** or **cross-slip** may be rate controlling.

Following Friedel, we assume that the dislocation structure is in the form of a three-dimensional network (Frank network) of mesh size **R.** From the geometry of the network we expect that the dislocation velocity (**v**) is related to the change in scale of the network by **dR/dt~v,** and considerations of the energy of the system show that the driving force for coarsening of the network by dislocation migration is then

$$F \approx \frac{Gb^2}{R} \tag{6.13}$$

6.3.3.1 Control by dislocation climb

Under conditions of small driving force and a negligible vacancy supersaturation, the dislocation velocity (**v**) is given by equation 5.8. Thus, from equations 5.8 and 6.13

$$v = \frac{dR}{dt} = \frac{D_s G b^3 c_j}{kTR} \tag{6.14}$$

and hence

$$R^2 = R_0^2 + c_1 t \tag{6.15}$$

where $c_1 = 2D_S\, Gb^3 c_j/kT$.

The dislocation density $\boldsymbol{\rho}$ is related to the network spacing by $\boldsymbol{\rho} \sim \mathbf{R}^{-2}$, and hence equation 6.15 may be written as

$$\frac{1}{\rho} - \frac{1}{\rho_0} = c_1 t \tag{6.16}$$

which is of the same form as the **type 2** empirical kinetics of equation 6.4 with $\mathbf{m} = \mathbf{2}$.

By assuming the relationship between flow stress (σ) and ρ given by equation 2.2, this can also be written as

$$\frac{1}{\sigma_0^2} - \frac{1}{\sigma^2} = c_3 t \tag{6.17}$$

where $c_3 = (2\ D_S\ c_j)/(\alpha^2\ GbkT)$

At high temperatures, climb is expected to be controlled by the formation (Q_{VF}) and movement (Q_{VM}) of vacancies, as is self diffusion (Q_S). However at lower temperatures, jog formation (Q_j) may also be a rate determining step. Therefore the activation energy for climb (Q_{CL}) is expected to be

$$\begin{aligned} Q_{CL} &= Q_{VF} + Q_{VM} = Q_S \text{ (at high temperatures)} \\ Q_{CL} &= Q_{VF} + Q_{VM} + Q_j \text{ (at low temperatures)} \end{aligned} \tag{6.18}$$

There are however, circumstances in which the climb may be controlled by diffusion along the dislocation lines (core or pipe diffusion), rather than through the lattice. In these circumstances the activation energy (Q_c) will be substantially lower than Q_s, and typically $Q_c/Q_s \sim 0.5$ (table 5.1). Prinz et al. (1982) have suggested that for extended dislocations, the climb during recovery is likely to be controlled by core diffusion.

6.3.3.2 Control by thermally activated glide of dislocations

Several authors (Kuhlmann 1948, Cottrell and Aytekin 1950, Friedel 1964) have considered the possibility that recovery may be controlled by thermally activated glide or cross-slip. It is proposed by these authors that the activation energy (Q) is a decreasing function of the internal stress (σ) and that the rate of recovery is

$$\frac{d\sigma}{dt} = -c_1 \exp\left(\frac{-Q(\sigma)}{kT}\right) \tag{6.19}$$

It is suggested that the stress dependence of the activation energy at low stresses may be of the form

$$Q(\sigma) = Q_0 - c_2\sigma \tag{6.20}$$

and hence

$$\frac{d\sigma}{dt} = -c_1 \exp\left(\frac{-(Q_0 - c_2\sigma)}{kT}\right) \tag{6.21}$$

On integration this gives (Cottrell and Aytekin 1950)

$$\sigma = \sigma_0 - \frac{kT}{c_2} \ln\left(1 + \frac{t}{t_0}\right) \tag{6.22}$$

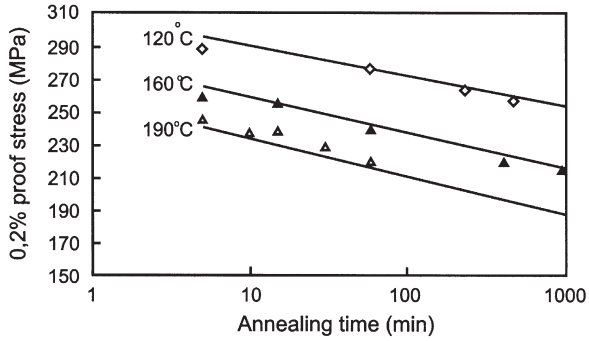

Fig. 6.11. Recovery of Al–3%Mg ($\varepsilon = 3$) plotted according to equation 6.22, (Barioz et al. 1992).

where σ_0 is the flow stress at $t = 0$ and t_0 is given by

$$\frac{kT}{c_1 c_2} \exp\left(\frac{Q_0 - c_2\sigma}{kT}\right)$$

This relationship is similar in form to the **type 1** kinetics of equation 6.2.

Therefore if recovery is controlled by thermally activated glide, we expect an activation energy which **decreases with increasing dislocation density** (or cold work), and which **increases during the anneal.** This relationship is consistent with the experimental results of Kuhlmann et al. (1949), Cottrell and Aytekin (1950) and Michalak and Paxton (1961) (figure 6.4c). It has been claimed that more recent measurements of recovery in Al–Mg alloys, shown in figure 6.11 (Barioz et al. 1992), are also consistent with this model. Q_0 was found to be independent of strain, but to depend on the magnesium content of the alloy, and ranged from 277 kJ/mol for Al–1%Mg to 231 kJ/mol for Al–5% Mg. In all cases Q_0 was found to be much larger than that for self diffusion for aluminium, which is ~142 kJ/mol.

Hirth and Lothe (1968) have discussed the velocity of dislocations under various other circumstances, and in particular have considered the thermally activated glide of jogged dislocations. The particular relationship between the dislocation velocity and the driving force is found to depend not only on the type of diffusion (core or bulk), but also on the way in which the jogs are assumed to move and on the effect of solutes.

Stacking fault energy will also be an important parameter in determining the rate of climb or cross-slip. Argon and Moffat (1981) proposed that the climb of extended edge dislocations in fcc metals is controlled by vacancy evaporation at extended jogs, and under these conditions the rate of climb is given by

$$v = \frac{c' D_x}{kT} F \gamma_{SFE}^2 \tag{6.23}$$

where D_x may be either core or bulk diffusivity.

Reference to the discussion of climb-controlled recovery in §6.3.3.1 shows that if the climb velocity is given by equation 6.23 instead of equation 5.8, the recovery rate will be proportional to γ_{SFE}^2.

In conclusion we see that there are several possible kinetic equations to describe uniform dislocation recovery, some of which predict kinetics similar to those which have been observed experimentally. In principle, it should be possible to identify the applicable model from the form of the experimental annealing response. However, much more work is needed before this can be done with confidence, and we highlight four areas of difficulty.

- **The relationships between mechanical properties and microstructure are in reality much more complex than those used in current recovery models (§6.2.2).**

Although recovery is frequently measured by changes in mechanical properties, reliable interpretation of such data in terms of the dislocation content and arrangement is not possible in most cases.

- **The mechanisms of dislocation annihilation and dislocation rearrangement may not be consecutive, but may occur concurrently (fig. 6.9).**

Because of this, a model of recovery based solely on dislocation annihilation or growth of a Frank dislocation network may not be appropriate, and the effect of the recovery mechanisms to be discussed in §6.4 and §6.5 will also need to be incorporated as appropriate into the overall recovery model.

- **The effects of solutes and stacking fault energy on dislocation mobility need more accurate formulation than has been possible to date.**
- **The heterogeneity of recovery throughout the microstructure cannot be ignored.**

As is evident in considering the **deformed state** (§2.4) and **primary recrystallization** (chapter 7), inhomogeneities in the deformed state lead to inhomogeneous annealing. Therefore changes in the rate of recovery, as measured by changes of a bulk property, during an anneal may well be due to different recovery rates in different parts of the microstructure. This factor, which was first suggested by Kuhlmann (1948) in order to explain the change in activation energy during recovery, needs to be incorporated into any comprehensive model of recovery.

6.4 REARRANGEMENT OF DISLOCATIONS INTO STABLE ARRAYS

6.4.1 Polygonization

If, as shown in figure 6.12a, unequal numbers of dislocations of two signs are produced during deformation, then, the excess cannot be removed by annihilation (fig. 6.12b). On annealing, these excess dislocations will arrange into lower energy configurations in the form of regular arrays or **low angle grain boundaries** (LAGBs). The simplest case is that shown in figure 6.12c in which dislocations of only one Burgers vector are involved. Such a structure may be produced by bending a single crystal which is deforming on a

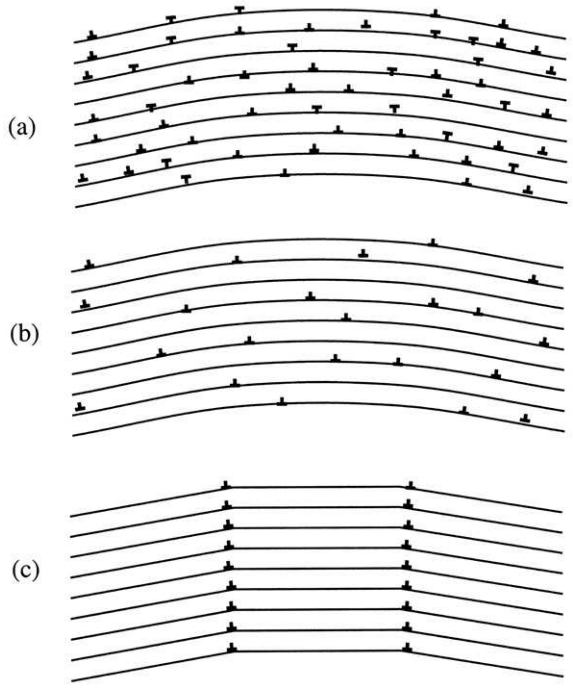

Fig 6.12. Recovery by polygonisation of a bent crystal containing edge dislocations. (a) As deformed, (b) After dislocation annihilation, (c) Formation of tilt boundaries.

single slip system, as was first demonstrated by Cahn (1949), and this mechanism is often known as **polygonization.**

The dislocation walls shown in figure 6.12c are known as **tilt boundaries**. These are a particularly simple type of **low angle grain boundary**, and such boundaries are discussed more fully in chapter 4. According to the Read-Shockley equation (equation 4.5), the energy of a tilt boundary **increases** with increasing misorientation and the energy per dislocation **decreases** with increasing misorientation (fig. 4.5). Therefore there is a driving force to form fewer, more highly misoriented boundaries as recovery proceeds.

6.4.2 Subgrain formation

In the case of a polycrystalline material subjected to large strains, the dislocation structures produced on deformation and on subsequent annealing are much more complex than the simple case shown in figure 6.12c because dislocations of many Burgers vectors are involved. Dislocations of two or more Burgers vectors react to form two-dimensional networks whose character depends on the types of dislocation involved (§4.3).

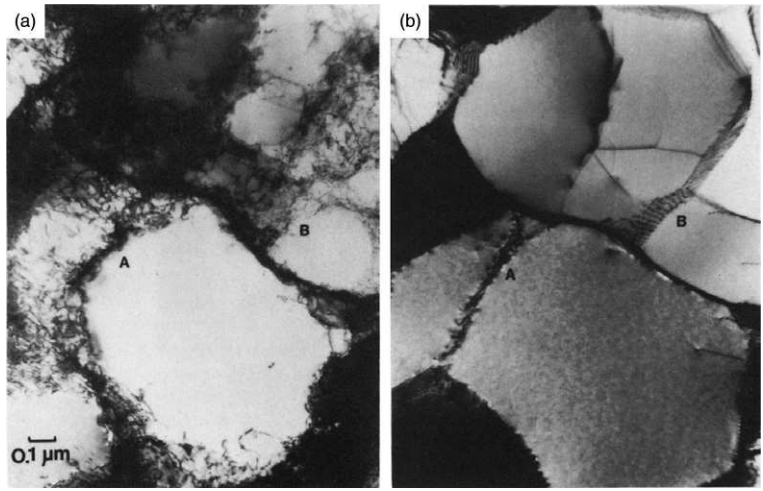

Fig. 6.13. Transmission high voltage electron micrographs (HVEM) of aluminium deformed 10% and annealed in-situ. (a) Deformed structure, (b) Same area after 2 min anneal at 250°C.

In an alloy of medium or high stacking fault energy, the dislocations are typically arranged after deformation in the form of a three dimensional **cell structure,** the cell walls being complex dislocation tangles (§2.4.2 and fig. 2.9a,b) and the size of the cells being dependent on the material and on the strain.

The transmission electron micrograph of figure 6.13a shows equiaxed cells of diameter ~1 μm in deformed aluminium. By annealing this specimen **in situ** in an HVEM, the recovery processes can be followed directly, and figure 6.13b shows the same area after annealing. The tangled cell walls, e.g. at **A** and **B** have become more regular dislocation networks or low angle grain boundaries and the number of dislocations in the cell interiors has diminished. The cells have now become **subgrains,** and at this stage there is little change in the scale of the structure.

The transition from loose tangles of dislocations in cell walls to subgrain boundary formation as shown in figure 6.13, can be considered to be a distinct stage in the recovery process (fig. 6.1d). It involves some annihilation of redundant dislocations and the rearrangement of the others into low angle grain boundaries. There have been many TEM studies of this stage of recovery, including those of Bailey and Hirsch (1960) on nickel, Carrington et al. (1960) and Hu (1962) on iron, and Lytton et al. (1965) and Hasegawa and Kocks (1979) on aluminium. As this process occurs, the mechanical properties are altered, the yield stress being lowered, but the work hardening rate rising, as shown by Lytton et al. (1965) and Hasegawa and Kocks (1979).

In some cases **dynamic recovery** during deformation occurs to such an extent that the dislocations are already in the form of a well developed subgrain structure after deformation, and post-deformation recovery then involves mainly a coarsening of the subgrain structure as discussed in the next section. The factors which tend to promote

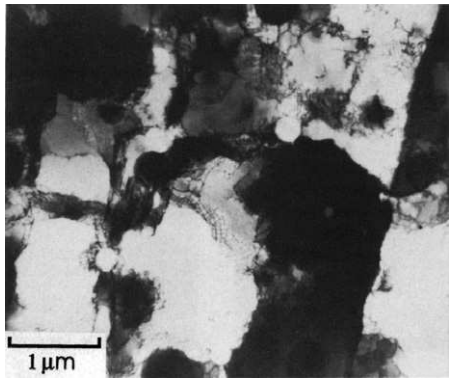

Fig. 6.14. Subgrain formation in copper containing a dispersion of SiO_2 particles, deformed 50% by cold rolling and annealed at 700°C, (Humphreys and Martin 1968).

the formation of a subgrain rather than a cell structure during deformation are:-

- high stacking fault energy,
- low solute content,
- large strain, and
- high temperature of deformation.

Well developed subgrain structures are not usually observed in metals of lower stacking fault energy such as stainless steel, because, as discussed above, recrystallization occurs before significant recovery can occur. However, if recrystallization is inhibited, for example by the presence of finely dispersed second-phase particles, then at a sufficiently high temperature, recovery will occur leading to the formation of well defined subgrains (Humphreys & Martin 1967) as shown in figure 6.14. If the deformation is relatively uniform so that the heterogeneities required for the nucleation of recrystallization are not formed, then pronounced recovery may occur even in pure copper, and van Drunen and Saimoto (1971) found that subgrain formation rather than recrystallization occurred during the annealing of $<100>$ copper crystals which had been deformed in tension.

6.5 SUBGRAIN COARSENING

The stored energy of a recovered substructure such as that of figure 6.13b is still large compared with that of the fully recrystallized material, and can be further lowered by coarsening of the substructure, which leads to a reduction in the total area of low angle boundary in the material.

6.5.1 The driving force for subgrain growth

The driving force for subgrain growth arises from the energy stored in the subgrain boundaries. If the microstructure can be approximated to an array of subgrains of

radius **R** and boundary energy γ_S, then the stored energy per unit volume ($\mathbf{E_d}$) is $\boldsymbol{\alpha\gamma_S/R}$, where α is a shape factor of ~1.5 (equation 2.7). The driving force **F** for subgrain growth arises from the reduction in stored energy as the subgrain grows and thus, following Ørsund and Nes (1989), we find

$$F = -\frac{dE_D}{dR} = -\alpha \frac{d}{dR}\left(\frac{\gamma_s}{R}\right) \tag{6.24}$$

If it is assumed that the stored energy is uniform and that the force is distributed evenly, the driving pressure **P** is given by

$$P = \frac{F}{A} = -\alpha R \frac{d}{dR}\left(\frac{\gamma_s}{R}\right) \tag{6.25}$$

If γ_S is constant during subgrain growth then

$$P = \frac{\alpha \gamma_s}{R} \tag{6.26}$$

However, as γ_S is a function of the misorientation of the adjacent subgrains (§4.3), the driving pressure (**P**) may not remain constant during subgrain growth.

6.5.2 Experimental measurements of subgrain coarsening

6.5.2.1 The kinetics of subgrain growth

Many measurements of the change of subgrain size (**D**) with time (**t**) at constant temperature reveal kinetics of the form

$$D^n - D_0^n = c_1 t \tag{6.27}$$

where **n** is a constant, $\mathbf{c_1}$ is a temperature-dependent rate constant and D_0 is the subgrain size at $t = 0$.

In some cases the value of the exponent **n** in equation 6.27 is found to be ~**2,** which is a similar form to the kinetics of grain growth following recrystallization (§11.1). Work in which an exponent close to 2 has been reported includes Smith and Dillamore (1970) on high purity iron, Sandström et al. (1978) on Al–1%Mn, Varma and Willits (1984) and Varma and Wesstrom (1988) on 99.99% aluminium, and Varma (1986) on Al–0.2%Mg. Figure 6.15 shows some typical experimental results.

However, most recent investigations of subgrain growth in aluminium have found that the subgrain growth rate decreases much more rapidly than implied by equation 6.27. For example Furu and Nes (1992), reported an exponent of ~4 in commercial purity (99.5%) aluminium. Other investigations of high purity (>99.995%) aluminium (Beck et al. 1959, Sandström et al. 1978, Humphreys and Humphreys 1994) have found growth kinetics which are consistent with either a large value of **n** in equation 6.27, or else a logarithmic relationship of the form

$$\log D = c_2 t \tag{6.28}$$

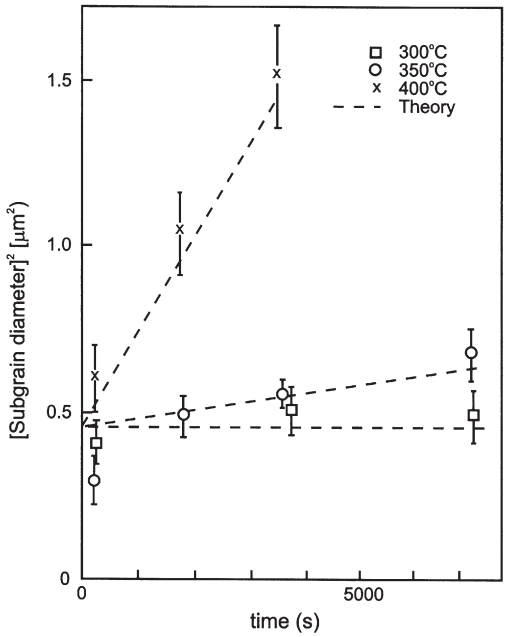

Fig. 6.15. Subgrain growth in an Al–1%Mn alloy plotted according to equation 6.27, with $n = 2$, (Sandström et al. 1978).

The number of experimental investigations of subgrain growth kinetics is rather small. In addition, there is often considerable scatter of the data, and the error bars shown in figure 6.15 are typical. We should also note that the amount of subgrain growth which is actually measured is usually very small, because subgrain growth is curtailed by the onset of recrystallization, and in the investigations quoted above, the ratio D/D_0 is rarely much greater than ~ 2.

Much more subgrain growth can occur in a material in which recrystallization cannot originate. $\{110\} < 001 >$ Goss-oriented single crystals deformed in plane strain compression do not develop the large-scale microstructural heterogeneities which promote recrystallization, and as there are no pre-existing high angle boundaries, recrystallization can be suppressed if the sample surfaces are carefully removed by etching. Subgrain growth ratios D/D_0 in the range 5–10 have been achieved in such crystals, allowing more accurate growth measurements to be made (Ferry and Humphreys 1996a, Huang and Humphreys 2000), and an example is shown in figure 6.16. The isothermal growth kinetics (fig. 6.16a) are always found to be consistent with an exponent in equation 6.27 which is larger than 2. However, it was found that the mean subgrain misorientation decreased slightly during annealing as shown in figure 6.16b. Because both the LAGB energies and mobilities are very dependent on misorientation (figures 4.6 and 5.6), the energy term γ_s in equations 6.26 and 6.34 decreases during subgrain growth, and if the growth is now plotted according to equation 6.34, as in figure 6.16c, a reasonable fit is found. This indicates that the high

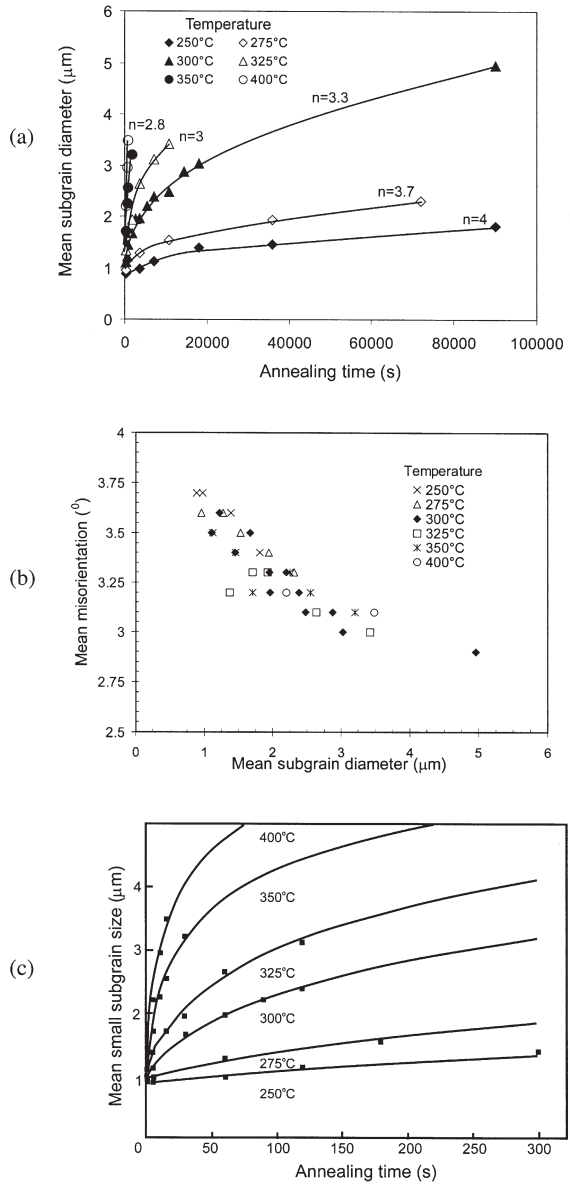

Fig. 6.16. Isothermal subgrain growth kinetics in deformed {110} < 001 > crystals of Al–0.05%Si. (a) The experimental data points are fitted to equation 6.27, and values of the exponent n are shown; (b) The change in mean subgrain misorientation during annealing of the crystals; (c) The data points of figure 6.16a are fitted to equation 6.34, taking account of the change in mean misorientation during growth, (Huang and Humphreys 2000).

growth exponent found using equation 6.27 is a consequence of the change in boundary character during annealing and of **c** in equation 6.35 not being constant. Although recrystallization does not occur in these samples, useful subgrain growth data are limited to the early stages of growth (figure 6.16c) because of the onset of **discontinuous subgrain growth,** which is discussed in §6.5.3.5. It should also be noted that such crystals deform in a rather simple manner with a limited number of slip systems, and these results may not be typical of the growth of all subgrains.

6.5.2.2 Correlation of orientation, misorientation and subgrain growth

As discussed above, the driving force for subgrain growth is expected to be proportional to the energy of the low angle grain boundaries (γ_s), therefore the growth rate will be a function of the subgrain misorientation (θ). This is a parameter which has not often been measured during subgrain growth experiments, but which is expected to be a function of prior strain and grain orientation (§2.2.3.2). Smith and Dillamore (1970) showed that the rate of subgrain growth in iron varied significantly between different texture components and this was assumed to be a result of different subgrain misorientation distributions. Failure to measure this parameter during measurements of subgrain growth must inevitably lead to decreased reliability of the experimental data and undoubtedly accounts for some of the scatter in the available results as discussed above.

More recent work has measured misorientations during subgrain growth. Furu and Nes (1992) measured the changes of both subgrain size and misorientation in commercially pure aluminium and found that as subgrain growth proceeded, the average subgrain misorientation increased. This result is consistent with there being **orientation gradients** in the specimen, a point which is further discussed in §6.5.3.6. In samples in which there are **no orientation gradients,** (Humphreys and Humphreys 1994, Huang and Humphreys 2000) the mean subgrain misorientation is found to decrease slightly during the anneal as shown in figure 6.16b.

6.5.2.3 Relationship between subgrain size and mechanical properties

In view of the use of mechanical properties to measure recovery and of the intrinsic importance of substructures in contributing to the strength of structural materials, we should briefly consider the relationship between the flow stress of a material and the subgrain structure. In the following discussion we assume that the dislocation density within the subgrains is negligible, and that the strength is determined by the cell or subgrain size. Substructure strengthening has been reviewed by McElroy and Szkopiak (1972), Thompson (1977) and Gil Sevillano et al. (1980).

We will consider three simple approaches to the problem.

(i) **It is assumed that subgrains behave like grains** and that the yield stress will be given by a Hall-Petch relationship

$$\sigma = \sigma_0 + c_1 D^{-1/2} \tag{6.29}$$

(ii) **It is assumed that the flow stress is determined by the operation of dislocation sources** (Kuhlmann-Wilsdorf 1970), whose length will be closely related to the subgrain

diameter, in which case

$$\sigma = \sigma_0 + c_2 D^{-1} \tag{6.30}$$

Equations 6.29 and 6.30 may both be written in the form

$$\sigma = \sigma_0 + c_3 D^{-m} \tag{6.31}$$

(iii) **It is assumed that the dislocations which comprise subgrain boundaries can be averaged over the microstructure.** In this case the area of subgrain per unit volume (A) is $\sim 3/D$. For small misorientations $\theta = b/h$ (equation 4.4), and the length of dislocation per unit area of boundary (L) is $1/h$. Therefore

$$\rho = AL = \frac{3}{Dh} = \frac{3b\theta}{D} \tag{6.32}$$

Assuming the relationship between flow stress and dislocation density of equation 2.2, then

$$\sigma = \sigma_0 + c_4 \left(\frac{\theta}{D}\right)^{1/2} \tag{6.33}$$

which is of the same form as equation 6.31 with $m = 1/2$ and $c_3 = c_4 \theta^{1/2}$.

All these equations have been used to analyse substructure strengthening and there is little agreement as to their application. Thompson's review indicates that for well developed subgrain boundaries $m \sim 1$, whilst for cell structures $m \sim 0.5$. However, he also cites experimental evidence in support of equation 6.33, and there is clearly need for further work in this area.

6.5.3 Subgrain growth by boundary migration

6.5.3.1 General considerations

Two quite different mechanisms by which coarsening of the substructure can occur have been proposed - **subgrain boundary migration,** which will be considered in this section, and **subgrain rotation and coalescence** which is considered in §6.5.4. Although it is generally accepted that the rate of subgrain growth is controlled by the migration of the low angle boundaries, the possibility that triple junction mobility may play some role, as discussed in §5.5, should be considered. However, there is as yet no experimental or theoretical evidence that this is a significant factor.

In a deformed and recovered polycrystal, the subgrain structure may be topologically rather similar to the grain structure of a recrystallized material, and coarsening by the migration of low angle grain boundaries is sometimes considered to be a similar process to that of **grain growth following recrystallization** which is discussed in chapter 11, although it will be shown here that there are significant differences.

The local driving forces for the migration of low angle grain boundaries (LAGBs) arise from the energy and orientation of adjacent boundaries. In the two-dimensional case shown schematically in figure 6.17, the triple point **A** is subjected to forces F_1, F_2 and F_3 from three boundaries. If the specific energies of the boundaries are equal, then the triple point will be in equilibrium when the boundaries make angles of 120° with each other (§4.5.1). The boundaries are therefore forced to become curved (dotted lines), and will tend to migrate in the direction of the arrows so as to minimise their length. Thus the triple point will migrate, and will become stable if it reaches a position (**A′**) in which the boundaries are straight (dashed lines) and the angles are at the equilibrium value of 120°.

The considerations of the topology of growth of a grain assembly in chapter 11, show that large subgrains will grow at the expense of small ones which will shrink and disappear. The subgrain structure adjusts to the forces arising from the boundary energies by the movement of triple point **Y** junctions, and the detailed mechanism of this will depend on the dislocations which comprise the boundaries. For example, in the simple case shown in figure 6.18, vertical movement of the junction **A** may be accomplished by dissociation of the higher angle boundary **AB** to provide dislocations for the boundaries **AC** and **AD.** In the general case, more complex dislocation interactions are required as the **Y** junctions move and it is possible that under certain conditions these could be rate determining (§5.5). However, no analysis of this process is yet available.

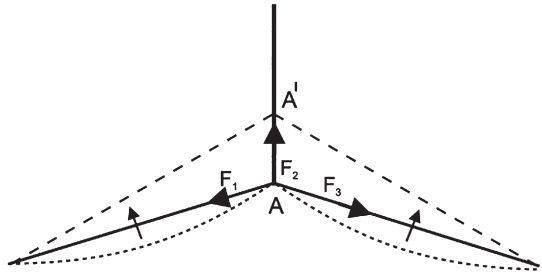

Fig. 6.17. The migration of low angle boundaries at a triple point.

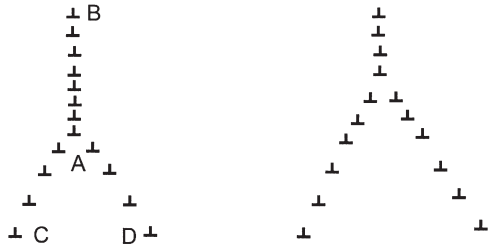

Fig. 6.18. Movement of a Y-junction during subgrain growth.

6.5.3.2 Subgrain growth in polygonized crystals

Symmetrical tilt boundaries, such as those shown in figure 6.12c can move by the glide of the edge dislocations which comprise the boundary (§5.2.1). The mobility is high and migration may occur at low temperatures (Parker & Washburn 1952). Subgrain growth of polygonized substructures (the arrays of tilt boundaries formed on the annealing of bent single crystals), has been extensively investigated, and growth of these subgrains has been shown to occur by the migration of **Y** junctions as shown in figure 6.18. The first quantitative study of this process was by Gilman (1955) on zinc crystals. Other investigations have been made on crystals of zinc (Sinha and Beck 1961), NaCl (Amelinckx and Strumane 1960), LiF (Li 1966) and silicon iron (Hibbard and Dunn 1956). In general these measurements show that both the boundary misorientation and spacing increase with the logarithm of time and that the activation energy increases as growth proceeds. The process has been analysed theoretically by Li (1960) and Feltner and Loughhunn (1962) and reviewed by Friedel (1964) and Li (1966). It should be emphasised that polygonization of bent single crystals is a very special case of subgrain formation and growth, and is expected to have little relevance to the growth of the subgrain structures which occur in polycrystals or in single crystals which have undergone more complex deformation.

6.5.3.3 Subgrain growth in the absence of an orientation gradient

There is a significant difference between **grain growth** which is discussed in chapter 11, and **subgrain growth** which is considered here. In the former case the boundaries are mainly high angle and have similar energies, the equilibrium angle between the boundaries is typically 120°, and the grain structure (in two dimensions) tends towards an assembly of equiaxed hexagonal grains (§4.5.1). In contrast, the energies of low angle grain boundaries are strongly dependent on both the misorientation and the boundary plane (§4.3.1), and the equilibrium angles between the boundaries are in general unlikely to be 120°. In lightly deformed materials the subgrains sometimes appear almost rectangular (e.g. figure 2.10). However, in heavily deformed materials the subgrains often appear topologically similar to a grain structure (fig. 6.22), although caution should be used in interpreting subgrain growth kinetics in terms of models developed for high angle boundaries. Nevertheless, in modelling the kinetics of subgrain growth by boundary migration, it is often assumed that if the appropriate values of boundary mobility (**M**) and the driving pressure for growth (**P**) are taken, then the growth of the subgrain structure may be treated in a similar manner to **grain growth** involving high angle boundaries, which is discussed in chapter 11 (Smith and Dillamore 1970, Sandström 1977b).

Using equations 6.26 and 5.1 and putting $\mathbf{dR/dt = v}$ we find

$$\frac{dR}{dt} = \frac{\alpha M \gamma_s}{R} \tag{6.34}$$

If there is no orientation gradient and θ remains constant during growth then integration gives

$$R^2 - R_0^2 = c\,t \tag{6.35}$$

where $c = 2\alpha M \gamma_s$ and R_0 is the subgrain radius at $t = 0$.

If c remains constant during growth, equation 6.35 is of the same form as the usual grain growth relationship (equation 11.5) and is similar to equation 6.27, with **n = 2,** which was shown to be consistent with some of the experimental measurements of subgrain growth kinetics.

6.5.3.4 Decreasing misorientation during subgrain growth

Even in the absence of an overall orientation gradient, the average misorientation θ of a subgrain structure may not remain constant. Using a two-dimensional vertex model (§16.2.4) to simulate subgrain growth in the absence of an orientation gradient, Humphreys (1992b) found that the average misorientation decreased as the subgrains grew (fig. 6.19), and that the exponent **n** in equation 6.27 was > 3, and this result has been confirmed by more recent Monte Carlo simulations (Holm et al. 2001).

It is reasonable to expect that low angle boundary migration will occur in such a way as to lower the local energy by removing or shortening boundaries of higher angle (higher energy). Consider the annealing of the boundary configuration shown in figure 6.20a, in which higher energy boundaries are shown as bold lines. The boundary angles are initially 120°, but line tension forces will tend to increase the angles DEC and GFH and decrease the angles CAK and HBL, resulting in the microstructure of figure 6.20b. In responding to the line tensions, the total length of higher angle boundary is thus decreased.

The experimental results discussed in §6.5.2.1 and shown in figure 6.16b confirm the computer predictions and provide clear evidence that in the absence of an orientation gradient, the subgrain misorientations tend to decrease as the subgrains grow. However,

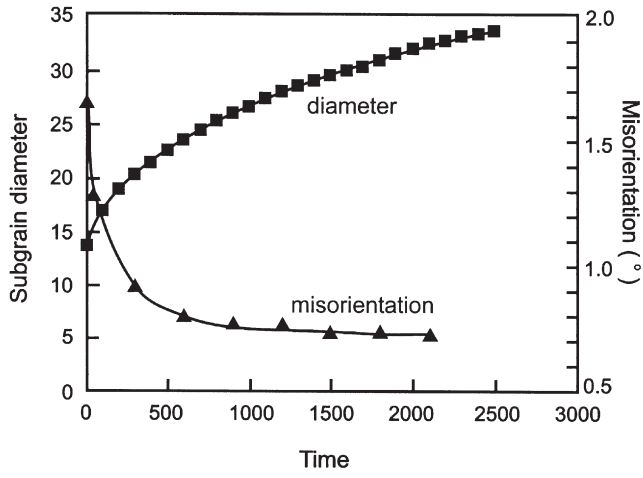

Fig. 6.19. Computer simulation of subgrain growth and misorientation decrease in the absence of a misorientation gradient, (Humphreys 1992b).

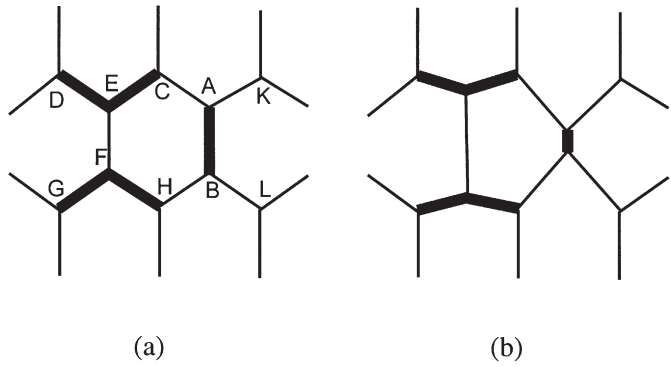

Fig. 6.20. The boundary movements which may lead to a decrease in the average misorientation if there is no orientation gradient.

it should be emphasised that there are large orientation gradients in most deformed grains (§2.4) and that the behaviour of figure 6.16b is not typical.

The role of boundary character in grain growth is discussed further in §11.3.2.

6.5.3.5 Discontinuous subgrain growth

The subgrain growth which has been considered in the earlier part of this chapter occurs by a gradual and uniform coarsening of the subgrains, and in phenomenological terms is a **continuous process** as defined in chapter 1. However, under certain circumstances, some subgrains may grow much faster than average, leading to a duplex subgrain structure as shown in figure 6.21, in which some subgrains may reach sizes of ~100 μm. This process, which superficially appears to be similar to recrystallization (figure 7.1) or abnormal grain growth (figure 11.19), differs from both as it involves only low angle boundaries. However, like these, it can be classified as a **discontinuous process,** and has been termed **discontinuous subgrain growth,** although abnormal subgrain growth would also be a reasonable description.

Discontinuous subgrain growth was first identified by Ferry and Humphreys (1996a), and further studied by Huang and Humphreys (2000) in $\{110\}<001>$ aluminium crystals. The rapidly growing subgrains were found to be those at the edge of the orientation spread of the subgrains, and to have slightly larger misorientations with respect to their neighbours than the normally growing subgrains, as may be seen in table 6.1.

The question of whether a cellular microstructure such as subgrain structure, will grow continuously or discontinuously is analysed in chapter 10. The somewhat surprising result of this theoretical analysis is that because of the large effect of misorientation angle on boundary mobility for small misorientations, (figure 5.5), discontinuous rather than continuous subgrain growth is expected in such a structure. The subgrains which are predicted to grow rapidly are those which are slightly larger and more misoriented than average, as is found experimentally. Vertex simulations (Maurice and Humphreys 1998) also predict discontinuous subgrain growth from similar initial microstructures.

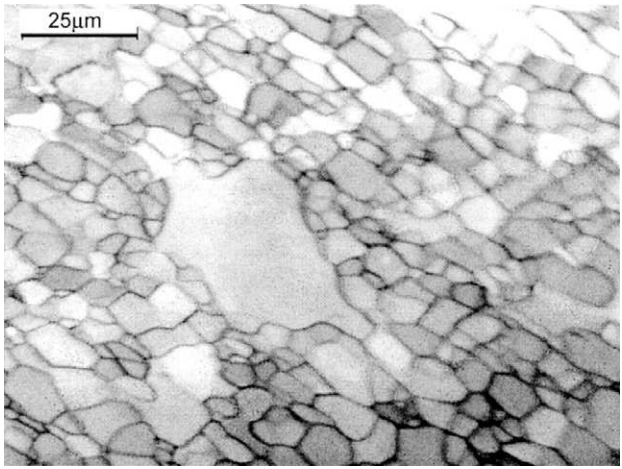

Fig. 6.21 EBSD pattern quality map showing discontinuous subgrain growth in Al–0.05%Si. In this type of map, the low angle boundaries appear as dark lines, (Huang and Humphreys 2000).

Table 6.1
The misorientations from their neighbours of subgrains growing continuously and discontinuously in {110} < 001 > crystals of Al–0.05%Si processed to varying starting microstructures (Huang and Humphreys 2000).

Process batch	Initial subgrain diameter (μm)	Misorientation to neighbours (degrees)	
		Continuous growth	Discontinuous growth
A	1.2	2.6	3.8
B	0.9	3.7	4.6
C	4.4	4.5	5.6

It is interesting that although abnormal subgrain growth is theoretically predicted, it has not been observed until recently. The reason, is that as discussed in §6.5.2.1, very little subgrain growth occurs in most materials because the process is curtailed by the onset of recrystallization. It is only in special circumstances, where recrystallization does not initiate, thus allowing substantial subgrain growth to occur, that abnormal subgrain growth can be detected.

6.5.3.6 Subgrain growth in an orientation gradient

In many deformed or recovered substructures there is an **orientation gradient** ($\mathbf{\Omega} = \mathbf{d}\theta/\mathbf{dR}$) (§2.2.3.2). If this is the case, the average subgrain misorientation (θ) will

increase during subgrain coarsening, and these subgrains will grow more rapidly than those in an environment where there is no orientation gradient. Recovery in an orientation gradient is thought to play a particularly important role in the **nucleation of recrystallization** as discussed in §7.6.

An example of this is shown in figure 6.22. Figure 6.22a shows the microstructure of an aluminium crystal of the $\{100\}<001>$ cube orientation which has been deformed in plane strain compression at 350°C. Under these conditions, the cube orientation is unstable (§13.2.4), and deformation bands are formed at which large (10–30°) orientation changes occur. Although the microstructure of the as-deformed material (fig. 6.22a) is reasonably uniform, on further annealing (fig. 6.22b), the subgrains in the deformation bands accumulate further misorientation as they grow and their growth is therefore very rapid. This is a similar process to that shown in the vertex simulation of figure 16.10.

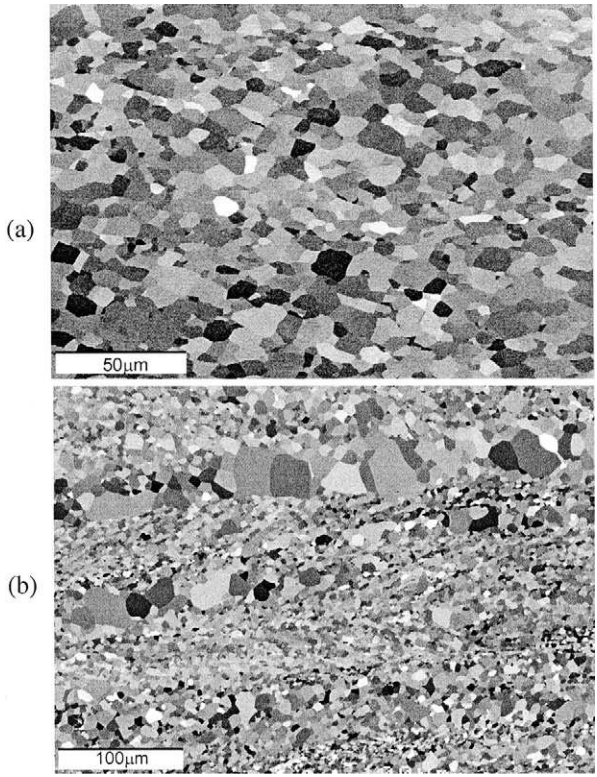

Fig. 6.22. Channelling contrast SEM micrographs showing subgrain growth in a hot deformed $\{100\}<001>$ aluminium crystal in which there are long range orientation gradients. (a) As deformed at 350°C and quenched, (b) further annealed at 350°C. Extensive subgrain growth is seen in bands where there are significant orientation changes, (Huang et al. 2000a).

Starting with equation 6.26, we now note that the LAGB energy varies with θ according to the Read-Shockley equation 4.6. For small values of θ, $\gamma_s = \theta\gamma_m/\theta_m$ and hence

$$P = \frac{\alpha\gamma_s}{R} = \frac{\alpha\theta\gamma_m}{\theta_m R} \tag{6.36}$$

(γ_m is the boundary energy predicted by the Read-Shockley equation when the misorientation reaches θ_m, the transition to HAGB behaviour).

Because of the orientation gradient, θ increases as the subgrain grows and

$$\theta = \theta_0 + \Omega(R - R_0) \tag{6.37}$$

where θ_0 and R_0 are the initial values of θ and R, and Ω is the orientation gradient.

Hence, from equation 5.1

$$\frac{dR}{dt} = \frac{\alpha M\theta\gamma_m}{\theta_m R} = \frac{\alpha M\gamma_m}{\theta_m R}[\theta_0 + \Omega(R - R_0)] \tag{6.38}$$

Initially, and for small orientation gradients, equation 6.38 reduces to equation 6.34. However, for the large orientation gradients found at deformation heterogeneities ($\Omega > 5^\circ/\mu m$), a rapid subgrain growth rate, which decreases more slowly with increasing R than does the rate in the absence of an orientation gradient, is predicted. The exact form of equation 6.38 depends on the orientation dependence of **M** and hence the model assumed for boundary mobility. **Better understanding in this area is required to develop the theories and models for the growth of subgrains in an orientation gradient, which are needed to predict the initiation of recrystallization.**

6.5.4 Subgrain growth by rotation and coalescence

An alternative mechanism for subgrain growth was proposed by Hu (1962), based on in-situ TEM annealing experiments of Fe–Si alloys. He suggested that subgrains might rotate by boundary diffusional processes until adjacent subgrains were of similar orientation. The two subgrains involved would then coalesce into one larger subgrain with little boundary migration, the driving force arising from a reduction in boundary energies, as discussed by Li (1962).

6.5.4.1 The process of subgrain rotation

The process is shown schematically in figure 6.23. Consider two adjacent low angle boundaries **AB** and **BC,** and let rotation occur in such a direction as to increase the misorientation of the higher angle boundary (AB) and reduce the misorientation of the lower angle boundary (BC). It can be seen from equation 4.5 and figure 4.6 that the change in boundary energy, $\mathbf{d\gamma/d\theta}$ is greater the lower the angle of the boundary. Therefore, if the two boundaries have similar areas, the increase in energy of boundary AB is less than the energy decrease of boundary BC. There is therefore an overall

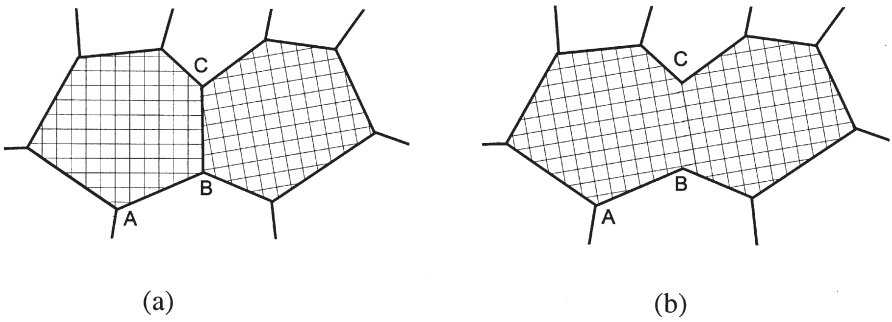

Fig. 6.23. Proposed mechanism for the rotation and coalescence of subgrains.

decrease in energy if rotation occurs in such a way as to decrease the misorientation of boundary BC and increase the misorientation of boundary AB, and this will eventually lead to coalescence as shown in figure 6.23b.

Experimental evidence for the occurrence of subgrain rotation and coalescence during recovery has not been accepted as unambiguous. The evidence has been obtained from two types of experiment: Direct observation of the annealing of thin foils in the TEM, and post-mortem observation in the TEM of material annealed in the bulk and then thinned.

6.5.4.2 Evidence from in-situ TEM observations

This technique is suspect because events occurring in thin foils are not generally representative of bulk behaviour. This is because dislocations can easily escape to the surface of a thin foil (which even in an HVEM is seldom thicker than $\sim$2 μm) and alter the dislocation content and hence the misorientation at low angle grain boundaries. As an example, consider the dislocations in the boundaries in figure 6.12c. The forces between the edge dislocations in the tilt boundaries are such as to push them apart vertically (Hirth and Lothe 1968). It is easy to see that if the specimen were heated to a temperature at which climb would occur, then dislocations would be lost and the boundary would eventually disappear. In addition, a thin specimen allows the stresses arising from the changes in dislocation configuration to be accommodated by bending. Several in-situ annealing experiments have shown dislocation extraction from very low angle boundaries (e.g. Sandström et al. 1978).

Evidence of subgrain rotation in deformed Al–6wt%Ni at very high temperatures was obtained by Chan and Humphreys (1984a) and Humphreys and Chan (1996) during in-situ annealing in the HVEM. This alloy contained a dispersion of second phase particles which coarsened but which did not dissolve at high temperatures. On annealing, well-defined subgrains were formed (fig. 6.24a), and at lower temperatures of annealing these were seen to grow by **the migration of low angle boundaries** at a rate controlled by the coarsening of the particles (see §11.4.3.2). However, at temperatures in excess of 550°C, **subgrain reorientation** was found to occur. Clear microscopic evidence of a change in the dislocation content of the boundaries is seen in figure 6.24b at boundary

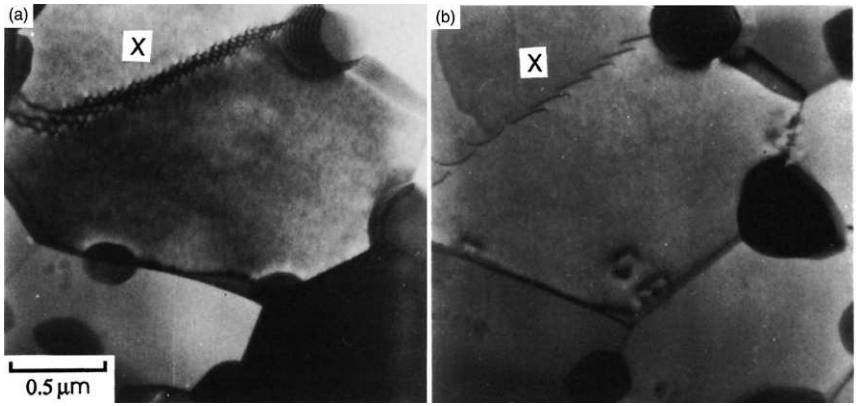

Fig. 6.24. Rotation of subgrains during the in-situ annealing of a thin foil of Al–6%Ni in the HVEM at 550°C. Note the dislocation loss at boundary X, (Humphreys and Chan 1996).

X. In addition, measurements of the misorientations of boundaries before and after reorientation clearly established that the contrast changes in the subgrains were due to changes in relative orientations and not to artifacts such as bending of the thin foil.

Although the experiments described above showed that subgrain rotation occurred, it should be emphasised firstly that this only took place at very high temperatures ($0.9T_m$), far above those where LAGB migration occurs readily, and thus the relevance to normal recovery at relatively low temperatures is questionable. Secondly, for the reasons discussed above, the dislocation rearrangement in the boundaries is almost certainly aided by the free surfaces of the specimen.

Most in-situ annealing experiments, particularly those in which the mechanisms of recrystallization were being investigated, have found **clear evidence of LAGB migration,** e.g. Kivilahti et al. (1974), Ray et al. (1975), Bay and Hansen (1979), Humphreys (1977), Berger et al. (1988), but have found **no evidence of subgrain rotation.**

6.5.4.3 Evidence from bulk annealed specimens

The difficulty with determining the annealing mechanism from examination of bulk-annealed samples is that only the structure before **or** after the event can be seen and the evidence is therefore indirect. Evidence cited in favour of coalescence is usually a micrograph of a large subgrain containing a very low angle boundary. This latter boundary is then stated to be in the process of disappearing by coalescence. Several clear instances of such structures have been obtained for example by Hu (1962), Doherty (1978), Faivre and Doherty (1979) and Jones et al. (1979). The problem with such observations is that during deformation, subgrains or cells are continually being formed and reformed, so that new subgrain boundaries will often form within old subgrains (§2.4.2). Therefore **micrographs of poorly developed low angle boundaries within well defined subgrains are as likely to be showing a boundary forming as a boundary disappearing and therefore do not provide convincing evidence of subgrain coalescence.**

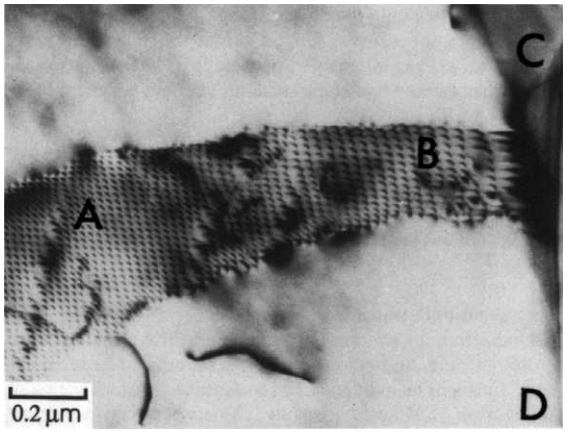

Fig. 6.25. Transmission electron micrograph of annealed aluminium showing that the spacing of dislocations in the low angle boundary AB becomes larger as the high angle boundary CD is approached, (Jones et al. 1979).

There have been several observations of recovered microstructures which show that the subgrain size in the vicinity of a grain boundary is larger than in the interior of the grain (Goodenow 1966, Ryum 1969, Faivre and Doherty 1979, Jones et al. 1979). Whether this effect is a result of the deformation microstructure adjacent to the HAGB being different to that in the grain interior (§3.7.1.4) or whether it is an indication of a difference in annealing behaviour near the HAGB is not yet clear. However, on the basis of the arguments of §6.5.4.1, a high angle boundary, whose energy is not orientation dependent should be a favourable site for subgrain rotation (Doherty and Cahn 1972).

Jones et al. (1979) have presented clear evidence that the dislocation content of very low angle LAGBs connected to HAGBs is not uniform, and that the dislocation content of the boundary may be lower adjacent to the HAGB, as shown in figure 6.25. It is envisaged that the HAGB is able to absorb dislocations from the LAGB, and the authors suggest that this may be the early stages of subgrain rotation.

6.5.4.4 Modelling reorientation at a single boundary

The kinetics of subgrain coalescence are best considered in two stages. In this section, we examine the reorientation at a single boundary, ignoring the constraints of adjacent subgrains, and in the next, we consider the total microstructure.

Li (1962) has discussed the kinetics of reorientation at a single boundary in terms of two possible mechanisms – **cooperative climb of edge dislocations and cooperative vacancy diffusion.** For small boundary misorientations, such as those typically found in recovered structures, dislocation climb is likely to be rate controlling, and we will only consider this mechanism.

Li examined the case of a single symmetrical tilt boundary of misorientation θ and height L. If the dislocation spacing remains uniform during climb, then the

work done by the dislocations in time **dt** during which the orientation changes by **dθ** is given by

$$dW = \frac{2L^3\, d\theta}{3b\theta B}\frac{d\theta}{dt} \tag{6.39}$$

where **B,** the mobility of dislocations by climb, is given by $B = D_x b^3 c_j/kT$. D_x is the diffusivity and c_j the concentration of jogs on the dislocations.

This is equal to the energy change (**dE**) when the boundary misorientation changes by $d\theta$

$$dE = 2L\gamma_m \ln\left(\frac{\theta_m}{\theta}\right) d\theta \tag{6.40}$$

where γ_m and θ_m are constants from the Read-Shockley equation (4.6).

Equating dE and dW we obtain

$$\frac{d\theta}{dt} = \frac{3\gamma_m \theta B b}{L^2} \ln\left(\frac{\theta}{\theta_m}\right) \tag{6.41}$$

which on integration gives

$$\ln\ln\left(\frac{\theta_m}{\theta}\right) = \left(\frac{3Bb\gamma_m}{L^2}\right) t + K \tag{6.42}$$

Li (1962) also analysed the reorientation of twist and other low angle boundaries and found that this differed from equation 6.41 by only a small factor.

Doherty and Szpunar (1984) re-examined the kinetics of reorientation by dislocation climb, and suggested that it was more appropriate to consider the behaviour of dislocation loops encircling a subgrain than to consider isolated boundaries as was done by Li. For climb controlled by bulk diffusion, they obtained kinetics very similar to those of Li, i.e. equation 6.41. However, they showed that core diffusion, which modifies the term **B** in equation 6.41, would lead to much faster rates of reorientation at low temperatures ($T < 350^\circ C$) in aluminium.

6.5.4.5 Modelling the kinetics of subgrain coalescence

During a coalescence event in a recovered subgrain structure, reorientation of one subgrain affects **all** the boundaries around the subgrain, and therefore we would expect some 14 LAGBs to be involved. Li (1962) showed that the driving force for rotation of a subgrain, calculated from the energy changes of all the boundaries involved is always finite about all axes except one, and that therefore the process is thermodynamically feasible. The total driving force from the α boundaries surrounding a subgrain is

$$\sum_\alpha L_\alpha^2 \frac{d\gamma}{d\theta} = \sum_\alpha L_\alpha^2 \gamma_m \ln\left(\frac{\theta_m}{\theta_\alpha}\right) \tag{6.43}$$

It may be seen from equation 6.43 that the boundary which provides the most driving force will be that with the smallest θ and largest area.

In order to properly calculate the kinetics of rotation of an enclosed subgrain, the driving force from equation 6.43 must be used in conjunction with the appropriate climb rate of the dislocations in all the participating boundaries, which is a difficult problem. However, reference to Li's climb kinetics of equation 6.41, show that the boundary which has the lowest rate of rotation also has the largest driving force. Li therefore argued that this boundary could be regarded as controlling the rate of rotation, and thus equation 6.41 could, to a first approximation be used to predict the rate of rotation of a subgrain. This approach has been widely adopted by later workers. However, it should be borne in mind that the values of L and θ to be used in the equation refer not to the **average subgrain,** but to that with the largest value of $L^2 \ln(\theta_m/\theta)$. Another problem in using this analysis is that rotation of one subgrain affects the environment and hence the subsequent rotation kinetics of all adjacent subgrains. Therefore, in order to determine the kinetics of subgrain rotation we need to know not only the initial distribution of subgrain sizes and orientations, but all subsequent values of these parameters.

More recently, Moldovan et al. (2001) have formulated a detailed theory for grain rotation in a polycrystalline columnar microstructure, based on continuum theories, elasticity and diffusive flow.

There have been several attempts to compare the experimentally measured kinetics of subgrain growth (§6.5.2) with those predicted for subgrain coalescence. The usual method of predicting growth kinetics from equation 6.41 has been to equate θ with the measured mean misorientation and to assume that at time **t,** all subgrains of diameter less than L will have coalesced, so that $\mathbf{L^2}$ is proportional to **t.** These kinetics are of similar form to those sometimes found in practice (equation 6.27 with $n = 2$), and are of course also similar to those which have been predicted for subgrain coarsening by LAGB migration when θ remains constant (e.g. equation 6.35). However, they are not consistent with more recent measurements of subgrain growth which give a much larger value of n in equation 6.27 (§6.5.2).

Because of the uncertainties over the theoretically predicted growth rates for both subgrain rotation and subgrain growth by migration, it would be unwise to use kinetics as a basis for distinguishing between these mechanisms.

6.5.4.6 Simulations of subgrain coalescence

Computer simulation of subgrain rotation and coalescence within a two-dimensional array of subgrains has been carried out. The driving force for the process is given by equation 6.43, and the rate of rotation is as calculated by Li (1962) on the assumption of control by dislocation climb. Saetre and Ryum (1992) used, as a starting structure, an array of square subgrains. We have used an extension of the vertex model (§16.2.4), which allows a more realistic subgrain structure. Figure 6.26 shows the results of our simulation for identical microstructures but with various misorientation spreads. As shown in figure 6.26a, there is an initial sharp increase in subgrain size, due to a large number of coalescence events involving the elimination of very low angle boundaries. Thereafter there is a linear increase in subgrain size in agreement with the results of Saetre and Ryum (1992). Note that after the initial period the rate of growth is little

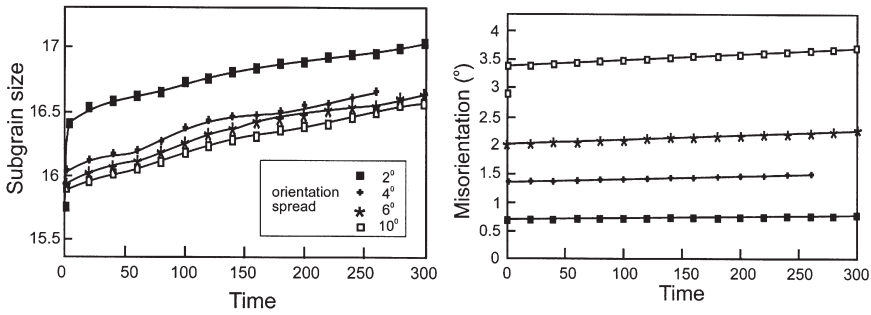

Fig. 6.26. Computer simulation of the kinetics of subgrain coalescence in a two dimensional microstructure. Orientation spreads of from 2 to 10 degrees have been introduced into the microstructure. (a) Subgrain growth,. (b) Mean misorientation.

affected by the misorientation. The mean subgrain misorientation is seen in figure 6.26b to increase almost linearly with time. The simulation was also run with a high angle boundary in the microstructure, but with the same spread of subgrain misorientations. It was found that coalescence took place preferentially at the HAGB as first predicted by Doherty and Cahn (1972). An analysis of the data showed that throughout the simulation, the chance of a coalescence event occurring at the high angle boundary was 2.5 times greater than within the grain interior.

Wolf's group at Argonne have recently conducted mesoscale simulations (Moldovan et al. 2002) and molecular dynamics simulations (Haslam et al. 2001) of growth in columnar polycrystals. These simulations allow both boundary migration and grain rotation to occur, therefore allowing comparison of these mechanisms. Grain rotation was found to be significant for grains of diameter ~15 nm at temperatures close to the melting point, and an example of the molecular dynamics simulation is shown in figure 6.27. These powerful molecular dynamics simulations demonstrate the interplay between grain rotation and boundary migration and, in agreement with the discussions above, suggest that **subgrain rotation will only be a significant factor for very small subgrains with small misorientations and at very high temperatures.**

6.5.5 Recovery mechanisms and the nucleation of recrystallization

There is no doubt that subgrain rotation and coalescence are thermodynamically feasible, and, as discussed above, there is evidence that in thin foils heated in the electron microscope, dislocations may be emitted from very low angle boundaries and that this may lead to coalescence under these special conditions. There is also some evidence that dislocation rearrangement may occur in low angle boundaries adjacent to high angle boundaries. However, there is no convincing evidence that this mechanism plays any significant role in subgrain coarsening either during uniform recovery, or during recovery in regions of large orientation gradient, which, as is discussed in §7.6.3, is thought to be a method by which recrystallization originates.

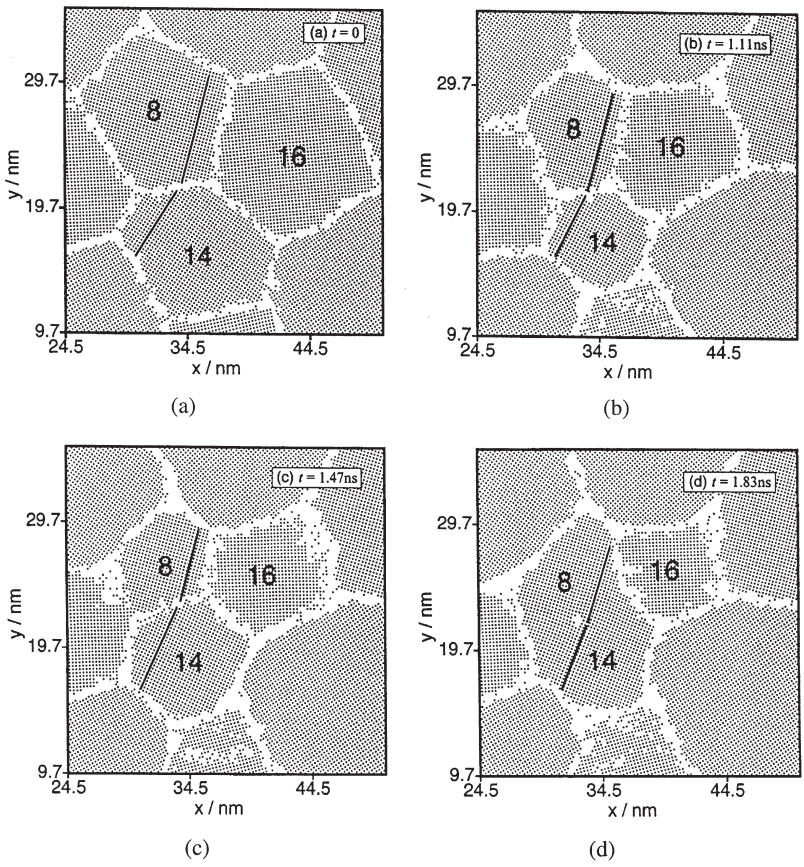

Fig. 6.27. Molecular dynamics simulation of grain growth involving grain rotation, coalescence and boundary migration in a small columnar polycrystal. The mis-coordinated atoms in the boundary regions are not shown, and the solid lines indicate $<110>$ directions. (a) $t=0$, (b) $t=1.11$ ns, (c) $t=1.47$ ns, (d) $t=1.83$ ns, (Haslam et al. 2001).

It is therefore reasonable at the current time, on the available theoretical and experimental evidence to assume that both subgrain coarsening and the nucleation of recrystallization from pre-existing subgrains are controlled by the migration of low angle grain boundaries.

6.6 THE EFFECT OF SECOND-PHASE PARTICLES ON RECOVERY

Second-phase particles may either have been present during the deformation of the material, in which case they are often distributed reasonably uniformly in the microstructure, or they may precipitate during the anneal, in which case their

distribution is often related to the dislocation structure. In this section we will be primarily concerned with a stable distribution of particles which does not alter during the anneal. The effects of concurrent precipitation and annealing are considered in §9.8.

Second-phase particles may affect recovery mechanisms in several ways. During the annihilation and rearrangement of dislocations to form low angle boundaries (§6.3), the particles may pin the individual dislocations and thus inhibit this stage of the recovery. The driving force (**F**) for the annealing of a three-dimensional dislocation network is given by equation 6.13. This will be opposed by the force due to the pinning effect of the particles (F_P). To a first approximation, this is given by

$$F_p = \frac{c_1 G b^2}{\lambda} \tag{6.44}$$

where c_1 is a constant whose value depends on the magnitude of the interaction between particles and dislocations, and λ is the spacing of particles along the dislocation lines (dislocation-particle interaction are discussed in more detail in §2.9.3). The resultant driving force then becomes $\mathbf{F}$-$\mathbf{F}_p$. This approach is only valid if the particle spacing is small compared to the scale of the dislocation network, and as this rarely occurs in practice, there has been little investigation of the effect of particles on this stage of recovery.

There has however been much more interest in the effect of particles on subgrain growth during recovery, as this is relevant to the origin of recrystallization in particle-containing alloys which is discussed in chapter 9.

6.6.1 The effect of particles on the rate of subgrain growth

There is substantial evidence that a fine particle dispersion may exert a strong pinning effect on subgrains (Humphreys and Martin 1968, Ahlborn et al. 1969, Jones & Hansen 1981), and an example is shown in figure 6.14. The use of particles to pin and stabilize the recovered substructure is a well established method for improving the strength and creep resistance of alloys at high temperatures. The particles used for this purpose need to be stable at high temperatures, and oxide particles, often introduced by **powder metallurgy or mechanical alloying** are incorporated into **dispersion hardened alloys,** such as nickel alloys (e.g. Benjamin 1970) and aluminium alloys (e.g. Kim and Griffith 1988).

The electron microscope observations of Jones and Hansen (1981) have revealed the pinning of individual boundary dislocations by particles as shown in figure 6.28. As yet, no theories of boundary mobility based on dislocation-particle interactions have been formulated, and the models used to account for subgrain growth in the presence of particles are essentially similar to those developed to account for the effect of particles on grain growth (§11.4) (Sandström 1977b). There are as yet, few quantitative measurements of the effect of particles on the rate of growth of subgrains.

It has been suggested (Bhadeshia 1997), that the stability of deformed mechanically alloyed iron and nickel-based superalloys against recrystallization can be explained by stabilisation of the fine (~0.2 mm) subgrain structure by triple junction pinning (§5.5).

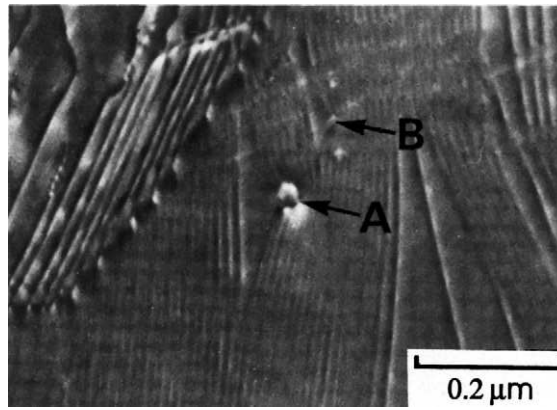

Fig. 6.28. Transmission electron micrograph showing pinning of grain boundary dislocations by Al_2O_3 particles A and B in a low angle boundary in aluminium, (Jones and Hansen 1981).

However, these microstructures appear to have a sufficient number of small second-phase particles to prevent subgrain growth (§11.4.2), and stabilization by the particles is a more likely explanation.

The interaction of high and low angle grain boundaries with particles is discussed in chapter 4. The pinning force (F_S) due to a single non-coherent spherical particle is given by equation 4.12, and the drag pressure (P_Z) due to the interaction of a random distribution of particles with a planar boundary, the **Zener drag,** is given by equation 4.24. If the interparticle spacing is much smaller than the subgrain diameter (2R), then from equations 6.26 and 4.24, the driving pressure for subgrain growth is given by

$$P = P_D - P_z = \frac{\alpha\gamma_s}{R} - \frac{3F_V\gamma_s}{2r} \tag{6.45}$$

and hence, using equation 5.1, and as before, putting $\mathbf{v}=\mathbf{dR}/\mathbf{dt}$

$$\frac{dR}{dt} = M\gamma_s\left(\frac{\alpha}{R} - \frac{3F_V}{2r}\right) \tag{6.46}$$

This equation predicts a parabolic growth law for short times, and at longer times, as P_D approaches P_Z it predicts a **limiting subgrain diameter** of $4\alpha r/3F_v$.

In practice there are several difficulties in applying equation 6.46 to the rate of subgrain growth. In particular, as discussed in §2.9.2, the initial cell or subgrain size formed on deformation may be closely related to the interparticle spacing, and therefore the assumption of a planar boundary interacting with randomly distributed particles on which equation 4.24 is based is not justified. In these circumstances, the pinning pressure

varies in a much more complicated manner with subgrain size as discussed in §4.6.2 and shown by figure 4.26.

6.6.2 The particle-limited subgrain size

Because of the industrial importance of particle-stabilised subgrain structures, there is considerable interest in calculating the particle-limited subgrain size. Because of the similarity of the pinning of high and low angle boundaries by particles, we have chosen to discuss the concept of the **limiting grain size** in some detail in §11.4.2, and in this section will comment only on those aspects of particular relevance to subgrains.

6.6.2.1 Stable particle dispersions

From §11.4.2, we expect that for small particle volume fractions the limiting subgrain size will be proportional to F_v^{-1} (equation 11.31), and at large volume fractions it will be proportional to $F_v^{-1/3}$ (equation 11.34). The critical volume fraction at which there is a transition is not known precisely, but may be ~0.05 (§11.4.2.3). Anand and Gurland (1975) measured the limiting subgrain size in steels with F_v in the range 0.1–0.2, and showed that their results were consistent with the $F_v^{-1/2}$ relationship of equation 11.33. However, as discussed in §11.4.2.3, the subgrain size predicted by equation 11.33 is unlikely to be stable, and, as shown in figure 6.29, their experimental results agree equally well with the preferred $F_v^{-1/3}$ relationship of equation 11.34.

6.6.2.2 The inhibition of recrystallization

Particle-limited subgrain growth may have a significant effect on the recrystallization behaviour of an alloy. A dispersion of particles may hinder the recovery processes involved in the initiation of recrystallization, and this topic is considered in §9.4.1.

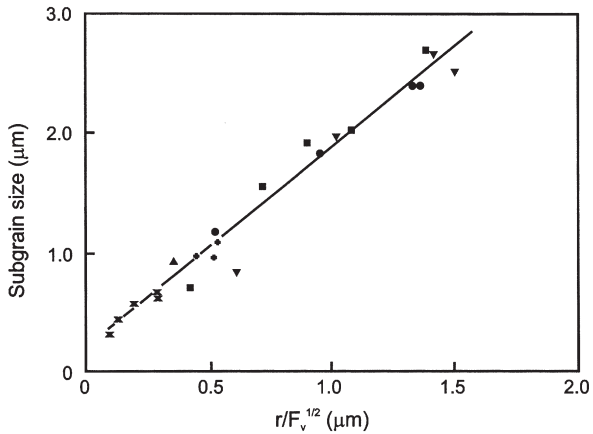

Fig. 6.29. The particle-limited subgrain size in carbon steels plotted according to equation 11.34, (after Anand and Gurland 1975).

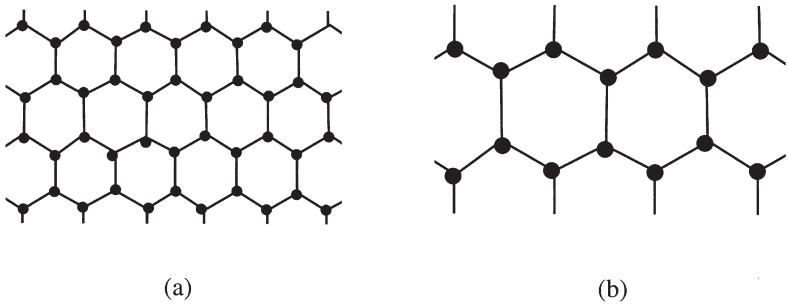

Fig. 6.30. Extended recovery controlled by the coarsening of second-phase particles.

6.6.2.3 Precipitation after subgrain formation

Precipitation on the recovered substructure may occur during the annealing of a supersaturated alloy. Examples of this behaviour have been found in the commercially important Al-Mn alloys (Morris and Duggan 1978), Fe–Cu, (Hutchinson and Duggan 1978), and Fe–Ni–Cr (Hornbogen 1977). In this situation, the precipitation generally occurs on the low angle boundaries. Such non-uniformly distributed precipitates (fig. 4.25d) exert a strong pinning effect on the boundaries as discussed in §11.4.3.1, and the limiting subgrain size is then given by equation 11.35.

6.6.2.4 Subgrain growth controlled by particle coarsening

If, after a particle-stabilised subgrain structure has formed, the particles subsequently coarsen during the recovery anneal, then general subgrain growth, whose kinetics are controlled by the coarsening of the particles, may occur as shown schematically in figure 6.30. An example of such a microstructure is seen in figure 6.24a. The kinetics of subgrain growth in these circumstances and the relationship between the particle parameters and the subgrain size are discussed in §11.4.3.1.

This phenomenon was first studied in Al–Cu alloys by Hornbogen and colleagues (e.g. Köster and Hornbogen 1968, Ahlborn et al. 1969, Hornbogen 1970). Substantial subgrain growth may occur as the particles coarsen, and the term **extended recovery** is sometimes used to describe the process.

Figure 6.31a shows an idealised one-dimensional deformed microstructure. The orientation is represented by the vertical axis and the distribution of second-phase particles and boundaries is shown in the horizontal direction. The microstructure therefore represents two grains, each containing small subgrains. On annealing at a low temperature, recovery will occur, and the initial subgrain growth will be largely unaffected by the particles until the subgrains have grown to a size comparable with the interparticle spacing (fig. 6.31b), at which point the recovered structure is stabilised as discussed in §6.6.2.1. The orientation spread within a grain is not likely to change significantly during subgrain growth, and as there is no overall orientation gradient within the grains, the subgrain misorientations remain small. Further annealing at higher temperatures may coarsen the particles, thus allowing the subgrains to grow as shown in figure 6.31c, and this process, which is shown schematically in figure 6.30, is

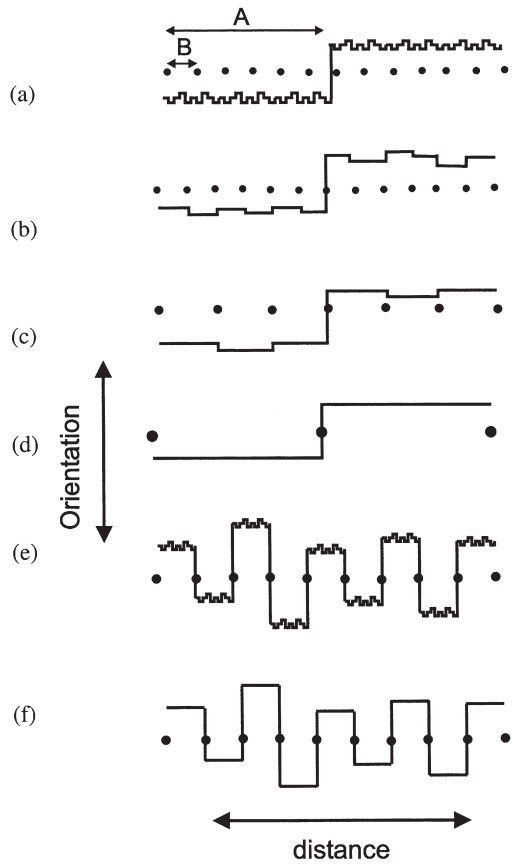

Fig. 6.31. Schematic diagram of extended recovery and continuous recrystallization as discussed in the text.

known as **extended recovery.** If the particle coarsening continues, then, eventually (fig. 6.31d), the microstructure will comprise mainly high angle boundaries. This is therefore similar to a recrystallized microstructure and it is not unreasonable to describe it by the term **continuous recrystallization.** However, it should be noted that this term does not imply any particular micromechanism and may be applied to any process in which a high angle boundary structure evolves without any obvious nucleation and growth sequence. The relationship between such continuous recrystallization which may occur during or after very large strain deformation, and the normal discontinuous recrystallization, is considered in detail in chapter 14.

The essential difference between extended recovery and continuous recrystallization is seen from the above discussions to be best defined in terms of the **relative amounts of low and high angle boundary** in the resultant microstructure, and there will be cases which are intermediate between both.

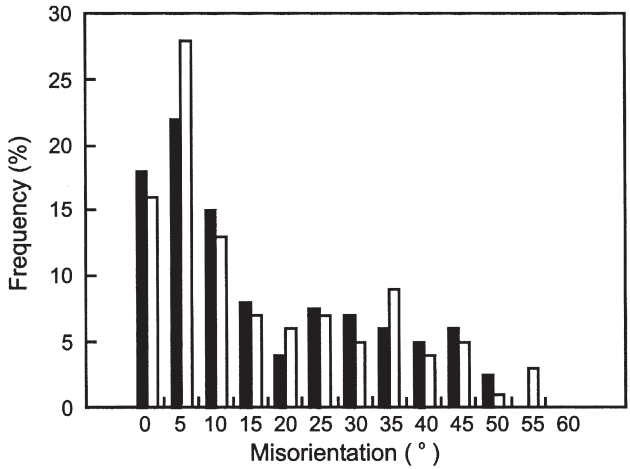

Fig. 6.32. The distribution of grain/subgrain misorientations in deformed Al–6wt%Ni annealed at 100°C (filled) and 500°C (open), (Humphreys and Chan 1996).

Good examples of extended recovery controlled by particle coarsening are found in alloys containing large (~0.1) volume fractions of intermetallic particles such as Al–Fe (Forbord et al. 1997) and Al–Ni (Morris 1976, Humphreys and Chan 1996). After hot extrusion, Al–6%Ni contains a volume fraction of 0.1 of ~0.3 μm $NiAl_3$ particles in a deformed matrix. On annealing, discontinuous recrystallization does not occur, but the particles and hence the substructure coarsen at high temperatures (see figures 11.13 and 11.14). Although the subgrains grow from ~0.8 μm at 100°C to ~2 μm at 500°C, the distribution of grain/subgrain misorientations is largely unchanged as shown in figure 6.32. The fact that the material retains a substantial fraction of low angle boundaries after the anneal, demonstrates that this is an example of extended recovery, which is readily distinguishable from continuous recrystallization in which a microstructure of mainly high angle boundaries is produced as shown in figure 14.5b.

ThisPageIntentionallyLeftBlank

Chapter 7

RECRYSTALLIZATION OF SINGLE-PHASE ALLOYS

7.1 INTRODUCTION

Recovery, which was discussed in the last chapter, is a relatively homogeneous process in terms of both space and time. When viewed on a scale which is larger than the cell or subgrain size, most areas of a sample are changing in a similar way. Recovery progresses gradually with time and there is no readily identifiable beginning or end of the process. In contrast, recrystallization involves the formation of new strain-free grains in certain parts of the specimen and the subsequent growth of these to consume the deformed or recovered microstructure (fig. 1.1c,d). The microstructure at any time is divided into recrystallized or non-recrystallized regions as shown in figure 7.1, and the fraction recrystallized increases from 0 to 1 as the transformation proceeds, as shown in the in-situ annealing sequence of figure 7.2. This is typical of a **discontinuous** annealing phenomenon as defined in §1.1.

Recrystallization of the deformed microstructure is often called **primary recrystallization** in order to distinguish it from the process of **abnormal grain growth** which may occur in fully recrystallized material and which is sometimes called **secondary recrystallization** (§11.5). We will always use the unqualified term **recrystallization** to mean primary recrystallization.

It is convenient to divide primary recrystallization into two regimes, **nucleation** which corresponds to the first appearance of new grains in the microstructure and **growth**

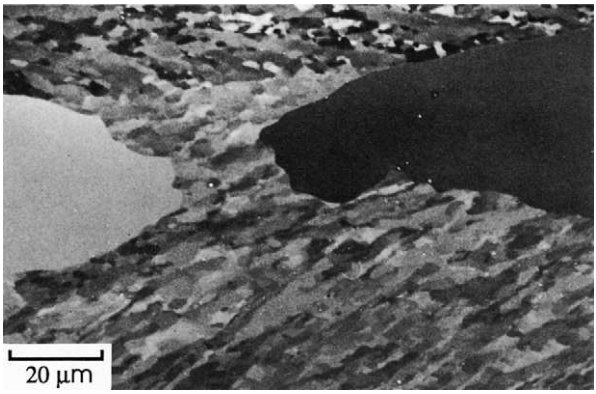

Fig. 7.1. An SEM channelling contrast micrograph of aluminium showing recrystallized grains growing into the recovered subgrain structure.

during which the new grains replace deformed material. Although these two events occur consecutively for any particular grain, both nucleation and growth may be occurring at any time throughout the specimen. The kinetics of recrystallization are therefore superficially similar to those of a phase transformation which occurs by nucleation and growth. In discussing the origin of recrystallization, the term **'nucleation'** which is conventionally used, is not appropriate because, as will be further discussed in §7.6.1, nucleation in the classic thermodynamic sense does not occur. A more accurate description of the process would be **'initiation',** although, for simplicity, we will use the accepted terminology.

The progress of recrystallization with time during isothermal annealing is commonly represented by a plot of the **volume fraction of material recrystallized (X_V)** as a function of **log(time).** This plot usually has the characteristic sigmoidal form of figure 7.3 and typically shows an apparent incubation time before recrystallization is detected. This is followed by an increasing rate of recrystallization, a linear region, and finally a decreasing rate of recrystallization.

In this chapter we will consider the origin of recrystallization, and general aspects such as the kinetics and other factors which affect both the process of recrystallization and the final microstructure. We will mainly be concerned with the behaviour of single-phase alloys, as the recrystallization of two-phase alloys is considered separately in chapter 9. The mobility and migration of the grain boundaries during recrystallization is considered in more detail in chapter 5, and the orientation of the recrystallized grains (the recrystallization texture), is discussed in chapter 12.

It has recently become apparent that the recrystallization of metals after very large strain deformation may be quite different from that after low or moderate strains, and that the discontinuous recrystallization which is the subject of this chapter, is replaced by a process of **continuous recrystallization.** This topic is the subject of chapter 14.

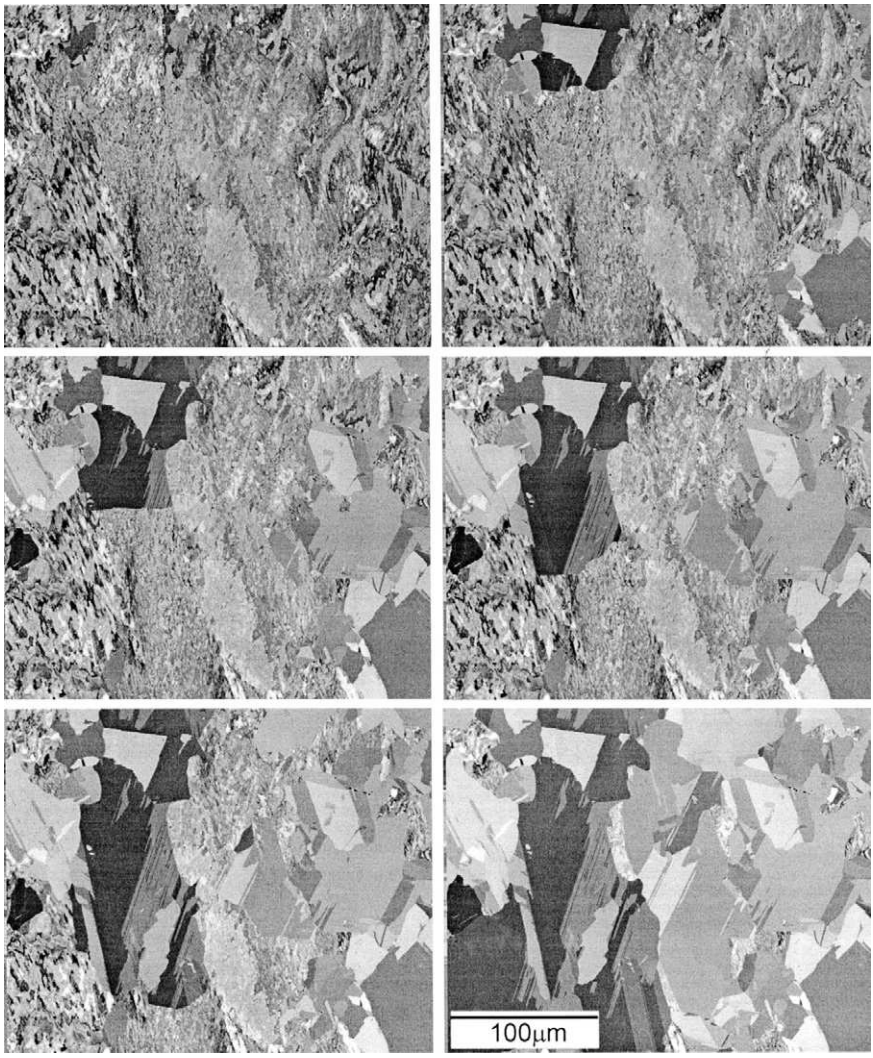

Fig. 7.2. Recrystallization of deformed copper observed during in-situ annealing in the SEM. Video sequences of this and other in-situ annealing experiments can be viewed at **www.recrystallization.info.**

7.1.1 Quantifying recrystallization

Recrystallization is a microstructural transformation, which is most directly measured by quantitative metallography (appendix 2). However, it is also possible to follow the progress of recrystallization by the measurement of various physical or mechanical properties.

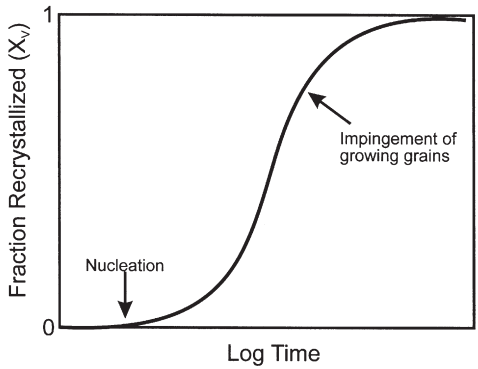

Fig. 7.3. Typical recrystallization kinetics during isothermal annealing.

7.1.1.1 The overall transformation

The extent of recrystallization is often described by $\mathbf{X_V}$, and for isothermal experiments it is convenient to use the time at which recrystallization is 50% complete **($t_{0.5}$),** as a measure of the rate of recrystallization. For isochronal experiments, where annealing is carried out at various temperatures for a constant time, e.g. 1 hr, then the **recrystallization temperature,** is usually defined as the temperature at which the material is 50% recrystallized.

Although such measurements of the recrystallization process have practical value, more fundamental measurements of recrystallization are obtained by separate reference to the constituent **nucleation and growth processes.**

7.1.1.2 Nucleation

Our first difficulty lies in defining what we mean by a **recrystallization nucleus.** A working definition might be **a crystallite of low internal energy growing into deformed or recovered material from which it is separated by a high angle grain boundary.**

If the number of nuclei per unit volume **(N)** remains constant during recrystallization, then this is the key parameter. However, if this is not the case, the **nucleation rate** $\dot{\mathbf{N}} = \mathbf{dN/dt}$ also needs to be considered. As nucleation of recrystallization is a very complex process, the nucleation rate is not expected to be a simple parameter. Early work indicated that the rate was not always constant during recrystallization as shown in figure 7.4.

However, such measurements need to be regarded with caution, particularly at the early stages of recrystallization, because the number of nuclei observed depends strongly on the technique used to detect them. For example in figure 7.4a are there really no nuclei present at times shorter than 1000 sec or were they just too small to be detected by optical microscopy? Is the initial rising nucleation rate shown in figure 7.4b a real effect or does it reflect the difficulty of detecting small nuclei, in which case perhaps this figure really represents a monotonically decreasing nucleation rate?

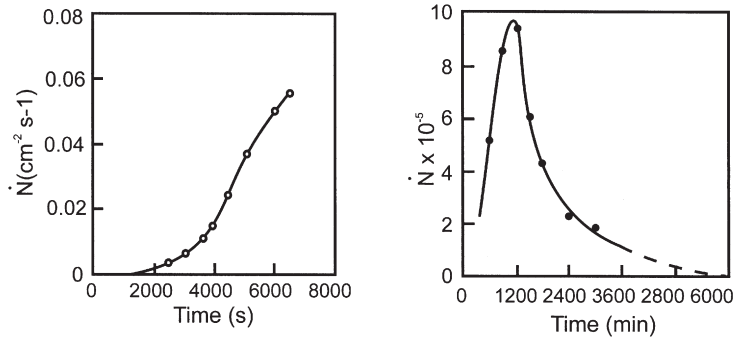

Fig. 7.4. The variation of nucleation rate **($\dot{N}$)** with time during the annealing of 5% deformed aluminium, annealed at 350°C. (a) Initial grain size 45 μm, (b) initial grain size 130 μm, (Anderson and Mehl 1945).

We must recognise that although formal models of the recrystallization kinetics (§7.3) usually refer to nucleation rates, these are often very difficult to measure experimentally. When we come to consider the mechanisms and sites of nucleation (§7.6), it will be clear that in most cases, it is not yet possible to obtain a realistic quantitative model for the number of nuclei and its variation with time and other parameters.

7.1.1.3 Growth

The growth of the new grains during recrystallization is more readily analysed than is their nucleation. It is generally accepted (§5.1.3) that the velocity (**v**) of a high angle grain boundary, which is also the growth rate **($\dot{G}$)** is given by

$$\mathbf{v} = \dot{\mathbf{G}} = \mathrm{MP} \tag{7.1}$$

where M is the boundary mobility and P is the net pressure on the boundary (§5.1.3).

Driving pressure – The driving pressure (P_d) for recrystallization is provided by the dislocation density (ρ), which results in a stored energy (E_D) given by equation 2.6. The resultant driving force for recrystallization is then given approximately as:

$$P_d = E_D = \alpha \rho G b^2 \tag{7.2}$$

where α is a constant of the order of 0.5.

For a dislocation density of 10^{15} m^{-2}, typical of a metal, and taking Gb^2 as 10^{-9} N, the driving pressure for primary recrystallization is of the order of 1MPa. If the dislocations are in the form of low angle boundaries, then, using equation 2.8, the driving pressure may be expressed in terms of subgrain size and misorientation.

Boundary curvature – If we consider a small, spherical, new grain of radius R, growing into the deformed structure, there is an opposing force which comes from the curvature of a high angle grain boundary of specific energy γ_b. The grain boundary area will be reduced and the energy lowered if the grain were to shrink, and there is thus a retarding pressure on the boundary given by the Gibbs-Thomson relationship:

$$P_c = \frac{2\gamma_b}{R} \tag{7.3}$$

This pressure is however only significant in the early stages of recrystallization when the new grains are small. For a grain boundary energy of 0.5 Jm^{-2} and the driving force discussed above, we find that P_c is equal to P_d when R is $\sim$1 μm. Below this grain size there would therefore be no net driving force for recrystallization. During the recrystallization of alloys, other retarding forces arising from solutes or second-phase particles may be important, and these will be discussed elsewhere.

The pressure on a grain boundary and therefore the boundary velocity, may not remain constant during recrystallization. In particular, as will be discussed later, the driving force may be lowered by concurrent recovery and both the driving force and the boundary mobility may vary through the specimen. Therefore the growth rate ($\dot{\mathbf{G}}$), which is an important parameter in any model of recrystallization is also a complex function of the material and the deformation and annealing conditions.

7.1.2 The laws of recrystallization

In this chapter we are primarily concerned with the principles of recrystallization, and although we will refer to selected work from the literature, no attempt will be made to present a detailed survey of the numerous experimental investigations which have been carried out over the past 50 years. Cotterill and Mould (1976) provide an extensive bibliography of the earlier work on a wide variety of materials.

In order to introduce the subject, it is of interest to recall one of the earliest attempts to rationalise the recrystallization behaviour of materials, viz the formulation of the so-called **laws of recrystallization** (Mehl 1948, Burke and Turnbull 1952). This series of qualitative statements, based on the results of a large body of experimental work, predicts the effects of the initial microstructure (grain size), and processing parameters (deformation strain and annealing temperature), on the time for recrystallization and on the grain size after recrystallization. These rules are obeyed in most cases and are easily rationalised if recrystallization is considered to be a nucleation and growth phenomenon, controlled by thermally activated processes, whose driving force is provided by the stored energy of deformation.

(i) A minimum deformation is needed to initiate recrystallization. The deformation must be sufficient to provide a nucleus for the recrystallization and to provide the necessary driving force to sustain its growth.

(ii) The temperature at which recrystallization occurs decreases as the time of anneal increases. This follows from the fact that the microscopic mechanisms controlling

recrystallization are thermally activated and the relationship between the recrystallization rate and the temperature is given by the Arrhenius equation.

(iii) **The temperature at which recrystallization occurs decreases as strain increases.** The stored energy, which provides the driving force for recrystallization, increases with strain. Both nucleation and growth are therefore more rapid or occur at a lower temperature in a more highly deformed material.

(iv) **The recrystallized grain size depends primarily on the amount of deformation, being smaller for large amounts of deformation.** The number of nuclei or the nucleation rate are more affected by strain than the growth rate. Therefore a higher strain will provide more nuclei per unit volume and hence a smaller final grain size.

(v) **For a given amount of deformation the recrystallization temperature will be increased by:**

A larger starting grain size. Grain boundaries are favoured sites for nucleation, therefore a large initial grain size provides fewer nucleation sites, the nucleation rate is lowered, and recrystallization is slower or occurs at higher temperatures.

A higher deformation temperature. At higher temperatures of deformation, more recovery occurs during the deformation (dynamic recovery), and the stored energy is thus lower than for a similar strain at a lower deformation temperature.

7.2 FACTORS AFFECTING THE RATE OF RECRYSTALLIZATION

When Burke and Turnbull (1952) reviewed the subject, they were able to rationalise a large body of experimental data into the comparatively simple concepts embodied in the above 'laws of recrystallization'. However, later research has shown that recrystallization is a much more complex process than was envisaged at that time, and in addition, we now know that it is difficult to extrapolate some of the earlier work, much of which was carried out on materials of high purity deformed to low strains by uniaxial deformation, to industrial alloys deformed to large strains. Although the laws of recrystallization still provide a very useful guide to the overall behaviour, we now recognise there are so many other important material and processing parameters that need to be taken into account that any attempt to understand recrystallization needs to address the phenomena at a much finer microstructural level than was possible 50 years ago.

In the following section, we will consider some of the important factors which are known to affect the rate at which recrystallization occurs in materials.

7.2.1 The deformed structure

7.2.1.1 The amount of strain

The amount, and to some extent the type of deformation, affect the rate of recrystallization, because the deformation alters the amount of stored energy and the

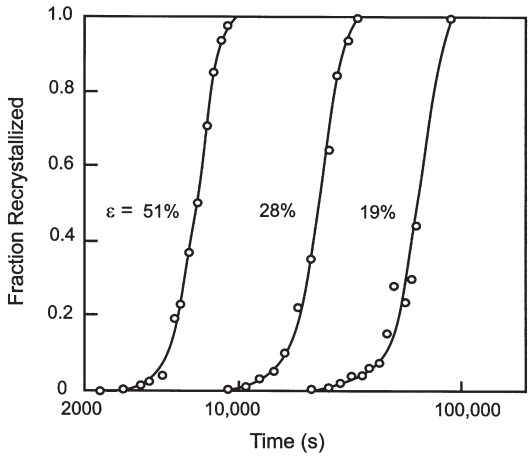

Fig. 7.5. The effect of tensile strain on the recrystallization kinetics of aluminium annealed at 350°C, (Anderson and Mehl 1945).

number of effective nuclei. As will be discussed in §7.6, the type of nucleation site may also be a function of strain. There is a minimum amount of strain, typically 1–3%, below which recrystallization will not occur. Above this strain the rate of recrystallization increases, levelling out to a maximum value at true strains of ~2–4. The effect of tensile strain on the recrystallization kinetics of aluminium is shown in figure 7.5.

7.2.1.2 The mode of deformation

The mode of deformation also affects the recrystallization rate. Single crystals deformed in single glide, recover on annealing, but may not recrystallize, because the dislocation structure (similar to that shown in fig. 6.7) does not contain the heterogeneities and orientation gradients needed to provide a nucleation site. The best examples of this effect are found in the hexagonal metals which deform by glide on the basal plane. For example Haase and Schmid (1925) showed that even after extensive plastic strain, crystals of zinc would recover their initial properties completely without recrystallization. At the other extreme, a metal which has undergone a deformation resulting in little or no overall shape change (i.e. most of the deformation is **redundant**) may nevertheless recrystallize readily. The effect of the deformation mode on recrystallization is complex. For example in both iron (Michalak and Hibbard 1957) and copper (Michalak and Hibbard 1961) it was found that straight rolling induces more rapid recrystallization than does cross rolling to the same reduction in thickness. Barto and Ebert (1971) deformed molybdenum to a true strain of 0.3 by tension, wire drawing, rolling and compression and found that the subsequent recrystallization rate was highest for the tensile deformed material and decreased in the above order for the other samples.

7.2.1.3 Strain path changes

In many metal working operations, the **strain path** is not constant, and may even be reversed. An example of this is in rolling, where shear deformation near the surface

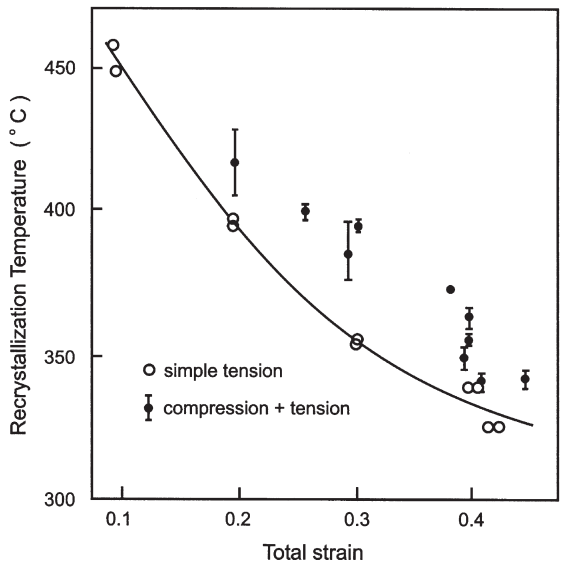

Fig. 7.6. The recrystallization temperature of copper as a function of the total applied strain in specimens deformed by tension or by a combination of tension and compression, (Lindh et al. 1993).

changes sign. Although the prime interest in strain path effects is their effect on formability, there is also interest in determining how such strain path effects influence the subsequent recrystallization behaviour.

Experiments to determine the role of strain path on the recrystallization of high purity copper have been reported by Lindh et al. (1993). They carried out tension and combined tension and compression experiments and measured the recrystallization temperature. For specimens deformed solely by tension, the recrystallization temperature decreased with increasing tensile strain (fig. 7.6) as would be expected. However, specimens deformed to the same **total permanent strain** ($\varepsilon_{\text{perm}}$) by tension and compression were found to recrystallize at higher temperatures. By reading across from the data points for the tension/compression samples to the curve for the tensile specimens of figure 7.6, an equivalent **recrystallization strain** ($\boldsymbol{\varepsilon}^{\mathbf{R}}_{\text{equ}}$) could be determined for the tensile/compression samples, and this was given by

$$\boldsymbol{\varepsilon}^{\mathbf{R}}_{\text{equ}} = \varepsilon_{\text{perm}} + \eta\varepsilon_{\text{red}} \tag{7.4}$$

where ε_{red} is the redundant strain and η a constant found to be 0.65. This shows that the redundant strain is only 0.65 times as effective in promoting recrystallization as is the permanent strain.

Embury et al. (1992) compared the recrystallization behaviour of cubes of pure aluminium deformed in uniaxial compression with similar specimens which were

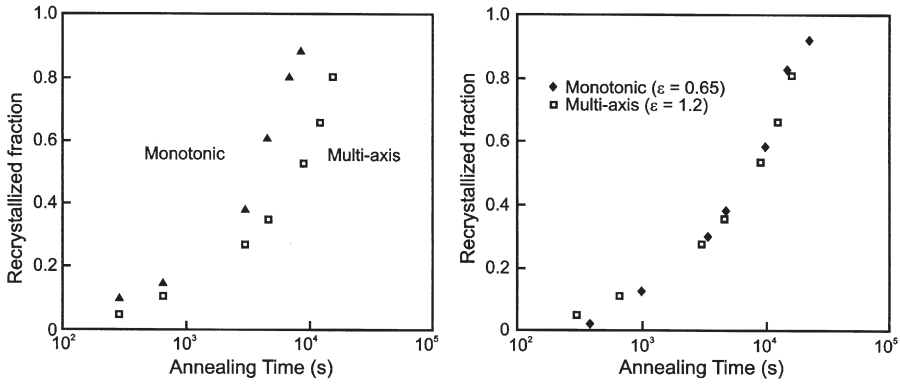

Fig. 7.7. The effect of redundant deformation on the recrystallization of pure aluminium. The recrystallization kinetics for specimens deformed monotonically are compared with those of specimens deformed by multi-axis compression. (a) Specimens deformed to the same equivalent strain (0.7), (b) specimens deformed to the same equivalent stress, (Embury et al. 1992).

deformed incrementally in different directions so as to produce no overall shape change. Their results (fig. 7.7a) show that for the same equivalent strain the specimens deformed by multi-axis compression recrystallized more slowly than the specimens deformed by monotonic compression, in agreement with the results of figure 7.6. However, if the specimens were deformed to the same level of **stress,** as shown in figure 7.7b, the recrystallization kinetics of the specimens were similar.

Zhu and Sellars (1997) investigated the effect of reversed uniaxial deformation on aluminium. They found similar effects on the recrystallization kinetics to those cited above, and also showed that the recrystallized grain size was much larger for a given total strain if the strain path involved tension and compression. They also investigated the effects of strain path change on the deformation microstructure, and found a lower dislocation density after strain reversal.

A simple interpretation of all these results is that the dislocation density and hence the flow stress are reduced on strain reversal. The lower driving pressure for recrystallization resulting in slower recrystallization and larger recrystallized grain sizes. However, a detailed explanation of the effect of deformation mode on recrystallization cannot be given, until the effects of redundant deformation on the microstructure are adequately understood.

A remarkable example of how a highly deformed microstructure can be 'undeformed' is found in the work of Farag et al. (1968). These authors found that the elongated grain structure produced in pure aluminium by a strain in torsion of 2.3 at 400°C could be returned to an equiaxed grain structure if an equal and opposite strain was subsequently given.

7.2.2 The grain orientations

7.2.2.1 Single crystals

As discussed in chapter 2, the microstructure and stored energy of a deformed grain depends strongly on the active slip systems and hence on its orientation. Therefore the initial orientation as well as the 'orientation path' during deformation, will affect both the nucleation sites and the driving force for recrystallization.

Hibbard and Tully (1961) measured the recrystallization kinetics of both copper and silicon-iron single crystals of various orientations, which had been cold rolled 80%, and found significant differences in rates of recrystallization as shown for silicon-iron in table 7.1.

Brown and Hatherly (1970) investigated the effect of orientation on the recrystallization kinetics of copper single crystals which had been rolled to a reduction of 98.6%. The recrystallization times on annealing at 300°C varied between 5 and 1000 min. These compared with a recrystallization time of 1 minute for a polycrystalline specimen deformed to the same strain. It was found, in agreement with the first two samples in table 7.1, that the recrystallization kinetics could not be clearly associated with the texture resulting from deformation. For example, both $\{110\}<112>$ and $\{110\}<001>$ crystals developed similar $\{110\}<112>$ rolling textures, but due to the differences in the nature of the deformed structure, the former recrystallized 50 times more slowly. Differences between the recrystallization kinetics and textures of the single crystals and the reference polycrystal in the above investigation, serve to highlight the importance of grain boundaries during recrystallization and show that care must be taken in using data from single crystal experiments to predict the behaviour of polycrystals.

The recent development of techniques such as EBSD which enable detailed characterisation of local orientations (appendix 2.1.4), has helped to clarify many issues concerning the recrystallization of single crystals, into which there has been considerable recent research (e.g. Driver 1995, Mohamed and Bacroix 2000, Driver et al. 2000, Godfrey et al. 2001). The general conclusions are in agreement with the earlier researches and show that the stored energy after deformation is strongly dependent on crystal orientation, and that this has a marked influence on the rate of recrystallization.

Table 7.1
Recrystallization of silicon–iron single crystals at 600°C (Hibbard and Tulley 1961).

Initial orientation	Final orientation	Time for 50% recrystallization (s)	Orientation after recrystallization
$\{111\}<112>$	$\{111\}<112>$	200	$\{110\}<001>$
$\{110\}<001>$	$\{111\}<112>$	1000	$\{110\}<001>$
$\{100\}<001>$	$\{001\}<210>$	7000	$\{001\}<210>$
$\{100\}<011>$	$\{100\}<011>$	No recrystallization	$\{100\}<011>$

7.2.2.2 Polycrystals

In polycrystalline materials there is evidence that the overall recrystallization rate may be dependent on both the starting texture and the final deformation texture. In iron, the orientation dependence of the stored energy after deformation has been determined (§2.2.3), and it has been predicted on this basis that the various texture components will recrystallize in the sequence shown in figure 7.8. Recent work (Hutchinson and Ryde 1995) has confirmed the trends shown in this figure. In aluminium alloys, Blade and Morris (1975) have shown that differences in the texture formed after hot rolling and annealing lead to differences in recrystallization kinetics when the material is subsequently cold rolled and annealed.

The observations of inhomogeneous recrystallization discussed in §7.4 provide further evidence of the variation of recrystallization rate for different components of the deformation texture.

7.2.2.3 The effect of boundary character on growth rate

The orientation relationships between deformed and recrystallizing grains may also have a strong effect on the growth rate during recrystallization. This is a consequence of the dependence of grain boundary mobility **(M)** on boundary character discussed in chapter 5, and it may be seen from equation 7.1, that this directly influences the growth rate.

Grain boundaries of high mobility will not only cause more rapid recrystallization, but may strongly influence the recrystallization texture. This effect, which is known as **oriented growth,** is discussed in detail in §12.3.2. It has been pointed out by Juul Jensen (1995b) that oriented growth effects may also result from low angle boundaries of low mobility, if recrystallizing grains encounter deformed regions of a similar orientation.

The important general conclusions to be drawn from this section are:

- **Recrystallization of different texture components** will occur at different rates, and will inevitably lead to inhomogeneous recrystallization (§7.4).
- **The strain path history** affects both the stored energy and the heterogeneities of the microstructure, and therefore apparently identical texture components may recrystallize quite differently. Without knowledge of the **starting texture, final**

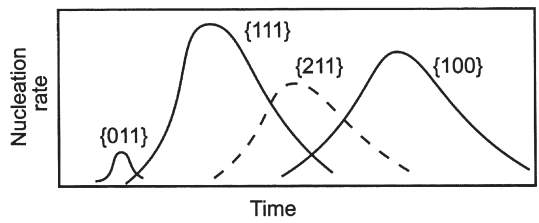

Fig. 7.8. Schematic representation of the proposed orientation dependence of the nucleation rate in deformed iron, (after Hutchinson 1974).

texture and the orientation path linking them, it may not be possible to predict the recrystallization behaviour of a particular component of the deformation texture.

- **The spatial distribution of orientations,** which affects the grain boundary character distribution, will influence both the initiation and growth of recrystallized grains.

7.2.3 The original grain size

It is generally found that a fine-grained material will recrystallize more rapidly than a coarse-grained material, as seen in figure 7.9.

There are several ways in which the initial grain size may be expected to affect the rate of recrystallization.

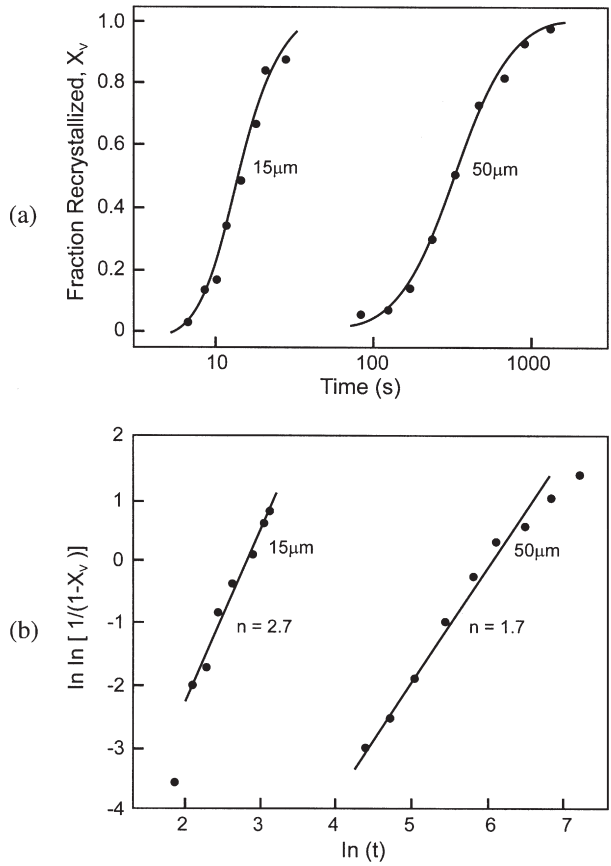

Fig. 7.9. The recrystallization kinetics at 225°C of copper of different initial grain sizes cold rolled 93%: (a) fraction recrystallized, (b) JMAK plot, (Hutchinson et al. 1989a).

- The stored energy of a metal deformed to low strains ($\varepsilon < 0.5$) tends to increase with a decrease in grain size (§2.2.2).
- Inhomogeneities such as deformation and shear bands are more readily formed in coarse-grained material (e.g. Hatherly 1982) and thus the number of these features, which are also sites for nucleation, increases with increasing grain size (§2.7.4 and §2.8.4).
- Grain boundaries are favoured nucleation sites (§7.6.4), and therefore the number of available nucleation sites is greater for a fine-grained material.
- The deformation texture and hence the recrystallization texture may be influenced by the initial grain size, and as discussed above, the recrystallization kinetics will then be affected by the grain orientations.

Evidence for all of these effects may be found in the literature, although it should be noted that in the investigation of Hutchinson et al. (1989a) shown in figure 7.9, where the growth rate of the grains in the fine-grained material was some 20 times faster than that of the coarse-grained material at the same temperature, the difference in kinetics was ascribed primarily to orientation effects.

7.2.4 Solutes

The usual effect of solutes is to hinder recrystallization (Dimitrov et al. 1978). Table 7.2 shows the effect of zone refining on the recrystallization temperatures of various metals after large rolling reductions. Although the amount and type of impurities in the commercial materials is not specified, and in some cases they may contain second-phase particles, the marked effect of purifying the metals is clearly seen.

The quantitative effect of a solute on the recrystallization behaviour is dependent on the specific solvent/solute pair. A good example of a very potent solute which has an important influence on commercial alloys is iron in aluminium. Figure 7.10 shows how very small concentrations of iron in solid solution in high purity aluminium may increase the recrystallization temperature by $\sim$100°C.

An extensive survey of the effect of transition element solutes on the recrystallization of iron has been carried out by Abrahamson and colleagues (e.g. Abrahamson and

Table 7.2
The effect of purity on the temperature of recrystallization (Dimitrov et al. 1978).

Metal	Recrystallization temperature (°C)	
	Commercial purity	Zone refined
Aluminium	200	−50
Copper	180	80
Iron	480	300
Nickel	600	300
Zirconium	450	170

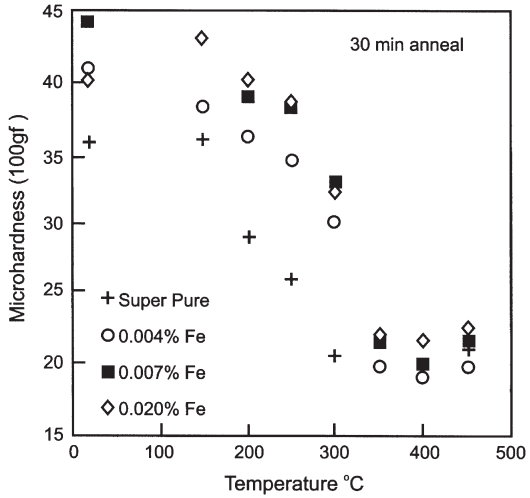

Fig. 7.10. The effect of trace amounts of iron in solid solution on the annealing response of aluminium deformed 80% by cold rolling, (Marshall and Ricks 1992).

Blakeny 1960). Although this work has indicated a correlation with the electron configuration of the solute, the effect remains unexplained.

Impurities may affect both the nucleation and growth of recrystallizing grains. It is difficult to measure or even define a **nucleation rate** for recrystallization, and the effect of impurities has not been quantified. Solutes may in some cases have a strong influence on the recovery processes which are an integral part of nucleation and which may affect the driving force for recrystallization. However, the majority of experimental work suggests that the main influence of solutes is on the grain boundary mobility (§5.3.3) and hence on the growth rate of recrystallizing grains (equation 7.1).

7.2.5 The deformation temperature and strain rate

At temperatures where thermally activated restoration processes such as dislocation climb occur during deformation, the microstructure will be dependent on the **deformation temperature** and **strain rate** in addition to the strain. After deformation at high temperatures and low strain rates, the stored energy will be reduced and recrystallization will occur less readily than after deformation to a similar strain at low temperature. These effects are considered in §13.6.

7.2.6 The annealing conditions

7.2.6.1 The annealing temperature

As may be seen from figure 7.11a, the annealing temperature has a profound effect on the recrystallization kinetics. If we consider the transformation as a whole and take the

time for 50% recrystallization ($t_{0.5}$) to be a measure of the rate of recrystallization, we might expect a relationship of the type:

$$\text{Rate} = \frac{1}{t_{0.5}} = C \exp\left(-\frac{Q}{kT}\right) \tag{7.5}$$

In figure 7.11b, we see that a plot of $\ln(t_{0.5})$ vs. 1/T gives a good straight line in accordance with equation 7.5, with a slope corresponding to an activation energy of 290 kJ/mol. Although such an analysis may be of practical use, an activation energy obtained from it is not easy to interpret, as it refers to the transformation as a whole,

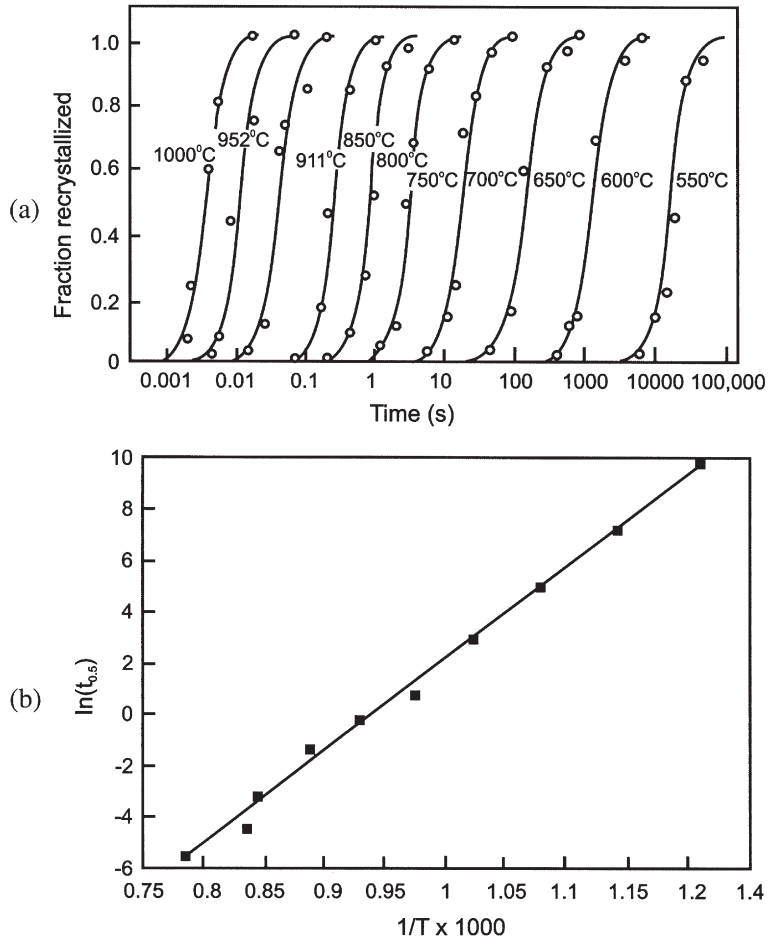

Fig. 7.11. (a) The effect of annealing temperature on the annealing of Fe-3.5%Si deformed 60%, (b) Arrhenius plot of the time for 50% recrystallization as a function of temperature, (data from Speich and Fisher 1966).

and is unlikely to be constant. For example such activation energies have been found to depend on strain (Gordon 1955) and to vary significantly with small changes in material purity. Vandermeer and Gordon (1963) found that an addition of only 0.0068 at% of copper to pure aluminium raised the activation energy for recrystallization from 60 to 120 kJ/mol.

An activation energy is only interpretable if it can be related to thermally activated processes at the atomic level. Consider the separate nucleation and growth processes which constitute recrystallization.

$$\dot{N} = C_1 \exp\left(-\frac{Q_N}{kT}\right) \tag{7.6}$$

$$\dot{G} = C_2 \exp\left(-\frac{Q_G}{kT}\right) \tag{7.7}$$

Although equation 7.7 has some validity because grain boundary migration rates are known to follow this type of relationship (§5.3.1), equation 7.6 is of little use because we have already noted that a constant nucleation rate is rarely found in practice. For example it was seen in §6.5 that the rate controlling process in recrystallization nucleation may be subgrain growth, in which case the activation energy for that process is the most relevant to nucleation.

7.2.6.2 The heating rate

The rate of heating of the specimen to the annealing temperature can also affect the rate of recrystallization. In order for this to occur, it is necessary for some other process to interact with recrystallization, and for this to have a different temperature dependence.

Consider the following two cases:

- **The heating rate affects the relative rates of recovery and recrystallization.**

If slow heating increases the amount of recovery occurring before recrystallization, the driving pressure will be reduced and recrystallization retarded. Although this effect is frequently cited in the literature, there is no experimental evidence to support it for single-phase alloys. Recovery would be enhanced at low heating rates only if it had a lower activation energy than recrystallization. In most alloys, the rates of both processes are controlled by lattice diffusion and have similar temperature dependencies; therefore heating rate is not predicted to affect one more than the other. In a very pure metal where HAGB migration is controlled by boundary diffusion (§5.3) and recovery by lattice diffusion, it would be expected that a low heating rate would in fact promote recrystallization, although this has not been reported.

- **Phase transformations can occur.**

Precipitation reactions have a different temperature dependence to recrystallization. If a supersaturated solid solution is deformed and annealed at a low heating rate, precipitation may occur before recrystallization and hinder it, whereas on rapid heating, recrystallization may be completed before any precipitation occurs. This effect, which is discussed in more detail in §9.8, may influence the rate of recrystallization in industrial

alloys, where it is often found that a rapid heating rate accelerates recrystallization and results in a smaller grain size, e.g. Al-Li alloys (Bowen 1990) and Al–Zn–Mg alloys (Wert et al. 1981).

Conversely, it is found that in steels, rapid heating may slow down recrystallization (Ushioda et al. 1989). In this case the heating rate determines the amount of carbon in solid solution, and this in turn affects the recrystallization (§15.3).

7.3 THE FORMAL KINETICS OF PRIMARY RECRYSTALLIZATION

7.3.1 The Johnson–Mehl–Avrami–Kolmogorov (JMAK) model

The type of curve shown in figure 7.3 is typical of many transformation reactions, and may be described phenomenologically in terms of the constituent nucleation and growth processes. The early work in this area is due to Kolmogorov (1937), Johnson and Mehl (1939) and Avrami (1939) and is commonly known as the JMAK model. A more general discussion of the theory of the kinetics of transformations may be found in the phase transformation literature, e.g. Christian (2002).

7.3.1.1 Theory

It is assumed that nuclei are formed at a rate $\dot{\mathbf{N}}$ and that grains grow into the deformed material at a linear rate $\dot{\mathbf{G}}$. If the grains are spherical, their volume varies as the cube of their diameter, and the fraction of recrystallized material $(\mathbf{X_V})$ rises rapidly with time. However, the new grains will eventually impinge on each other and the rate of recrystallization will then decrease, tending to zero as X_V approaches 1.

The number of nuclei **(dN)** actually appearing in a time interval **(dt)** is less than $\dot{\mathbf{N}}\mathbf{dt}$ because nuclei cannot form in those parts of the specimen which have already recrystallized. The number of nuclei which would have appeared in the recrystallized volume is $\dot{\mathbf{N}}\mathbf{X_V}\,\mathbf{dt}$ and therefore the total number of nuclei $(\mathbf{dN'})$ which would have formed, including the 'phantom' nuclei is given by:

$$dN' = \dot{N}dt = dN + \dot{N}X_V\,dt \tag{7.8}$$

If the volume of a recrystallizing grain is **V** at time **t,** then the fraction of material which would have recrystallized if the phantom nuclei were real $(\mathbf{X_{VEX}})$ is known as the **extended volume** and is given by:

$$X_{VEX} = \int_0^t V dN' \tag{7.9}$$

If the incubation time is much less than **t,** then

$$V = f\dot{G}^3 t^3 \tag{7.10}$$

where **f** is a shape factor ($4\pi/3$ for spheres). Thus

$$X_{VEX} = fG^3 \int_0^t t^3 \dot{N}\, dt \tag{7.11}$$

If $\dot{\mathbf{N}}$ is constant then

$$X_{VEX} = \frac{f\dot{N}\dot{G}^3 t^4}{4} \tag{7.12}$$

During a time interval **dt,** the extended volume increases by an amount $\mathbf{dX_{VEX}}$**.** As the fraction of unrecrystallized material is $1 - X_V$, it follows that $\mathbf{dX_{VEX}} = (1 - X_V)\,\mathbf{dX_{VEX}}$**,** or

$$dX_{VEX} = \frac{dX_V}{1 - X_V} \tag{7.13}$$

$$X = \int_0^{X_V} dX_{VEX} = \int_0^{X_V} \frac{dX_V}{1 - X_V} = \ln \frac{1}{1 - X_V} \tag{7.14}$$

$$X_V = 1 - \exp(-X_{VEX}) \tag{7.15}$$

Combining equations 7.12 and 7.15

$$X_V = 1 - \exp\left(\frac{-f\dot{N}\dot{G}^3 t^4}{4}\right) \tag{7.16}$$

This may be written more generally in the form

$$X_V = 1 - \exp(-Bt^n) \tag{7.17}$$

where $B = f\dot{N}\dot{G}^3/4$, which is often called the **Avrami, Johnson–Mehl or JMAK equation.**

In the case considered above, in which the growing grains were assumed to grow in three dimensions, the exponent **n** in equation 7.17, which we will refer to as the **JMAK or Avrami exponent** is seen from equation 7.16 to be **4.** The above treatment assumed that the rates of nucleation and growth remained constant during recrystallization. Avrami (1939) also considered the case in which the nucleation rate was not constant, but a decreasing function of time, $\dot{\mathbf{N}}$ having a simple power law dependence on time. In this situation **n** lies between 3 and 4, depending on the exact form of the function.

Two limiting cases are of importance, that already discussed in which $\dot{\mathbf{N}}$ is constant and **n = 4,** and that where the nucleation rate decreases so rapidly that all nucleation events effectively occur at the start of recrystallization. This is termed **site saturated nucleation.**

Table 7.3
Ideal JMAK exponents.

Growth dimensionality	Site saturation	Constant nucleation rate
3-D	3	4
2-D	2	3
1-D	1	2

In this case, $\mathbf{X_{VEX}}$ in equation 7.12 is given by $\mathbf{f N(\dot{G}t)^3}$ where **N** is the number of nuclei. This may be seen to give a JMAK exponent of **3** in equation 7.17.

The above analyses assume that until impingement, the grains grow isotropically in three-dimensions. If the grains are constrained either by the sample geometry or by some internal microstructural constraint to grow only in one or two-dimensions, then the JMAK exponent is lower as shown in table 7.3.

Cahn (1956) has extended the theory to include nucleation at random sites on grain boundaries and found that **n** fell from 4 at the start of the transformation to 1 at the end. However, no general analytical treatment of non-randomly distributed nucleation sites is available.

It should be noted that the essential feature of the JMAK approach is that the nucleation sites are assumed to be randomly distributed.

7.3.1.2 Comparison with experiment

Experimental measurements of recrystallization kinetics are usually compared with the JMAK model by plotting $\mathbf{\ln[\ln\{1/(1-X_V)\}]}$ against **ln t.** According to equation 7.17, this should yield a straight line of slope equal to the exponent **n.** This method of data representation is termed a **JMAK plot.** It should incidentally be noted that equation 7.14 shows that this is equivalent to a plot of $\mathbf{\ln X_{VEX}}$ against **ln t.**

The growth rate is not easily determined from measurements of X_V. However, if the interfacial area between recrystallized and unrecrystallized material per unit volume (S_V) is measured as a function of time, then Cahn and Hagel (1960) showed that the global growth rate $\dot{\mathbf{G}}$ is given by

$$\dot{\mathbf{G}} = \frac{1}{S_V}\frac{dX_V}{dt} \tag{7.18}$$

There are a number of early experimental investigations of recrystallization in which JMAK kinetics were found with $n \sim 4$. These include the work of Anderson and Mehl (1945) on aluminium, Reiter (1952) on low carbon steel and Gordon (1955) on copper. All these investigations were for fine-grained material deformed small amounts in tension. As pointed out by Doherty et al. (1986), in such conditions an increase in grain size on recrystallization is to be expected, with less than one successful nucleus arising

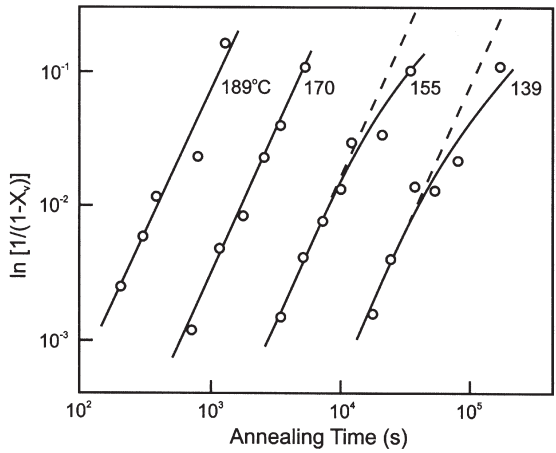

Fig. 7.12. JMAK plot of the recrystallization kinetics of aluminium containing 0.0068 at.% Cu, deformed 40% by rolling, (Vandermeer and Gordon 1962).

from each old grain. Therefore the overall spatial distribution of these nuclei is likely to approach random (fig. 7.14a), thus fulfilling the conditions for JMAK kinetics. Figure 7.9b shows that the recrystallization behaviour of fine-grained copper is consistent with JMAK kinetics, whilst the logarithmic plot for the coarse-grained material demonstrates a strong negative deviation at long times.

It is in fact very unusual to find experimental data which, on detailed analysis, show good agreement with JMAK kinetics. Either the JMAK plot is non-linear, or the slope of the JMAK plot is less than 3, or both. A very clear example is the work of Vandermeer and Gordon (1962) on 40% cold rolled aluminium containing small amounts of copper, shown in figure 7.12. The JMAK slopes were found to be 1.7, and the data at the two lower annealing temperatures are seen to fall below the straight line at long annealing times. There are numerous investigation of aluminium and of other materials in which values of **n** of the order of 1 have been found. These include copper (Hansen et al. 1981) and iron (Michalak and Hibbard 1961, Rosen et al. 1964).

It is therefore concluded that the JMAK analysis discussed above is too simple to quantitatively model a process as complex as recrystallization. In particular, the change in microstructure during recrystallization needs to be described by more parameters than the fraction of material transformed (X_V or X_{VEX}).

7.3.2 Microstructural path methodology

A significant attempt to improve the JMAK approach was made by Vandermeer and Rath (1989a) using what they termed **Microstructural path methodology (MPM).** In this approach, more realistic and more complex geometric models are employed by using additional microstructural parameters in the analysis and, if required, relaxing the uniform grain impingement constraint.

As for the JMAK model, it is convenient to use the concept of **extended volume** (X_{VEX}) whose relation to the recrystallized fraction (X_V) is given by equation 7.15. In addition, the microstructure is characterised by the **interfacial area** per unit volume between recrystallized and unrecrystallized material (S_V) and this is related to the extended interfacial area (S_{VEX}) by the relationship (Gokhale and DeHoff 1985).

$$S_{VEX} = \frac{S_V}{1 - X_V} \tag{7.19}$$

As before, this relationship is valid only for randomly distributed recrystallized grains.

The growth of individual recrystallizing grains may be written in integral form

$$X_{VEX} = \int_0^t V_{(t-\tau)} \dot{N}_{(\tau)} \, dt \tag{7.20}$$

$$S_{VEX} = \int_0^t S_{(t-\tau)} \dot{N}_{(\tau)} \, dt \tag{7.21}$$

where $V_{(t-\tau)}$ and $S_{(t-\tau)}$ are the volume and interfacial area respectively at time **t**, of a grain which was nucleated at time τ.

If it is assumed that the grains are spheroids which do not change shape, then the volume and interfacial area of a grain are

$$V_{(t-\tau)} = K_V \, . \, a^3_{(t-\tau)} \tag{7.22}$$

$$S_{(t-\tau)} = K_S \, . \, a^2_{(t-\tau)} \tag{7.23}$$

where **a** is the major semi-axis of the spheroid and K_V and K_S are shape factors. The radius function $a_{(t-\tau)}$ is related to the interface migration rate G(t) by

$$a_{(t-\tau)} = \int_\tau^t G(t) \, dt \tag{7.24}$$

Whereas X_{VEX} and S_{VEX} are global microstructural parameters which may be measured metallographically, $a_{(t-\tau)}$ is a local property, and may be estimated by measuring the diameter of the largest unimpinged grain intercept (D_L) on a plane polished surface. If it can be assumed that this is the diameter of the earliest nucleated grain, then $a_{(t-\tau)} = D_L/2$.

Vandermeer and Rath (1989a), using the method of Gokhale and DeHoff (1985) have shown that the nucleation and growth characteristics of the recrystallizing material are contained in the time dependence of equations 7.20 and 7.21, and have demonstrated how these equations may be evaluated to extract the **nucleation rate, growth rate,** and **size** of the recrystallizing grains. The method involves inverting the equations, based on the mathematics of Laplace transforms.

For isothermal annealing, it is assumed that the time dependence of X_{VEX}, S_{VEX} and D_L may be represented by power law functions of the form

$$X_{VEX} = Bt^n \tag{7.25}$$

$$S_{VEX} = Kt^m \tag{7.26}$$

$$D_L = St^s \tag{7.27}$$

It is also postulated that the derived functions can be represented by power law functions, thus

$$\dot{\mathbf{N}}_{(\tau)} = N_l \tau^{\delta-1} \tag{7.28}$$

$$a_{(t-\tau)} = G_a (t-\tau)^r \tag{7.29}$$

where N_l, G_a δ and **r** are constants.

If the shapes of the grains remain spheroidal during growth then $a_{(t)} = D_L/2$ and hence $\mathbf{r} = \mathbf{s}$ and $G_a = S/2$.

Vandermeer and Rath show that for spheroidal grains which retain their shape during growth

$$\delta = 3m - 2n \tag{7.30}$$

$$r = s = n - m \tag{7.31}$$

Reference to equations 7.25–7.29 shows that:

$\delta = 1$ corresponds to a constant nucleation rate
$\delta = 0$ to site saturated nucleation
$r = s = 1$ corresponds to a constant growth rate.

Therefore, by measuring X_V, S_V and D_L experimentally as a function of annealing time, **n, m** and **s** may be determined, δ and **r** calculated and the form of the nucleation kinetics identified.

If the simple JMAK model discussed above applies, then, for constant nucleation and growth rates we would obtain $n = 4$, $m = 3$, $s = 1$ and hence $\delta = 1$ and $r = 1$.

Figure 7.13, from the work of Vandermeer and Rath shows data for the recrystallization of a deformed iron crystal plotted to give n, m and s from the slopes of the lines in figures 7.13a, b, c respectively. The data have been normalised using an Arrhenius relationship so as to include results obtained at several temperatures. The values obtained are $n = 1.90$, $m = 1.28$, $s = 0.60$, which give $\delta = 0.04$ and $r = 0.62$. As δ is almost zero, it is concluded that nucleation is effectively site saturated, and as $r \sim s$ it is concluded that the grains grow as spheroids. The low value of **r** indicates a growth rate decreasing with time.

If $s \neq r$ then the grain shape is changing during recrystallization, and further information about the shapes of the grains may be extracted (Vandermeer and Rath 1990).

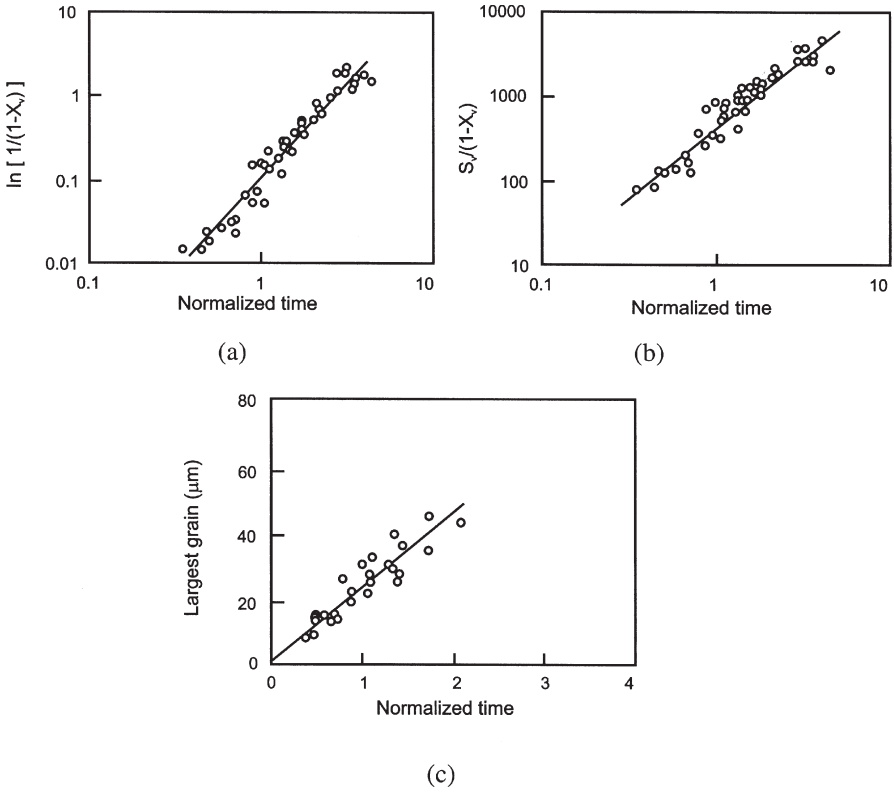

Fig. 7.13. Annealing kinetics of an iron crystal deformed 70% and annealed at various temperatures. By normalising the time axis by means of an Arrhenius relationship, data from a range of annealing temperatures are found to fall on a common curve. (a) Variation of X_V, (b) variation of S_V, (c) variation of largest recrystallized grain diameter, (Vandermeer and Rath 1989a).

The model has also been extended to include the effects of recovery during the recrystallization anneal (Vandermeer and Rath 1989b).

Microstructural path methodology allows more detailed information about nucleation and growth rates to be extracted from experimental measurements than does the original JMAK analysis, and is a very useful tool in determining whether or not nucleation is site-saturated (e.g. Vandermeer and Juul Jensen 2001). However, it should be noted that whilst the MPM approach is more flexible than the JMAK model, it is still based on the assumption that the spatial distribution of nuclei is random and that growth rates are global rather than local parameters.

From the above discussion of the JMAK and MPM models it is clear that the two factors most likely to cause problems in realistic modelling of recrystallization kinetics

are **inhomogeneous recrystallization** and **concurrent recovery,** and these are considered in the next section.

7.4 RECRYSTALLIZATION KINETICS IN REAL MATERIALS

7.4.1 Non-random spatial distribution of nuclei

It is widely recognised that the nucleation sites in recrystallization are non-randomly distributed. However, the analytical treatments of kinetics discussed above are unable to satisfactorily take this into account.

Evidence for non-random site distribution is found for all materials, particularly those with a large initial grain size, and examples include **iron** (Rosen et al. 1964), **copper** (Hutchinson et al. 1989a), **brass** (Carmichael et al. 1982) and **aluminium** (Hjelen et al. 1991, Somerday and Humphreys 2003b).

On the scale of a single grain, nucleation of recrystallization is inhomogeneous as is discussed in more detail in §7.6. Nucleation occurs at preferred sites such as prior grain boundaries, at transition bands, and shear bands. At lower strains, fewer of these deformation heterogeneities are formed and fewer of those formed act as nucleation sites. Whether or not these small-scale inhomogeneities lead to an overall inhomogeneous distribution of nuclei will depend on the number of nuclei relative to the number of potential sites, as shown schematically in figure 7.14. If nucleation only occurs at grain boundaries, then a given number of nuclei in a fine-grained material (fig. 7.14a) will lead to more homogeneous recrystallization than the same number in a coarse-grained material (fig. 7.14b). The limiting case is that of single crystals in which recrystallization nucleation is rarely randomly distributed (e.g. Driver 1995, Mohamed and Bacroix 2000, Driver et al. 2000, Godfrey et al. 2001).

On a larger scale, it is also found, that not all grains in a material recrystallize at a similar rate, and it is this larger-scale heterogeneity that is frequently the main cause of

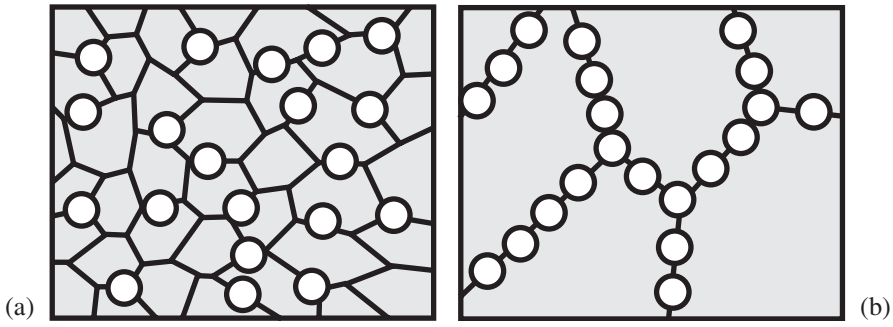

Fig. 7.14. Schematic representation of the effect of the initial grain size on the heterogeneity of nucleation. (a) Small initial grain size, (b) large initial grain size.

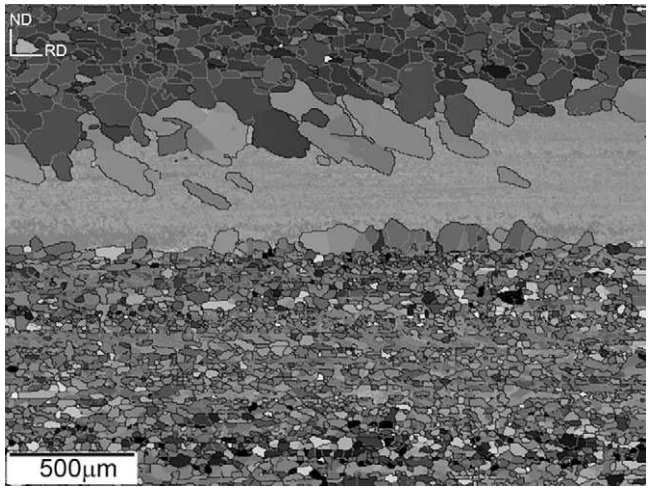

Fig. 7.15. EBSD map of a cold rolled single-phase, coarse-grained Al-0.05 wt%Mn alloy which has been partially recrystallized. The area originally contained three deformed grains. The upper and lower grains have recrystallized to different grain sizes, whilst no recrystallization has occurred in the central (Goss-oriented) grain. The colours represent the orientations within the sample, (Somerday and Humphreys 2003b). (See colour plate section.)

inhomogeneous recrystallization. This effect arises from the orientation differences between grains. As discussed in chapter 2, the slip systems and strain path which operate during deformation are dependent on crystallographic orientation. Thus the distribution and density of dislocations and of larger scale microstructural inhomogeneities is orientation dependent. Therefore the availability and viability of nucleation sites and also the growth rate of the recrystallizing grains depends strongly on orientation.

Fcc crystals of the $\{110\}<001>$ Goss orientation deformed in plane strain compression are an extreme example. In these materials no deformation heterogeneities form and no recrystallization is nucleated (Ferry and Humphreys 1996a). Goss-oriented grains in a deformed fcc polycrystal are also slow to recrystallize, and figure 7.15 shows an EBSD map of a deformed large-grained single-phase aluminium alloy which has partially recrystallized on annealing. The area of the sample originally comprised three grains, whose boundaries were aligned in the rolling direction (RD). The lower grain has recrystallized to a grain size of $\sim$15 μm and the upper grain has recrystallized to a grain size of $\sim$30 μm. No recrystallization has originated in the central Goss-oriented grain, but some large ($\sim$100 μm) grains from the upper and lower grains are growing into the Goss grain.

An extreme example of inhomogeneous recrystallization is found in low zinc α-brass (Carmichael et al. 1982) in which, depending on their initial orientation, grains may deform either by reasonably uniform slip or by deformation twinning and shear banding. On annealing, the latter grains recrystallize first and are often completely recrystallized before the former have started to recrystallize as shown in figure 7.16b.

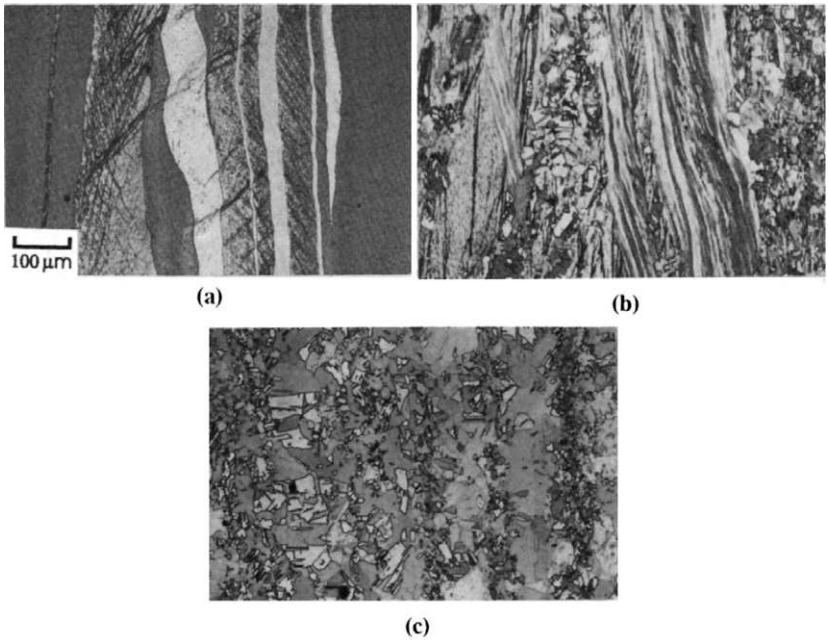

Fig. 7.16. Inhomogeneous recrystallization in 95:5 brass cold rolled 75% and annealed, (TD section with rolling direction vertical); (a) as deformed, (b) 6 min at 250°C, (c) 24 hr at 250°C, (Carmichael et al. 1982).

In alloys containing large second-phase particles which stimulate the nucleation of recrystallization (§9.3.4), clustering of the particles may, for similar reasons, lead to macroscopically inhomogeneous recrystallization.

7.4.2 The variation of growth rate during recrystallization

7.4.2.1 Experimental observations

There is considerable evidence that the growth rate **($\dot{G}$)** is not a constant, and therefore a realistic treatment of recrystallization kinetics must allow for the variation of $\dot{G}$ in both space and time. Although there may be some variation of the boundary mobility **(M)** during recrystallization, for example through an orientation dependence of mobility (§5.3.2), the main reason for such changes in growth rate is thought to be variations in the **driving pressure.** The driving pressure may vary through the material due to microstructural inhomogeneity and may also decrease with time due to recovery occurring concurrently with recrystallization. It is now thought that in many cases **both** these effects occur, making the interpretation or prediction of growth rates very difficult.

There have been several detailed measurements of grain boundary velocities during recrystallization, including those on **aluminium** (Vandermeer and Gordon 1959, Furu

and Nes 1992), **iron** (Leslie et al. 1963, English and Backofen 1964, Speich and Fisher 1966, Vandermeer and Rath 1989a) and **titanium** (Rath et al. 1979). The growth rates were usually determined either by measurement of the size of the largest growing grain, or by the Cahn–Hagel analysis (equation 7.18). In all these investigations the growth rates were found to decrease significantly with annealing time.

Various equations have been used to express the variation of $\dot{\mathbf{G}}$ with time such as

$$\dot{\mathbf{G}} = \frac{\mathrm{A}}{1 + \mathrm{Bt}^{\mathrm{r}}} \tag{7.32}$$

which, at long times reduces to

$$\dot{\mathbf{G}} = \mathrm{Ct}^{-\mathrm{r}} \tag{7.33}$$

In several cases **r** has been found to be close to 1, although in their investigation of the recrystallization kinetics of iron, Vandermeer and Rath (1989a) found $\mathrm{r} = 0.38$.

The basic JMAK model of §7.3.1 assumes a constant growth rate, and the following analysis illustrates the effect of recovery on the growth rate and on the kinetics of recrystallization. More detailed treatments are discussed by Furu et al. (1990).

If we allow $\dot{\mathbf{G}}$ to vary, then for site-saturated nucleation with **N** nuclei, equation 7.16 becomes

$$\mathrm{X_v} = 1 - \exp\left[-\mathrm{f\,N}\left(\int_0^{\mathrm{t}} \dot{\mathbf{G}}\mathbf{dt}\right)^3\right] \tag{7.34}$$

If the variation of growth rate with time is as given by equation 7.33, then combining equations 7.33 and 7.34 we find

$$\mathrm{X_v} = 1 - \exp\left[-\mathrm{f\,N}\left(\mathrm{C}\frac{\mathrm{t}^{(1-\mathrm{r})}}{(1-\mathrm{r})}\right)^3\right] \tag{7.35}$$

The JMAK plots for the recrystallization kinetics given by equation 7.35 are shown in figure 7.17 for various values of **r.**

Note that as the growth rate is increasingly slowed (increasing **r**), the JMAK plot remains a straight line. However the slope decreases and, from equation 7.35 is equal to $3(1-\mathrm{r})$.

7.4.2.2 The role of recovery

Until recently, a decreasing growth rate during recrystallization or a non-linear JMAK plot was thought to be due entirely to the effects of recovery on the driving force for recrystallization. The classic early work in this field is that of Vandermeer and Gordon

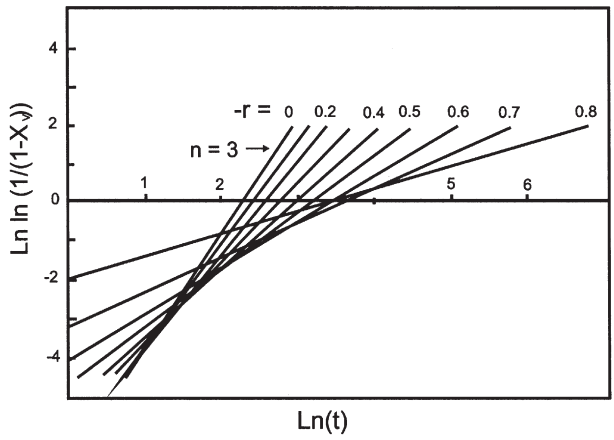

Fig. 7.17. The predicted effect of the recovery parameter **r** in equation 7.35 on the JMAK plot for recrystallization under conditions of site saturated nucleation.

(1962) who carried out an extensive metallographic and calorimetric study of the recrystallization of aluminium alloys containing small amounts of copper. In this work the low JMAK slopes and the deviation of these plots from linearity at long times (fig. 7.12) were attributed to recovery. However, it is now thought that in many cases, factors other than recovery may be more important.

Consider the measurements of the softening during annealing of cold worked copper and aluminium shown in figure 7.18. For the case of copper (fig. 7.18a) there is no softening prior to that due to recrystallization, but for aluminium (fig. 7.18b), there is extensive prior softening, and these observations are consistent with our knowledge of recovery in these materials. Although we may expect some recovery during the recrystallization of aluminium which will lower the driving force, it is unlikely that there will be significant recovery in copper, or other metals of medium to low stacking fault energy. In such materials, recovery is not a likely explanation for the low JMAK exponents, nor the non-linearity of the JMAK plots at longer times, such as shown in figure 7.9b.

We must now question the role of recovery in affecting recrystallization even in those materials for which recovery is known to occur readily.

Would uniform recovery explain the observed JMAK plots?
As discussed in chapter 6, recovery lowers the driving pressure (P) for recrystallization and is therefore expected to reduce $\dot{\mathbf{G}}$ according to equation 7.1. Although our knowledge of recovery kinetics is far from complete, the available evidence suggests that recovery processes are broadly consistent with the kinetics of growth rate reduction as given by equations 7.32 and 7.33. For example a JMAK slope of 2, which is commonly observed experimentally, implies a not unreasonable value of $r = 0.33$ in equation 7.33. However, recovery on the model discussed above or on the model of Furu et al. (1990), leads to linear JMAK plots and would therefore not explain the frequent observation of non-linearity such as shown in figure 7.12.

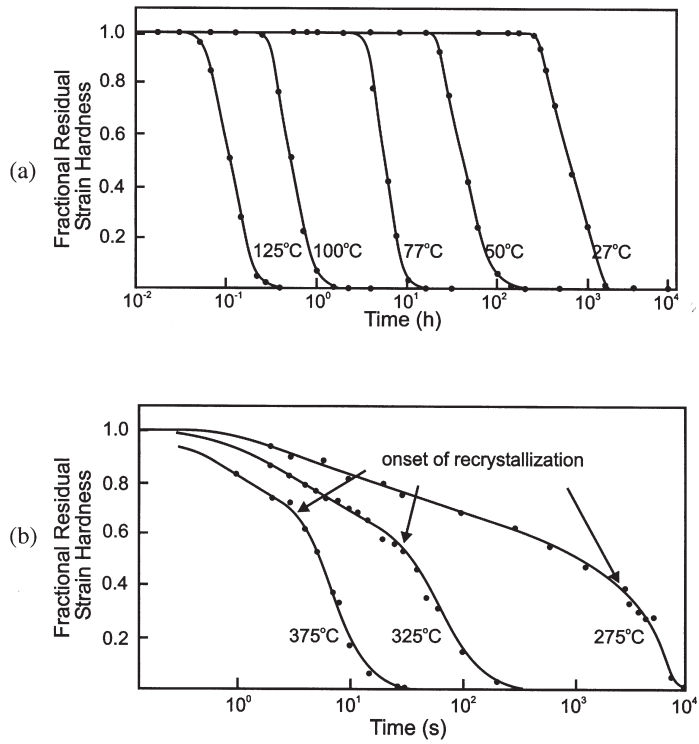

Fig. 7.18. The variation of the fractional residual strain hardening during annealing for (a) cold worked copper (Cook, and Richards 1946) and (b) commercial purity aluminium, (Furu et al. 1990).

Is the temperature dependence of $\dot{G}$ consistent with recovery?

In their investigation of the recrystallization kinetics of iron, Vandermeer and Rath (1989a) found that data over a wide range of annealing temperatures could be fitted to equation 7.33 if the data were normalised to take account of the temperature dependence of the growth rate (fig. 7.13c). If this decrease in growth rate were due to recovery, then it would fit equation 7.33 over the whole temperature range only if the activation energies for recovery and high angle grain boundary migration were equal. As discussed in §7.2.6.2, this is probable, with both processes being controlled by lattice diffusion, although it would also be consistent with the microstructural inhomogeneity discussed in the following section.

Is the amount of recovery sufficient to explain the recrystallization kinetics?

Several investigations (e.g. Perryman (1955) on aluminium and Rosen et al. (1964) on iron), have indicated that prior recovery treatment has little effect on recrystallization. In figure 7.19, the JMAK plots for iron which had been recovered at various temperatures before recrystallization, show that prior recovery has had little effect on the recrystallization kinetics.

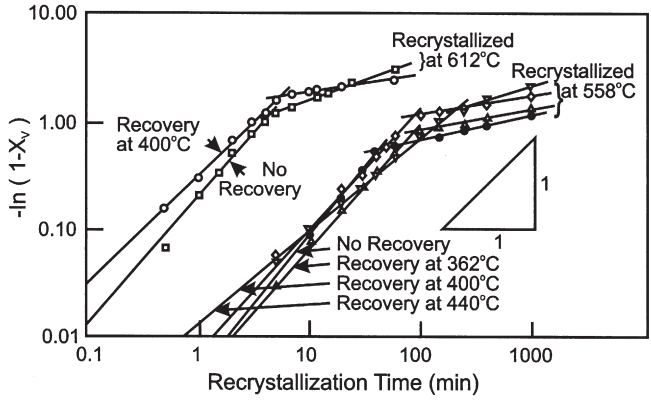

Fig. 7.19. The effect of recovery on the recrystallization of iron, (Rosen et al. 1964).

More recent experimental measurements of both the extent of recovery and the growth rate of recrystallization in aluminium (Furu and Nes 1992) have shown that the amount of uniform recovery is relatively small (20% at $X_V = 0.1$) and is not in itself sufficient to account for the observed decrease of the growth rate.

It is therefore likely that factors other than recovery are contributing to the decrease in growth rate at long annealing times.

7.4.2.3 The role of microstructural inhomogeneity

The nature of the deformation microstructure (§2.4) gives rise not only to the inhomogeneous distribution of recrystallization nuclei discussed in §7.4.1, but also to the variations in stored energy which are responsible for inhomogeneous growth rates.

Hutchinson et al. (1989a) investigated inhomogeneous recrystallization in cold rolled OFHC copper. They measured the release of stored energy during the recrystallization, and found that it was not proportional to the fraction recrystallized, and that the regions of high stored energy recrystallized first (fig. 7.20a). The measured growth rate of the recrystallizing grains decreased with time, and they were able to show that this was due entirely to the inhomogeneity of the stored energy distribution. As shown in figure 7.20b, the mean growth rate was found to be proportional to the true driving force, which was calculated from the calorimetric measurements. The recrystallization kinetics from this work, shown in figure 7.9b, indicate that although the fine-grained material gave a linear JMAK plot with a slope of 2.7, the coarse-grained material, in which the recrystallization was more inhomogeneous had a significantly lower slope of 1.7 and the data fell well below the straight line plot during the later stages of recrystallization.

Earlier work on aluminium (Vandermeer and Gordon 1962), also showed that the amount of heat evolved per unit volume recrystallized, decreased as recrystallization proceeded. Although this was interpreted as being due to recovery, it is quite possible

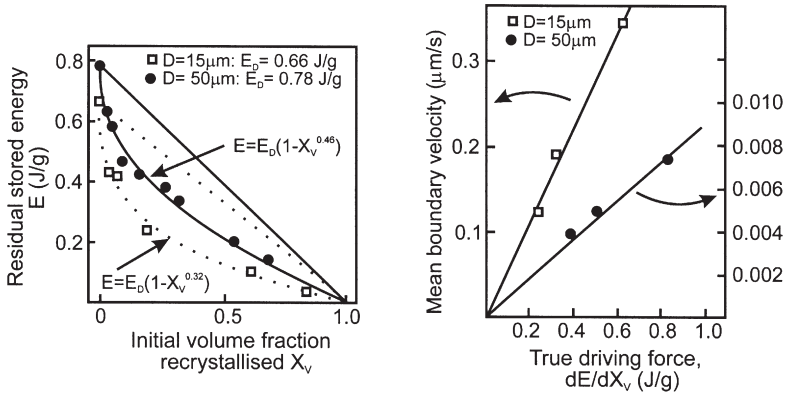

(a) (b)

Fig. 7.20. The effect of the inhomogeneous distribution of stored energy on the recrystallization of the copper specimens whose kinetics are shown in figure 7.9. (a) Correlation of the residual stored energy and the volume fraction recrystallized shows that a large part of the stored energy is released during the early stages of recrystallization, (b) correlation of the growth rate and the rate of decrease of stored energy shows the boundary velocity to be approximately proportional to the driving force, (Ryde et al. 1990).

that these results could also be explained at least in part, by an inhomogeneous distribution of stored energy.

As deformation microstructures are very varied and not well understood, it is difficult to give a general treatment of recrystallization in inhomogeneous microstructures, although specific cases have been modelled analytically by Vandermeer and Rath (1989b) and Furu et al. (1990).

In figure 7.21 we schematically illustrate one possible case. In figure 7.21a, spherical regions of high stored energy (dark shaded) are present in the deformed microstructure. These might for example, correspond to the highly deformed regions associated with large second-phase particles (§2.9.4). If recrystallization nucleates predominantly in or close to these regions then growth will be initially rapid, but will decrease when these regions of high stored energy are consumed (fig. 7.21b). In this case the heterogeneity is **local** and if the stored energy within these regions can be calculated, the growth rate and hence the recrystallization kinetics may be modelled analytically (Furu et al. 1990) on the basis of equation 7.34. Vandermeer and Juul Jensen (2001) interpreted the two-stage growth kinetics observed during recrystallization of an aluminium alloy in which nucleation occurred at large second-phase particles (see §9.3) in terms of such a model.

However, if few nuclei are formed, for example after low strains (fig. 7.21c), then growing grains will experience a driving force which is an average of the high and low energy regions and which will not vary during the recrystallization.

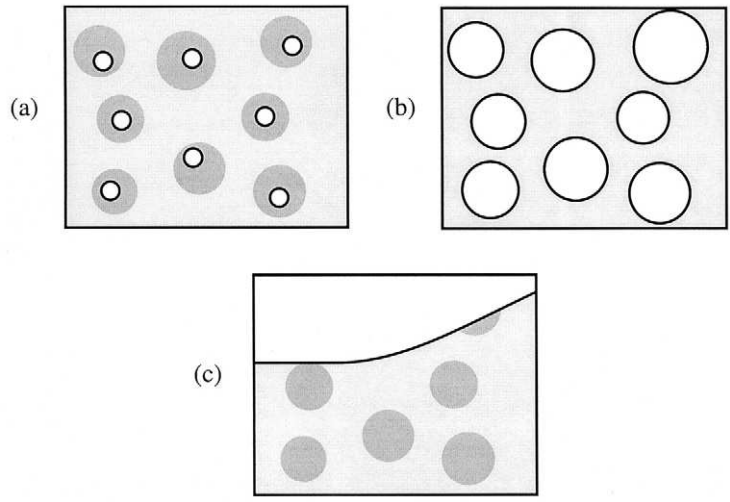

Fig. 7.21. The effect of local variations of stored energy on recrystallization. (a) If nucleation (white areas) occurs in regions of high stored energy (dark areas) then the growth rate diminishes as recrystallization proceeds, (b) after the regions of high stored energy are consumed, (c) if recrystallization nucleation is on a coarser scale than the distribution of stored energy then the growing grains sample an average stored energy which remains approximately constant as recrystallization proceeds.

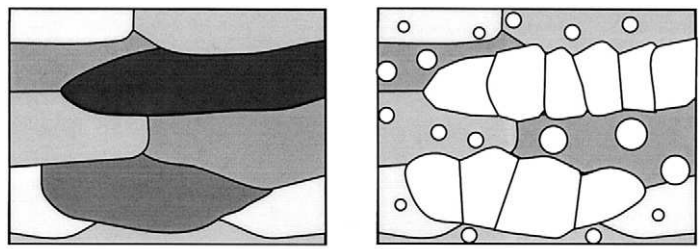

Fig. 7.22. A variation of stored energy from grain to grain as shown in (a), where regions of higher stored energy are shaded darker, results in inhomogeneous grain growth during recrystallization as shown in (b).

In figure 7.22, we illustrate a situation in which the deformed grains have different microstructures and stored energies. In this case the heterogeneity is on a much **coarser scale** than the example of figure 7.21. Even if nucleation is relatively uniform, growth will occur most rapidly in the grains of highest stored energy, leading to the type of microstructures shown in figure 7.22b. In this case not only will the growth rate decrease during recrystallization as the higher stored energy regions are

consumed, but growth of the grains will be restricted by impingement with their neighbours within the original grains.

Although analytical modelling cannot easily deal with the kinetics of inhomogeneous recrystallization, computer simulations of the type discussed in chapter 16 may be used to address the problem (Rollett et al. 1989a, Furu et al. 1990). As may be seen from the simulations of figure 16.13, inhomogeneous distribution of nuclei leads not only to low values of the JMAK slope, in agreement with many experimental measurements, but also to a decrease of the JMAK slope as recrystallization proceeds.

Thus we conclude that the deviation of recrystallization kinetics from the ideal linear JMAK plots and the low values of the exponent which are found in many experimental investigations, are in most cases directly attributable to the inhomogeneity of the microstructure. This leads to non-random distribution of nucleation sites and stored energy and to a growth rate which decreases with time.

7.5 THE RECRYSTALLIZED MICROSTRUCTURE

7.5.1 The grain orientations

In general the recrystallized grains are not randomly oriented, but have a **preferred orientation** or **texture.** The origin of recrystallization textures is discussed in detail in chapter 12, and some examples of texture control in industrial practice are given in chapter 15.

7.5.2 The grain size

The magnitude of the final grain size can be rationalised in terms of the effects of the various parameters on the nucleation and growth processes. Any factor such as a high strain or a small initial grain size, which favours a large number of nuclei or a rapid nucleation rate, will lead to a small final grain size as illustrated for α-brass in figure 7.23, where it may be seen that the annealing temperature has little effect on the final grain size. However if a change of annealing temperature or heating rate alters the balance between nucleation and growth, which is most likely in two-phase alloys (§7.2.6), then the final grain size will be affected accordingly.

The grain size may not be constant throughout a specimen. Just as the different texture components within a specimen recrystallize at different rates (§7.4), so the final grain size and shape within each texture component may be different as seen in figures 7.15, 7.16 and 7.25.

The spectrum of grain sizes as measured on a plane section is usually found to be close to a log normal distribution as shown in figure 7.24, and a similar grain size distribution has been reported for partly recrystallized material (Marthinsen et al. 1989).

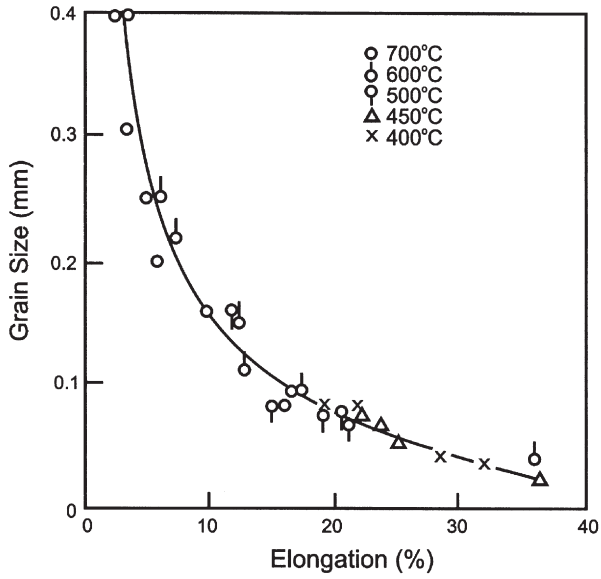

Fig. 7.23. The effect of tensile strain on the final grain size in α-brass recrystallized at various temperatures, (Eastwood et al. 1935).

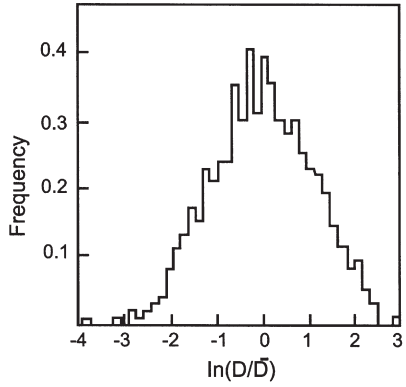

Fig. 7.24. The experimentally measured grain size distribution following the recrystallization of an Al-0.3%Fe alloy, (Saetre et al. 1986a).

7.5.3 The grain shape

If grains are uniformly distributed and growth is isotropic then the recrystallized structure consists of equiaxed polyhedra (§4.5). Although in many cases the recrystallized grains are approximately equiaxed, there are some instances where anisotropic growth leads to plate-shaped grains as may be seen in figures 7.15 and 7.25.

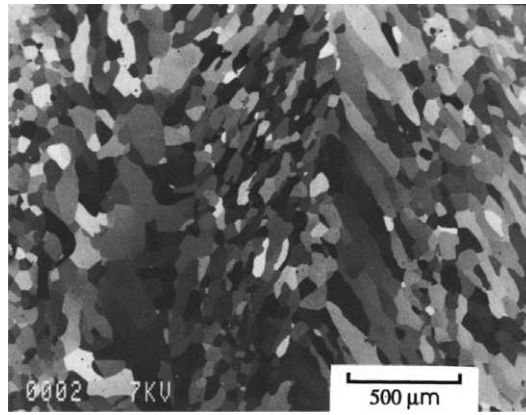

Fig. 7.25. SEM channelling contrast image of recrystallized high purity aluminium, showing the effect of anisotropic grain growth during recrystallization, (Hjelen et al. 1991).

This type of growth anisotropy is often crystallographic, and a particularly important case is for grains of fcc metals oriented by $\sim 40^\circ$ about a $< 111 >$ axis to the deformed matrix. In this situation, which is discussed in more detail in §5.3.2 and §12.3.2, the sides of a growing grain which form **tilt boundaries** to the deformed grain grow much faster than the other faces, resulting in plate-shaped grains such as that shown in figure 5.14. However, because such preferential growth is restricted to only tilt boundaries of very specific orientation relationships, it may not have a significant influence on the microstructure of recrystallized polycrystals.

In industrial, particle-containing alloys, anisotropic distribution of the particles, often along planes parallel to the rolling plane may reduce the growth rate perpendicular to the rolling plane as discussed in §4.6.2.3, resulting in pancake grains after recrystallization as shown in figure 4.28.

7.6 THE NUCLEATION OF RECRYSTALLIZATION

There has been a considerable research effort aimed at trying to understand the processes by which recrystallization originates. The importance of recrystallization nucleation is that it is a critical factor in determining both the size and orientation of the resulting grains. In order to control recrystallization effectively, it is necessary to understand the mechanisms of nucleation and the parameters which control it.

7.6.1 Classical nucleation

The possibility that the classical nucleation theory developed for phase transformations might be applicable to recrystallization was considered by Burke and Turnbull (1952).

In this situation, nucleation would be accomplished by random atomic fluctuations leading to the formation of a small crystallite with a high angle grain boundary. Such a nucleus would be stable if the difference in energy between the local deformed state and the recrystallized state were larger than the energy of the high energy interface produced in forming the nucleus. Although this theory appears to account for some aspects of recrystallization, such as the incubation period and preferential nucleation at regions of high local strain, it can be discounted because:

- **The driving force is low.** In comparison with phase transformations, the energy which drives the recrystallization process is very small (§2.2.1).
- **The interfacial energy is large.** The energy of a high angle grain boundary, which is an essential factor in the recrystallization process, is very large (§4.4.3).

Calculations based on nucleation theory (see e.g. Christian 2002) indicate that the radius of the critical nucleus (greater than 0.1 μm), is so large that the rate of nucleation will be negligible, and that this is therefore not a viable mechanism for the origin of recrystallization.

It is now accepted that the 'nuclei' from which recrystallization originates are therefore not nuclei in the strict thermodynamic sense, but small volumes which pre-exist in the deformed microstructure.

7.6.2 Strain induced grain boundary migration (SIBM)

This mechanism, an example of which is seen in figure 7.26 was first reported by Beck and Sperry (1950) and has been observed in a wide variety of metals. SIBM involves the bulging of part of a pre-existing grain boundary, leaving a region behind the migrating boundary with a lower dislocation content as shown schematically in figure 7.27. A characteristic feature of this mechanism is that the new grains have similar orientations

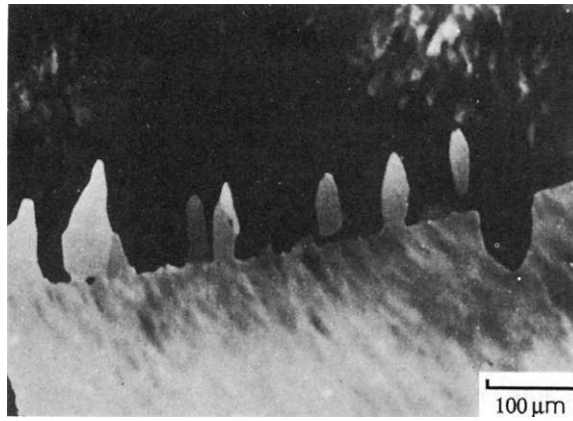

Fig. 7.26. An optical micrograph showing strain-induced grain boundary migration in aluminium, (Bellier and Doherty 1977).

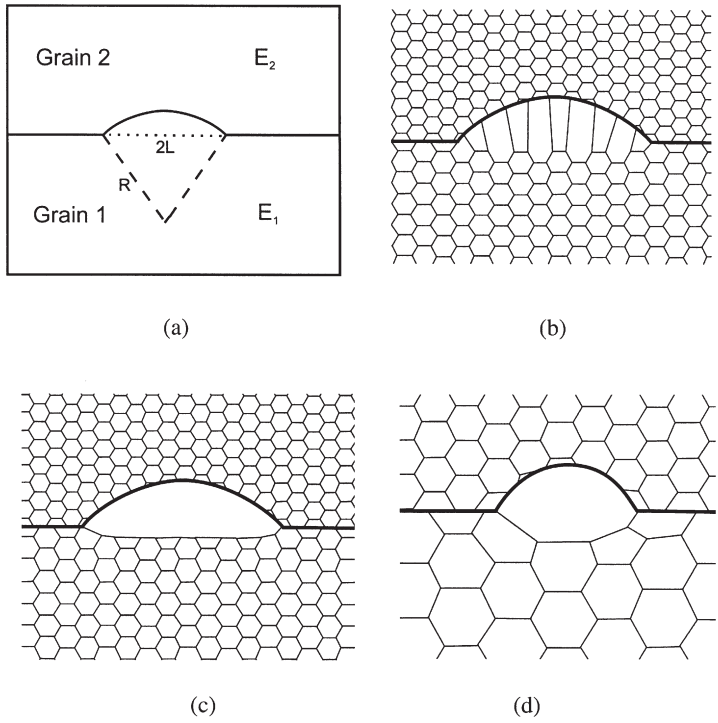

Fig. 7.27. (a) SIBM of a boundary separating a grain of low stored energy (E_1) from one of higher energy (E_2), (b) dragging of the dislocation structure behind the migrating boundary, (c) the migrating boundary is free from the dislocation structure, (d) SIBM originating at a single large subgrain.

to the old grains from which they have grown. This mechanism is particularly important after low strains, and Beck and Sperry found that at reductions $>40\%$ in pure aluminium the mechanism was apparently replaced by one in which grains of orientations different from either of the matrix grains were formed (see §7.6.4). In the early work, the similarity or otherwise of the new and old grain orientations was inferred from the contrast produced by etching, which may not be reliable. However, Bellier and Doherty (1977) were able to determine the grain orientations and, in rolled aluminium, confirmed that SIBM was the dominant recrystallization mechanism for reductions of less than 20%. Because of the orientation relationship between the new and old grains, operation of this mechanism is expected to result in a recrystallization texture which is closely related to the deformation texture. More recent research has shown that SIBM is also very important during recrystallization after high temperature deformation of aluminium and steels, when the deformation microstructures are more homogeneous than after lower temperature deformation (e.g. Theyssier and Driver 1999, Hutchinson et al. 1999b). The strengthening of the $\{100\}<001>$ **cube texture** during the recrystallization of aluminium alloys after high temperature deformation, which is of great industrial significance and which is discussed in (§12.4.1), is known to

be due to SIBM at the boundaries of cube-oriented regions in the deformed microstructure (e.g. Vatne and Nes 1994, Vatne et al. 1996a, 1996d).

7.6.2.1 Multiple subgrain SIBM

The driving force for SIBM is usually presumed to arise from a difference in dislocation content on opposite sides of the grain boundary. This could result directly from the deformation process, because it is known that the dislocation storage rate may be dependent on grain orientation (§2.2.3.3) and may also be different in the boundary regions.

The kinetics of the process were first analysed by Bailey and Hirsch (1962). In figure 7.27a, if the deformed grains have stored energies of E_1 and E_2 and $E_1 < E_2$, then the driving force is provided by the energy difference $\Delta E = E_2 - E_1$. If the bulging boundary is a spherical cap of radius **R,** with a specific boundary energy γ_b, the interfacial energy of the bulging region of the boundary is given by

$$E_B = 4\pi R^2 \gamma_b \tag{7.36}$$

and

$$\frac{dE_B}{dR} = 8\pi R \gamma_b \tag{7.37}$$

In the early stages of bulging, the energy difference per unit volume across the boundary is ΔE and

$$\frac{dE}{dR} = 4\pi R^2 \Delta E \tag{7.38}$$

For the bulge to grow $dE/dR > dE_B/dR$ and hence

$$R > \frac{2\gamma_b}{\Delta E} \tag{7.39}$$

This reaches a critical value when the boundary bulge becomes hemispherical, when $R = R_{crit} = L$, and

$$R_{crit} > \frac{2\gamma_b}{\Delta E} \tag{7.40}$$

On its concave side, the bulging boundary is joined to the lower grain by an array of dislocations or low angle boundaries, and it is not at all clear whether at the critical stage (equation 7.40), the boundary can still be considered as separating regions of high stored energy (E_1 and E_2) as shown in figure 7.27b, or whether it separates E_2 and perfect crystal (fig. 7.27c), in which case ΔE in equation 7.40 is now given by E_2. If this is the case, then the critical condition is likely to arise before the hemispherical configuration is reached. There is surprisingly little experimental evidence to resolve this

Fig. 7.28. TEM micrograph of SIBM in copper deformed 14% in tension and annealed 5 min at 234°C, (Bailey and Hirsch 1962).

point. Optical micrographs of Fe–Si (Dunn and Walter 1959) show some substructure in the bulged region, and the transmission electron micrographs of Bailey and Hirsch (1962) of copper, one of which is shown in figure 7.28, also show that the dislocation density of the bulge, although lower than that of the parent grain, is significant, in agreement with figure 7.27b. Simulations of SIBM using the vertex models described in §16.2.4 show some such dragging of low angle boundaries behind the migrating boundary, which is consistent with the results of Bailey and Hirsch (Humphreys 1992b).

Bate and Hutchinson (1997) have shown that if SIBM proceeds as shown in figure 7.27b, as the bulge develops, the dislocation or boundary length attached to the bulging boundary remains constant, whilst the boundary area is increased, and therefore the restraining pressure due to the substructure acting on the concave side of the boundary is reduced. They define the (constant) pressure on the convex side of the bulge as **P,** and that on the opposite side as **P.f,** a fraction **f** of **P.** The critical length for bulging is then found to be

$$R_{crit} = \frac{2\gamma_b}{\mathbf{P}\sqrt{1-\mathbf{f}}} \tag{7.41}$$

compared to the Bailey and Hirsch value of equation 7.40, which can be written as

$$R_{crit} = \frac{2\gamma_b}{\mathbf{P}(1-\mathbf{f})} \tag{7.42}$$

The implication of this analysis is that the critical bulge size is significantly reduced if the stored energy is large and ΔE is small **(f→1).** As **f** increases, the difference between R_{crit} as given by equations 7.41 and 7.42 decreases.

7.6.2.2 Single subgrain SIBM

If SIBM occurs in a material with a well recovered subgrain structure, such as a low-solute aluminium alloy, it may originate at a single large subgrain as shown in figure 7.27d. In this situation there is no substructure drag, and equating the size of the critical bulge with the large subgrain, the critical subgrain radius is given by

$$R_{crit} = \frac{2\gamma_b}{P} \tag{7.43}$$

and taking P, the stored energy of an array of subgrains of radius R_i and boundary energy γ_1 as $3\gamma_1/2r_i$ (equation 2.7), we obtain, for growth of a bulge into grain 2, (c.f. Faivre and Doherty 1979)

$$R_{crit} = \frac{4\gamma_b R_2}{3\gamma_2} \tag{7.44}$$

where R_2 and γ_2 are the size and boundary energy of the subgrains in the upper grain 2.

For single-subgrain SIBM, there is no requirement for a stored energy difference in the two grains, merely that there is a subgrain of the critical size adjacent to the grain boundary. However, the critical subgrain size for SIBM decreases if there is a stored energy difference across the boundary. The viability of single subgrain SIBM is therefore dependent on the sizes, size distributions and boundary energies (or misorientation) of the subgrains in the two grains. In figure 7.29, we show the critical

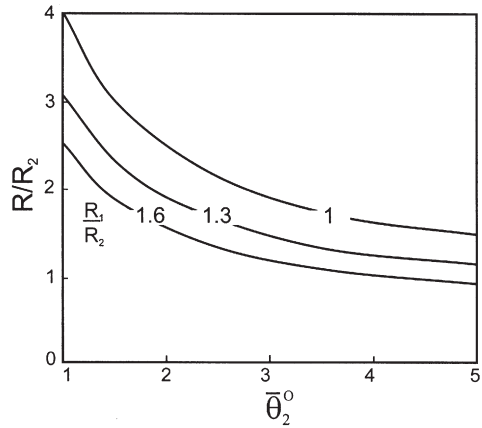

Fig. 7.29. The critical size for a large subgrain in grain 1 to undergo SIBM, as a function of the mean subgrain misorientation in grain 2 and the relative sizes of the subgrains in the two grains, (Humphreys 1999a).

subgrain size for SIBM as a function of the subgrain sizes of the two grains and the mean subgrain misorientation in grain 2 (Humphreys 1999a).

For the case when the subgrain structures have the same mean size ($R_1/R_2 = 1$) it can be seen that when the mean misorientation is larger than $\sim 2^\circ$ there is a reasonable probability of there being sufficiently large subgrains (R larger than ~ 2.5 times the mean subgrain size) on either or both sides of the high angle boundary to act as 'nuclei' for recrystallization. An energy difference across the boundary will of course make SIBM more viable and it can be seen from figure 7.29 that if $\bar{\theta}_2$ were 1° and $R_1 = 1.6R_2$ then a subgrain in grain 1 of size $2.5R_2$ (i.e. $1.6R_1$) would be capable of inducing SIBM.

The single subgrains large enough to induce SIBM can form during deformation (e.g. Humphreys and Hurley 2001). However, they might also arise from preferential recovery in the vicinity of a grain boundary, and Doherty and Cahn (1972) and Jones et al. (1979) have discussed how recovery by subgrain coalescence in the vicinity of a high angle boundary (§6.5.4) could initiate SIBM.

7.6.2.3 Multiple or single subgrain SIBM?

Multiple subgrain SIBM can occur under most conditions, because the critical nucleus size as given by equation 7.41 adjusts according to the conditions. However, if the stored energy difference (ΔE) between the grains becomes small, R_{crit} becomes improbably large. An important parameter is therefore the distance along the boundary over which any particular value of **f** is maintained. The maximum distance is the grain size, but it will usually be smaller. If we take 20 μm as a reasonable limit, then the conditions of **f** and θ_2 over which multiple subgrain SIBM can occur are as shown in figure 7.30.

The critical subgrain size for single subgrain SIBM is given by equation 7.44 and figure 7.29. The chances of there being a suitably large subgrain depend on the subgrain size distribution, and typically, subgrains up to around 3–4 times the mean are found. If we

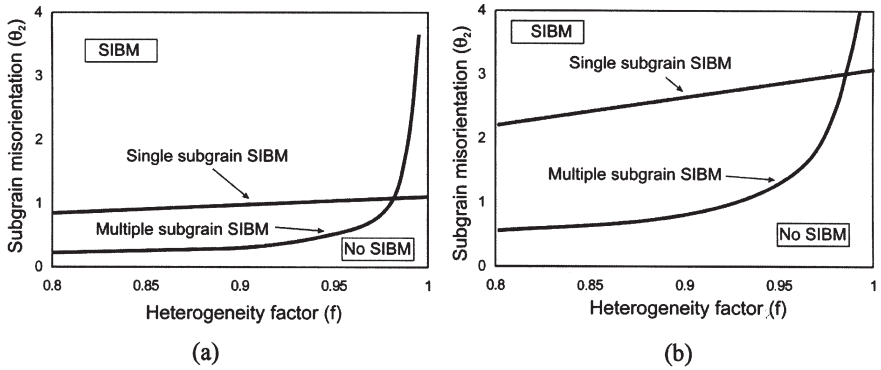

Fig. 7.30. The conditions for SIBM from single or multiple subgrains as a function of the fractional difference (**f**) in stored energy of the two grains. In the upper region, both mechanisms can occur, but single subgrain SIBM is usually more rapid: (a) single phase alloy, (b) particle-containing alloy where $P_Z = 0.5P_D$.

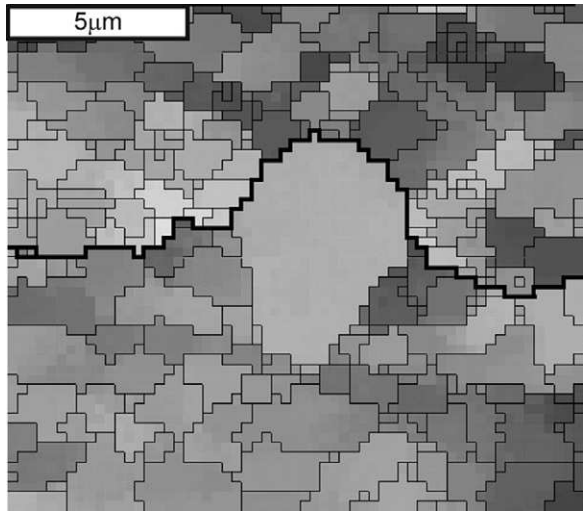

Fig. 7.31. EBSD map showing SIBM in Al-0.1 wt%Mg, cold rolled 20% and annealed at 300°C. The colours depend on orientation, HAGBs are black and LAGBs are grey. No substructure is apparent in the recrystallized grain, (Courtesy of P.J. Hurley). (See colour plate section.)

take $4R_2$ as the maximum available size, then SIBM can occur if $\theta_2 > 1^\circ$ when $R_1 = R_2$ (fig. 7.29). If we assume that changes in **f** are due to subgrain size differences alone, then the condition for single subgrain SIBM is as shown in figure 7.30a.

Calculations show that if both processes are viable, single subgrain SIBM is more rapid when the bulge sizes are close to critical, because of the lack of restraining pressure. Therefore we expect from figure 7.30a that single grain SIBM will dominate for substructures with misorientations larger than $\sim 1^\circ$, and when the grains have similar stored energies. Investigations of SIBM in aluminium cold rolled ~20% (Humphreys and Hurley 2001) are consistent with single subgrain SIBM as there is no detectable substructure within the bulge as is shown in the EBSD map of figure 7.31. Multiple SIBM is to be expected for lower subgrain misorientations, and in materials in which poorly defined dislocation cells are formed, which is consistent with the earlier work of Bailey and Hirsch on copper. The presence of a dispersion of second-phase particles reduces the driving pressure and favours multiple subgrain SIBM, as shown in figure 7.30b and discussed in §9.4.1.

Despite the undoubted importance of SIBM in recrystallization, much additional work is required to clarify the details of the mechanism and the conditions under which it occurs.

7.6.3 The preformed nucleus model

In the process of strain induced grain boundary migration discussed above, the high angle grain boundary which is a prerequisite for recrystallization, was already in

existence. However, in many cases, recrystallization originates in a region of the material where there is no such boundary, and we need to consider how a nucleus may be formed in such circumstances.

The possibility that recrystallization might originate at crystallites present in the deformed material was first postulated by Burgers (1941). In his **block hypothesis,** the nuclei could be either crystallites which were highly strained, or ones which were relatively strain free. It is now established beyond reasonable doubt that recrystallization originates from **dislocation cells or subgrains which are present after deformation.** Although there are still uncertainties about how these pre-existing subgrains become nuclei, several points are now clear.

(i) The **orientation of the nucleus is present in the deformed structure.** There is no evidence that new orientations are formed during or after nucleation, except by twinning (§7.7). Although there are instances where the orientations of new grains appear to lie outside the spread of the deformation texture (Huang et al. 2000c), the most likely explanation for such observations is that the recrystallization has originated from very small regions which were not detected during texture analysis of the deformed material.

(ii) Nucleation occurs by the **growth of subgrains** by the mechanisms discussed in §6.5.3. All direct in-situ TEM annealing observations of recrystallization nucleation (Ray et al. 1975, Humphreys 1977, Bay and Hansen 1979) have shown the mechanism to be one low angle boundary **migration,** and there is no evidence that subgrain **coalescence** has a significant role. The in-situ HVEM experiments have shown that recovery in the vicinity of the nucleus is significantly faster than in the remainder of the material.

(iii) In order for a high angle grain boundary to be produced by this rapid recovery, there must be an **orientation gradient** present. This is shown schematically in figure 7.32 which shows two 1-dimensional subgrain structures with similar misorientations between the individual subgrains. Recovery by subgrain growth of the structure shown

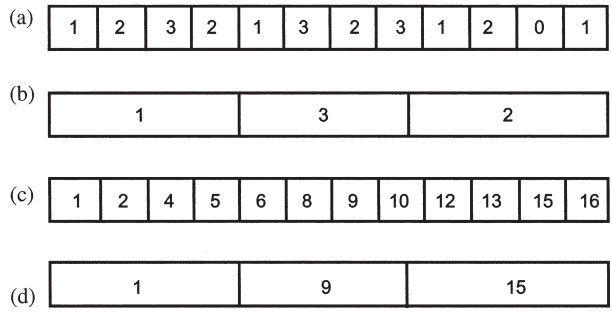

Fig. 7.32. The effect of an orientation gradient on the recovery of a 1-D microstructure. The numbers represent the orientation of the subgrains with respect to the left edge of the microstructure: (a) there is no overall orientation gradient, (b) on annealing, no high angle boundary is formed, (c) there is an orientation gradient, (d) recovery leads to the formation of higher angle grain boundaries.

in 7.32a produces large subgrains but no high angle boundary (fig. 7.32b), whereas the same amount of recovery in the presence of an orientation gradient (fig. 7.32c) results in the formation of higher angle grain boundaries (fig. 7.32d). This important point was first clearly stated by Dillamore et al. (1972). It should be noted that any region with a large orientation gradient will **always** have a high stored energy because of the geometrically necessary dislocations or low angle grain boundaries, which are needed to accommodate the misorientation. As discussed in §6.5.3.4, theory predicts that recovery will be most rapid in regions of large orientation gradient.

Nucleation of recrystallization in such a situation can therefore be considered as no more than discontinuous subgrain growth at sites of high strain energy and orientation gradient.

The **site** of the nucleus is very important in determining its viability, and it is found that the general mechanism discussed above can occur at a variety of sites.

7.6.4 Nucleation sites

Recrystallization will originate at inhomogeneities in the deformed microstructure. These may be associated with pre-existing microstructural features such as second-phase particles (§2.9.4) or grain boundaries, or may be inhomogeneities induced by the deformation, as discussed in chapter 2. As the orientation of a recrystallized grain will depend upon the recrystallization site, the types of site which operate may have a strong effect on the **recrystallization texture** as discussed in chapter 12.

7.6.4.1 Grain boundaries

Nucleation in the vicinity of prior grain boundaries, of new grains of orientations which are not close to those of the parent grains, has been frequently reported (e.g. Beck and Sperry 1950), and is more frequent at larger strains. Some evidence of the operation of such a mechanism has been obtained by Hutchinson (1989) in iron bicrystals in which the new grains were misoriented by 30° from the parent grains, and in aluminium bicrystals (Driver et al. 2000). Little is known about this type of recrystallization or about the orientations of the resulting grains. However, it is known that grain boundaries give rise to inhomogeneity of slip (Ashby 1970, Leffers 1981), and that different combinations of slip systems may operate near grain boundaries (§3.7.1), thereby giving rise to local misorientations in a manner which is probably similar in principle to that which occurs near large second-phase particles (§2.9.4). It is therefore likely that recrystallization originates in the regions of large orientation gradient which will be present near some grain boundaries or triple junctions. Whether or not there is a real distinction between this mechanism and that of SIBM has not been clearly established.

7.6.4.2 Transition bands

A transition band separates parts of a grain which have split during deformation into regions of different orientation (§2.7.3). A transition band is therefore a region of large orientation gradient which is an ideal site for recrystallization. Recrystallization at transition bands was first reported in iron by Hu (1963) and Walter and Koch (1963). The crystallographic orientations developed in transition bands are a direct consequence

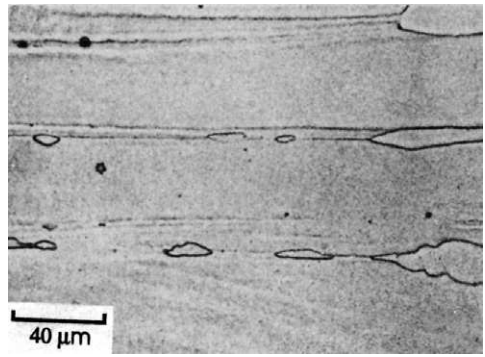

Fig. 7.33. Optical micrograph showing recrystallization at transition bands in a silicon–iron crystal, (Hu 1963).

of the slip processes and the strain path and therefore the recrystallized grains tend to have preferred orientations. Because of its importance in determining the recrystallization texture of metals (chapter 12) there have been many extensive studies of this mechanism including those of Bellier and Doherty (1977) and Hjelen et al. (1991) on aluminium, Inokuti and Doherty (1978) on iron and Ridha and Hutchinson (1982) on copper. An early example of nucleation at a transition band in iron, from the classic work of Hu is shown in figure 7.33.

An example of recrystallization in a transition band in a cube-oriented crystal of aluminium, deformed at high temperature, from the work of Huang et al. (2000b) is shown in the EBSD map of figure 7.34. The crystal has deformed inhomogeneously as shown in figure 7.34a and the regions within 15° of the original cube orientation are shaded dark. There is a large orientation gradient across the band (figure 7.34b), and on annealing, subgrain growth in this region is rapid (see §6.5.3.6 and figure 6.22), resulting in the accumulation of a large misorientation, so that a high angle boundary is produced after a small amount of growth, and recrystallization is then initiated.

7.6.4.1 Shear bands

Shear bands in rolled metals are thin regions of highly strained material typically oriented at ~35° to the rolling plane. They are a result of strain heterogeneity due to instability during rolling and their formation is strongly dependent on the deformation conditions as well as the composition, texture and microstructure of the material (§2.8). Nucleation of recrystallization at shear bands has been observed in many metals including copper and its alloys (Adcock 1922, Duggan et al. 1978a, Ridha and Hutchinson 1982, Haratani et al. 1984, Paul et al. 2002), aluminium (Hjelen et al. 1991) and steels (Ushioda et al. 1981). An early micrograph showing profuse nucleation at shear bands in copper is shown in figure 7.35.

Details of the mechanism of nucleation at shear bands are not known, and the orientations of the grains so formed appear to be very case dependent (Nes and Hutchinson 1989). For example in α-brass (Duggan et al. 1978a) the orientations of the grains were widely scattered, but in aluminium (Hjelen et al. 1991), the grains were of

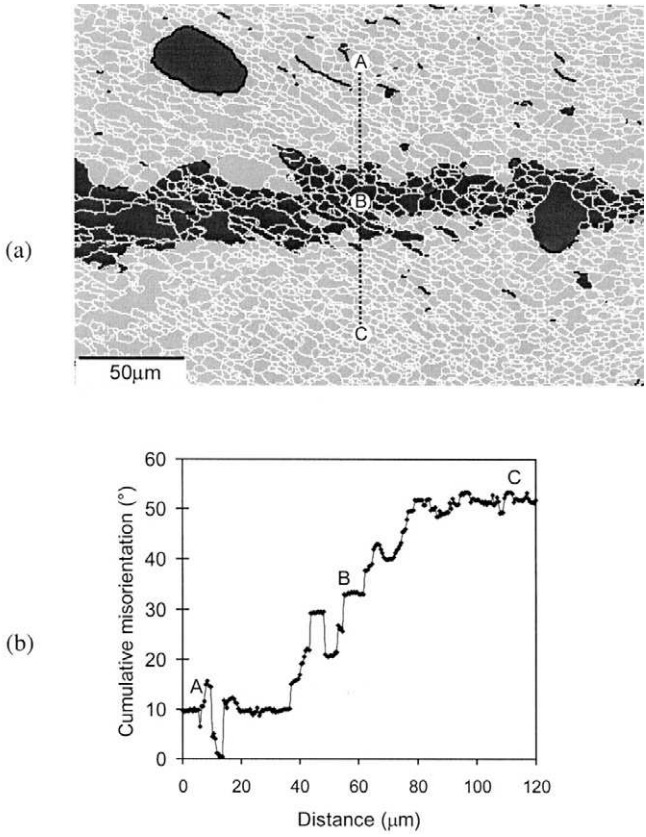

Fig. 7.34. EBSD of a hot-deformed and annealed aluminium crystal of cube orientation, showing recrystallization originating in a band of large orientation gradient: (a) map in which the regions close to the cube orientation are shaded dark. High angle boundaries are black and low angle boundaries are white, (b) the change in misorientation along the marked line A-B-C, (Huang et al. 2000b).

orientations close to the **S** $\{123\}<634>$ texture component. The orientations of the grains formed in shear bands, and their influence on the recrystallization texture are further discussed in §12.2.1.2.

7.7 ANNEALING TWINS

7.7.1 Introduction

During the recrystallization of certain materials, particularly the face centred cubic metals of intermediate or low stacking fault energy such as copper and its alloys and

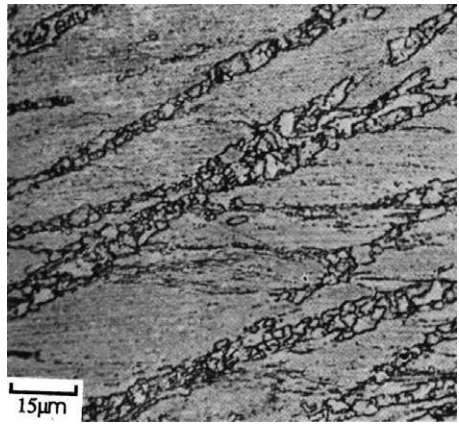

Fig. 7.35. Optical micrograph showing recrystallization occurring at shear bands in copper, (Adcock 1922).

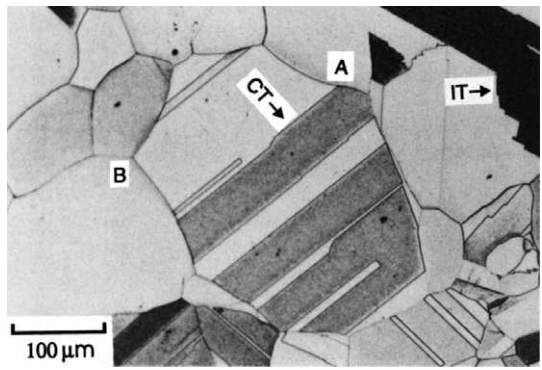

Fig. 7.36. Annealing twins in annealed 70:30 brass. Some coherent (CT) and incoherent (IT) twin boundaries are marked, (courtesy of M. Ferry).

austenitic stainless steels, annealing twins are formed as seen in figure 7.2. Such twins are also found in many intermetallic compounds, ceramics and minerals. These twins take the form of parallel sided lamellae as shown in figure 7.36. In fcc metals the lamellae are bounded by {111} planes or **coherent twin boundaries (CT)** and at their ends or at steps, by **incoherent twin boundaries (IT)** as shown in figure 7.36. The nature of these boundaries is discussed in more detail in §4.4. Twins may form during recovery, primary recrystallization or during grain growth following recrystallization, and their formation during the recrystallization of copper may be seen in the in-situ annealing sequence of figure 7.2. It should be noted that twin formation does not only occur during annealing, but may also occur during solid state phase transformations (Basson et al. 2000) or during solidification (Han et al. 2001), and of course during plastic deformation, although these types of twinning will not be considered further.

There has been recent interest in improving the properties of alloys by controlling the grain boundary character **(Grain Boundary Engineering),** and maximising the number of low Σ boundaries such as $\Sigma 3$ twins through thermomechanical processing, and this is further discussed in §11.3.2.3.

7.7.2 Mechanisms of twin formation

Although twins have been extensively studied, the atomistic mechanism of their formation remains unclear. The growth of twins may take place in two configurations as shown in figure 7.37. In figure 7.37a the growth direction is perpendicular to the coherent twin boundary and in figure 7.37b it is parallel.

7.7.2.1 Twinning by growth faulting

Gleiter (1969c, 1980) proposed that twinning occurred by the movement of ledges on the coherent twin boundary. As the twin propagates by addition of the close packed planes in a sequence such as ABCABC, the start or finish of the twin lamella requires only the nucleation and propagation of a ledge with a low energy growth fault such as to change the sequence e.g.

ABCABC|BACBACBA|BCABC.

Whilst this mechanism is capable of explaining twins propagating as shown in figure 7.37a, it is not consistent with the configuration of figure 7.37b.

7.7.2.2 Twinning by boundary dissociation

Goodhew (1979) found evidence for twin formation by boundary dissociation in gold. He identified the following dissociations:

$$\Sigma 9 \rightarrow \Sigma 3 + \Sigma 3$$
$$\Sigma 11 \rightarrow \Sigma 3 + \Sigma 33$$
$$\Sigma 33 \rightarrow \Sigma 3 + \Sigma 11$$
$$\Sigma 99 \rightarrow \Sigma 3 + \Sigma 33$$

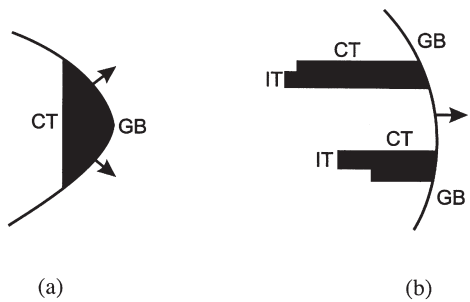

(a) (b)

Fig. 7.37. Possible orientations of twins during recrystallization: (a) the coherent twin (CT) boundary lies parallel to the recrystallization front, (b) the CT boundary is perpendicular to the recrystallization front, (after Goodhew 1979).

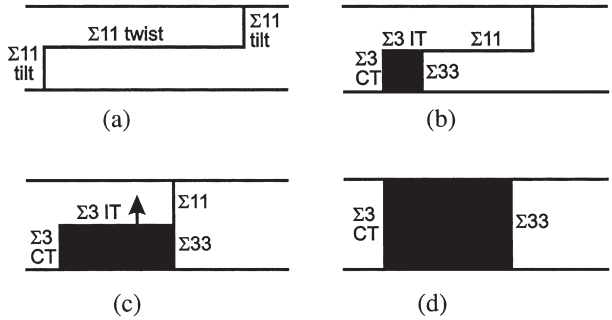

Fig. 7.38. Possible mechanism for the dissociation of a Σ11 boundary. During tilt boundary migration (a), one of the tilt boundaries dissociates (b), leaving a twin behind. The remaining Σ11 twist boundary is then eliminated (c), and the incoherent twin boundary (IT) then migrates to remove the remaining Σ11 boundary (d), (Goodhew 1979).

In all these cases a decrease in energy results (Hasson and Goux 1971), and a possible mechanism for this is shown schematically in figure 7.38.

It has been suggested that this type of boundary dissociation could occur by the emission of grain boundary dislocations, and variants of this type of mechanism have been suggested by Meyers and Murr (1978) and Grovenor et al. (1980).

7.7.3 Twin formation during recovery

Huber and Hatherly (1979, 1980) reported the formation of **recovery twins** in shear bands, during the annealing of deformed 70:30 brass at ~250°C, some 30°C below the recrystallization temperature. They were ~250 nm long and ~2–10 nm wide. Only one set of twins developed in a particular region, and these were always associated with local orientations of the form $\{110\}<112>$. The twins increased in number and width as annealing continued and there was a gradual loss of dislocations from the regions where they occurred (fig. 7.39). This loss appeared to correspond to the beginning of recrystallization, but it is significant that there was no clearly defined boundary around the developing nucleus.

7.7.4 Twin formation during recrystallization

7.7.4.1 The role of twinning

As twinning produces new orientations that were not present in the deformed microstructure, twinning may play an important part in the development of annealing textures (§12.3.5). An extensive research programme by Haasen and colleagues at Göttingen (e.g. Berger et al. 1988) has shown that multiple twinning in the early stages of recrystallization may be important in determining grain orientations in copper alloys. Their conclusion, based on in-situ high voltage electron microscopy annealing

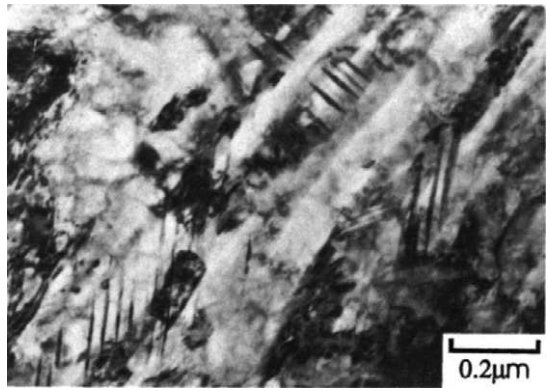

Fig. 7.39. Recovery twins in 85:15 α-brass, deformed in torsion and annealed at 240°C, (Huber and Hatherly 1979).

experiments (Berger et al. 1983) that twinning plays an important role in the recrystallization of aluminium is controversial. Twins are rarely observed in bulk samples of aluminium and it is likely that twin formation in this material is influenced by the free surfaces as discussed in §7.7.4.3.

7.7.4.2 Twin selection principles

If multiple twinning were to occur in a random manner then a random texture would result (§12.3.5). However, the recrystallization texture of heavily deformed copper (fig. 12.1) is a very strong cube texture with little contribution from twins. It is known (e.g. Hatherly et al. 1984) that only a few of the possible twin variants are formed, and therefore twinning during recrystallization cannot occur randomly and some selection principles must apply. Wilbrandt (1988) has reviewed these in detail and concluded that no single principle is capable of explaining all experimental observations. However, the following three factors have been shown to be important.

- **Boundary energy**

There is a large body of evidence which suggests that the lowering of grain boundary energy is a very important factor in determining the twin event and provides stability of the grain against further twinning. The work of Goodhew (1979) discussed above, and of the Göttingen group (Berger et al. 1988) has provided good evidence in support of this principle.

- **Grain boundary mobility**

The possibility that twinning occurs in a manner such as to provide a more mobile boundary has also been considered. For example during dynamic recrystallization of copper and silver single crystals (Gottstein et al. 1976, Gottstein 1984) (see §13.3.6), it was found that multiple twinning occurred until a fast growing grain orientation was formed. If this were the overriding factor however, we might expect twin chains to result in progressively more mobile boundaries, whereas it is known that twinning sometimes results in very immobile boundaries (Berger et al. 1988).

- **The role of the dislocation arrangement**

Evidence that twinning is affected by the dislocation structure has been presented by Form et al. (1980) who found that the twin density increased with the dislocation density. Rae et al. (1981) and Rae and Smith (1981) found that both dislocation structure and the grain boundary orientation were important in determining the ease of twinning.

7.7.4.3 Twinning and interfaces

In-situ annealing experiments on aluminium in the SEM (Humphreys and Ferry 1996), and comparison with the bulk microstructures, have shown that twin formation during recrystallization is much more prolific at a free surface than in the sample interior. It was also found that in two-phase aluminium alloys, twins were frequently associated with large second-phase particles. Although the reasons for this are not entirely clear, it is likely that the presence of a high energy surface or interface plays a significant role, as it does in twin formation during grain growth as discussed below. Significant numbers of twins may also be formed during the recrystallization of aluminium alloys containing dispersions of small second-phase particles (Higginson et al. 1995, Lillywhite et al. 2000), although the reasons are not clear.

7.7.5 Twin formation during grain growth

The early work on twin formation was mainly concerned with their formation during grain growth (Burke 1950, Fullman and Fisher 1951). The postulated mechanism of twinning, which is based on an energy criterion is shown in figure 7.40.

In figure 7.40a, grain growth is occurring such that the triple point between grains A, B and C is moving vertically. As growth proceeds, it is assumed that a growth fault may occur at some point leading to the formation of a grain (T) which is twinned with respect to grain A. If the relative orientations of the grains are such that the energy of the boundary AT is lower than that of AC then, because the energy of the coherent twin boundary AT is very low (table 4.2), there may be a reduction in total boundary energy

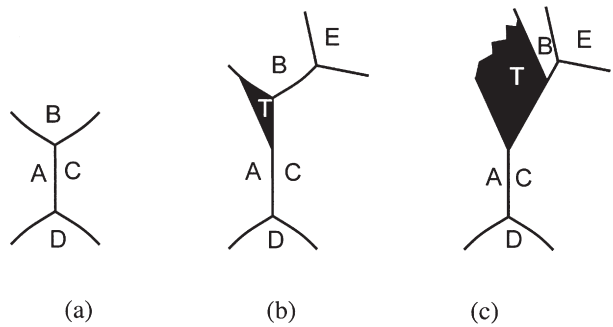

Fig. 7.40. Mechanism for twin formation during grain growth following recrystallization.

despite the extra boundary area created, and therefore the twin configuration will be stable and grow. This condition, in two dimensions, is:

$$\gamma_{AT} L_{13} + \gamma_{TC} L_{23} + \gamma_{TB} L_{12} < \gamma_{AC} L_{23} + \gamma_{AB} L_{12} \quad (7.45)$$

where γ_{ij} is the energy of the boundary between grains i and j and L_{xy} is the distance between points x and y.

The growth will be terminated if the triple point ABC reacts with another triple point such as BCE, resulting in a grain configuration with a less favourable energy balance (fig. 7.40c). On such a model, the number of twin lamellae should be proportional to the number of triple point interactions, and evidence for this was found by Hu and Smith (1956). The actual atomistic mechanism of twin formation during grain growth is likely to be similar to the mechanisms discussed above for twin formation during recrystallization.

ThisPageIntentionallyLeftBlank

Chapter 8

RECRYSTALLIZATION OF ORDERED MATERIALS

8.1 INTRODUCTION

There is significant interest in the use of ordered intermetallic compounds as high temperature structural materials. However, use of these materials is frequently limited by their poor toughness. Thermomechanical processing may be used not only to form the materials, but also to break-up the cast structure, reduce inhomogeneity, refine the grain size and optimise microstructure and texture (Morris and Morris-Munoz 2000). For superplastic applications (Nieh and Wadsworth 1997), control of grain size during processing and service is critical, and in some cases, control of grain shape and recrystallized state may also be important (e.g. McKamey and Pierce 1992, Zhang et al. 2000).

Few of the potentially useful intermetallics can be extensively deformed at room temperature, and there is most interest in hot deformation and either static or dynamic recrystallization. In this chapter we make some comparisons of deformation, recovery, recrystallization and grain growth in ordered alloys with the behaviour of conventional metals. Although there has been extensive research into thermomechanical processing of ordered materials, much of the work is on complex multi-phase materials such as the TiAl-based alloys (e.g. Yamaguchi 1999) in which the main interest is in optimising the phase distributions, and we will not consider these materials. Even for the simpler single-phase intermetallics, there are many unanswered questions regarding the annealing behaviour, as discussed in the review by Baker (2000).

8.2 ORDERED STRUCTURES

8.2.1 Nature and stability

The two ordered structures (or **superlattices**) which have been most extensively studied with respect to the annealing behaviour are the **$L1_2$** structure associated with A_3B alloys such as Cu_3Au, Ni_3Al, Ni_3Fe etc., and the **B2** structure typical of AB compounds such as CuZn, FeCo, NiAl etc. The $L1_2$ structure is face centred cubic with the A atoms located on the face centred sites (1/2, 1/2, 0 etc.) while the B2 structure is body centred cubic with the B atoms at the body centred site (1/2, 1/2, 1/2). The B2 structure is subject to a further significant ordering process in which a **DO_3** structure is produced. The unit cell consists of eight B2 unit cells arranged as a $2 \times 2 \times 2$ cube with alternate cells having A and B atoms at the cell centre. Examples of this structure include the important materials based on Fe_3Al.

In some materials the ordered structure is absent above a critical **ordering temperature (T_c),** but in others the ordered state is stable up to the melting point. In many respects materials of the latter type, which are called **permanently ordered materials,** are closely related to chemical compounds. Details of T_c for a number of significant materials are given in table 8.1.

In materials that are capable of being disordered, the retention of ordering during heating, or its development during cooling, is measured by the **ordering parameter (S).** S takes values between 1, corresponding to perfect ordering and 0, corresponding to the fully disordered state. However, the extent of ordering below T_c does not follow the same pattern in all materials. In some cases, e.g. FeCo, S decreases slowly as the alloy is heated, and the disordered state can be retained at room temperature by quenching. In other cases, e.g. Cu_3Au, the disordered state cannot be retained on quenching and there is an abrupt change to high values of S at temperatures just below T_c. The two types of behaviour are shown in figure 8.1.

In materials that can be disordered, the structure below T_c is characterised by volumes called **domains,** where there is a high degree of order. In a fully ordered material, neighbouring domains, in which the A and B atoms have different positions, are separated by a surface called an **antiphase boundary (APB)** and it is found in practice that such boundaries follow simple crystallographic planes in the parent lattice. APBs are of critical importance to the deformation and annealing behaviour of ordered materials, because they occur not only from the impingement, during ordering, of

Table 8.1
Ordering temperature (T_c) of some ordered alloys.

Material	T_c (°C)	Material	T_c (°C)
Cu_3Au	390	Fe_3Al	~540
Ni_3Fe	500	$(Co_{78}Fe_{22})_3$ V	910
CuZn	454	Ni_3Al	1638 (M.Pt.)
FeCo	~725		

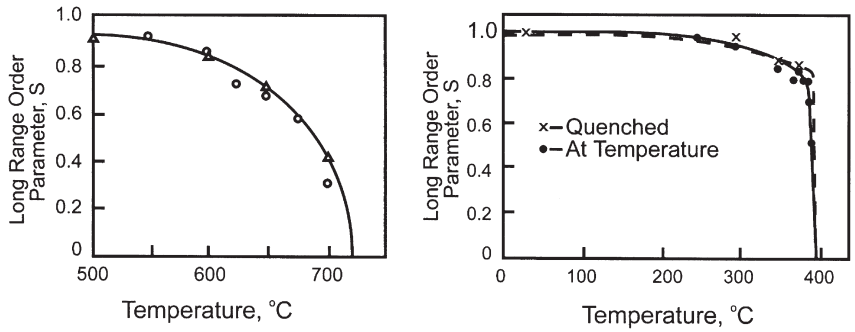

Fig. 8.1. Order parameter, **S**, as a function of temperature for, (a) FeCo, (after Stoloff and Davies, 1964); (b) Cu_3Au, (after Hutchinson et al. 1973).

growing domains but also from the passage of dislocations (see below). In partly disordered materials the domains are separated from each other by disordered regions.

8.2.2 Deformation of ordered materials

A perfect dislocation in the disordered lattice is merely a partial dislocation in the ordered structure and its movement in the superlattice leaves behind a plane that is an APB. In B2 structures for example, the expected dislocation has a Burgers vector of $a/2 < 111 >$ and its passage leads to the creation of an APB. In order to avoid the energy increase associated with the production of such a boundary, the moving dislocations in an ordered structure are coupled in pairs (**super-dislocations**) so that the second dislocation restores the ordered state. These two dislocations are linked by a small area of antiphase boundary.

The details of the slip processes in ordered B2 alloys have been discussed by Baker and Munroe (1990, 1997). The commonly observed dislocations have Burgers vectors corresponding to $< 100 >$, $< 110 >$ and $< 111 >$ but only the first and last of these are found at low temperatures. In many alloys (e.g. CuZn), there is a change from $< 111 >$ slip to $< 100 >$ slip at temperatures near 0.4–0.5 Tm. However, in others (e.g. FeAl), the temperature at which the transition to $< 100 >$ slip occurs is also governed by the composition. There is at present, no clear explanation for the change from $< 111 >$ to $< 100 >$ slip in these materials. For $< 111 >$ dislocations in B2 superlattices, the slip planes are {011}, {112} and {123} but whether or not the coupled $< 111 >$ partials can cross slip, depends on the energy of the APB that links them. For large APB energies the partials are close together and recombination and cross slip are easy. If the energy is very low, cross slip of the individual partials becomes possible. For intermediate values cross slip is more difficult and pile ups are to be expected.

A detailed study of the dislocations present in the $L1_2$ alloy $Al_{64}Ti_{28}Fe_8$ deformed in compression, has been made by Lerf and Morris (1991). At room temperature, undissociated $< 110 >$ dislocations move through the lattice, but $< 100 >$ dislocations

remain pinned. At 500°C, many dislocations dissociate into pairs of $a/2<110>$ partials, thereby constituting mobile super-dislocations on {111} planes. At 700°C, the super-dislocations are distributed evenly between the {001} and {111} planes. Cross slip between octahedral planes is increasingly prevalent at temperatures > 500°C.

The very limited low temperature ductility of many materials which remain ordered up to the melting point, is attributable in part to the retention of order and hence to the difficulty of dislocation movement, and also to grain boundary embrittlement in some intermetallics. However, some ordered alloys, such as boron-doped Ni_3Al, can be extensively deformed at room temperature (e.g. Ball and Gottstein 1993a, Yang and Baker 1997), and others can be deformed by techniques such as ball milling (Jang and Koch 1990, Koch 1991, Gialanella et al. 1992) or equal channel angular extrusion (ECAE) Semiatin et al. (1995).

It is often found that a recrystallized metal, particularly one with a small grain size, is more ductile than the cold-worked material. However, there are some examples of intermetallics that are more ductile when only recovered or partially recrystallized (Baker 2000). For example, McKamey and Pierce (1992) examined the room temperature strength and ductility of an Fe_3Al-based alloy using specimens that had been heat treated to relieve stresses or produce controlled amounts of recrystallization. Maximum ductility (8% elongation) was associated with the stress relieved (recovered) state, and in contrast the fully recrystallized material showed only 3.5% elongation.

During extensive plastic deformation, many of the super-dislocations become uncoupled or dissociated, and the material becomes **progressively disordered** (Koch 1991, Ball and Gottstein 1993a). An investigation by Dadras and Morris (1993) of a $Fe_{68}Al_{28}Cr_4$ alloy which had a DO_3 structure found that after milling, about 75% of the dislocations present were uncoupled and single.

The **stored energy** after deformation is seen from equation 2.6 to be proportional to the dislocation density (ρ) and the square of the Burgers vector (**b**). Values of **b** are different for disordered and ordered materials, and in $L1_2$ compounds, $\mathbf{b} = \mathbf{a/2<110>}$ in the disordered state, but after ordering **b** doubles to $\mathbf{a<110>}$. If the dislocation density is similar, we therefore expect the ordered material to have a larger stored energy than the disordered alloy, and there is some evidence for this (Baker 2000). However, the situation is complicated, because as discussed above, an ordered material may disorder during plastic deformation. A higher stored energy will tend to accelerate recrystallization or lower the recrystallization temperature (§7.2), and there is some evidence that an alloy which is **ordered** before deformation recrystallizes at a lower temperature than the same alloy **disordered** before deformation (Clareborough 1950, Baker 2000).

8.2.3 Microstructures and deformation textures

Although there has been much discussion of the mechanism of dislocation movement in ordered materials, there is surprisingly little known about the nature of the microstructures and textures developed during thermomechanical processing, as may be seen from the review of Yamaguchi (1999).

Boron-doped alloys based on Ni_3Al can be rolled at room temperature, and have been extensively studied by Gottstein and colleagues. Ball and Gottstein (1993a) rolled a boron-doped $Ni_{76}Al_{24}$, compound which has an $L1_2$ structure, to $>90\%$ reduction at room temperature. They found that at intermediate strains the microstructure consisted of clusters of microbands together with shear bands (fig. 8.2); the latter were of the intersecting type normally associated with alloys of low stacking fault energy. No evidence of cell formation was observed at any level of strain. At strains below 0.4, very thin ($\sim$0.05 μm) microbands were observed, and these authors also reported that at higher strains, somewhat thinner shear bands, classified by them as copper type shear bands, appeared between the brass type shear bands formed earlier.

The deformation texture of this material after rolling to 92% reduction is shown in figure 8.3. It was described as a weak copper-type texture consisting of the components, Brass, $\{110\}<112>$ and Copper, $\{112\}<111>$ and with a broad spread between the Goss, $\{110\}<001>$ and S, $\{123\}<634>$ orientations. This rolling texture is unexpected, because shear bands of the type shown in figure 8.2 which are common in materials with low-medium stacking fault energy, are normally associated with strong brass-type textures at this level of reduction (§3.6.4). Ball and Gottstein detected no evidence of deformation twinning, although these have since been reported by Chowdhury et al. (1998), who also found evidence of a structural change to a DO_{22} structure after large strains. The development of a 'copper type' texture (§3.2.1) in a microstructure resembling that of a low stacking fault energy fcc material (§2.5) is unusual and there is a need for further investigations.

Kawahara (1983) examined an FeCo-2V alloy; this material which has a B2 structure can be retained in the disordered condition by quenching. Extensive shear banding occurred in both ordered and disordered specimens after rolling. The first shear bands developed after only 10% reduction, and by 50% reduction the specimens displayed microstructures similar to that shown in figure 8.2, in which the shear bands were profuse and had the characteristics of the bands normally found in fcc metals with low stacking fault energy. The rolling texture of a specimen rolled to 70% reduction was said

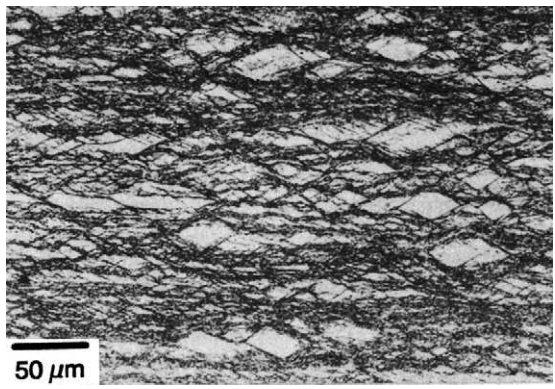

Fig. 8.2. Longitudinal section of 70% cold rolled, B-doped Ni_3Al showing shear bands, (Ball and Gottstein 1993a).

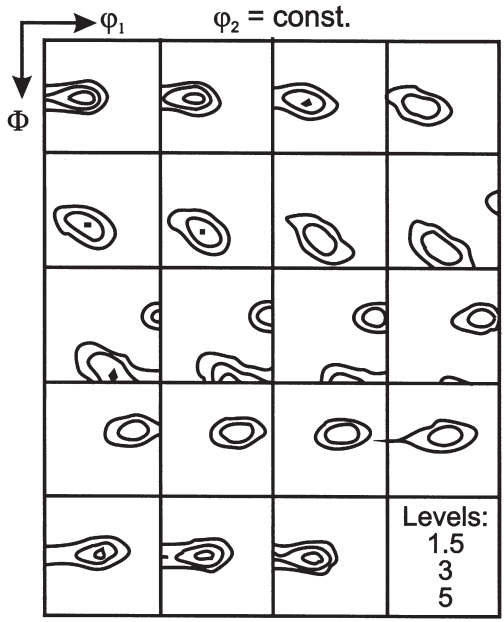

Fig. 8.3. Rolling texture of 92% cold rolled, B-doped Ni_3Al, (Ball and Gottstein 1993a).

to consist of $\{001\}<110>$, $\{112\}<110>$, $\{111\}<110>$ and $\{111\}<211>$ components and to be similar to that of iron-based materials.

The development of microstructures and textures during warm rolling of B2 ordered polycrystalline alloys based on Fe_3Al has been investigated. Huang and Froyen (2002) found that the grains elongated during deformation and that the boundaries remained straight. The dislocation structures were found to be reasonably random, with no evidence of cell formation. Most dislocations were found to be of Burgers vector $<111>$. Raabe (1996) reported textures near $\{111\}<110>$ on warm rolling similar material, and showed the experimental textures to be in good agreement with Taylor calculations based on the operation of $\{110\}<111>$ and $\{112\}<111>$ slip systems. Morris and Gunther (1996) have shown that the deformation textures in Fe_3Al are affected by the alloy composition, the processing temperature and the degree of order.

8.3 RECOVERY AND RECRYSTALLIZATION OF ORDERED MATERIALS

The recovery and recrystallization of ordered structures is complicated by the fact that several quite different processes may be occurring simultaneously in the material, viz., the restoration of the ordered state and those associated with recovery and recrystallization. The kinetics of these processes are quite different and the behaviour

is complex. Reviews of the literature by Cahn (1990) and Cahn et al. (1991) summarize the observations as follows:

- There is a drastic reduction in grain boundary mobility in the presence of atomic order, which severely retards recrystallization.
- A temperature range may exist where recrystallization does not occur even though it occurs at lower and higher temperatures.
- The pre-recrystallization behaviour depends on the composition of the alloy and the annealing temperature. The deformed alloy may soften, harden, or remain unchanged.

In the following account the $L1_2$ and B2 structures are considered separately.

8.3.1 $L1_2$ structures

8.3.1.1 Recovery

In a significant early study Roessler et al. (1963) examined Cu_3Au after rolling to 63% reduction ($\varepsilon \sim 1$). Both ordered and previously disordered material were used. It was found (fig. 8.4) that in both cases there was a hardness increase when annealing was carried out below the ordering temperature of 390°C; the increase was greatest for material deformed in the disordered state. The maximum values were associated with an increase in **S** from 0.50 to 0.85. It is well known that there is a relationship between hardness and domain size, and Stoloff and Davies (1964) have shown that the hardness is a maximum at a critical small domain size. The strain–age-hardening shown in figure 8.4 is attributable to rapid domain growth as order returns.

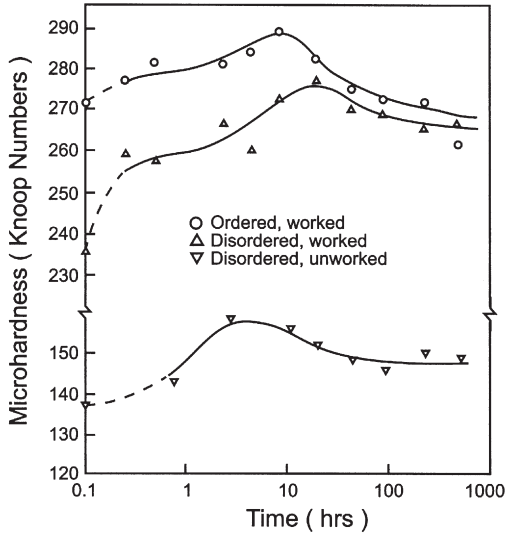

Fig. 8.4. Microhardness of rolled Cu_3Au as a function of annealing time at 288°C, (Roessler et al. 1963).

The alloy Ni_3Fe, which has $T_c \sim 500°C$, was found by Vidoz et al. (1963) to harden during annealing in much the same way as Cu_3Au. The effect was greatest at the stoichiometric composition and fell off rapidly as the composition deviated from ideality; off-stoichiometric alloys with $>32\%$ Fe or $>78\%$ Ni softened by recrystallization. In addition to the hardness increase, the stoichiometric alloy showed a strongly enhanced work hardening rate after annealing; this change is believed to be due to dislocation drag involving APB tubes.

Considerable attention has been paid to the family of $L1_2$ alloys based on the composition $(FeCoNi)_3V$ (Liu 1984). Cahn et al. (1991) rolled the alloy, $(Co_{78}Fe_{22})_3V$, in both the ordered and disordered conditions to reductions up to 50% ($\varepsilon \sim 0.8$) and annealed above and below T_c (910°C). In this alloy **S** remains high up to T_c and recrystallization was strongly retarded with a retardation factor of $\sim 300\times$ just below T_c. In the case of initially ordered material, both hardness and tensile measurements showed substantial softening prior to, and during the early stages of recrystallization as shown in figure 8.5a. However, initially disordered material showed substantial hardening before and during the early stages of recrystallization as shown in figure 8.5b. The increase in hardness, during recovery, of the material deformed in the disordered state (fig. 8.5b) is attributable to hardening induced by ordering during the annealing. The decrease of hardness of the initially ordered material (fig. 8.5a) is due to normal dislocation recovery processes. The hardness **decrease** of $(Co_{78}Fe_{22})_3V$ shown in figure 8.5a is in contrast to the **increase** of hardness during annealing of the initially ordered Cu_3Au shown in figure 8.4. It is thought that the latter behaviour is a consequence of the larger rolling deformation resulting in a substantial amount of disordering, which leads to order hardening on annealing.

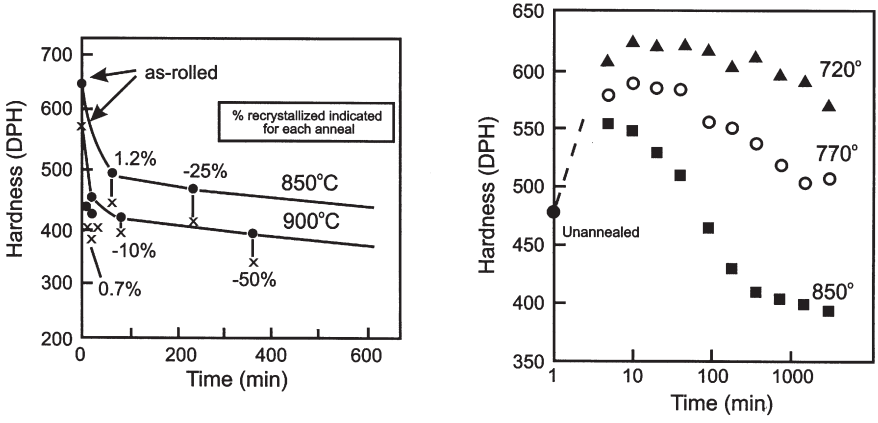

Fig. 8.5. Hardness changes during the annealing of deformed $(Co_{78}Fe_{22})_3V$. (a) Initially fully ordered material rolled to 25% reduction (• = microhardness, × = macrohardness); (b) Initially disordered material rolled to 50% reduction, (Cahn et al. 1991).

We conclude that during recovery of deformed weakly-ordered alloys at temperatures below T_c, there are two processes occurring.

- **Normal dislocation recovery,** which results in softening, and
- **Re-ordering,** if the material was disordered before or during deformation, which results in hardening.

The net effect on the hardness during a recovery anneal will therefore depend on the amount of deformation, the rate of re-ordering and the rate of dislocation recovery.

A strongly ordered alloy such as Ni_3Al tends to soften on recovery (Baker 2000). This may be because such a material disorders less extensively during deformation than does a weakly-ordered alloy.

8.3.1.2 Recrystallization

A second classic study of Cu_3Au, concerned in this case with recrystallization, was that of Hutchinson et al. (1973). The disordered alloy was rolled to 90% reduction ($\varepsilon \sim 2.5$) and isothermally annealed (fig. 8.6). The kinetics of ordering were such that order was fully restored at 330–380°C, and the retardation of recrystallization in the presence of order is clearly seen. Hutchinson et al. established that the retardation could not be attributed to inhibition of nucleation in the presence of order and that the significant factor was inhibition of grain boundary migration. This was believed to be due to the increased diffusion distances associated with boundary migration through an ordered lattice. The recrystallization textures were also determined; for annealing above T_c a very weak texture was found, but a strong copper-type deformation-type texture developed at temperatures below T_c. By comparing their results with those for pure copper and pure gold, Hutchinson et al. estimated that at T_c the retardation factor due to the presence of a superlattice is $\sim 100\times$. Cahn and Westmacott (1990) have carried out similar experiments with the alloy $(Co_{78}Fe_{22})_3V$ and find an even greater retardation factor of $300\times$.

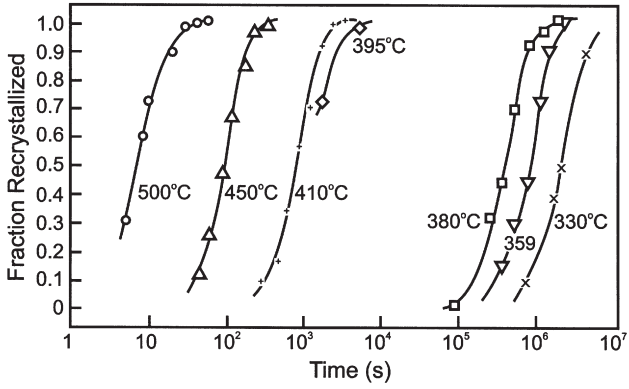

Fig. 8.6. Fraction recrystallized vs annealing time for Cu_3Au reduced 90% by rolling, (Hutchinson et al. 1973).

The annealing behaviour of the boron-doped Ni_3Al alloy referred to in §8.2.3 has been investigated by Gottstein et al. (1989), Ball and Gottstein (1993b) and Escher et al. (1998). In the initial work, details of the recrystallization kinetics were determined and recrystallization was reported to be slow. The JMAK exponent was 2.2 and the activation energy for recrystallization was found to be 110 kJ/mol which was less than half that found by Baker et al. (1984). In view of the high value of stored energy, which provides a large driving force for recrystallization, Gottstein et al. (1989) attributed the sluggish recrystallization behaviour to a reduced grain boundary mobility in the presence of ordered structures.

Before recrystallization, subgrain formation was found to occur preferentially near the grain boundaries, and recrystallization was found to initiate by strain induced boundary migration at low strain levels. After larger strains, nucleation was associated with shear bands (fig. 8.2) and microbands and equiaxed grains with diameter 0.2 μm developed at these inhomogeneities. Annealing twins were common in the new grains. In the volumes between the bands, nucleation was much slower and the grains that eventually developed were around three times larger. This situation is directly comparable to the case of low-zinc brass reported by Carmichael et al. (1982) (fig. 7.16 and §7.4.1).

In polycrystals of this material, the recrystallization texture was reported to be almost random, and Ball and Gottstein (1993b) attributed this to the locally high nucleation rate in the shear bands and microbands and the very low grain boundary mobility of ordered structures. Chowdhury et al. (2000) confirmed the weak recrystallization texture and related it to a reversion of the DO_{22} structure formed during deformation to the stable $L1_2$ structure and to the influence on the recrystallization, of twins formed in the later stages of deformation.

8.3.2 B2 structures

FeCo: The annealing behaviour of B2 alloys is different in many respects to that just described, and amongst such materials FeCo has been extensively studied. This alloy has a critical temperature of ~725°C, and the disordered state can be retained by quenching. On deformation, FeCo work hardens at similar rates in both the ordered and disordered states. The kinetics of re-ordering in FeCo deformed in the disordered state are retarded (Stoloff and Davies 1964) in contrast to the behaviour of alloys such as the $L1_2$ phase Cu_3Au in which acceleration is observed.

The recrystallization behaviour of FeCo containing small amounts of V or Cr has been studied by Buckley (1979) and Rajkovic and Buckley (1981). If cold worked material is annealed below Tc then interaction between the ordering and recrystallization reactions leads to the very complex pattern of behaviour summarised below.

- Above ~725°C (T_c) recrystallization is rapid.
- Between 600°C and 725°C the alloy orders rapidly and this is followed by slow recrystallization.
- Between 475° and 600°C, homogeneous ordering occurs at a moderate rate, dislocation recovery takes place but no recrystallization occurs. It is presumed that the driving force for recrystallization is insufficient for grain boundary migration through the superlattice.

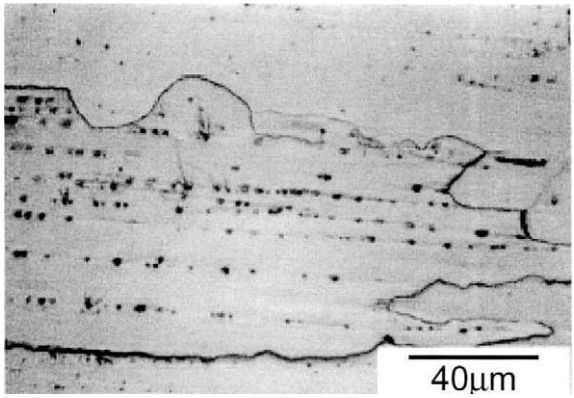

Fig. 8.7. Recrystallization originating by SIBM in hot-deformed Fe_3Al annealed at 650°C, (Huang and Froyen 2002).

- Between 250° and 475° the ordering reaction is slow and partial recrystallization is possible. Ordering is more rapid in the vicinity of the migrating grain boundaries.

Fe_3Al: On recovery, there is extensive recovery of the tangled dislocation structures formed on hot working, into well organised low angle boundaries (Morris and Lebouef 1994, Huang and Froyen 2002), accompanied by a decrease in hardness, and an increase in the degree of long-range order. Recrystallization originates at heterogeneities such as deformation bands (§7.6.4) and by SIBM (§7.6.2) as shown in figure 8.7.

β-brass: A detailed study of the annealing of β-brass was carried out by Morris and Morris (1991). As pointed out earlier, the amount of order decreases continuously in this phase as the temperature rises to, and through T_c, and the annealing behaviour (fig. 8.8) does not show the marked discontinuity seen in figure 8.6 for Cu_3Au. Electron microscopy showed that recovery of the dislocation structure was rapid at temperatures well below T_c, but decreased as T_c was approached and this was attributed to short-range ordering. The increasing rate of recrystallization as T_c is approached is to be expected, and the activation energy of 145 kJ/mol for boundary migration in this range is close to that for diffusion of copper in the ordered structure. The decreasing rate of recrystallization with increasing temperature above T_c is however, surprising.

8.3.3 Domain structures

An important difference between permanently ordered alloys and those which undergo an order/disorder transformation is the presence of an antiphase domain structure in recrystallized material.

Weakly-ordered compounds such as Cu_3Au and FeCo show profuse APBs after recrystallization (e.g. Hutchinson et al. 1973, Cahn 1990, Cahn and Westmacott 1990,

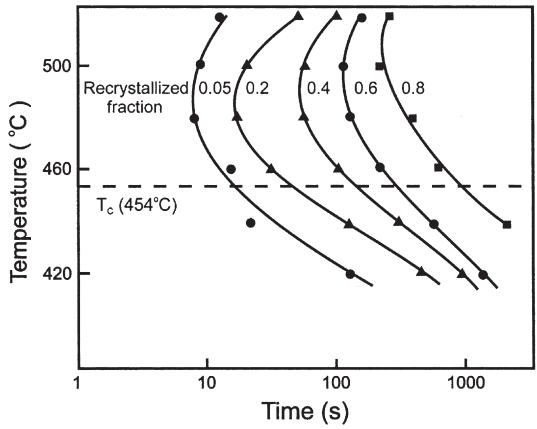

Fig. 8.8. Recrystallization kinetics of 20% compressed, β brass. The curves show contours for recrystallized fractions, (after Morris and Morris 1991).

Yang et al. 1996). However, strongly-ordered compounds such as Ni_3Al show few if any. Yang et al. (1996) suggested that this difference is because grain boundaries in weakly-ordered compounds are partially disordered, and that APBs are created within this disordered zone as the boundary migrates. The APBs will then act as a drag on the boundary, thus explaining why the boundaries, although disordered, move rather slowly compared to the fully disordered material. However, in strongly-ordered compounds, most of the boundaries are ordered and migration is hindered by the presence of long range order right up to the boundary plane, necessitating the two atomic species migrating to their correct sites as the boundary moves, with no consequent formation of APBs.

8.4 GRAIN GROWTH

Most of the studies of grain growth in ordered alloys report isothermal grain growth kinetics which are similar to those of disordered alloys, with the usual relationship between grain size and time as given by equation 11.7. Studies of grain growth in FeCo containing 2%V, have shown that the kinetics are described by this relationship with the exponent $\mathbf{n \sim 2.}$ If however, the rate constant is plotted against 1/T the results shown in figure 8.9 are observed (Davies and Stoloff, 1966). A normal Arrhenius relation exists above T_c but at lower temperatures the plot is curved and there is a discontinuous change in the rate constant at T_c, showing that even a small degree of order significantly slows grain growth. Huang and Froyen (2002) have reported a similar decrease in the grain growth rate in Fe_3Al when the ordering is increased.

Ball and Gottstein (1993b) investigated grain growth after recrystallization in the boron-doped Ni_3Al discussed in §8.3.1, and in the temperature range 800–1150°C. They found that the kinetics were of the form of equation 11.7, with a growth exponent **n** which

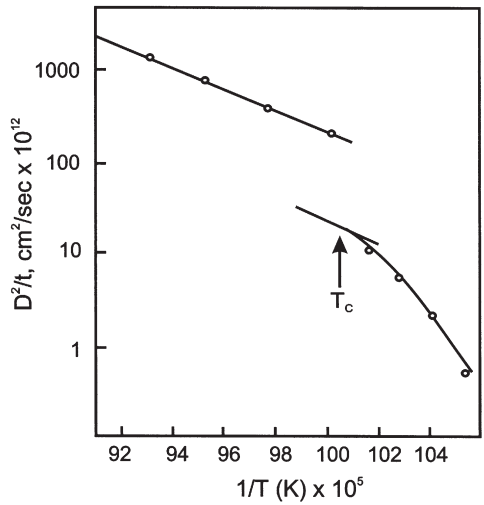

Fig. 8.9. The grain growth rate constant in FeCo–V as a function of temperature, (Davies and Stoloff 1966).

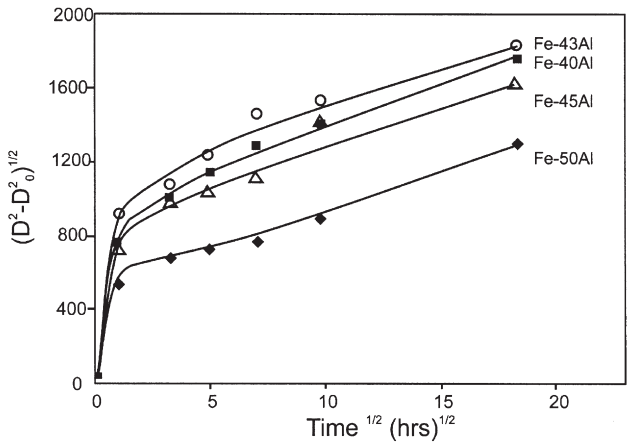

Fig. 8.10. Grain growth kinetics for various Fe–Al alloys at 1200°C, showing the effect of deviation from stoichiometry, (after Schmidt et al. 1989).

varied somewhat with temperature, having a mean value of 3. The activation energy for grain growth was found to be 298 kJ/mol, close to that for diffusion of Ni in Ni_3Al.

Baker (2000) has discussed the effect of stoichiometry on the rate of grain growth in ordered Fe–Co. Figure 8.10 shows the effect of stoichiometry on grain growth in Fe–Al, and it is seen that the rate of grain growth increases as the alloy deviates from

stoichiometry. As iron substitutes for aluminium, the alloy becomes more disordered and the rate of diffusion increases.

The effect of interstitial solutes such as boron, on grain growth rates is complex. In Ni_3Al, it is found that boron has little effect on boundary mobility (e.g. Cahn 1990, Yang and Baker 1996). However, boron has a very strong inhibiting effect on grain growth in FeAl (Yang and Baker 1996). This may be due to the nature of the interstitial sites in the two lattices.

8.5 DYNAMIC RECRYSTALLIZATION

Dynamic recrystallization is frequently observed during the hot deformation of ordered alloys. It appears to be rather similar to the process which occurs in metals, and is to be expected in materials where recovery is slow and there is a retention of large amounts of stored energy (§13.3).

Evidence of grain boundary migration and dynamic recrystallization has been obtained by Baker and Gaydosh (1987), and Imayev et al. (1995) in specimens of FeAl. At temperatures in the range 600–700°C, where a $<111>$ superdislocations operate (Baker and Munroe 1997), dynamic recrystallization is very slow. However, at temperatures in the range 750–900°C, where a $<100>$ dislocations operate, dynamic recrystallization proceeds rapidly. This difference in behaviour has been ascribed to the ability of the $<100>$ dislocations to climb more rapidly (Imayev et al. 1995), although the effects of changes in the grain boundary mobility with temperature should not be discounted.

Aretz et al. (1992) and Ponge and Gottstein (1998) have investigated dynamic recrystallization during the hot compression of large-grained boron-doped Ni_3Al. The stress–strain curve exhibited a peak, typical of metals undergoing dynamic recrystallization (§13.3), and dynamic recrystallization occurred at the old grain boundaries, with the new grains forming the typical 'necklace microstructure' described in §13.3.3. The mechanism of dynamic recrystallization appears to involve progressive lattice rotations in the grain boundary regions, and may be similar to that found for magnesium (Ion et al. 1982) and some minerals, which is discussed in §13.4.2. In the early stages of dynamic recrystallization, local boundary migration was observed and the orientations of the first layer of grains in the necklace were rather close to those of the original grains. However, as the structure developed with increasing strain, the orientations became more random, and this was attributed to the formation of annealing twins, and grain rotation arising from superplastic-type deformation in the dynamically recrystallized regions.

8.6 SUMMARY

The recovery, recrystallization and grain growth behaviour of ordered alloys shows many general similarities to disordered metals. Although the large number of material

and processing variables means that much remains to be clarified, the following conclusions can be drawn (Cahn 1990, Baker 2000):

- If deformed in the ordered state, ordered compounds recrystallize more rapidly than if deformed in the disordered state, and this is attributable to the larger stored energy.

- Grain boundary mobility is severely reduced by ordering, thus retarding both recrystallization and grain growth. Deviations from stoichiometry generally increase diffusivity and increase boundary mobility.

- During recovery of a weakly ordered alloy the hardness will usually decrease if $T > T_c$ and increase if $T < T_c$. Permanently ordered alloys tend to soften on recovery.

- In some weakly-ordered alloys, a temperature range may exist where recrystallization does not occur, even though it occurs at higher or lower temperatures.

- Weakly ordered alloys contain APBs after recrystallization, whereas strongly ordered alloys do not.

ThisPageIntentionallyLeftBlank

Chapter 9

RECRYSTALLIZATION OF TWO-PHASE ALLOYS

9.1 INTRODUCTION

Most alloys of commercial importance contain more than one phase, and therefore an understanding of the recrystallization behaviour of two-phase materials is of practical importance as well as being of scientific interest.

The second phase may be in the form of **dispersed particles** which are present during the deformation, or, if the matrix is supersaturated, the particles may **precipitate** during the subsequent anneal. In addition to conventional alloys which usually contain much less than 5% by volume of the second phase, we will make some reference to **particulate metal matrix composites** which contain large volume fractions of ceramic reinforcement and to **duplex alloys** in which the fractions of the two phases are similar.

The most important effects which second-phase particles have on recrystallization can be summarized as follows:

- **The stored energy and hence the driving pressure for recrystallization may be increased.**
- **Large particles may act as nucleation sites for recrystallization.**
- **Particles, particularly if closely spaced, may exert a significant pinning effect on both low and high angle grain boundaries.**

The first two effects tend to **promote** recrystallization, whereas the last tends to **hinder** recrystallization. Thus the recrystallization behaviour, particularly the kinetics and the resulting grain size and texture, will depend on which of these effects dominate.

The size, distribution and volume fraction of second-phase particles in an alloy are determined by alloy composition and processing, and by varying these, the metallurgist is able to control the microstructures and textures produced during recrystallization. The application of the principles discussed in this chapter to the processing of industrial alloys is therefore of considerable importance.

In this chapter we will examine the effects of particles on primary recrystallization, and in chapter 15 we will discuss some examples where the control of recrystallization by second-phase particles is of industrial significance. In most of this chapter we will be dealing with the situation in which a stable dispersion of particles is present during deformation and annealing. The particular case when recrystallization and phase transformation occur concurrently is considered in §9.8.

9.1.1 The particle parameters

As will be discussed in the following sections, the annealing behaviour of a particle-containing alloy is dependent on the **volume fraction, size, shape and spacing** of the particles, and we need to define these parameters. The determination and representation of the particle parameters is not a trivial problem, and for further details the reader is referred to Cotterill and Mould (1976) and Martin (1980). However, neither the theories nor the experimental results are currently of sufficient accuracy to warrant the use of very complicated parameters, and wherever possible, we will, for clarity, use the simplest relationships, and these are defined in appendix 2.8.

9.1.2 The deformed microstructure

Particles have a large effect on the microstructure developed during deformation, and this in turn affects the recrystallization behaviour. The deformation microstructures of two-phase alloys are discussed in detail in §2.9, and at this point we recall that there are three aspects of the deformation structure that are of particular importance in determining the behaviour of the material during subsequent annealing.

- **The effect of the particles on the overall dislocation density.** This provides the driving pressure for recrystallization.
- **The effect of the particles on the inhomogeneity of deformation in the matrix.** This may affect the availability and viability of the sites for recrystallization (§7.6.4).
- **The nature of the deformation structure in the vicinity of the particles** (§2.9.4). This determines whether particle stimulated nucleation of recrystallization (PSN) will be possible.

9.2 THE OBSERVED EFFECTS OF PARTICLES ON RECRYSTALLIZATION

Before we discuss the models and mechanisms of recrystallization in particle-containing alloys, we will look briefly at some of the experimental measurements and in particular at the parameters which appear to influence the recrystallization behaviour. It is not our intention to undertake a comprehensive review of the large number of experiments which have been carried out, but to emphasise what appear to be the key points which have emerged from these investigations. For a more detailed survey of the earlier literature, the reader is referred to Cotterill and Mould (1976) and to the reviews of Hansen (1975), Hornbogen and Köster (1978) and Humphreys (1979b).

9.2.1 The effect of the particle parameters

Both the recrystallization kinetics and the final grain size depend strongly on the **particle size** and the **interparticle spacing,** as was first demonstrated by Doherty and Martin (1962). It is difficult to separate the effects of these two parameters because there are few investigations in which they have been independently varied. It has frequently been found that by comparison with a single-phase alloy, recrystallization is retarded or even completely inhibited by closely spaced particles. With a sufficiently small spacing of thermally stable particles, it is possible to preserve the deformed/recovered microstructure up to the melting temperature of the matrix as shown in figure 9.1. The retention of the dislocation substructure at high temperatures provides a strengthening mechanism additional to that of the particles, in dispersion hardened alloys for high temperature structural applications (e.g. Kim and Griffith 1988). By comparison, alloys containing particles larger than ~1 μm and which are widely spaced, show accelerated recrystallization compared to the matrix as seen in figure 9.2a.

By varying the particle size and spacing, Doherty and Martin (1962) demonstrated that acceleration or retardation of recrystallization could be produced in the same alloy as

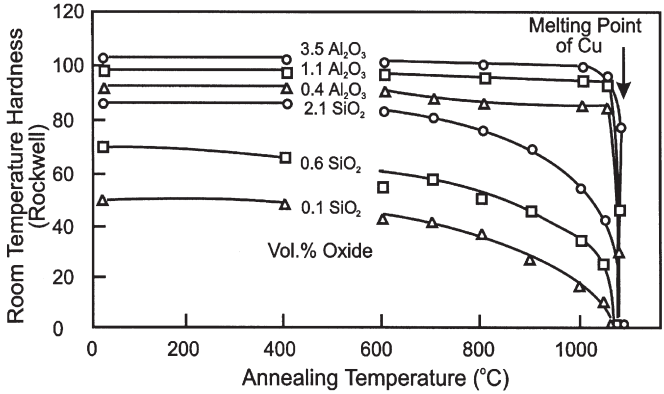

Fig. 9.1. The room temperature hardness of extruded and annealed dispersion-strengthened copper alloys, (after Preston and Grant 1961).

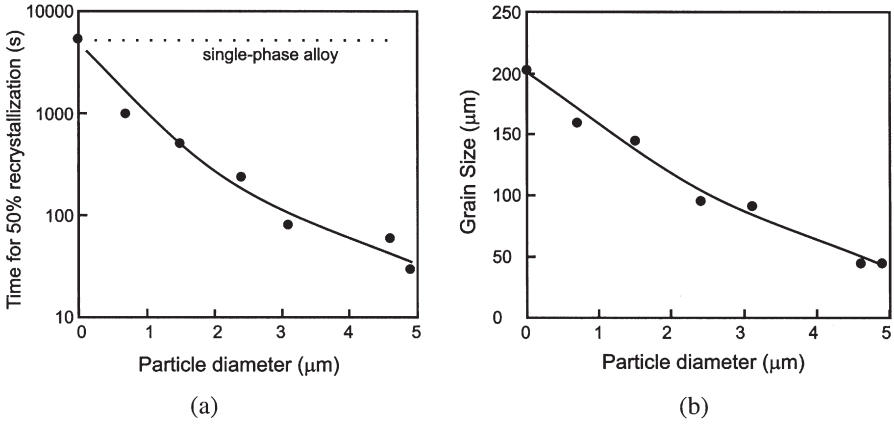

Fig. 9.2. The effect of particle size on recrystallization in Al–Si alloys reduced 50% by cold rolling and annealed at 300°C. (a) The time for 50% recrystallization, (b) The grain size after recrystallization, (data from Humphreys 1977).

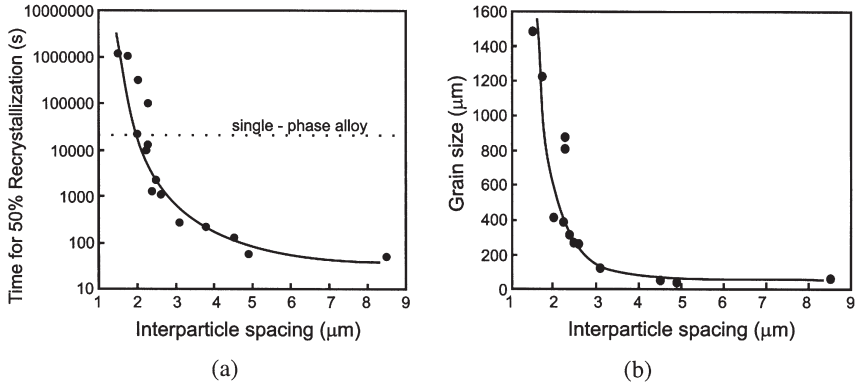

Fig. 9.3. The effect of interparticle spacing on the recrystallization of Al–Cu single crystals reduced 60% by rolling and annealed at 305°C. (a) The time for 50% recrystallization, (b) The grain size after recrystallization, (data from Doherty and Martin 1964).

shown in figure 9.3a. Figures 9.2b and 9.3b show that the final grain size becomes larger as recrystallization becomes more retarded. Figure 9.4 is a typical recrystallized microstructure in an alloy where recrystallization is retarded by small particles, and where the pinning of the grain boundaries by particles leads to a characteristic ragged boundary shape.

Analysis of a number of experimental investigations shows that the transition from accelerated to retarded recrystallization is primarily a function of the volume fraction

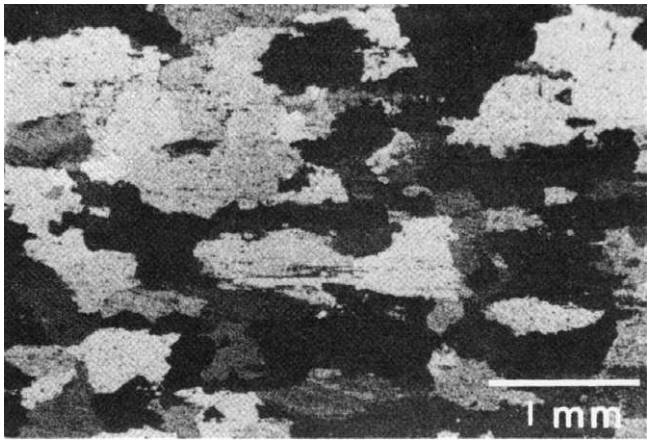

Fig. 9.4. Optical micrograph of cold rolled and recrystallized Al–Al_2O_3, (Hansen and Bay 1981).

(F_V) and particle radius (**r**), and that to a first approximation, retardation of recrystallization occurs when the parameter F_V/r is greater than $\sim 0.2\ \mu m^{-1}$ (Humphreys 1979b). If F_V/r is less than this value, it is often found that recrystallization is accelerated by comparison with the particle-free matrix, even if the particles are too small for particle stimulated nucleation of recrystallization (PSN) to occur. A later analysis of published experimental data by Ito (1988) suggested that a critical value of the interparticle spacing (λ), which is seen from equations A2.12 and A2.13 to be equivalent to $F_V^{1/2}/r$, may be a better indicator of the transition, although the experimental data are not good enough to distinguish between these two possibilities.

Acceleration of recrystallization is attributed both to the increased driving force arising from the dislocations generated by the particles during deformation (§2.9.2.1) and to PSN (§9.3). Accelerated recrystallization in alloys containing small particles is less commonly found in aluminium alloys than in copper alloys (e.g. Hansen 1975), and this is probably because the large amount of dynamic recovery in most aluminium alloys removes many of the geometrically necessary dislocations created at the particles. It will be shown in §9.3 that the condition for PSN is that the particle diameter should be greater than $\sim 1\ \mu m$. The criteria for acceleration/retardation and PSN indicate that the effect of volume fraction and particle size on recrystallization will be as shown schematically in figure 9.5. The position of the line AB depends on the amount of dynamic recovery in the material and will move to the right for aluminium and to the left for copper. Of course the figure is an over-simplification and, as will be discussed later in this chapter, there are other parameters which also have an effect on the recrystallization mechanisms and kinetics.

9.2.2 The effect of strain

There is considerable evidence from research on copper and aluminium alloys that the transition from retarded to accelerated recrystallization is affected by strain, and that an

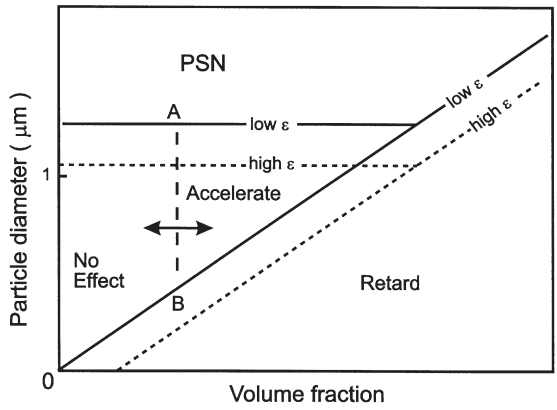

Fig. 9.5. Schematic diagram of the effect of particle size, volume fraction and prior strain on recrystallization kinetics and mechanism.

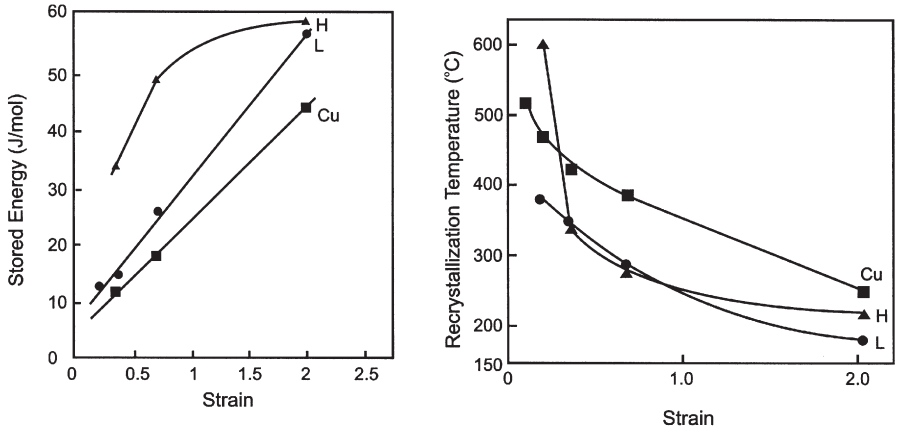

(a) (b)

Fig. 9.6. (a) The stored energy, (b) The recrystallization temperature in Cu–Al_2O_3 alloys compared with that of pure copper. The parameters of the alloys are d = 46 nm, $F_V = 1.5 \times 10^{-2}$ (H) and d = 38 nm, $F_V = 4 \times 10^{-3}$ (L), (Baker and Martin 1983b).

alloy which shows retarded recrystallization after small strains may show accelerated recrystallization after larger strains (fig. 9.5). An example of this effect in copper alloys containing small second-phase particles, is seen in figure 9.6. At low strains, particle pinning effects in alloy H cause the material to recrystallize at a higher temperature than pure copper. However, at larger strains, the increase in stored energy due to the particles increases the driving pressure for recrystallization, whilst the pinning pressure remains constant, and the material recrystallizes at a lower temperature than the pure copper.

9.2.3 The effect of particle strength

9.2.3.1 Coherent particles

Alloys of copper and nickel containing weak equiaxed coherent particles ($F_V/r \sim 2\ \mu m^{-1}$) which deform at the same rate as the matrix are found to show retarded recrystallization (Phillips 1966). During deformation, the particles become ribbons, but on annealing, they break-up and spheroidise. In such alloys, no geometrically necessary dislocations are produced (§2.9.1) and therefore there is no increase in the driving pressure for recrystallization. In addition, the effective interparticle spacing decreases during deformation, thus increasing the effectiveness of the particles in pinning boundaries. It is therefore to be expected that this type of alloy should exhibit retarded recrystallization more readily than one containing non-deformable particles.

9.2.3.2 Pores and gas bubbles

Pores or gas bubbles exert a pinning effect on boundaries in a similar manner to second-phase particles, and Bhatia and Cahn (1978) have reviewed their effect on recrystallization and grain growth. As no geometrically necessary dislocations are formed during deformation, pores and gas bubbles always tend to retard recrystallization and may also be dragged by the moving boundaries as discussed in §11.4.5. A dispersion of pores or gas bubbles has been found to inhibit recrystallization in many metals including platinum (Middleton et al. 1949), aluminium (Ells 1963), copper (Bhatia and Cahn 1978) and tungsten (Farrell et al. 1970). Thomson-Russell (1974) has shown that in doped tungsten, as the strain is increased, the bubble dispersion is progressively refined, leading to an increase in recrystallization temperature as shown in figure 9.7. Control of recrystallization in this way is a key part of the processing of tungsten filaments for incandescent light bulbs, as discussed by Dillamore (1978b).

9.2.3.3 Small plate-shaped particles

Even particles of a hard phase will fracture if small enough, because of the increasing stress due to the dislocations (equation 2.13 and fig. 2.34), particularly if they are in the

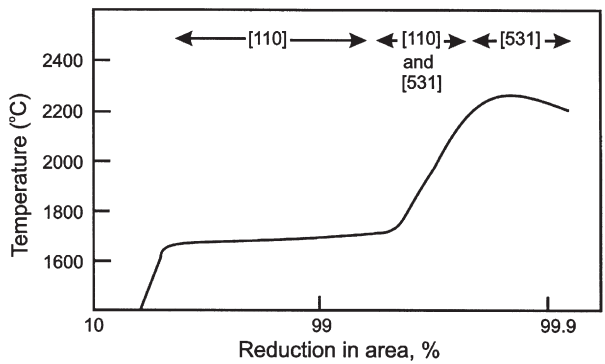

Fig. 9.7. Increase in recrystallization temperature and change in texture, with increasing strain in drawn tungsten wire, (after Thompson-Russell 1974).

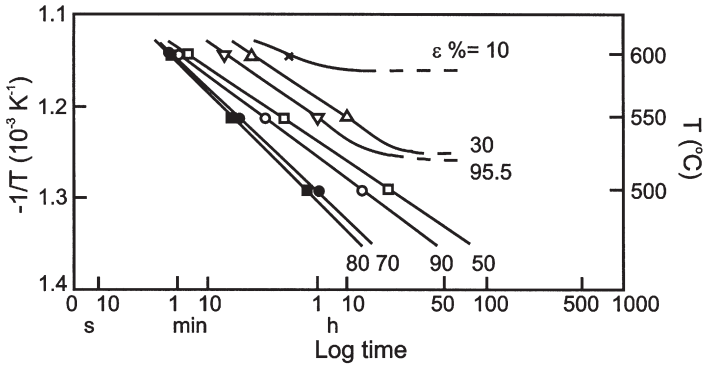

Fig. 9.8. The time to initiate recrystallization as a function of emperature (T) and cold work (ε%) in a steel containing a dispersion of 200 nm × 10 nm carbide plates, (Kamma and Hornbogen 1976).

form of plates. Kamma and Hornbogen (1976), investigating recrystallization in steels containing carbide plates (200 × 10 nm) found that for rolling reductions of up to 90%, the plates fractured, resulting in the formation of deformation bands. Recrystallization was nucleated at the intersection of these deformation bands, leading to rapid recrystallization. However, at larger strains, the refinement of the dispersion led to more homogeneous deformation, increased particle pinning and to slower recrystallization as shown in figure 9.8.

9.2.4 The effect of microstructural homogenisation

There has been considerable discussion in the literature as to whether or not "homogenisation of slip by a fine dispersion of particles" contributes to the retardation of recrystallization by removing the lattice curvatures necessary for nucleation, although this is now thought to be unlikely.

As discussed in §2.9.2.2, there is evidence that the presence of small, and very closely spaced particles affects the cell or subgrain structure resulting in less misoriented cells or subgrains (table 2.7). However, it is now clearly established (§7.6.4) that nucleation does not occur at cells or subgrains in regions of uniform orientation but at microstructural heterogeneities associated with large strain gradients. These sites, e.g. grain boundaries, deformation bands, shear bands and deformation zones at large particles, are still present in alloys showing retarded recrystallization (e.g. Chan and Humphreys 1984b). However, their effectiveness is reduced by the pinning effects of particles on both high and low angle grain boundaries, and the recrystallization kinetics are determined mainly by the fine particle dispersion.

We therefore conclude that the effects of particles on recrystallization may be analysed primarily in terms of particle stimulated nucleation and boundary pinning, and will consider these mechanisms in further detail.

9.3 PARTICLE STIMULATED NUCLEATION OF RECRYSTALLIZATION

PSN has been observed in many alloys, including those of aluminium, iron, copper and nickel and is usually only found to occur at particles of diameter greater than approximately 1 μm (Hansen 1975, Humphreys 1977), although a lower limit of 0.8 μm was inferred from the indirect measurements of Gawne and Higgins (1971) on Fe–C alloys.

In most cases a maximum of one grain is found to nucleate at any particle, although there is evidence that multiple nucleation occurs at very large particles. This is clearly seen in figure 9.9, one of the first micrographs to demonstrate PSN.

There are four particularly significant aspects of particle stimulated nucleation of recrystallization.

- Many **industrial alloys,** particularly those of iron and aluminium, contain large second-phase particles and thus PSN is a likely recrystallization mechanism in many engineering alloys.
- Unlike most other recrystallization mechanisms the nucleation sites are well defined regions of the microstructure which can be altered by alloying or processing. Thus the number of potential nuclei and hence the **recrystallized grain size** may be controlled.
- The orientations of the recrystallization nuclei produced by PSN will in general be different from those produced by other recrystallization mechanisms. We thus have the potential to exercise some control over the **recrystallization texture** by regulating the amount of PSN (§12.4.3, §15.2.2, §15.2.3).
- Because the interaction of dislocations and particles is temperature dependent, PSN will only occur if the prior deformation is carried out below a critical temperature or above a critical strain rate. This effect is considered in §13.6.4.

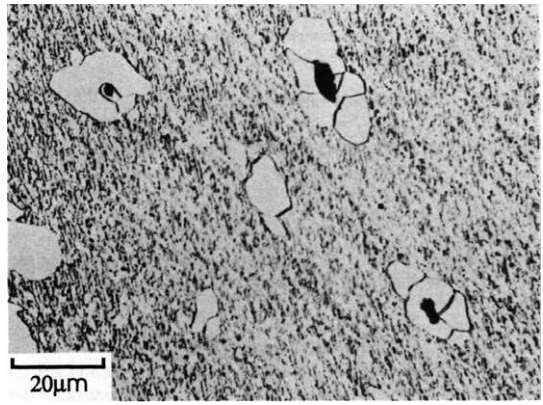

Fig. 9.9. Particle stimulated nucleation of recrystallization at oxide inclusions in iron, (Leslie et al. 1963).

9.3.1 The mechanisms of PSN

Although specimens which are annealed to produce recrystallization nuclei and which are subsequently examined metallographically, can provide information about the kinetics of recrystallization and the orientation of the new grains, there is little that can be deduced from these specimens about the mechanisms of nucleation. Most of the direct evidence has come from in-situ observations in the HVEM. From a study of recrystallization at particles in rolled aluminium, Humphreys (1977) concluded that:-

- Recrystallization originates at a pre-existing subgrain within the deformation zone, but not necessarily at the particle surface.
- Nucleation occurs by rapid sub-boundary migration.
- The grain may stop growing when the deformation zone is consumed.

Later in-situ work (Bay and Hansen 1979), together with work on bulk annealed specimens (Herbst and Huber 1978) has supported these general conclusions.

The electron micrographs of figure 9.10, part of an in-situ HVEM annealing sequence, show the occurrence of particle-stimulated nucleation in aluminium originating in the arrowed region close to the interface. It may be seen that the PSN grain does not grow very large, and is eventually surrounded by other grains. This is a common feature of PSN as discussed in §9.3.5.

The kinetics of nucleation, as determined by in-situ HVEM annealing of Al–Si, are illustrated in figure 9.11. The rapid annealing of the deformation zone, shown in figure 9.11a is due to the presence of a large orientation gradient and small subgrain size (§6.5.3.4), compared to the matrix, and the drop in the maximum misorientation within a deformation zone shown in figure 9.11b is consistent with the observation that the nucleus may not originate in the region of highest misorientation at the interface, but elsewhere in the deformation zone.

In-situ and bulk annealing experiments indicate that PSN occurs by a similar micro-mechanism to the nucleation of recrystallization in regions of heterogeneous deformation in single-phase materials, and the models of PSN are related to the models of recrystallization at transition bands discussed in §7.6.4.2.

Using the largely empirical model of the deformation zone discussed in §2.9.4 we can examine the occurrence of PSN more quantitatively. The deformation zone has a gradient of both orientation and dislocation density as given by equations 2.24 and 2.25. We will assume that recrystallization originates by the growth of subgrains within the deformation zone, and as shown in figure 9.12, also consider the possibility that this may occur at the particle surface (A), in the centre of the zone (B) or at the periphery (C).

9.3.1.1 Formation of a nucleus within the zone

A necessary criterion for the formation of a nucleus is that the maximum misorientation within the deformation zone (θ_{max}) is sufficient to form a high angle boundary with the matrix, and the conditions for nucleation therefore depend on both the particle size (equation 2.21 and the strain (fig. 2.36) and this condition is plotted in figure 9.13b.

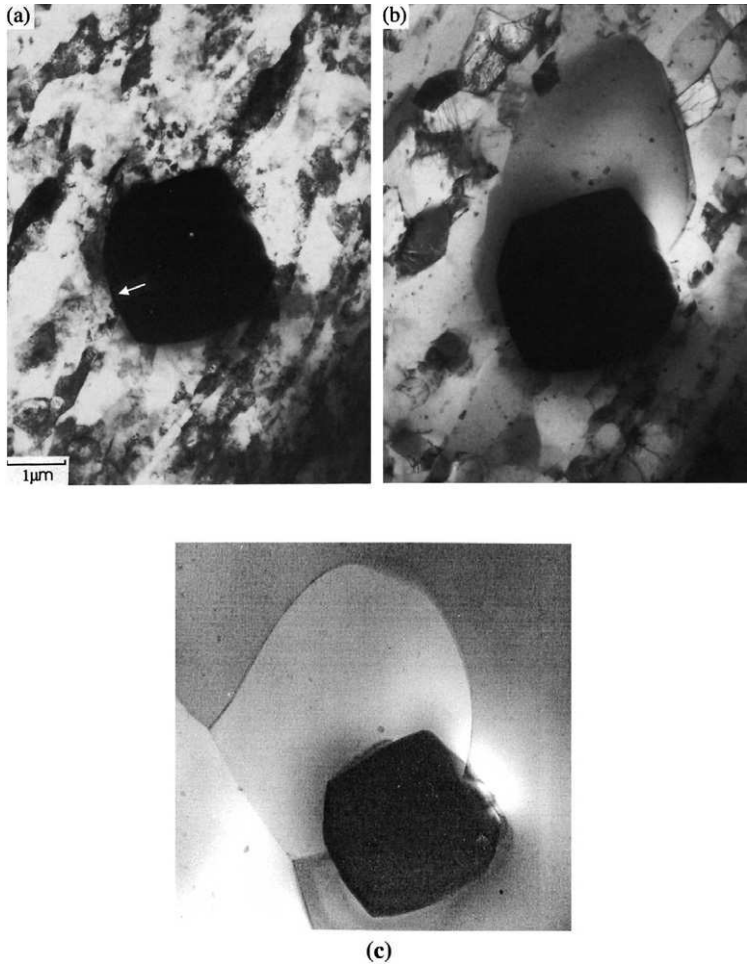

Fig. 9.10. In-situ HVEM annealing sequence of Al–Si. Note the very small subgrain size in the deformation zone above the particle. (a) Recrystallization originates in the arrowed region of the deformation zone close to the particle, (b) Recrystallization has consumed the deformation zone, (c) Further growth of the PSN grain is prevented by recrystallization which has originated elsewhere (Humphreys 1977). This and other videos of PSN may be viewed at www.recrystallization.info.

From the consideration of subgrain growth in an orientation gradient (§6.5.3.4) and equation 6.38, we see that to a first approximation, the growth velocity of a subgrain in a region of large orientation gradient is independent of subgrain size and is proportional to the magnitude of the orientation gradient. As a subgrain grows in an orientation gradient, it increases its misorientation with neighbouring subgrains. When this misorientation has reached that of a high angle grain boundary (e.g. 10–15°) we can say

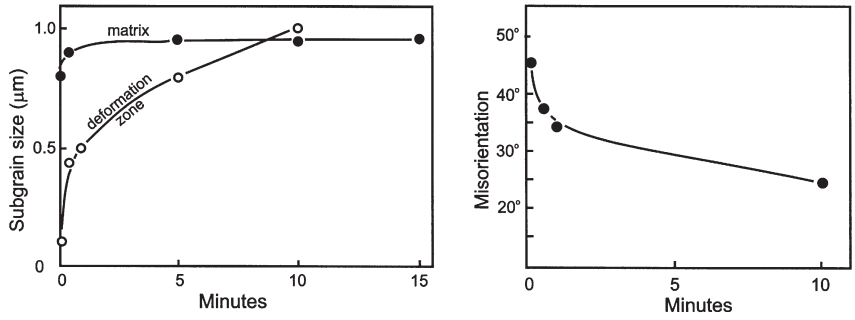

Fig. 9.11. Changes in the subgrain size and misorientation within the deformation zone of Si particles in Al as determined by in-situ HVEM annealing at 250°C. (a) Growth kinetics, (b) The maximum misorientation within the deformation zone, (Humphreys 1980).

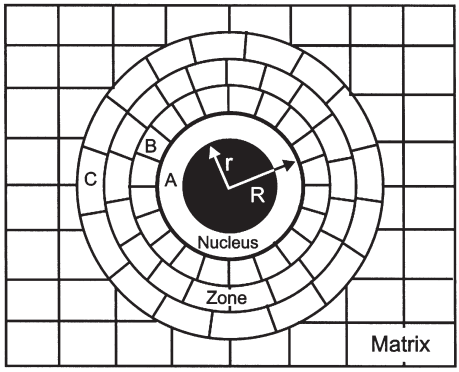

Fig. 9.12. Growth of a nucleus within the deformation zone.

that a potential recrystallization nucleus has been formed. The size to which a subgrain must grow to achieve a high angle boundary will be inversely proportional to the orientation gradient, and combining these two factors suggests that the **time** for the formation of a nucleus will be inversely proportional to the **square of the orientation gradient.** Therefore the formation of a nucleus close to the particle surface, where the orientation gradient is greatest (fig. 2.35), will be strongly favoured.

9.3.1.2 Growth of the nucleus

Once a nucleus which is significantly larger than the neighbouring subgrains is formed, then the above model which is based on uniform subgrain growth, is less appropriate than a model of the type shown in figure 9.12. The nucleus, which is assumed to have a high angle boundary of energy γ_b, is subjected to two pressures. A retarding pressure (P_C) due to its radius of curvature as given by equation 7.3, and a driving pressure (P_D)

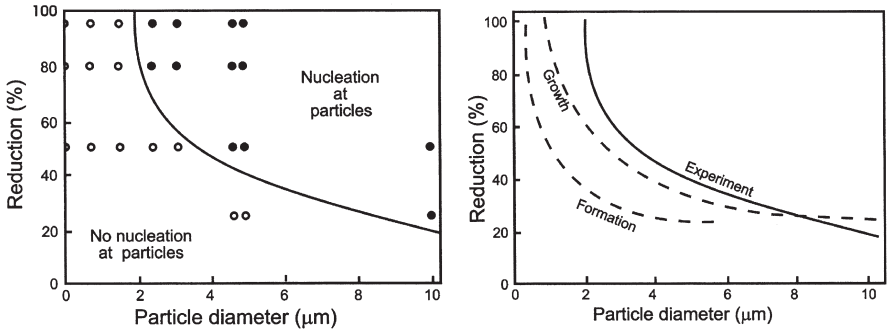

Fig. 9.13. (a) The effect of rolling reduction and particle size on the occurrence of PSN, (Humphreys 1977), (b) Comparison of the experimental data with theoretical predictions of nucleus formation and growth.

due to the dislocation density (ρ) or stored energy (E_D) of the material into which the nucleus is growing, as given by equation 7.2. The nucleus, of diameter D will grow if $P_D > P_C$, i.e.

$$D \geq \frac{4\gamma_b}{\alpha\rho G b^2} \tag{9.1}$$

where $\alpha \sim 0.5$.

The simplest analysis of PSN assumes that the critical condition for PSN is that at which the nucleus has a radius of curvature equal to half the particle diameter (i.e. R = r in fig. 9.12) and therefore D in equation 9.1 is replaced by the particle diameter (d). It is also assumed that at this stage the deformation zone has been consumed and that the driving force is provided by the matrix stored energy (E_D). The critical particle diameter (d_g) which will provide a nucleus able to grow beyond the deformation zone is therefore

$$d_g \geq \frac{4\gamma_b}{\alpha\rho G b^2} = \frac{4\gamma_b}{E_D} \tag{9.2}$$

Calculation of the stored energy or dislocation density in the matrix outside the deformation zone is more difficult as discussed in §2.2.1 and §2.9.2, although an estimate may be made by using equation 2.19 and taking the slip distance (L) as the spacing between the large particles. The dislocation density increases with strain and there will therefore be a **critical particle diameter (d_g) which is a function of strain,** below which the nucleus will not grow beyond the deformation zone and which therefore defines the conditions under which PSN will occur. The above analysis neglects the driving force provided by the higher dislocation density of the deformation zone, and if we take the variation of ρ within the zone as given by equation 2.25, then a more accurate estimate of the growth condition may be calculated.

Experimental measurements of the effects of particle size and strain on the occurrence of PSN in single crystals of Al–Si deformed by cold rolling, are shown in figure 9.13a. It is seen that the critical particle size for PSN ($d_{\underline{g}}$) decreases with increasing strain as expected. In figure 9.13b we compare the experimental data (represented by the solid line of fig. 9.13a) with the condition for **growth** calculated from equation 9.1, using the dislocation density in the deformation zone as given by equation 2.25. There is a reasonable fit between experiment and model, although as discussed above there are considerable uncertainties in the analysis. In figure 9.13b we also show the condition for the **formation** of a nucleus as discussed in §9.3.1.1. From a comparison of the criteria for formation and growth it is seen that following low temperature deformation **it is the condition for growth of the nucleus which is the determining factor for PSN.**

9.3.2 The orientations of grains produced by PSN

As the nuclei are thought to originate within the deformation zones, their orientations will be restricted to those present in these zones (§2.9.4).

9.3.2.1 Experiments on single crystals

Experiments on single crystals of Al–Si deformed in tension (Humphreys 1977, 1980) have established that the orientations of nuclei lie within the orientation spread of the deformation zone. Annealing of lightly rolled crystals of these alloys resulted in a strong recrystallization texture, which was rotated from the deformation texture by 30–40 degrees about a $<112>$ axis as shown in figure 9.14.

The use of EBSD has allowed much more detailed investigation of the orientations of nuclei, and figure 9.15, obtained from a partly recrystallized rolled crystal of nickel

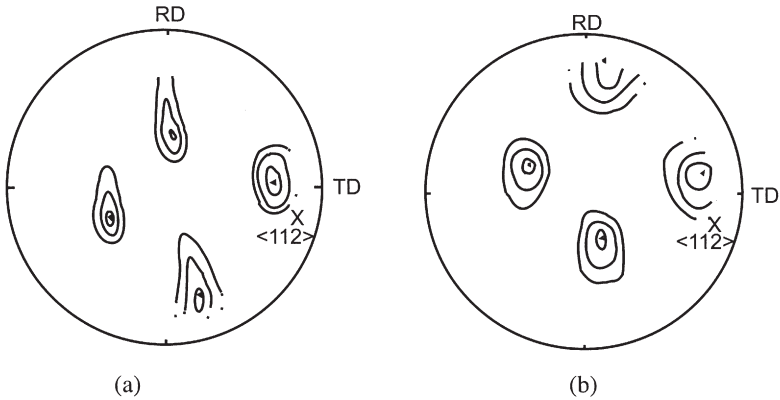

Fig. 9.14. 111 pole figures of (a) the deformation, and (b) the recrystallization texture of a 65% deformed single crystal of Al containing 4.6 μm Si particles. The deformed and recrystallized orientations are related by a rotation of ~40° about an axis close to the marked $<112>$ direction, (Humphreys 1977).

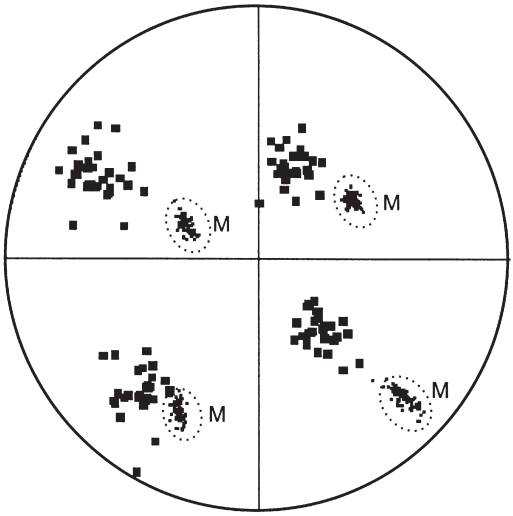

Fig. 9.15. 111 pole figure of EBSD data showing the relationship between the matrix orientations (**M**) and PSN nuclei (■) in a rolled and partially recrystallized Ni–SiO_2 single crystal, (Humphreys 2000).

containing large SiO_2 particles (Humphreys 2000), shows the orientations of both the deformed matrix and the recrystallization nuclei. Figures 9.14 and 9.15 show that **although the orientation spread of the nuclei is greater than that of the deformed matrix, the PSN nuclei are not randomly oriented.**

Further information about the orientations of PSN grains has been obtained from the annealing of oriented particle-containing single crystals which had been deformed in plane strain compression (see §2.9.4.2). Figure 9.16 shows 111 pole figures from particle-containing crystals of the $\{110\}<001>$ Goss orientation (Ferry and Humphreys 1996b). The orientation of the matrix crystal does not alter during deformation, or show significant orientation spread. Figures 9.16b–d show the orientations of PSN nuclei after various strains. Comparison of figures 9.16a and c shows that the nuclei have similar orientations to those of the particle deformation zones, and figures 9.16b–d show that although the nuclei have a greater spread of orientations at larger strains, they do not become random, and tend to be misoriented about the TD to the deformed matrix. Similar experiments on $\{001\}<110>$ crystals (Ardakani and Humphreys 1994) and $\{011\}<01\bar{1}>$ crystals (Ferry and Humphreys 1996c) have produced comparable results.

9.3.2.2 PSN in deformed polycrystals

Kalu and Humphreys (1988) determined the orientation of deformation zones at particles using a TEM microtexture technique and subsequently annealed the specimens in an HVEM until nucleation occurred. The microtextures were then re-measured and the orientations of the nuclei were found to lie within the deformation zones.

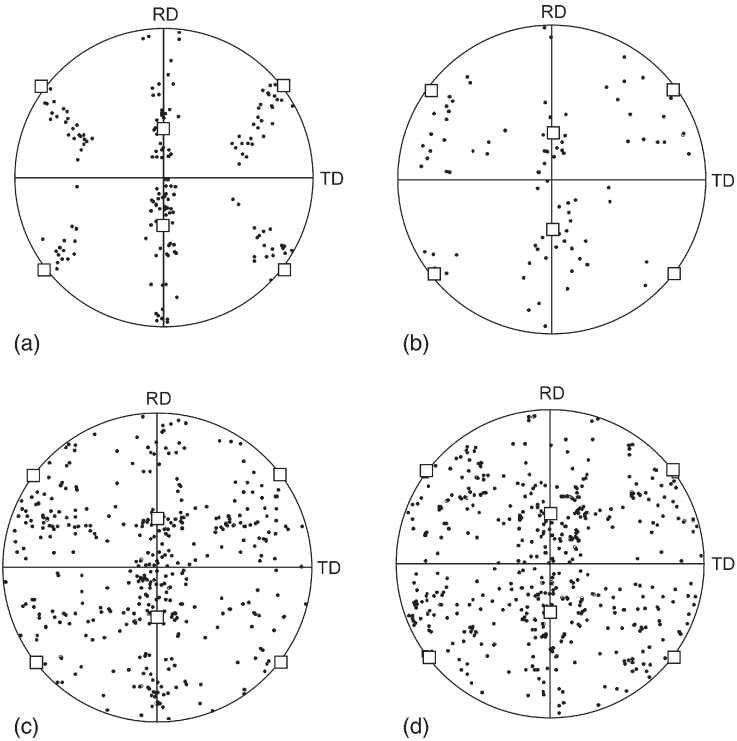

Fig. 9.16. 111 pole figures of EBSD data from $\{110\}<001>$ Al–0.6%Si crystals deformed in channel die plane strain compression. (a) Orientations in the deformation zones, $\varepsilon = 1.4$. Orientations of PSN nuclei after true strains of, (b) 0.7, (c) 1.4, and (d) 2.2. The matrix orientation, which does not change during deformation is shown as open squares, (Ferry and Humphreys 1996b).

Experiments on heavily rolled polycrystals containing large particles have usually shown that the nuclei are either weakly textured or are approximately randomly oriented (e.g. Wassermann et al. 1978, Herbst and Huber 1978, Chan and Humphreys 1984c, Humphreys and Brough 1997, Engler 1997, Hutchinson et al. 1998).

In summary, we find that in the case of deformed single crystals, a fairly sharp PSN texture occurs and this arises from the restricted range of orientations present in the deformation zones. In the case of heavily deformed polycrystals, each grain, or coherent portion of a grain will have several deformation zones, which, after large strains may have large misorientations. The range of orientations for potential nuclei is therefore much greater and a single grain will give rise to nuclei spread over a wide range of orientations, thus leading to a weakening of the texture. **Although the nuclei are not randomly oriented with respect to the deformed material, the spread of orientations around what may already be a weak texture may, when averaged over the whole polycrystalline specimen, result in an almost random distribution of nuclei orientations.**

9.3.2.3 The influence of PSN on the recrystallization texture

If PSN is the only nucleation mechanism, then the final recrystallization texture will, as discussed above, generally be weak. In alloys in which the number of particles is large, this is often the case. However, in alloys with low volume fractions of particles, or where there is also a pinning effect from small particles (§9.5) it is found that other texture components, are strongly represented in the final texture. This indicates a contribution from grains originating at microstructural features other than particles, a point which is discussed further in §9.3.5 and §12.4.3.

9.3.3 The efficiency of PSN

An important industrial application of PSN is in controlling the grain size of recrystallized alloys, and in particular, the production of fine-grained material. If each particle successfully nucleates one grain (i.e. an efficiency of nucleation equal to 1), the resultant grain size (**D**) will be directly related to the number of particles per unit volume and the grain size will be related to the volume fraction $\mathbf{F_V}$ of particles of diameter **d** by:

$$D \approx dF_V^{1/3} \tag{9.3}$$

The grain size predicted using this criterion is shown in figure 9.17.

If several grains nucleate at a particle, an efficiency of greater than 1 may occur. However, as multiple nucleation generally only occurs for particles larger than 5–10 μm, this is rarely achieved. If the particle size is close to the minimum (fig. 9.13), then the nucleation

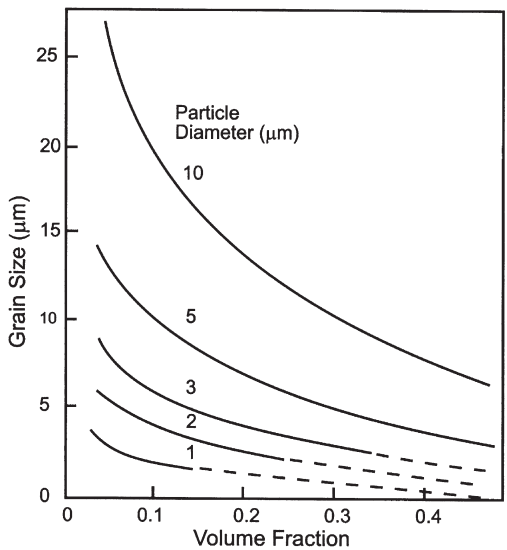

Fig. 9.17. The predicted grain size for a PSN efficiency of unity. The dashed lines show conditions under which Zener pinning effects may prevent discontinuous recrystallization, (Humphreys et al. 1990).

efficiency is very low (Humphreys 1977, Wert et al. 1981, Ito 1988), and the predicted small grain size is not achieved. As nuclei are essentially in competition with each other, we only obtain a high efficiency if all nucleation events occur simultaneously (site saturation nucleation), and if the grains grow at similar rates. This condition may be met for alloys with large, widely spaced particles, but if the particles are closely spaced, or, if growth of nuclei is affected by a fine dispersion of particles, then the nucleation efficiency may decrease markedly as will be discussed further in §9.5 and §9.6.

It is likely that particles situated in regions where large strains and strain gradients occur, such as at grain boundaries, shear bands etc. may provide more favoured nucleation sites than other particles, thus reducing the overall efficiency of nucleation. There is some evidence of this effect in Al–Mn and Al–Fe–Si alloys (Sircar and Humphreys 1994).

9.3.4 The effect of particle distribution

There is evidence that nucleation occurs preferentially at pairs or groups of particles as shown in figure 9.18. This may occur even if the individual particles are below the critical size for nucleation. This has been detected statistically (Gawne and Higgins 1971), from metallographic observations (Herbst and Huber 1978, Weiland 1995) and from in-situ annealing (Bay and Hansen 1979). A detailed study of the distribution of recrystallization nuclei in Al–Si specimens containing particles of diameters close to the critical size (Koken et al. 1988), has also shown that under these conditions, nucleation is favoured in sites of particle clustering. The effect of the clustering of nuclei on recrystallization kinetics is discussed in §7.4.1.

9.3.5 The effect of PSN on the recrystallized microstructure

If recrystallization originates solely by PSN, it would be expected from the preceding discussions that the fully recrystallized microstructure would comprise equiaxed grains

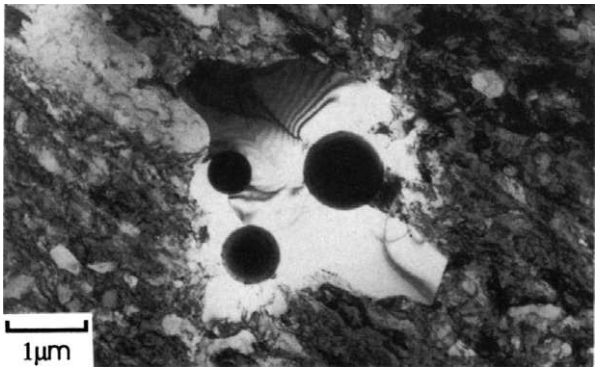

Fig. 9.18. Nucleation of recrystallization at a cluster of SiO_2 particles in nickel during an in-situ HVEM anneal, (Humphreys 1980).

of a size given by equation 9.3, and that the texture would be rather weak. We rarely find that this is the case, and it is instructive to examine one of the simplest cases. We consider the recrystallized microstructures in the particle-containing single crystals of the $\{110\}<001>$ Goss orientation which have already been considered in §9.3.2.1. Crystals of this orientation are particularly interesting because apart from large particles, no other sites for recrystallization are formed on deformation (§6.5.2.1). The microstructures of crystals deformed in plane strain compression to strains of 0.7 and 1.4 and fully recrystallized are shown in figure 9.19. At the lower strain, very small grains associated with the particles, and clearly formed by PSN are seen. However, they exist as 'island' grains within much larger grains, (a similar effect to that seen in the in-situ annealing sequence of figure 9.10c). At the larger strain, an equiaxed microstructure with a grain size corresponding to a PSN efficiency of 0.85 is seen. The preferential growth of these larger grains can be seen during the early stages of recrystallization (Ferry and Humphreys 1996c), and they have been identified as having

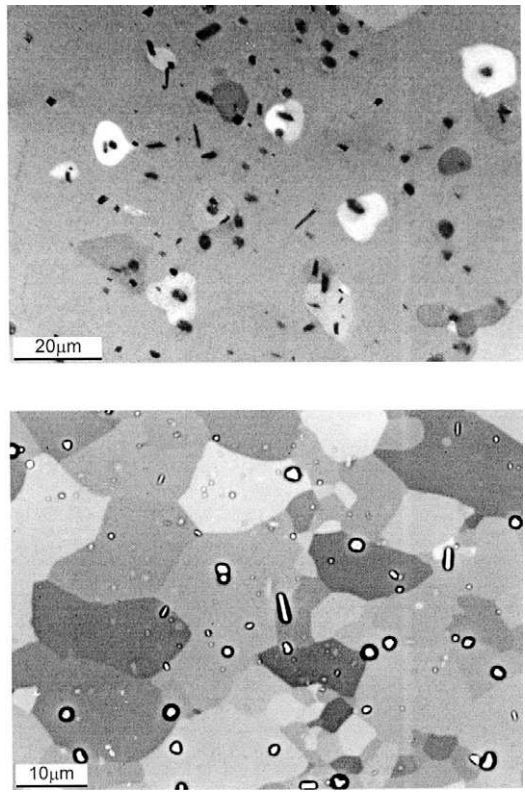

Fig. 9.19. The recrystallized microstructures in a deformed and annealed $\{110<001>$ crystal of Al–0.8%Si containing 3 μm silicon particles. (a) PSN grains left as islands within rapidly growing grains ($\varepsilon = 0.7$), (b) Equiaxed grains after larger strain ($\varepsilon = 1.4$), (Ferry and Humphreys 1996b).

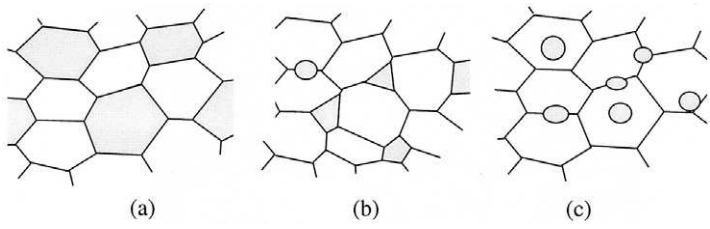

Fig. 9.20. The predicted effect of the relative grain boundary mobilities (R_M) on the microstructures developed during recrystallization. (a) $R_M = 1$. A normal microstructure, (b) $R_M = 1.2$. Small grains are often found at boundaries, (c) $R_M = 3$. The slow growing grains are often left as islands, (Humphreys et al. 1995).

orientations within the particle deformation zones, showing them also to be formed by PSN. These faster growing grains have a restricted range of orientations and are found to be oriented with respect to the matrix by $\sim 45^\circ$ $<111>$ or $24^\circ <150>$. The conclusion is that grains of certain orientations grow significantly faster than others, particularly in the lightly deformed material. This is a good example of "oriented growth" which is discussed in §12.3.2. The misorientations of the faster growing grains are not those associated with the most mobile boundaries in aluminium (§5.3.2), because PSN has produced only a limited range of orientations, and these grains are the fastest growing orientations of those available.

The development of a recrystallized microstructure in which recrystallizing grains have boundaries of two different mobilities, defined by the mobility ratio ($\mathbf{R_M}$), has been modelled (Humphreys et al. 1995) using a computer Avrami simulation (see §16.2.5). In figure 9.20, the effect of different values of R_M on the fully recrystallized microstructure is seen. If there is no difference in mobility ($R_M = 1$), the normal grain structure is formed (fig. 9.20a). However, as R_M increases, we first find small grains at the boundaries of the large grains (fig. 9.20b) and then island grains (fig. 9.20c). In addition to the change in microstructure as R_M varies, an associated change in the recrystallization texture is predicted.

Similar island grain microstructures have been found in other recrystallized two-phase crystals (Ardakani and Humphreys 1994), and also during the recrystallization of alloys containing bimodal particle distributions, e.g. Chan and Humphreys (1984b), Humphreys and Brough (1997), where the pinning effects of small particles magnify what may be quite small differences in boundary mobilities (§9.6).

9.4 PARTICLE PINNING DURING RECRYSTALLIZATION (ZENER DRAG)

9.4.1 Nucleation of recrystallization

In Chapter 6, we discussed the ways in which a dispersion of particles might hinder recovery and showed how pinning was particularly effective when the interparticle spacing and subgrain or cell sizes were similar. Because recrystallization usually initiates via local recovery, it is clear that particles may inhibit nucleation. There is little quantitative information on the sites for recrystallization nucleation in single-phase

alloys, and consequently it is difficult at present to develop a satisfactory model for the effect of particles on recrystallization nucleation in alloys containing only small particles. The effects of Zener drag on PSN are considered in §9.5.

9.4.1.1 Nucleation at deformation heterogeneities

The effect of particles on recrystallization nucleation at deformation heterogeneities such as deformation bands or shear bands may be discussed in terms of the **particle-limited subgrain size,** which is the largest size to which a subgrain can grow in a two-phase alloy (§11.4.2). If this parameter is small enough to prevent the growth of subgrains to a size such that a high angle grain boundary is formed, then nucleation will be suppressed.

If nucleation is taking place in a region of orientation gradient Ω, the amount of subgrain growth necessary to form a high angle boundary of misorientation θ_m is $\sim\theta_m/\Omega$. The criterion for suppression of nucleation would then, to a first approximation be

$$D_{lim} < \frac{\theta_m}{\Omega} \tag{9.4}$$

where, as discussed in §11.4.2.3, D_{lim} will be given by equation 11.30 for particle volume fractions less than ~0.05, and equation 11.34 for larger volume fractions. Thus the criterion for inhibition is

$$\frac{F_V}{r} > \frac{4\alpha\Omega}{3\theta_m} \qquad (F_V < 0.05) \tag{9.5}$$

$$\frac{F_V^{1/3}}{r} > \frac{\beta\Omega}{\theta_m} \qquad (F_V > 0.05) \tag{9.6}$$

For alloys containing low volume fractions of particles, using $\alpha = 0.35$, $\beta = 3$ as discussed in §11.4.2.3, taking θ_m as 15° and $\Omega = 5°\ \mu m^{-1}$ (Ørsund et al. 1989), then nucleation will be suppressed if $F_V/r > 0.15\ \mu m^{-1}$. This is in reasonable agreement with the experimental observations discussed in §9.2.1. The orientation gradients will tend to increase with increasing strain and therefore we expect that the critical value of F_V/r or $F_V^{1/3}/r$ necessary to suppress recrystallization will increase with increasing strain, as has been reported (§9.2.2).

9.4.1.2 Strain induced boundary migration (SIBM)

Recrystallization by strain induced boundary migration (SIBM) was discussed in §7.6.2. A dispersion of pinning particles will provide a pinning pressure (P_Z) opposing the driving pressure, and the critical bulge sizes for both single and multiple subgrain SIBM (equations 7.42 and 7.43 will then be modified by the replacement of **P** with **P–P$_Z$.** As P_Z increases, the critical bulge sizes for nucleation will increase, becoming infinite when $P_Z = P$. The effect of particle pinning on these mechanisms is shown in figure 7.30b for the case when $P_Z = P/2$. Although both mechanisms are inhibited by the particles, single grain SIBM is much more affected.

Studies of SIBM under conditions of particle pinning (Higginson et al. 1997, Higginson and Bate 1999) have shown that the SIBM bulge can be up to several hundred microns

in length when P_Z is large. This **broad front SIBM,** is also found in alloys in which the precipitation occurs during annealing (§9.8.3), and an example of this is shown in figure 9.27.

Under conditions where SIBM is affected by particle pinning, it is frequently found that this results in the preferential growth of certain texture components (§12.4.3), particularly cube-oriented grains (Higginson et al. 1997, Higginson and Bate 1999). This may be due to the decreased substructure drag during SIBM of cube grains, or to a reduced Zener pinning of boundaries of lower energy (§4.6.1.1).

9.4.2 Growth during recrystallization

During primary recrystallization, a growing grain in an alloy containing a dispersion of particles is acted on by two opposing pressures, the driving pressure for growth ($\mathbf{P_D}$) as given by equation 7.2 and the Zener pinning pressure **($\mathbf{P_Z}$)** arising from the particles, as given by equation 4.24. In the early stages of growth, we should also take into account the retarding pressure due to boundary curvature ($\mathbf{P_C}$) (equation 7.3). The net driving pressure for recrystallization (**P**) is thus

$$P = P_D - P_Z - P_C = \frac{\alpha \rho G b^2}{2} - \frac{3 F_V \gamma_b}{d} - \frac{2\gamma_b}{R} \qquad (9.7)$$

Recrystallizing grains will not grow unless P is positive and we therefore expect recrystallization growth to be suppressed when F_V/r is greater than a critical value, which will be larger for small driving pressures (i.e. low strains). Qualitatively, this is in agreement with the experimental results discussed in §9.2.1 in that alloys in which F_V/r is large are found to recrystallize more slowly than an equivalent particle-free matrix, and that a transition from retardation to acceleration occurs when a critical strain is exceeded.

Several investigators (e.g. Baker and Martin 1980, Chan and Humphreys 1984b) have found, from analyses of driving and pinning pressures (e.g. equation 9.7), that the Zener pinning pressure (P_Z) is too small to account for the retardation of recrystallization **growth** in their materials. However, the values of F_V/r in these investigations ranged from 0.2 to 0.6 μm^{-1}, which are consistent with particle-inhibition of **nucleation** according to equation 9.6.

We therefore conclude that Zener pinning plays a major role in retarding primary recrystallization. This may affect both the nucleation and the growth of the grains, and may modify the recrystallization texture. Experiment and theory suggest that the critical parameter in determining the recrystallization kinetics is F_V^n/r, where $1/3 < n < 1$, although further work is required in this area.

9.5 BIMODAL PARTICLE DISTRIBUTIONS

Many commercial alloys contain both large (> 1 μm) particles, which will act as sites for PSN, and small particles, spaced sufficiently closely to pin the migrating boundaries.

The recrystallization of such alloys has been analysed by Nes and colleagues (e.g. Nes 1976). In such a situation, the driving pressure (P_D) is offset by the Zener pinning pressure (P_Z) and the critical particle size for the growth of a nucleus (equation 9.2) now becomes

$$d_g = \frac{4\gamma_b}{P_D - P_Z} = \frac{4\gamma_b}{(\rho G b^2/2) - (3F_v\gamma/2r)} \tag{9.8}$$

where F_V and r refer to the small particles.

Thus, as the Zener pinning force increases, the critical particle diameter for PSN increases. As there will be a distribution of particle sizes in a real alloy, this means that less particles are able to act as nuclei, and that the recrystallized grain size will increase.

An alternative analysis of the effects of a fine particle dispersion on PSN may be made by extending that of §9.4.1. The orientation gradient (Ω) is in this case that at the large particles, and this is given by equation 2.24.

The number of particles capable of acting as nuclei (N_d) is the number of particles of diameter greater than d_g. If other nucleation sites are neglected and if we assume **site saturated** nucleation, then the grain size (D_N), will be given approximately by:-

$$D_N = N_d^{-1/3} \tag{9.9}$$

The recrystallization kinetics of bimodal alloys in which there is significant Zener pinning are often found to be **similar to those of alloys containing a similar dispersion of only small particles** (Hansen and Bay 1981, Chan and Humphreys 1984b, Humphreys and Brough 1997). The latter two investigations found an unusual recrystallized **'island' grain structure** in which small isolated grains from less successful nuclei were engulfed by more rapidly growing grains. This is a consequence of some grains having a much faster growth rate than others. This may be due to the factors discussed in §9.3.5, but may also be due to the PSN sites producing smaller nuclei than sites such as SIBM, so that P_C is larger for the PSN grains and consequently the initial driving pressure (equation 9.7) and thus growth rate is slower. It is often found that in such a situation, where particle pinning restricts the growth of some grains, there is also **orientation selection,** and the larger grains which dominate the recrystallized texture result in a much stronger texture than if PSN grains dominate (§12.4.3).

9.6 THE CONTROL OF GRAIN SIZE BY PARTICLES

There is considerable interest in the use of particles to control both the grain size and the texture of alloys. This is of importance in many structural steels, aluminium alloys used for cans, and superplastic alloys, and in chapter 15, we will discuss some cases in more detail. In the present discussion, we show how the effects of particles on recrystallization which were discussed earlier, can be used to control grain size during thermomechanical processing. The discussion below is largely based on models developed by Nes (1985),

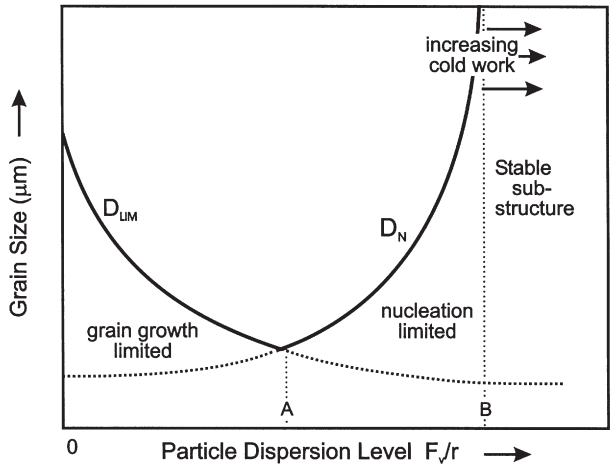

Fig. 9.21. The effect of the particle parameters on the recrystallized grain size.

Wert and Austin (1985) and Nes and Hutchinson (1989). The main parameter which determines the grain size after annealing an alloy which contains a volume fraction F_V of small particles of mean radius **r** is F_V/r. This is because F_V/r affects the Zener drag (equation 4.24), the number of viable recrystallization nuclei (equations 9.8, 9.9) and also the grain size (D_{lim}) at which normal grain growth will stagnate (§11.4.2). In figure 9.21, we show how the particle dispersion level (F_V/r) is expected to affect the grain size after recrystallization.

The curve $\mathbf{D_N}$ is the grain size after primary recrystallization by PSN. The number of viable nuclei from large particles or any other sites will decrease as F_V/r increases (equations 9.8, 9.9). At some dispersion level ($F_V/r = B$), the number of nuclei is effectively zero, and recrystallization can not occur. The curve D_{LIM} is the grain size at which normal grain growth will cease, as given by equations 11.31 or 11.34 as appropriate. The point at which these two grain sizes are equal is denoted $F_V/r = A$.

We note three important regimes.

- **Grain growth limited size. ($F_V/r < A$):** In this regime the grain size after primary recrystallization is determined by the number of available nucleation sites, and if the latter is large, then the former may be very small (equations 9.8, 9.9). However, the grains are unstable with respect to normal grain growth, and if annealed at a sufficiently high temperature then grain growth will occur up to the limiting size (D_{LIM}). In this situation the minimum grain size is achieved when $F_V/r = A$.
- **Nucleation limited size ($A < F_V/r < B$):** In this regime the material recrystallizes to a grain size (D_N) as determined by the number of nuclei. This is above the value of D_{LIM} and therefore normal grain growth will not occur. However, if the mean recrystallized grain size is small but the microstructure is not homogeneous, then the

suppression of normal grain growth may make the material vulnerable to **abnormal grain growth** if annealed at very high temperatures (§11.5.2).

- **No recrystallization ($F_V/r > B$):** In this regime the Zener pinning is now sufficient to suppress discontinuous recrystallization and the particles stabilise the deformed or recovered microstructure as discussed in §6.6.2.

We therefore see that there is an optimum dispersion level, $F_V/r = A$, required to produce a small and stable grain size. A further parameter which affects D_N and hence the critical values of F_V/r is the stored energy of deformation, which, for low temperature deformation is primarily a function of the strain. In figure 9.21, the arrows indicates the effect of increasing strain on the transition between regimes.

9.7 PARTICULATE METAL-MATRIX COMPOSITES

Particulate metal matrix composites (MMCs), such as aluminium alloys containing ~20 vol% of ceramic particles are of interest as structural materials in automotive and aerospace applications, where a high strength and stiffness combined with a low density is required. One of the advantages of particulate composites is that they can be mechanically processed in the same way as conventional alloys, and the recrystallization behaviour is therefore of interest (e.g. Humphreys et al. 1990, Liu et al. 1991).

In these materials we have the unusual situation of alloys containing both a large volume fraction of particles and also particles which are large enough (typically 3–10 μm) for PSN. The particles therefore play an important role in controlling the grain size by particle stimulated nucleation. If each particle produces one recrystallized grain, then the grain size as a function of particle diameter and volume fraction will be as shown in figure 9.17, from which it can be seen that very small grain sizes are achievable in these materials. The grain size of a series of Al–SiC particulate composites as a function of particle size and volume fraction are shown in figure 9.22, and these results are close to the predictions of equation 9.3 and figure 9.17.

The recrystallization kinetics of particulate MMCs are usually very rapid compared to the unreinforced matrix (Humphreys et al. 1990, Liu et al. 1989, Sparks and Sellars 1992, Ferry et al. 1992). This is a combination of the large driving force due to the geometrically necessary dislocations (equation 2.19) and the large number of nucleation sites.

In aluminium composites produced by powder metallurgy, there are, in addition to the large ceramic reinforcement particles, small (100 nm), inhomogeneously distributed oxide particles. These have several predictable but important effects, particularly in composites containing low volume fractions of ceramic reinforcement (e.g. Juul Jensen and Hansen 1990, Bowen et al. 1993), which can be interpreted in terms of the recrystallization of alloys containing bimodal particle distributions (§9.5).

- The recrystallization kinetics are slowed by Zener pinning.
- The recrystallized grain size is larger than predicted by equation 9.3.

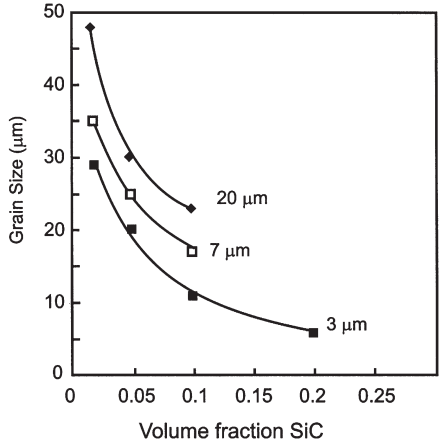

Fig. 9.22. The recrystallized grain size in Al–SiC particulate composites cold rolled 80% and annealed at 600°C, (courtesy M.G. Ardakani).

- Elongated subgrains and grains are produced (fig. 4.28).
- Stronger textures are formed than in the absence of the small particles.

Ferry et al. (1992) have studied the effect of precipitation on the recrystallization of an AA2014 Al–Al_2O_3 composite and found that as expected for bimodal particle distributions (§9.5), the recrystallization kinetics are determined primarily by the fine precipitate dispersion.

If large volume fractions of large ceramic particles are present then discontinuous recrystallization may be suppressed as found by Humphreys (1988a) and Liu et al. (1991). This has been found to occur when $F_V/r > 0.2\ \mu m^{-1}$, a similar condition to that found for conventional alloys (§9.2.1), and this is shown as the dotted region in figure 9.17. The resulting microstructures contain a mixture of high angle and low angle boundaries, and the material exhibits only recovery on annealing as discussed in §6.6.2.

9.8 THE INTERACTION OF PRECIPITATION AND RECRYSTALLIZATION

9.8.1 Introduction

In the earlier sections of this chapter we considered the recrystallization of two-phase alloys in which the second phase was present during deformation, and in which subsequent annealing did not substantially alter the phase distribution. However, in alloys in which precipitation can occur, the situation may arise in which the processes of recrystallization and precipitation occur concurrently. The situation is very complex because

- **The presence of a deformed microstructure may affect the nature and kinetics of the precipitation.**
- **The presence of precipitates may interfere with recovery and recrystallization.**

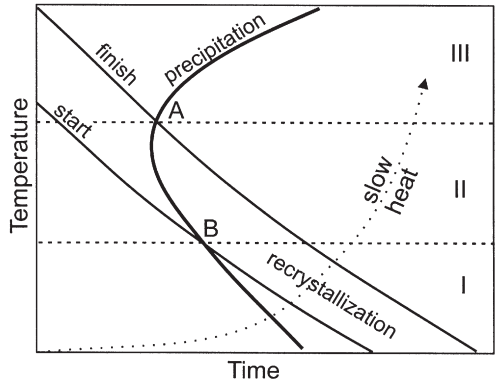

Fig. 9.23. Schematic TTT diagram for recrystallization and precipitation in cold rolled supersaturated aluminium alloys, rapidly heated to temperature, (Humphreys et al. 2003).

The problem was first analysed by Hornbogen and colleagues in Al–Cu and Al–Fe alloys (e.g. Ahlborn et al. 1969), and was reviewed by Hornbogen and Köster (1978). Despite its practical importance, there has been surprisingly little systematic work in this area since that time, until several recent investigations on the comparatively simple precipitation systems Al–Mn (Engler and Yang 1995, Somerday and Humphreys 2003), Al–Sc (Jones and Humphreys 2003), and Al–Zr (Humphreys et al. 2003). The following discussion is based mainly on the work described in the last three references.

During the annealing of cold rolled supersaturated solid solutions, either or both precipitation and recrystallization are found to occur, and figure 9.23 shows a schematic TTT curve for material which has been rapidly heated to the annealing temperature. The recrystallization start and finish lines are those found for dilute alloys in the absence of precipitation. The precipitation line represents the occurrence of sufficient precipitation to affect the recrystallization behaviour.

The significant points are those marked A and B, where the two processes interact. The temperatures T_A and T_B, and the corresponding times, are dependent on the particular alloy. For Al–1.3Mn, and Al–0.25Zr, T_A is ~400°C and $T_B \sim 350$°C, whereas for Al–0.25Sc, T_A and T_B are both above 500°C.

It may be seen that for the rapidly heated samples, the recrystallization behaviour can be divided into three regimes:

- **Regime I $T < T_B$ Precipitation before recrystallization**
  There is significant precipitation before any recrystallization has occurred, and recrystallization is prevented. In theory, precipitate coarsening could eventually occur and allow recrystallization to proceed, but for the alloys with T_A and T_B ~400°C, such a process would be extremely slow.

- **Regime II $T_A > T > T_B$ Precipitation and recrystallization occur concurrently**
  Recrystallization starts before precipitation, but subsequent precipitation will inhibit the completion of recrystallization.
- **Regime III $T > T_A$ Recrystallization before precipitation**
  In this regime, recrystallization occurs before precipitation, and is therefore unaffected by second-phase particles. Precipitation may subsequently occur in the recrystallized material.

The precipitation kinetics have a different temperature dependence to the recrystallization kinetics because, although both are controlled by diffusion, the driving force for precipitation decreases significantly at higher temperatures.

9.8.2 Regime I–Precipitation before recrystallization

9.8.2.1 The effect of heating rate

Figure 9.23 shows that annealing at temperatures below T_B will result in inhibition of recrystallization by the precipitates. However, if a slow heating rate (10°C/hr) is employed, then during the heating time, sufficient precipitation may occur to inhibit recrystallization even at high temperatures, as shown by the dotted curve of figure 9.23.

We therefore expect the heating rate to have a strong effect on recrystallization, and this is seen in table 9.1, which shows the temperatures at which recrystallization is complete in 1hr. Slow heating raises the recrystallization temperature of the Al–Zr and Al–Mn alloys by ~100° by causing precipitation to occur before recrystallization. Recrystallization of the Al–Sc alloy is unaffected by heating rate because even the rapid heating rate is insufficient to prevent precipitation before the onset of recrystallization. This analysis is in agreement with the known effects of heating rate on the recrystallization of industrial aluminium alloys where precipitation occurs during recrystallization (e.g. Bampton et al. 1982, Bowen 1990).

9.8.2.2 Microstructural evolution

Although the details of the evolution of microstructure during annealing in the regime where precipitation precedes recrystallization depends on the particular alloy and on whether precipitation is homogeneous or heterogeneous, in all cases, the microstructure develops in three stages.

Table 9.1
Effect of heating rate on the recrystallization temperature of some aluminium alloys (Humphreys et al. 2003).

Alloy	Recrystallization temperature (°C)	
	Fast heating (500°/s)	Slow heating (10°/hr)
0.25 Sc	575 ± 5	550 ± 20
0.25 Zr	380 ± 10	480 ± 20
1.3 Mn	425 ± 5	500 ± 20

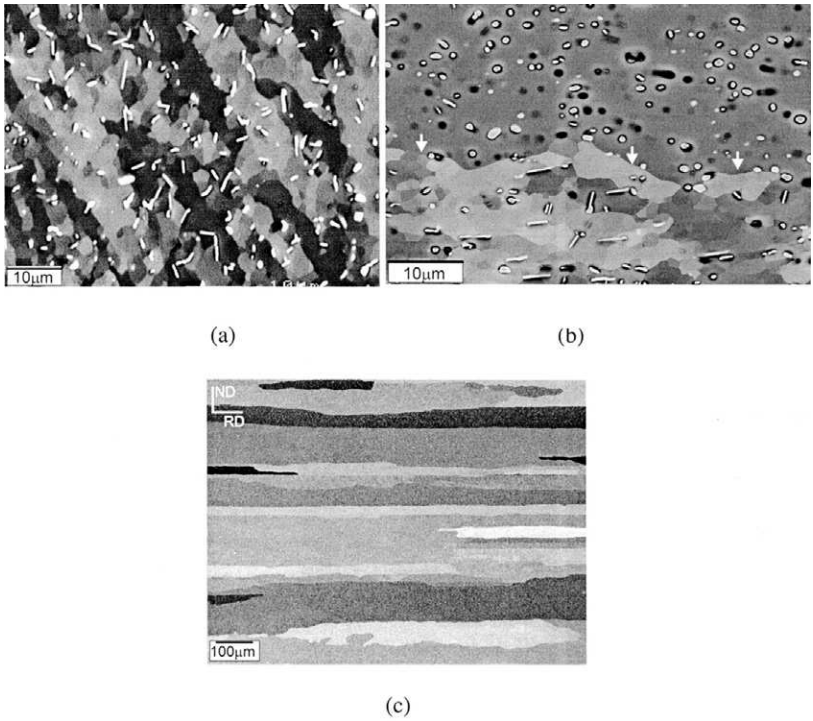

Fig. 9.24. SEM channelling contrast micrographs of supersaturated Al–1.3%Mn alloy, cold rolled 80% and heated at 10°/hr to temperature. (a) Precipitation of incoherent $MnAl_6$ plates on subgrain boundaries at 400°C, (b) Spheroidisation of plates at a HAGB (arrowed) during recrystallization at 500°C, (c) Fully recrystallized to produce large elongated grains at 550°C, (Humphreys et al. 2003).

Precipitation and recovery: Precipitation occurs and pins the high and low angle boundaries, thereby preventing recrystallization. An example of this in an Al–1.3%Mn alloy in which heterogeneous precipitation occurs on the deformed substructure is shown in figure 9.24a.

Particle coarsening or transformation: Before recrystallization can proceed, a significant amount of particle coarsening generally occurs. This is usually most rapid at boundaries, and may involve loss of full coherency (e.g. Al–Sc) or transformation to the equilibrium phase (e.g. Al–Zr). As the particles coarsen, the subgrains grow (§6.6.2). Although this is no more than recovery by particle controlled subgrain growth, it should be noted that some investigators have incorrectly described this process as *'continuous recrystallization'* or *'recrystallization in situ'*.

Recrystallization: At a sufficiently high temperature, or long times, enough particle coarsening occurs to allow recrystallization to originate at the high angle boundaries, deformation heterogeneities or large second-phase particles.

The driving pressure for the recrystallization is provided by the stored energy of deformation, and simple models (§7.6) predict that the minimum length (L_c) of a boundary of specific energy γ, which can migrate and initiate SIBM is

$$L_C \geq \frac{4\gamma}{E} \tag{9.10}$$

where ΔE is the net driving pressure across the boundary. However, the precipitation which precedes recrystallization, produces a Zener boundary pinning pressure (P_Z), and thus equation 9.10 becomes

$$L_C \geq \frac{4\gamma}{(P_D - P_Z)} \tag{9.11}$$

No recrystallization can occur when $P_Z > P_D$, but as the precipitate coarsens and P_Z is reduced, SIBM can occur, although L_C is initially very large. Therefore SIBM involving a few long boundary segments (broad front SIBM) can occur. Although P_Z and hence L_C are gradually reduced during high temperature annealing, the few large boundary segments which recrystallize first will dominate the recrystallization process, resulting in a very large grain size as shown in figure 9.24c, which is typical of alloys recrystallized in this regime. The grains are usually elongated in the rolling direction, and this is probably due to the additional pinning produced by precipitates at the existing high angle grain boundaries, which makes it difficult for a recrystallizing grain to migrate in the direction perpendicular to the rolling plane (§4.6.2.3).

Even at high annealing temperatures, e.g. 500–600°C in aluminium alloys, recrystallization proceeds relatively slowly because the movement of the recrystallization front is controlled by **particle coarsening or transformation on the migrating high angle boundaries** (Humphreys 1999a, Lillywhite et al. 2000, Humphreys et al. 2003) and is not related to the boundary mobility as is the case for recrystallization of a single-phase alloy (equation 7.1). The mechanisms of particle coarsening leading to the migration of high angle boundaries during recrystallization depend on the particular alloy and may involve spheroidisation of platelike particles (Al–Mn), as shown in figure 9.24b, particle coarsening (Al–Zr, fig. 9.25), passage of the boundary through semi-coherent particles (Al–Sc), or a phase transformation (Al–Mg–Si). Further details of these mechanisms may be found in the references cited above.

9.8.3 Regime II–Simultaneous recrystallization and precipitation

In this regime, it is seen from figure 9.23 that recrystallization starts before there is significant precipitation, but that precipitation will affect the recrystallization before the process is completed. This regime has been investigated in Al–Mn, Al–Sc and Al–Zr alloys (Humphreys et al. 2003), and recrystallization is found to be very inhomogeneous as shown in figure 9.26.

Typically, the amount of recrystallization in this regime depends primarily on the annealing temperature, but is almost independent of time. At temperatures just above

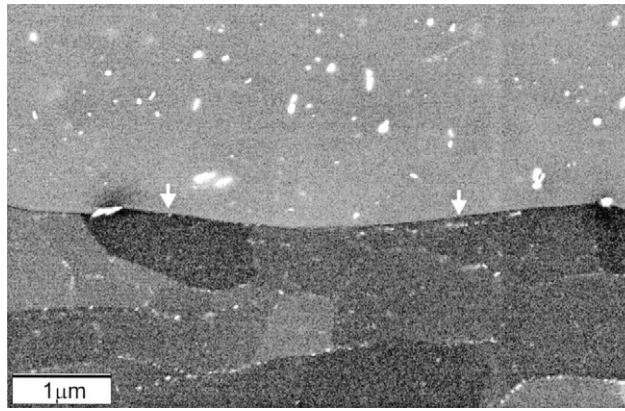

Fig. 9.25. Preferential coarsening of incoherent Al_3Zr particles at a HAGB migrating in the marked direction during recrystallization on slow heating to 350°C, (Humphreys et al. 2003).

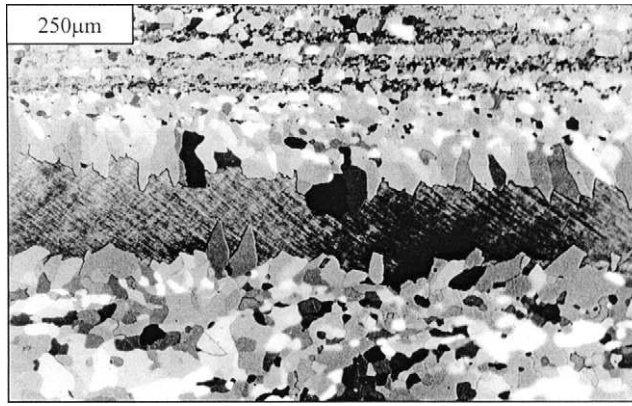

Fig. 9.26. Inhomogeneous recrystallization in partly recrystallized Al–0.12%Sc annealed 1min at 425°C, (Jones and Humphreys 2003).

T_B, only a small amount of recrystallization occurs, but at higher temperatures, there is more recrystallization, until at $\sim T_A$, full recrystallization is possible.

Regions of the microstructure with the highest stored energies or boundaries which are very mobile or on which precipitation is slow are particularly favoured, as these can recrystallize before precipitation intervenes. There is evidence of a number of unusual microstructural features including broad front SIBM (§9.4.1.2) involving boundaries close to $40° < 111 >$ (Somerday and Humphreys 2003, Jones and Humphreys 2003), growth of faceted grains (Jones and Humphreys 2003), and elongated 'tombstone-like' grains (Humphreys et al. 2003). An EBSD map showing broad front SIBM in an Al–Sc alloy is seen in figure 9.27.

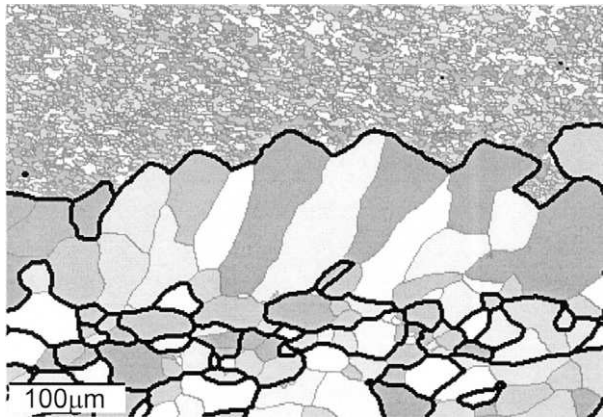

Fig. 9.27. EBSD map showing broad front SIBM in Al–0.12%Sc. A grain near to the cube orientation at the bottom is growing upwards into a deformed $\{110\} < 001 >$ Goss oriented grain. Note the substructure dragged behind the migrating boundary. The high angle boundaries are shown as thick black lines, (Jones and Humphreys 2003).

9.8.4 Regime III–Recrystallization before precipitation

Figure 9.23 indicates that on annealing at temperatures above T_A, recrystallization is complete before significant precipitation has occurred. In this situation, recrystallization is similar to that for a single-phase alloy, and an equiaxed grain structure is formed. The grains are generally smaller than those formed in regime I, but may subsequently undergo rapid grain growth at the high annealing temperatures.

9.9 THE RECRYSTALLIZATION OF DUPLEX ALLOYS

Earlier sections of this chapter have discussed the recrystallization of two-phase alloys in which one phase was dispersed in a matrix of the other. There are however many important alloys in which the volume fraction of the two-phases are comparable (e.g. fig. 11.15), and it is with the recrystallization of such **duplex alloys** that we are concerned here. Examples of duplex alloys include α/β brasses and bronzes, α/γ steels, α/β titanium alloys. The phase transformations and recrystallization which often occur during the thermomechanical processing of duplex alloys may be used to refine the microstructures, and this technology has been used extensively to produce fine grained duplex alloys capable of undergoing superplastic deformation (Pilling and Ridley 1989). In this section we are primarily concerned with recrystallization following low temperature deformation. The recrystallization of duplex alloys has been reviewed by Hornbogen and Köster (1978) and Hornbogen (1980), and grain growth in duplex microstructures is considered in §11.4.3.3.

The α/β brass alloys (e.g. 60:40 brass) provide good examples of recrystallization in coarse duplex microstructures. Some well known early work (Honeycombe and Boas

1948, Clareborough 1950) was carried out on this alloy system, and the later work of Mäder and Hornbogen (1974) provides a basis for the following discussion which illustrates some of the complexities in the behaviour of such systems.

9.9.1 Equilibrium microstructures

The simplest case is that in which the material is annealed at the same temperature at which it was equilibrated before deformation. If the volume fractions of both phases are equal, then the phases are usually constrained to undergo similar deformations. However, if one phase is continuous, then there will be a strain partitioning between the phases dependent on the relative volume fractions, sizes and strength of the phases, and this will influence the recrystallization behaviour. It is usually found that the phases recrystallize independently of each other in a manner that is largely predictable from a knowledge of the recrystallization of the individual phases (e.g. Vasudevan et al. 1974, Cooke et al. 1979).

In duplex α/β brass alloys, the microstructure comprises equiaxed grains of fcc, high zinc α-brass, which has a low stacking fault energy and whose deformation behaviour is discussed in §2.5; and grains of the ordered bcc (B2) β-brass phase. The annealing behaviour after rolling reductions of less than 40% is shown schematically in figure 9.28. The β-phase recovers readily and forms subgrains, whilst the low stacking energy α-phase undergoes little recovery, but recrystallizes readily, nucleation being mainly at the α/β boundaries. The β-phase generally recrystallizes at longer times, although for lower strains, extended recovery may occur (Mäder and Hornbogen 1974, Cooke and Ralph 1980). As discussed in §8.3.2, the recrystallization kinetics of the β-phase are affected by the ordering reaction.

After rolling reductions of greater than 70%, Mäder and Hornbogen found that the β-phase in a Cu–42%Zn alloy transformed martensitically into a distorted fcc phase (α_M) during deformation. On annealing, diffusion occurred between the two phases (fig. 9.29) tending to equalise their compositions, and recrystallization and precipitation occurred in all grains (fig. 9.29c), leading to the formation of a fine-grained duplex microstructure.

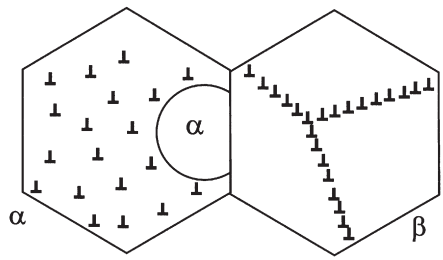

Fig. 9.28. Recrystallization of α/β brass after a low strain, (Mäder and Hornbogen 1974).

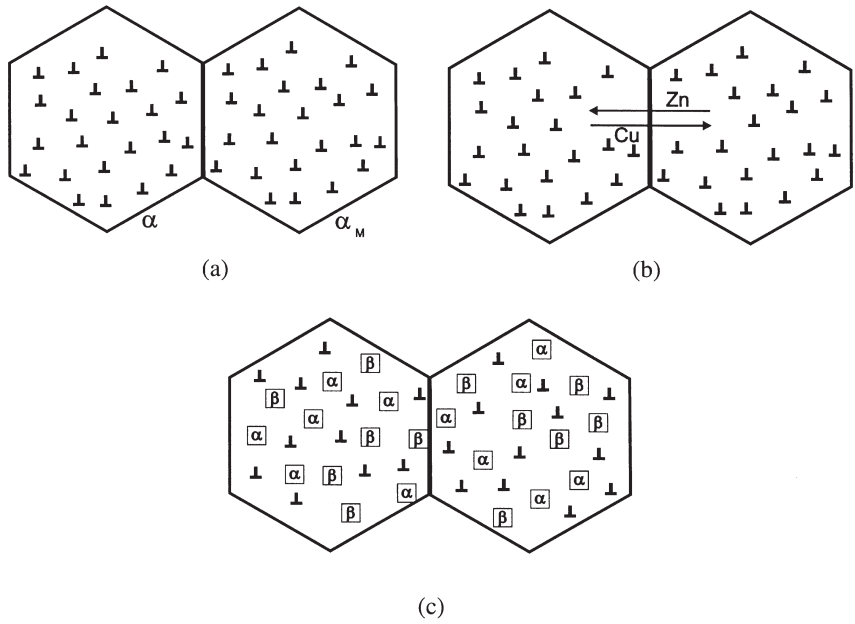

Fig. 9.29. Recrystallization of α/β brass after a large strain. (a) The β-phase transforms martensitically to α, (b) Interdiffusion occurs, (c) Recrystallization and precipitation occur in both phases, (Mäder and Hornbogen 1974).

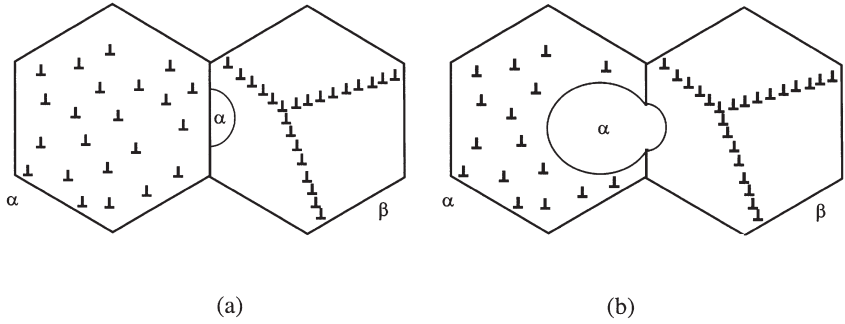

Fig. 9.30. Recrystallization of α/β brass at a temperature different from that of the pre-anneal. (a) The volume fraction of β is reduced by growth of α into the β grains, (b) The new α region nucleates recrystallization in the α grains, (Mäder and Hornbogen 1974).

9.9.2 Non-equilibrium microstructures

If the annealing is carried out at a temperature different from that at which the material was originally stabilized, then phase transformations will occur during the anneal, and

complex interactions between precipitation and recrystallization may result (§9.8), and much of the early work on α/β brasses was carried out in such conditions. The application of combined recrystallization and phase transformation to the control of microstructure in duplex materials has been discussed for iron and copper alloys by Hornbogen and Köster (1978), and for titanium alloys by Williams and Starke (1982) and Flower (1990), and will not be considered in detail here. However, the α/β brass system (Mäder and Hornbogen 1974) may again be used to illustrate the principles.

The necessary phase changes can take place either by movement of the original α/β interfaces or by precipitation within the phase whose volume fraction is being reduced. For example in figure 9.30a in which the fraction of β-phase is being reduced, α nucleates at the phase boundary and grows into the deformed β-phase. These grains subsequently act as recrystallization nuclei and consume the deformed α grains (fig. 9.30b). If the driving force is increased, then heterogeneous nucleation of α inside the β grains may occur.

ThisPageIntentionallyLeftBlank

Chapter 10

THE GROWTH AND STABILITY OF CELLULAR MICROSTRUCTURES

10.1 INTRODUCTION

In previous chapters, we considered the **deformed state** which provides the driving pressure for recrystallization and in separate chapters we discuss the local **recovery** processes which occur during the early stages of annealing and the larger scale processes of microstructural evolution such as **recrystallization** and **grain growth.** In this chapter we will show that there are clear relationships between these various annealing phenomena, and that they can be analysed within a unified framework. Such an approach is particularly useful when we try and analyse annealing behaviour which does not easily fit within the conventional definitions. In particular, we will examine why some microstructural changes occur uniformly or **continuously** throughout the microstructure, whereas others occur **discontinuously.**

If a material does not contain many free dislocations, so that the microstructure can be described in terms of subgrains and grains, we can characterise it in terms of an assembly of cells. Thus a **subgrain** in a deformed and recovered material differs from a **grain** in a fully recrystallized material only by the size of the cells and the misorientation between them.

Annealing of these microstructures occurs by the migration of high or low angle boundaries. Uniform coarsening of such cellular microstructures leads to continuous processes such as subgrain coarsening (§6.5) and normal grain growth (chapter 11), whereas inhomogeneous growth results in discontinuous processes such as recrystallization (chapter 7) and abnormal grain growth (§11.5). We therefore see that there is a relationship between all six of the annealing phenomena of table 1.1, and this will be explored in this chapter.

The assumption that a deformed microstructure can be considered to be cellular, is not unreasonable for high stacking fault energy/low solute metals such as many aluminium alloys and ferritic steels which have either been deformed at elevated temperatures or given a low temperature recovery anneal following cold work, but would not be a good approximation for metals of low stacking fault energy deformed at low temperatures (chapter 2).

10.2 THE MODEL

The microstructure shown in figure 10.1 comprises cellular regions which may be grains, subgrains or any mixture of these. The microstructure will have cells of a variety of sizes and also a distribution of misorientations. In order to simplify the analysis we will develop a mean field model in which we analyse the growth behaviour of **particular** cells of radius (R) and boundary type (misorientation θ, energy γ and mobility (M)) embedded in an **assembly** of cells of mean radius ($\overline{R}$) with grain boundary parameters–misorientation ($\bar{\theta}$), energy ($\overline{\gamma}$) and mobility ($\overline{M}$). As a further simplification, we do not take into account the effect of plane on the energy and mobility of the boundary (§5.3.2.2). Further details of the model discussed in this chapter are given by Humphreys (1997a).

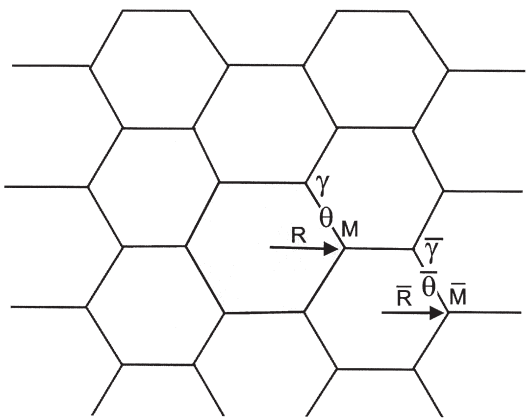

Fig. 10.1. The idealised cellular microstructure assumed in the analysis. The grains are approximated to spheres of radii R and $\overline{R}$, (Humphreys 1997a).

The model is based on the premise that the only important microscopic mechanism is that of boundary migration. This is realistic in most cases, but the possibility that other mechanisms may operate under certain conditions should not be ignored (§6.5.4).

Consider the growth by an amount ΔR, in a three dimensional microstructure, of the particular grain or subgrain of radius R. The consequent increase in boundary energy is given by:

$$\Delta E_{boundary} = 8\pi\alpha\gamma R\Delta R \tag{10.1}$$

If the grain assembly has a stored energy per unit volume of E_v, the stored energy released during the growth is:

$$\Delta E_{stored} = 4\pi\beta R^2 E_v \Delta R \tag{10.2}$$

where α and β are constants of the order of unity which represent the approximations inherent in the assumed idealised geometry of the model and which will vary slightly with the exact geometry assumed, as discussed by Hillert (1965). The reduction in energy during growth of the grain is

$$\Delta E = \Delta E_{stored} - \Delta E_{boundary} \tag{10.3}$$

The force on the boundary ($\Delta E/\Delta R$) is thus

$$F = 4\pi\beta E_v R^2 - 8\pi\alpha\gamma R \tag{10.4}$$

and the pressure on the boundary for growth of the grain is

$$P = \beta E_v - \frac{2\alpha\gamma}{R} \tag{10.5}$$

The energy stored per unit volume in the boundaries of a 3-D subgrain array is

$$E_v = \frac{3\overline{\gamma}}{2\overline{R}} \tag{10.6}$$

where $\overline{R}$ and $\overline{\gamma}$ are the mean radius and boundary energy of the array, and therefore the driving pressure for growth of the particular grain is

$$P = \frac{1.5\beta\overline{\gamma}}{\overline{R}} - \frac{2\alpha\gamma}{R} \tag{10.7}$$

and its boundary velocity is

$$\frac{dR}{dt} = MP = M\left(\frac{1.5\beta\overline{\gamma}}{\overline{R}} - \frac{2\alpha\gamma}{R}\right) \tag{10.8}$$

For the special case of boundaries of equal energy ($\gamma = \overline{\gamma}$), and taking $\alpha = 1/2$ and $\beta = 2/3$, equation 10.8 reduces to

$$\frac{dR}{dt} = MP = M\gamma\left(\frac{1}{\overline{R}} - \frac{1}{R}\right) \tag{10.9}$$

which is the expression derived by Hillert (1965) in his classic paper, for the growth of a grain of radius R in a 3-D assembly of grains of mean radius $\overline{R}$, and where the boundary energies are equal. For the more general case of interest here, and assuming the same values of α and β, equation 10.8 becomes

$$\frac{dR}{dt} = MP = M\left(\frac{\overline{\gamma}}{\overline{R}} - \frac{\gamma}{R}\right) \tag{10.10}$$

The growth rate of the large grain relative to that of the assembly is

$$\frac{d}{dt}\left(\frac{R}{\overline{R}}\right) = \frac{1}{\overline{R}^2}\left(\overline{R}\frac{dR}{dt} - R\frac{d\overline{R}}{dt}\right) \tag{10.11}$$

As first shown by Thompson et al. (1987), the large grain will grow faster than the normally growing grains and lead to instability of the microstructure by discontinuous growth if

$$\overline{R}\frac{dR}{dt} - R\frac{d\overline{R}}{dt} > 0 \tag{10.12}$$

Now the rate of growth of a uniform grain assembly ($d\overline{R}/dt$) was shown by Hillert (1965) to be (see §11.2.2.1)

$$\frac{d\overline{R}}{dt} = \frac{\overline{M}\overline{\gamma}}{4\overline{R}} \tag{10.13}$$

and this will be valid if the number of 'large' grains remains small. Taking dR/dt from equation 10.10, we can express the instability condition 10.12 as:

$$M\overline{\gamma} - \frac{\overline{R}M\gamma}{R} - \frac{R\overline{M}\overline{\gamma}}{4\overline{R}} > 0 \tag{10.14}$$

It is convenient to express the size and boundary parameters of the particular grain in terms of those of the assembly grains and we define

$$X = \frac{R}{\overline{R}}, \quad Q = \frac{M}{\overline{M}}, \quad G = \frac{\gamma}{\overline{\gamma}} \tag{10.15}$$

The instability condition of inequality 10.14 then becomes

$$Y > 0 \tag{10.16}$$

where $Y = 4QX - 4QG - X^2$, and the condition that $Y = 0$ is obtained when

$$X = 2Q \pm 2(Q^2 - QG)^{1/2} \tag{10.17}$$

and these two roots define the bounds of stable/unstable growth.

The condition for microstructural instability therefore depends on the **size, boundary energy** and **mobility** of the particular grain relative to the grain assembly. This is shown in figure 10.2, where it may be seen that there is not only a minimum value of size ratio (X) for instability to occur, but also a maximum size ratio to which the unstable grain/subgrain will grow. When the abnormal grain/subgrain achieves this maximum size ratio it continues to grow, but the ratio $R/\bar{R}$ remains constant. These critical size ratios are functions of the relative mobilities and boundary energies. In general, as might be expected, instability of a particular grain/subgrain is aided by a high mobility, a large size and small boundary energy. We see from the analysis that instability can only occur if $Q > G$ and that $X = 2G = 2Q$ at the minimum where $Q = G$.

The boundary mobilities and energies are not independent variables but are related to the nature of the boundary. We will take a particularly simple approach to boundaries and assume that the plane is unimportant and that the properties depend only on the misorientation (θ). We can then use the Read–Shockley relationship (equation 4.5) to relate boundary energy (γ) and misorientation (θ) as shown in figure 4.5. The effect of misorientation on boundary mobility (M) is less clear as discussed in §5.2.2. However, the empirical relationship of equation 10.18, which was derived from data such as shown in figures 5.5 and 5.6 (Humphreys 1997a), has been shown to describe the mobilities of boundaries in dilute aluminium alloys.

$$M = M_m\{1 - \exp[-B(\theta/\theta_m)^N]\} \tag{10.18}$$

where M_m is the mobility of a high angle boundary, $N = 4$ and $B = 5$.

We are now in a position to investigate the stability of various grain and subgrain structures by specifying a microstructure and inserting values of boundary energy and mobility into equation 10.17. It should be recognised that any predictions will be

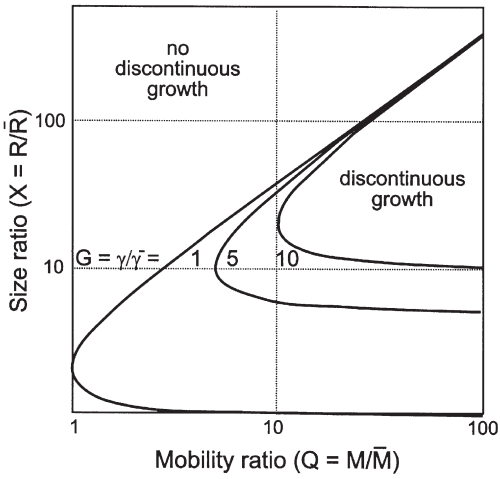

Fig. 10.2. The conditions for discontinuous growth as a function of the relative sizes, boundary energies and mobilities of the grains, (Humphreys 1997a).

sensitive to the precise forms of the relationships between misorientation, energy and mobility, and that these are not well established. However, it is likely that the main aspects of the following analysis will be valid.

10.3 STABILITY OF SINGLE-PHASE MICROSTRUCTURE

We take an array of equiaxed subgrains (or grains) of mean radius $\overline{R}$ and mean misorientation $\bar{\theta}$ and consider the growth behaviour of a particular subgrain of radius R, inserted into the array and misoriented by θ from the assembly. As the particular subgrain has a single orientation, it cannot be misoriented by the same amount from all the contiguous subgrains, and we will assume that θ represents the average misorientation between the particular subgrain and its surroundings. The use of an **average misorientation (θ)** between the particular subgrain and its neighbours is not unreasonable if either the number of neighbours is large or if $\bar{\theta}$ is small compared to θ. If the particular subgrain is of the same size as its neighbours ($R = \overline{R}$) then there will on average be 14 contiguous subgrains (§4.5.2). However, we will mostly be interested in cases where the particular subgrain is larger than average, and when $R = 2\overline{R}$ the number of neighbours will be ~50, and the concept of a mean misorientation may be more valid. Although the subgrain assembly has a mean misorientation of $\bar{\theta}$, the spread of orientations around this mean will be important, and this is considered later. We also assume in this analysis that $\bar{\theta}$ remains constant as the assembly coarsens. This will be a reasonable assumption unless there is an **orientation gradient** present, in which case $\bar{\theta}$ will tend to increase as the subgrains coarsen (§7.6.3). The subgrains in the assembly have a mean radius of $\overline{R}$, but individual subgrains may be larger or smaller than this, and the importance of the size distribution will be discussed later. Using equation 10.17, we calculate the minimum size of the particular subgrain which will grow discontinuously and the maximum size ratio to which it can grow. These parameters are now dependent on both θ and $\bar{\theta}$. When $\theta = \bar{\theta}$, then $G = 1$ and $Q = 1$ (i.e. this is an 'ideal' subgrain assembly with all boundaries having the same properties). In this situation, it is seen from equation 10.17 that the instability criterion $Q > G$ is not fulfilled, discontinuous growth cannot occur, and therefore the assembly will coarsen uniformly (continuously) on annealing.

In the following sections we apply this analysis to a number of microstructures of practical importance. In order to present the boundary misorientations in their commonly used form, they will be expressed in degrees rather than in normalised form. These situations are discussed in more detail elsewhere in the book, and in the sections below we consider only the applications of this analysis to these cases.

10.3.1 Low angle boundaries – Recovery

Figure 10.3 shows the conditions under which a particular subgrain which is misoriented by an angle θ from a subgrain assembly of mean misorientation $\bar{\theta}$ will grow abnormally according to equation 10.17. The condition for instability is that the particular subgrain should be of a critical size relative to the assembly and that $\theta > \bar{\theta}$. The upper bound indicates the extent of the discontinuous or abnormal growth.

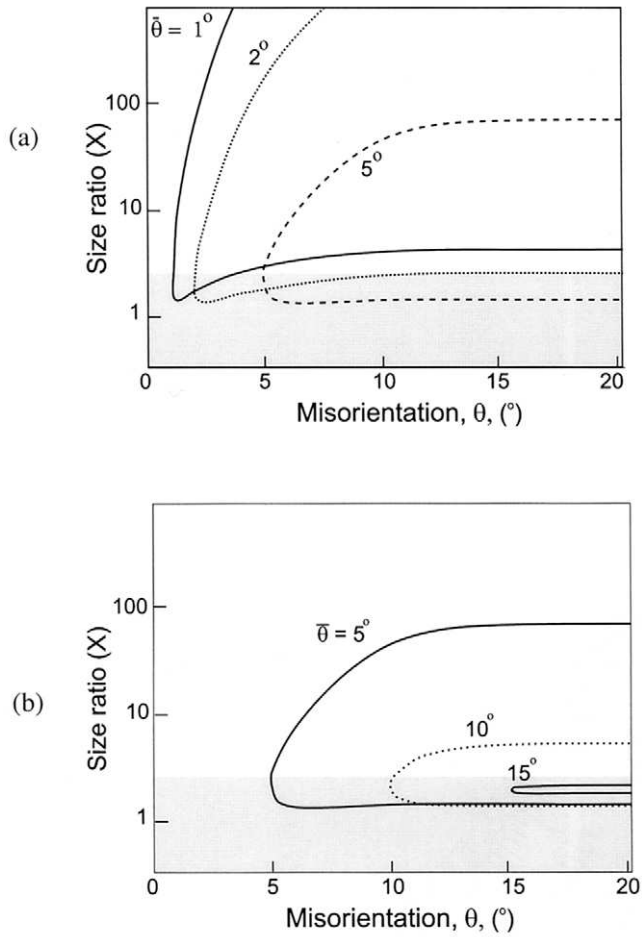

Fig. 10.3. Conditions for instability of a subgrain as a function of the relative size (X) and misorientation (θ) of the subgrain from the assembly, (a) Subgrain assemblies with mean misorientations of 1–5°, (b) Subgrain assemblies with mean misorientations of 5–15°. The shaded region represents the likely spread of sizes in the assembly, (Humphreys 1997a).

Figure 10.3a shows that if the mean misorientation of the assembly ($\bar{\theta}$) is small then discontinuous growth is possible for large subgrains which are only slightly misoriented from the assembly. e.g. for $\bar{\theta}=1°$, subgrains of size $2\overline{R}$ misoriented between 1.1° and 2.5° from the assembly will grow abnormally. For $\bar{\theta}=1°$ subgrains larger than $\sim 1.5\overline{R}$ will become unstable and grow until X is in the range of 50–100, and for $\bar{\theta}=5°$, subgrains larger than $1.5\overline{R}$ should grow discontinuously to reach values of 10–50X. We therefore see that **low angle subgrain microstructures are predicted to be intrinsically unstable with respect to discontinuous subgrain growth.** However, such discontinuous

(abnormal) subgrain growth, which is discussed in §6.5.3.5 is rarely found because it is usually superseded by the onset of recrystallization.

This analysis shows that the annealing behaviour depends not only on the mean properties of the assembly but also on the **range** of subgrain sizes and misorientations. There are few experimental measurements of the size distribution of subgrains, but measurements of subgrains in hot-worked (Duly et al. 1996) or cold worked (Hurley and Humphreys 2001) aluminium suggest that the distributions are approximately lognormal, with a maximum size in the range $2–3\overline{R}$, and in the following discussions we will assume such a size distribution for both grains and subgrains. The expected size range is indicated by the shaded region in figure 10.3. It can be seen from figure 10.3a that the minimum misorientation requirement is unlikely to be restrictive, and that the most critical factor in determining instability is whether the microstructure contains subgrains of a sufficient large size. The growth rates of both the assembly and the discontinuously growing subgrains may be determined from the preceding analysis, and it is found that the fastest growing subgrains are those with both the largest size and largest misorientation (Humphreys 1977).

10.3.2 High and low angle boundaries – Recrystallization

In this situation we assume an assembly of subgrains with a typical mean misorientation ($\bar{\theta}$) of 2° to 5°. If a small highly misoriented grain (i.e. a recrystallization 'nucleus') is present, then this may grow discontinuously, i.e. the normal process of primary recrystallization discussed in chapter 7. If this nucleus is misoriented by 15° or more from the subgrain assembly, then we see from figure 10.3a that microstructural instability is predicted for a nucleus in the size range $1.5\overline{R}$ to $2.5\overline{R}$, with the recrystallizing grain able to grow to a size between 100 and 1000 times the subgrain size. However, if the subgrain assembly has a mean misorientation of less than ~2°, we see that the 'nucleus' must be larger than $2.5\overline{R}$, and therefore the nucleation of the discontinuous recrystallization may be a limiting factor. The model may be extended to analyse recrystallization by strain induced boundary migration (Humphreys 1999a, Humphreys and Hurley 2001), and this is discussed further in §7.6.2.

10.3.3 High angle boundaries – Grain growth

It may be seen from figure 10.3a that as $\bar{\theta}$ increases, both the critical size for nucleating discontinuous growth and the maximum growth ratio decrease, and figure 10.3b shows that this trend continues for larger mean misorientations. If $\bar{\theta}$ is 10°, the maximum growth ratio is $\sim 5\overline{R}$ and thus the instability will not develop to any great extent. If $\bar{\theta} > 15°$, it may be seen that an abnormally growing subgrain can grow no larger than $\sim 2.5\overline{R}$. As this is within the normal size distribution of the assembly, this effectively means that no abnormal growth is possible and such an assembly is therefore stable. This latter result is consistent with the analysis of Thompson et al. (1987) which showed that abnormal grain growth could not occur in an assembly of grains whose boundary properties were identical ($Q = 1$ in equation 10.17), and which has been amply confirmed by experiment (§11.5). Even if there are some 'special boundaries' with low energy and high mobility (e.g. $\Sigma 7$ boundaries), these are unlikely to affect the stability of

the microstructure because the effective values of γ and M for a particular grain will be some average value involving all the boundaries which surround the grain.

In the regime of subgrains of moderate to large misorientation ($\bar{\theta} \sim 10^{\circ}$), nucleation of abnormal growth is seen from figure 10.3b to be easy and it is therefore likely that the number of abnormally growing grains will be large. However, such grains/subgrains can grow only a small amount relative to the assembly and figure 10.3b shows that such a process would lead to the development of a **broader size distribution** than that which would result from normal grain growth rather than to identifiable abnormal grain growth.

If we arbitrarily define the process of abnormal subgrain or grain growth as being one by which discontinuously growing subgrains or grains can reach a size greater than $5\overline{R}$, our analysis indicates that subgrain assemblies of mean misorientation less than 10° are intrinsically unstable, and will grow **discontinuously,** whereas if $\bar{\theta} > 10^{\circ}$, the assembly will be stable and will grow in a **continuous** manner (Humphreys 1997a).

The above analysis of the coarsening of microstructures containing a predominance of medium angle boundaries will be relevant to the abnormal grain growth of strongly textured alloys (§11.5.3), in which the mean boundary misorientations are much lower than in an assembly of randomly oriented grains (Humphreys 1997a).

10.3.4 The stability of microstructures after very large strains

It is normally found that an increasing plastic strain promotes recrystallization on subsequent annealing (chapter 7). However, a large number of investigations have shown that a highly strained metal can resist recrystallization, as discussed in chapter 14. During deformation of a subgrain-forming metal, the subgrain size usually remains approximately constant with strain, at a value determined by the deformation temperature and strain rate (§2.2.3, §13.2.3). However, the high angle grain boundary area increases with strain, due to geometrical factors (§2.2.1) and grain fragmentation (§2.4.2). Therefore as the strain increases, the ratio of high angle to low angle boundary area, and hence the mean misorientation ($\bar{\theta}$) increases. As discussed above, the stability of a microstructure increases as $\bar{\theta}$ increases, and therefore at sufficiently large strains, the fraction of high angle grain boundary may increase to a value sufficient to stabilise the microstructure against discontinuous growth (primary recrystallization). The fraction of high angle boundary required to prevent discontinuous recrystallization is estimated from the model to be ~0.6 to 0.7 (Humphreys et al. 1999). The inhibition of discontinuous recrystallization by very large strain deformation is considered in detail in chapter 14.

10.4 STABILITY OF TWO-PHASE MICROSTRUCTURES

The effects of a dispersion of second-phase particles on annealing has been incorporated into the theory discussed in the previous section (Humphreys 1997b). A volume fraction (F_V) of particles of diameter d exerts a pinning pressure P_Z on the boundaries, and for

planar boundaries we take $P_Z = 3F_V\gamma_i/d$, where γ_i is the energy of the boundary (equation 4.24). The growth rate of the grain or subgrain assembly in the presence of particles which exert a pinning pressure P_Z on the boundaries is then obtained by modifying equation 10.13 to take account of P_Z

$$\frac{d\overline{R}}{dt} = \frac{\overline{M}\overline{\gamma}}{4\overline{R}} - \overline{M}P_Z = \overline{M}\overline{\gamma}\left(\frac{1}{4\overline{R}} - \frac{3F_V}{d}\right) \tag{10.19}$$

and the growth rate of the particular grain/subgrain by a similar adjustment to equation 10.10.

$$\frac{dR}{dt} = \frac{M\overline{\gamma}}{\overline{R}} - \frac{M\gamma}{R} - MP_Z = M\left(\frac{\overline{\gamma}}{\overline{R}} - \frac{\gamma}{R} - \frac{3F_V\gamma}{d}\right) \tag{10.20}$$

We replace the particle pinning term by a dimensionless parameter

$$\psi = \frac{\overline{P}_Z\overline{R}}{\overline{\gamma}} = \frac{3F_V\overline{R}}{d} \tag{10.21}$$

and the growth rates are then, for the assembly

$$\frac{\overline{dR}}{dt} = \frac{\overline{M}\overline{\gamma}}{\overline{R}}\left(\frac{1}{4} - \Psi\right) \tag{10.22}$$

and for the particular grain

$$\frac{dR}{dt} = M\left(\frac{\overline{\gamma}}{\overline{R}} - \frac{\gamma}{R} - \frac{\Psi\gamma}{\overline{R}}\right) \tag{10.23}$$

The condition for instability, leading to abnormal or discontinuous growth of the particular grain or subgrain is given by inequality 10.12, and using equations 10.22 and 10.23 this becomes

$$\overline{R}M\left(\frac{\overline{\gamma}}{\overline{R}} - \frac{\gamma}{R} - \frac{\Psi\gamma}{\overline{R}}\right) - \frac{R\overline{M}\overline{\gamma}}{\overline{R}}\left(\frac{1}{4} - \Psi\right) > 0 \tag{10.24}$$

Using the normalised parameters for the special grain, the instability condition of inequality 10.24 may then be expressed in terms of the size ratio X as

$$X = \frac{2Q(G\Psi - 1)}{4\Psi - 1} \pm 2\frac{\left[(Q - QG\Psi)^2 + (4\Psi - 1)QG\right]^{1/2}}{4\Psi - 1} \tag{10.25}$$

The two roots of this equation as discussed earlier, define the bounds of stable/unstable growth, the lower bound X_{min} being the size ratio of the smallest grain or subgrain that can grow abnormally, and the upper bound X_{max} being the maximum ratio that this ratio can achieve.

The theory enables calculation of the growth rates of subgrains or grains (equations 10.22 and 10.23), and equation 10.25 predicts the conditions under which discontinuous processes such as discontinuous subgrain growth, recrystallization and abnormal grain growth will occur. The theory may be applied to individual regions of the microstructure, including the formation by subgrain growth of recrystallization nuclei at sites of large orientation gradients such as grain boundaries and large second-phase particles, and several applications, including the effect of second-phase particles on abnormal grain growth (§11.5.2) are discussed elsewhere in this book.

10.5 SUMMARY

In this chapter we have seen that the relationships between the processes of recovery, recrystallization and grain growth in single-phase or two-phase materials, all of which may occur continuously or discontinuously, can be explored and analysed semi-quantitatively using a simple analytical mean field model. This is a valuable concept because it removes the artificial and often blurred divisions between the various annealing processes, thereby enabling a broader approach to the subject.

It should be emphasised that the model, as presented here is oversimplified, and capable of significant refinement. For example, a recent modification to the theory which takes a more detailed account of local cell topology has been proposed by Feppon and Hutchinson (2002). As emphasised earlier, a major obstacle to full quantitative exploitation of such models is a lack of information about the basic materials parameters such as boundary energies and mobilities which are essential inputs (Humphreys and Hurley 2001).

ThisPageIntentionallyLeftBlank

Chapter 11

GRAIN GROWTH FOLLOWING RECRYSTALLIZATION

11.1 INTRODUCTION

Compared with primary recrystallization, the growth of grains in a recrystallized single-phase material might appear to be a relatively simple process. However, despite a large amount of theoretical and experimental effort, many important questions remain unanswered. The theoretical basis for understanding grain growth was laid down over 50 years ago in the classic papers of Smith (1948, 1952) and Burke and Turnbull (1952), and the apparent conflict of theory with experiment prompted several other theoretical models over a period of some 30 years. The application of computer simulation techniques (Anderson et al. 1984) provided a fresh approach to the problem and the interest and controversy surrounding the computer simulations gave a stimulus to the subject, which resulted in a number of international conferences (§1.2.2) and a large volume of literature.

Although primary recrystallization often precedes grain growth, it is of course not a necessary precursor, and the contents of this chapter are equally relevant to grain growth in materials produced by other routes, such as casting or vapour deposition. In this chapter we consider only the growth of grains under the driving pressures due to boundaries in the material. However, we note here that boundaries can be induced to

migrate by externally applied forces such as those due to stress as discussed in §5.2.1 or by magnetic fields (e.g. Smolukowski and Turner 1949, Watanabe 2001).

In this chapter we are primarily concerned with the **kinetics of grain growth** and the nature and **stability of the microstructure**; the factors affecting the **mobilities of the grain boundaries** are discussed in chapter 5.

11.1.1 The nature and significance of grain growth

When primary recrystallization, which is driven by the stored energy of cold work, is complete, the structure is not yet stable, and further growth of the recrystallized grains may occur. The driving force for this is a reduction in the energy which is stored in the material in the form of grain boundaries. The driving pressure for grain growth is often some two orders of magnitude less than that for primary recrystallization (§1.3.2), and is typically $\sim 10^{-2}$ MPa. Consequently, at a particular temperature, grain boundary velocities will be slower than during primary recrystallization, and boundary migration will be much more affected by the pinning effects of solutes and second-phase particles.

The technological importance of grain growth stems from the dependence of properties, and in particular the mechanical behaviour, on grain size. In materials for structural application at lower temperatures, a small grain size is normally required to optimise the strength and toughness. However, in order to improve the high temperature creep resistance of a material, a large grain size is required. Examples of the application of the control of grain growth which are considered in chapter 15, include the processing of silicon–iron transformer sheet and the development of microstructures for superplastic materials. There is also considerable interest in grain growth in thin metal, oxide and semiconductor films for electronic applications as discussed in §11.5.4. A good understanding of grain growth is therefore a pre-requisite for control of the microstructures and properties of metals and ceramics during solid state processing.

Grain growth may be divided into two types, **normal grain growth** and **abnormal grain growth or secondary recrystallization.** Normal grain growth, in which the microstructure coarsens uniformly, is classified as a **continuous process.** There is a relatively narrow range of grain sizes and shapes, and the form of the grain size distribution is usually independent of time and hence of scale as shown in figure 11.1a. After an initial transient period of growth, the microstructure reaches a **quasi-stationary state** in which the grain size distribution has an invariant form when expressed in terms of the grain size scaled by its mean value, and only the scale varies with some power of time. Such **self-similarity** is found for several growth processes such as particle coarsening or bubble growth (Mullins 1986), making this a challenging problem for modellers, who are often attracted more by the mathematical intricacies than the intrinsic importance of grain growth.

During abnormal grain growth, which is a **discontinuous** process, a few grains in the microstructure grow and consume the matrix of smaller grains and a bimodal grain size distribution develops. However, eventually these large grains impinge and normal grain growth may then resume (fig. 11.1b).

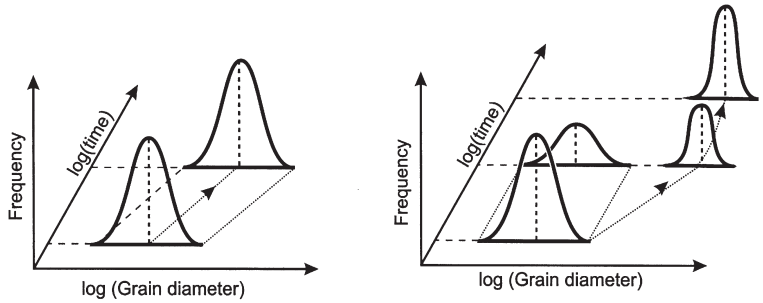

(a) (b)

Fig. 11.1. Schematic representation of the change in grain size distribution during (a) Normal grain growth and (b) Abnormal grain growth, (After Detert 1978).

11.1.2 Factors affecting grain growth

The main factors which influence grain growth, and which will be considered later in this chapter include:

- **Temperature**

Grain growth involves the migration of high angle grain boundaries and the kinetics will therefore be strongly influenced by the temperature dependence of boundary mobility as discussed in §5.3.1. Because the driving force for grain growth is usually very small, significant grain growth is often found only at very high temperatures.

- **Solutes and particles**

Although grain growth is inhibited by a number of factors, the pinning of grain boundaries by solutes (§5.3.3) and by second-phase particles (§4.6) is particularly important.

- **Specimen size**

The rate of grain growth diminishes when the grain size becomes greater than the thickness of a sheet specimen. In this situation the columnar grains are curved only in one direction rather than two, and thus the driving force is diminished. The grain boundaries, where they intersect the surface, may also develop grooves by thermal etching, and these will impede further grain growth.

- **Texture**

A strongly textured material inevitably contains many low angle boundaries of low energy, and there is therefore a reduced driving force for grain growth.

11.1.3 The Burke and Turnbull analysis of grain growth kinetics

Burke (1949) and Burke and Turnbull (1952) deduced the kinetics of grain growth on the assumption that the driving pressure (**P**) on a boundary arises only from the

curvature of the boundary. If the principal radii of curvature of a boundary of energy γ_b are $\mathbf{R_1}$ and $\mathbf{R_2}$ then

$$P = \gamma_b\left(\frac{1}{R_1}+\frac{1}{R_2}\right) \tag{11.1}$$

If the boundary is part of a sphere of radius $\mathbf{R}$, then $\mathbf{R = R_1 = R_2}$ and

$$P = \frac{2\gamma_b}{R} \tag{11.2}$$

Burke and Turnbull then made the following assumptions:

- **γ_b is the same for all boundaries.**
- **The radius of curvature (R) is proportional to the mean radius ($\bar{R}$) of an individual grain, and thus**

$$P = \frac{\alpha\gamma_b}{\overline{R}} \tag{11.3}$$

where α is a small geometric constant.

- **The boundary velocity is proportional to the driving pressure P** (equation 5.1), and to $\mathbf{dR/dt}$. i.e. $\mathbf{dR/dt = cP}$, where c is a constant.

Hence,

$$\frac{d\overline{R}}{dt} = \frac{\alpha c_1 \gamma_b}{\overline{R}} \tag{11.4}$$

and therefore

$$\overline{R}^2 - \overline{R}_0^2 = 2\alpha c_1 \gamma_b t$$

which may be written as

$$\overline{R}^2 - \overline{R}_0^2 = c_2 t \tag{11.5}$$

where $\bar{\mathbf{R}}$ is the mean grain size at time $\mathbf{t}$, $\overline{R}_0$ is the initial mean grain size and $\mathbf{c_2}$ is a constant.

This **parabolic growth law** is expected to be valid for both 2-D and 3-D microstructures, although, according to equation 11.1 the constant c_2 will be different for the two situations. In the limit where $\overline{R}^2 \gg \overline{R}_0^2$

$$\overline{R}^2 = c_2 t \tag{11.6}$$

Equations 11.5 and 11.6 may be written in the more general form

$$\overline{R}^n - \overline{R}_0^n = c_2 t \tag{11.7}$$

$$\overline{R} = c_2 t^{1/n} \tag{11.8}$$

The constant **n**, often termed the **grain growth exponent** is, in this analysis equal to **2**.

11.1.4 Comparison with experimentally measured kinetics

The use of equations 11.5 and 11.6 to describe grain growth kinetics was first suggested empirically by Beck et al. (1949). These authors found that **n** was generally well above 2 and that it varied with composition and temperature. It is significant that very few measurements of grain growth kinetics have produced the grain growth exponent of 2 predicted by equations 11.5 or 11.6, and values of **1/n** for a variety of metals and alloys as a function of homologous temperature are shown in figure 11.2. The trend towards lower values of **n** at higher temperatures, seen in this figure, has been reported in many experiments.

Data for some zone-refined metals in which the impurity levels are no more than a few ppm are shown in table 11.1. The values of **n** range from 2 to 4, with an average of 2.4 ± 0.4. Grain growth kinetics have been extensively measured in ceramics, and compilations of the data (Anderson et al. 1984, Ralph et al. 1992) reveal a similar range of grain growth exponents as is shown in table 11.2.

Much effort has been expended in trying to explain why the measured grain growth exponents differ from the 'theoretical' value of 2 given by the Burke and Turnbull analysis, and the earlier explanations fall into two categories:

(i) The boundary mobility (M) varies with the boundary velocity
The boundary mobility, as discussed in §5.1.3, may under certain circumstances be a function of boundary velocity, in which case the linear dependence of velocity on driving pressure (equation 5.1), which is assumed in the Burke and Turnbull analysis will not apply. An example of this is the case of solute drag on boundaries (§5.4.2). Figure 5.32 shows that the velocity is not linearly proportional to the driving pressure except for very low or very high boundary velocities. However, the shape of these curves

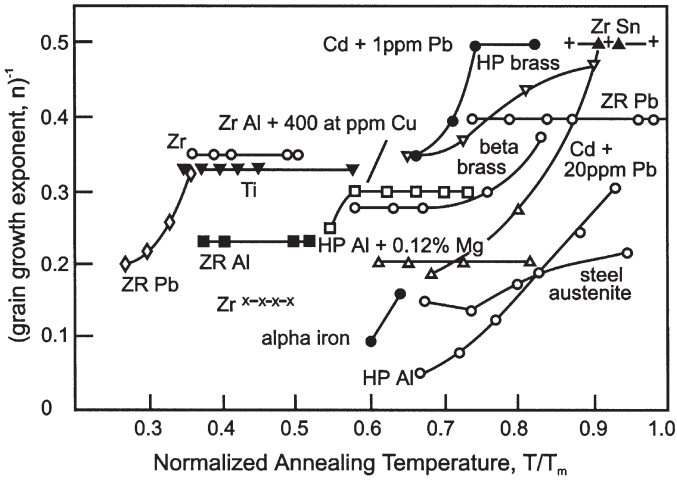

Fig. 11.2. The temperature dependence of the grain growth exponent **n** for isothermal grain growth in a variety of materials, (Higgins 1974).

Table 11.1
Grain growth exponents for isothermal grain growth in high purity metals (from Anderson et al. 1984).

Metal	Exponent n	Reference
Al	4	Gordon and El Bassyoumi (1965)
Fe	2.5 (varies with T)	Hu (1974)
Pb	2.5	Bolling and Winegard (1958)
Pb	2.4	Drolet and Gallibois (1968)
Sn	2.3	Drolet and Gallibois (1968)

Table 11.2
Grain growth exponents for isothermal grain growth in ceramics (from Anderson et al. 1984).

Ceramic	Exponent n	Reference
ZnO	3	Dutta and Spriggs (1970)
MgO	2	Kapadia and Leipold (1974)
MgO	3	Gordon et al. (1970)
CdO	3	Petrovic and Ristic (1980)
$Ca_{0.16}Zr_{0.84}O_{1.84}$	2.5	Tien and Subbaro (1963)

would only predict a higher grain growth exponent if conditions were such that the boundary changed from breakaway to solute drag behaviour during grain growth, and it is unlikely that these conditions would commonly be met.

As discussed in §5.3.1.2, there is evidence of changes in grain boundary structure and mobility at very high temperatures, even in metals of very high purity. It is conceivable that this could account in some cases for transitions to lower **n** values, although there is no direct evidence for this.

Grain growth in ceramics has been extensively investigated, and in many cases the measured values of **n** have been ascribed to particular mechanisms of boundary migration. For example Brook (1976) lists eleven proposed mechanisms for boundary migration with growth exponents of between 1 and 4.

(ii) There is a limiting grain size
An alternative empirical analysis of the data was given by Grey and Higgins (1973), who proposed that equation 5.1 be replaced by

$$v = M(P - C) \tag{11.9}$$

where **C** is a constant for the material.

If this relationship is used in the Burke and Turnbull analysis then equation 11.4 becomes

$$\frac{d\overline{R}}{dt} = c_1\left(\frac{\alpha\gamma_b}{\overline{R}} - C\right) \tag{11.10}$$

When, as a result of grain growth, the driving pressure **P** falls to the value **C**, there is no net pressure, and grain growth ceases at a **limiting value.** Grey and Higgins showed that this form of equation accounted quite well for the kinetics of grain growth in several materials. The term **C** is similar to the Zener pinning term which accounts for a limiting grain size in two-phase materials (§11.4.2), and Grey and Higgins suggested that the physical origin of **C** might be solute clusters which are unable to diffuse with the boundary.

However, there is often little evidence for $\mathbf{n = 2}$ even in very pure materials, and it has been suggested that one or more of the underlying assumptions of the Burke and Turnbull analysis may be incorrect. Although we will later conclude that there is little evidence to suggest that the Burke and Turnbull result is in serious error, a great deal of work has gone into producing more refined models of grain growth which address not only the kinetics but also the grain size distribution.

11.1.5 Topological aspects of grain growth

The Burke and Turnbull analysis assumes that the mean behaviour of the whole array of grains can be inferred from the migration rate of part of one boundary and does not consider the interaction between grains or the constraints imposed by the space-filling requirements of the microstructure. This aspect of grain growth was first addressed by Smith (1952) who discussed grain growth in terms of grain topology and stated that **'Normal grain growth results from the interaction between the topological requirements of space-filling and the geometrical needs of surface tension equilibrium'.**

From the introduction to grain topology in §4.5, we note that in a two-dimensional grain structure, the only stable arrangement which can fulfil both the space-filling and boundary tension equilibrium requirements is an array of regular hexagons as shown in figure 11.3, and any other arrangement must inevitably lead to grain growth. For example, if just one 5-sided polygon is introduced (fig. 11.4a), then it must be balanced by a 7-sided one to maintain the average number of edges per grain at 6 (§4.5.1) as shown in figure 11.4a. In order to maintain the 120° angles at the vertices, the sides of the grains must become curved. Grain boundary migration then tends to occur in order to reduce the boundary area, and the boundaries migrate towards their centres of curvature (fig. 11.4b). Any grain with more than six sides will tend to grow because its boundaries are concave and any grain with less than six sides will tend to shrink as it has convex sides. The shrinkage of the 5-sided grain in figure 11.4a leads to the formation of a 4-rayed vertex (fig. 11.4b) which decomposes into two 3-rayed vertices and the grain becomes 4-sided (fig. 11.4c). A similar interaction allows the grain to become 3-sided (fig. 11.4e) and to eventually disappear leaving a 5-sided grain adjoining a 7-sided grain (fig. 11.4f).

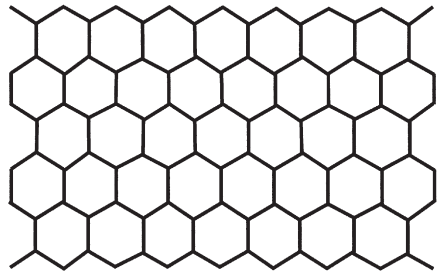

Fig. 11.3. A 2-dimensional array of equiaxed hexagonal grains is stable.

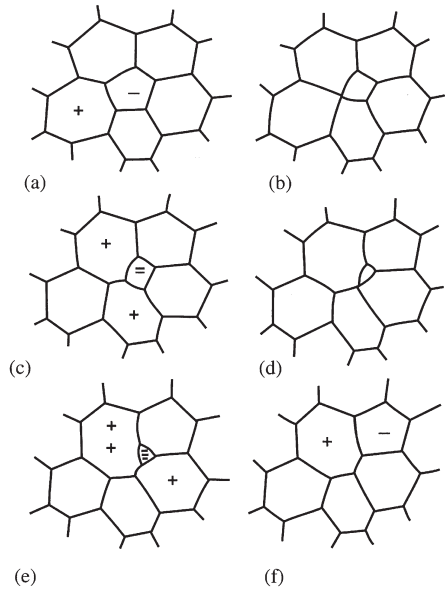

Fig. 11.4. Schematic diagram of growth of a 2-dimensional grain structure. (a) A grain of less than or more than 6 sides introduces instability into the structure, (b)–(f) Shrinking and disappearance of the 5-sided grain, (Hillert 1965).

Von Neumann (1952) and Mullins (1956) proposed on the basis of surface tension requirements, that the growth of a 2-D cell of area **A** with **N** sides is given by

$$\frac{dA}{dt} = c(N - 6) \tag{11.11}$$

or, if written in terms of grain radius (R)

$$\frac{dR}{dt} = \frac{c(N - 6)}{2R} \tag{11.12}$$

Rivier (1983) later showed that the **Von Neumann–Mullins law** is actually a geometric result and not due to surface tension.

In three dimensions, no regular polyhedron with plane sides can fill space and have its sides at the appropriate angles to balance the boundary tensions. As discussed in §4.5, the nearest shape is the Kelvin tetrakaidecahedron (fig. 4.17) but the angles are not exact and the boundaries must become curved to obtain equilibrium at the vertices. Therefore **grain growth is inevitable in an ideal 3-dimensional grain structure.**

11.2 THE DEVELOPMENT OF THEORIES AND MODELS OF GRAIN GROWTH

A complete theory of grain growth must take into account both the topological space-filling requirements discussed by Smith and the kinetics of local boundary migration as discussed by Burke and Turnbull. In this section we review the various attempts that have been made to improve on the theory discussed in §11.1.3. We should note that all the theories discussed below assume that the rate limiting factor in grain growth is the migration of the boundaries. However, grain growth also involves the migration of grain vertices, and the possibility that the mobility of these defects might become rate limiting under certain circumstances as discussed in §5.5, should not be ignored, although it appears likely that this is only significant for nano-structured materials.

11.2.1 Introduction

Because the geometry of an array of grains is very similar to that of a soap froth, and the stability and evolution of the latter is of interest in its own right, this analogy has been widely studied. For example Smith (1952) suggested, on the basis of data from soap froth experiments that the distribution of grain sizes and shapes should be invariant, and that the grain area should be proportional to time. In both systems the driving force for growth is the reduction in boundary energy. The analogy between the two cases is very close, and similar growth kinetics and grain size distributions are found, as discussed by Weaire and Rivier 1984, Atkinson 1988 and Weaire and Glazier 1992. However, the mechanisms of growth are different because in froths, growth occurs by gas molecules permeating through the cell membranes in order to equalise the pressures. There are other significant differences, and there are therefore limits to the extent that soap froth evolution can be used as an analogy for grain growth.

Theories and models of grain growth may be divided into two general categories, **deterministic** and **statistical**. Deterministic models are based on the premise that the behaviour of any grain in the assembly is dependent upon the behaviour of **all** the other grains. If the geometry of the whole grain assembly is known, then topological constraints are automatically accounted for, and by the application of relatively simple local rules such as equation 11.4, the evolution of the grain structure is predicted. This very powerful approach requires extensive computing power if reasonable sized grain assemblies are to be studied, and deterministic models will be further discussed in §11.2.4.

Statistical models are based on the assumption that the behaviour of the whole grain assembly can be calculated by generalising the behaviour of a small part of the microstructure. The Burke and Turnbull analysis is an example of such a model, and the later refinements which predict grain size distributions and which approximate the topographical constraints are discussed in §11.2.2 and §11.2.3.

The development of statistical theories of grain growth has a long and complex history and the merits of different approaches are still hotly debated. The essential problem is that the theories need to reduce the topological complexity of the real grain structure and its effect on the driving forces for grain growth to some average value, with a manageable number of parameters, for the particular grain under consideration. In assessing the theories we will concentrate on their predictions of the kinetics of grain growth and of the grain size distributions, and the comparison of these experimentally.

11.2.2 Early statistical theories

The majority of statistical grain growth theories fall into the category of **mean field theories** which determine the behaviour of a single grain or boundary in an environment which is some average representation of the whole assembly. The theories may be divided into two groups. During grain growth, the larger grains grow and the smaller grains shrink and statistically the grains can be considered to move in grain size–time–space under the action of a force which causes a drift in the mean grain size. Such models, typified by the theories of Feltham and Hillert are commonly known as **drift models.** Another approach, taken by Louat, is to consider the grain faces to undergo a random walk in the grain size–time–space. Grain growth then formally becomes a diffusion-like process, and this is often known as the **diffusion model.**

11.2.2.1 Feltham and Hillert's theories

Hillert (1965) developed a statistical theory of grain growth which was based on the assumption that the grain boundary velocity is inversely proportional to its radius of curvature. He used previous analyses of the Ostwald ripening of a distribution of second-phase particles to obtain the relationship

$$\frac{dR}{dt} = cM\gamma_b\left(\frac{1}{R_{crit}} - \frac{1}{R}\right) \tag{11.13}$$

where $c = 0.5$ for a 2-D array and 1 for a 3-D array. R_{crit} is a critical grain size which varies with time according to

$$\frac{d(R_{crit}^2)}{dt} = \frac{cM\gamma_b}{2} \tag{11.14a}$$

$$\frac{dR_{crit}}{dt} = \frac{cM\gamma_b}{4R_{crit}} \tag{11.14b}$$

A grain such that $R < R_{crit}$ will shrink, and one with $R > R_{crit}$ will grow. Hillert showed that topographic considerations resulted in the mean grain radius $\bar{R}$ being equal to R_{crit},

and therefore equation 11.14 predicts parabolic grain growth kinetics of the form of equations 11.4 and 11.5.

Hillert also solved equation 11.13 to obtain the grain size distribution f(R,t). As shown in figure 11.6a, this is much narrower than the log-normal distribution which is close to that found experimentally (§11.2.4 and fig. 11.6b). In Hillert's grain size distribution the maximum was $1.8\bar{R}$ for a 3-D array and $1.7\bar{R}$ for a 2-D array. He argued that if the initial grain size distribution contained no grains larger than $1.8\bar{R}$ then normal grain growth would result and the distribution would adjust to the predicted f(R,t). However, if grains larger than $1.8\bar{R}$ were present then he predicted that abnormal grain growth would result, although this latter conclusion has been shown to be incorrect (§11.5.1).

Hillert's result is very similar to that obtained by Feltham (1957), who started from the assertion that the normalised grain size distribution was log-normal and time invariant. He obtained

$$\frac{dR^2}{dt} = c \ln\left(\frac{R}{\bar{R}}\right) \tag{11.15}$$

where c is a constant. Setting $R = R_{max} = 2.5\bar{R}$ he obtained parabolic growth kinetics.

11.2.2.2 Louat's random walk theory

Louat (1974) argued that boundary motion can be analysed as a diffusional process in which sections of the boundary undergo random motion. This will lead to grain growth because the process of grain loss by shrinkage is not reversible. The theory predicts parabolic grain growth kinetics and an invariant Rayleigh grain size distribution (fig. 11.6a) which is close to that found experimentally (§11.2.4). Although the theory has been criticised by a number of authors on the grounds that it lacks a strong physical basis for its assumptions, it was later defended and further developed by its author (Louat et al. 1992). Pande (1987) has developed a statistical model which combines the random walk element of Louat's theory with the radius of curvature approach of Hillert.

11.2.3 The incorporation of topology

11.2.3.1 Defect models

Hillert (1965) proposed an alternative approach to two-dimensional grain growth based on the topological considerations discussed in §11.1.5. Within an array of six-sided grains, the introduction a 5-sided and 7-sided grain as shown in figure 11.4a, constitutes a stable defect. As growth occurs and the 5-sided grain ultimately disappears (fig. 11.4b–e), the 5–7 pair defect moves through the structure (fig. 11.4f). Hillert argued that the rate of growth depended on the time taken for the defect to move (i.e. for a 5-sided grain to shrink) and on the number of such defects in the microstructure. If the latter remained constant, which is a reasonable assumption for a time invariant grain distribution, then a parabolic growth rate similar to that for his statistical theory (equation 11.14) results. Morral and Ashby (1974) extended this model to 3-D by introducing 13 or 15-sided grains into an array of 14-sided polyhedra.

11.2.3.2 The Rhines and Craig analysis

Rhines and Craig (1974) emphasised the role of topology in grain growth. They argued that when a grain shrinks and disappears as shown in figure 11.4, then not only must this volume be shared out between the neighbouring grains, but because the topological attributes (shape, faces, edges, vertices etc.) of the neighbours also alter, this will in turn influence grains which are further away. They introduced two new concepts, the **sweep constant** and the **structural gradient.**

They defined a **sweep constant** Θ, as the number of grains lost when the grain boundaries in the specimen sweep out unit volume of material. They argued that Θ will remain constant during grain growth. An alternative parameter Θ^*, the number of grains lost when the boundaries sweep through a volume of material equal to that of the mean grain volume, was suggested by Doherty (1975). Clearly both these parameters cannot remain constant during grain growth, neither can be measured directly by experiment, and the matter is unresolved. The second parameter introduced by Rhines and Craig was the dimensionless **structural gradient** ς, which is the product of the **surface area per unit volume (S_v)** and the **surface curvature per grain (m_v/N_v)**. i.e.

$$\varsigma = \frac{m_v S_v}{N_v} \tag{11.16}$$

where N_v is the number of grains per unit volume and

$$m_V = \int_{S_V} \frac{1}{2}\left(\frac{1}{r_1} + \frac{1}{r_2}\right) dS_V \tag{11.17}$$

where r_1 and r_2 are the principal radii of curvature.

Rhines and Craig argued that ς should remain constant during growth and as shown in figure 11.5a, found ς to be constant in their experiments. However, Doherty (1975) suggested an alternative structure gradient $\varsigma^* = m_v/N_v$, which is the mean curvature per grain.

The Rhines and Craig analysis, using Doherty's modifications as suggested by Atkinson (1988) is as follows. The mean pressure (P) on the boundaries is

$$P = \frac{\gamma_b m_v}{S_v} \tag{11.18}$$

and the mean boundary velocity

$$v = MP = \frac{M\gamma_b m_V}{S_V} \tag{11.19}$$

The volume swept per second per unit volume of specimen is $v.S_v$, and if Θ^* grains are lost per unit volume, for each $\bar{V}$ (where $N_v = \bar{V}^{-1}$), the rate of loss of grains will be

$$\frac{dN_v}{dt} = \frac{\theta^* v S_v}{\bar{V}} = \theta^* M \gamma_b m_v N_v \tag{11.20}$$

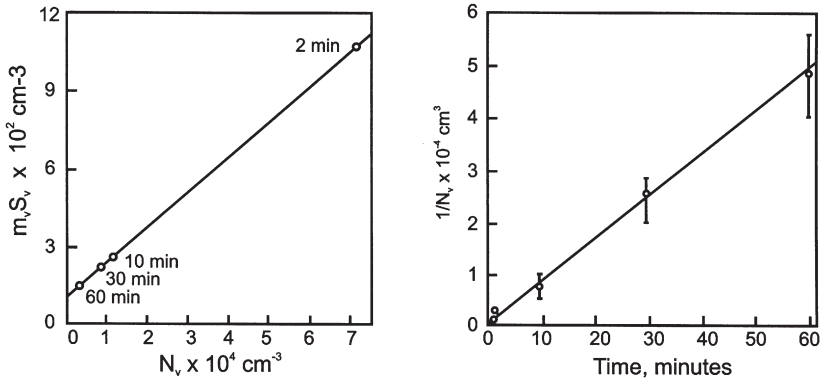

Fig. 11.5. (a) Plot of $m_v S_v$ against N_v for grain growth in aluminium, (b) Plot of mean grain volume ($1/N_v$) against annealing time for aluminium, (after Rhines and Craig 1974).

For each grain lost, per unit volume, there is a net increase in volume of $\bar{V}$ which on average is distributed over the remaining N_v grains. Therefore

$$\frac{d\bar{V}}{dt} = \frac{dN_V}{dt}\frac{\bar{V}}{N_V} = \frac{\theta^* M \gamma_b m_V}{N_V} \tag{11.21}$$

If Θ^*, M, γ_b, and m_v/N_v ($= \varsigma^*$) are constant with time then equation 11.21 can be integrated to give

$$\bar{V} = \frac{\theta^* M \gamma_b m_V t}{N_V} + \bar{V}_0 = ct + \bar{V}_0 \tag{11.22}$$

where $\bar{V}_0$ is the mean grain volume at $t = 0$.

As shown in figure 11.5b, Rhines and Craig (1974) found such a relationship in aluminium of 99.99% purity. A linear dependence of $\bar{V}$ on time implies that the grain radius is growing as $t^{1/3}$, i.e. **the grain growth exponent n of equation 11.7 is equal to 3.** As emphasised by Rhines and Craig (1974), this is an important difference from the value of **2** predicted by most other theories. The linear dependence of $\bar{V}$ on time is only predicted in the above analysis if ς^* remains constant, whereas the results shown in figure 11.5b shown a constancy of ς. Doherty (1975) has suggested that this could be reconciled if in equation 11.18, the driving pressure **P** was replaced by **(P−c)**, in accord with equation 11.9.

The Rhines and Craig experiments were carried out by the very time-consuming method of serial sectioning of specimens rather than by analysis of 2-D sections as is commonly done. They found that conventional 2-D analysis of their specimens resulted in the grain radius being proportional to $t^{0.43}$, i.e. $\mathbf{n = 2.3}$, which is rather close to that commonly

found (table 11.1). They concluded from the discrepancy between their 2-D and 3-D measurements that **N_v can only be determined from 3-D methods such as serial sectioning and cannot be inferred from measurements on a 2-D section.** There has been widespread discussion of this point, and the analysis of 3-D microstructures produced by computer simulation (Anderson et al. 1984, Srolovitz et al. 1984a) has been of help. These have shown that there will only be a serious discrepancy between 2-D and 3-D metallographic methods if the structure is **anisotropic**, and the difference in the grain growth exponents measured by Rhines and Craig (1974) in 2-D and 3-D therefore implies that their microstructure was anisotropic. There is of course a serious implication in this for all experiments based on 2-D sections, and the work of Rhines and Craig emphasises that grain shape anisotropy must be determined if 2-D measurements are to be used for comparison with theory.

This seminal work left a number of unanswered questions about theoretical and experimental aspects of grain growth kinetics. In particular, it was not clear whether a grain growth exponent of 3 would be the result of any model based on topographic considerations or whether it is specific to this particular analysis. As discussed by Atkinson (1988), it is not obvious that the microstructure will be in topographic equilibrium, particularly at low temperatures, and if this is the case then the local topographic constraints discussed in §11.2.3.1 may be more appropriate. Kurtz and Carpay (1980) proposed a detailed statistical theory of grain growth, which placed an emphasis on topographic considerations, and was essentially an extension of the Rhines and Craig model. However, unlike Rhines and Craig, Kurtz and Carpay predicted a parabolic ($\mathbf{n = 2}$) grain growth relationship.

Because of the difficulty of serial sectioning methods, experimental confirmation of $\bar{V} \propto t$ is limited to the work of Rhines and Craig (1974), and as shown by the results in tables 11.1 and 11.2, it would be inadvisable to place too much reliance on a study of a single material, in particular aluminium of only moderate purity, in which boundary mobility is known to be very sensitive to small amounts of impurity (§5.3.3). However a grain growth exponent of $\sim$3 would not be inconsistent with many investigations of metals.

11.2.3.3 The Abbruzzese–Heckelmann–Lücke model

These authors developed a 2-D statistical theory of grain growth (Lücke et al. 1990, 1992, Abbruzzese et al. 1992). A key element of their approach is the introduction of topological parameters relating the number of sides of a grain ($\bar{n}_i$) to its size (r_i). From experimental measurements they found that

$$\bar{n}_i = 3 + 3r_i \tag{11.23}$$

and that the mean size ($\bar{r}_n$) of grains with **n** sides was given by

$$n = 6 + \frac{3(\bar{r}_n - 1)}{\xi^2} \tag{11.24}$$

where ξ is a correlation coefficient equal to 0.85.

Although this **special linear relationship** is derived from experiments, the authors suggested that it would be generally applicable to equiaxed real grain structures. The parabolic grain growth kinetics predicted on this model are similar to those of the Hillert theory i.e. equation 11.14.

11.2.3.4 Other recent statistical theories

The discussions above show that although statistical theories of normal grain growth in pure single-phase polycrystals have been developed over a period of some 50 years, there is no general agreement as to the correct solution, or even if this type of approach can ever yield a satisfactory solution. New theories and modifications of the old theories are still being produced at an alarming rate as may be seen from the literature and the proceedings of recent conferences on grain growth. One of the main problems in reaching an agreement remains the representation of the topology of the grain structure both accurately and with a reasonable number of parameters.

11.2.4 Deterministic theories

If instead of considering the behaviour of an 'average' grain, we consider the growth and shrinkage of **every grain in the assembly** then many of the topological difficulties of the statistical models are bypassed. Hunderi and Ryum (1992b) discuss the relative merits of **statistical** and **deterministic** models of grain growth and illustrate this with an analysis of grain growth in one dimension, developed from the earlier deterministic model of Hunderi et al. (1979). These authors pointed out that the statistical theories described in §11.2.3 do not allow for the fact that a grain of a particular size can grow in an environment where it is surrounded by smaller grains, but will shrink if surrounded by larger grains, i.e. R_{crit} in equation 11.13 varies with position. They proposed a **linear bubble model** in which a bubble **i** makes contact with a number of other bubbles $\mathbf{i-n}$ to $\mathbf{i+n}$, where **n** depends on the relative sizes of the bubbles. The pressure difference between bubbles of different sizes leads to the transfer of material between the bubbles and sets of coupled equations are solved to predict the size distribution and grain growth kinetics of the bubbles, which are found to be close to those for parabolic growth predicted by Hillert. Extension of such an analytical model to large numbers of grains in 3-D is however, not currently practicable. The most promising deterministic models of grain growth in recent years have been those based on computer simulation of grain growth using the **equation of motion** and **Monte-Carlo** simulation methods, details of which are discussed in §16.2.

11.2.4.1 Equation-of-motion computer simulation

In this approach, which has mainly been applied to 2-D at present, a starting grain structure is specified, and this microstructure is then allowed to equilibrate by allowing the boundaries and vertices to move according to specific equations. For example, a boundary is adjusted to allow the angles at the triple points to be 120° and then the boundary is allowed to move by an amount proportional to its radius of curvature, this cycle being repeated over all boundaries a large number of times. This is essentially a quantification of the logical arguments which suggested the sequence shown in figure 11.4. The key feature of this type of approach is that once the initial microstructure is

constructed, the laws of motion formulated, and procedures for dealing with vertex contact and grain switching (fig. 16.8) specified, then no further assumptions are needed regarding topology, and the grain growth behaviour is thus truly deterministic.

A number of different authors have developed **vertex models** based on such methods (§16.2.4), and these are reviewed by Anderson (1986) and Atkinson (1988). The slightly different physical principles used have resulted in rather different grain size distributions and growth kinetics, although the latter are generally close to parabolic. These simulations have also shown that the initial growth kinetics are very sensitive to the starting grain structure. In order to make a significant contribution to our understanding of grain growth, this approach needs to be developed in 3-D, and preliminary work in this area has been carried out Nagai et al. (1992) and Maurice (2000).

11.2.4.2 Monte-Carlo computer simulation

The Monte-Carlo simulation technique, the principles of which are discussed in §16.2.1, has been extensively used to study grain growth. Early tests of a 2-D model (Anderson et al. 1984) showed that the shrinkage of a large isolated grain of area **A**, followed the relationship

$$A - A_0 = -ct \tag{11.25}$$

where A_0 is the grain size at $t = 0$ and c is a constant.

This leads to a parabolic relationship between grain size and time similar to that predicted by many theories (equation 11.5) and shows that the simulation leads to a linear dependence of boundary velocity on driving pressure (i.e. equation 5.1).

Significantly however, the growth of a 2-D grain structure such as is shown in figure 16.4, was found after an initial transient, to give a grain growth exponent of **2.44.** This differed significantly from the value of **2** predicted by the statistical theories discussed in §11.2, and was closer to the experimentally measured values (tables 11.1 and 11.2). Analysis of the computer-generated microstructures suggested that deviation from the exponent of 2 was due to topological effects. In particular, the movement and rotation of vertices was found to result in the redistribution of curvature between adjacent boundaries, and it was suggested by Anderson et al. (1984) that this lowered the local driving pressures for boundary migration, and was responsible for the higher grain growth exponent. These simulations indicated the importance of the random motion of boundaries which was first considered by Louat (1974) and also emphasised the importance of the local environment of a grain. Extension of these simulations to 3-D (Anderson et al. 1985) resulted in a grain growth exponent of **2.81** as compared to the Rhines and Craig (1974) prediction of **3.** At the time, these results therefore supported the Rhines and Craig (1974) view that grain growth exponents larger than **2** were an inevitable consequence of topological factors.

However, later simulations by the same group (Anderson et al. 1989a) run for longer times with larger arrays indicated that the earlier results were incorrect as they **did not represent steady state grain growth and were influenced by the starting grain structure.** The later

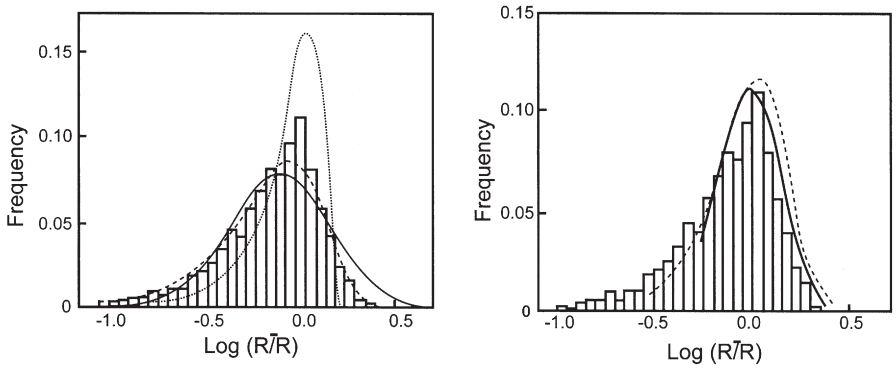

Fig. 11.6. Histogram of the grain size distributions from 2-D Monte-Carlo simulations compared with: (a) Theoretical distributions - log-normal (Feltham 1957), Hillert (1965) dotted, and Rayleigh (Louat 1974) dashed, (b) Experimental data - for aluminium (Beck 1954) and MgO (Aboav and Langdon 1969), dashed line, (after Srolovitz 1984a).

results revealed a growth exponent of **2.04** in 2-D and **2.12** for a 3-D simulation, which are very close to the $\mathbf{n=2}$ parabolic kinetics which are predicted on most theories, and Anderson concluded that the asymptotic long-time growth exponent is **2.**

The grain size distributions obtained by the Monte-Carlo simulations have been analysed by Srolovitz et al. (1984a) and Anderson et al. (1989a). The grain size distribution function, expressed in terms of $R/\bar{R}$ is found to be time invariant and close to experimental measurements as shown in figure 11.6. The grain size distribution determined from 2-D sections of the 3-D grain structure is closest to the Rayleigh distribution suggested by Louat (1974).

11.2.5 Recent theoretical developments

As noted in §11.1.1, modelling of grain growth remains a remarkably active area, and over the past decade over 20 papers have, on average, been published annually, most of these being refinements of earlier models. The mean field approach has been improved by taking account of spatial correlation among grains of different sizes (Marthinsen et al. 1996), and whilst this gives the correct kinetics, the size distributions are not in agreement with experiment unless further modifications are made (Mullins 1998a). Stochastic theories, often using the Fokker–Planck formulation, are based on a given grain growing in an environment which varies from grain to grain, and this gives a more complete description of grain growth (Mullins 1998a,b, Pande and Rajagopal 2001). However, a universally accepted stochastic theory of coarsening is not yet available (Pande and Rajagopal 2001). Models which take into account the fact that the grain boundary energies and mobilities in real materials are not isotropic have also been formulated (Kazaryan et al. 2002).

11.2.6 Which theory best accounts for grain growth in an ideal material?

The question should now be considered as to which theory or model, if any, is close to accounting for grain growth in pure single-phase materials. That there is no obvious answer is clear from the large number of approaches that are actively being pursued. Ryum and Hunderi (1989) have given a very clear analysis of the statistical theories of grain growth and shown that all make questionable assumptions.

We will briefly consider a number of basic questions:

(i) Is a grain growth exponent of 2 inevitable?
The discussions in this section have shown that the vast majority of theories predict parabolic kinetics. The main dissent from this is the work of Rhines and Craig (1974) which predicted $\mathbf{n = 3}$**.** However, their analysis is no longer accepted, and the extension of their work by Kurtz and Carpay (1980) predicted $\mathbf{n = 2}$**.** Indications from early Monte-Carlo simulations that a higher value of n was associated with topographic factors (Anderson et al. 1984) have proved to be an artefact of the model, as later simulations (Anderson et al. 1989a) found $n \sim 2$. In a review of the theory of the coarsening behaviour of **statistically self similar structures,** i.e. those in which the structure remains geometrically similar in a statistical sense, Mullins and Vinals (1989) concluded that for curvature driven growth, such as occurs during grain growth, an exponent of $\mathbf{n = 2}$ is inevitable.

The evidence in favour of $n = 2$ being the prediction of theory for an ideal single-phase material in which the boundary velocity is proportional to driving pressure and boundary energies are isotropic, appears to be conclusive.

(ii) Can grain size distributions be used to prove or disprove a theory?
As discussed earlier in this section, the various theories predict different grain size distributions, although it is usually predicted that the grain size distribution expressed in terms of normalised grain size ($R/\bar{R}$) will remain invariant during growth.

As shown in figure 11.6, the experimental data appear to be closest to the Rayleigh distribution, with the narrow Hillert distribution giving the worst fit. More recent reviews of experimental distributions (Pande 1987, Louat et al. 1992) have confirmed this, and the results of later Monte-Carlo simulations (Anderson et al. 1989a) have produced data consistent with the Rayleigh distributions. In comparing experiment with theory it should be noted that as discussed in §11.2.3.2, measurements from 2-D sections will only reflect the 3-D grain distribution if the grain structure is isotropic. Although there have been numerous correlations of measured and predicted distributions, Frost (1992) has shown that the grain size distribution predicted by individual statistical models can be varied by very small adjustments to the models and cannot therefore be used to prove the validity of a model.

(iii) Why is a grain growth exponent of 2 rarely measured?
As discussed in §11.1.4 and summarised in tables 11.1 and 11.2, grain growth exponents of **2** are rarely found experimentally and average values are close to **2.4.** If we accept that theory predicts $\mathbf{n = 2}$**,** then we must conclude that **the larger measured exponents are a consequence of the materials used not being ideal** i.e. not consistent with the basic

assumptions about the material which are incorporated in the models. We should recall that the driving pressure for grain growth is very small (§11.1) and therefore any small deviations from an 'ideal material' may have a very large effect on kinetics. There are several important parameters of the material which may lead to loss of ideality and have an influence on the kinetics:

- **The initial grain structure is not equiaxed or is far from the steady state grain size distribution.** Changes in grain size distribution during growth are known to affect experimentally measured grain growth kinetics (e.g. Takayama et al. 1992, Matsuura and Itoh 1992) and have been shown to produce large exponents during the early stages of growth in Monte-Carlo simulations (Anderson et al. 1984, 1989a).
- **The presence or development of a texture.** This would result in the occurrence of non-uniform boundary energies and mobilities thereby invalidating equations 11.3 and 11.4 which form the basis of grain growth theory.
- **The presence of very small amounts of a second-phase or other pinning defect.** As discussed in §11.1.4 this could account for high values of **n.**

These last two important factors are considered in more detail in the following sections.

11.3 GRAIN ORIENTATION AND TEXTURE EFFECTS IN GRAIN GROWTH

11.3.1 Kinetics

11.3.1.1 Experimental measurements

The rate of grain growth may be affected by the presence of a strong crystallographic texture (Beck and Sperry 1949). This arises at least in part from a large number of grains of similar orientation leading to more low angle (i.e. low energy and low mobility) boundaries (§4.2). Thus the driving pressure (equation 11.3) and hence the rates of growth are reduced. The texture may also alter during grain growth thereby affecting the kinetics (Distl et al. 1982, Heckelmann et al. 1992). The evolution of textures during grain growth is discussed in §12.4.4, and an example of the complex grain growth kinetics which are found when there are concurrent texture changes is seen in figure 12.22b.

11.3.1.2 Theories

Novikov (1979) modified a statistical model of grain growth to include variations of boundary energy and showed how the presence of texture would affect the kinetics of grain growth. Abbruzzese and Lücke (1986) and Eichelkraut et al. (1988) have incorporated the effects of texture into Hillert's model of grain growth. They argued that if a material contained texture components A,B,C ... etc., then the uniform boundary energies (γ_b) and mobilities (M) in equations 11.13 and 11.14 should be replaced by specific values relating to the texture components, ($\gamma_b{}^{AB}$, M^{AB} etc.) and that the critical radius R_{crit} in equation 11.13 would be different for each group of boundaries. They then calculated the grain growth of each texture component and showed that this might have a very strong effect on the grain size distribution and growth kinetics. Figure 11.7 shows the predicted change in these parameters for a material containing two texture components, A and B. The initial relative mean grain

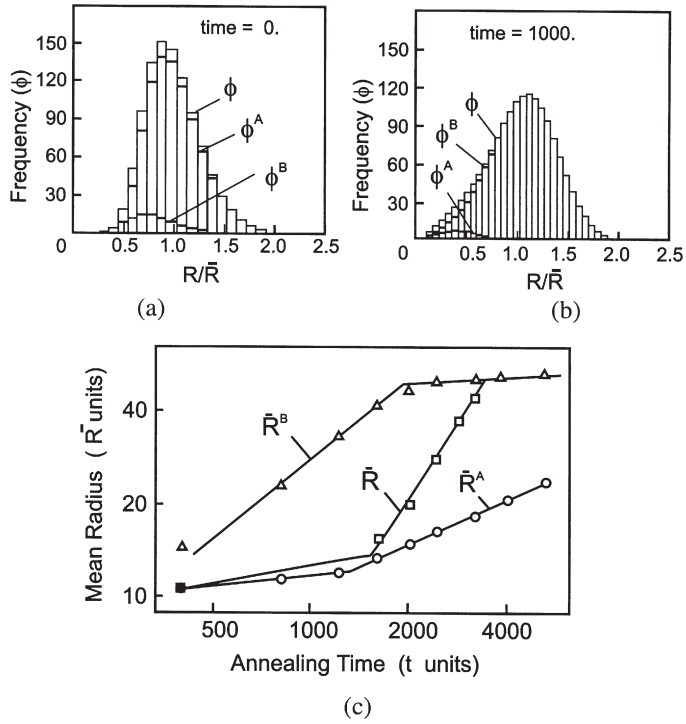

Fig. 11.7. Predicted grain growth in a microstructure containing texture components A and B. (a) Initial grain size distribution, (b) Grain size distribution after growth, (c) Growth kinetics, (after Abbruzzese and Lücke 1986).

sizes are $\bar{R}_B/\bar{R}_A = 0.8$, and the mobilities are $M^{AB}/M^{AA} = 5$ i.e. the mobility of A grains growing into B grains is five times that of A grains growing into A. It may be seen that in this case the A component is strongly depleted during growth (fig. 11.7a,b), that the grain size distribution is drastically altered, and that the relationship between $\bar{R}$ and t is complex (fig. 11.7c). There is some evidence of agreement between the predictions of the model and experimental measurements (Abbruzzese and Lücke 1986), although too much reliance should not be placed on quantitative agreement because the relationships between the mobility, energy and misorientation of grain boundaries are not known accurately.

11.3.1.3 Computer modelling

Grest et al. (1985) extended their Monte-Carlo simulation studies of grain growth to include variable boundary energies. They set the boundary energies according to the Read–Shockley relationship (equation 4.6) and varied the energy range by altering θ_m, the angle at which the energies saturate according to this equation. The simulation is therefore close to representing the annealing behaviour of a microstructure comprising a mixture of both high angle and low angle boundaries. However, as the mobilities of the

boundaries were not varied, the low angle (low energy) boundaries did not have the correspondingly low mobilities expected in a real material (§5.2). They found that the introduction of variable boundary energy led to an increase in the growth exponent (**n**) to **4.** The number of low angle boundaries increased during the anneal, compared with the constant energy simulation and the grain size distribution was broader. This simulation may be compared with the vertex simulation of recovery shown in figure 6.19, in which the low angle boundaries had both low energies and low mobilities and in which a large growth exponent **n** and a decrease in boundary misorientation were also found.

11.3.2 The effect of grain growth on grain boundary character distribution

As automated techniques for the rapid determination of crystallite orientations have become widely available in recent years, there has been a growing interest in the effect of grain growth and other annealing processes on **grain boundary character,** and particularly on its **distribution (GBCD),** (e.g. figs. 4.2 and A2.1) which is as much a quantitative measure of the microstructure of a material as is the grain size.

11.3.2.1 The frequency of special boundaries

There is a large body of evidence to show that the relative fractions of low-Σ boundaries often change during grain growth. In metals of medium to low stacking fault energy, where significant numbers of $\Sigma 3^n$ boundaries are present, the populations of both these and $\Sigma 1$ boundaries tend to increase during grain growth. Thus, in nickel, Furley and Randle (1991) reported an increase in $\Sigma 3$ (twin) boundaries and a decrease in $\Sigma 5$ boundaries during grain growth, and Randle and Brown (1989) found an increase in both low angle ($\Sigma 1$) and other low Σ boundaries during the annealing of austenitic stainless steel. Pan and Adams (1994) reported a greatly increased number of special boundaries ($\Sigma 1$, $\Sigma 3$ and $\Sigma 9$) during grain growth of Inconel 699.

Some of the clearest evidence as to the change of boundary character during grain growth in such materials has been obtained by Watanabe et al. (1989) who examined the misorientations of boundaries after grain growth and abnormal grain growth in an Fe–6.5%Si alloy which was annealed after rapid solidification. After a short annealing time (fig. 11.8a) the distribution of misorientation is close to the random value (fig. 4.2), but at long times (fig. 11.8c) it shifts markedly towards lower misorientations and a strong {100} texture develops. The frequency of low Σ and low angle boundaries was also found to increase markedly as grain growth proceeded as shown in figure 11.8d.

In fcc metals of high stacking fault energy, where there are few $\Sigma 3$ boundaries, but in which there are low angle ($\Sigma 1$) boundaries, the mean misorientation and therefore energy of these boundaries has been shown to decrease during subgrain growth when there is no orientation gradient, as discussed in §6.5.2.1 and shown in figure 6.16b.

11.3.2.2 Interpretation of the data

It was argued in §6.5.3.4 that the annealing of a microstructure with a distribution of boundary energies, the boundary tensions would inevitably lead to a decrease in the

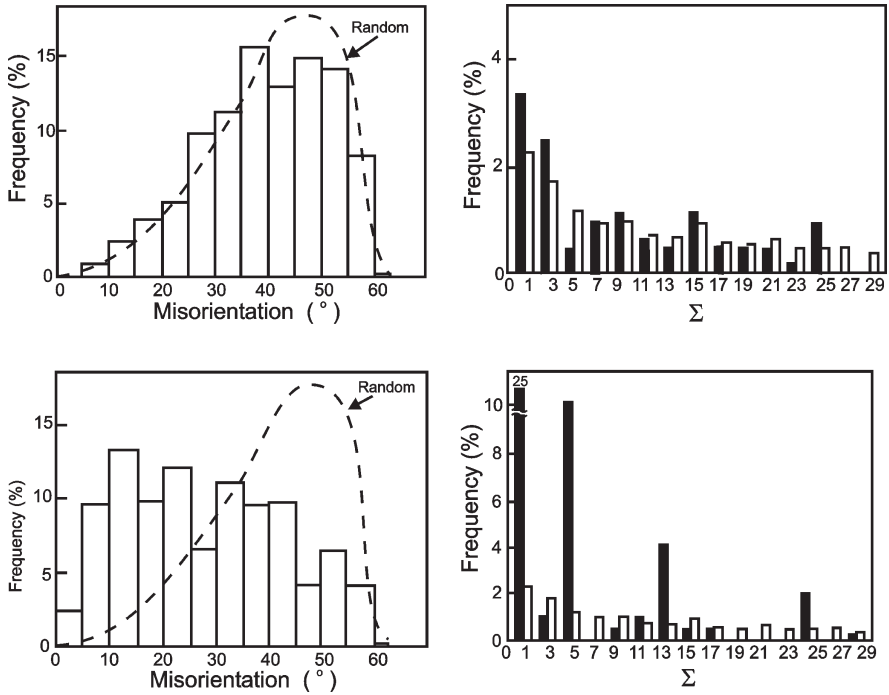

Fig. 11.8. The effect of grain growth on grain boundary character in rapidly solidified Fe–6.5wt%Si. (a) After an anneal for 600 secs at 1090°C, the measured distribution of grain misorientations is close to that for randomly oriented grains, and, (b) the frequency of special boundaries (shaded) is close to the random value (open), (c) After annealing for 3500 at 1090°C the mean misorientation is reduced and, (d) the frequency of low angle (Σ1) and other special boundaries is increased, (after Watanabe 1989).

total amount of high energy boundary relative to low energy boundary. This has been observed as discussed above, and has been shown to occur in both Monte-Carlo (Grest et al. 1985, Holm et al. 2001) and vertex (Humphreys 1992b) computer simulations.

In order to illustrate semi-quantitatively, the complexities of the problem we have run a simple vertex simulation with an initial microstructure containing five generic types of grain boundary:

1. Random high angle boundaries of constant energy and mobility
2. Low energy boundaries with low mobility (typified by LAGBs or Σ3 twins)
3. Low energy boundaries with high mobility (typified by low Σ boundaries in pure metals)
4. High energy boundaries with low mobility
5. High energy boundaries with high mobility

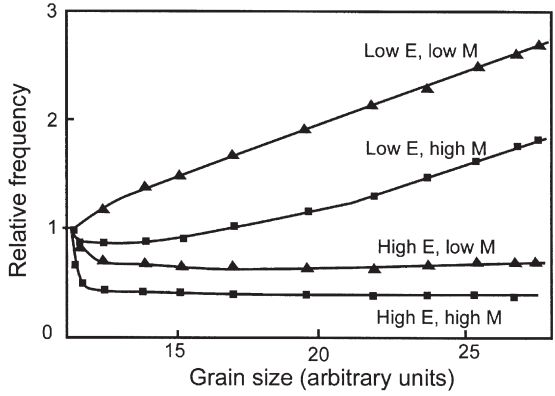

Fig. 11.9. Computer simulation of the change in boundary type during grain growth. The boundary frequencies are expressed as multiples of the frequency of a 'random' boundary.

High or low energies or mobilities were given values of x5 or 1/5 respectively that of the random boundaries. It was found that the distribution of boundary types changed during grain growth as shown in figure 11.9.

It is seen that there is a tendency for the proportion of low energy boundaries to increase and for high energy boundaries to decrease during grain growth. However, the boundary mobility plays a significant role, and it is interesting that the largest increase is predicted for low energy/low mobility boundaries such as LAGBs ($\Sigma 1$) and other low-Σ boundaries, which is in accord with the experimental results of figure 11.8.

From the above considerations of the effects of grain orientation and boundary character on grain growth, we conclude that there is experimental and theoretical evidence that bulk and local orientation effects are important during grain growth, and that these affect both the kinetics of grain growth and the microstructure. There is growing evidence that the **ideal materials with isotropic and unchanging boundary energy which are addressed in the standard theories of grain growth simply do not exist,** and the most fruitful developments in the theory of grain growth in single-phase materials will be those which take a more realistic account of orientation effects during grain growth.

11.3.2.3 Grain boundary engineering

The grain boundary character distribution can be of industrial significance because certain mechanical and physical properties of polycrystals depend on the nature of the grain boundaries. It has long been known that the properties of low energy low Σ boundaries differ from those of more general or 'random' high angle boundaries (e.g. §5.3.2), and it is well established (e.g. Palumbo and Aust 1992, Aust et al. 1993, Watanabe 1998) that the presence of such boundaries may improve the engineering

performance of the material. Important properties of such boundaries may include:

- Lower rates of grain boundary sliding during creep.
- Resistance to high temperature fracture.
- Resistance to solute segregation, precipitation and intergranular embrittlement.
- Lower electrical resistivity.
- Resistance to corrosion.
- Resistance to stress corrosion.

It was first suggested by Watanabe (1984) that thermomechanical processing could be used to control grain boundary distributions so as to improve the properties of materials, and this has given rise to the concept of **grain boundary engineering (GBE),** which is currently a very active research area, particularly for metals of medium and low stacking fault energy (see e.g. Watanabe 1998). GBE has been successfully exploited commercially in areas including the improvement in service performance of austenitic stainless steels and nickel alloys in power plant by Ontario Hydro (Lehockey et al. 1998), and an improvement in the corrosion and creep resistance of lead-acid battery grids (Lehockey et al. 1999).

Both recrystallization and grain growth may be used to increase the fraction of low Σ boundaries, and many cycles of deformation and annealing are often employed in order to optimise the material. For many applications, it is not simply the number of low energy boundaries which is important, but also their spatial distribution. For example, if failure occurs along grain boundaries of 'random' character, then it is important that the low-Σ boundaries are situated so as to break up the network of these boundaries. Thus the **3-dimensional connectivity of the boundaries** is also an important parameter (Randle 1999, Kumar et al. 2002, Schuh et al. 2003).

The science underlying the thermomechanical processing schedules used in grain boundary engineering is surprisingly poorly understood, and most of the processing schedules, some of which are patented, are purely empirical. In order to establish scientifically-based methods for controlling the boundary character distributions, there is a need for systematic research to establish how and why **recrystallization** affects the number and distribution of special boundaries. The effect of **grain growth** on the number of special boundaries is more predictable as discussed in §11.3.2.2 and shown in figures 11.8 and 11.9, although more detailed quantitative models are required.

11.4 THE EFFECT OF SECOND-PHASE PARTICLES ON GRAIN GROWTH

It was shown in §4.6 that second-phase particles exert a strong pinning effect (**Zener pinning**) on boundaries, with the pinning pressure being determined primarily by the size, volume fraction, interface and distribution of the particles. Because the driving pressure for grain growth is extremely low, particles may have a very large influence both on the kinetics of grain growth and on the resultant microstructures. It should be noted that at the high temperatures at which grain growth occurs, the dispersion of second-phase particles may not be stable. We will first deal with the behaviour of a material containing a stable dispersion of particles and at the end of this section

consider the cases where the particles themselves form, coarsen or migrate during the process of grain growth. It should be noted that the quantitative relationships presented below are based on the interaction of boundaries with a random distribution of non-coherent equiaxed particles. For other types of particle the retarding pressure due to the particles may be different as discussed in §4.6.1 and appropriate modifications to the theory should therefore be made.

Although the discussion below is presented in terms of **normal grain growth,** many of the considerations are also relevant to the **growth of a subgrain structure during recovery.** Those aspects of the theory which are particularly relevant to subgrain growth are further discussed in §6.6.

11.4.1 Kinetics

A dispersion of stable second-phase particles will reduce the rate of grain growth because the driving pressure for growth (P in equation 11.3) is opposed by the pinning pressure (P_z) due to the particles (equation 4.24). If this is incorporated into a simple grain growth theory such as the Burke and Turnbull (1952) analysis (§11.1.3), the rate of grain growth becomes

$$\frac{dR}{dt} = M(P - P_z) = M\left(\frac{\alpha\gamma_b}{R} - \frac{3F_v\gamma_b}{2r}\right) \tag{11.26}$$

This predicts a growth rate which is initially parabolic, but which subsequently reduces and eventually stagnates when $P = P_Z$.

Hillert (1965) extended his theory of normal grain growth to include the effects of particle pinning on the kinetics of grain growth and on the grain size distribution. The pinning pressure due to the particles results in a modification to the growth rate for single-phase materials (equation 11.13)

$$\frac{dR}{dt} = cm\gamma_b\left(\frac{1}{R_{crit}} - \frac{1}{R} \pm \frac{z}{c}\right) \tag{11.27}$$

where $c = 0.5$ for 2-D and 1 for 3-D and $z = 3F_V/4r$

For grains in the size range $1/R \pm z/c$, the net pressure for boundary migration will be zero and therefore no growth or shrinkage will occur. Grains larger or smaller than this will shrink or grow at a reduced rate. Hillert suggests that the mean growth rate will be given by

$$\frac{d\bar{R}^2}{dt} = \frac{cM\gamma_b}{2}\left(1 - \frac{z\bar{R}}{c}\right)^2 \tag{11.28}$$

which predicts a more gradual retardation of growth rate than equation 11.26. Hillert (1965) also points out that the grain size distribution will be affected by particle pinning. Abbruzzese and Lücke (1992) have extended this model and showed that the width of

the grain size distribution during normal grain growth should be reduced by particle pinning, for which there is some experimental evidence (Tweed et al. 1982).

11.4.2 The particle-limited grain size

It was shown many years ago by Zener (1948) that when the pressure on a boundary due to particle pinning equalled the driving pressure for grain growth, growth would cease and a **limiting** grain size would be reached. The existence of a limiting grain size is of great practical importance in preventing grain growth during the heat treatment of industrial alloys.

11.4.2.1 The Zener limit

In the situation which was first considered by Zener, the grain boundary is considered to be macroscopically planar as it interacts with the particles and therefore the pinning pressure (P_z) is given by equation 4.24. The driving pressure for growth (P) arises from the curvature of the grain boundaries, and is given by equation 11.3. Grain growth will cease when $P = P_z$. i.e.

$$\frac{\alpha \gamma_b}{R} = \frac{3 F_v \gamma_b}{2r} \tag{11.29}$$

If the mean grain radius is taken to equal the mean radius of curvature (R) then we obtain a limiting grain size

$$D_z = \frac{4\alpha r}{3F_V} \tag{11.30}$$

Setting $\alpha = 1$ (some authors use other values), results in the well known **Zener limiting grain size**

$$D_{Zener} = \frac{4r}{3F_V} \tag{11.31}$$

It has long been recognised that this is only an approximate solution, and numerous alternative approaches have been attempted. Hillert (1965) derived a limiting grain size from equation 11.27 by equating $1/R_{crit}$ with z/c for the case when R is large, giving a limiting grain radius for the 3-D analysis, of $4r/3F_V$, i.e. a grain diameter of twice that of equation 11.31 (α in equation 11.30 equal to 0.5). Gladman (1966) developed a geometric model consisting of tetrakaidecahedral grains and considered the effect of particles on the growth and shrinkage of the grains. He concluded that the limiting grain size was given by

$$D_G = \frac{\pi r}{3F_V}\left(\frac{3}{2} - \frac{2}{Z}\right) \tag{11.32}$$

where Z is the ratio of the maximum grain size to the average grain size, a parameter which is not readily calculated, but which is expected to lie between 1.33 and 2. Hillert's

(1965) grain growth theory gives $Z = 1.6$, and Gladman has suggested $Z = 2$. Using this value, Gladman's model, which has the same dependence on F_V and r as equation 11.30, predicts a limiting grain size which is smaller than that of equation 11.31, corresponding to equation 11.30 with $\alpha = 0.375$.

Numerous refinements to the Zener treatment have been carried out (e.g. Louat 1982, Hellman and Hillert 1975, Hillert 1988) and **these generally predict a limiting grain size which is of a similar form to equation 11.30 with $0.25 < \alpha < 0.5$,** i.e. considerably smaller than that predicted by equation 11.31. The many refinements of the Zener relationship have been comprehensively reviewed by Manohar et al. (1998).

11.4.2.2 Comparison with experiment

There are surprisingly few experimental results available to test these relationships accurately in materials containing low volume fractions of particles, and in particular to verify the dependence of D_Z on F_V. Gladman (1980) compared measurements of the limiting grain size (D_Z) from a number of investigations with his theory and found reasonable agreement. Tweed et al. (1982) in a detailed study of the recrystallized grain sizes and size distributions in three aluminium alloys containing very low volume fractions of Al_2O_3, found limiting grain sizes which in some cases corresponded to very small values of α in equation 11.30. However the data showed considerable scatter and it is difficult to reconcile the trend of the data with any model of limiting grain size. The limiting grain sizes obtained by Koul and Pickering (1982) after grain growth of iron alloys containing volume fractions of $\sim 5 \times 10^{-3}$ of carbide particles are shown in figure 11.10. It may be seen that although the data are limited and scattered, there is fair agreement with the theoretical line corresponding to equation 11.30 with $\alpha = 0.37$, i.e. Gladman's model. Manohar et al. (1998) have analysed the available experimental results for iron and aluminium alloys containing small volume fractions of second-phase particles, and conclude that they are consistent with equation 11.30 with $\alpha \sim \mathbf{0.26}$ (see fig. 11.12).

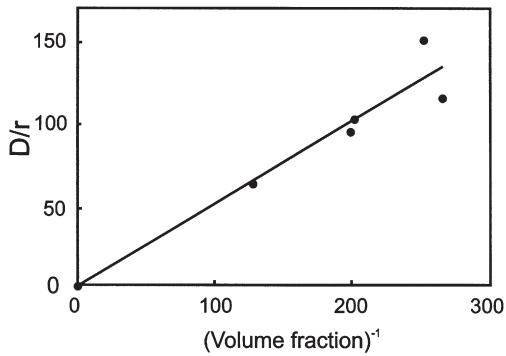

Fig. 11.10. The particle-limited grain size in carbide-containing Fe–Ni–Cr alloys, (data from Koul and Pickering 1982).

11.4.2.3 Particle-boundary correlation effects

The analyses discussed in §11.4.2.1 assumed that the pinning pressure (P_z) was that for a macroscopically planar boundary. However, as discussed in §4.6.2.2, when the interparticle spacing is similar to the grain size, this assumption is not valid, and non-random correlation of particles and boundaries must be taken into account. This will be particularly important in materials with large volume fractions of particles. In this situation, a limiting grain size (D_{Z1}) is found by equating the driving pressure (equation 11.3) with the pinning pressure as given by equation 4.27.

$$D_{Z1} = r\left(\frac{8\alpha}{3F_V}\right)^{1/2} \approx \frac{1.6\alpha^{1/2}r}{F_V^{1/2}} \tag{11.33}$$

The limiting grain size given by equation 11.33 is very similar to that suggested by Anand and Gurland (1975) for subgrain growth (fig. 6.29 and §6.6.2.1). It is however likely that D_{Z1} which represents the situation when all particles are on boundary corners but not all boundary corners are occupied by particles (fig. 4.25a), represents a lower bound for the limiting grain size and that grain growth will actually continue to occur until all grain corners are pinned, i.e. the grain size D_C of equation 4.28 (fig. 4.25b).

$$D_{ZC} = D_C \approx N_V^{-1/3} \approx \frac{\beta r}{F_V^{1/3}} \tag{11.34}$$

where β is a small geometric constant.

Various authors (Hellman and Hillert 1975, Hillert 1988, Hunderi and Ryum 1992a) have discussed this type of relationship, and Hillert (1988) suggests that $\beta = 3.6$.

The experimental measurements of limiting grain size in alloys containing large volume fractions of particles ($F_V > 0.05$) are very scattered (Hazzledine and Oldershaw 1990, Olgaard and Evans 1986) and although there is some indication that the limiting grain size is inversely proportional to F_V^n, where $n < 1$, the results are by no means conclusive. If equation 11.34 is assumed to hold, then analyses of the results of Hellmann and Hillert (1975) on steels and the data for Al–Ni of figure 11.14 give β as 3.3 and 3.4, respectively. The subgrain data of Anand and Gurland (1975) which were analysed by them in terms of equation 11.33 also fit equation 11.34, as shown in figure 6.29, with $\beta = 2.7$.

Figure 11.11 shows the predicted variation of the limiting grain sizes D_Z and D_{ZC} with volume fraction according to equations 11.30 and 11.34 using values of the geometric constants ($\alpha = 0.35$, $\beta = 3$) which are consistent with experiment. It may be seen that the curves cross at a volume fraction of ~0.06. At volume fractions less than this the particle-correlated limit (D_{ZC}) is unstable with respect to growth, and the uncorrelated limit (D_Z) is appropriate, whereas at higher volume fractions the limit will be D_{ZC}. In practice there will be a gradual transition between correlated and uncorrelated pinning as considered in §4.6.2.2, and this has been discussed by Hunderi and Ryum (1992a). The actual volume fraction at which the transition from D_Z to D_{ZC} occurs is not yet firmly established either theoretically or experimentally, but theoretical estimates

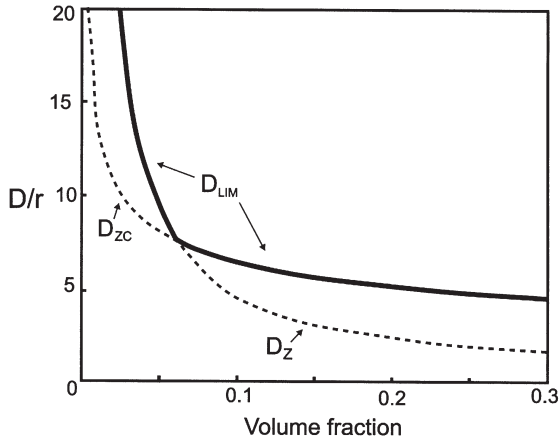

Fig. 11.11. The predicted variation with particle size and volume fraction of the particle-boundary correlated limiting grain size (D_{ZC}) for $\beta = 0.3$, and the non-correlated limiting grain size (D_Z) for $\alpha = 0.35$.

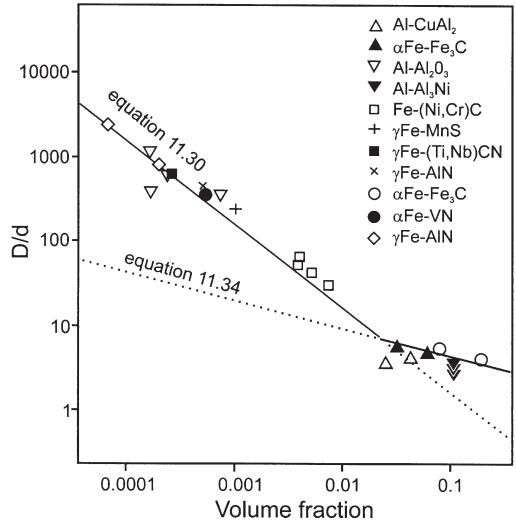

Fig. 11.12. Experimental measurements of the limiting grain/particle size ratio as a function of the volume fraction. The result are consistent with a transition from a F_V^{-1} to a $F_V^{-1/3}$ relationship at a volume fraction of ~0.05, in agreement with the theoretical analysis of figure 11.11, (after Manohar et al. 1998).

(Hillert 1988, Hazzledine and Oldershaw 1990, Hunderi & Ryum 1992a) put it within the range $0.01 < F_V < 0.1$, which is consistent with figure 11.11. A recent analysis by Manohar et al. (1998) of several experimental investigations, is shown in figure 11.12. The experimental results are seen to be consistent with the analysis of figure 11.11,

suggesting a transition from a F_V^{-1} to a $F_V^{-1/3}$ dependence of the limiting grain size, at $F_V \sim 0.05$.

The above considerations suggest that the effective limiting grain size (D_{lim}), will be the larger of D_Z or D_{ZC}, the solid line in figure 11.11, and that the transition will occur at a volume fraction of ~0.05.

11.4.2.4 Computer simulations

Extensive computer simulation of particle-controlled grain growth has been carried out using the Monte-Carlo technique (§16.2.1). The initial work (Srolovitz et al. 1984b) which was a 2-D simulation found a limiting grain size proportional to $F_V^{-1/2}$. However, it has since been shown (Hillert 1988, Hazzeldine and Oldershaw 1990) that the situation in 3-D is quite different and that the **2-D simulations of particle-limited grain growth are not applicable to grain growth in a 3-D microstructure, because a particle in a 2-D simulation is equivalent to a fibre in 3-D!** Later three dimensional Monte-Carlo simulations (Anderson et al. 1989b, Hazzledine and Oldershaw 1990) found a limiting grain size in accordance with equation 11.34, although their value of β (~9) is considerably larger than that found experimentally (§11.4.2.3). The earlier 3-D Monte-Carlo simulations were often limited to a lattice of $\sim 100^3$ units, with a particle diameter equal to one unit. Therefore for volume fractions less than ~0.05, as may be seen from equation 11.34, the limiting grain size approaches the size of the array, and accurate results cannot be obtained. Such simulations were therefore limited to the range in which D_{ZC} is expected to apply and could neither verify nor contradict the prediction that the limiting grain size (D_{lim}) changes from D_Z to D_{ZC} at a critical volume fraction.

Recent larger scale Monte Carlo simulations (Miodownic et al. 2000) have shown a F_V^{-1} dependence of the limiting grain size, in agreement with the original Zener prediction of equation 11.30, with $\alpha \sim 1$, i.e. equation 11.31, for particle volume fractions in the range 0.025 to 0.15. However, there are only 4 data points, and these results contradict the analytical considerations, other simulations and experiments discussed above, inasmuch as they find no transition at high volume fraction to a $D \propto F_V^{-1/3}$.

Although there is now more general agreement that at low volume fractions, the Zener relationship of equation 11.30 is obeyed, **the question of the transition to a relationship such as equation 11.34 at large volume fractions, remains unclear, requiring further investigation.**

11.4.2.5 A solute limited grain size?

As discussed in earlier sections, grain growth is promoted by the reduction in energy (ΔE_B) as the area of grain boundary decreases during growth. However for a solid solution, the situation is more complicated because some of the solute will segregate to the boundaries and lower the specific boundary energy (§5.4.2) whilst the remaining solute will raise the energy of the material in the grain interior (ΔE_G).

Consider a small-grained polycrystal containing a small amount of a solute which segregates strongly to the boundaries (see fig. 5.30). Initially, most of the solute will be in the grain boundaries. However, as the grains grow, the boundary area becomes

insufficient to accommodate all the solute, and some will be rejected, raising the free energy of the grain interiors.

At some stage of growth, the net free energy change, ΔE_G-ΔE_B, may become positive and the driving force for grain growth vanishes, i.e. we have a limiting grain size which is determined by solute. Such a concept was proposed by Weissmuller (1993) as being a method of promoting grain stability in nanostructured materials. The theory was further examined by Kirchheim (2002), who claimed that it would account for the stability of nano-scale grains in Ni–P and Ru–Al alloys, and has also been discussed by Gleiter (2000) in his review of nanostructured materials. The somewhat similar case of vacancy-limited grain growth is discussed in §5.3.4.1.

11.4.3 Particle instability during grain growth

We have assumed so far, that the second-phase particles are stable during grain growth. There are many situations in which this is not so, and in this section we examine the consequences of instability of the second-phase during grain growth for three important cases.

11.4.3.1 Precipitation after grain or subgrain formation

In some situations the second-phase particles may be precipitated after the formation of a grain or subgrain structure. In this case the particles are unlikely to be distributed uniformly and will form preferentially on the boundaries. The pinning pressure due to the particles will therefore be greater than for a random particle distribution (Hutchinson and Duggan 1978) as discussed in §4.6.2.3. If it is assumed that all the particles are on boundaries and are randomly distributed on these boundaries, then the pinning pressure is given by equation 4.36 and by equating this with the driving pressure given by equation 11.3, the limiting grain size is

$$D_{ZP} = r\left(\frac{8\alpha}{F_V}\right)^{1/2} \tag{11.35}$$

It is expected that in practice this situation will be more applicable to the **growth of subgrains during recovery** (§6.6) than to **grain growth,** although no quantitative tests of equation 11.35 have yet been reported.

11.4.3.2 Coarsening of dispersed particles during grain growth

An important situation is one in which grain growth has stagnated due to the particle dispersion, but the particles coarsen (Ostwald ripening). In this situation the grain size (D) is equal to D_{lim} as defined in §11.4.2.3, and the rate of growth is controlled by the rate of change of particle size. Thus

$$\frac{dR}{dt} = c\frac{dr}{dt} \tag{11.36}$$

where the constant c is $2\alpha/3F_V$ for low volume fractions and $\beta/2F_V^{1/3}$ for large volume fractions.

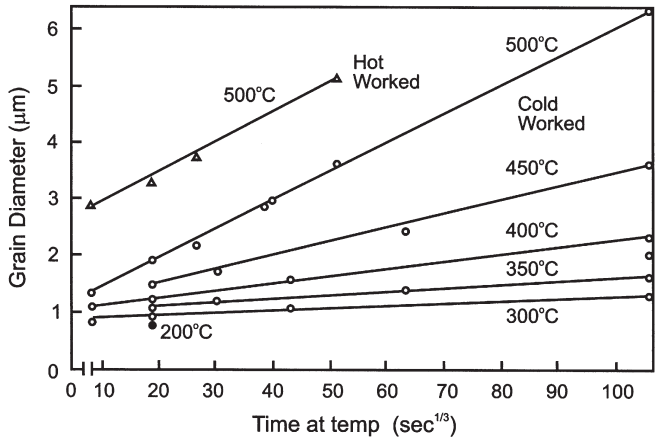

Fig. 11.13. The kinetics of grain growth when controlled by particle coarsening for an Al–6wt%Ni alloy containing a volume fraction of 0.10 of $NiAl_3$ particles, (Morris 1976).

The rate of particle coarsening will depend on the rate controlling mechanism (Hillert 1965, Gladman 1966, Hornbogen and Koster 1978, Ardell 1972, Martin and Doherty 1976). If the particle growth is controlled by volume diffusion (diffusivity $= D_s$) then (Wagner 1961)

$$\bar{R}^3 - \bar{R}_0^3 = c_1 D_s t \tag{11.37}$$

whereas for particle growth controlled by diffusion along the grain boundaries (diffusivity $= D_b$), which is commonly found for large volume fractions, as discussed below, then

$$\bar{R}^4 - \bar{R}_0^4 = c_2 D_b t \tag{11.38}$$

Figure 11.13 shows the kinetics of grain growth in an Al–6wt%Ni alloy which contains a volume fraction of 0.1 of $NiAl_3$ particles of initial diameter 0.3 μm. The grain growth kinetics, which are controlled by the particle coarsening are seen to be in accord with equation 11.37 over a wide temperature range. Figure 11.14 shows the relationship between the size of the grains and the second-phase particles in the same alloy system. The grain size is found to be proportional to the particle size as would be predicted by equation 11.34. From the slope of the line, the constant β in the equation is found to be 3.4. A similar linear relationship between particle and subgrain size has been reported in a commercial Al–Fe alloy (Forbord et al. 1997).

Coarsening of the particles by grain boundary diffusion will of course only affect those particles which are on grain boundaries, and other particles will coarsen more slowly. However, as grain growth occurs the boundaries will lose some particles and acquire others, and therefore the overall particle coarsening rate may be uniform, although the rate constant in equation 11.37 should include a correction factor to account for the fraction of the time a particle is not attached to a boundary.

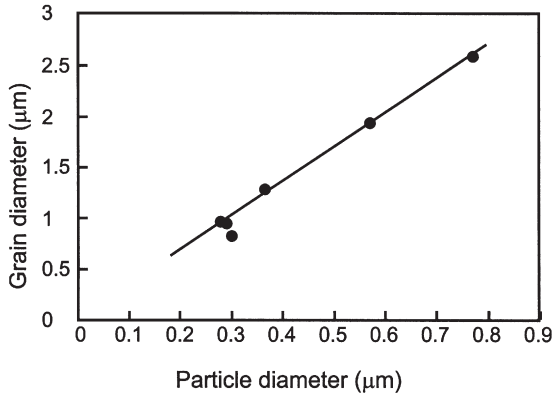

Fig. 11.14. The relationship between grain size and particle diameter for an Al–6wt%Ni alloy containing a volume fraction of 0.10 of $NiAl_3$ particles, (Humphreys and Chan 1996).

11.4.3.3 Coarsening of duplex microstructures

In a duplex alloy in which the volume fractions of the two phases are comparable, the rate of coarsening of the structure is controlled by interdiffusion between the phases over distances which are of the order of the size of the phases. In this situation the coarsening rate is predicted to be dependent on the coarsening mechanism and morphology and volume fractions of the phases (e.g. Ardell 1972, Martin and Doherty 1976). A detailed analysis of such phase growth is beyond the scope of this book, but typically, it is expected that the growth exponent will be ~3 for bulk diffusion control (equation 11.37) and ~4 for interface control (equation 11.38). Grewel and Ankem (1989, 1990) have studied grain growth in a variety of titanium-based alloys containing a wide range of volume fractions, such as the microstructure shown in figure 11.15 and find that, as shown in figure 11.16, the growth exponent is not particularly sensitive to volume fraction. However, it is found that as the temperature is raised from 700°C to 835°C the growth exponent **n** in Ti–Mn alloys decreases from 3.6 to 3.1, indicating a change in growth mechanism from interface to bulk diffusion control with increasing temperature.

Although Higgins et al. (1992) reported a growth exponent of ~4 for duplex Ni–Ag alloys, which is consistent with interface diffusion-controlled coarsening as discussed above, they found that the rate constants were several orders of magnitude greater than predicted by the theory of Ostwald ripening. They suggested that the non-spherical shape of the particles (e.g. fig. 11.15) and the resulting curvature provide a driving force for **particle migration and coalescence**.

11.4.4 Grain rotation

Randle and Ralph (1987) found that in a nickel-based superalloy in which grain growth was inhibited by the second-phase particles, there was a much higher frequency (~50%)

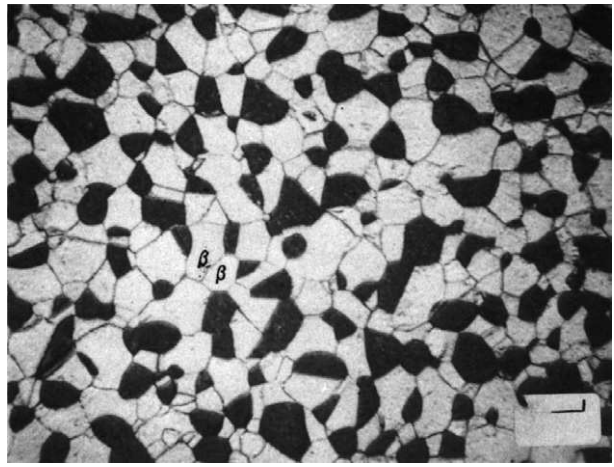

Fig. 11.15. Microstructure of a Ti–6%Mn alloy containing 44% of α-phase (dark) and 56% of β-phase, (Grewel and Ankem 1990).

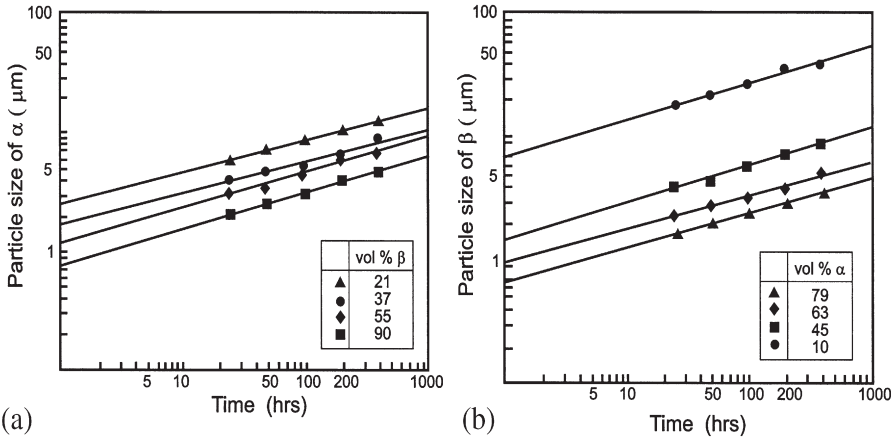

Fig. 11.16. Growth kinetics of the phases in a series of Ti–Mn alloys containing different volume fractions at 973K, (a) α-phase, (b) β-phase, (Grewel and Ankem 1989).

of low-Σ boundaries than in the same alloy in which precipitation had not occurred. It was suggested that this might be the result of grains rotating to produce lower energy boundaries (cf. subgrain rotation in §6.5.4), although there is as yet no direct experimental evidence to support this proposed mechanism, and as discussed in §11.3.2, a high frequency of special boundaries may often arise as a result of grain growth by boundary migration, or during the recrystallization of particle-containing alloys (§7.7.4.3). However, 2-D molecular dynamics simulations (§6.5.4.5 and fig. 6.27) have suggested that nanoscale grains may rotate at temperatures close to the melting temperatures.

11.4.5 Dragging of particles by boundaries

Equation 11.26 shows that grain growth in a particle-containing material occurs when the driving pressure (P) is greater than the pinning pressure (P_z), and in the subsequent discussions it has been assumed that growth ceases at a limiting grain size when these two pressures are equal. However, the pressure exerted by a boundary on a particle may, at high temperatures, be sufficient to drag the particle through the matrix, and in these circumstances boundary migration will continue at a rate determined by the mobility of the particle in the matrix (M_p) (Ashby 1980, Gottstein and Schwindlerman 1993).

The effect of driving pressure on boundary velocity is shown schematically in figure 11.17. For low driving pressures, ($P < P_z$) the boundary moves together with the particles and the velocity is given by

$$v = \frac{M_P P}{N_s} \tag{11.39}$$

where N_s is the number of particles per unit area of boundary.

However, when $P > P_z$ the boundary breaks away from the particles and velocity is given by $M(P - P_z)$, where M is the intrinsic mobility of the boundary (i.e. equation 11.26).

There are several mechanisms by which the particles can move through the matrix (Ashby 1980), including the migration of atoms (matrix or particle) by diffusion through the matrix, through the particle or along the interface. Ashby (1980) has shown that in general, coupled diffusion of both matrix and particle atoms is required. The resulting particle mobilities are low and are generally negligible for stable crystalline particles. However, for gas bubbles or amorphous or liquid particles, measurable particle velocities may occur at very high temperatures (Ashby 1980).

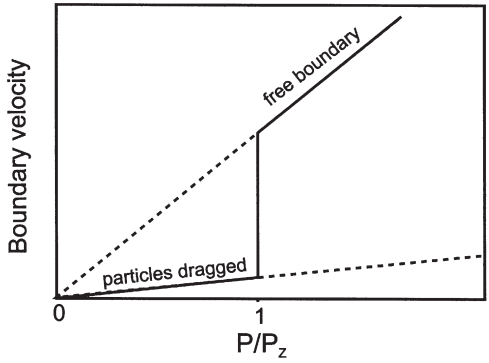

Fig. 11.17. The grain boundary velocity as a function of the driving pressure (P). At low driving pressures the boundary velocity is controlled by the dragging of particles, but when the driving pressure exceeds the pinning pressure due to particles (P_z), the boundary breaks free from the particles.

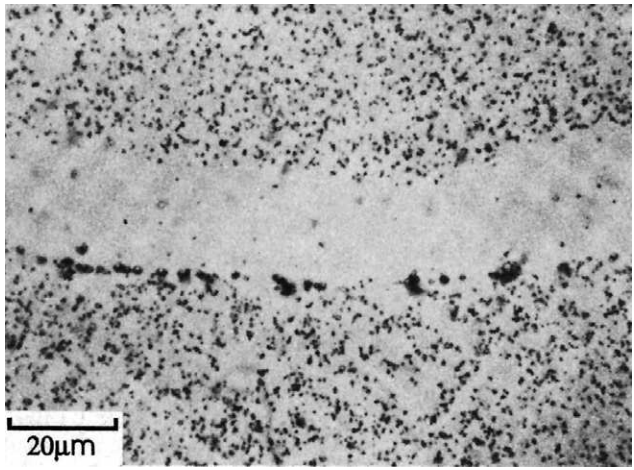

Fig. 11.18. Particle dragging by a boundary in copper containing amorphous SiO_2 particles. The particle-free band behind the migrating boundary and the increased particle concentration at the boundary are clearly seen, (Ashby and Palmer 1967).

Ashby and Centamore (1968) observed particle drag in copper containing various oxide dispersions annealed at high temperatures. As particles are swept along with the boundary, the number of particles on the boundary (N_s) increases as is seen in figure 11.18, and therefore the boundary velocity decreases according to equation 11.39. The mobilities of amorphous SiO_2, GeO_2 and B_2O_3 particles were all measurable at high temperatures, but significantly no migration of stable, crystalline Al_2O_3 particles was detectable. This phenomenon is therefore unlikely to be important in alloys containing stable crystalline particles. However, if such a mechanism were to occur in an engineering alloy, the resulting increased concentration of particles at grain boundaries would be expected to lead to increased brittleness and susceptibility to corrosion.

11.5 ABNORMAL GRAIN GROWTH

In the previous section we discussed the uniform growth of grains following recrystallization. There are however, circumstances when the microstructure becomes unstable and a few grains may grow excessively, consuming the smaller recrystallized grains (fig. 11.1b). This process, which may lead to grain diameters of several millimetres or greater is known as **abnormal grain growth.** Because this **discontinuous growth of selected grains** has similar kinetics to primary recrystallization and has some microstructural similarities, as shown in figure 11.19, it is sometimes known as **secondary recrystallization.** Abnormal grain growth is an important method of producing large grained materials and contributes to the processing of Fe–Si alloys for electrical applications (§15.4). The avoidance of abnormal grain growth at high temperatures is an important aspect of grain size control in steels and other alloys, and Dunn and Walter (1966) give an extensive review of abnormal grain growth in a wide variety of materials.

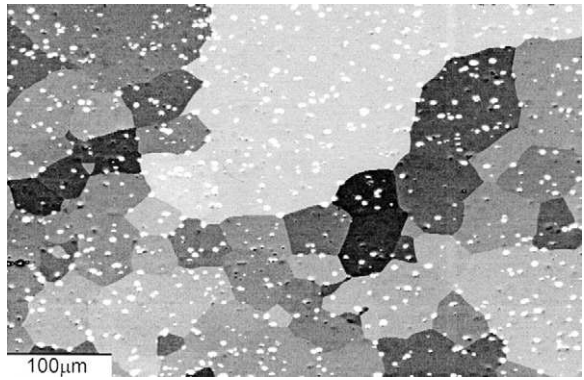

Fig. 11.19. Abnormal grain growth in Al–1%Mg–1%Mn annealed at 600°C.

11.5.1 The phenomenon

The driving force for abnormal grain growth is usually the reduction in grain boundary energy as for normal grain growth. However, in thin materials an additional driving force may arise from the orientation dependence of the surface energy (§11.5.4). Abnormal grain growth originates by the preferential growth of a few grains which have some special growth advantage over their neighbours, and the progress of abnormal grain growth may be described in some cases by the JMAK kinetics of equation 7.17 (Dunn and Walter 1966).

An important question to consider is whether or not abnormal grain growth can occur in an 'ideal grain assembly' i.e. one in which there are no impurities and the boundary energy is constant. As was shown by Thompson et al. (1987), the answer to this question can be deduced from the theory of grain growth, and we will base our discussion on the analysis presented in chapter 10.

Consider the growth of a particular grain of radius R in an assembly of grains of mean radius $\bar{R}$. The growth rates of the grain and the assembly are given by equations 10.10. and 10.13 respectively, and the condition for the abnormal growth of the particular grain is given by equation 10.14. For the 'ideal' material, all boundary energies and mobilities are equal and the condition for abnormal growth then becomes

$$\frac{4R}{R} - \frac{R^2}{R^2} - 4 > 0 \tag{11.40}$$

This condition is never achieved, although the left hand side equals zero when $R = 2\bar{R}$.

Thus a very large grain will always grow more slowly than the average grain relative to the grain assembly, and will eventually rejoin the normal size distribution. Therefore abnormal grain growth cannot occur in an 'ideal grain assembly'.

Monte-Carlo simulation of abnormal grain growth (Srolovitz et al. 1985) has been found to produce a similar result. Abnormal grain growth can therefore only occur

when normal grain growth is inhibited, unless the abnormally growing grain enjoys some advantage other than size over its neighbours. The main factors which lead to abnormal grain growth – **second-phase particles**, **texture** and **surface effects**, are considered below.

11.5.2 The effect of particles

As discussed in §11.4.2, a dispersion of second-phase particles will prevent growth above the limiting grain size. However, under certain circumstances, abnormal grain growth may still be possible. This phenomenon has been analysed by many people, the best known work being that of Hillert (1965) and Gladman (1966). In the following section, we explore, using the cellular stability model of chapter 10, the conditions under which abnormal grain growth occurs, and will reach conclusions which are in general agreement with the earlier work.

11.5.2.1 Conditions for abnormal grain growth

As discussed in §11.5.1, abnormal grain growth is an example of unstable or discontinuous growth of a cellular microstructure, and may be analysed accordingly. We will assume for the moment that all the grain boundary energies and mobilities are equal, and that the material, containing grains of mean radius $\bar{\mathbf{R}}$, and a volume fraction $\mathbf{F_V}$ of spherical particles of diameter **d.**

From equation 10.22 we see that $d\bar{R}/dt$ will become zero and thus normal grain growth will cease when

$$\Psi = \frac{1}{4} \tag{11.41}$$

where $\Psi = 3F_V\bar{R}/d$ (equation 10.21), and therefore the limiting grain size is

$$\bar{R}_{LIM} = \frac{d}{12\,F_V} \tag{11.42}$$

The limiting grain size, $\bar{R}_{LIM}$ as given by equation 11.42 is seen to be identical to the limiting grain size (D_Z) of equation 11.30, with the constant $\alpha = 0.25$, which is within the limits consistent with experimental observations (§11.4.2.1).

For $\Psi > 0.25$, it may be seen from inequality 10.12 that because $d\bar{R}/dt$ is always zero, abnormal grain growth will always occur provided that dR/dt is positive. As shown in figure 11.20, the **minimum** size of grain to initiate abnormal growth is small for $\Psi < 0.5$. However, the **maximum** size ratio which can be achieved by abnormal growth is less than 5 if $\Psi < 0.1$ (or $F_V/d < 1/30\bar{R}$). Below this value of Ψ we therefore find a **broadening of the grain size distribution rather than true abnormal growth.** As Ψ increases above 0.25, the minimum size of grain required to initiate abnormal growth increases, and it is seen from equation 10.23 that growth becomes impossible for even the largest abnormally growing grain if $\Psi \geq 1$ or

$$\frac{F_V}{d} > \frac{1}{3\bar{R}} \tag{11.43}$$

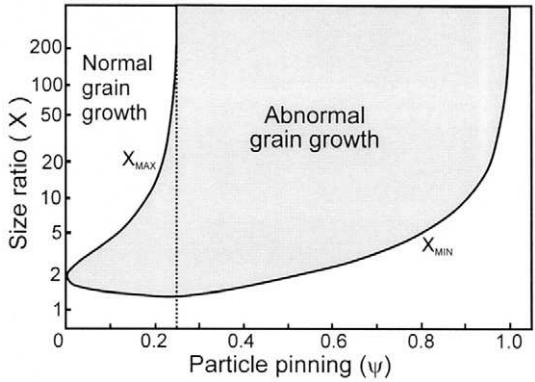

Fig. 11.20. The effect of particles (expressed in terms of the dimensionless parameter Ψ) on the minimum grain size ratio (X_{MIN}) required to initiate abnormal grain growth in an ideal grain assembly, and the maximum ratio (X_{MAX}) to which such grains may eventually grow. Note that for small values of Ψ, X_{MAX} is sufficiently small that size broadening rather than discontinuous grain growth will occur, (Humphreys 1997b).

which corresponds to a mean grain size (D_M) of

$$D_M = 2R = \frac{2d}{3F_V} \tag{11.44}$$

and therefore above this dispersion level no grain growth of any type can occur. D_M is seen to be four times the limiting grain size for normal grain growth given by equation 11.42. These predictions (and figure 11.20) are similar to the conclusions reached in the much more detailed model of Anderson et al. (1995). From our model we can identify 5 distinct regimes:

$\Psi = 0$	**Normal grain growth possible**
$0 < \Psi < 0.1$	**Broadening of grain size distribution**
$0.1 < \Psi < 0.25$	**Abnormal growth and normal grain growth**
$0.25 < \Psi < 1$	**Abnormal growth but no normal grain growth**
$\Psi > 1$	**No growth possible**

These regimes are shown in figure 11.21 as a function of the mean grain size ($\bar{R}$) and the dispersion level (F_V/d). The upper limit of Ψ for abnormal growth shown in figure 11.21 is the condition for migration of a planar boundary ($R = \infty$) and this assumes that abnormal grain growth is not limited by the availability of a suitably large grain as a 'nucleus'. However, as seen from figure 11.20, at larger values of Ψ the minimum grain size required to initiate abnormal grain growth increases and the largest available grain will depend on the size distribution in the grain assembly. It is often found that grain size distributions are log-normal and that the maximum is typically $\sim 2.5\bar{R}$ (e.g. fig.11.6). From equation 10.25, it can be shown that this corresponds to $\Psi \sim 0.6$ and this condition, which is a more realistic limit to abnormal grain growth is shown as a dotted line in figure 11.21. It should be noted that this analysis is based on the pinning due to

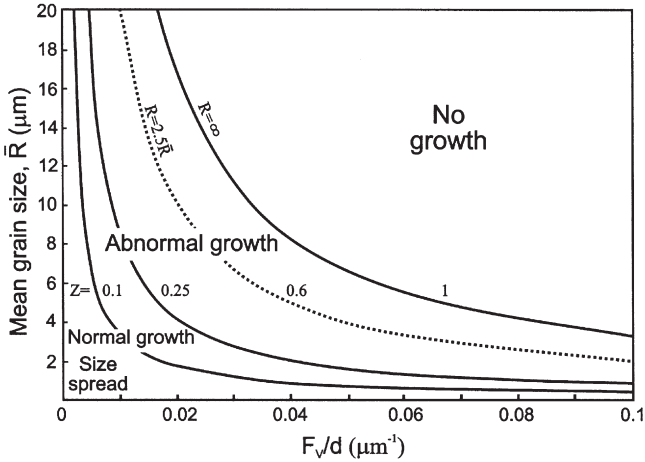

Fig. 11.21. The various growth regimes for an ideal grain assembly as a function of the matrix grain size ($\bar{R}$) and the particle dispersion level (F_V/d). The dotted line corresponds to $\Psi = 0.6$, which is the condition for the abnormal growth of a grain of diameter 2.5 times that of the assembly, (Humphreys 1997b).

particles being the Zener pinning pressure (equation 4.24), and as discussed in §4.6.2.2 and §11.4.2.3, this may not be appropriate for large particle volume fractions.

Alloys which have been processed to produce grain sizes of less than a micrometre are currently of considerable scientific and technological interest (§15.6), and the conditions for abnormal grain growth in these materials are further discussed in §14.5.2.

11.5.2.2 Experimental observations

Abnormal grain growth has been reported for a large number of alloys containing particle volume fractions of between 0.01 and 0.1, and details may be found in Dunn and Walter (1966), Cotterill and Mould (1976) and Detert (1978). However, there is very little evidence in the literature as to the precise conditions necessary to induce or prevent this phenomenon. The fact that abnormal grain growth does not occur more readily in particle-containing alloys may be due to a number of factors.

(i) In many cases the grain size produced during primary recrystallization is significantly greater than the particle-limited grain size, and Hillert (1965) noted that this is a very effective way of suppressing abnormal grain growth. According to the analysis above, abnormal grain growth will not be possible if the grain size is larger than four times the limiting grain size for normal grain growth. As discussed in §9.2.1, the grain size produced by primary recrystallization is a complex function of the particle parameters and the thermomechanical processing route, and in alloys in which the ratio F_V/r is large, particle pinning often results in a large grain size after primary recrystallization. As an example, consider the recrystallization data shown in figures 9.2 and 9.3 for particle-containing

aluminium alloys which exhibit accelerated and retarded recrystallization. Data for two specimens from each investigation (the extreme data points of each figure), are summarized in table 11.3. It can be seen that particularly for the material showing retarded recrystallization (material code1), the measured grain size is very much larger than the limiting grain size (D_Z) as given by equation 11.42, (or equation 11.30 with $\alpha = 0.25$). If the measured grain sizes are compared with D_M, the critical grain size for abnormal grain growth (equation 11.44), it may be seen that abnormal grain growth will not be possible in materials 1 or 2, but is highly likely in materials 3 and 4.

(ii) The occurrence of abnormal grain growth may be limited by 'nucleation' rather than growth considerations. Strong evidence for this comes from the large number of experimental observations which show that abnormal grain growth is particularly likely to occur as the annealing temperature is raised and as the particle dispersion becomes unstable. This is clearly shown in the classic early work of May and Turnbull (1958) on the effect of MnS particles on abnormal grain growth in silicon iron. Gladman (1966, 1992) has discussed the unpinning of boundaries under conditions of particle coarsening, with particular reference to steels in which the control of abnormal grain growth is of great technological importance, and the grain growth behaviour of some steels is shown in figure 11.22.

Plain carbon steels without grain refining additives show a coarsening of the grain size by normal grain growth. However, if conventional grain growth inhibitors (AlN) are present (fig. 11.22a), then small grains persist up to a temperature of ~1050°C at which temperature coarsening of the particles allows abnormal grain growth to occur, producing a very large grain size. At temperatures of ~1200°C, most of the particles have dissolved and normal grain growth then results. However, if a coarser dispersion

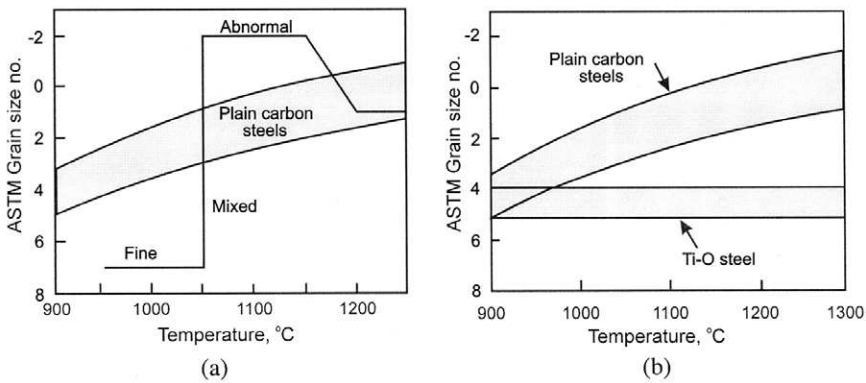

Fig. 11.22. Abnormal grain growth in steels. (a) TiN grain growth inhibitors are very effective in preventing normal grain growth, but their coarsening and dissolution lead to abnormal grain growth at high temperatures, (b) Coarse, insoluble, non-metallic inclusions are less effective in preventing normal grain growth, but their stability prevents abnormal grain growth, (Gladman 1992).

Table 11.3
Conditions for abnormal grain growth in some particle-containing aluminium alloys.

Code	Alloy	F_V	d (μm)	Grain Size (μm)	D_M (μm)	D_Z (μm)	Reference
1	Al–Cu	0.053	0.56	1483	11	2.5	Doherty and Martin (1964)
2	Al–Cu	0.03	1.01	68	67	15.7	
3	Al–Si	0.0012	0.7	160	583	114	Humphreys (1977)
4	Al–Si	0.01	4.9	44	490	16.3	

of more stable particles (e.g. oxides or titanium carbonitrides) is present (fig. 11.22b) then all grain growth is inhibited to very high temperatures.

According to the analysis of §11.5.2.1 as summarised in figure 11.21, if an alloy which is stable against abnormal growth is annealed at a temperature where the particles coarsen or the volume fraction decreases (i.e. lower F_V/d), abnormal grain growth will only become possible if the mean grain size does not increase proportionately. The onset of abnormal grain growth may then depend on local destabilization of the grain structure by removal or weakening of critical pinning points (Gladman 1966), leading to local inhomogeneous grain growth. The resulting broader grain size distribution may then enable the 'nucleation' of abnormal grain growth.

11.5.2.3 Computer simulation

Monte-Carlo simulations of abnormal grain growth in the presence of particles have been carried out in 2-D (Srolovitz et al. 1985) and 3-D (Doherty et al. 1990). In 2-D, although normal grain growth stagnated due to particle pinning, abnormal grain growth could not be induced. However, in the 3-D simulations, large artificially-induced grains were found to be stable and to consume the smaller pinned grains, which is in keeping with the analytical models discussed above and with the experimental observations. This result again emphasises the necessity of using 3-D simulations for the modelling of particle pinning.

11.5.3 The effect of texture

The inhibition of normal grain growth by texture (§11.3) may lead to the promotion of abnormal grain growth, and a review of the extensive work in this field is given by Dunn and Walter (1966) and Cotterill and Mould (1976). Perhaps the best example of this is the intensification of the Goss texture in silicon iron, which is discussed in (§15.4). In many cases normal grain growth is restricted by a number of factors such as particles and free surfaces in addition to texture, in which case it is difficult to quantify the role of texture in abnormal grain growth.

If a **single strong texture component** is present in a fine-grained recrystallized material, then abnormal grain growth commonly occurs on further annealing at high

temperatures. This has been clearly demonstrated for the cube texture in aluminium (Beck and Hu 1952), copper (Dahl and Pawlek 1936, Bowles and Boas 1948, Kronberg and Wilson 1949), nickel alloys (Burgers and Snoek 1935) and silicon iron (Dunn and Koh 1956).

Abnormal grain growth is possible in such a situation because within a highly textured volume the grain boundaries have a lower misorientation and hence a lower energy and mobility than within a normal grain structure. If some grains of another texture component are present, then these introduce boundaries of higher energy and mobility which may migrate preferentially by a process which is therefore closely related to primary recrystallization of a material containing subgrains (chapter 7).

Analyses of abnormal grain growth in a textured material have been carried out by e.g. Abbruzzeze and Lücke (1986) and Eichelkraut et al. (1988). The analysis discussed below is based on the model of Humphreys (1997a), which is presented in chapter 10. A somewhat similar analysis which considered only the effects of boundary mobility and not boundary energy, was given by Rollett et al. (1989b).

Abnormal grain growth tends to occur when there is at least one strong texture component. If this texture component is very sharp, then the mean misorientation ($\bar{\theta}$) is small and there are many low angle boundaries within a particular texture variant, whereas if the texture component is more diffuse then the boundaries have a higher mean misorientation. Typically, a texture component is defined as containing orientations within $\sim 15^\circ$ of some ideal orientation and therefore we could take $\bar{\theta} = 15^\circ$ as an upper limit for the grain/subgrain assembly in our model. There will be other grains in the microstructure which have either 'random' orientation, are part of another texture component or are a crystallographic variant of the main component. Thus we expect the microstructure to contain many high angle boundaries ($\bar{\theta} > 15^\circ$) and these will provide the 'nuclei' for discontinuous growth. The situation will therefore be similar to that shown in fig.10.3b for $\bar{\theta}$ in the range 5° to 15°, where we note that nucleation of abnormal grain growth will be easy, but the maximum size ratio of the abnormally growing grains will be small if the main texture component is diffuse (large $\bar{\theta}$). For example figure 10.3b indicates that if $\theta = 10^\circ$, the maximum size of abnormally growing grains will be approximately five times the mean grain size.

Diffuse textures: Hutchinson and Nes (1992) noted that in steel, Cu and Al, grains in the main texture components were larger than average, and similar results were reported during grain growth of Al–Mn (Distl et al. 1982, Weiland et al. 1988). These results may be demonstrating the transitional normal/abnormal behaviour predicted for grain assemblies with medium angle boundaries discussed above, for which broad size distributions rather than true abnormal growth, are predicted.

Strong textures: If the main texture component is strong, then $\bar{\theta}$ is small and stronger abnormal growth is predicted (fig.10.3a). This is amply confirmed by experiment, a good example being silicon iron (§15.4). The model presented in chapter 10, predicts that the maximum size ratio of the abnormal grains to the grain assembly should decrease as the main texture component is weakened, and quantifies the relationship between these parameters. Although this is broadly in line with experiments, there are few measurements quantitatively relating texture strength and grain size distribution.

11.5.4 Surface effects

It has long been recognised that abnormal grain growth is often easier in thin sheets than in bulk materials. This phenomenon is of particular importance in the production of sheet Fe–Si alloys (Dunn and Walter 1966) as is discussed in §15.4. The control of grain size and texture in the thin polycrystalline films used for electronic applications provides a more recent example of the importance of surface effects in grain growth (Abbruzzese and Brozzo 1992, Thompson 1992). Abnormal grain growth may occur in thin sheets if normal grain growth is inhibited by the free surfaces or by particles or texture as discussed above, and is particularly favoured if the texture leads to a significant variation of surface energy among the grains, as illustrated by the recent work of Greiser et al. (2001).

11.5.4.4 Surface inhibition of normal grain growth

When grains are of the order of the thickness of the sheet, then the grains are significantly curved only in one direction, and from equation 11.1, the driving pressure is seen to fall towards half that of a grain within a 3-D assembly. Thermal grooving at the junction between the boundary and the free surface, due to the balance between the surface tension and grain boundary tension may also exert a pinning effect on the boundary. The classic work on thermal grooving is due to Mullins (1958) and this treatment has been extended by Dunn (1966), Frost et al. (1990) and Frost et al. (1992). An application of Frost's computer model to the simulation of grain growth in thin metallic strips is shown in figure 16.9.

The following is a simplified treatment of the phenomenon.

Consider a single grain in a sheet of thickness **S,** whose boundaries are pinned by thermal grooving as shown in figure 11.23. The angle θ_g at the thermal groove as shown in figure 11.23b is determined by the balance between the forces arising from the boundary energy γ_b and the surface energy γ_{sur} and is given by

$$\theta_g = \arcsin\left(\frac{\gamma_b}{2\gamma_{sur}}\right) = \frac{\gamma_b}{2\gamma_{sur}} \tag{11.45}$$

The boundary can be pulled out of the groove if, at the surface, it deviates from the perpendicular by an angle of $\sim\theta_g$, which corresponds to a radius of curvature of

$$R_2 = \frac{S}{2\theta_g} \tag{11.46}$$

which can be equated with a pinning pressure due to thermal grooving of

$$P_g = \frac{\gamma_b^2}{S\gamma_{sur}} \tag{11.47}$$

This is opposed by the pressure **P** (equation 11.3) due to the in-plane curvature $\mathbf{R_1}$, (fig.11.23a). Thus, no grain growth will occur if $P_g \geq P$, and therefore the limiting grain

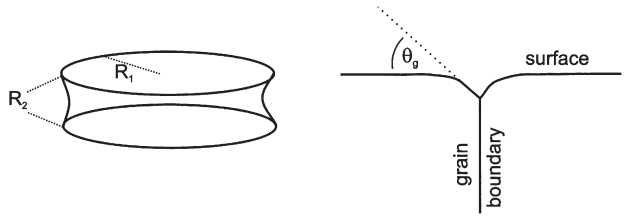

Fig. 11.23. Thermal grooving of a thin specimen. (a) The shape of an isolated grain in a thin sheet, (b) Thermal grooving at the surface.

size for normal grain growth (D_L) is given as

$$D_L = \frac{S c_1 \gamma_{sur}}{\gamma_b} \tag{11.48}$$

where c_1 is a small constant.

Mullins (1958) proposes that $c_1 = 0.8$, and computer simulations by Frost et al. (1992) give $c_1 \sim 0.9$. Typically, it is found that $\gamma_{sur} \sim 3\gamma_b$, suggesting a limiting size for normal grain growth in thin films of 2 to 3 times the thickness, which is consistent with experimental measurements in metals (Beck et al. 1949) and semiconductor films (Palmer et al. 1987).

11.5.4.5 Abnormal grain growth in thin films

There is considerable evidence that abnormal grain growth can readily occur in thin films or sheets in which normal grain growth has stagnated for the reasons discussed above (Beck et al. 1949, Dunn and Walter 1966, Palmer et al. 1987, Thompson 1992). That this abnormal grain growth is **not driven by boundary curvature** is clear from observations which show that the direction of motion may be in the opposite direction to that predicted by the curvature (Walter and Dunn 1960b), and from measurements which show that the boundary velocity is constant with time (Rosi et al. 1952, Walter 1965). Two dimensional computer simulations of grain growth are particularly effective for studying abnormal grain growth in thin films (Srolovitz et al. 1985, Rollett et al. 1989b, Frost and Thompson 1988).

The driving pressure for abnormal grain growth comes from the orientation dependence of the surface energy. If the difference in surface energy between two adjacent grains is $\Delta\gamma_{sur}$ then the driving pressure for boundary migration is $P_s = 2\Delta\gamma_{sur}/S$. As this has to overcome the drag due to thermal grooving the growth velocity will be

$$v = M(P_s - P_g) = \frac{M}{S}\left(2\Delta\gamma_{sur} - \frac{\gamma_b^2}{\gamma_{sur}}\right) \tag{11.49}$$

The velocity of abnormal grain growth is thus predicted to be inversely proportional to the sheet thickness, which is consistent with experiments on metal sheet (Foster et al. 1963) and semiconductor thin films (Palmer et al. 1987).

The condition that abnormal grain growth should occur is given from equation 11.49 as

$$2\Delta\gamma_{sur} > \frac{\gamma_b^2}{\gamma_{sur}} \tag{11.50}$$

or

$$\frac{\Delta\gamma_{sur}}{\gamma_{sur}} > c_2\left(\frac{\gamma_b}{\gamma_{sur}}\right)^2 \tag{11.51}$$

where c_2 is a small constant which is given by Mullins (1958) as 1/6 and Frost et al. (1992) as ~1/4.

Taking $\gamma_{sur}/\gamma_b = 3$, then equation 11.51 indicates that abnormal grain growth will occur if $\Delta\gamma_{sur} > 0.02\gamma_{sur}$, i.e. only a few percent difference in surface energy is required to promote abnormal grain growth in thin specimens.

Surface energy variations between grains are a consequence of grain orientation. Therefore the analysis above, which takes account of the variation of **surface energy** due to orientation but not the variation of the **grain boundary energy** due to texture, must be an oversimplification.

The surface energy of a grain is of course very dependent on the surface chemistry, and it has long been known that abnormal grain growth in Fe–Si alloys is affected by the atmosphere (Detert 1959, Walter and Dunn 1959, Dunn and Walter 1966). Recent work on grain oriented, silicon steel sheet (§15.4) has shown the importance of small alloying additions in determining surface energies.

11.5.5 The effect of prior deformation

There has been interest in the effects of small strains on grain growth and abnormal grain growth (Riontino et al. 1979, Randle and Brown 1989). The observation that a small prior plastic strain may prevent normal grain growth and promote the onset of anomalous grain growth has long been known (§1.2.1.3) and is probably best interpreted in terms of **primary recrystallization by strain induced boundary migration** (§7.6.2) rather than as a grain growth phenomenon.

Chapter 12

RECRYSTALLIZATION TEXTURES

12.1 INTRODUCTION

The recrystallization textures that develop when deformed metals are annealed have been the subject of extensive study. There are two reasons for this: first, and most important practically, these textures are largely responsible for the directionality of properties observed in many finished products and second, their origin is a source of much scientific interest. With respect to the latter, and despite frequent claims to the contrary, present understanding of the origin of recrystallization textures is little more than qualitative in nature. There are many reasons for this and most of them have already been discussed in earlier chapters. They are related to the nature of the nucleation event, the orientation dependence of the rate of nucleation in inhomogeneities of various type and orientation environment, and to the nature, energy and mobility of the boundaries between grains of various orientations. The determination of microtextures by Electron Backscatter Diffraction (EBSD) (appendix 1) which enables a correlation to be made between local orientation and microstructure, is now enabling some of these questions to be answered.

We begin by noting that there are several important matters which are often neglected in discussions of texture evolution.

- **The effect of subsequent grain growth.** The development of an annealing texture does not cease when recrystallization is complete. It continues during grain growth and

the final texture is not necessarily representative of the texture present when primary recrystallization is complete. Much of the immense amount of material available in the literature refers to textures that have been altered by growth.

- **The effect of strain.** Much of the data, and particularly that for fcc metals, refers to the annealing of very heavily rolled materials, e.g. 95–99% reduction by rolling. Such extreme deformation is not generally typical of industrial practice.

- **The starting texture.** Although a great deal of attention has been given to the relationship between the deformation texture and the recrystallization texture, there is increasing evidence that the orientation of the material before deformation plays a significant role in determining the recrystallization texture.

- **The effect of purity.** The purity of a particular metal may strongly influence the recrystallization texture. In many cases very small amounts of second elements may, by affecting the boundary mobility, change the annealing texture completely, e.g. 0.03% phosphorus in copper.

12.2 THE NATURE OF RECRYSTALLIZATION TEXTURES

In this section we describe the nature of the textures formed on annealing, and compare them with the deformation textures discussed in chapter 3. Although some comment is made on the effects of composition, strain and other processing variables, a detailed consideration of the ways in which recrystallization textures evolve is left until later in the chapter.

12.2.1 Recrystallization textures in fcc metals

The range of recrystallization textures seen in fcc metals and alloys is much wider and more complex than is the case for the corresponding deformation textures, and in many cases the origin of the textures is still a matter of debate.

12.2.1.1 Copper and its alloys

As discussed in §3.2, the rolling texture of pure copper consists basically of a tube in orientation space which includes as major components the orientations $\{123\}<634>$ (S) and $\{112\}<111>$ (Copper), together with a less significant $\{110\}<112>$ (Brass) component (table 3.1). In highly alloyed metals of low stacking fault energy such as 70:30 α-brass, the Brass orientation is dominant and there is additionally a less important $\{110\}<001>$ (Goss) component. The intermediate alloys have textures in which there is a more or less gradual transition from one extreme to the other. A similar, simple transition is not found in the recrystallized metals.

In the case of heavily rolled copper, and other fcc metals and alloys of medium to high stacking fault energy, the recrystallization texture consists of a strong cube texture $\{001\}<100>$ (fig. 12.1). If the stacking fault energy is sufficiently low, minor

Table 12.1
Components of recrystallization textures in fcc metals.

Notation	Miller indices	Euler angles		
		φ_1	Φ	φ_2
Cube	{001} < 100 >	0	0	0
-	{236} < 385 >	79	31	33
Goss (G)	{011} < 100 >	0	45	0
S	{123} < 634 >	59	37	63
P	{011} < 122 >	70	45	0
Q	{013} < 231 >	58	18	0
R (aluminium)	{124} < 211 >	57	29	63

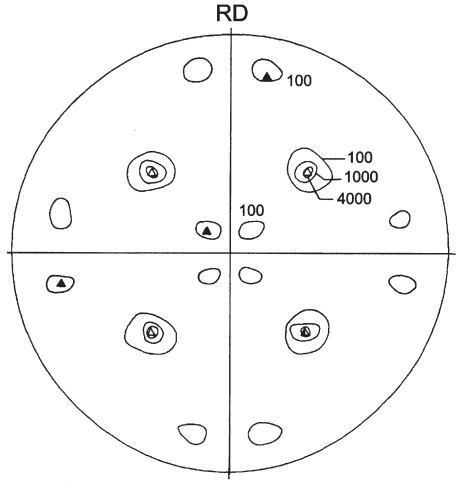

Fig. 12.1. 111 Pole figure of 97% cold rolled copper, annealed at 200°C (intensity in arbitrary units). Open symbols indicate the ideal 'cube' orientation {001} < 100 > and filled symbols {122} < 212 > the 'twin' orientation, (Beck and Hu 1966).

components that correspond to the twins of this orientation are also present. The strong cube texture of copper is eliminated by quite small amounts of many alloying elements, e.g. Al 5%, Be 1%, Cd 0.2%, Mg 1.5%, Ni 4.2%, P 0.03%, Sb 0.3%, Sn 1%, Zn 4% (Barrett and Massalski 1980). It will be recognised that for the most part these alloying elements reduce the stacking fault energy and change the nature of the deformation texture. A similar change in deformation texture occurs if copper is rolled at low temperatures (−196°C) and as would be expected, the cube texture is then absent after annealing.

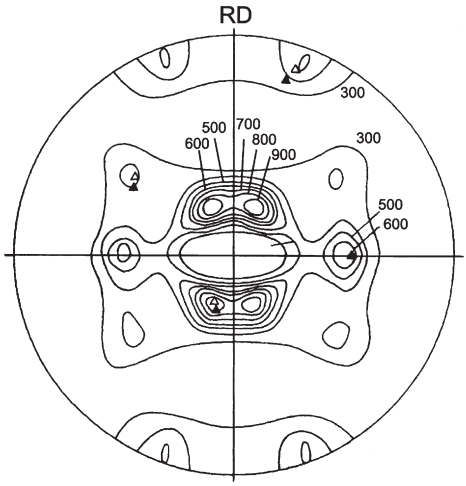

Fig. 12.2. 111 Pole figure of 95% cold rolled 70:30 brass, annealed at 340°C, (intensity in arbitrary units). Opens symbols indicate ideal $\{225\}<374>$ and filled symbols $\{113\}<211>$ orientations, (Beck and Hu 1966).

Low stacking fault energy copper alloys – There have been many investigations of copper–zinc alloys. The recrystallization texture of 70:30 brass (fig. 12.2) is usually reported to be $\{236\}<385>$, but it will be shown later that this can be significantly altered by variation of the annealing temperature. The strong cube texture of copper is lost rapidly as the alloy content increases and in the 3% zinc alloy is very weak. Similarly the $\{236\}<385>$ texture is not a major component in alloys containing less than 10% zinc. In the intermediate range of 3–15%Zn a series of complex orientations is developed. These annealing textures have been investigated extensively by Lücke and colleagues, (e.g. Schmidt et al. 1975, Virnich and Lücke 1978, Hirsch 1986). Their results for this and several other alloy systems are summarised in figure 12.3. It is found that stacking fault energy is the dominant parameter and if the results are normalised with respect to stacking fault energy then consistent behaviour is observed for a range of alloys. In figure 12.3 the texture components are plotted as a function of the **reduced stacking fault energy,** $\gamma_{\mathrm{RSFE}} = \gamma_{\mathrm{SFE}}/\mathrm{Gb}$.

It will be seen that there is a marked change in the nature of the recrystallization texture at $\gamma_{\mathrm{RSFE}} \sim 3.10^{-3}$ corresponding to ~8%Zn, 3%Al or 2%Ge. At about this value the $\{236\}<385>$ component begins to develop in the alloys and thereafter rises rapidly to a near maximum value at $\gamma_{\mathrm{RSFE}} \sim 2.2 \times 10^{-3}$. At lower values, the cube texture is the strongest component although its strength is significant only for low alloy contents. Typical ODFs for the system Cu–Zn are given in figure 12.4, and the volume fractions of the various texture components are shown in figure 12.5. The Euler angles for these and other recrystallization texture components are given in table 12.1.

Copper–manganese alloys – Unlike most elements, the addition of manganese to copper does not lower the stacking fault energy and, as discussed in §3.6.4, increasing manganese content leads to increasing Brass and Goss deformation textures. On

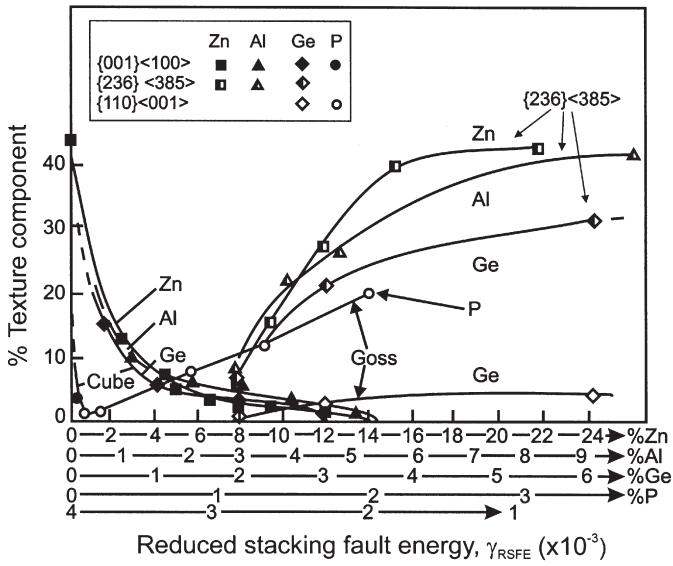

Fig. 12.3. Volume fraction of major texture components ($\{100\}<001>$; $\{236\}<385>$; $\{110\}<001>$) in recrystallized copper based alloys, plotted as a function of the reduced stacking fault energy, $\gamma_{RSFE} = \gamma_{SFE}/Gb$, (Lücke 1984).

recrystallization, Engler (2001a) has shown that the cube texture disappears as the Mn level increases and α-fibre components such as Goss and $\{236\}<385>$ dominate. However, the textures are rather weak except for very large rolling reductions.

Effect of processing variables – There have been many investigations of the effects of microstructure and processing variables such as prior grain size and texture, strain, time, temperature of annealing and rate of heating on these basic textures. It is not possible to review all of these and only a few specific examples are discussed. In the case of the cube texture it has been known for more than fifty years that this texture is reduced by:

- small rolling reductions ($\leq$50%) with intermediate annealing,
- a large grain size at the beginning of the penultimate rolling stage, and
- a low final annealing temperature.

An example of the effects of prior grain size, rolling reduction and annealing temperature in 70:30 brass is found in the work of Duggan and Lee (1988). After annealing for 1 hr at 300°C (low temperature) the texture of material cold rolled 92% changed from the normal $\{236\}<385>$ (fig. 12.6a) to $\{110\}<110>$ (fig. 12.6b) as the prior grain size increased, but the magnitude of the change was strain dependent and non-existent at 97% reduction. Annealing at high temperatures (600°C) led to a $\{113\}<332>$ texture for small grain sized material and high reductions (fig. 12.6c). After low reductions the $\{110\}<112>$ and more general $\{110\}<hkl>$ orientations

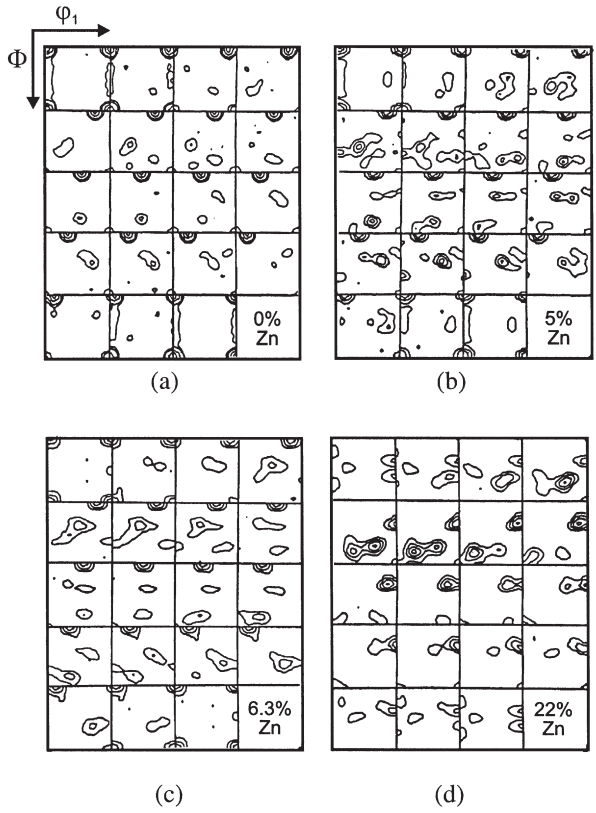

Fig. 12.4. Recrystallization textures of rolled and annealed copper–zinc alloys. (a) Cu, (b) 5%Zn, (c) 6.3%Zn, (d) 22%Zn, (Virnich and Lücke 1978).

were produced. The $\{110\}<112>$ texture was present to higher strain levels as the grain size increased. It seems probable that the high temperature $\{113\}<332>$ texture involved grain growth, and in the 97% rolled material, where grain growth was limited by the specimen thickness and the short annealing times, the texture was $\{236\}<385>$. For all grain sizes investigated (30–3000 μm) the texture of heavily rolled material was $\{236\}<385>$ after annealing at 300°C, and $\{113\}<332>$ for 600°C annealing. These results illustrate the importance of grain growth effects on annealing textures.

ODF data from Yeung et al. (1988) have confirmed the importance of annealing temperature. Specimens of 70:30 brass of 100 μm grain size, were cold rolled and annealed in a salt bath at 300°C and 900°C. The volume fractions of some of the main texture components measured from the ODF data are summarised in table 12.2. Nucleation was found to occur in all of the various types of deformation inhomogeneities present in the microstructure after annealing at 900°C, and for 95% rolled material the volume fraction of the $\{236\}<385>$ orientation was reduced from

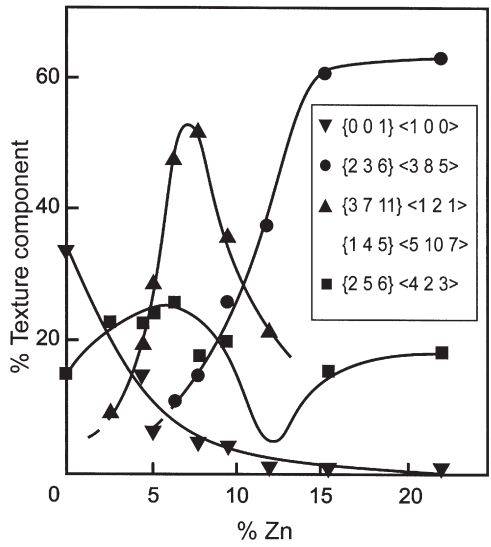

Fig. 12.5. Volume percentage of texture components in recrystallized copper–zinc alloys, (Virnich and Lücke 1978).

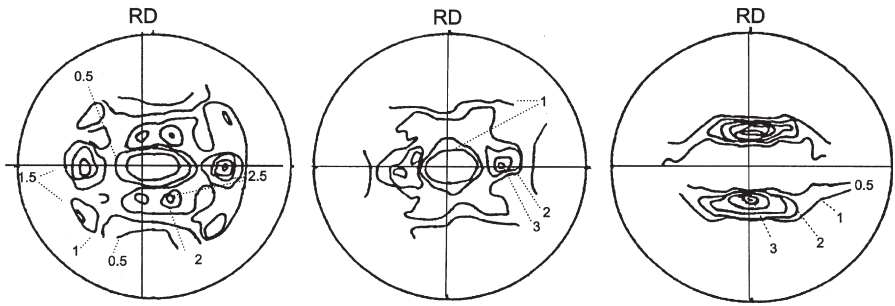

Fig. 12.6. Effect of prior grain size on the recrystallization texture of 92% cold rolled and annealed 70:30 brass. (a) 30 μm grain size, 18 hr at 300°C, (b) 3000 μm grain size, 18 hr at 300°C, (c) 30 μm grain size, 1 hr at 600°C, (Duggan and Lee 1988).

0.35 at 300°C to ~0.1 at 900°C. The major components after the high temperature annealing were characteristic of the rolling texture, i.e. 32% by volume of a component with orientation between B and S and 16.8% of one that was developed by an ND rotation of the cube component. The changes were attributed to the absence of recovery during the rapid heating to the high annealing temperature, which resulted in recrystallization nucleating uniformly over all components of the deformation microstructure. When coupled with the rapid boundary migration rate associated with high temperature annealing, the retention of rolling texture components is to be expected.

Table 12.2
Volume percentages of some texture components in recrystallized 70:30 brass after the rolling reductions shown and subsequent annealing, (Yeung et al. 1988).

Component	Volume % of component after annealing					
	T = 300°C			T = 900°C		
	cr. 80%	cr. 87%	cr. 95%	cr. 80%	cr. 87%	cr. 95%
{001} < 100 >	2.4	3.1		0.5	3.3	
Brass–Goss					24.0	5.9
{236} < 385 >			35.2			9.4
ND rotated cube						16.8
Brass–S						31.8
Others	20.0	34.7	20.9	54.3	29.0	7.1
Random	77.6	62.2	43.9	45.2	43.7	29.0

Table 12.2 illustrates well, a little recognised aspect of recrystallization textures. It is commonly asserted that such textures are sharp and well defined, particularly after large strains. However, as shown in the table, the volume fraction of random and other minor components is high in all cases.

Fibre textures – The recrystallization textures of copper-based wires, and other products which have fibre textures, are normally similar to the corresponding deformation textures. In the case of copper, low temperature annealing of wires leads to fibre textures based on < 100 > or < 112 >, but high temperature annealing leads to mixed < 111 > to < 112 > type textures.

12.2.1.2 Single-phase aluminium alloys

When annealed after cold rolling, high purity aluminium develops the characteristic cube texture found in materials of high to medium stacking fault energy. As in the case of copper, the texture is strengthened by high rolling reductions and high annealing temperatures.

The presence of magnesium in solid solution reduces recovery, increases the strength of the alloy and leads to the formation of shear bands during cold rolling (§2.8). These lead to a reduction in the strength of the normally dominant cube texture for two reasons.

- The shear bands cut through the elongated cube bands which are responsible for the cube-oriented recrystallized grains (§2.8 and §12.4.1) and therefore suppress the formation of the cube texture (Ridha and Hutchinson 1982).

- Recrystallization nucleates in the shear bands (§7.6.4.3), and texture components such as {011} < 100 > (Goss), {011} < 122 > (P) and {013} < 231 > (Q) occur (Hirsch

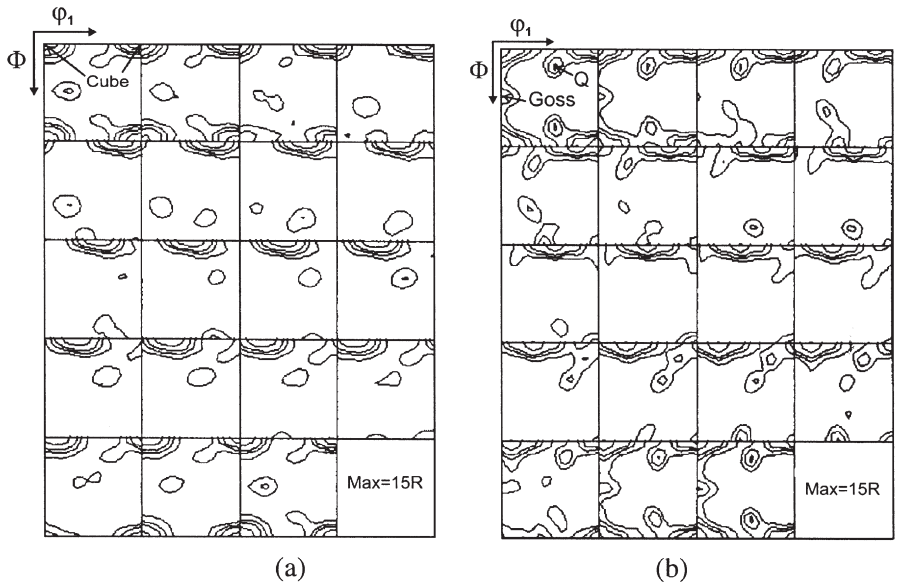

Fig. 12.7. The effect of cold rolling reduction on the recrystallization textures of coarse-grained Al–3%Mg: (a) prior reduction 90%, (b) prior reduction 97.5%, (Engler 2001b).

1990a, Lücke and Engler 1992, Engler 2001b). The overall textures may be quite weak, suggesting that grains of more random orientation are also generated within the highly deformed shear bands.

In Al–3%Mg, the recrystallization texture is strongly affected by the amount of deformation (Engler 2001b) as shown in figure 12.7. After a cold rolling reduction of 90%, the cube texture remains dominant after recrystallization (fig. 12.7a), but after a reduction of 97.5%, strong Q and Goss components are formed (fig. 12.7b). This behaviour is rather similar to that of a solution treated Al–1.8%Cu alloy (Engler et al. 1995).

Because the small amounts of elements such as iron and silicon, which are present in aluminium of commercial purity, result in the formation of second-phase particles either before or during the recrystallization anneal, **almost all commercial aluminium alloys are multiphase, and the amount of research on genuinely single-phase aluminium alloys is rather limited.**

12.2.2 Recrystallization textures in bcc metals

Because annealed low carbon steel sheet is a product of major industrial importance the optimisation of properties is of continuing interest. Texture, grain size, composition, second phase dispersions and processing at each of the several production stages are all important and their respective roles in selected products are discussed in detail in chapter 15.

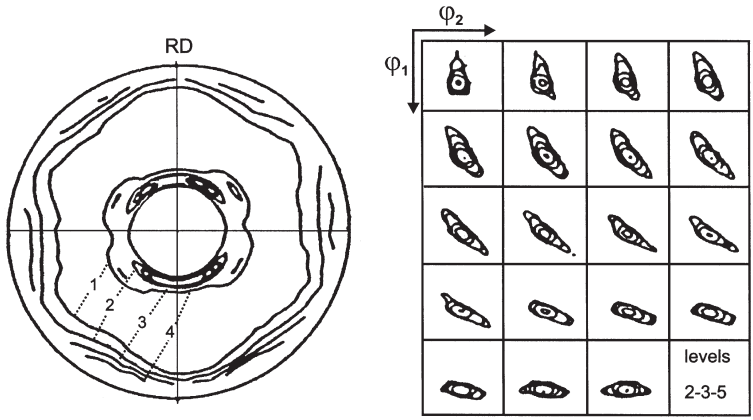

Fig. 12.8. Recrystallization textures of an interstitial-free steel after 80% prior reduction by cold rolling. (a) 110 pole figure, (b) ODF, (Emren et al. 1986).

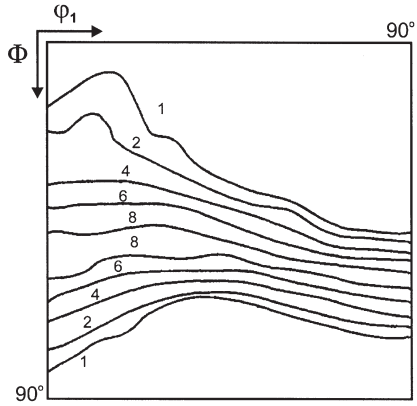

Fig. 12.9. $\varphi_2 = 45^\circ$ section of ODF for recrystallized IF steel, (Hutchinson and Ryde 1997).

Emren et al. (1986) have made a detailed study of texture development in vacuum degassed, aluminium-killed and interstitial-free steels and in Armco iron. The extent of rolling, the time and temperature of annealing and the heating rate were all varied. The 110 pole figures for each material after 80% rolling and annealing at 700°C were basically similar, and that for an interstitial-free steel is shown in figure 12.8a; the corresponding ODF is shown in figure 12.8b. It is clear that the recrystallization texture is basically similar to the rolling texture shown in figure 3.9 and that the recrystallization

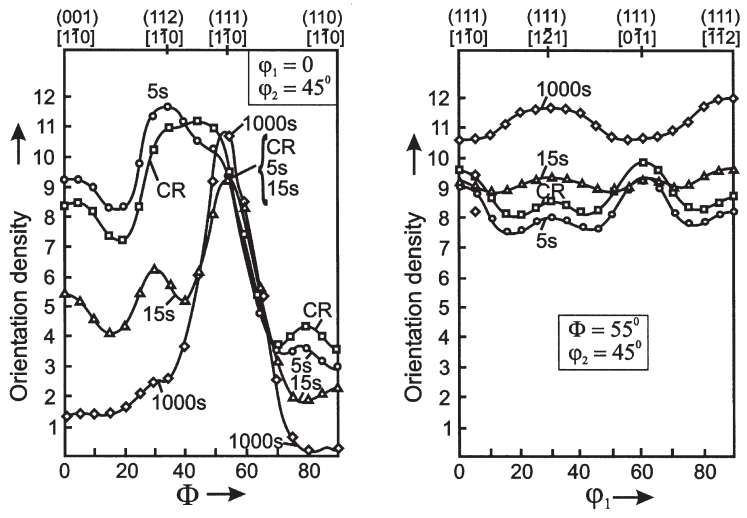

(a) (b)

Fig. 12.10. Orientation density f(g) along α- and γ fibres for different stages of recrystallization in 85%, cold rolled steel after annealing at 700°C. (a) Along α-fibre, (b) Along γ-fibre, (Emren et al. 1986).

texture can still be described by reference to the fibres used earlier for the rolled state (§3.3 and fig. 3.10), viz:

- **The α-fibre,** a partial fibre texture with a $<110>$ fibre axis parallel to the rolling direction and intensity maxima at $\{001\}<110>$, $\{112\}<110>$ and $\{111\}<110>$.
- **The γ-fibre**, a fairly complete fibre texture with the $<111>$ fibre axis parallel to the sheet normal; the major components in this fibre texture have $<110>$, $<112>$ and $<123>$ aligned with the rolling direction.

A typical recrystallization texture plotted in the $\phi_2 = 45°$ section is shown in figure 12.9. Comparison with the corresponding deformation textures of figure 3.10 shows that the recrystallization orientations are generally close to the α and γ fibres, but that much of the α-fibre has been eliminated on recrystallization, especially in the range (001)[1$\bar{1}$0] to (112)[1$\bar{1}$0]. The γ-fibre is relatively unchanged.

Examination of the development of texture during annealing at 700°C of a vacuum degassed steel (fig. 12.10), shows a loss of orientations near $\{112\}<110>$ and $\{001\}<110>$ and an increase in the strength of the $\{111\}<112>$ component. The $\{111\}<110>$ component remains constant.

There is a significant difference in the nature of the recrystallization textures for bcc and fcc metals. The rolling textures for both can best be described by prominent fibres and in bcc metals these fibres are largely retained in the recrystallization texture. In contrast, the recrystallization textures of rolled fcc metals are better described by individual peak-type components which are not always prominent in the deformation texture.

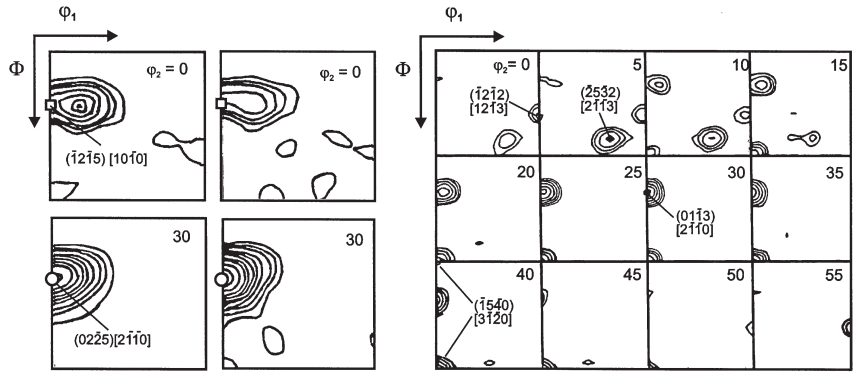

Fig. 12.11. $\varphi_2 = 0°$ and $\varphi_2 = 30°$ sections for 90%, cold rolled titanium after recrystallization at (a) 600°C, (b) 800°C, (c) complete ODF for recrystallization at 1000°C, (Inoue and Inakazu 1988).

The industrially important iron-silicon, electrical steels will not be discussed in this chapter, and a detailed account of the generation of the strong $\{110\} < 001 >$ (Goss) texture typical of this material is given in §15.4.

12.2.3 Recrystallization textures in hexagonal metals

The early studies of recrystallization textures in hexagonal metals reported that, in general, the rolling textures were retained with some redistribution of intensity (Barrett and Massalski 1980) and this is largely true of the rather limited number of more recent studies (Philippe 1994). Orientation distribution function results from Inoue and Inakazu (1988) for rolled and recrystallized titanium showed that the major component after annealing within the α-phase field was $\{0225\} < 2110 >$ irrespective of the extent of rolling or the annealing temperature. This orientation is related to the major component of the rolling texture, $(1214)[10\bar{1}0]$ by a 30° [0001] rotation. However, the intensity increased considerably as the reduction or the annealing temperature was increased. When annealing was carried out at 1000°C, i.e. within the β-phase field, the texture was modified by variant selection associated with the phase transformation. Figure 12.11 shows selected sections of the ODFs for material recrystallized in the α and β temperature ranges.

12.2.4 Recrystallization textures in two-phase alloys

In addition to the size and spacing of the particles, the recrystallization textures that form when multi-phase alloys are annealed depend particularly on whether the second phase is present during deformation, or whether precipitation occurs on annealing (see Hornbogen and Kreye 1969, Hatherly and Dillamore 1975, Hornbogen and Köster

Table 12.3
Major components of the recrystallization texture for some particle-containing alloys, (from Humphreys and Juul Jensen 1986).

Material	Rolling reduction	Particles		Recrystallization texture
		$F_V \times 100$	Diameter (μm)	
Al (99.9965)	90	0	–	Cube
Fe–AlN	70	0.06	0.017	Rolling
Al–Al_2O_3	90	0.4	0.1	Deformation
Cu–SiO_2	70	0.5	0.23	Rolling + twins
Al–FeSi	90	0.5	0.2–7	Cube, rolling, random
Al–Si	90	0.8	2	Cube, rolling, random
Al–Ni	80	10.0	1	Rolling, random
Al–SiC	70	20.0	10	Random

1978, Humphreys and Juul Jensen 1986, Juul Jensen et al. 1988, Humphreys 1990). The particles may affect the recrystallization texture in two ways:

- Large (>1 μm) pre-existing particles are favoured nucleation sites during recrystallization and the highly misoriented deformation zones associated with them lead to a wide range of nucleus orientations (§9.3).
- A dispersion of closely spaced particles may pin boundaries, affecting not only the recrystallization kinetics, but also the final grain size and texture.

Humphreys and Juul Jensen (1986) and Juul Jensen et al. (1988) have collated data on the recrystallization textures of a number of alloys, and some selected examples, shown in table 12.3 will be used to illustrate the effects of particles on texture.

12.2.4.1 Particle stimulated nucleation (PSN)

The contribution of particle-stimulated nucleation to recrystallization and the orientations of the nuclei, have been considered in chapter 9, and here we are concerned mainly with the effects on the final recrystallization texture. It seems certain that the nuclei originate within the particle deformation zones and their orientations are therefore restricted to those present in these zones. The situation is summarised as follows.

For small deformations, or in particle-containing single crystals, the range of PSN orientations may be very restricted and PSN may in this situation result in a relatively strong texture (figs. 9.14, 9.15, 9.16). Although the new orientations have a crystallographic relationship with the deformed matrix, which is a function of the slip

activity (§2.9.4), this inevitably leads to a spread of orientations around those of the deformed matrix.

As discussed in §9.3.2.2, the nuclei developed in heavily deformed polycrystalline materials are either randomly oriented or weakly textured. Habiby and Humphreys (1993) showed that even if PSN grains are highly misoriented from the matrix grains, a weakened rolling texture rather than a random texture would result. Starting with a computer-generated texture typical of the rolling texture of an aluminium alloy, they generated a 'recrystallization texture' by allowing each orientation in the rolling texture to generate new grains misoriented by up to 45° about random axes from the parent grain. The result was a weakened rolling texture with peak intensity reduced from 5.5 to 3.1x random.

The annealing behaviour of particulate metal–matrix composites is an extreme example of texture control by PSN (Humphreys 1990, Bowen and Humphreys 1991, Bowen et al. 1991). In many such materials the volume fraction of large (>3 μm) particles is much greater than in conventional alloys and may exceed 0.2. PSN readily occurs at the large particles and the strength of the recrystallization texture (a weak rolling texture) is reduced as the volume fraction of particles is increased, becoming effectively random for volume fractions in excess of 0.1.

12.2.4.2 Pinning by small particles

As was discussed in §9.4, a dispersion of closely-spaced small (< 1 μm) particles may have a strong influence on the recrystallization kinetics and the grain size, and the effects depend on whether the particles are present before or after the deformation. Although the recrystallization texture is likely to be influenced by particle size, strength and spacing, there is little data on well characterised material and it is not yet possible to quantify the effects of these parameters.

Small deformable particles – The presence of a dispersion of small deformable particles such as those formed during the age-hardening of e.g. Al-4%Cu, affects the homogeneity of deformation (§2.9.1), and often leads to the formation of shear bands. In this case the recrystallization texture is very similar to that of the solid solution alloys discussed in §12.2.1.2 (Lücke and Engler 1992).

Small non-deformable particles – If the particles are non-deformable and too small for PSN, or if the particles are precipitated during the recrystallization anneal, their effect is mainly one of boundary pinning (§4.6). Humphreys and Juul Jensen (1986) analysed the published data for such alloys, and found that, in general a texture similar to that of the deformed material was retained after recrystallization (see table 12.3). For example in bcc alloys, the {111} components are often strengthened, and in both fcc and bcc alloys the recrystallization texture is often stronger than the deformation texture, although the balance between the components may be altered. As discussed in §9.4, for small particle spacings, discontinuous recrystallization may not be possible and the annealing mechanism is then one of recovery, although coarsening of the particle dispersion may lead to **extended recovery** (§6.6.2.4). In either of these cases it is to be expected that the annealing texture will be similar to the deformation texture. The reason for the retention of the rolling texture for some alloys of larger interparticle spacing and which undergo normal discontinuous recrystallization (e.g. Cu–SiO_2 in table 12.3) is not entirely clear.

However, as discussed in §12.4.3.3, more recent research has provided strong evidence that in aluminium alloys, Zener pinning may lead to the formation of a strong cube texture on recrystallization.

12.3 THE THEORY OF RECRYSTALLIZATION TEXTURES

12.3.1 Historical background

The nature of the recrystallization texture is determined primarily by two factors:

- **The orientations of the new grains.**
- **The relative nucleation and growth rates of these grains.**

The manner in which these factors operate to produce a unique recrystallization texture from a particular deformation texture and microstructure has been the subject of controversy for more than 50 years and for the whole of that time two major theories have been strongly advocated. It has been claimed that the recrystallization texture has its origin in either the preferred nucleation of grains with a particular orientation (**oriented nucleation theory**) or the preferred growth of grains of specific orientations from a more randomly oriented array of nuclei (**oriented growth theory**). Most of the experimental work related to the controversy has been concerned with fcc metals and the early work was mainly carried out on copper and its single-phase alloys. The importance of the cube texture in the thermomechanical processing of commercial, multiphase aluminium alloys (§15.2) has resulted in an increased activity in this area in recent years.

It was pointed out in §7.6 that the nuclei from which the recrystallized grains originate are small regions which pre-exist in the deformed state, i.e. the orientations of the nuclei are already present in the deformed structure. With the exception of changes that may be introduced by twinning there is no way that other significantly different orientations can develop. To the early workers faced with a recrystallization texture that was apparently quite different to the deformation texture from which it developed this presented a major problem, and several models were proposed to explain how a new orientation might be generated. Most of these are no longer considered tenable and will not be discussed here; details of this early work are reviewed by Beck and Hu (1966).

The oriented nucleation theory began with the assertion by Burgers and Louwerse (1931) that the preferred nuclei in lightly compressed aluminium single crystals consisted of crystal 'fragments' that were more heavily deformed than the bulk of the crystal. A formal crystallographic theory was devised which associated the 'fragments' with local lattice curvatures and involved a $<112>$ rotation. Subsequently, Barrett (1940) found that the recrystallized grains in a single crystal specimen were related to the deformed matrix by a $45^\circ <111>$ rotation. Results of this type led to speculation that the observed rotations were associated with a maximum growth rate, and as experimental methods improved, the value of the angular rotation was refined and **the oriented growth theory** was established. Considerable further evidence for the high mobility of boundaries with certain orientation relationships has been obtained and this is discussed in §5.3.2.

An early alternative oriented nucleation theory was based on the **inverse Rowland transformation** (Verbraak and Burgers 1957, Verbraak 1958). This so called 'martensitic' theory relied on a formal crystallographic analysis (the Rowland transformation) which describes a mechanism capable of deriving two twin-related lattices of type $\{112\}<111>$ from a single $\{001\}<100>$ lattice. The martensitic model assumes that the two neighbouring twin-related $\{112\}<111>$ copper components of the rolling texture jointly undergo an inverse Rowland transformation to generate an $\{001\}<100>$ cube texture nucleus. The necessary shear requires the presence of $<112>$ partial dislocations and the analysis requires therefore that the stacking fault energy be sufficiently low to allow the formation of the partials. If these are absent, as in aluminium, the process cannot occur and the development of the cube texture in that metal would require a different mechanism. For this and other reasons the theory never attracted strong support and a later attempt by Verbraak (1975) to revive interest was not successful.

12.3.2 Oriented growth

Most discussions of oriented growth are based on observations of specific rotation relationships associated with rapid grain boundary migration. Much of the experimental work has been carried out by the group led by Lücke, and the crystallographic relationships found for various materials are given in table 5.3. The most important of these is the $40°<111>$ relationship that is used to relate the deformation and annealing textures of fcc metals (e.g. Ibe and Lücke 1966, Lücke 1984).

There are several difficulties in accepting that oriented growth due to specific crystallographic relationships between grains is solely responsible for the final texture, and these are outlined below.

12.3.2.1 The number of active rotation axes

Only a small number of the possible rotation axes are actually active and for any particular axis, rotation generally occurs only in one sense.

Many single crystal studies have been made in this area. Consider the orientations $\{112\}<111>$, $\{123\}<634>$ and $\{110\}<112>$ which form the basis of all fcc rolling textures. Single crystals of the first type retain that orientation during rolling to 80% reduction, and when recrystallized, orientations derived from 6 of the 8 possible $40°<111>$ rotations are found (Köhlhoff et al. 1981). $\{123\}<634>$ crystals are a little less stable during rolling, but only one of the possible rotations occurs during recrystallization (Lücke et al. 1976). The $\{110\}<112>$ orientation is very stable during rolling and all 8 rotations occur on annealing, albeit with some scattering (Köhlhoff et al. 1981).

A similar situation is found for polycrystalline materials as can be illustrated by considering the cube texture, $\{001\}<100>$. Oriented growth theory maintains that this orientation is related to the $\{123\}<634>$ (S) orientation present in the rolling texture of copper and aluminium by a near $40°<111>$ rotation. However only one of the eight possible rotations of each variant of S yields the cube texture and there is at present no way of predicting which.

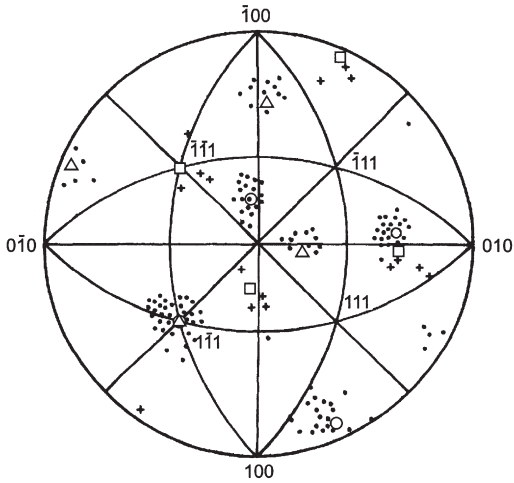

Fig. 12.12. Orientation relationship between artificially nucleated grains and the deformed matrix of aluminium crystals. The matrix is plotted in standard projection. (•) $<111>$ poles of new grains close to a 40°[1$\bar{1}$1] relationship, (+) $<11\bar{1}>$ poles of new grains close to a 40°[1$\bar{1}$1] relationship, (○) Ideal orientation for 40°[1$\bar{1}$1] clockwise rotation, (Δ) Ideal orientation for 40°[1$\bar{1}$1] anticlockwise rotation, (□) Ideal orientation for 40°[1$\bar{1}\bar{1}$1] anticlockwise rotation, (Yoshida et al. 1959).

These results can only be interpreted on the basis that the number of nuclei available is limited, i.e. oriented growth does not occur independently of oriented nucleation.

12.3.2.2 The precision of high mobility relationships

Although definite orientation relationships between deformed and recrystallized textures are often quoted and used to support the oriented growth theory, there are several factors that suggest that precise relationships do not exist during recrystallization.

- The spread in both the deformation and annealing textures is such that it is unrealistic to select a single orientation relationship to relate them. Figure 12.12 shows the orientations of recrystallized grains artificially nucleated in an aluminium single crystal. The orientation of the deformed crystal is plotted in standard projection. It was asserted that the results demonstrated a 40° [1$\bar{1}$1] relationship with the deformed crystal although **'in most cases the scatter....around the ideal orientation was rather large'.** The common [1$\bar{1}$1] directions are in fact up to 16° apart and [1$\bar{1}$1] for the annealed grains is spread over an angle of approximately 28°. Although there is clearly an orientation relationship based at or near $<111>$, involving a rotation of ~40°, the scatter is considerable.

- Experiments on single crystals (§5.3.2.2) show that the **high mobility of 40° $<111>$ boundaries is restricted to tilt boundaries,** and that 40° $<111>$ twist boundaries do

not have a high mobility. Thus, only a restricted set of these boundaries are likely to have high mobility, as discussed by Hjelen et al. (1991). It should also be noted that the recrystallized grains in polycrystals are usually equiaxed, showing little evidence of the preferential migration of tilt boundaries.

- Although the reasons for the high mobility of a low-Σ or CSL boundary can be broadly understood in the case of boundaries migrating in perfect material (§5.4.1), it is difficult to see how the necessary ordered boundary structure can be maintained during recrystallization.

- Because of the rapid local orientation variations in the deformed microstructure, a precise relationship between a growing grain and the adjacent deformed matrix cannot be defined. As discussed in chapter 2, during deformation a single grain breaks up into regions of different misorientation as cells or subgrains and other heterogeneities develop. The orientation of a deformed grain therefore varies over small distances. Such orientation changes have been measured in both single crystals and polycrystals as discussed in chapter 2, and figure 7.34 demonstrates the large changes in misorientation encountered during the growth of a recrystallizing grain.

In summary, we see that although there is clear evidence of oriented growth in single crystals and lightly deformed polycrystals where an orientation relationship between the recrystallizing grain and the deformed matrix may exist and be maintained during growth, it is now clear that during the recrystallization of highly deformed polycrystals, any orientation relationships will not only be very localised, but will be transient as a grain grows into new surroundings. Whether, during the later stages of growth, the existence of favourable orientation relationships over only part of the boundary of a growing grain will lead to a significantly faster overall growth rate for the grain, remains to be clarified.

12.3.2.3 Oriented growth due to other factors

Although discussions of oriented growth have generally stressed the role of high mobility boundaries of specific character, there are other factors which may result in grains of some orientations growing faster or slower than others, and thereby influence the recrystallization texture.

Size – Grains of different orientations tend to originate at different type of site. If the recrystallization nuclei are large, e.g. those originating at cube bands (§12.4.1.2), they will tend to grow more rapidly than others because of the smaller drag pressure from boundary curvature (§7.1.1.3 and equation 7.3). This will be particularly important in a fine-grained, recrystallized microstructure.

Position – Recrystallizing grains adjacent to regions of high stored energy will recrystallize more rapidly than others (§7.4.2.3). As stored energy is known to be orientation dependent, this can lead to the development of preferred orientations during recrystallization.

More general orientation relationships – The problems associated with ascribing high mobility to a precise orientation relationship such as 40° $<111>$ were discussed above. However, there is mounting evidence that boundaries with more general orientation relationships may have higher or lower mobilities than average, and that these may make a substantial contribution to orientation growth effects, and we note the following:

- Boundaries of misorientation less than $\sim 15^\circ$ have low misorientations, as do 60° $<111>$ (twin) boundaries. Juul Jensen (1995b) has pointed out that the effect of such low mobility boundaries on the growth of recrystallizing grains may be as significant as those of high mobility. This type of oriented growth is sometimes called **'orientation pinning'.**

- Boundaries deviating by up to $\sim 20^\circ$ from $40^\circ <111>$ have higher than average mobilities (§5.3.2).

- In a randomly oriented assembly of grains, a large fraction (~ 0.35) of the high angle boundaries have misorientations within 20° of $40^\circ <111>$.

As discussed by Hutchinson and Ryde (1997), on the basis of the orientation dependence of both the frequency and the mobility of boundaries noted above, and the requirement of a successful recrystallizing grain to avoid a low mobility, it is to be expected that a substantial fraction of the boundaries of recrystallizing grains will inevitably have misorientations of 20°–40° about axes near $<111>$. Although much further work is required to substantiate the above ideas, a model of recrystallization growth based on more general considerations of boundary mobility and frequency overcomes many of the objections to the conventional oriented growth theory.

12.3.3 Oriented nucleation

The realisation that the nucleus of a recrystallized grain must have an orientation that is close to or identical with that of the volume element in the deformed structure from which it grew has existed for many years. Attention was refocussed on this by the development of electron microscope techniques that allowed orientation determinations from very small volumes of material and by advances in the theoretical analysis of texture development during deformation. Many of the developments in this field have been stimulated by the need to find the nuclei responsible for the cube texture. Although it is universally accepted that oriented nucleation occurs, many of the details of how nuclei of particular orientations develop remain a matter of debate. Such nuclei may be produced at heterogeneities such as deformation bands, or may be formed at specific components of the normal deformation texture, as discussed below.

12.3.3.1 Oriented nucleation at deformation/transition bands

- **The Dillamore–Katoh model**

The benchmark work was the paper by Dillamore and Katoh (1974) who calculated the rotation paths during the compression of polycrystalline iron, and showed that a

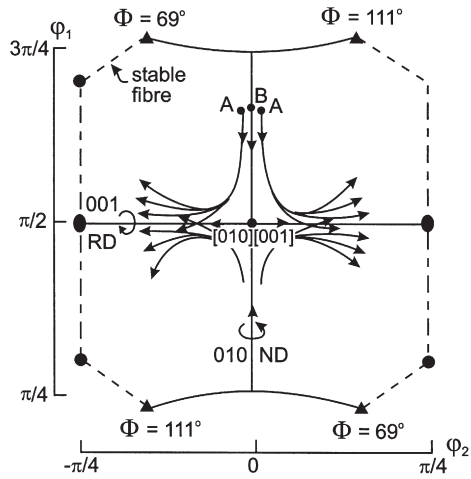

Fig. 12.13. Section through orientation space at $\Phi = 90°$ showing schematically the slip rotations in the vicinity of the cube orientation in fcc metals, (Dillamore and Katoh 1974).

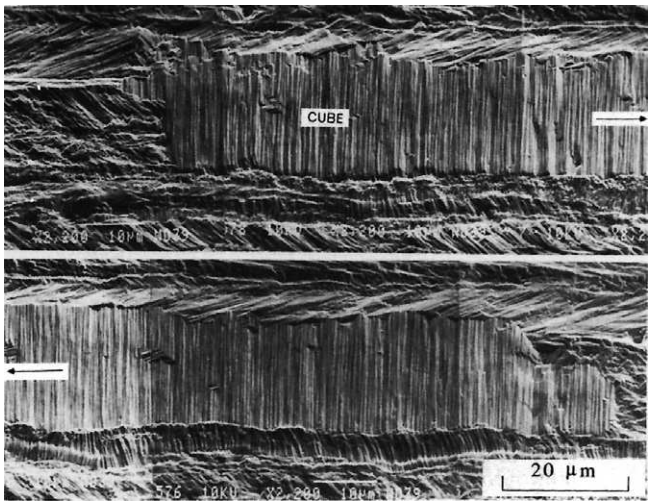

Fig. 12.14. Long, thin, cube oriented-grain developing in 95% cold rolled copper after annealing for 100 sec at 140°C. Longitudinal section, cut at 45° to RD to expose cube-oriented grains as {110} <001>, (Duggan et al. 1992).

transition band centred on <411> would be formed when the rotation paths of neighbouring volumes diverged (§2.7.3) as shown in figure 2.19a. They argued that this would provide a very favourable site for the nucleation and growth of a recrystallized grain and pointed out that a <411> fibre texture was indeed prominent in the recrystallization texture of compressed iron as shown in figure 2.19c. Inokuti and

Doherty (1978) found $<411>$ oriented nuclei in transition bands after annealing compressed iron samples.

A second important result came from their analysis of rolling texture development in copper. In this case it was predicted that similar transition bands would form in which the central region of the curved lattice contained the cube orientation as shown in figure 12.13. This shows that certain crystals will approach the cube orientation by rotation around the normal direction and then subsequently diverge by rotation about the rolling direction, eventually arriving at a stable orientation outside the plane of the figure. A small initial curvature, indicated by A-B-A will rapidly become larger, but the centre point B, linking the two diverging orientations will continue to rotate into and remain at the cube orientation.

If nucleation were to occur at this site, which, because of its large orientation gradient is likely, then the cube texture should be found. The first experimental support for this was provided by Ridha and Hutchinson (1982) who found long narrow regions of precisely the predicted type in cold rolled copper. This observation has been confirmed many times since in both copper and aluminium by SAD and EBSD experiments (e.g. Hjelen et al. 1991). Somewhat related observations have also been made by the use of an orientation-sensitive deep etching technique (Köhlhoff et al. 1988b) and a typical microstructure is shown in figure 12.14.

- **Other deformation banding models**

Although it has been widely accepted that the Dillamore–Katoh model provides a satisfactory explanation of the appearance of cube-oriented volumes in the deformed material, other models have subsequently been proposed. Amongst these the work of Lee et al. (1993) is significant. These workers assert that the cube-oriented volumes (nuclei) in cold rolled copper are formed by deformation banding and maintain that the Dillamore–Katoh model corresponds to a deformation band in which all regions of the grain involved have the same homogeneous strain and that this is the macroscopic strain (i.e. the model corresponds to the first of the two deformation bands defined by Chin (1969) and discussed in §2.7.2).

Lee et al. (1993) used a simple one-dimensional model, that considered only one banding mode, to examine the formation of deformation bands in the presence of heterogeneous strain and concentrated on the formation of cube-oriented volumes and the orientation environment in which they occurred. It was found that cube-oriented volumes appeared more profusely than in the Dillamore–Katoh model, and from a much wider range of starting orientations. These cube-oriented volumes were similarly related to neighbouring volumes by a $30–40^\circ <111>$ rotation. However the angular relationship deteriorated at high reductions and they suggested that a unified theory was needed. In this the cube volumes are generated by both types of deformation banding at low-medium rolling reductions with the Dillamore–Katoh model more significant at high reductions. The net result is an increased number of suitably oriented nuclei.

Akef and Driver (1991) point out that the Dillamore–Katoh analysis was based on the use of the Taylor model, i.e. the analysis assumes full constraints (§3.7.1). It is well known that this leads to ambiguities in the slip rate particularly for high symmetry orientations like $\{001\}<100>$. Furthermore the analysis referred to the case of bcc iron undergoing pencil glide, $\{hkl\}<111>$ and by reversing the signs of the rotations

Dillamore and Katoh extended it to the case of fcc metals and $\{111\}<110>$ slip. Akef and Driver question the validity of this transposition and also the use of the Taylor analysis. They have analysed the rotation paths and rotation rates for crystals originally oriented near $\{001\}<100>$ and conclude that the behaviour of their single crystal specimens can be predicted more accurately by a simple model of deformation band development in which the normal strain components are equal to the macroscopic strains and the shear strain components are assumed to be unconstrained.

12.3.3.2 Oriented nucleation at selected components of the deformation texture

Much recent research has shown that preferred nucleation occurs within certain of the deformation components. This is not usually associated with deformation heterogeneity, but with the local orientation environment and particularly the juxtaposition of particular texture components. Such preferential nucleation may be due to the relative microstructures and stored energies of the adjoining grains and may also be influenced by their relative orientations. The two most important examples, which are discussed in some detail elsewhere, are cube-band nucleation in aluminium (§12.4.1) and the preferential growth of γ-fibre grains into deformed α-fibre grains in low-carbon steels (§12.4.2). As is discussed below, such processes involve elements of both 'oriented nucleation' and 'oriented growth' during the early stages of recrystallization.

12.3.4 The relative roles of oriented nucleation and oriented growth

The relative roles of nucleation and growth in determining the recrystallization texture require the examination of microstructure and local texture (microtexture) of both the deformed and recrystallizing material. As emphasised by Duggan et al. (1993), there is a fundamental difficulty in interpreting the results of experiments based on examination of partially recrystallized samples, because in such circumstances, the creation of a growing grain destroys what might have been significant evidence relative to both the nucleus and its immediate environment. However, microtexture investigations, using techniques such as EBSD or deep etching (see appendix 1) have helped to clarify several issues and provide unambiguous evidence of both oriented nucleation and oriented growth, as illustrated in the following two examples.

- The annealing of deformed single crystals containing large second-phase particles at which PSN occurs (e.g. Ardakani and Humphreys (1994), Ferry and Humphreys 1996c) is instructive. In such materials, PSN is found to occur, but only a very few of these grains grow significantly, and in many cases, the majority of the small PSN grains are left as "islands" by the rapidly growing grains as shown in figures 9.19 and 9.20 and discussed in §9.3.5. The fact that this behaviour occurs only after moderate strains, and that after large strains the PSN grains grow at similar rates to the other grains, is consistent with recrystallization dominated by **oriented growth.**

- There have been many microtexture investigations of the recrystallization of single crystals (e.g. Driver 1995, Mohamed and Bacroix 2000, Driver et al. 2000, Godfrey et al. 2001). Recrystallization originates at heterogeneities which are specific to the material and the crystal orientation. The limited number of crystallographic orientations in a heterogeneously deformed single crystal result in a limited range of

recrystallized grain orientations and hence a strong recrystallization texture, giving clear examples of **oriented nucleation.**

Further examples of the relative roles of nucleation and growth in determining the annealing texture will be found in the discussions of texture evolution (§12.4) and in the examples of the control of recrystallization during industrial processing discussed in chapter 15.

The final recrystallization texture is determined by both the range of nuclei orientations available and the subsequent growth advantage enjoyed by any grains. Both of these factors will depend on the material and the processing parameters and the relative importance of each will vary from case to case. It is now recognised that any recrystallization nucleus in a heavily deformed polycrystal will be surrounded by a wide spread of orientations and that these surroundings will change during growth, and this must be taken into account in any model of recrystallization.

In summary, a rigid polarisation between theories of ORIENTED GROWTH and ORIENTED NUCLEATION is now considered to be untenable. The orientations of the nuclei are restricted to those present in the deformed material, and there is no evidence that nuclei of random orientations ever occur. There is also undisputed evidence that under certain circumstances, some orientation relationships are associated with a high or low boundary mobility.

Much of the discussion about the origin of recrystallization textures is now centred on the orientation dependence of recrystallization mechanisms at the micron scale, where a distinction between 'nucleation' and the 'early stages of growth' is meaningless. This emphasises again the artificiality of the 'oriented nucleation' versus 'oriented growth' arguments.

12.3.5 The role of twinning

Annealing twins are common in the recrystallized grains of low to medium SFE metals (§7.7). The formation of an annealing twin provides the only means of generating an orientation which is significantly different to those present in the deformed metal prior

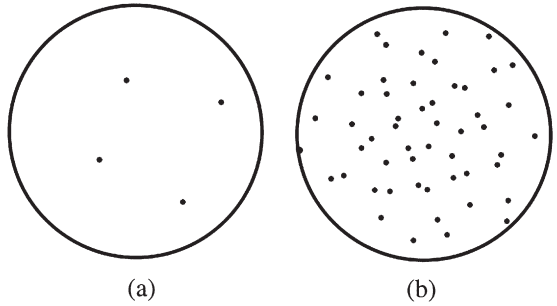

Fig. 12.15. Effect of repeated random twinning on texture. (a) 111 poles of initial orientation, (b) after 3 generations of twins.

Table 12.4
Orientation relationships in twin chains*, (Berger et al. 1983).

Orientation Relationship	Nearest coincidence relationship
$20° < 100 >$	$22.6° < 100 >$; $\Sigma 13a$
$50° < 111 >$	$46.8° < 111 >$; $\Sigma 19b$
$130° < 430 >$	$129.8° < 540 >$; $\Sigma 25b$
$145° < 541 >$	$145.7° < 541 >$; $\Sigma 23$

*The coincidence relationships shown are not necessarily those of minimum rotation angle.

to recrystallization. It is not surprising therefore, that the role of twinning in the generation of recrystallization textures has been actively investigated. Such studies have been carried out extensively by Gottstein and colleagues at Aachen and by Haasen, Berger and colleagues at Göttingen (see for example Gottstein 1984, Berger et al. 1988, Haasen 1993).

There are twelve possible twinning elements ($\{112\} < 111 >$) in fcc metals and if all these were to operate successively during annealing, the strength of the texture would be rapidly reduced. Gottstein (1984) has pointed out that only six generations of twinning would be needed to achieve a random texture, and this is illustrated in figure 12.15. However, most recrystallization textures in metals which form annealing twins, are sharp and clearly defined (e.g. fig. 12.1) and it follows that unrestricted twinning does not occur.

Some selection principles must apply, and a preferred sequence of twinning events (**twin chain**) must occur. The factors responsible for selecting a particular twin variant are still in dispute (§7.7.4.2), but the two most likely are the development of a high mobility boundary (Gottstein 1984) or a reduction of grain boundary energy (Berger et al. 1988).

An extensive investigation by Berger et al. (1988) found that whereas recrystallized grains in aluminium were related to the matrix by approximately $40° < 111 >$, no such relationship existed for copper. In experiments with tensile deformed $< 100 >$ and $< 111 >$ crystals of 99.9998% pure copper, the favoured relationships were $20° < 100 >$, $50° < 111 >$, $130° < 430 >$ and $145° < 541 >$. The orientations produced by these rotations are all related by twin chains of various lengths. The $145° < 541 >$ orientation relationship is twin-related to those for $20° < 100 >$ and $50° < 111 >$ by three link chains and to that for $130° < 430 >$ by a single link chain. All of these rather complex relationships are close to coincident site lattices as shown in table 12.4.

Berger et al. (1988) went on to extend these observations to the development of the annealing texture in rolled polycrystalline copper and pointed out that similar orientation relationships existed. The cube texture is twin-related to two of the major components of the rolling texture ($\{112\} < 111 >$ and $\{110\} < 112 >$) by a $130° < 430 >$ rotation and to the third component $\{123\} < 634 >$ by a $50° < 111 >$ rotation. These are significant results but some caution is needed in extrapolating the single crystal results to explain the origin of recrystallization textures in rolled polycrystals. The crystals

were only lightly deformed (20% elongation for $<100>$ crystals and 4% elongation for $<111>$ crystals). The microstructure was, therefore, very homogeneous and none of the major inhomogeneities of deformation that act as nucleation sites in heavily rolled material would have been present. A second concern, the precision of the rotations involved, has already been referred to, and in this case the rotations $130°<430>$, $50°<111>$ and $20°<100>$ lead, respectively to 8°, 5° and 4° deviation from the ideal.

12.4 THE EVOLUTION OF TEXTURES DURING ANNEALING

Having discussed the nature of recrystallization textures, and the various mechanisms which may be important, we now discuss a few important examples of texture development and examine the extent to which the experiments can be reconciled with the models. The control of texture in order to improve properties is of great technological significance, and some more specific cases of industrial importance are discussed in chapter 15.

12.4.1 The cube texture in fcc metals

The cube texture (figs. 12.1, 12.4a), has been the subject of intense research for many years. It can be produced in many fcc metals and alloys of medium to high stacking fault energy and the precision and sharpness are remarkable. In addition to copper and aluminium the cube texture is found in gold and nickel, in iron–nickel alloys containing more than 30% nickel and in some ternary alloys of iron, nickel and copper (Barrett and Massalski 1980). The conflicting experiments and different theories referred to in this section show that this very old problem is still the subject of controversy. This has been fuelled to some extent by the very considerable industrial significance attached to the development of the cube texture during the processing of deep drawn aluminium alloy beverage cans (§15.2.2).

Neither pole figure nor ODF data of cold rolled material generally give any indication of a significant $\{001\}<100>$ component and therefore the origin of the cube texture has been difficult to explain, and we highlight two proposed models, together with a discussion of some important factors.

12.4.1.1 The transition band model

Only a small amount of cube-oriented material is needed to provide the necessary recrystallization nuclei and the theoretical analysis of Dillamore and Katoh (1974) (see §2.7.3 and §12.3.3.1) showed that cube orientations could develop in transition bands as shown in figure 12.13. Under such conditions a cube nucleus would have available in the neighbouring microstructure a large misorientation gradient appropriate for rapid growth. Long thin cube oriented regions, thought to originate in this way were detected in the microstructure of heavily rolled copper by Ridha and Hutchinson (1982) and shown to develop into cube-oriented grains. Ridha and Hutchinson also suggested that the rapid development of the cube nuclei from these sites would be aided by the

Table 12.5
Orientation relationships for cube oriented volumes, (Duggan et al. 1993).

Common Axis	Cold Rolled (no. of volumes)	Partially Annealed (no. of volumes)
15–60° < 110 >	34	25
25–40° < 111 >	36	1
Others	48	22
Total	118	48

dislocation structure within the cube bands. They argued that the predominant slip systems active for material of the cube orientation {001} < 100 > would involve only the Burgers vectors a/2[101] and a/2[$\bar{1}$01], which are orthogonal to one another. As there is little interaction between dislocations of orthogonal Burgers vectors, rapid and extensive recovery is expected to take place in the cube-oriented subgrains, thus giving them an added advantage in forming recrystallization nuclei.

12.4.1.2 The cube-band model

In commercial aluminium alloys it is generally found that the cube texture developed on recrystallization is stronger after hot rolling than after cold rolling (e.g. Hirsch and Engler 1995). Although this can be partly explained by a reduction of the random components of the texture that are derived from particle stimulated nucleation (§13.6.4), there is now considerable evidence that other factors also promote the formation of the cube texture in recrystallized, hot rolled aluminium alloys, the most significant of which is the **increased stability of the cube orientation** during rolling at high temperatures (see §13.2.4). It is now accepted that the origin of the cube grains on recrystallization after high temperature deformation are the cube-oriented elements of the deformed structure, which are retained as long, ribbon-like bands, and there is no evidence that a Dillamore and Katoh transition band mechanism operates under these conditions (Vatne and Nes 1994, Samajdar and Doherty 1995, Vatne et al. 1996a,d). The strength of the cube texture on recrystallization is found to be directly related to the strength of the cube texture after hot deformation (Weiland and Hirsch 1991, Bolingbroke et al. 1994, 1995). The mechanism of recrystallization from cube bands (Vatne et al. 1996a), has been shown to be that of strain-induced boundary migration (SIBM), (see §7.6.2), in which subgrains from the cube bands consume neighbouring subgrains.

12.4.1.3 The significance of neighbouring S-oriented grains

Most investigations of the cube recrystallization texture in copper and aluminium have noted that there is a preference for the cube grains to grow into adjacent deformed grains of **S** orientation (Vatne and Nes 1994, Samajdar and Doherty 1995 and Vatne et al. 1996a,d), although this may not be a pre-requisite.

Duggan et al. (1993) examined the orientation environment in rolled copper that favoured the development of successful cube-oriented grains. The deformed

microstructure was searched for cube-oriented volumes and the orientations of the surrounding regions determined. Analysis of the results indicated that about 60% of the cube-oriented regions had either $<111>$ or $<110>$ common with their adjacent regions (table 12.5). The specimen was then lightly annealed to produce isolated cube-oriented grains and the orientations of the volume elements immediately adjacent to any unrecrystallized cube volumes determined. Table 12.5 indicates that during partial annealing, virtually all of the deformed cube-oriented regions that had at least one (25-40°) $<111>$ related neighbour (such regions were generally close to the **S** orientation) had been consumed by the growing recrystallized cube grains.

12.4.1.4 Preferential formation of cube nuclei

Most investigations of cube nucleation from prior cube bands after deformation at low or high temperatures (Duggan et al. 1993, Vatne and Nes 1994, Samajdar and Doherty 1995, Vatne et al. 1996a,d) suggest a model based on SIBM into adjacent **S**-oriented grains. There are a number of factors which would encourage this:

- **A large driving pressure** is provided by the higher stored energy of adjacent S components. It is known, particularly for aluminium deformed at high temperatures, that the cube grains have a low stored energy compared to other components such as **S** (table 13.1).

- **A large subgrain size.** The cube subgrains tend to be larger than for other orientations (table 13.1), and additionally, have a larger size spread which results in the presence of some exceptionally large cube subgrains (Vatne et al. l996d). As discussed in §7.6.2, this would favour the initiation of SIBM of the cube bands.

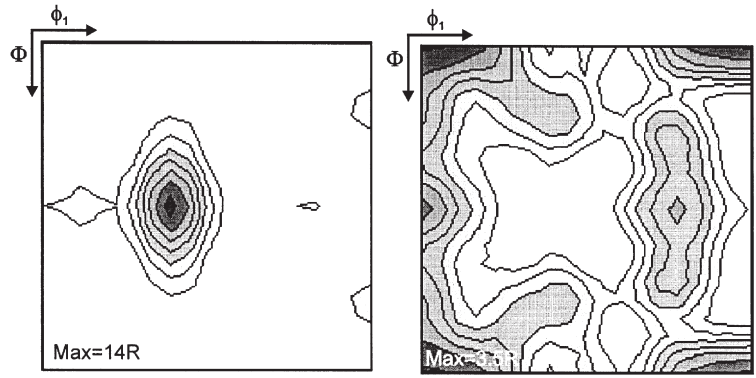

Fig. 12.16. The 'compromise texture'. (a) $\varphi_2 = 0°$ section of the ODF of cold rolled Aluminium AA3004 (maximum intensity = 14R), (b) $\varphi_2 = 0°$ section of the ODF after the deformed orientations have been transformed 40° about all $<111>$ axes (maximum intensity = 3.5R), (Bate 2003).

- **A higher mobility** of a $40^\circ < 111 >$ Cube/S boundary, even very locally, would promote the early stages of growth.

- **A lower energy** of a special boundary such as $40^\circ < 111 >$ would reduce the retarding pressure due to boundary curvature (§7.1.1.3 and equation 7.3) and promote the early stages of growth.

12.4.1.5 Preferential growth of cube grains

Lücke and Hirsch and their colleagues at Aachen have long argued that the cube texture is due to selected growth. Amongst the modifications that have been made to oriented growth theory, the concept of the **compromise texture** has had considerable attention, (see for example, Lücke 1984, Lücke and Engler 1990, 1992). It is argued that the cube grains have the best chance of growing because this orientation provides the best compromise towards meeting the $40^\circ < 111 >$ condition with respect to all components of the deformation texture. In the case of the **S** component the agreement is nearly exact for all four components; the worst situation is found for the copper component where the deviation from the proposed relationship is 23° for $30^\circ < 111 >$ and 30° for $40^\circ < 111 >$.

The compromise texture model assumes that nuclei of random orientations are present throughout the microstructure, and that grains oriented $40^\circ < 111 >$ to the deformed material grow most rapidly. In such a situation, the recrystallization texture would be expected to be close to the deformation texture transformed by $\pm 40^\circ$ about all $< 111 >$ axes, and this is demonstrated in figure 12.16. Figure 12.16a shows the $\phi_2 = 0$ section of an experimentally measured ODF of cold rolled aluminium AA3004, which is seen to be very similar to the ODF of figure 12.3. Figure 12.16b shows the same section after the data are transformed by $40^\circ < 111 >$. The transformation does indeed produce a significant amount of Cube texture, and also peaks at the Goss and **P** orientations (see table 12.1), such as may occur during recrystallization of commercial aluminium alloys (e.g. fig. 15.3). However, these predicted textures are very weak (by a factor of 4), and become even weaker if any spread from the ideal $40^\circ < 111 >$ rotation is allowed. It is therefore difficult to accept that a compromise-texture model plays a dominant role in the evolution of strong Cube textures on recrystallization.

There is some direct evidence (Juul Jensen 1995b) that in aluminium and copper, the recrystallizing cube grains grow faster than others, and this has been ascribed to a larger misorientation (but no specific orientation relationship) between the cube grains and the deformed matrix than for other grains (see §12.3.2.3). The extent to which such preferential growth contributes to the strength of the cube texture is not yet clear.

In summary, there is strong evidence that the prolific formation and early growth of cube-oriented grains is largely responsible for the final cube texture, and less evidence that these grains subsequently enjoy a significant growth advantage. The fact that the 'nucleation' of cube grains by SIBM from prior cube bands is an example of growth selection at the subgrain level, highlights the difficulty of distinguishing between 'oriented nucleation' and 'oriented growth', and reinforces the conclusions of §12.3.4.

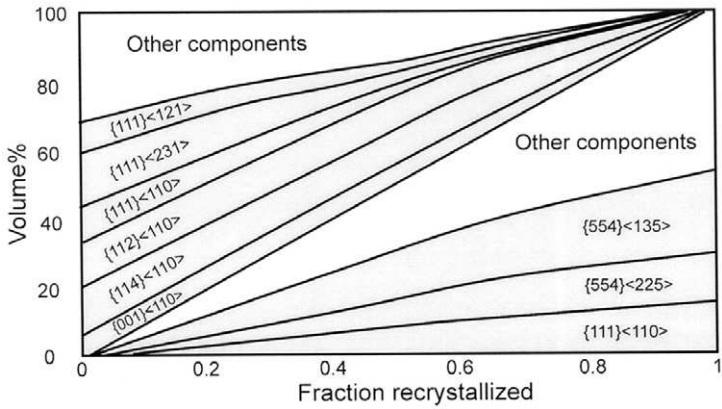

Fig. 12.17. Changes in the volume percentages of deformation texture components (upper region) and recrystallization texture components (lower region) during annealing of 75% cold rolled IF steel, (Hutchinson and Ryde 1997).

12.4.2 The recrystallization textures of low-carbon steels

The evolution of the recrystallized texture in low-carbon steels has been investigated in some detail by a number of research groups, and particularly by Hutchinson and Jonas and colleagues (Hutchinson and Ryde 1997, Hutchinson 2000, Hutchinson and Artymowicz 2001, Jonas and Kestens 2001, Reglé 2001), and extensive use has been made of EBSD in this work.

The main rolling texture components of low carbon steels lie along the α and γ fibres defined in figure 3.10. The microstructure is complex with two types of dislocation structure. One of these is typical of a material with a high value of stacking fault energy, having elongated substructures with sharp boundaries, extensive local misorientation and rolling plane orientations of type $\{111\}<uvw>$ that lie in the γ-fibre (Every and Hatherly 1973, Hutchinson 2000). These regions are characterised by the microstructurally persistent nature of the sub-boundaries referred to in §2.4.1. The second is more typical of a lower stacking fault energy material, having an equiaxed cell structure, diffuse boundaries, only minor local misorientations and rolling plane orientations that lie in the α-fibre. Such microstructures may be described as transient in nature (§2.4.1).

Figure 12.17 from the work of Hutchinson and Ryde (1995) shows the variation of the volumes of the main texture components during the annealing of an interstitial-free (IF) steel.

Recrystallization nucleation begins in grains with near γ-fibre orientations and appears to involve abnormal growth of the subgrains with large misorientations which are formed in the γ-fibre. This mechanism, which was originally proposed by Dillamore et al. (1967), has been substantiated by more recent EBSD investigations, (e.g. Barnett 1998, Reglé 2001). In the early stages of recrystallization, the new γ-fibre grains are

often found adjacent to the prior grain boundaries, although the precise mechanism of their formation is not clear.

Up to ~50% reduction, it has been shown that the early nucleated grains have an orientation distribution which is close to the final recrystallization texture (Hutchinson and Ryde 1995), but there has been extensive debate concerning the preferential growth of the recrystallizing γ-fibre grains such as $\{111\}<112>$ into the deformed α-fibre orientations such as $\{112\}<110>$. These orientations are related by a rotation of ~27° about a common $<110>$ axis, and this has been interpreted by some as an example of oriented growth due to a high mobility of such boundaries. However, Lindh et al. (1994) showed that there was no association between the volume fractions of the disappearing deformed and the growing recrystallized components, as may be seen in figure 12.17. More recent measurements of growth rates by Magnusson et al. (2001) also found no evidence of increased growth rates for the γ-fibre nuclei, but detected a significant decrease in growth rates as recrystallization progressed, and this was interpreted in terms of recovery and an inhomogeneous distribution of stored energy.

The current view (Hutchinson 2000) is that the recrystallization textures of steels having cold reductions of up to ~ 80% are controlled by the orientation of the nuclei rather than by growth selection, although there is some evidence that after larger cold reductions, there may be some contribution from growth selection (e.g. Kestens and Houbaert 2000).

12.4.3 Recrystallization textures of two-phase alloys

Many alloys of industrial importance contain second-phase particles, and the effect of these on the recrystallization texture is therefore of industrial significance. By controlling composition or processing, the size and distribution of the particles can be altered, and this provides a means of controlling the textures as is discussed in §15.2. In §12.2.4 we discussed the two basic effects of particles on recrystallization textures: particle stimulated nucleation (PSN) and boundary pinning (Zener drag); and in this section we examine the influence of these factors in texture evolution.

12.4.3.1 The influence of PSN

The orientations of PSN nuclei in a heavily rolled polycrystal are relatively random (§9.3.2, §12.2.4.1). However, except in metal–matrix composites containing high volume fractions of large particles (table 12.3), the recrystallization textures in alloys in which PSN is occurring are seldom close to random. This indicates that grains from other sites and with different orientation are also formed and that these contribute to the final texture. It is difficult to draw general conclusions about the types of site which are competing with PSN, but it may be seen from table 12.3 that for low particle volume fractions, both cube and rolling components are present (e.g. Al–Fe–Si, Al–Si), and for high particle volume fractions, rolling components are formed (e.g. Al–Ni). As not all particles which are large enough for PSN actually produce grains (§9.3.3), the selective nucleation at particles in particularly favourable sites (e.g. grain boundaries) may also be significant.

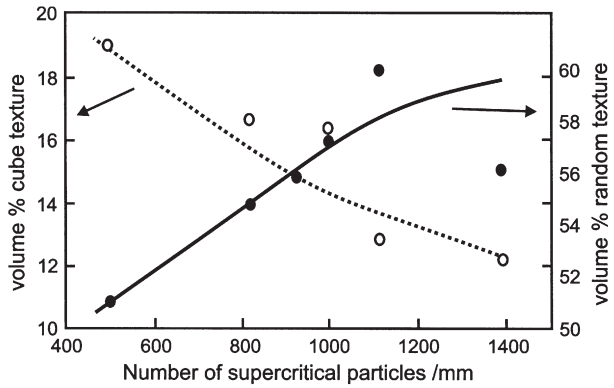

Fig. 12.18. Correlation between recrystallization texture and the number of constituent particles that can act as PSN sites in hot-rolled AA3004, (Bolingbroke et al. 1993).

In a study of heavily rolled Al–Fe–Si, (AA1050), containing ~0.5% of 1–7 μm particles, Juul Jensen et al. (1985) found that the first grains nucleated at the particles with random orientations while cube oriented grains were nucleated later. The cube grains grew rapidly and the final microstructure consisted of small grains (<10 μm), usually associated with large particles or clusters of particles, together with large grains (>100 μm). The cube-oriented grains were amongst the largest and the randomly-oriented grains amongst the smallest, although the reason for the rapid growth of the cube-oriented grains is not clear. It has been suggested that the cube grains may grow more rapidly by virtue of a preferential location compared to the PSN grains (Nes and Solberg 1986). Alternatively, it is possible that the PSN grains may have lower misorientations to their neighbours and a consequent lower growth rate (orientation pinning).

Ardakani and Humphreys (1994) and Ferry and Humphreys (1996b) have shown very clearly that PSN grains in single crystals, although nucleated at an early stage, may grow more slowly than other grains under conditions of low strain and low particle volume fraction (figs. 9.19, 9.20 and §9.3.5).

It has been suggested by Lücke and colleagues (e.g. Lücke and Engler 1990) that the texture of aluminium alloys in which PSN occurs can be explained by growth selection on the **compromise-texture** model discussed in §12.4.1.5, on the assumption that the orientations of the PSN grains are random.

12.4.3.2 The effect of deformation temperature

Under deformation conditions of low Zener–Hollomon parameter (Z) (high temperature/low strain rate), PSN on subsequent annealing becomes less viable (§13.6.4). The critical value of Z for PSN depends on the particle diameter (fig. 13.31), and as Z increases, the number of supercritical particles and therefore the number of PSN nuclei decreases. Consequently, other nucleation sites, particularly cube, dominate the final texture, and this is demonstrated in figure 12.18 where the strength of the cube

component in aluminium AA3004 is seen to decrease as the number of supercritical-sized particles increases.

12.4.3.3 The role of Zener drag

It was shown in §9.4, that a dispersion of closely spaced, second-phase particles would prevent or delay recrystallization. In the latter case, annealing for longer times or at higher temperatures generally results in eventual recrystallization. There is considerable evidence that for aluminium alloys and in such situations, the particles have a significant effect on the recrystallization texture, and we consider three cases.

- **Small particles present during deformation**

In this situation, a strong cube texture is formed, and Bowen et al. (1993), Humphreys and Brough (1997), Engler (1997), and Higginson et al. (1997) have all shown that the strength increased with increasing particle content. As Zener pinning increases, the critical size for a recrystallization nucleus increases (§9.4). This favours SIBM which can occur over large sections of boundary (broad front SIBM) as discussed in §9.4.1.2, and cube nucleation from prior cube bands by SIBM therefore occurs in preference to other types of nucleation.

- **Large and small particles present before deformation**

The recrystallization of alloys with bimodal particle distributions was discussed in §9.5, and the recrystallization textures in Al–Si and Al–Cu alloys with such microstructures have been investigated (Humphreys et al. 1995, Humphreys and Brough 1997). In both cases a much stronger cube texture is produced on recrystallization than that found in similar alloys containing only large particles.

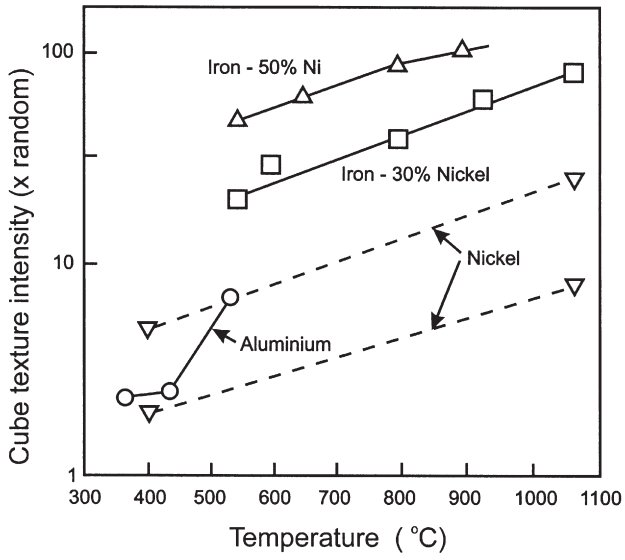

Fig. 12.19. Strengthening of cube texture with grain growth for fcc metals and alloys, (Hutchinson and Nes 1992).

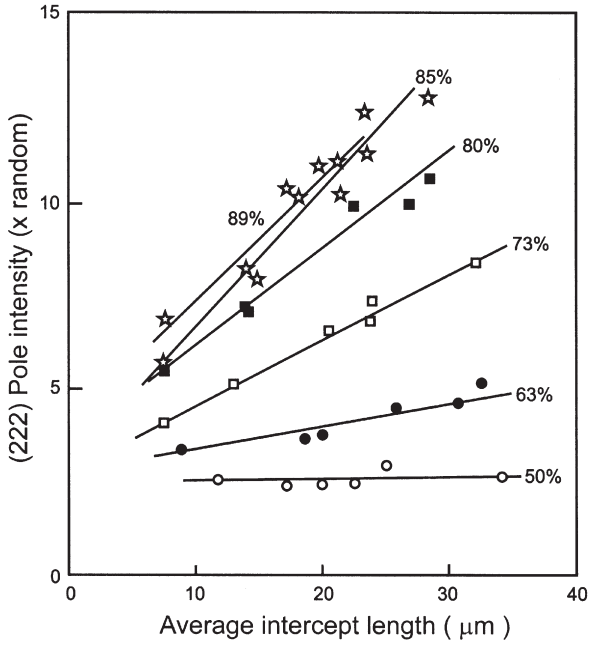

Fig. 12.20. Strengthening of {111} texture intensity with grain growth in low-carbon steel with different rolling reductions, (Hutchinson and Nes 1992).

In such alloys, the likely sites for the nucleation of recrystallization are either cube bands or large particles. As Zener pinning increases, the critical particle size becomes larger (equation 9.8), and eventually there are no particles sufficiently large for PSN. However, as discussed above, broad front SIBM will still be possible, and therefore a cube texture is produced.

- **Precipitation during the recrystallization anneal**

Precipitation during the recrystallization anneal has also been shown to promote the cube texture in industrial aluminium alloys (Daaland and Nes 1996, Engler 1997, Vatne et al. 1997). This may be due to the fact that the cube nuclei are large compared to the nuclei at particles, and therefore particle pinning is less effective (i.e. P_C in equation 9.7 is smaller). However, it is also possible that precipitation occurs more readily on the 'random' boundaries of the PSN nuclei than on the 'special' Cube/S boundaries of the cube nuclei (Daaland and Nes 1996, Somerday and Humphreys 2003).

12.4.4 Texture development during grain growth

The textures developed during recrystallization are not necessarily permanent and in many cases changes occur during subsequent grain growth. In some cases the components initially present may be replaced by quite different components, whilst in

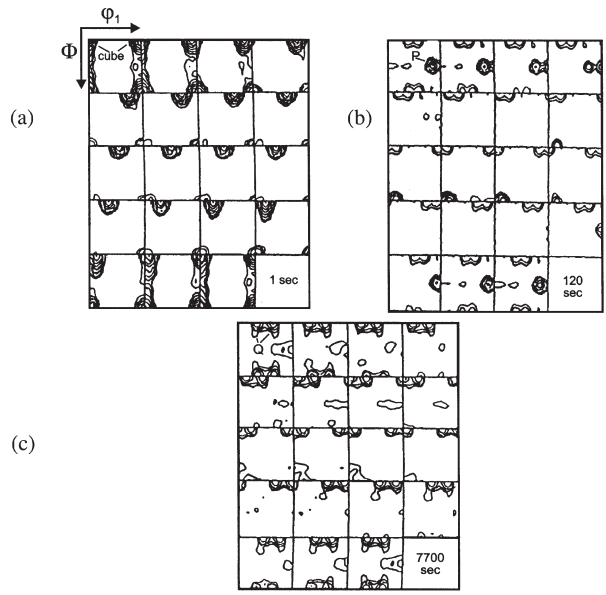

Fig. 12.21. Texture evolution during grain growth in Al–1%Mn annealed at 620°C: (a) 1 sec, primary recrystallization completed, (b) 120 sec, first stage of grain growth, (c) 7700 sec, final stage of grain growth, (Abbruzzese et al. 1988).

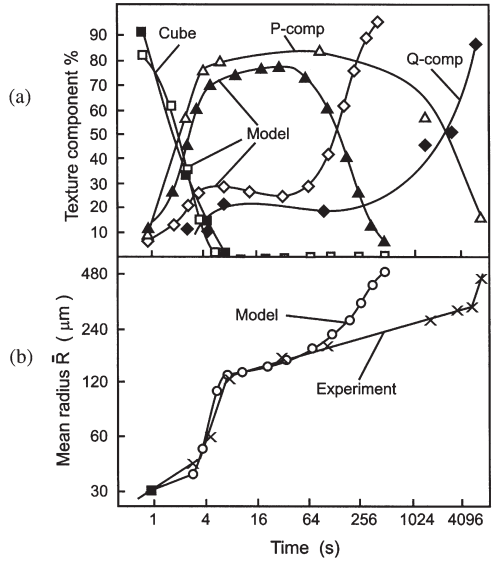

Fig. 12.22. Texture controlled grain growth in Al–1%Mn as a function of annealing time. (a) Volume fractions of components (filled points are experimental data), (b) Grain radii, (Abbruzzese et al. 1988).

others an initially rather diffuse texture may be retained and strengthened. The more dramatic changes of the former type are usually associated with abnormal grain growth (Beck 1954). Amongst the best known examples is that associated with abnormal grain growth in rolled copper sheet, where the cube texture is replaced by new orientations generated by a 30°–40° $<111>$ rotation (Bowles and Boas 1948, Kronberg and Wilson 1949). Other examples include silver and 70:30 brass in which the $\{236\}<385>$ texture typical of low SFE metals reverts to the rolling texture $\{110\}<112>$, and Al–3%Mg alloys in which an initial cube texture is replaced by components near $\{013\}<231>$ and $\{124\}<211>$ (Heckelmann et al. 1992). However the more general result, particularly for commercial materials, is that texture sharpening occurs rather than texture change (Hutchinson and Nes 1992). Figure 12.19 shows that the strength of the cube texture in a number of fcc metals and alloys is increased during grain growth and figure 12.20 demonstrates a similar strengthening of the $\{111\}$ texture components in a bcc, low-carbon steel.

Abnormal grain growth, which would be necessary for major changes in texture does not usually occur in commercial alloys because they usually contain sufficient amounts of dispersed phases to suppress such growth (§11.5.2). Additionally, the differences in boundary energy and mobility between the texture components present may be insufficient to promote abnormal grain growth (§11.5.3).

Current theories of grain growth after primary recrystallization, including the influence of texture, are discussed in chapter 11, and we are concerned here only with the evolution of texture during grain growth. Several models for grain growth in textured materials have been proposed as discussed in §11.3 (Abbruzzese and Lücke 1986, Eichelkraut et al. 1988, Bunge and Dahlem-Klein 1988). Abbruzzese et al. (1988), have compared model predictions with experimental results from Al–1%Mn which was rolled to 95% reduction and annealed at 620°C. As shown in figure 12.21a the primary recrystallization texture has a strong $\{001\}<100>$ component with a prominent spread generated by a rotation about the rolling direction. After further annealing for 120 sec the cube component is completely lost and an $\{011\}<122>$ component, which was previously insignificant, predominates (fig. 12.21b). At this stage a third component, $\{013\}<231>$, can be detected and as annealing continues this replaces the $\{011\}<122>$ component (fig. 12.21c). Figure 12.22 shows that the experimental results are in good agreement with the model used during the early stages of annealing; the lack of agreement at longer times was attributed to the fact that the mean grain size approached the sheet thickness. Weiland et al. (1988) have reported somewhat similar results from the same alloy and have shown by EBSD that the different components have different grain sizes.

It is obvious that the nature of the texture changes taking place during grain growth is very complicated and, as yet, relatively unexplored. Although theories to explain these changes are being developed, it should be noted that the orientation dependence of grain boundary energies and mobilities on which they are based, is often poorly known (§5.3.2).

ThisPageIntentionallyLeftBlank

Chapter 13

HOT DEFORMATION AND DYNAMIC RESTORATION

13.1 INTRODUCTION

The softening (restoration) processes of recovery and recrystallization may occur **during** deformation at high temperatures. In this case the phenomena are called **dynamic recovery** and **dynamic recrystallization** in order to distinguish them from the **static annealing** processes which occur during post-deformation heat treatment and which have been discussed in earlier chapters. The static and dynamic processes have many features in common, although the simultaneous operation of deformation and softening mechanisms leads to some important differences. Although dynamic restoration processes are of great industrial significance, they are not well understood because they are difficult to study experimentally and to model theoretically.

Dynamic recovery and dynamic recrystallization form part of the much larger subject of **hot working.** This is a very large and important area which cannot be covered in detail here. Some aspects of the historical development of the understanding of dynamic restoration are discussed by McQueen (1981) and Tegart (1992).

Dynamic recovery and dynamic recrystallization occur during metalworking operations such as **hot rolling, extrusion** and **forging.** They are important because they lower the flow stress of the material, thus enabling it to be deformed more easily and they also have an

influence on the texture and the grain size of the worked material. Dynamic recrystallization may also occur during creep deformation (Gifkins 1952, Poirier 1985), the main difference between **hot working** and **creep** being the strain rate. Hot working is generally carried out at strain rates in the range of 1–100 s^{-1}, whereas typical creep rates are below 10^{-5} s^{-1}. Nevertheless, in many cases similar atomistic mechanisms occur during both types of deformation. Dynamic recrystallization also occurs during the natural deformation of minerals in the Earth's crust and mantle, and is therefore of interest to Structural Geologists (e.g. Nicolas and Poirier 1976, Poirier 1985).

13.2 DYNAMIC RECOVERY

In metals of high stacking fault energy, such as aluminium and its alloys, α-iron and ferritic steels, dislocation climb and cross-slip occur readily (§2.2.2). Dynamic recovery is therefore rapid and extensive at high temperatures and is usually the only form of dynamic restoration which occurs. The stress-strain curve in this case is typically characterised by a rise to a plateau followed by a constant or steady state flow stress as shown in figure 13.1.

During the initial stages of deformation there is an increase in the flow stress as dislocations interact and multiply. However, as the dislocation density rises, so the driving force and hence the rate of recovery increases (§6.3), and during this period a microstructure of low angle boundaries and subgrains develops. At a certain strain, the rates of work hardening and recovery reach a dynamic equilibrium, the dislocation density remains constant and a **steady-state flow stress** is obtained as seen in figure 13.1. During deformation at strain rates larger than $\sim$1 s^{-1} the heat generated by the work of deformation cannot all be removed from the specimen and the temperature of the specimen rises during deformation. This may then cause a reduction in the flow stress as

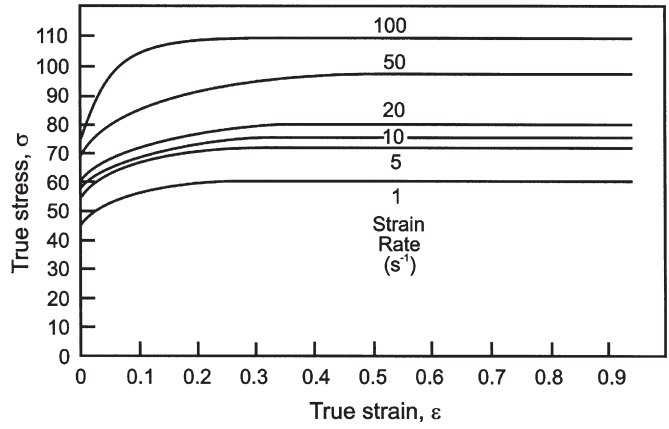

Fig. 13.1. Stress-strain curves for Al–1%Mg at 400°C, (Puchi et al. 1988).

straining proceeds. In modelling the high temperature deformation behaviour as discussed below, it is very important that such effects are taken into account (e.g. Shi et al. 1997).

13.2.1 Constitutive relationships

At temperatures where thermally activated deformation and restoration processes occur, the microstructural evolution will be dependent on the **deformation temperature (T)** and **strain rate** ($\dot{\varepsilon}$) in addition to the **strain** (ε). The strain rate and deformation temperature are often incorporated into a single parameter – **The Zener–Hollomon parameter (Z),** which is defined as:

$$Z = \dot{\varepsilon} \exp\left(\frac{Q}{RT}\right) \tag{13.1}$$

where Q is an activation energy.

For the purposes of analytical or computer modelling of hot working operations it is necessary to express the relationship between flow stress, temperature, strain and strain rate algebraically. If the flow stress follows a mechanical equation of state, i.e. it is dependent only on the **instantaneous** values of **T,** ε and $\dot{\varepsilon}$ and not on their **history,** then the relationship between these parameters may be expressed by relatively simple empirical equations (e.g. Jonas et al. 1969, Frost and Ashby 1982). It is found that during hot work, such a mechanical equation of state is closely followed, and during steady state deformation, the relationship between the flow stress (σ) and Zener–Hollomon parameter is often found to be

$$Z = c_1 \sinh(c_2\sigma)^n \tag{13.2}$$

where c_1, c_2 and n are constants.

Equation 13.2 may also be expressed in the form

$$\sigma = \frac{1}{c_2}\ln\left[\left(\frac{Z}{c_1}\right)^{1/n} + \left(\left(\frac{Z}{c_1}\right)^{2/n} + 1\right)^{1/2}\right] \tag{13.3}$$

At low values of stress, equation 13.3 reduces to a power relationship of the form

$$\dot{\varepsilon} = c_3\sigma^m \exp\left(-\frac{Q_1}{RT}\right) \tag{13.4}$$

where c_3, m and Q_1 are constants.

and at high stress values it simplifies to

$$Z = 0.5^n\ c_1 \exp(nc_2\sigma) = c_4 \exp(c_5\ \sigma) \tag{13.5}$$

Thus **Z** is seen to be closely related to the flow stress and hence to the dislocation density (equation 2.2). The Zener–Hollomon parameter is particular convenient for discussions of hot working processes in which the temperature and strain rate are generally known, whereas the flow stress may not be measurable.

A detailed consideration of the mechanical properties during hot deformation, the constitutive relationships and the microstructures developed during high temperature deformation is outside the scope of this book and further details may be found in Jonas et al. (1969), Roberts (1984, 1985), Sellars (1978, 1986, 1990, 1992a, 1992b), Blum (1993), Shi et al. (1997) and Davenport et al. (2000).

13.2.2 Mechanisms of microstructural evolution

The basic mechanisms of dynamic recovery are dislocation climb, cross-slip and glide, which result in the formation of low angle boundaries as also occurs during static recovery (§6.4). However, the applied stress provides an additional driving pressure for the movement of low angle boundaries and those of opposite sign will be driven in opposite directions, and this stress-assisted migration of dislocation boundaries may contribute significantly to the overall strain (Exell and Warrington 1972, Biburger and Blum 1992, Huang and Humphreys 2002). Such migration results in some annihilation of dislocations in opposing boundaries and Y-junction boundary interactions (§6.5.3) and these enable the subgrains to remain approximately equiaxed during the deformation. In-situ SEM deformation experiments have shown that some reorientation of subgrains may also occur during hot deformation. The subgrains can therefore be considered to be **transient** microstructural features.

The processes of work hardening and recovery lead to the continual formation and dissolution of low angle boundaries and to a constant density of unbound or 'free' dislocations within the subgrains. After a strain of typically 0.5 to 1, the subgrain structure often appears to achieve a steady state. The microstructural changes occurring during dynamic recovery are summarised schematically in figure 13.2, and typical microstructures are shown in figure 13.3.

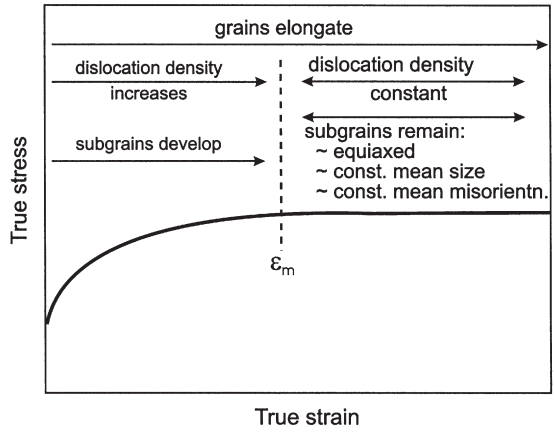

Fig. 13.2. Summary of the microstructural changes which occur during dynamic recovery, (after Sellars 1986).

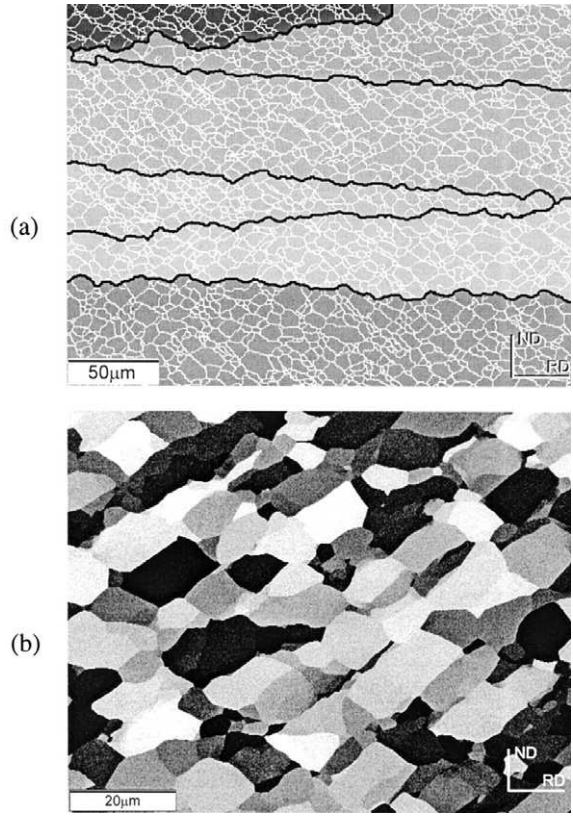

Fig. 13.3. Microstructure in ND-RD plane of Al–0.1%Mg deformed in plane strain compression at 350°C, $\varepsilon = 1$, $\dot{\varepsilon} = 0.25$. (a) EBSD map showing LAGBs (white) and serrated HAGBs (black), (b) SEM channelling contrast image showing the subgrain structure.

Although the dislocation and subgrain structures often remain approximately constant during steady-state deformation, the original grain boundaries do not migrate significantly and the grains continue to change shape during the deformation. This of course means that although the flow stress may remain constant, **a true microstructural steady state is not achieved** during dynamic recovery. This is particularly true if the strain is sufficient to reduce the separation of high angle boundaries to a value comparable with the subgrain size, an important situation which is further considered in chapter 14.

13.2.3 The microstructures formed during dynamic recovery

13.2.3.1 The subgrains

During high temperature deformation, dynamic recovery results in more organised dislocation arrangements within the subgrain boundaries (McQueen 1977), in the same

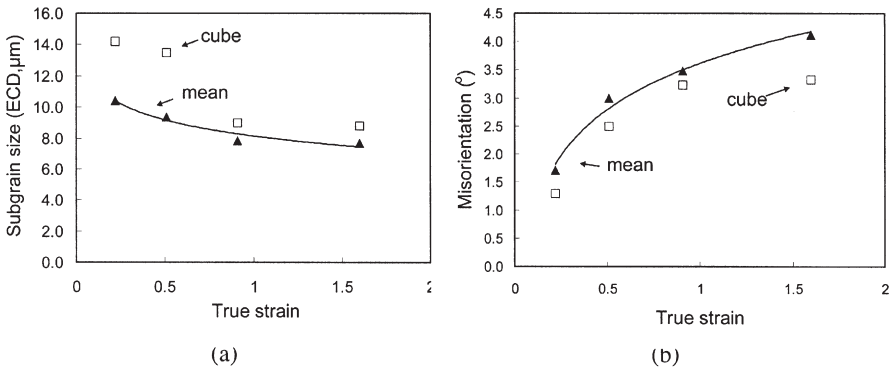

Fig. 13.4. The effect of strain on the size and misorientation of subgrains in Al–0.1Mg deformed in plane strain compression at 350°C at a rate of 10^{-2} s^{-1}. Both mean data, and data for cube-oriented subgrains are shown (Humphreys and Ashton 2003).

way as in static recovery (§6.4 and figure 6.13). In aluminium alloys, the cells or subgrains formed during low temperature deformation are arranged in bands, which are usually aligned on planes of high shear stress (see §2.4.2). This type of alignment is also found after high temperature deformation (Duly et al. 1996, Zhu and Sellars 2001), although it becomes less obvious at higher temperatures or lower strain rates (i.e. lower **Z**) as may be seen from a comparison of figures 2.10 and 13.3b.

The cell or subgrain size is generally found to be independent of strain at strains larger than ~0.5 (e.g. Duly et al. 1996), and as shown in figure 13.4a, although it depends on the temperature and rate of deformation (§13.2.3.4). However, the subgrain misorientations increase with strain as shown in figure 13.4b.

The subgrains formed during high temperature deformation are usually found to contain significant numbers of dislocations which are not associated with the low angle grain boundaries, and the density of these unbound dislocations has been found to be related to the flow stress (§13.2.3.4).

13.2.3.2 High angle boundary serrations

During deformation under conditions of low **Z,** the grain boundaries migrate locally in response to the boundary tensions of the substructure and to local dislocation density variations, and become serrated with a wavelength which is closely related to the subgrain size as shown in figures 13.3a and 13.5a. However, if small second-phase particles are present, these may prevent local migration of the high angle boundaries, so that these remain planar as shown in figure 13.5b.

13.2.3.3 The homogeneity of deformation

As discussed in chapter 2, the microstructures developed during low temperature deformation are usually very inhomogeneous and these regions of inhomogeneity are

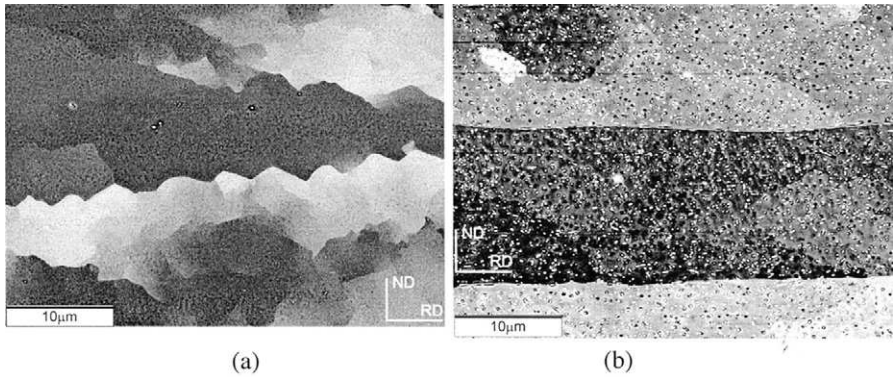

Fig. 13.5. High angle grain boundaries in aluminium alloys deformed at 400°C in plane strain compression. (a) Al–5%Mg, showing serrations at the high angle boundaries, (b) Al–2%Cu. Second-phase particles prevent boundary serrations from developing.

frequently sites for the origin of recrystallization during subsequent annealing. It is generally found that as the temperature of deformation increases, the deformation becomes more homogeneous (e.g. Drury and Humphreys 1986, Hansen and Jensen 1991, Ball and Humphreys 1996). Some of this may be explained in terms of an increase in the number of operating slip systems, which gives rise to homogeneous deformation more typical of the ideal 'Taylor type' plasticity (§3.7.1.2) than that which occurs at lower temperature. During deformation at high temperatures, slip systems which do not operate at low temperatures because of a higher Peierls–Nabarro stress may also become active. This is particularly important in non-metals and non-cubic materials, (Hazif et al. 1973, Ion et al. 1982) and even in face-centred cubic metals there is some evidence that slip systems other than $\{111\}<011>$ may operate at high temperatures (§13.2.4). Figure 13.6 shows how the frequency of the formation of the large-scale **deformation bands** visible under the optical microscope, decreases as the deformation temperature increases. Samajdar et al. (2001) have also shown that the long range misorientation gradients in aluminium, decrease as **Z** decreases. It is also usually found that **shear banding** becomes less frequent at higher deformation temperatures, as shown in figure 2.23.

13.2.3.4 The effect of the deformation conditions

The mechanisms of dislocation generation and recovery discussed above, operate over a wide range of temperatures and strain rates (e.g. Blum 1993). However, it should be noted that at very low strain rates and high temperatures (i.e. creep conditions), other mechanisms such as Herring–Nabarro and Coble creep may be important, although they will not be considered here. At low temperatures and high strain rates (high **Z**) the dislocation generation (work hardening) factor is dominant whereas at high temperatures and low strain rates (low **Z**) dynamic recovery dominates. Therefore after hot deformation, the microstructure will be dependent on both strain and Zener–Hollomon parameter.

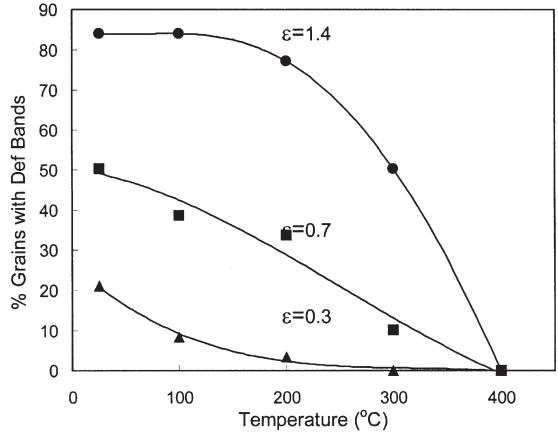

Fig. 13.6. The effect of deformation temperature and strain on the formation of large-scale deformation bands in Al–0.3Mn deformed in plane strain compression (Ball and Humphreys 1996).

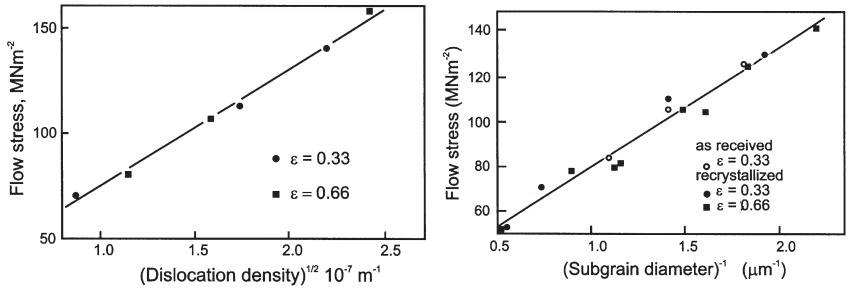

(a) (b)

Fig. 13.7. The relationship between the high temperature flow stress and microstructure in Al–1%Mg–1%Mn. (a) The dislocation density within subgrains (Castro–Fernandez et al. 1990), (b) The subgrain size, (Castro–Fernandez and Sellars 1988).

- **Dislocation content**

It has been found for steels and for aluminium that the high temperature flow stress is related to the density of dislocations **within** the subgrains (ρ_i) by the relationship (Castro–Fernandez et al. 1990)

$$\sigma = c_1 + c_2 G b \rho_i^{1/2} \tag{13.6}$$

where c_1 and c_2 are constants.

This is similar to the relationship between the flow stress and overall dislocation density found at low temperatures (equation 2.2), and figure 13.7a shows this relationship for an Al–Mg–Mn alloy.

- **Subgrain size**

If subgrains are formed, it is usually found (Sherby and Burke 1967) that the high temperature flow stress is inversely proportional to the mean subgrain diameter (**D**) (equation 6.30) and an example of this is shown in figure 13.7b. It has been shown (Takeuchi and Argon 1976) that if equation 6.30 is expressed in terms of normalised stress and subgrain size and a dimensionless constant K, then K is constant for any particular class of material.

$$\frac{\sigma}{G}\frac{D}{b} = K \tag{13.7}$$

Derby (1991) has analysed subgrain data for a range of metals and minerals and these are plotted according to equation 13.7 in figure 13.8. **K** has a value of ~10 for fcc metals and ~25–80 for ionic crystals of the NaCl structure.

Furu et al. (1992) have analysed subgrain sizes in aluminium alloys for a wide range of conditions, and shown that the relationship between subgrain size (D) and Zener–Hollomon parameter (**Z**) for $10^{13} < Z < 10^{17}$ can be expressed empirically as

$$D = K_1 - K_2 \log Z \tag{13.8}$$

where k_1 and k_2 are constants.

At constant flow stress (or **Z**), equations 13.6 and 6.30 imply a unique relationship between the subgrain size and the dislocation density within the subgrains of the form

$$\rho_i^{1/2} = c_3 D^{-1} \tag{13.9}$$

Such a relationship is predicted by theoretical models of subgrain formation during deformation (e.g. Holt 1970, Edward et al. 1988), and experimental investigations in

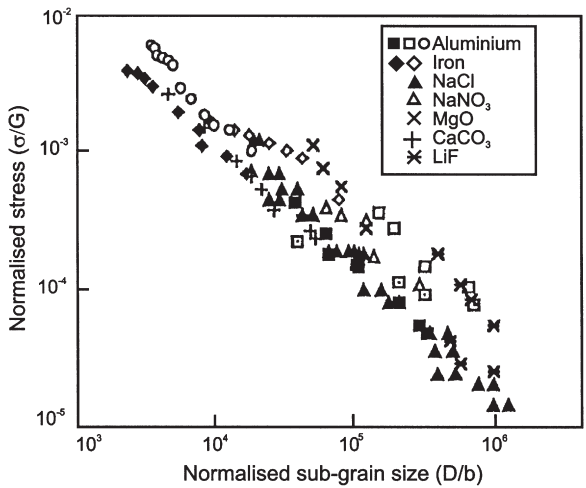

Fig. 13.8. The relationship between subgrain size and high temperature flow stress, (after Derby 1991).

aluminium (Castro–Fernandez et al. 1990), copper (Straker and Holt 1972) and ferritic steels (Barrett et al. 1966, Urcola and Sellars 1987), have reported values of c_3 between 10 and 20.

13.2.3.5 The effect of variable deformation conditions

During many hot working operations, the deformation temperature and strain rate do not remain constant, and because the microstructural parameters such as dislocation density are closely linked to the deformation conditions as discussed in the previous section, an understanding of microstructural evolution under conditions of varying temperature or strain rate is important. Hot deformation experiments on aluminium alloys, in which the strain rate is raised during deformation (Baxter et al. 1999), have shown that the microstructures reach equilibrium after little further deformation. However, if the strain rate is decreased during deformation, further strains of ~0.5 are required before the microstructure achieves steady state values. Huang and Humphreys (2002) found that the main mechanism of subgrain growth during a strain rate decrease was by low angle boundary migration. The rate of subgrain growth under these conditions is very much larger than for static annealing as shown in figure 13.9, the boundary migration rates being strongly affected by the imposed stress (§13.2.2).

13.2.4 Texture formation during hot deformation

The crystallographic textures resulting from cold or warm deformation were discussed in chapter 3. In some cases deformation at high temperatures may produce significantly

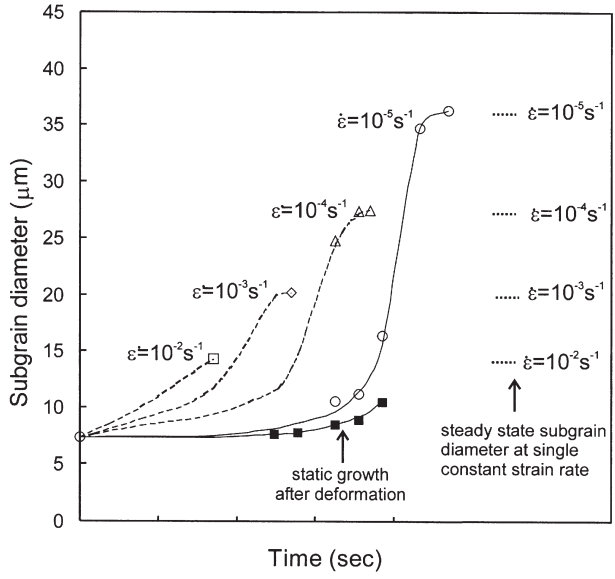

Fig. 13.9. The effect of strain rate change on samples of commercially pure aluminium, initially deformed to a strain of 0.9 at 400°C a rate of 0.5 s^{-1}. The growth rates of the subgrains under static conditions are also shown (Huang and Humphreys 1997).

different textures, even in materials which undergo only dynamic recovery. Because these textures may have a strong influence on the recrystallization of hot-worked material, we will give a brief discussion here, and focus particularly on the cube texture component in hot-deformed aluminium alloys. This topic is of great industrial significance, and has been the subject of extensive research in recent years.

As discussed in §13.2.1, the deformation temperature and strain rate are conveniently described collectively by the Zener–Hollomon parameter (**Z**). The textures developed in aluminium alloys during deformation under conditions of low **Z,** often differ from those in alloys deformed at ambient temperatures (high **Z**), and in particular, it is found that during plane strain compression (e.g. rolling), there is increasing stability of the $\{011\}<211>$, Brass, and $\{001\}<100>$, Cube, components at the expense of the other normal rolling components as **Z** decreases.

The texture of a commercially hot-rolled Al–1%Mn–1%Mn alloy is shown in figure 13.10. It may be seen that the normal rolling texture components, Brass, Copper and S (see fig. 3.3) are all present, but that along the β-fibre, the Brass component is particularly strong, and that there are also peaks close to Cube.

Some care has to be taken in interpreting hot deformation textures as true deformation textures, because of the possibility of some recrystallization occurring prior to quenching, and this is particularly true for Al–Mg alloys (e.g. Hirsch 1991). Details

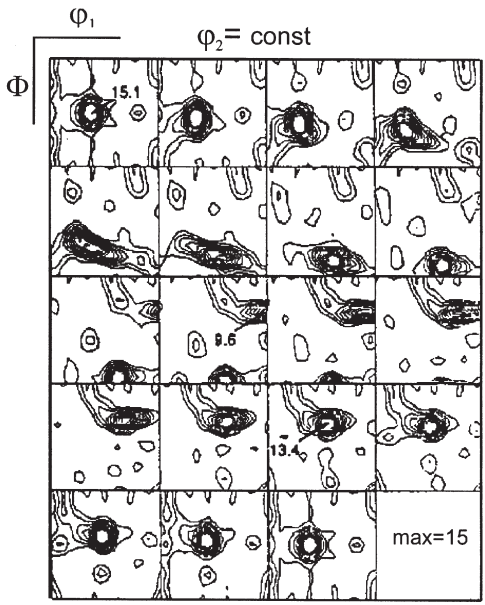

Fig. 13.10. ODF of commercially hot-rolled Al–1%Mg–1%Mn alloy showing a large Brass component and a significant Cube component in addition to the normal rolling texture, (Daaland and Nes 1995).

of the texture evolution also depend strongly on the starting texture (Bolingbroke et al. 1995), but the above trends are generally observed, and are consistent with studies of hot-deformed single crystals (Maurice and Driver 1993, 1997a).

An investigation of textures after hot deformation in a number of dilute aluminium alloys (Vernon–Parry et al. 1996) showed that under the range of conditions studied, the strength of the cube texture decreased with increasing strain, and decreased with increasing **Z.** Similar results were reported by Basson et al. 1998, and their results are shown in figure 13.11.

It is also found that the subgrains within different texture components have different characteristics. Table 13.1 shows TEM measurements for subgrains in an Al–1Mg alloy deformed in plane strain compression at 400°C to a strain of 1. The last column shows the stored energy, which is a function of the subgrain misorientation divided by the size (equation 2.8). These measurements, together with those of Bardal et al. (1995) on Al–1%–1%Mg, and the data of figure 13.4, indicate that while cube-oriented subgrains in aluminium tend to be larger than other subgrains, they have similar or somewhat lower misorientations. This is thought to be an important factor in the subsequent recrystallization of hot-deformed aluminium (§13.6.2) and the development of recrystallization texture (§12.4.1).

The increased stability of the Brass and Cube texture components in aluminium alloys during high temperature deformation has been explained by the operation of non-octahedral slip, $\{110\}<110>$, at high temperatures, for which there is some evidence from surface slip markings (Hazif et al. 1973, Maurice and Driver 1993). If such slip is included in crystal plasticity calculations, then an increased stability of these texture components can be predicted (Maurice and Driver 1993, 1997b). However, the agreement between predicted and actual textures is not particularly good if reasonable

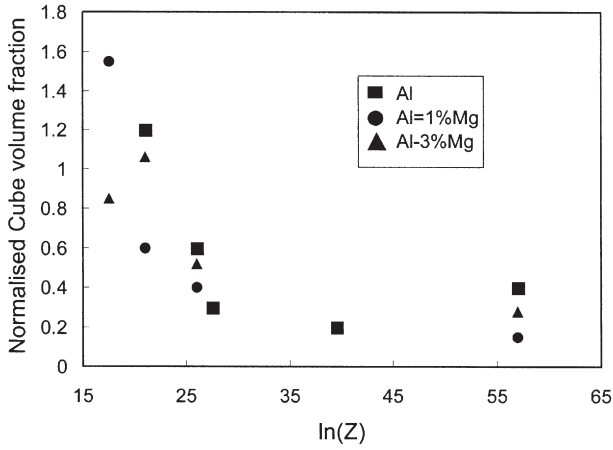

Fig. 13.11. Normalised cube texture volume fraction as a function of Zener–Hollomon parameter (Z), for alloys deformed in plane strain compression to a strain of 1, (after Basson et al. 1998).

Table 13.1
Subgrain parameters in an Al–1Mg alloy deformed at 400°C to $\varepsilon = 1$ (Driver et al. 1996).

Orientation	Misorientation (deg)	Size (μm)	Stored Energy ($mJcm^{-3}$)
Brass	3.1	12	12.2
S	6.3	17	13.3
Copper	4.3	14	12.9
Cube	4	23	7.6

slip conditions are assumed (Kocks et al. 1994, Knutsen et al. 1999, Samajdar et al. 2001). Additionally, the occurrence of non-octahedral slip cannot easily explain why the strength of the cube texture may, in certain circumstances actually increase with strain (Knutsen et al. 1999). Several authors have linked the changes in texture to changes in microstructure (Samajdar et al. 2001) and to the onset of some form of dynamic grain boundary migration (Kocks et al. 1994, Knutsen et al. 1999), and further work is required to clarify this matter.

13.2.5 Modelling the evolution of microstructure

There is a significant interest in modelling the evolution of microstructure during the hot deformation of metals which undergo dynamic recovery. The aims are to predict both the microstructures and the flow stresses of materials processed under the wide range of conditions employed in industrial processing, and a comprehensive review of the subject is given by Shercliff and Lovatt (1999). The early work was based on the development of the empirical constitutive equations discussed in §13.2.1, but more recently, most attention has been given to the development of 'physically based' state variable models in which models which quantify parameters such as dislocation density, subgrain size and misorientation are combined to model the overall microstructural evolution. Examples of this type of modelling may be found in the work of Sellars (1990, 1997), Nes (1995b), Nes and Furu (1995), and Shercliff and Lovatt (1999). Such modelling has been extended by using finite element methods to provide more realistic descriptions of the strain, strain rate and temperature distributions during deformation processing (McLaren and Sellars 1992, Beynon 1999, Davenport et al. 1999). Details of these models are outside the scope of this book, but an outline of how such models may be used in the context of industrial deformation processing is given in §16.3.3.

13.3 DISCONTINUOUS DYNAMIC RECRYSTALLIZATION

In metals in which recovery processes are slow, such as those with a low or medium stacking fault energy (copper, nickel and austenitic iron), dynamic recrystallization may take place when a critical deformation condition is reached. A simplified description of the phenomenon of dynamic recrystallization is as follows. New grains originate at the old grain boundaries, but, as the material continues to deform, the dislocation density of

the new grains increases, thus reducing the driving force for further growth, and the recrystallizing grains eventually cease to grow. An additional factor which may limit the growth of the new grains is the nucleation of further grains at the migrating boundaries.

This type of dynamic recrystallization, which has clear nucleation and growth stages, can be classified as a discontinuous process. There are other mechanisms which produce high angle grain boundaries during high temperature deformation, and which may be considered to be types of dynamic recrystallization. These phenomena are discussed in §13.4.

13.3.1 The characteristics of dynamic recrystallization

The general characteristics of dynamic recrystallization are as follows:

- As shown in figure 13.12, the stress-strain curve for a material which undergoes dynamic recrystallization generally exhibits a broad peak that is different to the plateau, characteristic of a material which undergoes only dynamic recovery (fig. 13.1). Under conditions of low Zener–Hollomon parameter, multiple peaks may be exhibited at low strains, as seen in figure 13.12.
- A critical deformation (ε_c) is necessary in order to initiate dynamic recrystallization. This occurs somewhat before the peak (σ_{max}) of the stress strain curve. For a range of testing conditions, σ_{max} is uniquely related to the Zener–Hollomon parameter (**Z**).
- ε_c decreases steadily with decreasing stress or Zener–Hollomon parameter, although at very low (creep) strain rates the critical strain may increase again (Sellars 1978).
- The size of dynamically recrystallized grains (D_R) increases monotonically with decreasing stress. Grain growth does not occur and the grain size remains constant during the deformation.

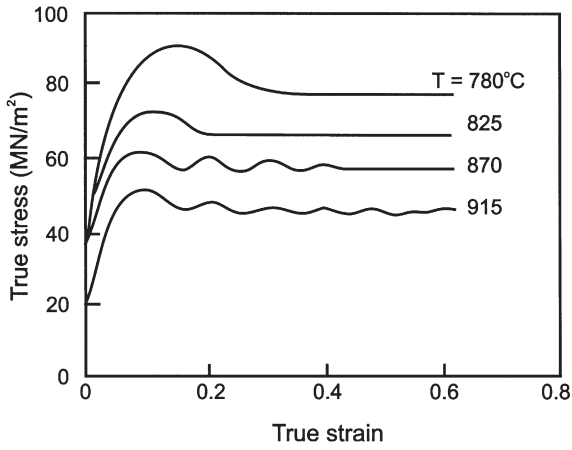

Fig. 13.12. The effect of temperature on the stress-strain curves for 0.68%C steel, deformed in axisymmetric compression, $\dot{\varepsilon} = 1.3 \times 10^{-3}\ s^{-1}$, (Petkovic et al. 1975).

- The flow stress (σ) and D_R are almost independent of the initial grain size (D_0), although the kinetics of dynamic recrystallization are accelerated in specimens with smaller initial grain sizes.
- Dynamic recrystallization is usually initiated at pre-existing grain boundaries although for very low strain rates and large initial grain sizes, intragranular nucleation becomes more important.

13.3.2 The nucleation of dynamic recrystallization

13.3.2.1 Nucleation mechanisms

Dynamic recrystallization originates at high angle boundaries. These may be the original grain boundaries, boundaries of dynamically recrystallized grains, or high angle boundaries created during straining (e.g. those associated with deformation bands or deformation twins). Bulging of grain boundaries is frequently observed as a prelude to dynamic recrystallization, and it is usually assumed that a mechanism closely related to strain-induced grain boundary migration (§7.6.2) operates. Recent investigations (Wusatowska et al. 2002), have suggested that the origin of dynamic recrystallization in copper may be the formation of lattice rotations at grain boundary serrations due to boundary sliding, a mechanism proposed by Drury and Humphreys (1986), which is discussed in §13.4.2.

13.3.2.2 Models of dynamic recrystallization

Several models of dynamic recrystallization have been proposed. Regardless of the details of the mechanism of nucleation, the condition for the growth of a dynamically recrystallized grain is thought to depend on the distribution and density of dislocations, both in the form of subgrains and free dislocations §13.2.3, which provide the driving force for growth. Figure 13.13, based on the model of Sandström and Lagneborg (1975), shows schematically the dislocation density expected in the vicinity of a migrating boundary. The boundary at **A** is moving from left to right into unrecrystallized material which has a high dislocation density ρ_m. As the boundary moves, it reduces the dislocation density in its wake to around zero by recrystallization. However, the continued deformation raises the dislocation density in the new grain, so that it builds

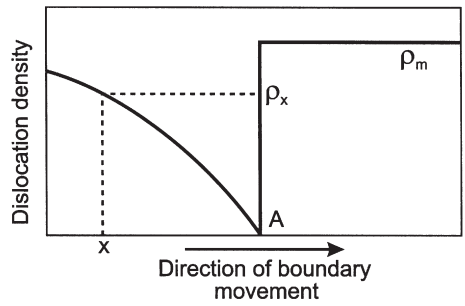

Fig. 13.13. Schematic diagram of the dislocation density at a dynamic recrystallization front, (after Sandström and Lagneborg 1975).

up behind the moving boundary and reaches ρ_x at a distance **x** behind the boundary, tending towards a value of ρ_m at large distances. The following very approximate analysis, which does not take dynamic recovery into account is based on that proposed by Sandström and Lagneborg (1975) and Roberts and Ahlblom (1978).

The migrating grain boundary moves under a driving pressure of $\sim\rho_m Gb^2$ arising from the dislocation density difference across the boundary and from equation 5.1, the resulting velocity is given as

$$\frac{dx}{dt} = M\rho_m Gb^2 \tag{13.10}$$

If the mean slip distance of the dislocations is **L,** the rate of increase of dislocation density behind the migrating boundary due to the continuing deformation is obtained by differentiating equation 2.1.

$$\frac{d\rho}{dt} = \frac{\dot{\varepsilon}}{bL} \tag{13.11}$$

and hence

$$\frac{d\rho}{dx} - \frac{\dot{\varepsilon}}{MLGb^3\rho_m} \tag{13.12}$$

and

$$\rho = \frac{\dot{\varepsilon}x}{MLGb^3\rho_m} \tag{13.13}$$

The dislocation density behind the moving boundary reaches the value of ρ_m when $x = x_c$ and hence

$$x_c = \frac{MLGb^3\rho_m^2}{\dot{\varepsilon}} \tag{13.14}$$

If nucleation is assumed to occur by a bulge mechanism, then the critical condition for the formation of a nucleus of diameter x_c would (equation 7.40) be

$$E > \frac{2\gamma_b}{x_c} \tag{13.15}$$

Where **E** is the stored energy, which is taken to be a fraction **K** of $\rho_m Gb^2$. Using equation 13.14, the condition for nucleation then becomes

$$\frac{\rho_m^3}{\dot{\varepsilon}} > \frac{2\gamma_b}{KMLGb^5} \tag{13.16}$$

The terms on the right hand side of equation 13.16 may be regarded as approximately constant at a particular temperature, and thus the condition for the nucleation of dynamic recrystallization is that a critical value of $\rho_m^3/\dot{\varepsilon}$ must be achieved. In materials such as aluminium and pure iron, recovery occurs readily and this parameter, strongly dependent on dislocation density, never reaches the critical value, and therefore only **dynamic recovery** occurs. However in materials of lower stacking fault energy such as

copper, nickel and stainless steel, recovery is slow and the dislocation density increases to the critical value necessary for **dynamic recrystallization** to occur.

There is some confusion in the literature about the occurrence of dynamic recrystallization in aluminium. As discussed above, rapid dynamic recovery generally prevents the accumulation of sufficient dislocations to sustain dynamic recrystallization. However, there have been numerous reports of dynamic recrystallization in aluminium of very high purity, and these have been reviewed by Kassner and Evangelista (1995), who conclude that discontinuous dynamic recrystallization can occur during room temperature deformation in very high purity aluminium. If we consider the conditions for dynamic recrystallization given by equation 13.16, we see that the critical value of $\rho_m^3/\dot{\varepsilon}$ required for dynamic recrystallization will be reduced by an increased boundary mobility (M), and as discussed in §5.3, very high boundary mobilities are found in very pure metals. Thus it is quite likely that there are conditions under which the increase in boundary mobility outweighs any increase in the recovery rate, thereby allowing dynamic recrystallization to occur.

13.3.3 Microstructural evolution

Dynamic recrystallization generally starts at the old grain boundaries as shown schematically in figure 13.14a. New grains are subsequently nucleated at the boundaries of the growing grains (fig. 13.14b), and in this way a thickening band of recrystallized grains is formed as shown in figure 13.14c. If there is a large difference between the initial grain size (D_0) and the recrystallized grain size (D_R), then a **'necklace'** structure of grains may be formed (fig. 13.14b–c), and eventually the material will become fully

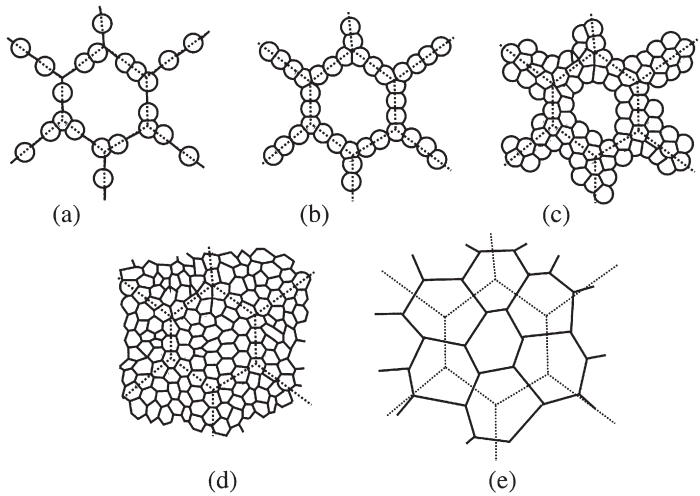

Fig. 13.14. The development of microstructure during dynamic recrystallization. (a)–(d) Large initial grain size, (e) small initial grain size. The dotted lines show the prior grain boundaries.

recrystallized (13.14d). A micrograph of copper which has undergone partial dynamic recrystallization is shown in figure 13.15.

Unlike static recrystallization, the mean size of the dynamically recrystallized grains does not change as recrystallization proceeds as shown in figure 13.16.

In some cases, microstructural evolution is more complicated than that described above, because the onset of dynamic recrystallization may lead to changes in deformation mechanism. For example, if dynamic recrystallization results in a very small grain size, then subsequent deformation may occur preferentially by the mechanism of **grain boundary sliding.** This will tend to occur if deformation by dislocation glide and climb is particularly difficult, and has been reported in α-brass (Hatherly et al. 1986) in which

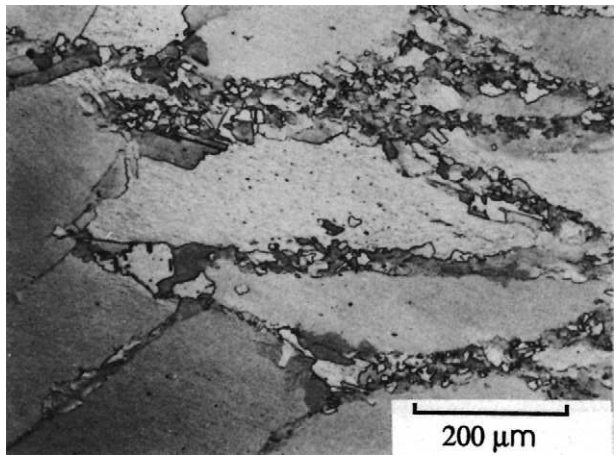

Fig. 13.15. Dynamic recrystallization at prior grain boundaries in polycrystalline copper at 400°C, $\dot{\varepsilon} = 2 \times 10^{-2}$, $\varepsilon = 0.7$, (Ardakani and Humphreys 1992).

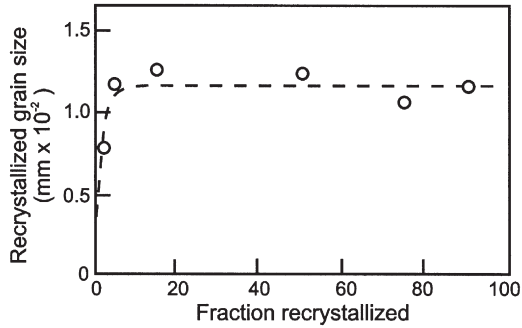

Fig. 13.16. Relationship between dynamically recrystallized grain size and fraction recrystallized in nickel deformed at 880°C, $\dot{\varepsilon} = 5.7 \times 10^{-2}$ s^{-1}, (Sah et al. 1974).

the low stacking fault energy hinders climb, in magnesium (Drury et al. 1989) where there are few slip systems, in dispersion hardened copper (Ardakani and Humphreys 1992) in which dislocation motion is hindered by second-phase particles, and in intermetallics (Ponge and Gottstein 1998).

13.3.4 The steady state grain size

Experimental observations generally show that the steady state grain size (D_R) during dynamic recrystallization is a strong function of the flow stress and is only weakly dependent on deformation temperature. The empirical relationship is often given as

$$\sigma = KD_R^{-m} \tag{13.17}$$

where $m < 1$ and K is a constant. Twiss (1977) examined the relation between the mean grain size and flow stress of a number of materials and proposed a universal relationship which can be expressed in normalised form as

$$\frac{\sigma}{G}\left(\frac{D_R}{b}\right)^n = K_1 \tag{13.18}$$

where $n = 0.8$ and $K_1 = 15$, which is of a rather similar form to the subgrain relationship of equation 13.7. Derby (1991) has found that such a relationship holds for a very wide range of materials of metallurgical and geological significance as shown in figure 13.17, and has shown that the data in figure 13.17 are bounded by loci of the form

$$1 < \frac{\sigma}{G}\left(\frac{D_R}{b}\right)^{2/3} < 10 \tag{13.19}$$

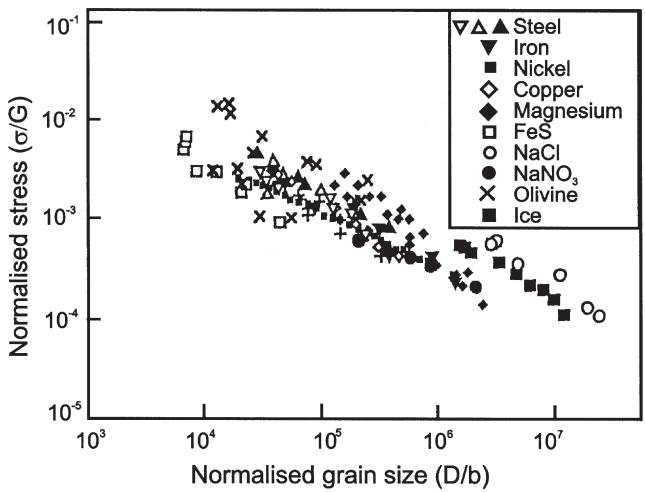

Fig. 13.17. The relationship between dynamically recrystallized grain size and high temperature flow stress, (after Derby 1991).

However, Wusatowska et al. (2002) have recently reported that in copper, although the grain size exponent (**m**) in equation 13.17 is 0.75 at low flow stresses, it reduces to 0.23 at high stress, suggesting a change in the mechanism of dynamic recrystallization.

Dynamic recrystallization is a continuous process of deformation, nucleation of grains and subsequent migration of grain boundaries, leaving new dislocation-free grains which then deform further. Although the details of dynamic recrystallization cannot be directly observed in metals, these processes have been observed to occur in transparent crystalline materials (§13.5).

For a steady state to occur there must be a dynamic balance between the nucleation of new grains and the migration of the boundaries of the previously nucleated grains. Derby and Ashby (1987) have analysed this balance as follows. In the time taken for a moving boundary to sweep out a volume equivalent to the mean steady state grain size (D_R), the nucleation rate ($\dot{N}$) should be sufficient for one new nucleation event to occur in each equivalent volume averaged over the microstructure. If nucleation is confined to pre-existing grain boundaries then this condition may be expressed as

$$\frac{CD_R^3\dot{N}}{\dot{G}} = 1 \tag{13.20}$$

where C is a geometric constant ~3.

The steady state grain size will therefore be dependent on the ratio of the nucleation and growth rates. Derby and Ashby (1987) argue that as the steady state grain size depends on the ratio of the nucleation and growth rates, both of which may have a similar temperature dependence, then it is to be expected that the steady state grain size will be only weakly dependent on temperature, as is found in practice. If the size of the dynamically recrystallized grains (D_R) is taken to be equal to x_c as given by equation 13.14, and we assume a relationship between flow stress and dislocation density of the form of equation 2.2 and a relationship between flow stress and strain rate as given by equation 13.4 with $m = 5$, then equation 13.14 may be written in the form $\boldsymbol{\sigma} = \mathbf{K'/D}$, which is similar to equation 13.18. Derby and Ashby (1987) have used a more sophisticated version of this analysis to calculate the steady state grain size starting from equation 13.20 and arrive at a relationship close to that of equation 13.18.

13.3.5 The flow stress during dynamic recrystallization

As shown in figure 13.12, the stress strain curves of a dynamically recrystallizing material may be characterised by a single peak or by several oscillations. Luton and Sellars (1969) have explained this in terms of the kinetics of dynamic recrystallization. At low stresses, the material recrystallizes completely before a second cycle of recrystallization begins, and this process is then repeated. The flow stress, which depends on the dislocation density, therefore oscillates with strain. At high stresses, subsequent cycles of recrystallization begin before the previous ones are finished, the material is therefore always in a partly recrystallized state after the first peak, and the stress strain curve is smoothed out, resulting in a single broad peak.

Sakai and Jonas (1984) have suggested that the shape of the stress strain curve depends primarily on the ratio of the recrystallized and starting grain sizes (D_0/D_R). If (D_0/D_R) > 2 then the microstructure develops as shown in 13.14a–d, the material is only partly recrystallized except at very high strains, and a smooth curve with a single peak results. However, if $D_0/D_R < 2$ then the new grains all develop at about the same time because there are enough sites (i.e. old boundaries) for recrystallization to be complete in one cycle as shown in figure 13.14e. This fully recrystallized and softened material then undergoes further deformation, hardens, and then recrystallizes again. As this cycle is repeated, an oscillatory stress strain curve results. The shape of the stress-strain curve therefore depends on the deformation conditions (Z) and on the initial grain size. Figure 13.18 illustrates schematically the relationship between the stress-strain behaviour and these parameters.

13.3.6 Dynamic recrystallization in single crystals

A considerable research effort has been expended in studying the fundamental aspects of the dynamic recrystallization of single crystals of silver, gold, nickel and copper and its alloys, and this is reviewed by Mecking and Gottstein (1978) and Gottstein and Kocks (1983). As discussed earlier in this chapter, dynamic recrystallization is essentially a grain boundary phenomenon, and therefore its occurrence in single crystals, although scientifically interesting, is unlikely to be of direct relevance to the thermomechanical processing of industrial alloys.

As shown in figure 13.19, the stress-strain curve of a copper crystal deformed in tension at high temperatures exhibits a sharp drop, which has been shown to correspond to the occurrence of dynamic recrystallization. There is no clear correlation between the strain and the onset of dynamic recrystallization, but the shear stress for dynamic recrystallization (τ_R) has been shown to be reproducible for given deformation conditions. However, τ_R is a function of the material, the crystal orientation, the

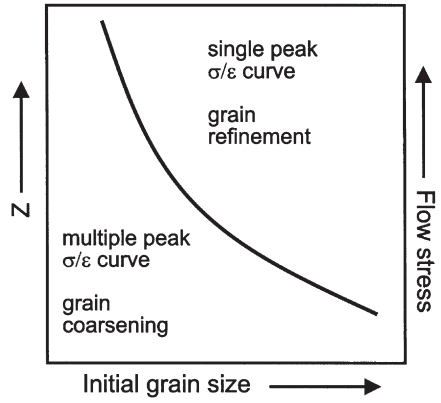

Fig. 13.18. The conditions for multiple and single peak dynamic recrystallization, (after Sakai et al. 1983).

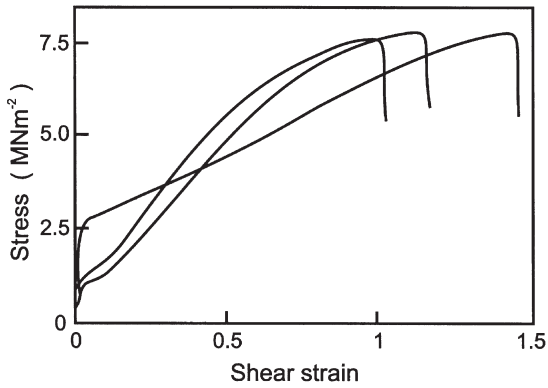

Fig. 13.19. Shear-stress/shear-strain curves of copper crystals of similar orientation deformed at 857°C, (Gottstein et al. 1979).

deformation temperature and the strain rate (Gottstein et al. 1979, Stuitje and Gottstein 1980, Gottstein and Kocks 1983), and unlike the case for polycrystals, τ_R is not uniquely related to the Zener–Hollomon parameter.

The experimental evidence suggests that in the high temperature regime, dynamic recrystallization in a single crystal is triggered by the formation of a single critical nucleus which is a subgrain in the deformed structure. This subgrain then sweeps rapidly through the microstructure. However in the low temperature regime, copious twinning of the nucleus takes place, and rapid growth only occurs when a twin with a high mobility orientation relationship with the matrix (§5.3.2) is formed. The onset of dynamic recrystallization in single crystals is therefore seen to be **nucleation controlled** in contrast to polycrystals (§13.3.4) in which it is **growth controlled.**

In single crystals of copper containing a fine dispersion of oxide particles which inhibit subgrain growth, dynamic recrystallization has been found to nucleate at the transition bands which form in the crystals during high temperature deformation (Ardakani and Humphreys 1992).

13.3.7 Dynamic recrystallization in two-phase alloys

There is some evidence that a process similar to the particle stimulated nucleation of recrystallization (PSN) which occurs on static annealing of alloys containing large particles (§9.3), may occur during high temperature deformation. In copper, dynamically recrystallized grains have been found at particles of SiO_2 or GeO_2 several microns in diameter (Ardakani and Humphreys 1992). The microstructures developed in these alloys are very different to those in single-phase copper (fig. 13.15), or in copper containing small particles, in which dynamic recrystallization is associated only with the prior grain boundary regions.

There is little evidence for particle stimulated dynamic recrystallization in aluminium alloys. Humphreys and Kalu (1987) and Castro–Fernandez and Sellars (1988) found

small highly misoriented grains adjacent to large second-phase particles, but these grains were generally of a similar size to the subgrains remote from the particles and there was little evidence of their growth. It is likely that such nuclei form by dynamic recovery of the misoriented subgrains formed at particles during deformation (§2.9.4), but that the stored energy of the matrix is too low to allow the nuclei to grow (§9.3). Although dynamic recrystallization in Al–Mg alloys has been attributed to PSN (McQueen et al. 1984, Sheppard et al. 1983), it is more likely that the recrystallized grains found in these alloys were formed by progressive lattice rotation as discussed in §13.4.2.

Particle stimulated dynamic recrystallization will only be possible if dislocations accumulate at the particles during deformation. This will only occur for larger particles, lower temperatures and higher strain rates (high **Z**) and therefore, unlike single phase alloys, there will be a particle-dependent lower limit to **Z** below which the nucleation of PSN will not be possible (fig. 13.31). This aspect is considered in more detail in §13.6.4.

13.3.7.1 Phase transformations during hot deformation

In addition to the processes of recovery and recrystallization, there may be concurrent phase transformations during deformation at elevated temperatures. The complex interactions between the processes of deformation, restoration and phase transformation are of great importance in the thermomechanical processing of a number of materials, in particular steels (Gladman 1990, Jonas 1990, Fuentes and Sevillano 1992) and titanium alloys (Williams and Starke 1982, Flower 1990, Weiss et al. 1990). Although we have discussed the underlying principles of many of the individual restoration processes involved, a detailed treatment of this subject is beyond the scope of this book.

13.4 CONTINUOUS DYNAMIC RECRYSTALLIZATION

13.4.1 Types of continuous dynamic recrystallization

The dynamic recrystallization discussed in §13.3 is the normal discontinuous dynamic recrystallization which occurs for example in cubic metals of low stacking fault energy. However, in recent years it has become apparent that under certain conditions a microstructure of high angle grain boundaries may evolve during high temperature deformation in ways other than the nucleation and growth of grains at pre-existing boundaries, and in this section we examine some of these alternative mechanisms of dynamic recrystallization. Although such processes generally fall into the overall phenomenological classification of **continuous dynamic recrystallization,** it must be recognised that within this category there are several quite different types of mechanism which need to be considered separately.

There are at least two processes which can be classed as continuous dynamic recrystallization. The first, known as **geometric dynamic recrystallization,** has many similarities with the continuous recrystallization which occurs on annealing alloys which have undergone very large strains, and for this reason it is discussed in detail in chapter 14. The other process, found in both metals and minerals, and which involves a gradual rotation of the material adjacent to high angle boundaries, is discussed below.

13.4.2 Dynamic recrystallization by progressive lattice rotation

There is considerable evidence that in certain materials, new grains with high angle boundaries may be formed during straining, by the progressive rotation of subgrains with little accompanying boundary migration. This is a **strain-induced** phenomenon which should not be confused with the subgrain rotation which has been postulated to occur during static annealing (§6.5.4).

The phenomenon involves the progressive rotation of subgrains adjacent to pre-existing grain boundaries as the material is strained, with the old grains developing a gradient of misorientation from centre to edge. In the centre of the old grain, subgrains may not be well developed or may have very low misorientations. Towards the grain boundary, the misorientations increase, and at larger strains, high angle boundaries may develop. This type of mechanism was first found in minerals (see §13.5), and has since been found in a variety of non-metallic and metallic materials. In the Geological literature the phenomenon is termed **rotation recrystallization.**

The mechanisms by which this progressive subgrain rotation occurs are not yet entirely clear, but it is most frequently found in materials in which dislocation motion is inhibited by either a **lack of slip systems** (e.g. magnesium alloys) or by **solute drag** (e.g. aluminium–magnesium alloys). It is likely that it is associated with inhomogeneous plasticity and accelerated dynamic recovery in the grain boundary regions, and it is possible that grain boundary sliding is also involved. However, the occurrence of a transition in dynamic recrystallization behaviour in minerals between discontinuous and rotation mechanisms (§13.5), raises the possibility that dynamic recrystallization by subgrain rotation in cubic metals may occur when boundaries are solute-loaded and unable to migrate rapidly (§5.4.2). Although this phenomenon usually results in a partially recrystallized **necklace** microstructure (fig. 13.14a–c), at large strains a completely recrystallized structure (fig. 13.14d) may be formed (Gardner and Grimes 1979).

13.4.2.1 Magnesium alloys

There is evidence that progressive lattice rotation may occur at grain boundaries in magnesium alloys (Ion et al. 1982, Galiyev et al. 2001, Tan and Tan 2003), and that this may eventually lead to the formation of new grains. The mechanism proposed by Ion et al. (1982), which is shown schematically in figure 13.20, is based on local shearing near grain boundaries (fig. 13.20a), which occurs because of the lack of the 5 independent slip systems required for homogeneous plasticity (§3.7). Dynamic recovery of the geometrically necessary dislocations then occurs (fig. 13.20b), resulting in the formation of new subgrains or grains (fig. 13.20c). Such a process is progressive, with no clear division between the nucleation and growth stages. At higher deformation temperatures, non-basal slip is easier, deformation becomes more homogeneous, and the dynamic recrystallization becomes similar to the discontinuous process discussed in §13.3 (Galiyev et al. 2001).

13.4.2.2 Aluminium alloys

In aluminium alloys containing solute additions such as Al–Mg alloys (Gardner and Grimes 1979, Drury and Humphreys 1986) and Al–Zn alloys (Gardner and Grimes

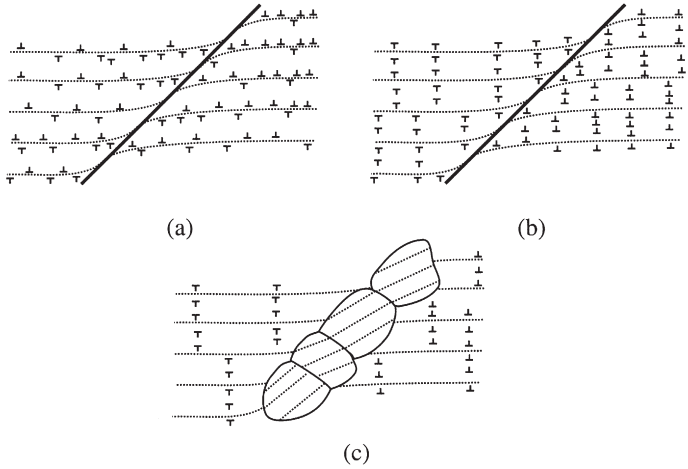

Fig. 13.20. Schematic diagram showing the proposed mechanism of dynamic recrystallization in magnesium, by progressive lattice rotation and dynamic recovery at grain boundaries, (after Ion et al. 1982).

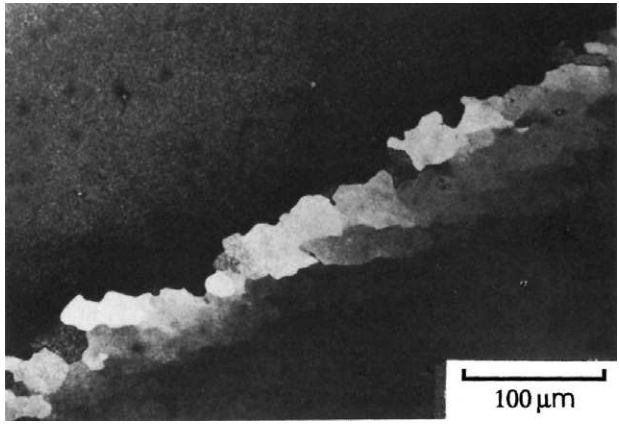

Fig. 13.21. Development of misorientations by lattice rotation adjacent to the grain boundary during deformation of Al–5%Mg, (Drury and Humphreys 1986).

1979), significant lattice rotations may develop at the grain boundaries during deformation at temperatures in the range 300–400°C. Even though there is little evidence of subgrain formation in the grain interiors, well developed subgrain/grains may develop at the boundaries as seen in figure 13.21.

Investigation of these microstructures by EBSD has enabled the development of such microstructures to be determined in some detail. Figure 13.22 shows an EBSD map of a grain boundary region in Al–5%Mg deformed in plane strain compression at 350°C. The original high angle boundary is denoted by a thick line and the low angle

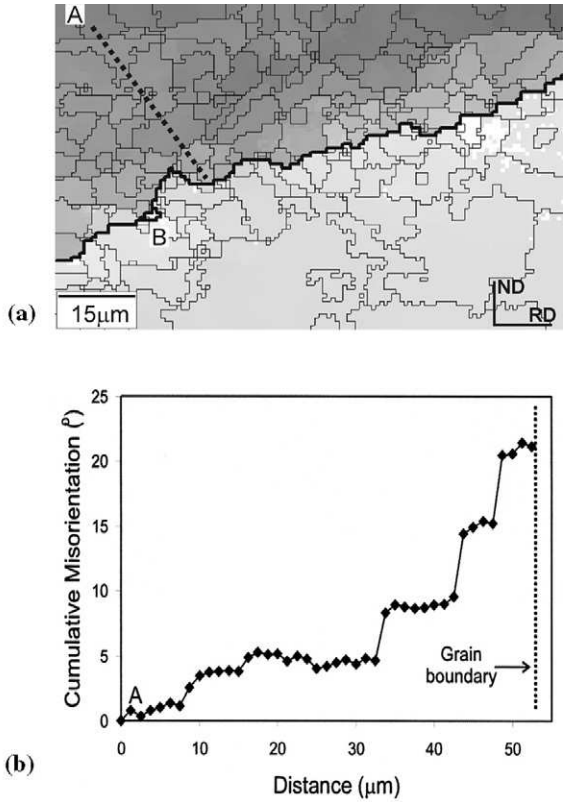

Fig. 13.22. EBSD measurements of lattice rotations at a grain boundary in Al–5%Mg, deformed in plane strain compression at 350°C. (a) EBSD map showing high angle (> 15°) boundaries as thick lines and low angle boundaries as thin lines. Colour changes reveal misorientations developed at the boundary serrations, (b) The cumulative misorientations along the line from A to the boundary. (See colour plate section for fig. 13.22a.)

boundaries by thin lines. A plot of the cumulative misorientation from the interior of the grain (A) to the boundary, along the dotted line (fig. 13.22b), shows the large orientation gradients which develop at the boundaries, particularly within the serrations. In figure 13.22, these have not yet developed into separate identifiable grains, except at B.

It has been proposed that the mechanism involves an interaction between grain boundary deformation and the grain boundary serrations (Drury and Humphreys 1986) as shown in figure 13.23. High angle grain boundaries develop serrations due to interaction with the deformation substructure (fig. 13.5a), as shown in figure 13.23a. Grain boundary sliding can then only occur on parts of the boundary, e.g. A, whilst other regions (e.g. B) have to accommodate the strain by plastic deformation (fig. 13.23b), leading to shear and local lattice rotation as shown in figure 13.23c. Whether

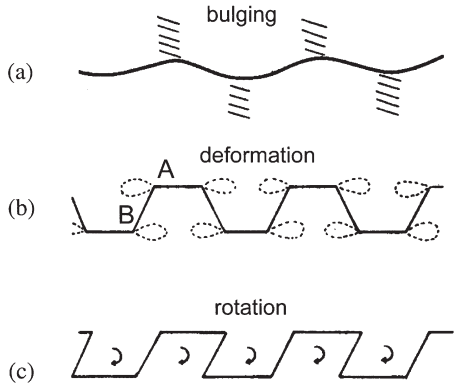

Fig. 13.23. Proposed mechanism of dynamic recrystallization by progressive lattice rotation in Al–Mg alloys. (a) HAGB serrations form, (b) Grain boundary sliding occurs on horizontal boundaries, but slip occurs on bulged sections, leading to local lattice rotations associated with the bulges, (c), (Drury and Humphreys 1986).

the deformation at the boundaries involves actual grain boundary sliding, or local plasticity close to the boundaries is not yet established.

It is interesting to note that it has recently been suggested that the mechanism of figure 13.23 may be responsible for the nucleation of discontinuous dynamic recrystallization in copper (Wusatowska et al, 2002).

13.4.2.3 Particle-stabilised microstructures

It has been suggested that a process similar to that of progressive lattice rotation discussed above, may occur in alloys containing finely dispersed second-phase particles, and that this mechanism may be responsible for the development of fine grained microstructures during the thermomechanical processing of superplastic aluminium alloys (§15.5.3). It was proposed that the particles pinned the subgrains, preventing extensive growth, and evidence of a progressive increase of the subgrain/grain misorientation has been claimed (Nes 1979, Higashi et al. 1990). However, this behaviour is generally observed in alloys which have already been extensively cold or warm worked, and more recent work carried out with the benefit of EBSD (Ridley et al. 2000), suggests that the development of subgrain misorientations during hot deformation of fine-grained aluminium alloys containing dispersions of small stable Al_3Zr particles, does not differ significantly from that in single-phase alloys (§13.2), and that any increase in the fraction of high angle boundaries is primarily due to a decrease in the number of low angle boundaries. The development of superplastic microstructures by hot working is further discussed in §15.5.3.

13.5 DYNAMIC RECRYSTALLIZATION IN MINERALS

Dynamic (or **syntectonic**) recrystallization has long been recognised as an important process during the natural deformation under metamorphic conditions, of rock-forming

minerals (see e.g. Nicolas and Poirier 1976, Poirier and Guillopé 1979, Poirier 1985, Urai et al. 1986, Urai and Jessel 2001). Although there are substantial differences not only between minerals and metals, but also between the deformation conditions in the Earth's crust and mantle, and in a hot-rolling mill, there is a substantial commonality of behaviour between the two classes of materials, and over the past 30 years there has been a very fruitful interchange of scientific ideas between Geology and Materials Science. One of the main interests of the Geologists is in using the microstructure to interpret the deformation history of the mineral. The dynamically recrystallized grain sizes (fig. 13.17), which have been shown to be closely related to stress (equation 13.18) have, together with the subgrain sizes and dislocation densities, been used by Geologists as **paleopiezometers** to determine the stresses to which the mineral has been subjected.

Research in this area has involved the investigation of microstructures in naturally deformed minerals, laboratory deformation of minerals under conditions of high temperature and high pressure, and the in-situ deformation under the optical microscope of low melting point minerals and other transparent analogue crystalline materials. The latter experiments (e.g. Means 1989) have been able to provide direct observations of the occurrence of dynamic recrystallization, albeit at low spatial resolution, that cannot be obtained for metals. In many cases it is also possible to simultaneously obtain local orientation (microtexture) information from minerals in the optical microscope using standard mineralogical methods. Figure 13.24 is an optical micrograph of a naturally deformed quartzite and shows clear evidence of dynamic recrystallization in the regions of the original grain boundaries. Figure 13.25 is an example of an in-situ deformation experiment on camphor, showing the development of a similar microstructure to figures 13.15 and 13.24.

13.5.1 Boundary migration in minerals

Natural minerals are generally very impure, and segregation and precipitation may occur at the grain boundaries leading to a loss of mobility. In addition, bubbles and

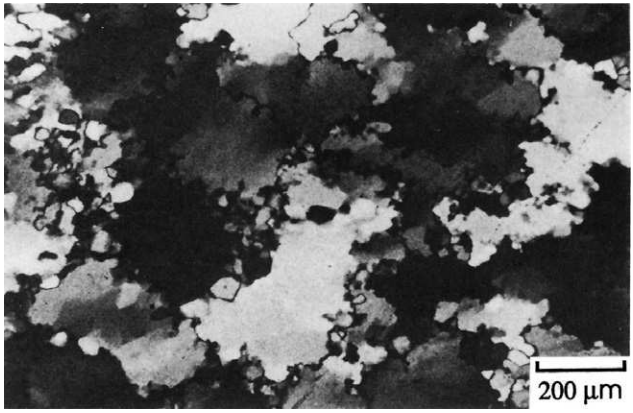

Fig. 13.24. Dynamic recrystallization in naturally deformed quartzite, (Urai et al. 1986).

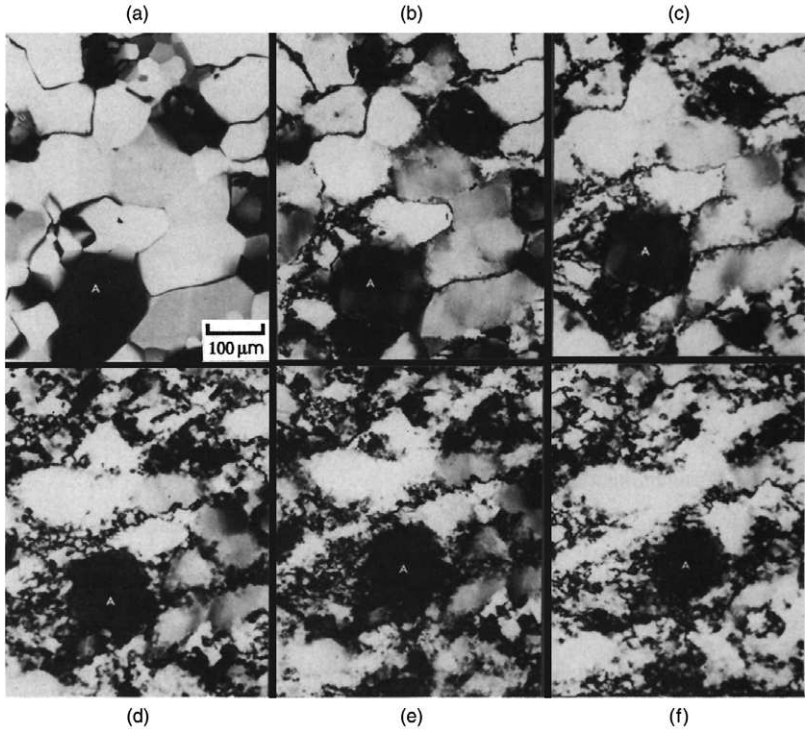

Fig. 13.25. Dynamic recrystallization of camphor at room temperature, (Tungatt and Humphreys 1981).

cavities may also be present. The bonding in minerals is of course different to that in metals, and this will also influence the boundary migration (Kingery 1974, Brook 1976). In many instances, the boundaries in minerals are likely to resemble those of impure ceramics.

It is now well established that in some natural minerals there is a fluid film at the boundary (see Urai et al. 1986, Urai and Jessel 2001) and that this has a large influence on grain boundary migration (Rutter 1983). The structure of a fluid-filled boundary can be described in terms of the two crystal–liquid interfaces and the fluid layer between them, and the behaviour of the boundary will therefore be less constrained by the matching of the two crystals than for a dry boundary. The boundary configuration may then be determined by the energy of the crystal–liquid interfaces, as is the case for crystal growth from the melt, and an orientation dependence of boundary migration rate is therefore expected. Migration mechanisms related to solid–liquid interfaces such as spiral growth involving screw dislocations (cf. Gleiter's boundary migration model discussed in §5.4.1.3) are predicted to be important.

If it is assumed that the migration rate is limited by diffusion in the fluid layer, a rapid increase in migration rate with film thickness is predicted as shown qualitatively in

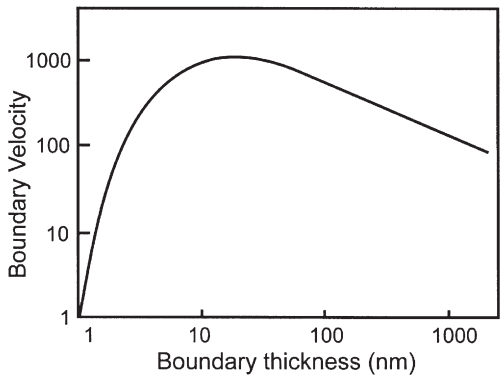

Fig. 13.26. The predicted effect of fluid film thickness on boundary migration rate, (Urai et al. 1986).

figure 13.26. The increase in mobility may be as much as four orders of magnitude for a 2nm film (Rutter 1983). For thick fluid layers, diffusion across the film is expected to become rate controlling, the mobility then becoming inversely proportional to the film thickness.

13.5.2 Migration and rotation recrystallization

It is well established that in minerals, two types of dynamic recrystallization occur. At high temperatures and high stresses a discontinuous form of dynamic recrystallization similar to that discussed in §13.3 occurs, and this is referred to in the Geological literature as **migration recrystallization**. However, at lower temperatures and stresses there is often a transition to a mechanism similar to that discussed in §13.4 (referred to as **rotation recrystallization**). This transition, which is thought to correspond to the breakaway of boundaries from their solute atmospheres (fig. 5.32), is shown in figure 13.27 for experimentally deformed halite (NaCl). The driving force for dynamic recrystallization increases with applied stress and the intrinsic boundary mobility is also a strong function of temperature, thus accounting qualitatively for the shape of figure 13.27. It has also been shown (Trimby et al. 2000) that the transition between rotation and migration recrystallization in NaCl is dependent on the water content of the material. The boundary mobility in ionic solids is very sensitive to small solute concentrations, particularly aliovalent ions, and in figure 13.28, it is seen that the transition temperature in $NaNO_3$ (calcite structure) between rotation and migration recrystallization is markedly raised by small amounts of Ca^{2+} ions.

13.6 ANNEALING AFTER HOT DEFORMATION

Recovery and recrystallization following hot deformation are of great technological importance because in many hot working operations such as multi-pass rolling,

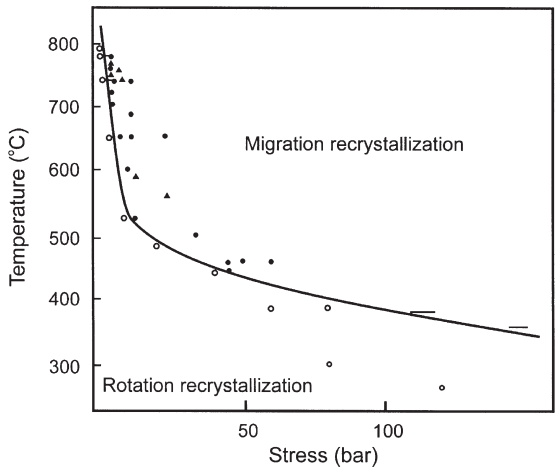

Fig. 13.27. The boundary between migration and rotation recrystallization in halite, (Guillopé and Poirier 1979).

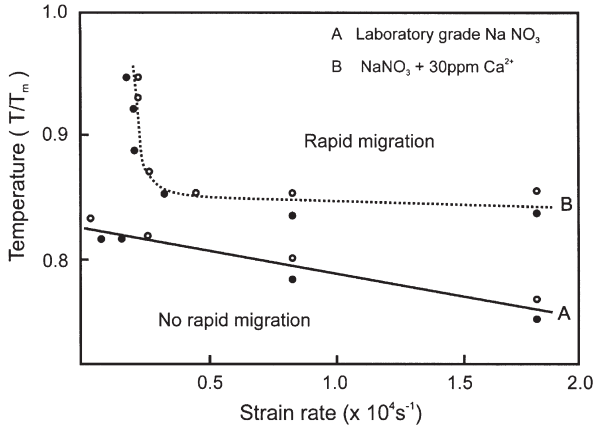

Fig. 13.28. The effect of calcium additions on boundary migration in sodium nitrate, (Tungatt and Humphreys 1984).

annealing takes place between the rolling passes. Additionally, the rates of cooling of the material are generally very low in large-scale metal forming operations, allowing recovery, recrystallization and grain growth to occur immediately after hot deformation.

13.6.1 Static recovery

Because dynamic recovery has already taken place during the deformation, further microstructural changes due to static recovery are generally small. However, some

further recovery, including dislocation rearrangement and subgrain growth (Ouchi and Okita 1983) and consequent softening (Sellars et al. 1986) may take place, usually with similar kinetics to those found for static recovery (§6.2.2).

13.6.2 Static recrystallization

Static recrystallization may occur when a hot deformed material is subsequently annealed. This is often very similar to the static recrystallization discussed in earlier chapters, the main difference being that the lower stored energy resulting from hot deformation, affects the kinetics of recrystallization. From §13.2.1 we expect the driving pressure and hence the recrystallization behaviour to be strongly dependent on **Z,** and this effect is well documented (see Jonas et al. 1969). Figure 13.29 shows the effect of **Z** on the recrystallization kinetics of commercially pure aluminium deformed to a constant strain and annealed at a constant temperature. The effect of strain is also important, and in materials which undergo dynamic recrystallization, the static recrystallization behaviour depends on whether the strain was larger or smaller than that required for dynamic recrystallization (ε_c).

Because of the industrial importance of controlling the grain size and texture during the recrystallization of hot-rolled aluminium alloys, there has been significant activity in investigating the mechanisms of recrystallization in these materials. Much attention has focussed on the nucleation of cube-oriented grains, and it is now thought that these originate from elongated remnants of cube grains in the hot-worked microstructure (Vatne et al. 1996a), by a process of strain induced boundary migration such as described in §7.6.2. A more detailed consideration of the formation of cube grains during recrystallization of hot deformed aluminium can be found in §12.4.1.

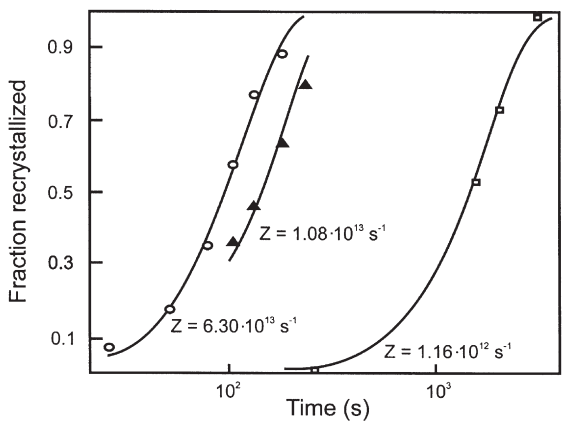

Fig. 13.29. The effect of deformation temperature and strain rate (Zener–Hollomon parameter) on the recrystallization kinetics of commercial purity aluminium deformed to a strain of 3 and annealed at 410°C, (Gutierrez et al. 1988).

Metallographic measurements indicate that static recrystallization can often be described approximately by the JMAK relationship (equation 7.17), with the exponent in the range 1.5–2 (Roberts 1984, 1985). Because of the technological importance of the subject, empirical relationships for the recrystallization behaviour as a function of deformation behaviour have been determined (e.g. Roberts 1985, Sellars 1986, 1992a, Beynon and Sellars 1992), and for C–Mn and HSLA steels of grain size $\mathbf{D_0}$, it is often found that the time for 50% static recrystallization ($t_{0.5}$) at the deformation temperature is given (Sellars and Whiteman 1979) by an equation of the form

$$t_{0.5} = c_1 D_0^C \varepsilon^{-n} Z^{-K} \exp\left(\frac{Q_{rex}}{RT}\right) \tag{13.21}$$

where c_1, C, K and n are constants and Q_{rex} is the activation energy for recrystallization.

The recrystallized grains generally nucleate at the old grain boundaries and are equiaxed. Their size $\mathbf{D_R}$ is given by

$$D_R = c_2 D_0^{C'} \varepsilon^{-n'} Z^{-K'} \tag{13.22}$$

where c_2, C′, K′ and n′ are constants.

The range of values of the constants in these equations is discussed by Roberts (1985) and Sellars (1986, 1992a). If dynamic recrystallization has occurred prior to static recrystallization, then there is little effect of strain or D_0, i.e. C, C′, n and n′ tend to zero. Relationships such as these are necessary components of models for industrial hot rolling (§16.3) and much recent research effort has been aimed at developing physically-based state-variable constitutive annealing models to describe recrystallization following hot deformation (e.g. Sellars 1997, Furu et al. 1996, Vatne et al. 1996b). The annealing of the hot worked materials are modelled by the incorporation of processes such as dislocation recovery, SIBM and PSN into deformation microstructures modelled using the principles discussed in §13.2.5.

13.6.3 Metadynamic recrystallization

Whenever the critical strain for dynamic recrystallization (ε_c) is exceeded, recrystallization nuclei will be present in the material. If straining is stopped, but annealing continued, these nuclei will grow with no incubation period into the heterogeneous, partly dynamically recrystallized matrix. This phenomenon is known as **metadynamic recrystallization** (Djaic and Jonas 1972, Petkovic et al. 1979). The microstructure of a material which has undergone some dynamic recrystallization is very heterogeneous and may contain:

A – Small dynamically recrystallized grains (nuclei) which are almost dislocation free.
B – Larger recrystallized grains with a moderate dislocation density which are growing dynamically.
C – Unrecrystallized material with a high dislocation density (ρ_m).

Each of these types of region will have a different static annealing behaviour, and the overall annealing kinetics and grain size distributions may be extremely complex, as

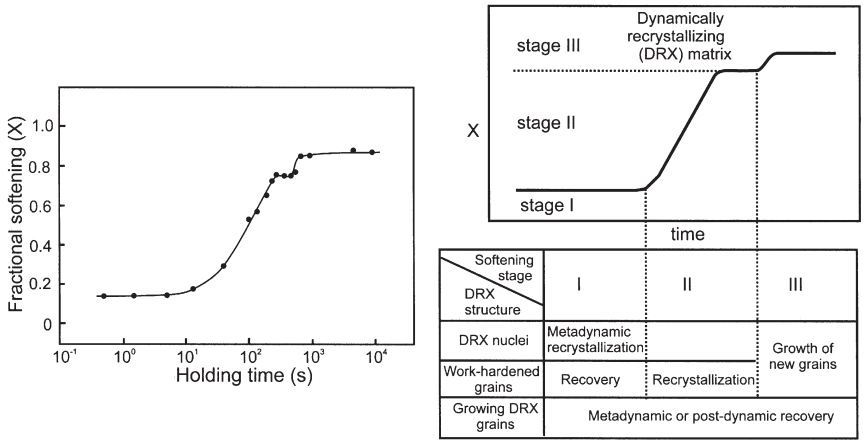

(a) (b)

Fig. 13.30. The restoration processes occurring in a dynamically recrystallizing material if it is held at temperature after deformation has stopped. (a) The effect of strain on the static softening of austenite deformed at 860°C, (Xu and Sakai 1991), (b) Schematic relationship between the various softening stages and the main restoration processes, (Xu et al. 1995).

illustrated by figure 13.30a. Sakai and colleagues (Sakai et al. 1988, Sakai and Ohashi 1992, Sakai 1997) have identified several annealing stages in hot-deformed nickel, copper and steels.

- **Regions A,** may continue to grow during the early stages of post deformation annealing by the mechanism of metadynamic recrystallization.

- **Regions B** will, if their dislocation density (ρ) is below a critical value (ρ_{RX}), recover, and this has been termed **metadynamic recovery.** If $\rho > \rho_{RX}$ then these regions may subsequently recrystallize statically.

- **Regions C** will undergo static recovery, followed by static recrystallization. When the material is fully recrystallized then further grain growth may occur (§13.6.5). The relationship between the various restoration processes and the overall softening is shown schematically in figure 13.30b.

13.6.4 PSN after hot deformation

The conditions under which particle stimulated nucleation of recrystallization (PSN) could occur following low temperature deformation were discussed in §9.3. However, if the temperature of deformation is raised, then PSN may become less viable, and we need to consider the effect of deformation temperature on the two criteria for PSN – the **formation** of nuclei within deformation zones, and the **growth** of the nuclei beyond the particle.

13.6.4.1 Deformation zone formation

At high temperatures, dislocations may be able to bypass particles without forming deformation zones. Humphreys and Kalu (1987) have shown that the critical strain rate for the formation of a deformation zone at a particle of diameter **d** is given by:-

$$\dot{\varepsilon}_c = \frac{K_1 \exp\left(\frac{-Q_s}{RT}\right)}{Td^2} + \frac{K_2 \exp\left(\frac{-Q_b}{RT}\right)}{Td^3} \tag{13.23}$$

where K_1 and K_2 are constants and Q_s and Q_b are the activation energies for volume and boundary diffusion. This relationship has been found to be obeyed in aluminium alloys for a wide range of particle sizes and deformation conditions with $K_1 = 1712 m^2 s^{-1} K$ and $K_2 = 3x10^{-10} m^3 s^{-1} K$.

For particles which are potential PSN sites ($d > 1\mu m$), the second term will generally be negligible, and a simplified version of equation 13.23 may therefore be used. The critical particle diameter for the formation of a particle deformation zone (d_f) may, if we assume that the activation energies in equations 13.1 and 13.23 are identical, be expressed in terms of the Zener–Hollomon parameter as

$$d_f = \left(\frac{K_1}{TZ}\right)^{1/2} \tag{13.24}$$

13.6.4.2 Nucleus growth

The growth criterion for PSN (e.g. equation 9.24) is also affected by the deformation conditions, because the stored energy (E_D) is reduced at elevated temperatures, although this effect is more difficult to quantify. As the microstructure following high temperature deformation consists mainly of subgrains, the growth condition (equation 9.2) may be written in terms of the subgrain size (D), using equation 2.7, as

$$d_g = \frac{4\gamma_b D}{3\gamma_s} \tag{13.25}$$

and using equation 13.7 then

$$d_g = \frac{4\gamma_b K G b}{3\gamma_s \sigma} \tag{13.26}$$

The relationship between the flow stress (σ) and Zener–Hollomon parameter is given by equations 13.2 to 13.5, and if, for example we use equations 13.1 and 13.4 then

$$d_g = \frac{4\gamma_b K' G b}{3\gamma_s Z^{1/m}} \tag{13.27}$$

Somewhat different versions of equation 13.27 may be obtained, depending on the particular relationships between subgrain size, flow stress and **Z** which are used, and at present there is no entirely satisfactory solution.

In figure 13.31 we show the variation of the critical particle diameters for the formation and growth of particle deformation zones, with **Z,** according to equations 13.24 and 13.27 (neglecting the small effect of the temperature term in equation 13.24 and using values of the constants appropriate for aluminium). It may be seen that at values of **Z**

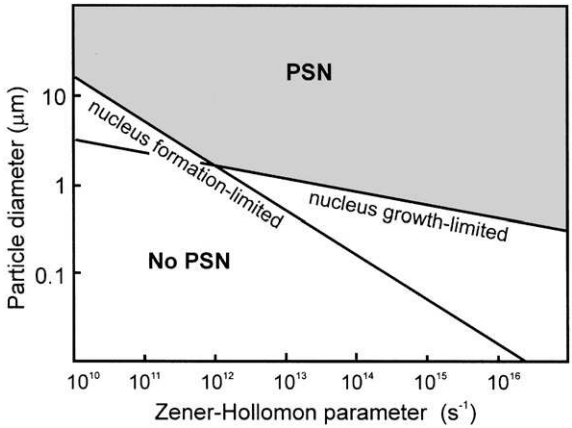

Fig. 13.31. The effect of deformation conditions on PSN.

less than $\sim 10^{12}$ s^{-1}, the condition for PSN is governed by that for **deformation zone formation,** but at higher values it is determined by the criterion for **growth** of the nucleus. Experimental investigations have confirmed this model. Measurements by Kalu and Humphreys (1986) on Al–Si alloys deformed at $10^8 < Z < 10^{12}$ showed that zone formation was the controlling factor, whereas the measurements of Oscarsson et al. (1987) on AA3004 and of Furu et al. (1992) on AA3003, in which specimens were deformed in the range $10^{12} < Z < 10^{16}$, were both consistent with growth control.

13.6.5 Grain growth after hot working

When recrystallization is complete, grain growth can take place, and has been described by the empirical equation

$$D^n = D_R^n + c t \exp\left(-\frac{Q_g}{kT}\right) \tag{13.28}$$

where c, n and Q_g are constants.

For steels, very large values of the exponent n ($\sim$10) have been reported (see Sellars 1986).

Chapter 14

CONTINUOUS RECRYSTALLIZATION DURING AND AFTER LARGE STRAIN DEFORMATION

14.1 INTRODUCTION

A large number of low-angle boundaries are formed when a polycrystalline metal is deformed (chapter 2) or when the material is subsequently recovered by annealing at low temperatures (§6.4). On annealing at elevated temperatures, such a microstructure will usually recrystallize discontinuously as discussed in chapters 7 to 9, this process being driven mainly by the energy stored in the low-angle boundaries.

However, after deformation to large strains, particularly at elevated temperatures, a microstructure consisting predominantly of high-angle grain boundaries may be formed. Minor boundary movements either during the deformation or on subsequent annealing may then result in a fine-grained microstructure consisting mainly of crystallites which are surrounded by high-angle boundaries. Such a microstructure is similar to that resulting from conventional recrystallization, but because no recognisable 'nucleation' and 'growth' of the recrystallized grains occurs, and the microstructure evolves relatively homogeneously throughout the material, the process can reasonably be classified as **continuous recrystallization.** It is worth emphasising that terminology such as continuous or discontinuous recrystallization is purely phenomenological, referring

only to the spatial and temporal heterogeneity of microstructural evolution, and implying no specific mechanism of recrystallization.

The occurrence of continuous recrystallization during high temperature deformation, which is known as **geometric dynamic recrystallization,** has been recognised for some time. However, recent research has shown that severe cold-working of a metal can also result in a microstructure which consists almost entirely of high-angle grain boundaries, and which, on annealing, may undergo continuous recrystallization. The microstructures which evolve after such low temperature processing, are often **sub-micron grain (SMG) structures,** and because such materials may have attractive mechanical properties, there has been extensive research recently in this field.

We consider that the phenomena discussed in this chapter can be explained almost entirely in terms of the fundamental processes discussed in earlier chapters, and that no unusual micro-scale mechanisms are involved. Nevertheless, this subject, which was briefly alluded to in the first edition of this book, now requires a separate chapter, in which the principles underlying the continuous recrystallization of metals deformed at either ambient or elevated temperatures are considered. In order to simplify discussion and to enable comparison with the conventional deformation processing discussed elsewhere in the book, we will mainly be concerned with microstructures produced by conventional rolling procedures.

There has been considerable research into producing SMG structures using more exotic deformation routes (see e.g. the reviews of Humphreys et al. 1999, 2001b, Horita et al. 2000a, Prangnell et al. 2001), and we will consider the application of these methods to the production of SMG alloys as a case study in chapter 15.

14.2 MICROSTRUCTURAL STABILITY AFTER LARGE STRAINS

When a polycrystalline metal is deformed, the grain boundary area increases with increasing strain at a rate which depends on the mode of deformation (§2.2.1). For example, during rolling, the grain thickness in the normal direction (H) is related to the strain (ε) and the initial grain size D_0 (fig. 14.1) by the geometric relationship

$$H = D_0 \exp(-\varepsilon) \tag{14.1}$$

During the plastic deformation, cells or subgrains are formed, and after a moderate strain ($\varepsilon \sim 1$) these generally do not change very much. Therefore, with increasing strain, the percentage of the boundaries which are of high angle (HAGB%) increases (fig. 14.1c). Additionally, new high-angle boundaries may form by grain fragmentation as discussed in chapter 2.

Although it is convenient to discuss the microstructures in terms of the **fraction or percentage of high angle boundaries (HAGB%),** it should be recognised that this is only a rather crude and arbitrary description, and that it is the overall grain boundary character distribution, e.g. figures 4.2 and A2.1, which is important. Nevertheless, for analytical purposes, it often convenient to use the simpler descriptions.

The analysis of the stability of cellular microstructures discussed in chapter 10, showed that microstructures with a large fraction of low angle boundaries are intrinsically unstable with respect to discontinuous growth (i.e. discontinuous recrystallization). If the mean low angle boundary misorientation is increased, the boundary properties become more uniform, and the structure cannot recrystallize discontinuously.

During deformation, the mean boundary misorientation increases, and thus the microstructure becomes progressively more stable against discontinuous growth as strain increases. The criteria for the suppression of discontinuous recrystallization, which have been discussed by Humphreys (1997a) and Humphreys et al. (1999), are therefore the conditions of strain, temperature and initial grain size, which result in a sufficient fraction of high angle boundary, (0.6–0.7) to ensure microstructural stability. Alternative criteria for continuous recrystallization can be formulated in terms of the impingement of corrugated high angle boundaries at large strains as discussed in §14.4.2. However, purely geometric criteria, such as those used to derive equation 14.3 are less rigorous, although both approaches give rather similar results.

14.3 DEFORMATION AT AMBIENT TEMPERATURES

Early reports of the deformation of metals which were subjected to true strains in the range 3–7, resulting in grain sizes in the range 0.1–0.5 μm, include copper and nickel (Smirnova et al. 1986), magnesium and titanium alloys (Kaibyshev et al. 1992) and Al–Mg (Wang et al. 1993). Typically, such large strains were produced by a high shear redundant strain method (see §15.6) such as equal channel angular extrusion (ECAE). However, similar fine-scale microstructures can also be produced by conventional cold rolling to large strains. A good example of this phenomenon in aluminium has been given by Oscarsson et al. (1992), who found that after very large rolling reductions ($>95\%$), a stable fine-grained microstructure was formed on annealing, whereas at lower strains, normal discontinuous recrystallization occurred. Other examples of the production of sub-micron grains in aluminium alloys by low temperature annealing following cold rolling include Ekstrom et al. (1999), Engler and Huh (1999), Humphreys et al. (1999) and Jazaeri and Humphreys (2001, 2002).

14.3.1 The development of stable microstructures by large strain deformation

For simplicity, we consider only the case of deformation by cold rolling or plane strain compression. The size (D) of the cells or subgrains formed on deformation is reduced very little at strains above ~2 (fig. 2.4), and Nes (1998) has shown that the data from this figure is consistent with the following relationship for $\varepsilon > 2$.

$$D = k\varepsilon^{-1} \tag{14.2}$$

where k is a constant.

The spacing (H) of the high angle boundaries in the normal direction (ND), of a material with initial grain size D_0, decreases with strain (fig. 14.1a–c) according to

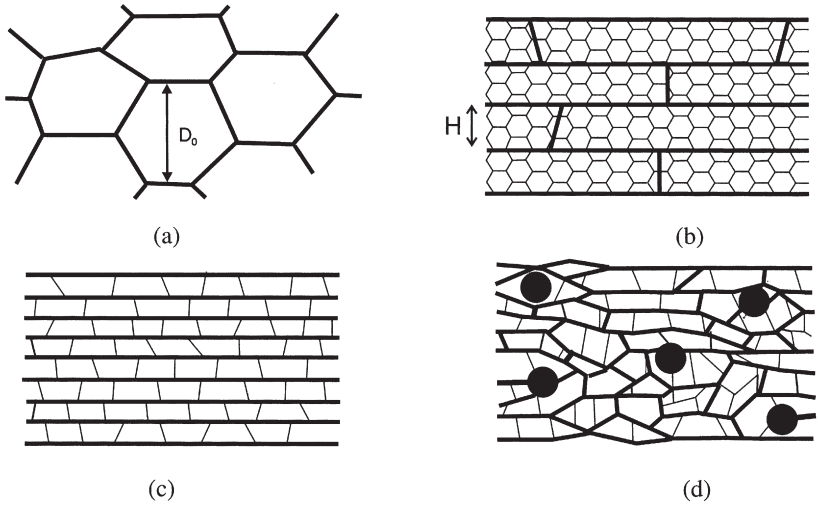

Fig. 14.1. Schematic diagram of the development of microstructure with increasing strain; (a) initial grain structure, (b) moderate deformation, (c) large deformation, (d) effect of large second-phase particles on deformation.

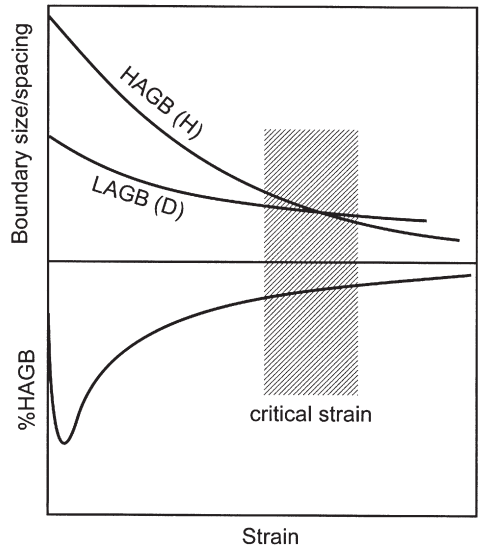

Fig. 14.2. Schematic diagram of the effect of strain on the cell/subgrain size (D), HAGB spacing (H) and %HAGB during deformation at ambient temperatures.

equation 14.1. Consequently, as shown in figure 14.2, the HAGB spacing decreases more rapidly than the subgrain size with strain, and the fraction of boundaries which are of high angle therefore increases with strain. At a sufficiently large strain (ε_{cr}), the fraction of high angle boundary becomes sufficient (~0.6–0.7) to make the microstructure stable against discontinuous growth (i.e. recrystallization) as discussed in §14.2. The precise rate of increase in the fraction of HAGB with strain and therefore the critical strain ε_{cr}, is difficult to calculate precisely (Humphreys 1997a, 1999), as it depends on the shape and planarity of the boundaries, and will be increased by any new high angle boundaries created by fragmentation of the old grains (§2.4, §2.7).

14.3.2 The effect of the initial grain size

As shown by equation 14.1, a small initial grain size (D_0) will reduce the boundary spacing H to the critical value at a lower strain than will a larger initial grain size (Harris et al. 1998). The effect of strain and initial grain size on the spacing of high angle boundaries (H) and on the percentage of high angle boundaries in an Al–Fe–Mn alloy are shown in figure 14.3. The HAGB% initially decreases with increasing strain as low angle boundaries are formed during deformation, but then progressively increases as H becomes smaller. If the initial grain size is reduced, it may be seen that the HAGB% at high strains is larger, and the HAGB spacing (H) at a given strain, is smaller.

It is seen from figure 14.3b that, at the largest strains, the HAGB separations for the materials of different initial grain size tend to converge. In table 14.1, the measured HAGB spacing (H) is compared with that predicted (H_G) by the geometric reduction of the original grain size (equation 14.1) at a true strain of 2.6. The ratio H_G/H, which will be unity if H is determined purely by geometrical factors, is seen to be greatly affected by the initial grain size. The large value of H_G/H for the 260 μm material is consistent with extensive grain fragmentation in such a large-grained material (§2.7). For the 12 μm material, the value of H_G/H implies no grain fragmentation, which is consistent with previous results for small grain sizes (Humphreys et al. 1999). The 3 μm material is seen to have a grain spacing which is considerably larger than the geometric value. There are two factors which can contribute to this. At large strains as the deformation texture strengthens, some **grain orientations converge,** transforming high angle into lower angle boundaries. Statistical calculations of this effect for the materials of table 14.1, indicate

Table 14.1
The effect of strain and initial grain size on the spacing of high angle boundaries in the normal direction in Al–Fe–Mn alloy AA8006 cold rolled to a strain of 2.6 (data from Jazaeri and Humphreys 2002).

Initial grain size (μm)	Measured spacing (H) (μm)	Predicted spacing (H_G) (μm)	H_G/H
260	1.7	19.3	11.3
12	1.0	0.9	0.9
3	0.6	0.2	0.4

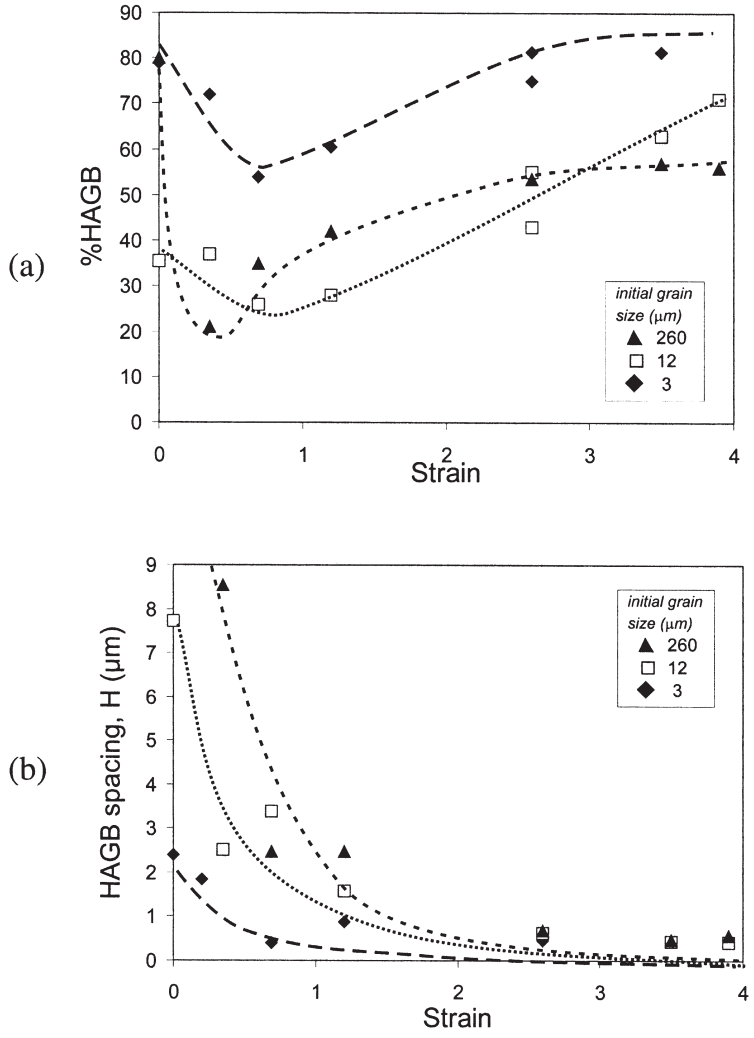

Fig. 14.3. The effect of strain and initial grain size on the microstructure of an Al–Fe–Mn alloy (AA8006); (a) The percentage of high angle boundaries, (b) The high angle boundary spacing (H), (Jazaeri and Humphreys 2002).

that the loss of high angle grain boundaries in this way should be no more than ~15%, which is insufficient to account for the very small value of H_G/H. The second effect which can cause this is the **local dynamic grain growth** (fig. 14.8) which can occur when high angle boundaries approach closely. This effect, which is discussed in §14.4.3, is normally found only at elevated temperatures, but is clearly able to occur at ambient temperatures in a low-solute aluminium alloy under these conditions.

14.3.3 The effect of second-phase particles

Large (> 1 μm) second-phase particles will increase the rate of formation of high angle boundaries by breaking up the planarity of the boundary structure as shown schematically in figures 2.37 and 14.1d, and also by creating high angle boundaries associated with the large local lattice rotations close to the particles (§2.9.4). An EBSD map demonstrating the effect of large particles on the microstructure is shown in figure 14.4. Such particles therefore reduce ε_{cr}, although it is difficult to quantify the effect.

14.3.4 The transition from discontinuous to continuous recrystallization

The transition from discontinuous to continuous recrystallization with increasing rolling reduction, was first reported by Oscarsson et al. (1992), and has been investigated in detail by Jazaeri and Humphreys (2001, 2002).

For the larger initial grain sizes and lower strains, normal discontinuous recrystallization occurred on subsequent annealing (fig. 14.5a), but for larger strains and smaller grain sizes, a predominantly high angle boundary microstructure was formed at comparatively low annealing temperatures, with only minor boundary movements (fig. 14.5b), by a process of continuous recrystallization.

The transition between discontinuous and continuous recrystallization is best measured by monitoring the changes in HAGB content on annealing, and this is shown in figure

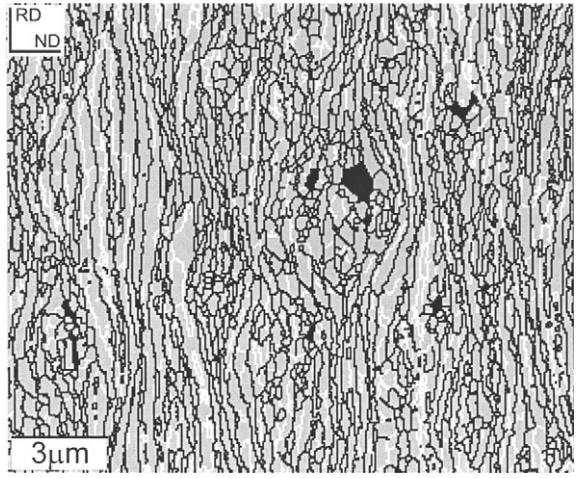

Fig. 14.4. EBSD map showing the effect of large (> 1 μm) second-phase particles on the microstructure of Al–Fe–Mn (AA8006) cold-rolled to a strain of 3.9. The particles are shown as black regions, HAGBs shown as black lines and LAGBs as white lines, (Jazaeri and Humphreys 2001).

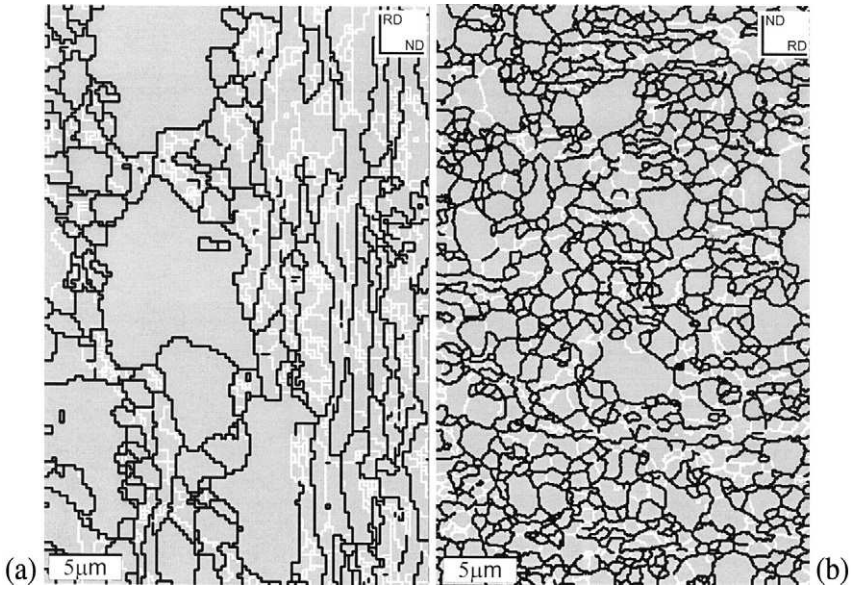

Fig. 14.5. EBSD maps of Al–Fe–Mn (AA8006) annealed after cold rolling; (a) $\varepsilon = 0.69$, $T = 250°C$, showing discontinuous recrystallization; (b) $\varepsilon = 3.9$, $T = 300°C$, showing continuous recrystallization. HAGBs shown as black lines and LAGBs as white lines, (Jazaeri and Humphreys 2001).

14.6a,b. When continuous recrystallization occurs, there is a relatively sharp change in the HAGB% as the deformed substructure is consumed by the recrystallizing grains. However, when continuous recrystallization occurs, there is little change in the HAGB%. During annealing the grains/subgrains gradually become more equiaxed and larger (fig. 14.6c). These changes are gradual, and quite different to those occurring during discontinuous recrystallization.

A further difference is that on discontinuous recrystallization, the strong deformation texture is generally replaced by a different texture, such as a strong cube texture (§12.2.1). However, when continuous recrystallization occurs, the **rolling texture is retained** with little change (Engler and Huh 1999, Jazaeri and Humphreys 2001), because there is little microstructural change on annealing following the deformation.

Figure 14.7 summarises the effects of initial grain size and strain on the transition from discontinuous to continuous recrystallization in an AA8006 Al–Fe–Mn alloy.

14.3.5 The mechanism of continuous recrystallization in aluminium

The microstructural changes which occur when a highly deformed material undergoes continuous recrystallization are rather small, and occur incrementally as the annealing temperature is increased. As seen from figure 14.6c, there is no significant change in the

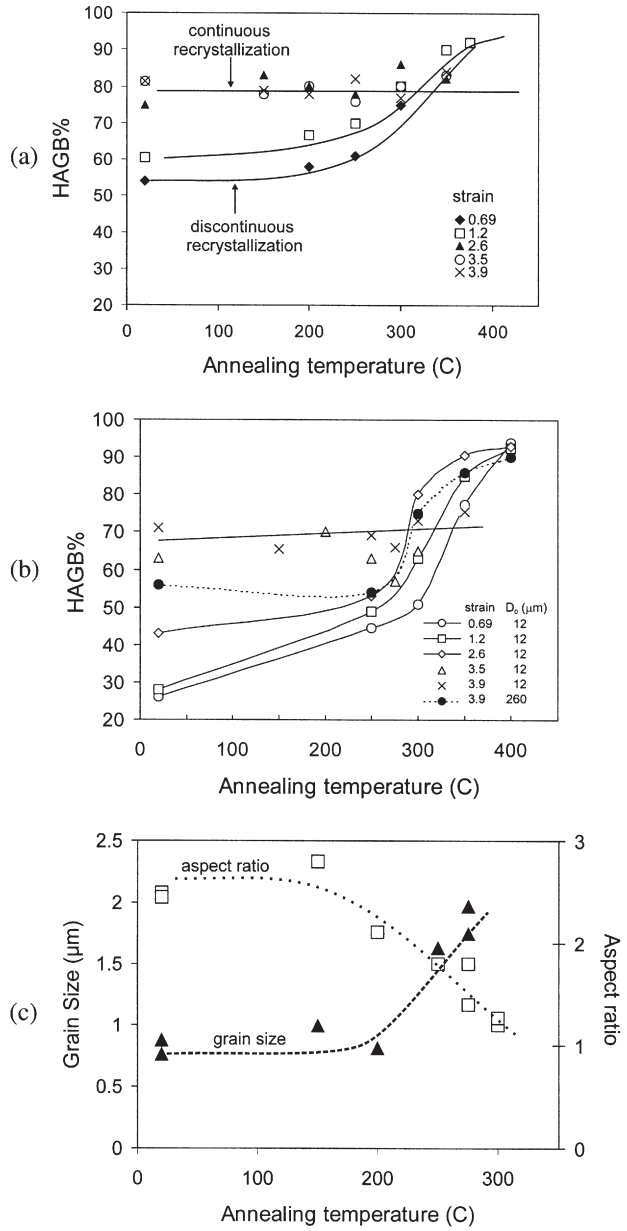

Fig. 14.6. Microstructural changes during the annealing of AA8006, as a function of strain and initial grain size (D_0) (a) % HAGB for $D_0 = 3$ μm; (b) %HAGB for $D_0 = 12$ μm and 260 μm, (Jazaeri and Humphreys 2002); (c) Grain/subgrain size and aspect ratio for $D_0 = 12$ μm, $\varepsilon = 3.9$, (data from Jazaeri and Humphreys 2001).

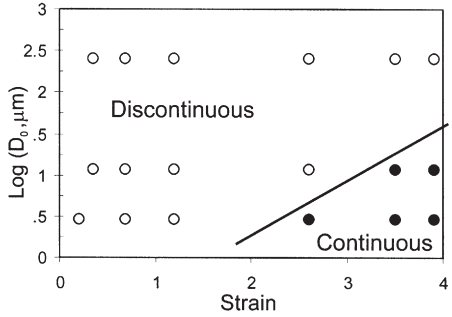

Fig. 14.7. The effects of initial grain size and strain on the transition from discontinuous to continuous recrystallization in AA8006, (Jazaeri and Humphreys 2002).

fraction of high angle boundaries, but the deformed grains/subgrains become more equiaxed and slightly larger.

In its simplest form, the highly deformed microstructure is similar to that shown schematically in figure 14.1c. It comprises lamellar high angle boundaries aligned parallel to the rolling plane, together with intersecting boundaries which are mainly of low angle. On annealing such a microstructure, it is thought that the energy is lowered by localised boundary migration as shown in figure 14.8, and this can be considered to occur in two stages.

- **Collapse of the lamellar microstructure**

The lamellar structure will tend to collapse due to the surface tension at the node points such as A, where the boundaries (of energy $\gamma_{\mathbf{R}}$) aligned in the rolling plane, are pulled by the boundaries (of energy $\gamma_{\mathbf{N}}$) aligned in the normal direction as shown in figure 14.8b.

The equilibrium configuration of the node **A** is determined by equation 4.10, and the critical condition for collapse of the structure is when the nodes **A** and **A**′ touch. This depends on the grain length in the rolling direction (L) and the normal direction (N) and on the relative boundary energies. If $\gamma_R = \gamma_N$ then the critical aspect ratio (L/N) for impingement is ~2. However, the boundaries in the normal direction are usually of lower angle, and if for example $\gamma_R = 2\gamma_N$ (corresponding to boundaries in the normal direction of ~3°), the critical aspect ratio is ~4. A convincing vertex simulation of this process due to Bate, is seen in figure 16.11, and this has been shown to give good agreement with the annealing behaviour of a highly deformed Al–3%Mg alloy (Hayes et al. 2002). Additional break-up of the lamellar grain microstructure and production of high angle boundaries during the deformation by large second-phase particles (figs. 14.1d and 14.4) will increase $\gamma_{\mathbf{N}}$, and lower the critical grain aspect ratio required for continuous recrystallization.

It is interesting that the mechanism of figure 14.8a and b has some geometric similarities to that originally proposed by Dillamore et al. (1972) for subgrain growth.

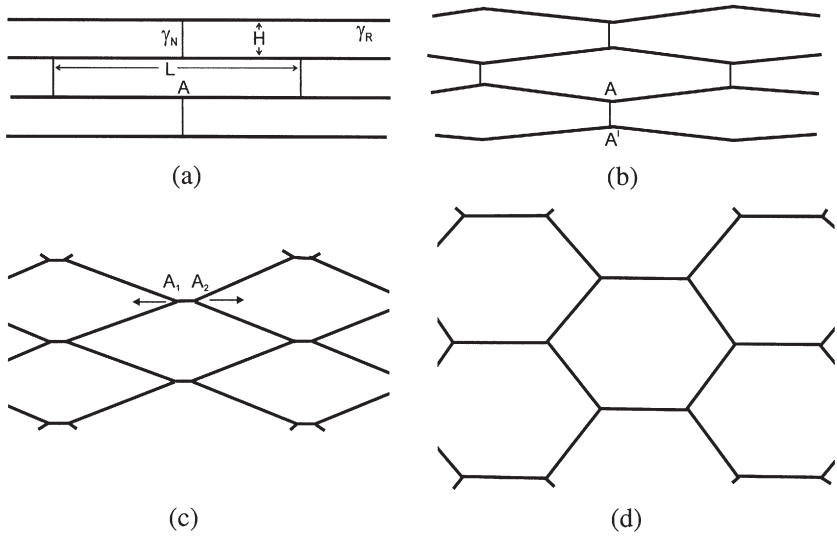

Fig. 14.8. Schematic diagram showing the continuous recrystallization of a highly deformed lamellar microstructure; (a) Initial structure, (b) collapse of the lamellar boundaries, (c) spheroidisation begins by Y-junction migration, (d) further spheroidisation and growth.

- **Spheroidisation and growth**

When the nodes **A** and **A′** touch, node switching (fig. 14.8) will occur, and two new nodes $\mathbf{A_1}$ and $\mathbf{A_2}$ will form and be pulled apart by the boundary tensions as shown in figure 14.8c. Further spheroidisation and growth will occur due to boundary tensions, as shown in figure 14.8d, leading to a more equiaxed grain structure. Such a fine-grained microstructure will be unstable with respect to normal and perhaps abnormal grain growth as discussed in §14.5.

14.4 DEFORMATION AT ELEVATED TEMPERATURES

14.4.1 Geometric dynamic recrystallization

As shown in figure 13.3a and 13.5a, grain boundaries develop serrations during dynamic recovery, and the wavelength of these serrations is similar to the subgrain size. If the material is subjected to a large reduction in cross section, for example by hot rolling or hot compression, then the original grains become flattened, as shown schematically in figure 14.9. Because the subgrain size during high temperature deformation is almost independent of strain (§13.2), the fraction of boundaries which are high angle, increases with strain, and eventually the size of the boundary serrations will become comparable with the grain thickness as shown schematically in figure 14.9b. Interpenetration of the scalloped boundaries will occur, resulting in a microstructure of small equiaxed grains of a size comparable with the subgrain size (fig. 14.9c), and an example of this process in

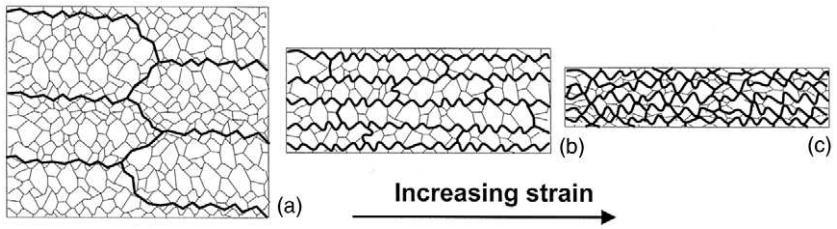

Fig. 14.9. Geometric dynamic recrystallization. As deformation progresses, the serrated HAGBs (thick lines) become closer, although the subgrain size remains approximately constant. Eventually the HAGBs impinge, resulting in a microstructure of mainly high angle boundaries.

an Al–Mg–Fe alloy is shown in figure 14.10. At lower strains (fig. 14.10a), the flattened old grains containing subgrains are seen, but at large strains (fig. 14.10b) a microstructure of almost equiaxed grains has formed.

An equiaxed microstructure with a large number of high angle boundaries therefore evolves without the operation of any new microscopic recrystallization mechanism and this process clearly differs from the **discontinuous dynamic recrystallization** discussed in §13.3. Microstructures of this type are commonly formed in aluminium and its alloys deformed to large strains (Perdrix et al. 1981). Humphreys (1982) showed that the origin of such microstructures was a process of grain impingement as discussed above, and this has been confirmed by later more extensive investigations (McQueen et al. 1985, 1989, Humphreys and Drury 1986, Solberg et al. 1989) and the term **geometric dynamic recrystallization** has been used to describe the phenomenon. The mechanical properties and texture resulting from this process are of interest, and are reviewed by Kassner et al. (1992).

One factor which often distinguishes geometric dynamic recrystallization from conventional discontinuous recrystallization is the **crystallographic texture.** As discussed in chapter 12, textures resulting from discontinuous recrystallization are often quite different from the deformation textures. However, during geometric dynamic recrystallization, there is little high angle boundary migration, and the texture remains largely unchanged (Gholinia et al. 2002b).

It is therefore seen that there is a great deal of similarity between the processes of continuous recrystallization which occurs on static annealing after very large strains (§14.3), and that of geometric dynamic recrystallization discussed in this section.

14.4.2 The conditions for geometric dynamic recrystallization

The occurrence of geometric dynamic recrystallization will depend on both the original grain size (D_0) of the material and on the deformation conditions. If we assume (Humphreys 1982) that the condition for geometric dynamic recrystallization is that grain impingement occurs when the subgrain size (D) becomes equal to the grain

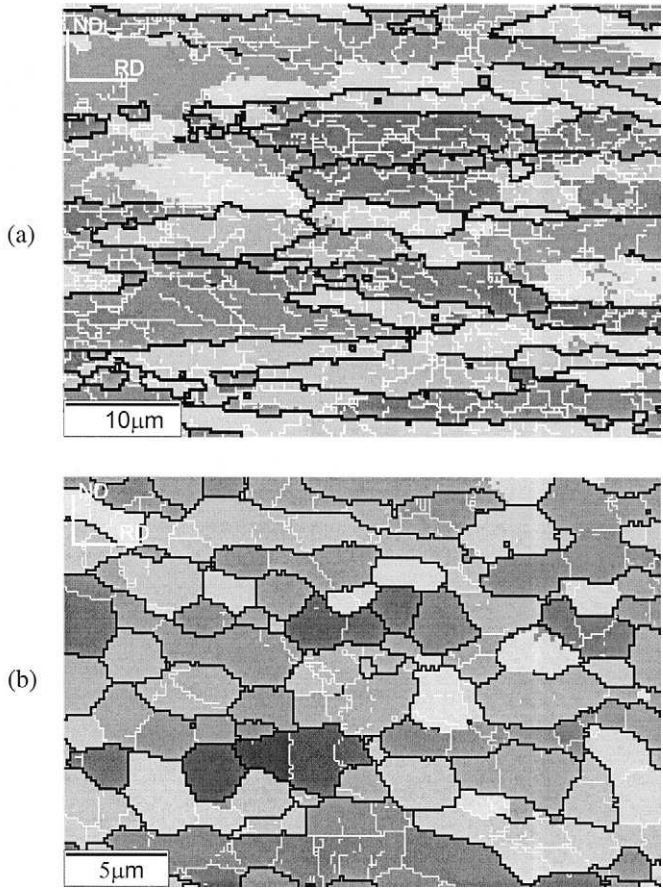

Fig. 14.10. EBSD maps showing geometric dynamic recrystallization in an Al–3Mg–0.2Fe alloy deformed at 350°C in plane strain compression; (a) $\varepsilon = 0.7$, (b) $\varepsilon = 3$. (HAGBs shown black and LAGBs white), (Gholinia et al. 2002b).

thickness (H), then, using equation 14.1, the critical compressive strain (ε_{cr}) for the process is

$$\varepsilon_{cr} = \ln\left(\frac{K_1 D_0}{D}\right) \tag{14.3}$$

where K_1 is a constant of the order of unity.

The relationship between flow stress and subgrain size is given by equation 13.7 and therefore

$$\varepsilon_{cr} = \ln(\sigma D_0) + K_2 \tag{14.4}$$

or, using equations 13.1 and 13.4

$$\varepsilon_{cr} = \ln(Z^{1/m} D_0) + K_3 \tag{14.5}$$

When the specimen is deformed at high stresses (large Z), geometric dynamic recrystallization does not occur until large strains because the subgrain size is small, whereas at low stresses, geometric dynamic recrystallization occurs at smaller strains. The critical strain for geometric dynamic recrystallization is also seen from equation 14.3 to be reduced if the original grain size is small.

It should be noted that the condition for geometric dynamic recrystallization may be derived either from geometric conditions as above, or from the theory of the stability of cellular microstructures as discussed in §10.3.4.

14.4.3 The grain size resulting from geometric dynamic recrystallization

The considerations above predict that geometric dynamic recrystallization should occur when the high angle boundary separation is similar to the subgrain size, and that this should result in a grain size which is approximately equal to the subgrain size. The question arises as to what happens if deformation is continued to larger strains, so that the HAGB spacing might become smaller than the subgrain size. In fact, it has been shown that this does not happen, even at very large strains, as seen in figure 14.11, in which the HAGB separation, the subgrain size and the HAGB spacing given by equation 14.1 are shown.

It is seen that although the HAGB spacing initially decreases more rapidly than the theoretical value, when it reaches the subgrain size it decreases no further. This is because of dynamic grain growth. When the grain spacing is larger than the subgrain

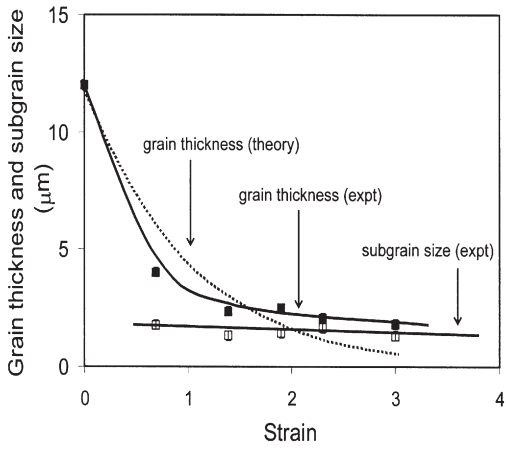

Fig. 14.11. Effect of strain on HAGB spacing and subgrain size in Al–3Mg–0.2Fe alloy deformed at 350°C in plane strain compression, (Gholinia et al. 2002b).

size, e.g. figure 14.9a, large scale HAGB migration is prevented by the pinning effects of the substructure. However, if the HAGB spacing is smaller than the subgrain size, no such pinning is exerted, and the elongated grains will tend to spheroidise as discussed in §14.3.5 and shown schematically in figure 14.8c, under the influence of their boundary tensions by lateral migration of the Y-junctions (A). As the grain spacing becomes similar to the subgrain size, substructure pinning will reoccur, and in this way a constant HAGB separation is achieved by dynamic equilibrium. A more detailed model of dynamic grain boundary migration under similar conditions has been proposed by Gourdet and Montheillet (2002). It should also be noted that a similar process of **dynamic grain growth** under conditions where the grain size is similar to the subgrain size, is of importance during **superplastic deformation,** although in this situation the grain size is stabilised by a dispersion of second-phase particles. Further discussion of the effect of second-phase particles on dynamic grain growth is given by Bate (2001b).

14.5 THE STABILITY OF MICRON-GRAINED MICROSTRUCTURES AGAINST GRAIN GROWTH

Although sub-micron-grained alloys may have impressive mechanical properties (§15.6.3, they cannot be used at elevated temperatures unless the microstructures are stable. Grain growth has been discussed in detail in chapter 11, and here we are only concerned with the behaviour of very fine-grained materials.

14.5.1 Single-phase alloys

Single-phase fine-grain microstructures have a large stored energy, due to the large area of grain boundary, and during high temperature annealing they are very susceptible to grain growth, as discussed in chapter 11. Hayes et al. (2002) have measured the growth at 250°C of 0.5 μm grains produced in an Al–3%Mg alloy by severe deformation, and found **normal grain growth,** with an exponent of 2.6. As may be seen from figure 14.12, the rate of grain growth at this temperature is very rapid.

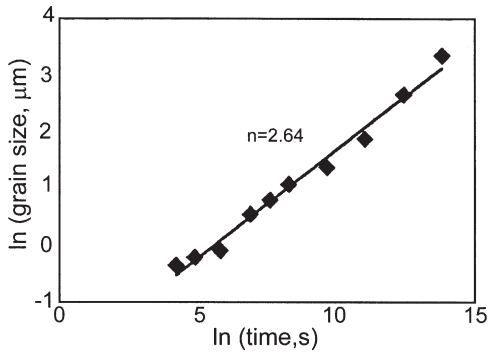

Fig. 14.12. Annealing of a single-phase 0.5 μm-grained Al–3%Mg alloy at 250°C, showing normal grain growth, (Hayes et al. 2002).

In contrast, Engler and Huh who obtained continuous recrystallization in high purity aluminium capacitor foil found that the microstructure underwent **abnormal grain growth** on further annealing. The difference between the two investigations is due to **texture.** The material of Hayes et al. (2002) was processed by equal channel angular extrusion (see §15.6.2) which results in a very weak texture. Such a material is not expected to undergo abnormal grain growth (§11.5). However, the material of Engler and Huh (1999) was heavily cold-rolled and had a strong rolling texture which was retained on continuous recrystallization. On further annealing, this material underwent texture-induced abnormal grain growth (§11.5.3).

These limited results show that the high temperature stability of the fine-grained microstructures produced by thermomechanical processing will be very dependent on the method of deformation, because of the effect that the processing route has on the texture.

14.5.2 Two-phase alloys

The most effective method of preventing normal or abnormal grain growth of a fine-grained microstructure is with a dispersion of stable second-phase particles as discussed in §11.4 and §11.5. Figure 14.13 shows a version of figure 11.21 which is enlarged to show the region relevant to micron-grained alloys, and which shows the predicted influence of the pinning particles (F_V/d) and the grain size (D) on the stability of fine-grain structures. The figure explains the three types of grain growth behaviour discussed in chapter 11. If there are no or few second-phase particles, it is seen that normal grain growth is predicted to occur during high temperature annealing as discussed above. However, as F_V/d increases, normal grain growth will be prevented, but abnormal grain growth is increasingly likely for smaller grain sizes.

In an alloy such as the Al–Fe–Mn alloy discussed above, in which $F_V/d \sim 0.1\ \mu m^{-1}$, the 0.5 μm diameter grains are predicted to undergo abnormal grain growth after a small

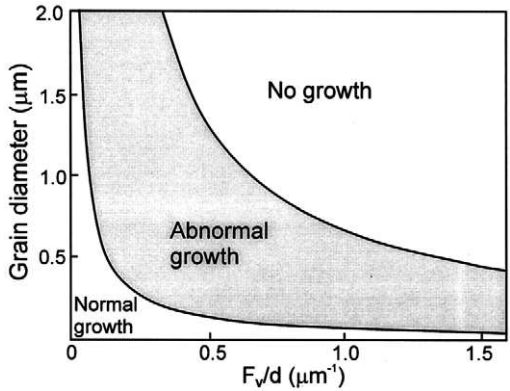

Fig. 14.13. The effect of second-phase particles on normal and abnormal grain growth of micron-grained alloys, (Humphreys et al. 1999).

amount of normal grain growth, as is found (Jazaeri and Humphreys 2001). In order to maintain a very small grain structure at high temperatures, sufficient particles must be present to prevent abnormal grain growth, and this requires $F_V/d > 1.5\ \mu m^{-1}$ for 0.5 μm diameter grains. This represents very significant amounts of second-phase particles, e.g. a volume fraction of 0.1 of 60 nm particles, which may be compared with the level of $F_V/d \sim 0.1\ \mu m^{-1}$ which is typically required to prevent discontinuous recrystallization during conventional processing (§9.2.1), and is rarely achievable in conventional industrial alloys (e.g. Hasegawa et al. 1999). However, interest in the superplastic deformation of micron-grained alloys (e.g. Grimes et al. 2001, Higashi 2001) has stimulated the development of special alloys containing sufficiently large quantities of stable intermetallic particles to maintain microstructural stability at elevated temperatures.

ThisPageIntentionallyLeftBlank

Chapter 15

CONTROL OF RECRYSTALLIZATION

15.1 INTRODUCTION

Although in this book we are primarily concerned with the scientific aspects of annealing phenomena, it is important to remember that this science provides the base for the solid state processing of all metals. Recrystallization plays a vital part in the manufacture of all wrought steel products and contributes enormously to the production of aluminium, copper and other non-ferrous metals. The control of microstructure and texture during recrystallization is therefore of major economic importance.

In this chapter we have selected a number of industrially important examples to illustrate how control of microstructure and texture during annealing are vital for the optimisation of properties. Although some of our examples may seem common-place, many of these products are in fact amongst the most highly developed and sophisticated materials available.

15.2 PROCESSING OF SOME INDUSTRIAL ALUMINIUM ALLOYS

Most commercial aluminium alloys contain substantial amounts of impurity, and in this respect they differ from many steels and titanium alloys. However, aluminium of very high purity (<10 ppm Fe) has an almost 100% cube texture after recrystallization (§12.2.1), and the texture of such material makes it useful for foil in **electrolytic**

capacitors, where the capacitance depends on the surface area. This can be increased by up to two orders of magnitude through an etching process that forms narrow channels along $<100>$ directions into the foil, and thus a **strong cube texture** is desirable.

15.2.1 Commercial purity aluminium (AA1xxx)

Increasing amounts of iron raise the recrystallization temperature and also reduce the strength of the cube texture. Aluminium of commercial purity, e.g. AA1050, typically has a combined iron and silicon content of more than 1 wt%, and the recrystallization behaviour of this type of material is deceptively complex, the annealing textures depending in particular on the heat treatment prior to cold rolling, the Fe/Si ratio and the annealing temperature.

15.2.1.1 The role of iron

Small amounts of iron may change the annealing texture from almost pure cube to a strong retained rolling (R) texture. Recrystallization may originate at cube sites (§12.4.1) and sites such as shear bands or grain boundaries, where orientations close to the deformation texture may be formed. For very low iron concentrations, the cube texture predominates. However, very small amounts (<100 ppm) of iron in solid solution have a large effect on recrystallization kinetics (fig. 7.10) and greater amounts may lead to precipitation on the recrystallizing front. It is postulated that the consequent solute drag and/or precipitation leads to slower growth of the dominant cube grains and allow the R component to develop, thereby reducing the strength of the cube component. However, such a reduction of the cube texture by precipitation would be contrary to the strengthening of the cube texture by precipitation, which is observed in a number of aluminium alloys, and discussed in §12.4.3.3.

The importance of the annealing temperature is well illustrated by the work of Hirsch and Lücke (1985) with an Al-0.007%Fe alloy. The 95% cold-rolled alloy was annealed at 280°C, 360°C and 520°C and figure 15.1 shows ODF results for the as-rolled material and for each annealing temperature. With the exception of a small amount of cube texture, the rolling texture (R) was retained at 360°C (fig. 15.1c), whereas the results for higher and lower temperatures were quite different. In both cases the cube texture was the major component observed and the strength of the R component was substantially reduced. This was interpreted by the authors as being due to the precipitation of an iron-rich phase at 360°C which hindered boundary migration. At the lower and higher temperatures where precipitation occurs after, or before recrystallization is complete, the effect on boundary migration is less drastic and a stronger cube texture develops.

15.2.1.2 The combined role of iron and silicon

The presence of silicon in addition to iron leads to the formation during casting of a stable α–Al–Fe–Si phase in the form of plates or rods of maximum dimension up to $\sim$10 μm (constituent particles). Consequently, the level of iron in solid solution is reduced, the exact amount being dependent on the homogenising and cooling conditions. In addition to the recrystallization behaviour discussed above, PSN at the Al–Fe–Si

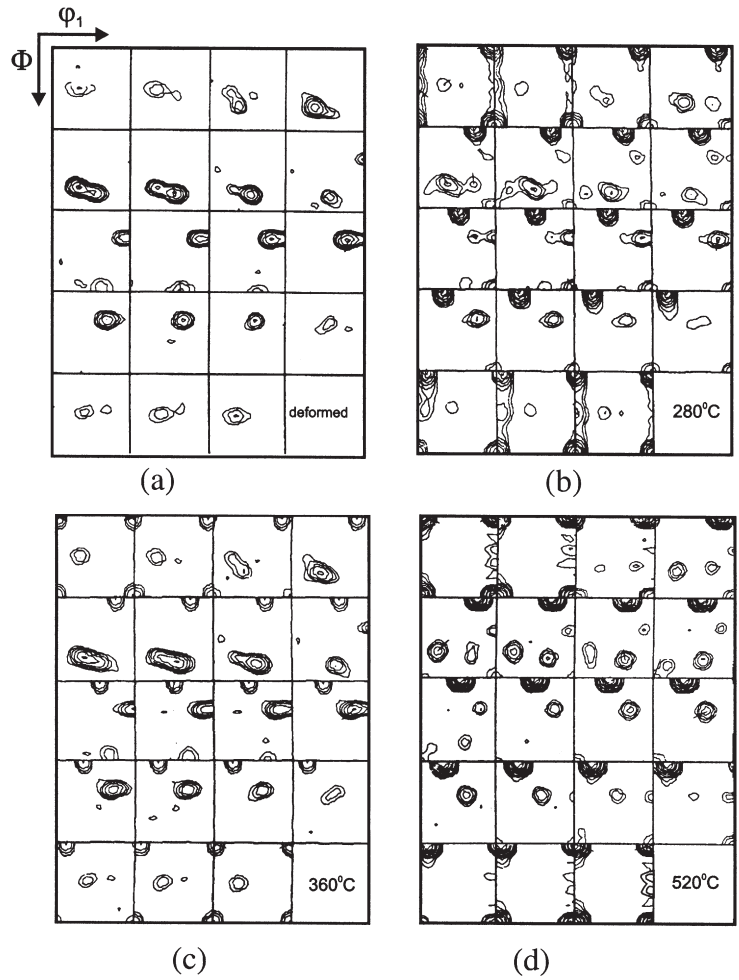

Fig. 15.1. Effect of annealing temperature on the recrystallization texture of 95% cold-rolled, Al-0.007%Fe alloy; (a) As rolled, annealed at: (b) 280°C, (c) 360°C, (d) 520°C, (Lücke 1984).

particles may also occur, leading to a random texture component, with a consequent weakening of the R component in particular.

Inakazu et al. (1991) have made a detailed study of the effects of small amounts of iron and silicon on the recrystallization texture of drawn aluminium. Both <100> and <111> texture components were obtained, but the balance depended on the annealing temperature. At temperatures above 450° the <111> deformation component was strengthened, but below 300°C the <100> component increased. The results were interpreted in terms of precipitation during the recrystallization anneal.

The recrystallization of commercial purity aluminium and related alloys is a very good example of how the final annealing texture is the result of competition between grains originating at different sites (§12.4), and shows how the balance between the components is affected by small changes in composition or annealing temperature. Oscarsson et al. (1991) have investigated the effect of the deformation temperature on the texture after recrystallization in commercial Al–Fe–Si alloys. They show that in addition to texture effects arising from changes in solute, the deformation temperature affects the amount of PSN (see §13.6.4) and hence the 'random' component of the recrystallization texture.

15.2.2 The production of aluminium beverage cans (AA3XXX)

The modern aluminium beverage can is produced in vast numbers worldwide, and has a dominant position in the North American market. Some 175 billion cans are manufactured annually, using the equivalent of approximately 15% of the world's primary aluminium production, although because of recycling, the actual amount of primary metal used is somewhat lower. The production of these cans, and the significant decrease in can weight which has been made possible by improvements in thermo-mechanical processing, provides an excellent example of the practical significance that comes from an understanding of the principles of deformation processing, recovery and recrystallization. The microstructural aspects of can production are reviewed by Marshall (1996).

The basic metallurgical steps involved in the production of the sheet are casting, homogenization, hot rolling, annealing and cold rolling. Understanding the problems involved requires some knowledge of can making and we begin with a brief account of that process. This is followed by a description of sheet production and a discussion of metallurgical factors such as microstructure and texture.

15.2.2.1 Can making

Can making begins with a cupping operation (Hartung 1993). This is done on a multi-stage press which cuts the blank and then forms a shallow, drawn cup with diameter ~90 mm. Modern presses form up to 14 cups in a single stroke at speeds as high as 275 strokes per minute. The cups are then transferred to the can press or 'body maker'. These are long stroke, mechanical presses that generate a trimmed can in a series of steps, viz:

- At the beginning of the stroke the cup is redrawn to the final can diameter.
- The side wall is then thinned and elongated in a series of wall ironing dies: in a typical body maker three ironing operations are involved. The punch is designed to develop a gradual reduction in metal thickness from the dome area to the sidewall, but an annular region of thicker material is maintained near the open end. This region is usually ~50% thicker than the sidewall and its purpose is to provide a sufficient volume of material for subsequent necking and flanging. The sidewall itself is usually a little more than 0.1 mm thick.
- At the end of the stroke the bottom of the can is formed into the well known, pressure resistant, stackable dome configuration. The can is removed from the retreating punch by a combination of air pressure and mechanical fingers.

Fig. 15.2. Deep drawn cups produced from circular blanks of AA3104 alloy with different textures. (a) Mixed rolling and cube texture, showing little earing, (b) strong cube texture, showing extensive 0°/90° earing.

After removal, the can is trimmed to remove the **ears** (see fig. 15.2b) and roughened edges generated at the open end. The whole process is done at very high speed and a modern body maker/trimmer combination produces in excess of 350 can bodies per minute.

The remaining processes are of less interest metallurgically. They involve washing, preparation of the surface for the inks and varnishes used in labelling and the application of the interior coating. Finally the cans are necked down at the open end and flanged so that the lid can be inserted after filling.

The overall result of this processing is a thin walled pressure vessel with an internal volume of ~375 ml capable of withstanding an internal pressure of 0.62 MPa and a longitudinal load of ~135 kg in the unpressurised condition; the final wall thickness is ~0.1 mm. The reduction in can mass in recent years has been spectacular; the weight of the blank from which the can is drawn has fallen from 22 g in 1968, to 19.2 g in 1978, to 16.5 g in 1988, to ~12 g in 1993 and is currently close to 10 g.

15.2.2.2 The production of can body sheet

The production of can body sheet is highly competitive and explicit production details are not freely available. The details given in this section are basically correct but not explicitly true for any individual manufacturer. The alloys for can bodies are based on the Al–Mg–Mn non-heat-treatable group and the main alloys used are AA3004, including the narrower specification AA3104, whose composition ranges are shown in table 15.1. The easy-open ends that are fitted after the can has been filled are made from a different alloy (AA5182) and are not discussed here.

The sheet is produced from **DC-cast ingots** that are 300–760 mm thick, 1300–1850 mm wide and of length determined by the mill layout and its ingot and coil handling facilities. After scalping the ingots are **homogenised** at temperatures above ~550°C and soaked for a carefully controlled period. The ingot is then cooled to ~500°C and held for a sufficient time to ensure a uniform temperature for **hot rolling in a breakdown mill.** During this rolling process which lasts for about 15 min the temperature falls to ~300°C and the ingot is reduced to a slab of ~25 mm thickness. At this stage the slab is transferred to a **hot finishing mill.** This may be either a single stand reversing mill or a

Table 15.1
Nominal compositions of aluminium alloys for can bodies.

	Si%	Fe%	Cu%	Mn%	Mg%	Zn%
AA3004	0.3 max	0.7 max	0.25 max	1–1.5	0.8–1.3	0.25 max
AA3104	0.6 max	0.8 max	0.05–0.25	0.8–1.4	0.8–1.3	0.25 max

multiple stand continuous mill. Mills of the latter type with 3–4 stands produce coiled metal ~2.5 mm thick that recrystallizes without furnace annealing, but in single stand rolling the final coiling temperature is too low for full in-coil recrystallization, and a further furnace anneal is required in this case. The current demand is for final sheet $\leq$0.3 mm thick with strength corresponding to H19 (UTS 295 MPa, YS 285 MPa, Elongation 2%). This is achieved by **cold rolling** to ~87% reduction in thickness. There is a continuing demand for further reduction in the thickness of can stock sheet; in 1978, for example, a typical value was 0.38 mm. In the same year the required thickness control ranged from $\pm$7.5 μm to $\pm$10 μm; the 1993 requirement was $\pm$5 μm.

The metallurgical effort in can production is directed towards minimizing the mass of aluminium in each can and eliminating shutdowns. The aim is to use the smallest round blank stamped from the thinnest possible sheet, that will provide sufficient strength after cupping and wall ironing to minimum height. In order to achieve this, strict control is exercised over all aspects of the development of microstructure and texture, and we examine these at the various processing stages.

15.2.2.3 Development of microstructure and texture

The evolution of microstructure and texture during the processing schedule determine the properties of the final sheet product.

The as-cast microstructure – The most important features of the cast ingot are the size, type and distribution of the coarse constituent particles, eutectic element microsegregation and the cell size. The boundaries of the cells, which are ~100 μm in size, are decorated with the constituent particles, which are the product of complex eutectic reactions, the main intermetallic phases being $(FeMn)Al_6$ and Mg_2Si. Much of the manganese remains in solid solution.

Homogenisation – The main objectives of homogenisation are the elimination of microsegregation, transformation of the coarse β-$(FeMn)Al_6$ particles, and the precipitation of manganese in the form of dispersoids. Microsegregation is largely removed during the slow heat up of the ingot, which also dissolves the Mg_2Si particles. The consequent release of silicon is believed to aid the transformation of β-$(FeMn)Al_6$ to α-$Al_{15}(FeMn)_3Si_2$. The harder α-phase is desirable as it aids die cleaning and prevents galling. Some of the manganese in solid solution is incorporated into the Fe-bearing constituent particles, and much of the remainder is precipitated as fine α-$Al_{15}Mn_3Si_2$ dispersoid particles. These particles are critical in determining the annealing response after hot rolling and hence the recrystallization texture.

Hot rolling and recrystallization – Little further precipitation occurs during hot rolling in the **break-down mill** even though the temperature falls to ~300°C over 15 min or so. The major metallurgical changes at this stage are the breaking down of the large constituent particles and the establishment of a moderate recrystallized grain size in the matrix. In the **hot finishing mill,** the metal does not recrystallize between passes, and recrystallization occurs on final coiling or, if necessary, during a further furnace anneal at ~350°C.

The can making process requires a **strong cube texture** after recrystallization, and the conditions for obtaining this have been the subject of considerable research. The recrystallization texture is dominated by two components, grains of cube orientation and grains of 'random' orientations. It is thought that much of the random component originates from particle stimulated nucleation of recrystallization (PSN) at the constituent particles (§9.3.2) and that the cube grains originate at preserved cube bands in the hot rolled microstructure as discussed in §12.4.1. A higher rolling temperature (low Z) will promote cube retention, and also restrict PSN (fig. 13.31). The effect of this on the recrystallization texture is shown in figure 12.18, where it is seen that as the number of particles capable of PSN decreases, the strength of the cube texture increases and the random texture decreases. More detailed discussion of texture control in such materials, and the effect on the final deep drawing properties is given by Hutchinson et al. (1989b) and Hutchinson and Ekström (1990).

Cold rolling – The requirement for deep drawing of the can bodies is good formability and low earing. The strong textures developed during thermomechanical processing of the sheet may lead to the generation of ears and valleys around the top of a can (fig. 15.2). These may cause trouble during can making and eventually they must be trimmed off. At present, can makers specify that the fractional height of the ears above the valleys of a drawn cup should lie in the range of 0.5% to 3% of the can height.

The major texture components after cold rolling are shown in table 15.2. Although the cube texture of the hot-rolled and recrystallized sheet is relatively stable during cold rolling, its strength is reduced as the normal cold-rolled texture components (Brass, Copper, S) develop (§3.2.1). Table 15.2 suggests that at this stage strong ±45° earing would be present, together with minor 0–180° earing. The extent of the ±45° earing can be minimised if the development of the rolling texture components is kept to a minimum during hot-rolling and annealing, i.e. if the cube texture is maximised.

Table 15.2
Major texture components in cold-rolled can body sheet.

Texture	Name	Earing
{100} < 001 >	Cube	4-fold 0/90° etc.
{110} < 001 >	Goss	2-fold 0/180°
{110} < 112 >	Brass	4-fold 45° etc.
{112} < 111 >	Copper	4-fold 45° etc.
{123} < 412 >	S (~R)	4-fold 45° etc.

While the trend is to minimise earing and the consequent trimming and metal loss, a minimum amount is specified (usually 0.5%). There is a very important practical reason for this (Malin 1993). If $\pm 45^\circ$ earing is eliminated, the new texture generates two-fold earing at 0° and 180° derived from the Goss component. Although four 45° ears are able to withstand the hold-down pressure supporting the blank during forming, two 0–180° ears cannot do this without some circumferential flow and pinching. The resulting pinched ears tend to jam the body maker during the subsequent re-drawing and ironing.

It is well known that earing also depends on mechanical parameters such as lubrication, blank holder pressure and alignment (Rodrigues and Bate 1984, Bate 1989, Malin and Chen 1993, Courbon 2000) but a discussion of these is beyond the scope of this book.

This important example of industrial thermomechanical processing clearly demonstrates the vital role of texture control during can manufacture, particularly at the hot-rolled and annealed stage.

15.2.3 Al–Mg–Si automotive sheet (AA6xxx)

The current demand for weight reduction in vehicles, in order to increase fuel economy and reduce emissions, has led to an increasing interest in the use of aluminium sheets for autobody applications, because replacement of steel by aluminium could potentially lead to a 50% weight saving in the vehicle (e.g. Burger et al. 1995, Morita 1998). The two generic types of aluminium alloy most commonly used are the non-heat-treatable Al–Mg alloys of the AA5xxx series and the age-hardening Al–Mg–Si alloys of the AA6xxx series (Burger et al. 1995, Lloyd and Gupta 1997, Engler and Hirsch 2002). The Al–Mg alloys are mostly considered for internal applications, whereas the stronger Al–Mg–Si series, which are discussed here, have a number of advantages for use as outer skin sheet.

- They are readily formable in the solution treated state.
- They have good corrosion resistance.
- They achieve a high strength by age-hardening during the paint bake cycle.

15.2.3.1 The production schedule

The first stages of the production schedule of the sheets is broadly similar to that described for Al–Mg–Mn alloys in §15.2.2, consisting of DC casting, homogenisation, breakdown hot rolling and multistand hot rolling. The hot rolled strip, which is 3–6 mm thick, is cold rolled to a final gauge of ~0.8–1.2 mm. The sheet is then passed through a continuous annealing line where it is rapidly heated to a solution treatment temperature of 500–570°C, when it recrystallizes, and it is then quenched to retain the Mg and Si in solid solution. After forming, the required strength is achieved during the final automotive paint baking cycle, which consists of a 20–30 min anneal at temperatures between 160 and 200°C.

15.2.3.2 The importance of the texture

The formability of aluminium sheet is generally inferior to that of steel, and it is therefore important to control the texture of the aluminium during processing so as to optimise the formability. A strong Goss texture is considered to be detrimental to

formability, whereas a weak cube texture is beneficial (Engler and Hirsch 2002). However, for automotive sheet used for exterior panels, the **spatial distribution of texture** is generally considered to be more important than the overall texture.

During forming, parallel undulations of a few millimetres spacing may form in the rolling direction. These lines may be pronounced enough to be visible after painting, thereby making the sheet unsuitable for exterior body panels. This effect, which is known as **ridging** or **roping** has been shown to be associated with the presence of bands of similar crystallographic orientation in the sheet (Baczynski et al. 2000). Grains of different orientation have different flow stresses (Taylor factors), and this results in an uneven strain distribution. Both Cube and Goss-oriented grains have been associated with roping. To minimise the problem, the sheet must be produced in the T4 temper with a relatively weak texture.

15.2.3.3 The evolution of the texture and microstructure

The development of the microstructure and texture during thermomechanical processing is dependent on the temperature, strain and strain rate, but the following is typical of a conventional processing cycle (Engler and Hirsch 2002).

- During the **breakdown rolling,** recrystallization occurs between passes. The resultant transfer gauge plate is fully recrystallized with a strong cube texture and a grain size of ~200 μm. There is typically a texture gradient from Cube in the centre to TD-rotated Cube near the surface.
- The subsequent **multi-stand hot rolling** is carried out at lower temperatures, and some precipitation of Mg_2Si and other phases may occur. At lower rolling temperatures no recrystallization occurs and a typical β-fibre rolling texture results, although at higher rolling temperatures some recrystallization may occur. This hot-band material is **coiled,** and during this process and the subsequent cooling, partial recrystallization occurs, and a mixed rolling and cube recrystallization texture results, the relative amounts depending on the finishing temperature. During the coiling, further heavy precipitation of finer Mg_2Si particles occurs.
- The strip is then **cold rolled** to final sheet gauge, resulting in a strong rolling texture, although some bands of Cube texture remain from the hot band. The sheet is given a **final solution heat treatment** at 500–570°C in order to re-dissolve the Mg_2Si particles. This also recrystallizes the material, resulting in a final grain size of 20–30 μm.

The recrystallized texture depends on the earlier stages of processing, and in particular on the amount of Mg_2Si precipitation following the hot rolling stage. As discussed in §12.4.3.3, the presence of finely dispersed second-phase particles during annealing, tends to inhibit particle stimulated nucleation of recrystallization (PSN) more than the recrystallizing Cube-oriented grains, resulting in a very strong Cube texture. This is what normally happens in material processed by the conventional route described above, and summarised in table 15.3, resulting in the strong Cube texture of figure 15.3a.

However, if the hot band material is given an extra intermediate anneal **before** cold rolling, in order to coarsen the Mg_2Si particles, as shown in table 15.3, PSN contributes more to the recrystallization process and a weaker recrystallization texture results as shown in figure 15.3b. As discussed above, such a weak Cube texture is desirable both for formability and for the elimination of roping in the sheet.

Table 15.3
Processing routes for AA6xxx automotive sheet, showing the effect on the final texture, of an intermediate anneal before cold rolling.

Breakdown hot rolling 25–40 mm plate (transfer guage) Recrystallized to 200 μm grains Strong cube texture		
Tandem mill hot rolling 3–6 mm strip (hot band) Hot-deformed microstructure Rolling texture		
Coiling Partly recrystallized microstructure Fine Mg_2Si precipitation Rolling + Cube texture		
Intermediate anneal Fully recrystallized Precipitates coarsen Cube texture		**No intermediate anneal** Partly recrystallized Fine Mg_2Si precipitates Rolling + Cube texture
↓	**Cold rolling** 0.8–1.22 mm sheet Deformed microstructure	↓
Rolling texture		Rolling texture
↓	**Solution treatement** Recrystallized to ~20–30 μm grains Precipitate dissolution	↓
Weak cube texture		**Strong cube texture**
Forming		
Age-hardening during paint-bake		

In addition to the parameters discussed above, there are other means of controlling the final texture, which are not discussed here, including the alloy composition, the exit temperature of tandem rolling and the amount of the cold rolling reduction.

15.3 TEXTURE CONTROL IN COLD ROLLED AND ANNEALED SHEET STEEL

15.3.1 Introduction

The world production of low carbon steel far exceeds that of any other metallic material and while much of that production is used for what may seem simple purposes there is a continuing demand for improvement in processing and properties. The major

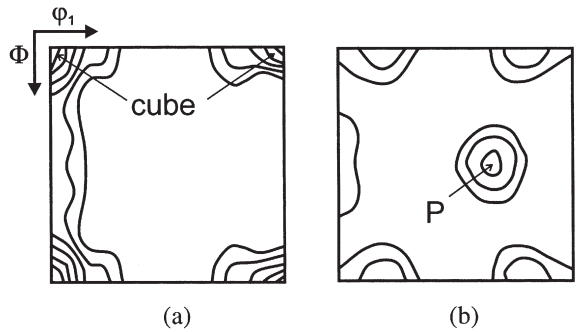

Fig. 15.3. Recrystallization textures ($\phi_2 = 0$ sections) in AA6xxx alloy after the solution heat-treatment anneal (T4 temper). (a) Strong Cube texture in conventionally processed material (max intensity = 26R), (b) Weak Cube and P texture in material given an intermediate anneal after hot rolling to coarsen the Mg_2Si particles (max intensity = 8R), (after Engler and Hirsch 2002).

changes have been:

- The development of oxygen blown converters.
- The use of ladle degassing,
- The introduction of continuous casting and the direct production of slabs.
- The continuing replacement of batch annealing by continuous annealing lines for sheet steel.
- The development of low carbon and ultra low carbon forming steels.

Each of these has influenced the production and properties of deep drawing steels but we are concerned here with only the last two. Although continuous annealing lines have been used for steel sheet products for many years, the best quality drawing steels were traditionally produced by lengthy batch annealing and it was always recognised that development of the required texture and strength were critical problems facing the introduction of continuous annealing. Today these problems have been solved and more than 40 continuous annealing lines are in operation.

The first interstitial-free steels appeared in the late 1960's when it was reported that drawability could be improved by small additions of titanium and niobium. In order to achieve the desirable carbon contents of less than 0.01%, these steels required an alloy content of 0.05–0.1%. Such amounts lead to loss of surface quality due to the presence of inclusions and also to high alloy costs (Obara et al. 1984). However steel making technology has now reached the point where carbon contents in the range 0.001–0.003% can be produced by short time, ladle-degassing treatments. Such steels require much smaller amounts of alloying elements ($\leq$0.03%Nb or $\leq$0.05%Ti). If additional strength is required this can be achieved by the addition of small amounts of phosphorus (<0.1%) and by bake hardening.

In the following discussion of these topics we begin with a brief review of the measurement of drawability and this is followed by an account of the effects of changes

in annealing practice and steel chemistry. Attention is centred particularly on normal low carbon steels and the relatively new ultra low carbon steels. Only brief mention is made of the conventional interstitial-free steels. Much of the relevant research work has been carried out in the industrial laboratories of Japanese steel producers and much of the relevant literature is to be found in steel industry journals and conference reports.

15.3.2 Background

15.3.2.1 Assessment of formability

It is obvious that the presence of a crystallographic texture in a rolled sheet will affect the strain distribution and plastic flow during forming. This texture-induced anisotropy may take two forms. In the first of these, termed **planar anisotropy,** the flow properties in the sheet plane vary with direction. In the second an appropriate texture will introduce a differential strengthening between the 'in-plane' and 'through-thickness' directions; such an effect is referred to as **normal anisotropy.**

The criterion for drawability is given by the ratio of the true strains in the width and thickness direction (the **r** value).

$$\mathrm{r} = \frac{\varepsilon_{\mathrm{w}}}{\varepsilon_{\mathrm{t}}} \tag{15.1}$$

In the presence of planar anisotropy the value of **r** varies with direction in the sheet plane and an average **r** value, $\bar{\mathbf{r}}$ is used.

$$\bar{\mathbf{r}} = \frac{\mathbf{r}_0 + 2\mathbf{r}_{45} + \mathbf{r}_{90}}{4} \tag{15.2}$$

$\bar{\mathbf{r}}$ is a convenient measure of normal anisotropy and therefore of drawability. High values of $\bar{\mathbf{r}}$ correlate with good drawability. Planar anisotropy which is given by

$$\Delta\mathrm{r} = \frac{\mathbf{r}_0 + \mathbf{r}_{90} - 2\,\mathbf{r}_{45}}{2} \tag{15.3}$$

correlates with the extent of earing in deep drawing.

Theoretical values of $\bar{\mathbf{r}}$, calculated by Hutchinson and Bate (1994), on the basis of the Taylor model (§3.7.1) are given in table 15.4. The desired properties of good drawability and minimum earing are seen to be associated with {111} < uvw > type textures; it is for this reason that the strong < 111 > ND fibre texture found in annealed low carbon steels is so important. In this respect it is to be noted that {554} is only a few degrees removed from {111}. It can also be seen that {001} < 110 > and {110} < 001 > textures are undesirable.

Because good drawability is associated with {111} rolling plane textures and bad drawability with {100} rolling plane textures, the ratio of the intensities of the 222 and 200 X-ray reflections from a rolling plane specimen (I_{222}/I_{200}) is often used as a measure of formability and correlates well with $\bar{\mathbf{r}}$.

Table 15.4
Values of $\bar{r}$ and Δr for major texture components (Hutchinson and Bate 1994).

Orientation (10° spread)				Predicted anisotropy (pencil glide)	
{hkl} < uvw >	Euler Angles			$\bar{r}$	Δr
	φ_1	Φ	φ_2		
{001} < 110 >	45	0	0	0.45	−0.88
{112} < 110 >	0	35.3	45	3.33	−5.37
{111} < 110 >	0	54.7	45	2.80	−0.44
{111} < 112 >	90	54.7	45	2.80	−0.44
{554} < 225 >	90	60.5	45	2.87	1.53
{110} < 001 >	90	90	45	25.43	49.38

15.3.2.2 Texture of low carbon steel

As discussed in §3.3, the rolling texture of low carbon steel consists of two major orientation spreads lying along the α and γ-fibres of figure 3.10. The second of these is an almost complete < 111 > rolling plane normal fibre texture with {111} parallel to the rolling plane and several prominent directions parallel to the rolling direction; these include < 110 >, < 112 > and < 123 >. The first or α-fibre is a partial fibre texture about the rolling direction with a < 110 > fibre axis and prominent {001}, {112} and {111} rolling plane components (see fig. 3.10). The annealing texture and its generation are discussed in detail in §12.4.2 and here we repeat only that in the case of steels rolled to ~70% reduction a number of strong components including {111} < 110 >, {554} < 135 > and {554} < 225 > develop in the γ-fibre early in the annealing cycle and subsequently grow at the expense of α-fibre orientations such as {111} < 110 > (see fig. 12.17).

For low reductions a Goss component occurs together with a {111} rolling plane texture, but as the reduction is increased the Goss component weakens and the {111} textures strengthens with the centre of the spread near {111} < 112 >. At 90% reduction the desirable {111} texture strengthens further but this is offset by the appearance of deleterious components with near {100} orientations. As a consequence there has been a long held belief in an optimum rolling reduction of ~70% reduction for the traditional low carbon forming steels, viz rimming and aluminium killed steels (fig. 15.4). The recent developments in steel making and processing have enabled the use of higher reductions (up to 90%) and at the same time the achievable $\bar{r}$ value has been raised from the typical values shown in figure 15.4 to ~2.5 in ultra low carbon steels containing small amounts of niobium and titanium. This improvement is best understood by considering the origin of the texture and the effects of processing variables on texture development in three important cases:

- Batch annealed Al killed steels.
- Continuously annealed low carbon steels.
- Interstitial free steels.

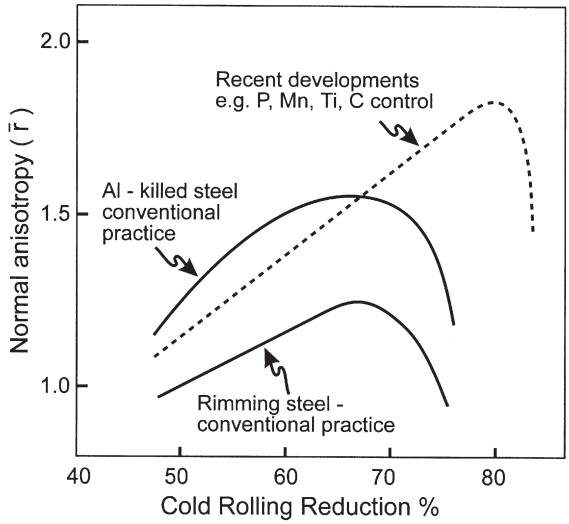

Fig. 15.4. Relationship between cold rolling reduction and $\bar{\mathbf{r}}$ for different steel types, (Hutchinson 1984).

15.3.2.3 The origin of the texture

The most important single property of a good deep drawing steel is a strong {111} rolling plane texture after annealing. As pointed out by Nes and Hutchinson (1989) the limitations of commercial processing involving huge tonnage production and multi-operation processing are such that modification of rolling textures and/or grain boundary character is not generally possible. This effectively rules out the option of controlling texture development by **growth** processes. It is however, often possible to modify the recrystallization texture by controlling the **nucleation** process.

In general, nucleation is associated with microstructural inhomogeneities and the most significant of these are microstructurally persistent features such as transition bands, shear bands, grain boundaries and the deformation zones around hard particles. In these very low carbon steels, carbides are few and particle stimulated nucleation is not likely to be significant. Shear band nucleation was investigated by Haratani et al. (1984) who found that shear bands form preferentially in $\{111\}<112>$ volumes and result in the creation of $\{110\}<001>$ Goss-oriented nuclei. Shear band formation is favoured by large grain size and high contents of interstitial elements and it follows that a small grain size and low C and N contents are desirable. In these steels, transition band nucleation is not significant and the important nuclei are those of the γ-fibre, associated with grain boundaries, as discussed in §12.4.2.

15.3.3 Batch annealed, Al-killed, low carbon forming steels

This category includes the common rimming and aluminium killed steels. In addition to the effects of rolling reduction, $\bar{\mathbf{r}}$ values in these steels are strongly influenced by the

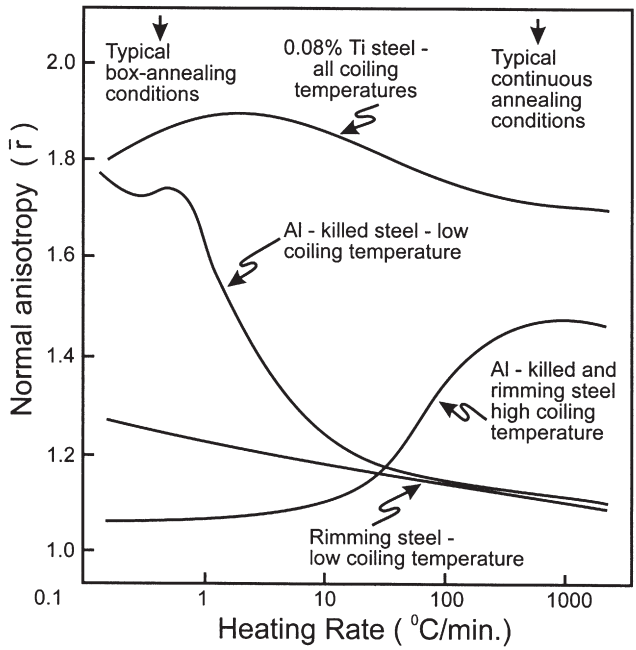

Fig. 15.5. Effect of coiling temperature and heating rate for final anneal on $\bar{r}$ for different steel types, (Hutchinson 1984).

coiling temperature after hot rolling and the heating rate during annealing. Figure 15.5, compiled by Hutchinson (1984) from the work of several authors, summarises the position. It will be seen that at low coiling temperatures ($\leq$600°C), the high $\bar{r}$ values typical of killed steels are found only for the slow heating rates typical of batch annealing. The situation is reversed for high coiling temperatures (~700°C) but the maximum value that can be developed is lower. These effects which provide the basis for the traditional use of batch annealing for the extra deep drawing quality killed steels are discussed below.

15.3.3.1 The aluminium nitride reaction

The origin of the high $\bar{r}$ values associated with aluminium killed steels has been the subject of an immense research effort. The steels have strong {111} texture components and very weak {100} components and a so-called 'pancake' grain structure in which the large, recrystallized grains are elongated in the rolling direction. Understanding of the phenomena involved began with the work of Leslie et al. (1954). An essential requirement is that both aluminium and nitrogen be in solid solution before cold rolling begins and this means that any AlN present must be decomposed prior to hot rolling. It is essential, also, that the dissolved aluminium and nitrogen should not precipitate during hot rolling or immediately thereafter. Leslie et al. found that precipitation occurred most rapidly at ~800°C and established that the extent of precipitation was

related to the development of the pancake grain structure. In practice AlN precipitation is prevented by a high soaking temperature, ~1250°C and spraying the hot band with water after hot rolling, but before coiling at ~580°C.

It is now believed (Hutchinson and Ryde 1995) that the long argument about the manner in which the aluminium and nitrogen atoms act to control texture development by retarding nucleation has been settled in favour of a precipitation process. Under slow heating conditions, as in batch annealing, the aluminium atoms diffuse and combine with the nitrogen to form small precipitates which retard recrystallization. The precipitates which occur at the old grain and cell boundaries are readily identified within the recrystallized grains as sheets, that are elongated in the rolling direction and, dictate the formation of the coarse, elongated, pancake grain structure that is ideally suited for sheet forming processes. The second-phase particles inhibit both nucleation and growth but the large final grain size indicates that nucleation is the more affected. Dillamore et al. (1967) and Hutchinson (2000) have related the accompanying enhancement of the desirable {111} texture components during recrystallization to the higher stored energy associated with {111} oriented volumes in the deformation microstructure (§2.2.3.3) and the consequent faster recrystallization (fig. 7.8).

15.3.3.2 Continuously annealed low carbon steels

The development of continuous casting opened the way to the large scale introduction of continuous annealing lines but the high heating rates involved effectively precluded the use of AlN as a texture controlling precipitate. Such lines involve heating rates of the order of several hundred degrees per minute and a reduction in annealing time from several days to ~10 min. An excellent summary of the extensive Japanese research work that led to their introduction is given by Abe et al. (1978) and general understanding and clarification of this work owes much to the contributions and critical reviews of Hutchinson and co-workers (e.g. Hutchinson and Ryde 1995, Hutchinson 1999, 2000).

The high heating rate in continuous annealing precludes any use of AlN precipitation as a mechanism of texture control. Advantage is taken, instead, of the fact that after annealing, rolled, pure iron develops a strong recrystallization texture. It is essential, therefore, that the carbon content be low and that any second-phase particles present should not occur as a fine dispersion that could inhibit grain growth. In practice any cementite particles present may begin to dissolve and in combination with the manganese already in solid solution weaken the {111} texture. Ideally coiling should occur at a high temperature to ensure that any cementite particles are coarse and do not inhibit growth. The best results are obtained if coiling is carried out at temperatures above 700°C. Under these conditions the eutectoid transformation occurs during the slow cooling of the tightly wound coil rather than during water spraying and the cementite is much coarser and more widely dispersed. In the short time available in the continuous annealing cycle, any other second-phase particles must also be coarsened in order to reduce growth effects due to Zener drag. Prominent among these phases are MnS and AlN. The high coiling temperature ensures that any precipitation is on a coarse scale while the equilibrium established in the ferrite is such that the carbon content is very low. The realization that this almost pure iron is the key parameter controlling the texture was the major factor behind the successful introduction of the modern ultra low carbon drawing steels.

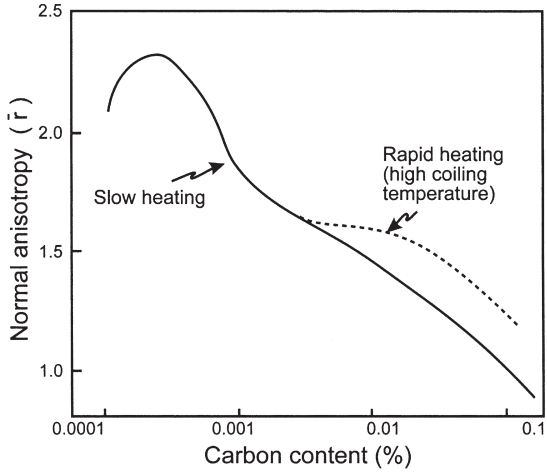

Fig. 15.6. Effect of carbon content on $\bar{\mathbf{r}}$-value of steel, (Hutchinson 1984).

The dramatic effect of carbon on drawability is well illustrated in figure 15.6. Two important factors are immediately obvious. First the value of $\bar{\mathbf{r}}$ is dramatically increased at low carbon levels and second there is an optimum value associated with a carbon level near 3 ppm. A detailed account of the role of carbon in texture control is given by Hutchinson (1984).

Table 15.5 provides a summary of the optimum conditions for batch and continuous annealing of low carbon steels.

15.3.3.3 The role of manganese

Manganese is the major alloying element present in these steels and its influence is thought to be the result of solid solution effects, phase forming effects and complex interactions with other elements such as carbon, nitrogen, oxygen and phosphorus. The extensive investigations of Hu and colleagues (Hu and Goodman 1970, Cline and Hu 1978, Hu 1978) showed that manganese adversely affects the drawability (fig. 15.7).

It was thought originally that the effect of manganese was due to solute drag that provided the opportunity for nucleation and growth of unfavourably oriented grains. However, it is now known that the effect is due to the simultaneous presence of carbon and manganese, which interact to form C–Mn dipoles. The importance of this interaction was demonstrated in a number of important papers during the period 1970–1984, and details are given by e.g. Fukuda and Shimazu (1972), Abe et al. (1983), Hutchinson and Ushioda (1984) and Osawa (1984).

15.3.4 Ultra low carbon steels

Although the very high $\bar{\mathbf{r}}$ values associated with the low carbon steels of figure 15.6 suggest that good drawability is readily available by carbon reduction, this is an overly

Table 15.5
Optimum conditions for texture and anisotropy development in low carbon steels (Hutchinson 1993).

Parameter	Batch annealing	Contin. annealing
Carbon	low (*)	low (***)
Manganese	low (*)	low (**)
Microalloying	Al (***)	()
Soaking temp., °C	high (***)	low (*)
Finish rolling	$>A_3$ (**)	$>A_3$ (**)
Coiling, °C	low, <600, (***)	high, >700, (***)
Cold rolling, %	~70	~85
Heat. rate, anneal	20–50°C/hr. (***)	5–20°C/sec. (**)
Anneal temp., °C	~720 max	850 max

(), not critical, (*) significant, (**) important, (***) vital.

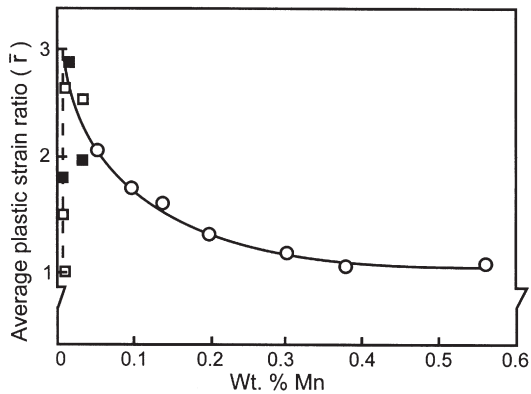

Fig. 15.7. Effect of manganese on $\bar{\mathbf{r}}$-value, (Cline and Hu 1978).

simple view as other property requirements such as ductility and resistance to strain ageing must also be considered. In general the ductility is improved by the low yield strength and high elongation resulting from a decreased carbon content while strain aging can be eliminated by lowering the combined carbon/nitrogen content to $< 0.001\%$ and light temper rolling (~0.5% reduction). However these effects are limited and the production of the superior grades (e.g. fig. 15.9) requires the additional use of strong carbide forming elements such as niobium and titanium. Little more than the stoichiometric equivalent is needed and these small amounts are considerably less than those used in the earlier interstitial-free steels where the alloy content was often as high as 10× the stoichiometric equivalent. Both elements are effective in reducing the planar anisotropy of elongation and $\Delta\mathbf{r}$ and Satoh et al. (1985) found that this was particularly so for niobium.

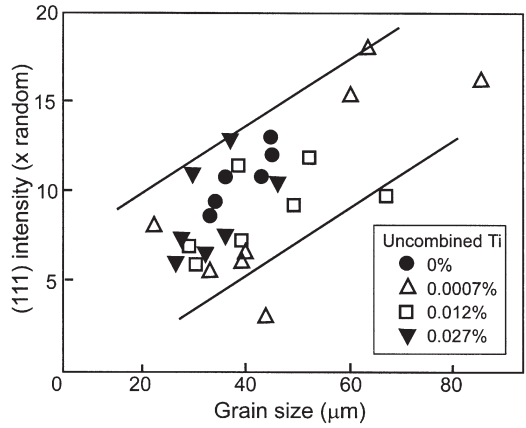

Fig. 15.8. Texture intensities for {111} parallel to sheet plane in very high purity steels having different levels of uncombined titanium, as a function of the grain size, (Takazawa et al. 1995, in Hutchinson and Ryde 1997).

Several explanations of the strong {111} texture have been given (Hutchinson and Ryde 1995). These include interference by second-phase particles, the influence of hot rolling conditions on the starting conditions, solid solution effects of the alloying elements and scavenging of carbon and nitrogen by the alloying elements. Figure 15.8 from a detailed investigation by Takazawa et al. (1995) shows data for {111} texture strength in very high purity iron–titanium alloys. In the absence of any effect due to titanium in solid solution. Hutchinson and Ryde conclude that the excellent deep drawability of titanium-alloyed IF steels (and by inference niobium containing steels) is due to the scavenging action of removing carbon and nitrogen from solid solution.

Figure 15.9 from the work of Fudaba et al. (1988) gives details of the quality of the best IF steels now available. These steels have $\bar{\mathbf{r}}$ values as high as 2.5 and tensile elongation of 53%, and have in addition a very low value of planar anisotropy (see the results for $\mathbf{r}_{45°}$ in fig. 15.9). The absence of planar anisotropy is particularly significant in the production of drawn rectangular shapes.

The outer panels of automobile bodies must be baked to harden the surface coating and this is usually done at ~190°C. Because of the possibility of strain ageing, any carbon in solution should be eliminated or stabilised. In the case of continuously annealed, normal drawing grades of low carbon steel, strain ageing is eliminated by the introduction of an over-aging stage. For the higher grade steels containing titanium and niobium this treatment is not necessary. Since the carbides are stable to ~830°C there is very little carbon in solution during annealing and high cooling rates can be used.

15.3.5 Extra low carbon, high strength steels

In addition to drawability and resistance to strain aging, automobile outer panels should have high strength. This is provided by the addition of solution hardening elements such as phosphorus (0.06–0.08%) and manganese (0.5–0.8%). Unfortunately phosphorus in

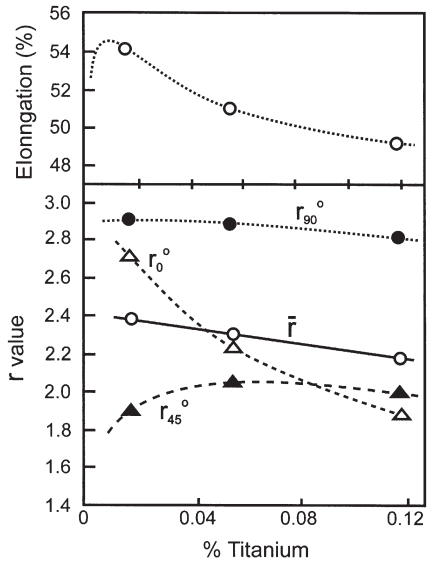

Fig. 15.9. Effect of titanium content on the mechanical properties of 0.8 mm, 0.007%-Nb steel cold-rolled 81%, (Fudaba et al. 1988).

these steels increases the tendency to develop forming cracks but this can be controlled by the further addition of very small amounts of boron (Fudaba et al. 1988).

Further strength can be obtained by taking advantage of the normally deleterious phenomenon of strain aging. Bake-hardenable steels are produced with a small, but controlled amount of residual solute carbon. Resistance to room temperature aging is obtained but the yield strength is increased when the dislocations become stabilised during baking. As a consequence the yield strength is low during forming but high after baking. The required amount of solute carbon can be obtained by adjustment of the annealing cycle but as it has been pointed out earlier, small amounts of solute carbon have a deleterious effect on the development of the desired {111} texture during annealing. The solution is simple and elegant (Obara et al. 1984, Abe and Satoh 1990). As before, the carbon is stabilised as niobium carbide before recrystallization is complete; this ensures a strong {111} texture. The temperature is then raised so that a small amount of carbon goes into solution. As recrystallization is almost complete before this happens the texture is unaffected.

15.4 RECENT DEVELOPMENTS IN GRAIN-ORIENTED, SILICON STEEL SHEETS

15.4.1 Introduction

The production of grain-oriented, electrical steels is probably the best known example of the beneficial effects of recrystallization control during processing. The subject has been

reviewed many times (see, for example Dillamore 1978b, Luborsky et al. 1983) and we begin with only a brief summary of the requirements and the processes used and a similarly brief account of their significance. This is followed by a review of recent developments relating particularly to changes in composition, the possibility of producing cube-oriented sheet and the control of domain size.

15.4.2 Production of silicon steel sheets

The sheets or laminations used as transformer cores are usually made from a 3%Si, carbon-free, sheet steel. The essential requirements are easy magnetisation, low hysteresis loss and low eddy current loss. The first and second of these are governed principally by composition, orientation and purity. It would be advantageous to use a somewhat higher silicon content but such alloys are brittle and cannot be cold rolled. Magnetisation is easiest in the $<100>$ directions (fig. 15.10) and great care is taken to see that a strong preferred orientation is developed with a $<100>$ rolling direction. In practice the texture that is commonly found is the well known $\{110\}<001>$ Goss texture. The state of internal stress and the smoothness of the sheet surface are also important. Eddy current losses are also affected by these parameters but more importantly by grain size, sheet thickness and stresses introduced by the insulating coatings applied to the sheets. The properties are optimised by small grain size, reduced thickness and minimum internal stress. Finally, it would be desirable to have the smallest possible domain size and maximum domain wall mobility (Kramer 1992).

Present day practice stems from the work of Goss (1934a,b) who patented a technique for developing a strong $\{110\}<001>$ texture. This process is called the **Armco**, or two-stage cold rolling method, and a typical production schedule is summarised in table 15.6. The data shown are approximately correct, although different manufacturers use slightly modified compositions, temperatures, gas mixtures, coatings etc.

There are three important requirements in the Armco process:

- Provision must be made for the nucleation of $\{110\}<001>$ grains.

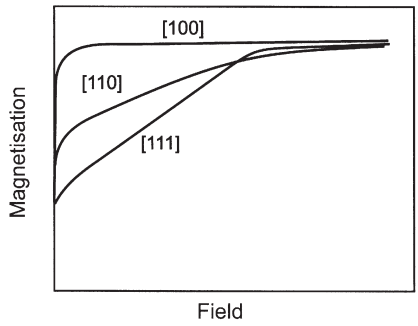

Fig. 15.10. Relationship between magnetisation and field for simple crystallographic directions in iron, (after Honda et al. 1928).

- These grains must be able to grow.
- Grains of other orientations must not grow.

The desired $\{110\}<001>$ orientation first appears during the initial hot rolling as a friction-induced shear texture at and near the surface. In the normal course of events it would be largely lost during cold rolling and be replaced by the usual two-component $\{112\}<110> + \{111\}<110>$ texture (§3.3). The use of two, light, cold rolling stages ensures that although these components are produced, their presence is controlled. In addition, the Goss orientations are not completely lost. They survive at the centres of transition bands separating the above orientations and in this environment nucleation is favoured so that some $\{110\}<001>$ grains appear in the annealing texture after the decarburising anneal. These grains are somewhat larger than those of the other orientations, and during the final texture anneal they grow by abnormal grain growth to dominate the final texture.

The necessary conditions for their growth are provided by microstructural control. A fine dispersion of manganese sulphide is generated by cooling the slab rapidly before hot rolling. These particles are resistant to rapid coarsening and, by preventing normal grain growth (§11.4) keep the matrix grain size small during the early stages of the final high temperature annealing. As Ostwald ripening and dissolution proceed, abnormal grain growth becomes possible and the desired Goss-oriented grains grow and dominate the microstructure. Abnormal grain growth is also promoted by the presence of a sharp texture (§11.5.3). The possibility of generating undesirable orientations by surface nucleation processes is eliminated by the addition of sulphur to the MgO surface coating. This prevents the growth of surface grains and the sulphide formed is eventually lost by reaction with the hydrogen atmosphere.

A second processing schedule, sufficiently different to avoid direct problems with patent laws, was developed and patented by Nippon Steel Corporation (Taguchi et al. 1966, Sakakura 1969). Details of this **Nippon Steel** process which uses a single cold rolling stage, and aluminium nitride as an additional grain growth inhibitor are also summarised in table 15.6. Typically these steels contain ~0.025% aluminium and ~0.01% nitrogen. The resultant AlN particles are much less stable than MnS and because they coarsen rapidly the processing involves rapid cooling after hot rolling (Step (b) in table 15.6). For the same reason two-stage cold rolling with intermediate annealing is not possible. The resulting large cold rolling reduction results in a decreased $\{110\}<001>$ component and a larger grain size but this is off-set by an increased perfection of the final orientation. The MgO coating used in the final annealing treatment contains metal nitrides as well as sulphur. The nitrides help to control the decomposition of the AlN particles.

There has been continuing controversy about the validity of the patents involved and an investigation by Harase and Shimazu (1988) is significant. These workers investigated two batches of material, one containing only MnS as an inhibitor and the other containing both MnS and AlN. Samples from each batch were processed by both the single, and double cold rolling routes. Abnormal grain growth, with a strong Goss texture, occurred in the presence of AlN particles irrespective of the rolling schedule used. If only MnS particles were present, abnormal grain growth occurred only after two-stage cold rolling. In this material the texture was described as $\{334\}<9,13,3>$ which is similar to the normal $\{111\}$ type textures found in annealed low carbon steels.

Table 15.6
Processing of grain oriented steel.

Armco process	Nippon steel process
(a) Soak at ~1340°C; hot roll to 2 mm	(a) Soak at ~1350°C; hot roll to ~2 mm
(b) Cold roll to 0.5–1 mm	(b) Hot band anneal 1125°C, air cool to 900°C, water quench to 100°C
(c) Anneal at 950°C in dry H_2/N_2 (80:20)	(c) Cold roll
(d) Cold roll to finished size	(d) Decarburise at 850°C in wet H_2; dew point 66°C.
(e) Decarburise at 800°C in wet H_2; dew point 50°C	(e) Coat with $MgO + 5\%TiO_2$
(f) Coat with MgO	(f) Texture anneal at 1200°C in H_2/N_2 (75:25)
(g) Texture anneal at 1150°C in pure H_2	

Both processes are being continually refined but it is generally accepted at this time, that the Nippon Steel process leads to a more perfect Goss texture but to a larger grain size. Some of the changes are referred to in the next section.

15.4.3 The development of the Goss texture

The strong $\{110\}<001>$ texture develops from near-surface recrystallized grains during the final high temperature anneal, and although this is a critical factor in the processing, there is still no generally accepted explanation of the scientific basis of this phenomenon, as witnessed by the large number of recent papers expressing contradictory views, and the brief critical review of Morawiec (2000). Factors that are considered to be important include the relative size of the initial Goss grains, their orientation with respect to the other grains, and the role of the second-phase particles. The latter two factors are consistent with the fact that the onset of abnormal grain growth requires either a strong texture (§11.5.3) or boundary pinning by second-phase particles (§11.5.2).

Size – May and Turnbull (1958), and Inokuti et al. (1987) have suggested that the primary Goss grains have a size advantage over grains of other orientations, but this has not been confirmed by later workers (Harase and Shimizu 1988, Böttcher et al. 1992), and is not now considered to be a major factor.

Orientation – It is generally accepted that orientation is the most important factor in determining the growth of the secondary Goss grains. There are comparatively few Goss grains in the primary microstructure, but many of these are related to the more plentiful

$\{111\}<112>$ grains by orientation relationships close to the high coincidence CSL ($\Sigma 9$) relationship of 38.94° about a $<110>$ axis, and this has been considered to be important (Harase and Shimizu 1990, Bölling et al. 1992).

Boundary mobility – As discussed in §11.5.3, abnormal grain growth can occur due to differences in boundary mobility, and a higher mobility of the near $\Sigma 9$ boundaries has been suggested as the cause of the abnormal growth of Goss grains (Abbruzzese and Lücke 1986, Harase and Shimizu 1990). However, as pointed out by Hutchinson and Homma (1998), there is little evidence of an enhanced mobility of such boundaries.

Second-phase particles – Abnormal grain growth occurs as the grain growth inhibiting particles coarsen and dissolve. The Zener pinning pressure on grain boundaries by particles is directly proportional to the boundary energy (equation 4.24), and there is some evidence (Humphreys and Ardakani, 1996) that this may allow preferential growth of low energy CSL boundaries. Although there is no direct evidence of a lower energy for $\Sigma 9$ boundaries in steel, Hutchinson and Homma (1998) show that this could account for the development of the microstructure and texture during abnormal growth in silicon-iron. Although it does not appear to have been considered by researchers, it is also possible that indirect effects such as more rapid particle dissolution at the CSL boundaries compared to other boundaries, could play a role in nucleating abnormal growth.

15.4.4 Recent developments

Thin gauge, high silicon content, perfect crystal alignment and small domain size are the fundamental features of an ideal electrical steel sheet (Bölling et al. 1992). Recent developments have involved:

- Small but significant alterations to composition
- Improvements in the perfection of the final texture
- Reductions in sheet thickness
- Control of the domain structure
- The development of cube-textured material
- Production of amorphous sheet by melt spinning techniques
- The direct casting of strip.

Some of these are discussed below.

15.4.4.1 Composition

It has been generally accepted that the magnetic properties of electrical steels would be considerably improved by increasing the silicon content; unfortunately increase beyond the current maximum of ~3.1% leads to embrittlement during cold rolling.

Nakashima et al. (1991a) examined steels produced by the single-stage cold rolling process and containing up to 3.7% Si, and particular attention was paid to the abnormal grain growth aspects. It was found that the effectiveness of grain growth inhibition in the single-stage process decreased as the silicon content increased and that

abnormal grain growth did not occur at all in the 3.7% Si sheet (final thickness 0.285 mm). However, at the higher silicon contents used in this study, the ratio of the α and γ phases is changed and there is a real possibility that this may have affected the state of the inhibiting precipitates of MnS and AlN. To overcome this, Nakashima et al. adjusted the carbon content of their steels so as to maintain a constant α/γ ratio at a temperature of 1150°C. The problem of silicon-induced cold brittleness could be largely overcome by strip casting of thin sheet or completely overcome by the use of melt spinning to produce amorphous material. Both techniques are being actively investigated and both are likely to be used in the near future.

Many small changes of composition have been investigated, particularly with respect to the growth inhibitors but details of many of these are to be found only in the voluminous and sketchy patent literature. Selenium and antimony react with manganese to form appropriate inhibiting phases and Fukuda and Sadayori (1989) claim that when used in conjunction with AlN the mean deviation from the $<001>$ for the Goss grains is improved from 7–3.5°.

15.4.4.2 Sheet thickness

It is well known that eddy current losses are substantially reduced in thin sheets, but until the early 1980s the thinnest sheets produced were 0.30 mm thick. Currently sheets of 0.23, 0.18 and 0.15 mm are available but production is not easy. Nakashima et al. (1991b) have shown that while abnormal grain growth produces a nearly perfect Goss texture in thick (0.60 mm) sheet, texture loss occurs increasingly in thinner material. This was attributed to a decline in the efficiency of the growth inhibiting process that permitted grains of undesirable orientations to reach the surface and become stabilised. The effect is overcome in current production practice by the addition of nitrogen to the furnace atmosphere during the final anneal (see table 15.6).

15.4.4.3 Cube texture

If a strong $\{100\}<uvw>$ texture could be induced, the resulting steel would have two $<100>$ directions in the plane of the sheet. Obvious advantages would exist for such a product and this would particularly be so for the cube texture, $\{100\}<001>$. The development of such a texture was first reported many years ago by Assmus et al. (1957) and Detert (1959) in thin (<0.6 mm) silicon iron sheet. Normal grain growth was retarded in the thin sheets and large grains with a {100} surface plane appeared. It was recognised that a process of surface-energy-controlled, abnormal grain growth (sometimes referred to as **tertiary recrystallization**) was occurring and it was found that, in the presence of environmental sulphur, grains with a {100} surface plane grew into the matrix structure. If the sulphur was removed {110} type grains grew. It was thought at one time that oxygen might be an active species in promoting {100} grains (Walter and Dunn 1960a) but this is now considered unlikely. Of the other Group VI elements the surface adsorption of selenium leads to the preferred growth of {111} surface oriented grains (Benford and Stanley 1969). The role of surface energy in promoting abnormal grain growth in thin sheets is discussed in §11.5.4. Kramer (1992) has reviewed the development and potential uses of cube-oriented sheet. Despite the apparent advantages offered by such sheet, several difficulties remain. The grain size is some four times greater than that of Goss textured sheet and the domain size is larger;

both effects are undesirable. As in other products the texture is never perfect and the domain structure in slightly misoriented sheet, where misorientation may occur about each of the surface {100} directions, is complicated. Kramer believes that these factors ensure that, in all but a few cases, cube textured sheet cannot compete with the best, current Goss-textured material.

A different approach to the production of cube oriented sheet has been described by Arai and Yamashiro (1989) who reported results for a 3.26% Si–Fe alloy directly cast to 0.37 mm thickness before final cold rolling. No inhibitors were used in this work and surface-energy-controlled grain growth occurred. Despite the lack of inhibitors a very strong $\{100\}<uvw>$ texture developed as the final sheet thickness decreased to 0.15 mm. In view of the current developments in strip casting this is a very interesting result.

15.4.4.4 Domain structure

As understanding of the physical metallurgy of electrical steels has developed there has been an upsurge of interest in the domain structure. Figure 15.11 from the work of Bölling et al. (1992) shows the domain structure at the surface of a typical, 0.23 mm, thick sheet. Points to be noted are the large grain size, the extent of local misorientation and the variation in domain wall spacing from 0.25–1.1 mm. Ideally the spacing should be small and this can be induced partly by means of the insulating coating applied to the surface, which develops high surface stresses. However, the length of the domains is governed primarily by the grain size which is large in strongly textured material. The problem can be solved simply by lightly scratching the surface in a direction normal to RD; the small local misorientation produced acts as an artificial grain boundary. Domain refining of this type is now carried out in commercial production by pulsed laser irradiation, which produces a very small local strain at the surface without affecting the insulating coatings, and the core losses are reduced by ~10%.

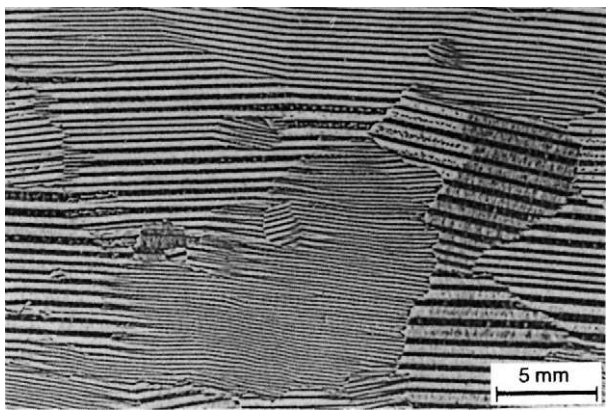

Fig. 15.11. Magnetic domains in high permeability grain oriented steel, (Bölling et al. 1992).

15.5 COMMERCIAL SUPERPLASTIC ALUMINIUM ALLOYS

15.5.1 Superplasticity and microstructure

Superplastic materials are polycrystalline solids which have the ability to exhibit unusually large ductilities. If deformed in uniaxial tension, a normal ductile metal will fail by necking after an elongation of less than 50%. However, superplastic alloys often exhibit elongations of several hundred percent and exceptionally, several thousand percent. In order to resist necking, the flow stress of the material must have a high strain rate sensitivity, or **m** value, where

$$\sigma = K\dot{\varepsilon}^{m} \tag{15.4}$$

and σ is the flow stress, $\dot{\varepsilon}$ the strain rate and K a constant.

This may be rewritten (Mukherjee et al. 1969) in an expanded form as

$$\dot{\varepsilon} = \frac{K'DGb}{kT}\left(\frac{b}{d}\right)^{p}\left(\frac{\sigma}{G}\right)^{1/m} \tag{15.5}$$

where **D** is the diffusivity, **d** the grain size, and **p** the grain size exponent (usually between 2 and 3).

For superplasticity, **m** must be greater than 0.3 and for the majority of superplastic alloys **m** lies in the range 0.4 to 0.7. A wide variety of metals, alloys and even ceramics can be made superplastic and there has been extensive development of superplastic aluminium and titanium alloys over the past 30 years. Recent reviews include those by Stowell (1983), Kashyap and Mukherjee (1985), Sherby and Wadsworth (1988), Pilling and Ridley (1989), Ridley (1990), Nieh et al. (1997) and Grimes (2003).

The production of superplastic microstructures in **any** crystalline material and the stability of such a microstructure during subsequent high temperature deformation, exploit the principles of recrystallization and grain growth discussed in this book. However, we will restrict the present discussion to superplastic aluminium alloys which provide very good examples of the application of microstructural control by thermomechanical processing to commercial practice. Although the earliest work on superplasticity concentrated on **microduplex** alloys which consist of approximately equal amounts of two phases, the aluminium alloys currently of commercial interest are all **'pseudo-single-phase'** alloys, i.e. they consist of an aluminium matrix with only relatively small amounts of dispersed second phases. Although special alloys have been developed for superplastic applications, it is now known that many conventional alloys may be made superplastic if thermomechanically processed in the appropriate manner.

At high temperatures, a superplastic alloy is characterised by a low flow stress (< 10 MPa) and a high resistance to non-uniform thinning. This allows the near-net-shape forming of sheet material using techniques similar to those developed for the bulge forming of thermoplastics. Superplastic forming (SPF) is thus an attractive option for the forming of complex shapes from sheet at low stresses, incurring much smaller tooling costs than for conventional cold pressing operations. However, the slow strain rates often necessary

for superplastic forming and the higher material costs have so far restricted the commercial exploitation of SPF to a relatively small number of specialised applications.

The mechanisms of superplastic deformation involve grain boundary sliding, dislocation glide and climb and diffusional processes; the balance between them remaining a matter of debate. The microstructural requirement is for a small grain size, typically less than 10 μm. Equation 15.5 shows that the smaller the grain size, the higher is the strain rate which can be used at a given stress. It is important that the grains are equiaxed, with high angle boundaries. It is also important that dynamic grain growth during SPF is minimised, otherwise, as seen from equation 15.5, the flow stress will increase during forming. The maximum superplastic strain is usually limited by grain boundary cavitation, which again is minimised by a small grain size.

The key to successful SPF is therefore the development of a very small grain size and the inhibition of dynamic grain growth during the forming process.

15.5.2 Development of the microstructure by static recrystallization

This processing route, typified by that developed by Rockwell (Wert et al. 1981), which is illustrated in fig. 15.12, is based on the mechanism of **particle stimulated nucleation of recrystallization** (§9.3) and has been used to produce superplastic microstructures in the high strength aerospace 7xxx series alloys (Al–Zn–Mg–Cr) such as AA7075 and AA7475.

Following a solution heat treatment, the alloy is overaged at ~400°C to produce a dispersion of large (~1 μm) intermetallic particles in addition to a stable dispersion of small (~0.1 μm) chromium-rich dispersoids. The material is then warm-rolled in several passes at 200°C to an 85% reduction. This temperature is low enough (§13.6.4) to ensure that deformation zones develop at the large particles, but high enough to prevent excessive work hardening by the small dispersoids. The alloy is then heated rapidly in a

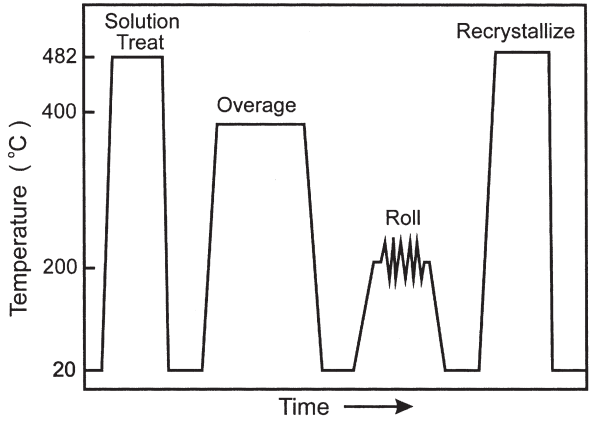

Fig. 15.12. Schematic diagram showing the four step thermomechanical processing treatment used for grain refinement of AA7075, (after Wert et al. 1981).

salt bath at 480°C to completely recrystallize. Particle stimulated nucleation occurs at the large particles and subsequent grain growth is inhibited by both the large and the small particles. Wert et al. (1981) found that the number of large particles per unit volume was approximately ten times the number of grains, indicating a very low efficiency of PSN. As the particle size of ~1 μm is on the borderline for PSN (§9.3.3) it is likely that recrystallization nucleates first at the larger particles, and the smaller particles are then engulfed before nucleation occurs at them.

AA7475 processed by this route has a grain size of ~10μm and is capable of tensile elongations of ~1000% if deformed at the relatively slow strain rate of 2×10^{-4} s^{-1} at 520°C.

15.5.3 Development of the microstructure by dynamic recrystallization

An alternative method of producing a fine grain structure in aluminium involves the type of continuous dynamic recrystallization discussed in chapter 14. The first recorded example of the use of this processing route was for the **Supral** alloys, such as Supral 100 (Al–6%Cu–0.4%Zr) and Supral 220 (Al–6%Cu–0.4%Zr–0.3%Mg–0.2%Si–0.1%Ge) which were developed specifically for superplastic application (Watts et al. 1976).

The alloys are cast from high temperatures (≥780°C) and rapidly chilled to avoid the precipitation of primary $ZrAl_3$. The alloy is given an initial heat treatment at ~350°C in which most of the Zr is precipitated as a fine dispersion of $ZrAl_3$ particles (volume fraction ~0.05 and particle size ~10 nm) which, once formed are relatively stable. A solution treatment may then be given at ~500°C which takes ~4% copper into solid solution, leaving the remaining 2% in the form of large (> 1 μm) $CuAl_2$ particles. The alloy is then warm worked at ~300°C, the small spacing of the $ZrAl_3$ particles preventing recrystallization (§9.5). This may be followed by a final reduction by cold rolling. Finally the heavily rolled sheet is superplastically formed at ~460°C. During the initial stages of this deformation (typically within a strain of 0.4), a microstructure of small (~5 μm) equiaxed grains with high angle boundaries evolves from the deformed microstructure. Tensile elongations of greater than 1000% can readily be obtained for Supral 220 at strain rates of 10^{-3} s^{-1} at 460°C. The grain size produced during SPF is strain rate dependent, and in many cases it is beneficial to begin the deformation at a high strain rate which produces a small grain size, and then reduce the strain rate once the recrystallized structure has evolved.

Despite considerable research, there is much debate as to the way in which the fine-grained 'recrystallized' microstructure evolves with strain, and in particular, as to how the average boundary misorientation increases with strain. Although many novel mechanisms have been proposed, none have been substantiated, and it is our view that the development of the microstructure is largely explainable by the normal mechanisms of deformation and annealing discussed earlier in this book.

One of the difficulties in studying the process has been that most investigations have started with heavily worked alloy, and the work of Ridley et al. (1998, 2000), who started with the cast microstructure is therefore significant. These authors also demonstrated the contributions of the alloying elements copper and zirconium in producing the superplastic microstructure. It was shown that most of the high angle

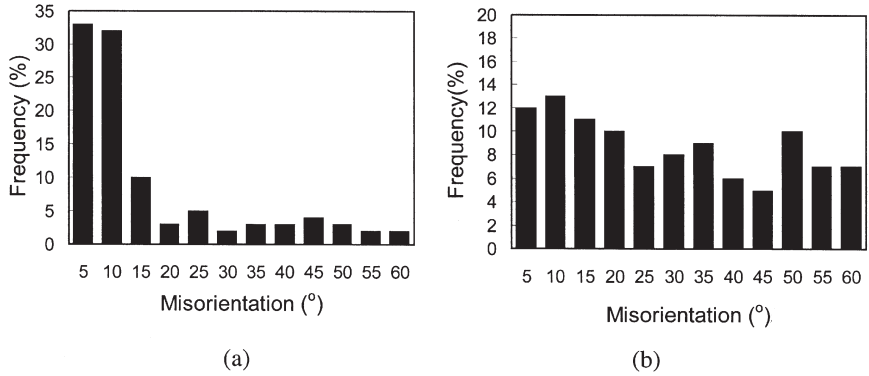

(a) (b)

Fig. 15.13. Distribution of grain boundary misorientations in a Supral-type alloy (Al–6Cu–0.4Zr); (a) After low temperature deformation, (b) After further tensile deformation at 450°C to $\varepsilon = 0.7$, (Ridley et al. 2000).

grain boundary in the final recrystallized, superplastically deforming material is already present before the final high temperature deformation at 460°C, and that during this deformation, dislocation glide and climb processes of the type discussed in §13.2, 'clean up' the dislocation and low angle boundary debris by dynamic recovery, to produce a subgrain structure (10–20 μm) which is consistent with the temperature and strain rate (or Zener–Hollomon parameter) of the superplastic deformation (equation 13.7). The microstructural development is therefore rather similar to that of geometric dynamic recrystallization (§14.4.1 and fig. 14.9) in that a large prior deformation at low temperature produces a small high angle boundary spacing (~5 μm), and that the final high temperature deformation conditions are such that the low angle boundary spacing (or subgrain size) exceeds the HAGB spacing, thereby producing a microstructure which consists almost entirely of high angle grain boundaries.

The essential stages in producing the small final grain size in an Al–Cu–Zr Supral-type alloy are thought to be as follows:

- On casting, the large amount of copper, results in a **small cast grain size** (~50 μm).
- The cold/warm working reduces the HAGB spacing significantly (equation 14.1). The presence of the Al_3Zr dispersoids prevents any static recrystallization during processing from cast billet to sheet, and therefore **very large total compressive reductions accumulate.** The small initial grain size (D_o in equation 14.1), also aids the production of a small HAGB spacing. At this stage the distribution of grain boundary character is as shown in figure 15.13a, containing a large fraction of low angle boundaries, which is typical of a deformed polycrystal.
- On deformation at 450°C, the LAGB size increases to the large size appropriate to the low value of Z or flow stress (equation 13.7). There is little HAGB migration, although some grain spheroidisation and localised dynamic grain growth (fig. 14.8) occur, producing an **equiaxed microstructure of grain size ~8 μm.** The microstructure now consists mainly of high angle boundaries (fig. 15.13b), and can be considered to have been 'recrystallized' as a result of a 'continuous' rather than a 'discontinuous' process.

This method of producing a fine grain size during the superplastic deformation itself is not unique to the Supral alloys, and similar processing routes are used to achieve superplasticity in other aluminium alloys. In particular, the newer strong lightweight aluminium–lithium alloys such as AA8090 (Al–2.5%Li–1.2%Cu–0.6%Mg–0.1%Zr) which are also resistant to static recrystallization, may undergo a similar type of dynamic recrystallization and show extensive superplasticity (Ghosh and Ghandi 1986, Grimes et al. 1987).

15.6 SUB-MICRON-GRAINED ALLOYS

In chapter 14, we discussed how stable fine-grained microstructures could be obtained by deformation to large strains (often termed **severe deformation**) at ambient or elevated temperatures. In the past few years, there has been a considerable interest in using such methods to produce alloys with micron-scale grains, and in this section we discuss the development and application of technologies based on these principles.

Sub-micron-grained (SMG) alloys may have extremely good mechanical properties, **and if it were possible to control the properties of bulk alloys by processing rather than by composition, the result would be fewer and simpler industrial alloys, with consequent economic and environmental benefits.** However, there are formidable problems in scaling-up the technologies and this remains a distant goal.

15.6.1 Background

Many industrially important metal-forming methods, such as rolling and extrusion impart large plastic strains and, as discussed in chapter 14, very fine grained microstructures may in certain cases be formed. However, during such processing, one or more dimensions of the work piece is continuously reduced and eventually foil or filamentary materials, having limited use for structural applications, are produced. There are however a number of large strain processing methods in which a sample can be deformed without any net change in its dimensions and there is no limit to the strain that can be achieved, provided the material has sufficient ductility. The concept of using such **redundant shape change** processes to achieve ultra-high strain deformations and produce microstructural improvements in alloys is by no means new and the method of forging and folding used to produce Samurai swords is one such process.

It should be noted that strain path changes involving redundant strains are not as efficient as direct straining in producing a small grain size on recrystallization as discussed in §7.2.1.3. However, as extremely large total strains can be used, this is not usually a limiting factor.

Deformation to large strains using redundant deformation methods was pioneered in the early 1950s by Bridgeman (1950) using **torsional straining under a compressive load,** and **equal channel angular extrusion (ECAE)** was developed in the early 1970s in the former Soviet Union as a method for deforming materials to large strains by simple shear (Segal et al. 1981). The current interest in the production and study of SMG

materials by severe plastic deformation began in the early 1990s, utilising the techniques of ECAE and torsion under compression. Because torsional straining can process only very small amounts of material, recent interest has centred on ECAE due to its ability to produce billets of material large enough to facilitate reliable mechanical property investigations. There is now a vast body of literature on the subject, and at least one international conference every year. However, the majority of the published papers deal with the material properties, making only limited attempts to characterise the microstructures, and in many cases no clear distinction is made between grains and subgrains. The deformation geometry and strain paths are often very complex, and there have been few serious attempts to determine the mechanisms by which the microstructures evolve.

The range of alloys which have been investigated is very large, and because the material is usually constrained during the deformation, even comparatively brittle materials such as intermetallics may be successfully processed. The subject has recently been reviewed in detail by Valiev et al. (2000) and Prangnell et al. (2001).

15.6.2 Processing methods

There are many methods which have been used to produce SMG alloys, and these are summarised below.

15.6.2.1 Torsional straining

One method that has been used with a wide range of materials is that of torsion under hydrostatic pressure, adapted from the Bridgeman anvil (Bridgman 1950, Saunders and Nutting 1984, Valiev et al. 1992). In this technique (fig. 15.14a), a thin disc, typically the size of a coin, is deformed in torsion using the friction provided by the application of a large hydrostatic pressure ($\sim$5 GPa). The equivalent strains that have been induced with this method are typically of the order of 7, and grain sizes of $\sim$0.2 μm have been produced by deformation at room temperature. This technique cannot readily be scaled up and is therefore most suitable for small-scale laboratory investigations.

15.6.2.2 Reciprocating extrusion

In this method, shown schematically in figure 15.14b, a billet is extruded from one chamber to another and then is re-extruded into the first chamber (Richert and Richert 1986). The distance between the two extruding rams is kept constant by use of an external housing, thus creating a constant volume die cavity during reciprocal ram movements. As the die cavity volume is constant, the billet has no free surface and is therefore kept under compression on either side of the extrusion orifice. The pressures required are very large, and there is little reported use of this method.

15.6.2.3 Multiple forging

Multiple forging has evolved from the conventional forging operations of breakdown forging and upsetting, and if this method is repeated a large number of times it is possible to significantly refine grain sizes (e.g. Sakai 2000). The technique is

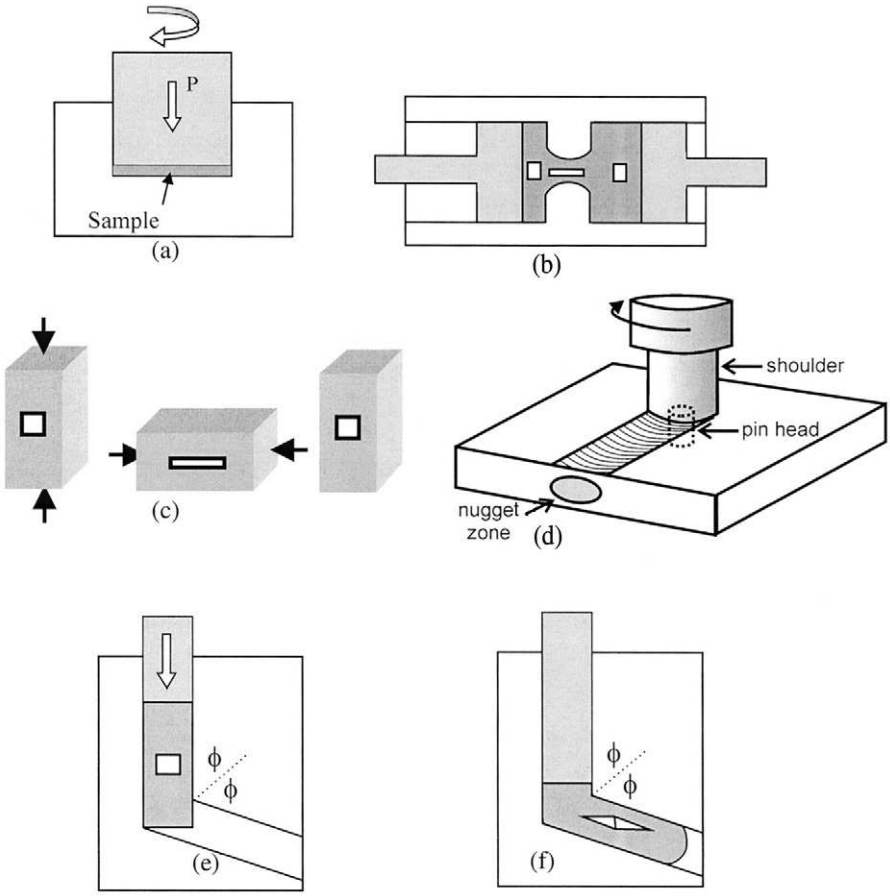

Fig. 15.14. Methods of deforming materials to very large strains; (a) Torsion under hydrostatic pressure, (b) Reciprocating extrusion, (c) Multiple forging, (d) Friction stirring, (e) and (f) Equal channel angular extrusion. The white regions indicate the shape changes during deformation.

based on upsetting a rectilinear block of metal followed by rotation to another orthogonal face and subsequent compression. The process is repeated on all orthogonal faces in such a manner that cubic dimensions are restored every third compression. The technique is schematically illustrated in figure 15.14c and because the material is not constrained, the deformation must be performed at high temperature to prevent cracking. This technique of severe plastic deformation is not as effective for grain refinement as other severe plastic deformation techniques as the strains are redundant in nature, the deformed elements being restored to their original shape every third deformation. However, it can be carried out on standard equipment and can be used for reasonably large billets.

15.6.2.4 Friction stirring

The technique of friction stir welding is of great interest to the aerospace industry as a means of joining non-weldable aircraft alloys (Mahoney et al. 1998, Norman et al. 2000). A friction stir weld is created by butting two components together and stirring one component into the other by the action of a rotating tool under a compressive load applied by the tool. The tool effectively grips material from one side of the join and as it rotates forces material under the tool to the other side of the join. As the tool applies a compressive load, it is possible for each material element to experience more than one rotation as the tool progresses along the join. In this manner, the technique is akin to torsion under compression discussed above. However, as the tool moves over the sample, significantly larger volumes of material are deformed. The technique, which is illustrated in figure 15.14d, typically produces 1–3 μm grain structures in the dynamically recrystallized nugget zone (Norman et al. 2000). It would be feasible to use this technique (in the absence of a join) as a method of severe plastic deformation of sheet materials. This would simply be accomplished in relatively thick sheet materials by friction stirring the whole sheet with overlapping 'weld' runs.

15.6.2.5 Equal channel angular extrusion

The most widely used method is that of Equal Channel Angular Extrusion (ECAE) developed in the former Soviet Union by Segal and colleagues (Segal et al. 1981). Of the possible methods for obtaining very high plastic strains it has arguably the simplest deformation mode, which under ideal conditions is a simple homogenous in-plane shear. This aids the quantitative interpretation of the development of the deformation microstructures. The technique can also be scaled up to produce substantial samples for property determination.

During ECAE the sample is extruded in a closed die which has two intersecting channels of equal size (fig. 15.14e) offset at an angle 2φ. Assuming there is no friction and a sharp die corner, the sample will be subjected to a homogenous shear, apart from at its ends, which can be shown to be simply dependent on the die angle (2φ) by:

$$\gamma = 2\cot\phi \tag{15.6}$$

For multiple passes (n) the strains can be summed and an equivalent strain (ε_E), which enables comparison with other deformation processes, can be defined (Segal et al. 1981) as

$$\varepsilon_E = \frac{2n}{\sqrt{3}}\cot\phi \tag{15.7}$$

The above analysis can also be used to predict, in a material of initial grain size D_0, the separation of the grain boundaries, (H) as a function of strain, for a constant strain path.

$$H = \frac{D_0}{\sqrt{1+\gamma^2}} \tag{15.8}$$

Although the concept of an equivalent strain is useful for comparing different processes such as rolling and ECAE, the differences in the deformation modes between these

processes lead to quite different slip activities and the microstructures and textures developed will therefore differ. During ECAE the grains are elongated by shear, and the separation of the original grain boundaries (H), as given by equation 15.8, reduces with increasing strain at a lower rate than for deformation by rolling (equation 14.1).

The net shape of the billet, which, in laboratory-scale experiments, is typically ~15–20 mm in diameter, remains almost constant during processing, and therefore there is no geometric constraint on the total strain that can be achieved. Usually, equivalent strains of 5–10 are sufficient to increase the high angle boundary content sufficiently to produce a material which will undergo continuous recrystallization to develop a sub-micron-grain size, the principles being those previously discussed in chapter 14. The most comprehensive microstructural characterisation of aluminium alloys and steels processed by ECAE have been obtained by high resolution EBSD (Appendix 2), by Prangnell and colleagues, e.g. Humphreys et al. (1999), Gholinia et al. (2000) and Prangnell et al. (2001).

The die angle is an important factor in ECAE processing, not only by determining the strain per pass, but also the geometry of deformation (Nakashima et al. 1998). It is not necessary to keep the work piece orientation the same for each repeated pass, and several permutations are possible, the most common being either no sample rotation or a rotation of 90° between passes. It has been claimed that a 90° rotation between passes is most effective in breaking up the microstructure and producing an equiaxed sub-micron grain structure (Iwahashi et al. 1998) when a 90°die is used. However, it has been found that for a 120° die, the grain structure is more effectively broken up and a higher fraction of high angle grain boundaries is formed if the sample orientation is maintained during successive passes (Gholinia et al. 2000). Prangnell et al. (2001) have given a detailed discussion of the effects of strain path on microstructural evolution during ECAE processing.

15.6.2.6 Accumulative roll bonding

Accumulative roll-bonding (ARB), which was developed in Japan, is a novel, yet simple rolling process for introducing high strains into rolled material. The first reported use of ARB was by Saito and co-workers (Saito et al. 1998) who achieved submicron grained microstructures in a commercially pure aluminium alloy (AA1100). Later papers, (e.g. Saito et al. 1999) explain the process in more detail and discuss its application to a range of aluminium alloys and to steel.

Two sheets of metal of similar dimensions are degreased and wire brushed to aid bonding. They are then stacked, fastened together by rivets, heated to below the recrystallization temperature and rolled by 50%. This produces a sheet almost identical in dimensions to the starting sheet prior to rolling. The process is then repeated until the desired strain is reached. The ARB process is cyclic in nature and theoretically can be applied without any strain limit.

Accumulative roll-bonding, as a process of severe plastic deformation appears to have several advantages. Most importantly, it is one of the few severe plastic deformation processes that are easily scalable to industrial needs, as ARB is an adaptation of an already existing process. In addition, due to the nature of rolling, the productivity of the process once scaled, would approach that of conventional rolling. ARB has the

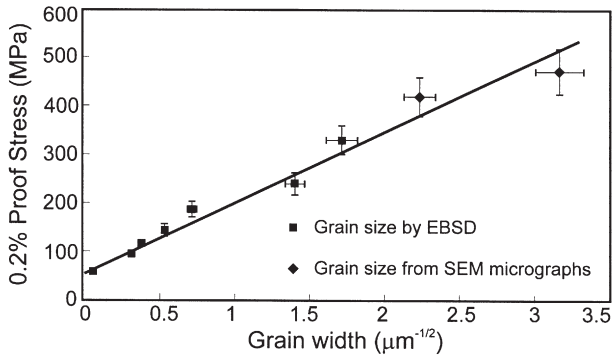

Fig. 15.15. The effect of grain size on the yield strength of Al–3%Mg, (Hayes et al. 2000).

potential for producing large pieces of material in sheet form with uniform 'through-thickness' ultra-fine grained microstructures.

A number of problems may arise during processing, including edge cracking and the introduction of surface oxide. The temperature range for processing depends on the material, and may be rather narrow, the lower limit being that at which good bonding occurs, and the upper, that at which recrystallization or excessive microstructural coarsening occurs.

15.6.3 Properties and applications of SMG alloys

The Hall–Petch relationship of equation 6.29 has previously been found to apply to most conventional alloys with grain sizes larger than ~5 μm, and recent investigations of aluminium alloys deformed by ECAE have confirmed its validity for grain sizes as small as ~0.2 μm (Hayes et al. 2000, Horita et al. 2000b) as shown in figure 15.15. The ten-fold increase in yield strength in this alloy, and comparable increases found for AA1100 and AA3004 alloys (Horita et al. 2000b) due to the grain size reduction, demonstrate that **such processing can confer on alloys of intrinsic low or moderate strength, properties typical of high strength age-hardened aluminium alloys.**

Another potential application of SMG alloys is for high strain-rate superplasticity (e.g. Higashi 2001). The production of grain sizes of ~10 μm in commercial aluminium alloys for superplastic deformation was discussed in §15.5. For such conventional superplastic alloys the optimum strain rate is typically $\sim 10^{-3}$ s^{-1}, and such low strain rates are a limiting factor in the application of the technology. However, as the grain size is reduced, it is seen from equation 15.5 that the superplastic strain rate for a given flow stress, increases, and a reduction of the grain size from ~10 μm to ~1 μm would allow the use of strain rates of ~1 s^{-1}. For such applications at elevated temperatures the thermal stability of the microstructure of the alloy is a critical factor, and as discussed in §14.5, a large amount of boundary pinning by second-phase particles is required, necessitating the use of specially designed alloys.

15.6.4 Summary

The production of sub-micron-grained alloys by deformation processing has been shown to be possible for a very wide range of materials, and it has been demonstrated that such alloys may have desirable mechanical properties at ambient temperatures and be suitable for high strain rate superplasticity. The two most important challenges are to scale-up the processing so that large quantities of material can be produced, and to produce the materials at a viable economic cost.

ThisPageIntentionallyLeftBlank

Chapter 16

COMPUTER MODELLING AND SIMULATION OF ANNEALING

16.1 INTRODUCTION

In order to control the microstructure, texture and properties of an alloy during a complex industrial thermomechanical treatment, there is a need for quantitative models which will accurately predict the effect of the processing parameters on the material which is produced. The empirical approach, which has long been used, is now recognised as being of limited value and, in many cases, the cost of industrial scale parametric experimental investigations is prohibitively expensive. Many major metal-producing companies, particularly in the aluminium and steel industries, have now recognised that in order to have any predictive value, models are needed which are based on sound physical concepts (Melton 1999, Ricks 1999). Because of the complexity of industrial thermomechanical processing schedules and our lack of a sound understanding of many of the annealing phenomena, this remains a long term objective.

16.1.1 The role of computer simulation

In discussing recovery, recrystallization and grain growth in earlier chapters, we have tried to show wherever possible, how an understanding of the physical mechanisms can lead to the development of quantitative models of the process. The ideal model would be

analytical and based on sound physical principles which perfectly describe the annealing process, thus allowing prediction of the resultant microstructure, texture and kinetics. It is clear that because of the complexity of the processes involved, we are still far from this goal and in part this is due to the heterogeneous nature of many annealing processes. Whereas it is feasible to describe simple processes such as the annealing of a dislocation dipole with some accuracy by analytical means, the nucleation of primary recrystallization or the onset of abnormal grain growth are catastrophic events which depend not upon the average microstructure, but upon heterogeneities in the microstructure. Analytical methods such as the JMAK approach and its extensions discussed in chapter 7 or the cellular stability model of chapter 10 are useful in giving a broad description of a process, but cannot yet handle the spatial complexities of recrystallization in real materials. For these reasons, much effort has in recent years been put into the development of computer simulations of annealing. There have been several methods of approach, each with its own particular advantages and disadvantages. Some of the models involve simulation at or close to the atomistic level and once the rules for the motion of the basic units are defined then little further input is necessary. Other computer models use analytical equations to describe parts of the annealing process and allow the computer to deal with the heterogeneity of the annealing.

16.1.2 The status of computer simulation

Computer simulations have been criticised as being incapable of making any significant predictions, and it is of course true that they will not reveal any micromechanisms which occur on a smaller scale than the basic units of the model. However, by dealing with the annealing of a complete microstructure and thus taking into account long range cooperative effects and those due to heterogeneity, the models are capable of revealing hitherto unknown phenomena. Bate (2001a) provides a concise critical review of the current status of the modelling of deformation and annealing. Whilst most of the models produce realistic microstructures or textures, the use of these models is at present limited by several factors.

- The size of the model, although this becomes less of a problem as computing power increases.
- The lack of accurate input data, e.g. deformation structures, boundary properties.
- Inadequate understanding or modelling of the basic physical processes. For example, most 'recrystallization' models are essentially growth models, with no detailed or physically-based modelling of nucleation.

Unlike an analytical solution, it is usually impossible for the reader to verify a computer simulation, and there is always a real danger that the output of a model may be the result of faulty, inaccurate or inadequately detailed modelling. A large number of models are regularly presented in the literature as being successful. However, sensitivity analyses of these models are rarely given, nor are the models tested with a range of parameters against good experimental data. For these reasons the results of computer simulation should be treated with great caution. This is illustrated by the problems encountered in using 2-D models to simulate the grain growth of 3-D microstructures as discussed in §11.2.4.2 and §11.5.2.3.

One of the most useful roles of computer simulations is to draw attention to areas where further theoretical or experimental work is needed. A good example of this is the computer simulation of **grain growth,** which has in the past 20 years, by producing results which have questioned the accepted understanding of the subject, stimulated a large amount of theoretical and experimental work, thus rejuvenating an important field which had become dormant. As our understanding of the physical phenomena involved in annealing increases, modelling techniques become more sophisticated, and as the power of computers grows, the role of modelling and computer simulation will become increasingly dominant.

The modelling which has been carried out to date may be divided into two general categories. There are the **micro models** which aim to deal with individual processes such as deformation or annealing, or perhaps only part of these, i.e. recovery, recrystallization or grain growth. Then there are the **coupled models** which may involve two models, e.g. combining a deformation and an annealing model, or may use many models in an attempt to simulate a large scale industrial process such as multi-pass hot rolling. In this chapter we will examine some of the micro models of annealing, with particular emphasis on topological models which can explicitly deal with spatial inhomogeneity. Other micro models which use parameters averaged over a larger length scale or use statistical descriptions of microstructure have been discussed elsewhere in the book, e.g. chapter 10. We will not consider computer simulations of plastic deformation here, and will only briefly comment on the use of coupled models.

16.2 MICRO MODELS

16.2.1 Monte Carlo simulations

In a series of papers, Anderson and colleagues (e.g. Anderson et al. 1984, Anderson 1986) developed Monte Carlo methods for the simulation of grain growth in two and three dimensions. More recently, the same approach has been used to study primary recrystallization, abnormal grain growth, dynamic recrystallization and dynamic grain growth.

16.2.1.1 The method and its application to grain growth

In this method, known as the Potts, or large-Q Potts model, the material is divided into a number of discrete points which represent the centres of small areas or volumes of material and these points are arranged on a regular lattice. These are the fundamental building blocks of the model. They are regions within which the microstructure is assumed to be homogeneous and structureless. Each block may have an attribute such as an orientation, but no subsidiary microstructure. Each region is given a number corresponding to a grain orientation as shown in figure 16.1, and a grain may comprise one or more blocks. A grain boundary is therefore characterised by the relative numbers (orientation) of the blocks, leading to boundaries of the type 4/6 and 3/7 etc. The grain boundary energy may then be specified in terms of the number pairs. For example, in the simplest case we might take like number pairs (e.g. 3/3) to have a zero energy and all unlike pairs to have the same high energy, which would be a reasonable approximation for high angle grain boundaries. Although, in a 2-D simulation, the boundary energy is

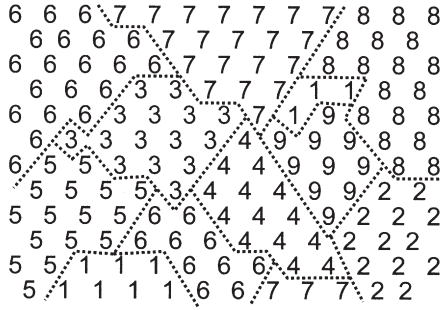

Fig. 16.1. The basis of the Monte Carlo simulation method.

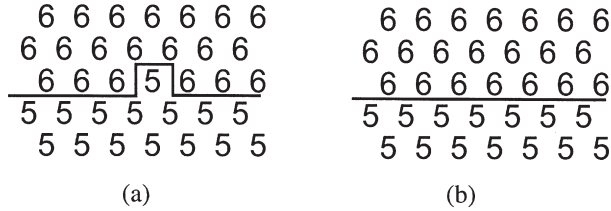

Fig. 16.2. Grain boundary migration in the Monte Carlo model.

satisfactorily simulated by the interaction between nearest neighbour pairs, in 3-D simulations it has been found necessary to consider interactions of up to third nearest neighbours.

The model is run by selecting a block at random, and reorienting it to one of the adjacent grain orientations. The energy of the new state is then determined. If the energy change (ΔE) is less than or equal to zero then the transition is accepted. However, if ΔE is greater than zero, then the reorientation is accepted with a probability which is typically $\exp(-\Delta E/kT)$, but other methods have been used, e.g. Raabe (2000). The unit of time in the simulation is the **Monte Carlo Step** which represents N attempted transitions, where N is the number of blocks or lattice sites in the model.

Transitions within a grain will not occur because of the severe energy penalty, but transitions at grain boundaries may occur, giving rise to boundary migration. Figure 16.2 shows how this arises. If the interaction energy between like sites is 0 and that between unlike sites is 1, then the energy of the configuration in 16.2a is greater than that of 16.2b by 2 units, thus providing a driving force for reducing boundary curvature. Consequently, as the model is run, the grains grow, as shown in figure 16.3, exhibiting many of the features of grain growth. Using larger arrays of at least 200×200 points, realistic microstructures are produced as shown in figure 16.4.

The techniques may be extended to three dimensions (Anderson et al. 1985), although the size of the array which can be used is rather limited, and the largest simulations are currently $\sim 400 \times 400 \times 400$ points (Miodownic et al. 2000). Comparison of the

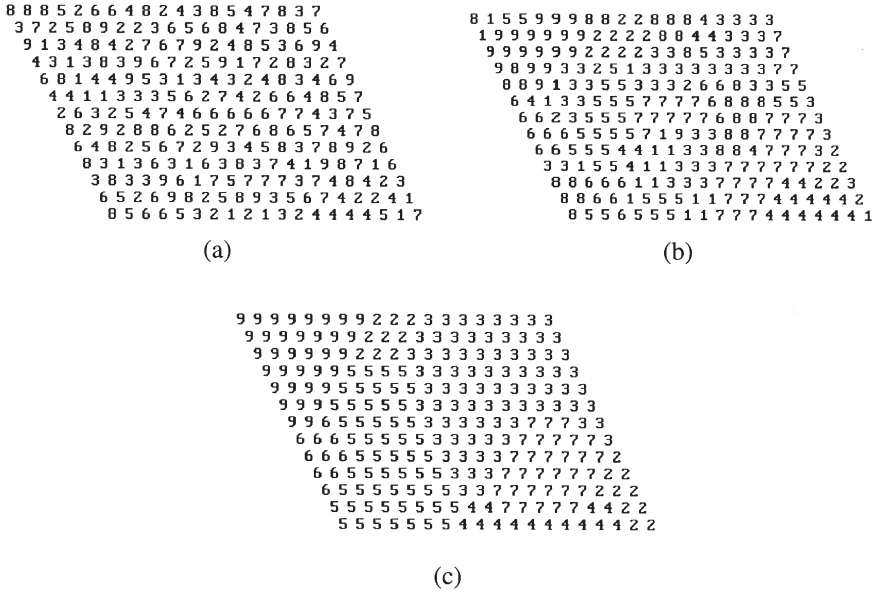

Fig. 16.3. Monte Carlo simulation of grain growth using a small array.

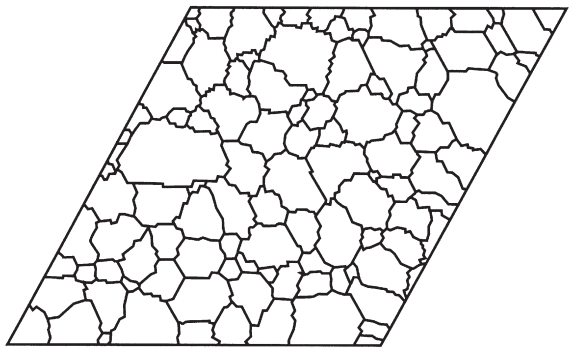

Fig. 16.4. A typical grain structure from a two-dimensional Monte Carlo simulation of grain growth.

2-D and 3-D simulations shows the grain size and size distribution in the 2-D case to be nearly identical to that found from a cross section of the 3-D simulation.

Quantitative measurements of the structures evolved in both 2-D and 3-D simulations exhibit many of the features of grain growth, including grain size distribution and kinetics, although as discussed in §11.2.4.2, earlier simulations predicted the kinetics incorrectly.

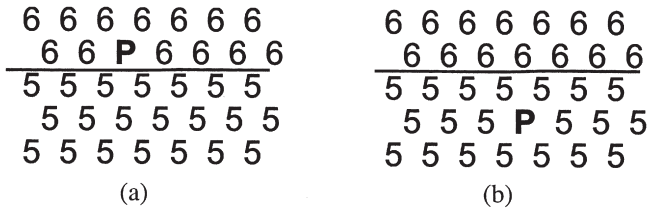

Fig. 16.5. Interaction of a grain boundary and second-phase particle in the Monte Carlo model.

This method has also been used to simulate the effect of second-phase particles on grain growth. This is done by selecting a fraction of individual blocks to be particles. These are assigned a different number to any of the matrix blocks and these sites are not allowed to switch orientation during the simulation. The 'particles' therefore have an interfacial energy equal to the grain boundary energy. If we calculate the total energy of the array shown in figure 16.5a where the 'particle' is on the grain boundary, we find that it is 2 units lower than that of 16.5b where the particle is inside a grain. Therefore there is an attraction between particles and boundaries leading to a pinning force similar to that discussed in §4.6. The volume fraction of particles may be varied, as it is simply the fraction of sites which are designated as particles. However, in most of the simulations, the particle size, which is one block, is not varied. The method has been used to investigate the limiting grain size in particle-containing alloys (§11.4.2), and as discussed in §11.4.2.4, the earlier simulations were consistent with the limited grain size predicted analytically for alloys containing large volume fractions of particles, where there is a strong correlation between particles and grain boundaries (equation 11.34). More recent larger scale simulations (Miodownic et al. 2000) tend to confirm the Zener relationship of equation 11.30, and the significance of these results is discussed in §11.4.2.4.

Abnormal grain growth may also be simulated by the Monte Carlo method (§11.5.2.3). This is done by introducing a very large grain, typically of a width equal to that of the array, into a particle-containing microstructure where normal grain growth has stagnated.

16.2.1.2 Application to primary recrystallization

The Monte Carlo simulation technique described above has been extended to the simulation of primary recrystallization (e.g. Srolovitz et al. 1986, Rollett et al. 1989a). A grain structure is first developed by growth as discussed above, and a stored energy **H** is given to all sites within each grain. In order to simulate heterogeneous deformation, the stored energy within a grain can be varied. Recrystallization 'nuclei', which are grains comprising three blocks with $H = 0$, are then introduced into the structure. Just as for grain growth, the pinning effect of second-phase particles may be studied.

Although reasonably realistic kinetics and microstructures are obtained, the use of such models for recrystallization is not as successful as for grain growth for a number of reasons.

- The volume of the model is generally too small relative to the scale of structure which is of importance in determining the recrystallization of real materials.

- In many Monte Carlo simulations, a second-phase particle is represented by a single lattice point, which is inadequate, because the effect of particles on recrystallization is strongly dependent on particle size as well as spacing (§9.2). Later simulations have allowed a variable particle size.
- The models fail to adequately model the nucleation stage, which is dependent on variations in the microstructure over distances of the order of 100 nm, and use empirical rules for nucleation, recovery and stored energy.

Monte Carlo modelling of recrystallization has now largely been replaced by the use of cellular automata models which are discussed in §16.2.2. These are closely related to the Monte Carlo method, but are capable of taking into account some of the more complex aspects of recrystallization.

16.2.1.3 Application to dynamic recrystallization

The Monte-Carlo simulation method has also been applied to dynamic recrystallization (Rollett et al. 1992, Peczac and Luton 1993). The 2-D simulations are similar to the static recrystallization simulations discussed above, except that the stored energy is allowed to increase with strain (time). In order to model dynamic recrystallization, 'nuclei', consisting of a group of say three units, are introduced at random into the lattice. These nuclei have no internal energy when they are introduced, but subsequently acquire energy during the 'deformation'. Nuclei grow or shrink according to the energy criteria which are discussed above. There is no explicit criterion for nucleation such as a critical strain, and the growth of the nuclei is determined by energetic criteria. There are a number of parameters which need to be given to the model. These include the rates of work hardening and recovery and the rate of nucleation and its dependence on the other parameters. Such models provide a means of examining the effect of variables on dynamic recrystallization. The outputs, which may be compared with experiment or theory are the stress-strain data and the grain size. However, the advantages of the Monte-Carlo approach over the well established methods which use semi-empirical equations to model hot working (§16.3) have yet to be demonstrated.

16.2.1.4 Success and limitations of Monte Carlo models

The merit of the Monte Carlo method lies in its inherent simplicity, its easy programmability and its straightforward implementation in 3-D. In its simplest form it can develop a realistic microstructure given little more than boundary energies. In its ultimate form, where the blocks are atoms, and the atoms are allowed to move freely, this becomes **molecular modelling** (§16.2.3**).** A Monte Carlo model develops the complete microstructure and is essentially deterministic apart from the local random fluctuations at the boundaries. It therefore automatically includes the topographic factors which have been a continuing problem in developing theories of grain growth (§11.2).

The Monte Carlo method is most successful when used in its most simple form, e.g. for grain growth in single phase materials, as in this situation the model requires very little input. However, for such applications it will ultimately be superseded by molecular dynamics modelling (§16.2.3). As the method is applied to more complex problems such as static and dynamic recrystallization, more assumptions need to be incorporated, more relationships, either empirical or analytical, need to be included in the model,

and the unit blocks of the model need to have a larger number of attributes. **Cellular automata** models are better equipped to deal with such problems.

Bate (2001a) has emphasised the limitations of Monte Carlo modelling in its treatment of grain boundaries. Although the effects of boundary misorientation on energy and mobility can be incorporated (e.g. Holm et al. 1998), the effects of the boundary plane, which have a significant effect on these parameters (e.g. $\Sigma 3$ twins and $40^\circ <111>$ tilt boundaries) cannot be included, and this can be shown to have a significant effect on the evolution of microstructure and texture (Bate 2001a).

16.2.2 Cellular automata

Cellular automata (CA) models are closely related to Monte-Carlo models, in that the volume of material is divided into cells or blocks. Although Monte Carlo blocks may have attributes as discussed above, CA models offer a much more efficient and flexible method of doing this, and they are therefore better at simulating complex processes such as recrystallization (Hesselbarth and Gobel 1991, Marx et al. 1999, Raabe 1999).

A cellular automaton consists of a grid of cells and is typically characterized by parameters such as:

- **Cell geometry** – the number, size, shape and arrangement of the cells needs to be specified.
- **The number and type of states that a cell can possess** – in the simplest case, cells may be characterised as either recrystallized or unrecrystallized. Alternatively a detailed deformation microstructure may be included and each cell will be characterised by microstructural parameters such as dislocation density, cell or subgrain size and crystallographic orientation.
- **The definition of the neighbourhood of a cell** – the question of whether the transition of a cell is affected by its nearest neighbours or whether a more extended neighbourhood is considered varies for different models.
- **The rules of transition for a cell** – as annealing proceeds, transitions may occur within cells, e.g. changes of dislocation density. Also events originating from adjacent cells such as the growth of recrystallized grains need to be accommodated.

Having specified the initial microstructure, annealing is then usually simulated on a statistical basis which neglects the details of the event. For example, nucleation may be assumed to be site saturated or to occur at a predetermined rate and the orientations may be random or related to the orientation of the specific cells. Such a model is computationally efficient, allowing large volumes to be examined and allowing effects such as orientation-dependent boundary mobility to be included. The output of such models includes the recrystallization kinetics, texture, grain size and grain size distribution.

Cellular automata are essentially spatial frameworks into which simple models, such as analytical or empirical equations which describe the details of the annealing mechanisms may be inserted. They have the advantage over models which are not spatially resolved (e.g. the analytical model of chapter 10, that inhomogeneities of microstructure and the spatial distribution of texture may readily be taken into account.

16.2.3 Molecular dynamics

Perhaps the ultimate tool for simulating annealing processes is molecular dynamics (MD), which has been used for over 40 years to study non-equilibrium dynamics in atomic systems. In this method, the trajectories of atoms in a defined cell of material are determined by integrating Newton's equations of motion over finite time steps. The atom motion is driven by the interatomic forces, and these are usually modelled in terms of the Lennard–Jones pair potential.

The main advantage of this method over other simulations is that the only inputs required are the interatomic force laws. The simulations make no assumptions about the physical properties of the grain boundaries or the mechanisms of migration. Significant advantages over other simulations are that the simulation uses real length and time scales. However, molecular dynamics is computationally demanding and currently only very small atom arrays and very short times can be studied even with the best available computers.

The first simulation of curvature driven boundary migration was by Jhan and Bristowe (1990), and the technique has recently been applied to 2-D simulations of curvature driven boundary migration for boundaries of different types and misorientation (fig. 16.6), and also to triple junction migration, and shown to give good agreement with experiments (Upmanyu et al. 1999, 2002). Recent 3-D simulations of the growth of columnar grains (fig. 6.27) have shown that both boundary migration and grain rotation may occur at very high temperatures for very small grains (Haslam et al. 2001).

Although molecular dynamics is extremely powerful, its computational requirements are such that it cannot presently model processes such as recrystallization in 3-D. For example, in the simulation of figure 6.27, an array of ~390,000 atoms in a cell of ~70 nm × 70 nm × 1.5 nm was used to model the growth of 25 grains of diameter 15 nm for a period of ~7 ns at a temperature of $0.95T_m$.

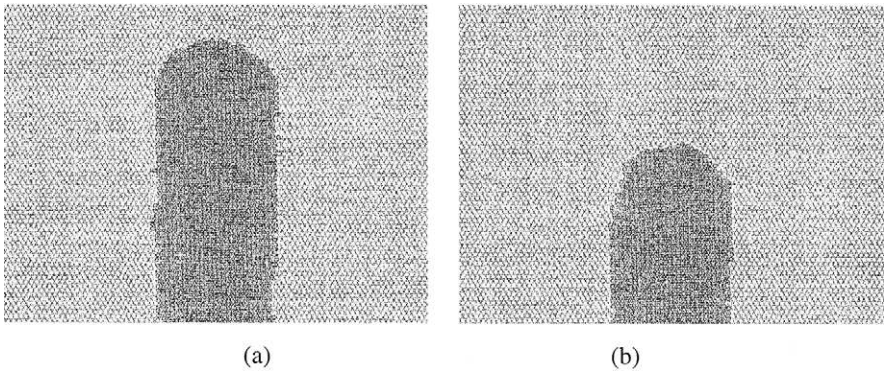

Fig. 16.6. 2-D molecular dynamic simulation of the shrinking of a half-loop grain of misorientation 28.5° at different times, (Upmanyu et al. 1999).

16.2.4 Vertex simulations

Vertex or network models are based on the assumption that the smallest microstructural unit of importance during annealing is a grain or subgrain, and they represent the microstructure as a cellular structure. Many models assume an 'ideal grain assembly' with no variation of boundary properties and can therefore only model grain growth. However more sophisticated models which take into account the orientation dependence of boundary properties are now commonly used. A review of vertex models and comparison with Monte Carlo models is given by Maurice (2001).

The earliest simulations in this field were the bubble rafts used by Bragg and Nye (1947) to study grain growth. The coarsening of soap froths between glass plates has been used as a grain growth simulation (e.g. Weaire and Glazier 1992) and has also been studied in its own right. Although the mechanisms of grain growth and froth coarsening are clearly different as the latter involves gas diffusion, it is interesting that detailed measurements of the kinetics of soap froth coarsening show a remarkable similarity to those for grain growth (Ling et al. 1992). The computer models discussed below are mostly two-dimensional, but are being extended to 3-D. It should be re-emphasized that 2-D simulations of the annealing of 3-D microstructures may be misleading, and the results should be interpreted with caution.

16.2.4.1 The basic model

If we consider a 2-D array of grains, then the grains themselves may be represented only by their vertices and this reduces the amount of data needed to be held in the computer. For example, figure 16.4 was obtained using a Monte Carlo simulation in two-dimensions with an array of 150×150 points, i.e. 22,500 lattice points. There are approximately 100 grains in the structure, with an average of six sides, and thus there are some 200 vertices. Representing this structure by the node points or vertices therefore gives significant compression of the data and allows larger numbers of grains to be used in the model. A microstructure consisting of a two-dimensional network of grains or subgrains is constructed. The (sub)grains are represented by the vertices N_j as shown in figure 16.7, and the positions of these, together with the identification of their neighbours, is stored in the computer. Apart from the constraint that each vertex should connect three boundaries, there are no constraints on their spatial distribution. Each subgrain is assigned a crystallographic orientation (O_j), and the distribution of orientations can be varied, so as to represent any required orientation gradients. The three orientations associated with each vertex are also stored in the computer.

This is a flexible framework into which grains or subgrains of any spatial or angular distribution may be introduced, and it is possible to produce microstructures which are reasonably realistic representations of deformed or recovered structures. Such a model can readily accommodate over 100,000 grains or subgrains. Because the orientations of adjacent grains are known, the boundary misorientation angle is also determined, and the boundary energies and mobilities may be calculated if the relationships are known (e.g. equations 4.5 and 10.18).

Once the initial microstructure has been constructed, often by a Voronoi network, subsequent events are determined by the equations governing the motion of the

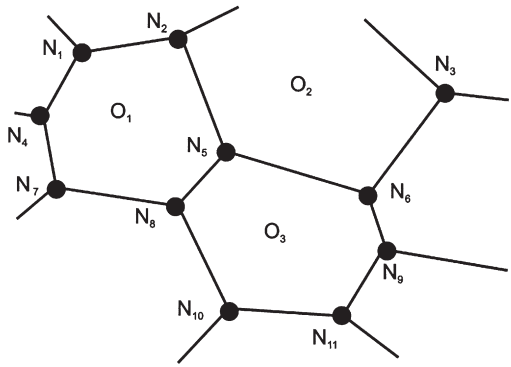

Fig. 16.7. The basis of an orientation-dependent network model, (Humphreys 1992a).

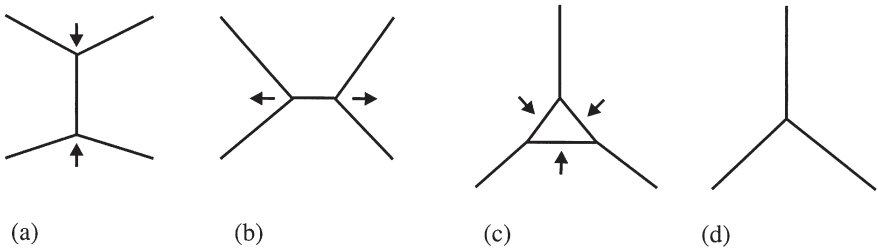

Fig. 16.8. (a), (b) node switching events; (c), (d) shrinking and disappearance of a three-sided grain.

boundaries and vertices. As no random paths are chosen, the models are truly deterministic. During annealing, nodes may be driven into contact and in such cases appropriate action must be incorporated into the computer code. For example, nodes moving in the directions shown in figure 16.8a will switch partners as shown in figure 16.8b. Similarly, three-sided grains will generally tend to shrink and to vanish as shown in figure 16.8c and d. The principal difference between the various vertex models stems from the way the dynamics is taken into account.

16.2.4.2 Boundary dynamics models

In the boundary-dynamics models, the displacement of the boundaries is computed from their local curvatures, and then the position of the triple points (or vertices) is adjusted to fulfil equilibrium requirements. The main contributions to the development of this type of models are due to Frost, Thomson and colleagues, (Frost et al. 1988), and more recently Saetre and Ryum (1993). This type of approach tends to imitate the physical mechanisms of boundary migration very realistically and yields good results in a wide range of situations such as normal and abnormal grain growth, or grain growth stagnation in thin films. The main drawback is its large computational requirement if one wants to simulate the evolution of large structures or 3-D cases.

16.2.4.3 Vertex-dynamics models

The vertex-dynamics models constitute an alternative, more economic, vertex simulation technique which keeps track of the triple (or quadruple) points only, ascribing the boundary migration to the motion of these points. The reliability of these vertex-dynamics models is, of course, very much dependent on the way vertex motion equations are derived from the migration of the adjacent interfaces. Several different solutions involving line-tension driven vertex motion have been proposed over the years (see for example Fullman 1952, Soares et al. 1985). More sophisticated formulations were derived by Kawasaki and co-workers (1989) who considered a vertex network connected by straight edges, its dynamics being governed by the balance between the reduction of interfacial energy by boundary migration and the dissipation due to the viscous drag which opposes the interface motion. Humphreys (1992a,b) proposed the use of a vertex-dynamics model to study the time evolution of structures with boundary mobilities and energies depending on the interface character. In the first version of his model, the grain boundaries were considered as straight edges, the line tensions being summed up at each vertex to give the driving force on the vertex.

16.2.4.4 Boundary versus vertex-dynamics models

All the vertex-dynamics models referred to above, treat the boundaries as straight edges, thus neglecting the fact that the migration of a boundary is driven by its curvature. Moreover, the mechanical equilibrium at triple junctions is not satisfied. The implicit assumption behind this type of model is that the boundary mobility is much higher than the triple junction mobility, which is true in most situations as discussed in §5.5. In the boundary-dynamics models, it is recognised that the boundary curvature governs the boundary migration, and the triple junction is considered to be in local equilibrium at all times. Weygand et al. (1998b) have recently proposed a modified Kawasaki model in which they consider the motion of the triple junctions together with that of 'virtual vertices' distributed along the grain boundaries. The main advantages of this approach are that it does not need to assume a particular shape for the boundaries, and that it does not enforce equilibrium at the triple junction. One of the striking results of their study is that during normal grain growth, the structure evolves so as to fulfil the local equilibrium at the triple junctions. It is therefore not unreasonable to assume from the start a local mechanical equilibrium in the vicinity of the vertex. Such an idea was proposed by Svoboda (1993) as an improvement to Humphreys' method, and has been used by Maurice and Humphreys (1997, 1998).

16.2.4.5 Modelling orientation-independent grain growth

The growth of an ideal grain assembly (all boundaries have equal properties) is perhaps the simplest problem to tackle. A detailed comparison of the application of various models to this problem is given by Atkinson (1988). Such models are tested by comparing the growth kinetics and grain size distributions in a high angle boundary array with that produced by experiment or with other computer simulations such as 2-D Monte Carlo simulations and are usually found to produce similar results. Frost and colleagues have made extensive use of their model to simulate grain growth in thin metallic films, an area of importance in the technology of integrated circuits, and in which the limitation of the model to two dimensions does not pose a serious problem. They have incorporated grain boundary grooving into the model and an example of their simulation is shown in figure 16.9.

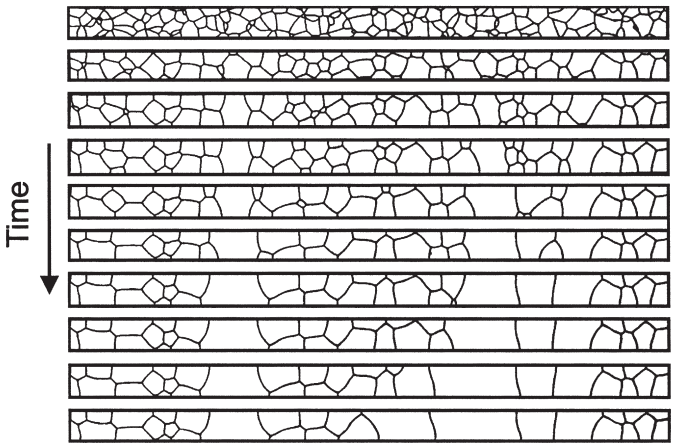

Fig. 16.9. Simulation of grain growth in thin metallic strip. Thermal grooving is included in the model, and the grain structure stagnates before a complete bamboo structure is formed, (Walton et al. 1992).

16.2.4.6 Modelling recovery and recrystallization

In order to simulate recovery or the nucleation of recrystallization, the model has to take account of the grain and subgrain orientations, because the energy and mobility of low angle boundaries are strongly dependent on orientation, and an early two-dimensional version of such a model was discussed by Humphreys (1992a,b). A model such as this may of course only be used to simulate the recovery of a material in which the dislocations are arranged into low angle boundaries (e.g. a high stacking fault energy material such as Al or Fe).

Vertex models in which grain and subgrain orientations can be included may be used to investigate recovery and the possible mechanisms of recrystallization nucleation, including SIBM and the annealing of a transition band in a deformed material as shown in figure 16.10. It should be emphasised that recrystallization nucleation, which is no more than heterogeneous recovery in a region of large orientation gradient, follows as a natural consequence of the spatial and angular heterogeneities in the starting microstructure and is not specifically programmed into the model. Pinning by particles may also be introduced into such a model (Humphreys 1992a, Weygand et al. 1999, Bate 2001b), and by producing a suitable orientation gradient at a large particle, particle stimulated nucleation of recrystallization may be simulated (Humphreys 1992a,b).

An interesting recent application of vertex modelling to the annealing of highly deformed aluminium by Bate (see Hayes et al. 2002) is shown in figure 16.11. These authors investigated the instability on annealing of the elongated grain structures produced by very large strain deformation (e.g. figs. 14.1 and 14.8) and which do not undergo discontinuous recrystallization on subsequent annealing (§14.3.4). The model shows necking and 'pinching off' of high angle lamellar boundaries due to the surface tension of the less mobile low angle boundaries. The grain aspect ratio is progressively reduced during annealing, and this process of continuous recrystallization ultimately produces an equiaxed grain structure.

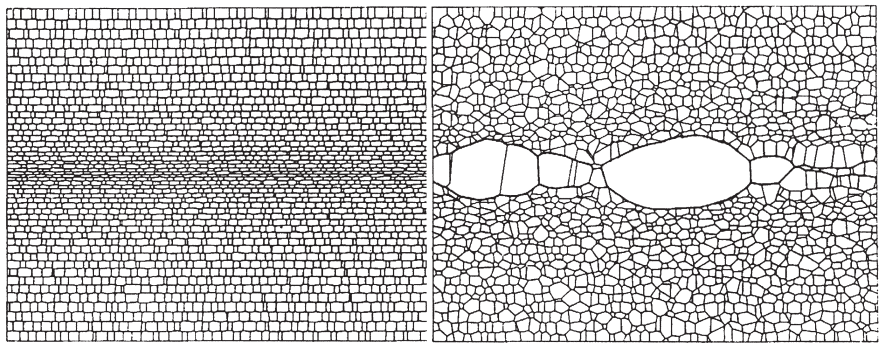

(a) (b)

Fig. 16.10. Simulation of recrystallization nucleation in a transition band. (a) The initial microstructure consists of subgrains which are smaller and more elongated in the transition band. There is also an imposed vertical orientation gradient of 5° per subgrain over the ten central bands of subgrains, (b) The microstructure evolved on 'annealing' shows the development of large elongated grains of similar orientations but with high angle boundaries (bold lines) to the recovered structure, (Humphreys 1992a).

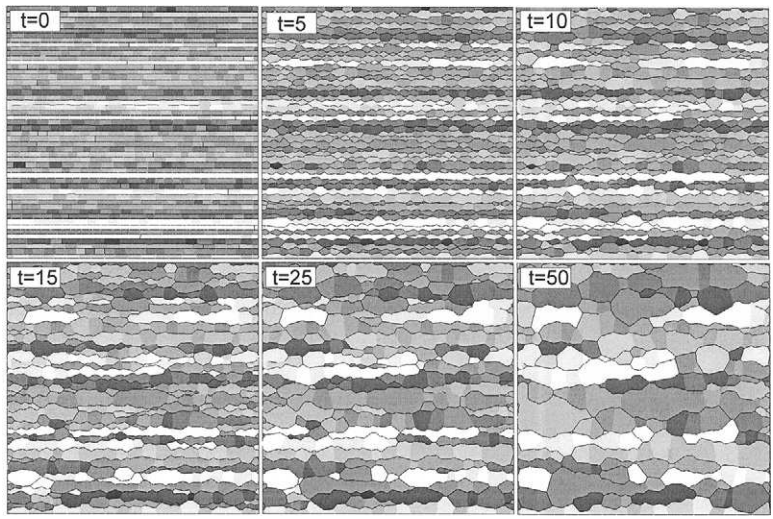

Fig. 16.11. Vertex simulation of continuous recrystallization of a highly deformed metal with a lamellar grain structure. Grey levels correspond to orientation, and only high angle boundaries are delineated. The times are indicated in arbitrary units, (Hayes et al. 2002).

16.2.4.7 Dynamic grain growth

Vertex models have been successfully used to model dynamic grain growth during the high temperature deformation of particle-containing alloys (Bate 2001b). The Zener drag due to the particles is treated as an average drag on the boundaries rather than treating the particles individually. This is justified if the particles are small and closely spaced relative to the grain size.

16.2.4.8 Three dimensional vertex models

It has repeatedly been emphasised in this and earlier chapters that 2-D modelling of the evolution of 3-D microstructures is unsatisfactory and may lead to incorrect results. The vertex models discussed above have all been two-dimensional, and there is a need to extend the approach to three dimensions. However, there are formidable difficulties in extending the concepts discussed above to 3-D. Maurice and Humphreys (1998) derived the equations for the motion of a curvature driven quadruple junction, but few 3-D network models are currently available. Fuchizaki et al. (1995) and Wakai et al. (2000) have developed 3-D models for normal grain growth under the conditions where all boundaries have equal energy and mobility, and Maurice (2000) has demonstrated a 3-D model with orientation-dependent boundary properties, which is an extension of the model of Kawasaki et al. (1989). Figure 16.12 shows a section through a 3-D model of the evolution of microstructure in a subgrain structure containing a transition band, demonstrating the rapid subgrain growth which occurs in the region of large orientation gradient, and which can be compared with the 2-D simulation of figure 16.10 and the real microstructure of figure 7.34 which was produced in a similar situation.

16.2.4.9 Success and limitations of vertex models

Vertex or network modelling is an excellent and efficient form of modelling annealing in situations where the microstructure can be realistically simulated by an array of cells

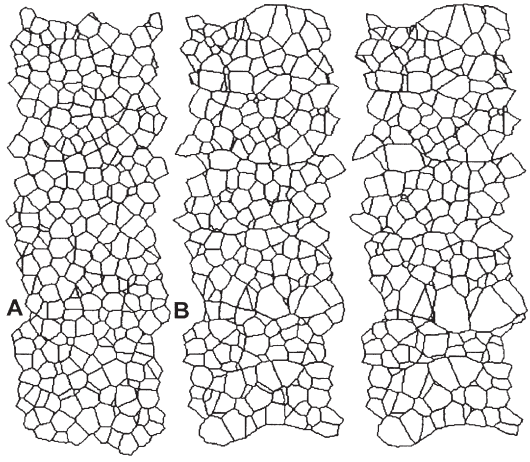

Fig. 16.12. Section through a 3-D vertex simulation of the annealing of a transition band (AB) at different stages of the annealing. (from the work of Maurice, 2000).

and where boundary migration is the mechanism of annealing. Apart from the initial microstructure, only the properties of the boundaries are required as input. With orientation-dependent boundary properties, events such as the nucleation of recrystallization may readily be simulated, and a comparison of the kinetics of grain growth obtained by vertex and Monte Carlo models show great similarity (Maurice 2001). The advantages over Monte Carlo models are the larger microstructures which can be investigated, the more transparent physical mechanisms and the better treatment of boundary properties. Mechanisms such as subgrain rotation and coalescence (fig. 6.26) and concurrent deformation (Bate 2001b) may be included, and two-phase microstructures investigated, although this is not simple if only the boundary vertices are tracked.

The main limitation of the network models compared to Monte Carlo models is the difficulty of producing the 3-D models which are required for quantitative predictions. An interesting approach involving both models has been the use of small 3-D Monte Carlo models to verify the microstructures produced by larger 2-D vertex models of recrystallization (Bate 2001a, Hayes et al. 2002).

16.2.5 Computer avrami models

The application of the JMAK relationship of equation 7.17 which describes the kinetics of recrystallization, is limited by the spatial and temporal inhomogeneity of the nucleation and growth processes. By using analytical relationships to describe nucleation and growth rates etc., but using a computer to deal with the spatial distribution effects, more realistic models for recrystallization can be obtained. Although this does not have the flexibility of the cellular automata models (§16.2.2), by which it has largely been overtaken, it is a rapid and simple method of assessing the effects of different nucleation and growth theories on the development of microstructures and textures.

An early two-dimensional simulation of this type was demonstrated by Mahin et al. (1980), and the Trondheim group (Saetre et al. 1986a, Marthinsen et al. 1989, Furu et al. 1990) extended the simulation to three dimensions and extensively refined the model. In its most general form, nuclei are distributed within a cube at a given rate, and these then grow according to a specified growth law, the transformation being complete when grains impinge on one other. Microstructures are then obtained from two-dimensional sections of the volume, which are analysed by a binary tree construction.

Applications of the model to recrystallization have shown good agreement with the analytical models discussed §7.3 for randomly distributed nuclei, and it has been shown that an inhomogeneous distribution of nuclei reduces the JMAK exponents as recrystallization proceeds as shown in figure 16.13 (Furu et al. 1990).

16.2.6 Neural network modelling

The modelling of recrystallization by empirical equations has recently been enhanced by the application of sophisticated numerical methods to model microstructural evolution

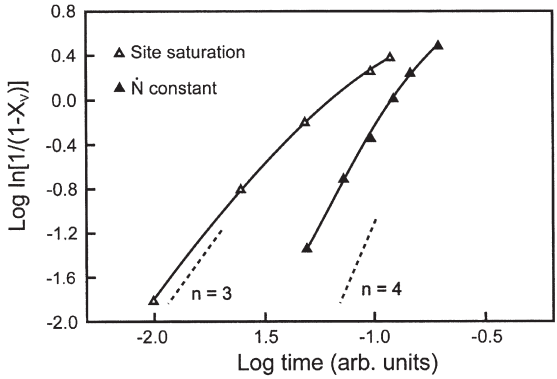

Fig. 16.13. The effect of inhomogeneous nucleation on recrystallization kinetics. The Avrami exponent decreases as recrystallization proceeds, (Furu et al. 1990).

(e.g. Sabin et al. 1997). Numerical methods allow the prediction of microstructure without having to develop the underlying metallurgical theory in detail. Neural networks provide a parameterised, nonlinear mapping between inputs (e.g. plastic strain and annealing temperature and time) and an output (e.g. grain size or extent of recrystallization). The network is first 'trained' on a characteristic data set, consisting of inputs and the ideal network outputs. This training is often done by the conventional method of minimising an error function. The network can then be used to derive outputs, given inputs that were not present in the training data, i.e. it can make predictions.

Neural networks are well suited to problems such as recrystallization, which is known to be influenced by many factors in a manner which makes analytical or physical modelling very difficult. Gaussian process models are variants on traditional neural networks which automatically embody Bayesian methods. Rather than simply giving a single, optimal predicted output when presented with new inputs, the Gaussian process model yields a probability distribution of the predicted value. Specifically, the model assumes that this probability distribution is a Gaussian. The mean and standard deviation of this Gaussian are inferred from the training data, thus providing an error on the prediction. The magnitude of these errors is dependent upon the noise in the data and the distribution of the training data, so that where data is sparse the errors will be larger. Bayesian methods have the advantage that they reduce over-fitting of the training data and produce a model which generalises well (MacKay 1995).

Although such models are designed primarily for practical application and are particularly suited for analysis of metallurgical plant data, they can give a good account of the relationships between the materials and processing input parameters and the output parameters such as microstructure and texture. Such modelling can therefore highlight important and unexpected relationships between the parameters which may indicate previously unknown physical relationships and may therefore provide a useful feedback to improving scientific understanding.

16.3 COUPLED MODELS

An important impediment to the successful implementation of the annealing models discussed in §16.2 is the lack of information about the initial deformed condition. Not only are we currently unable to model or predict the deformation microstructure accurately or in sufficient detail, but we do not even have sufficiently detailed experimental measurements of deformed microstructures to provide an adequate base for modelling annealing. However, many annealing models are now being coupled to deformation models or to real deformation microstructures.

16.3.1 The annealing of 'real' microstructures

Automated methods for obtaining detailed quantitative microstructures such as EBSD mapping (Appendix 2) can readily provide microstructures suitable for input to the 2-D Monte Carlo, cellular automata or vertex models described in §16.2. The input data can include orientations, together with a measure of the local stored energies obtained from pattern quality (Engler 1998), or may be higher resolution EBSD maps in which reconstructed subgrains and grains are used (Baudin et al. 2000, Caleyo et al. 2002).

16.3.2 The annealing of computer generated deformation microstructures

Alternatively, an annealing model may be coupled with a model describing the deformed state. The coarser aspects of the deformed state may be predicted from Finite Element (FE) (Gottstein et al. 1999, Raabe and Becker 1999, Radhakrishnan et al. 1998) or Self Consistent Plasticity modelling (Solas et al. 1999). However, standard FE procedures operate on much too coarse a scale to give more than an approximate account of the deformed state, although they may provide some indication of the spatial distribution of stored energy. Crystal Plasticity Finite Element models (CPFEM) which can model the deformed state more accurately, have been developed (Raabe and Becker 1999, Bate 1999, Bate 2001a), but, particularly in 3-D, remain very computer intensive, and are currently unable to predict the scale of grain fragmentation. Such models may provide a reasonable description of the driving pressures for recrystallization, but are currently unable to model the deformed state with sufficient accuracy to deal with the nucleation of recrystallization. Bate (2001a) has critically reviewed the coupling of CPFEM deformation models to annealing models, and demonstrated the extreme sensitivity of vertex or Monte Carlo annealing simulations to small changes in the deformation microstructures arising from slightly different CPFEM conditions.

Another approach has been to derive more detailed local microstructural parameters, such as dislocation densities, by coupling FE modelling to work hardening models (e.g. Gottstein et al. 1999, Luce et al. 2001) and using this as input to an annealing model.

16.3.3 Modelling an industrial thermomechanical process

The development of quantitative physically-based models of thermomechanical processing is already established in the steel industry and is being developed for the

aluminium industry. Although detailed consideration of such models is beyond the scope of this book, it is instructive to see how some of the basic concepts discussed earlier in this book fit into the larger perspective of industrial practice.

16.3.3.1 Outline of a model

The modelling of industrial multi-pass hot rolling which has been of particular interest to modellers involves successive hot rolling reductions with intermediate stages during which the material may recrystallize. Each rolling pass is modelled in terms of four steps (e.g. Sellars 1992a).

- **The starting microstructure,** is characterised by several parameters which may include grain, subgrain and dislocation structure, together with texture.
- **Deformation** to a particular strain takes place at an imposed strain rate and temperature.
- **Annealing** occurs between rolling passes.
- **The final microstructure** is produced and becomes the starting microstructure for the next cycle.

The microstructural changes during deformation and annealing, and the **strain** and **strain rate** vary during the overall process. Models to predict changes of microstructure and texture at each stage are required. **Micro-models,** such as the recrystallization models discussed in §16.2 can be used to describe these processes, although currently, the semi-empirical state-variable constitutive models discussed in §13.2.5 and §13.6.2 are more commonly used.

The **temperature** is non-uniform through the material and changes continuously with time and stock geometry. The surface oxide film and lubricants will also affect heat transfer to the environment and to the rolling mill. Finite difference computing methods are used to calculate instantaneous values of temperature.

16.3.3.2 Application to steels

Models such as that discussed above have been successfully used by the steel industry for some time (see Jonas 1990, Sellars 1990, Torizuka et al. 1997). The predicted change in grain size during multiple rolling of C–Mn steel is shown in figure 16.14. The steel is reduced from 250 mm slab in equal passes of 15% reduction, with 20 seconds between passes. The broken line, which represents the predicted recrystallization kinetics shows that after each roughing pass (**R**) the grain size is refined by complete recrystallization and when the grain size is below 100 μm, some grain growth occurs between passes. Complete recrystallization also occurs during the first four finishing passes (**F**), but at the lower temperatures recrystallization is incomplete between passes. For comparison, data has been computed (solid line) using a recrystallization rate which is 5 times slower. Although recrystallization is incomplete between all finishing passes, the overall changes in grain size remain similar.

The relative insensitivity of the output to differences in the input microstructural equations and the good quantitative agreement between predicted and observed microstructures has made modelling an accepted tool for the industrial thermomechanical processing of steel.

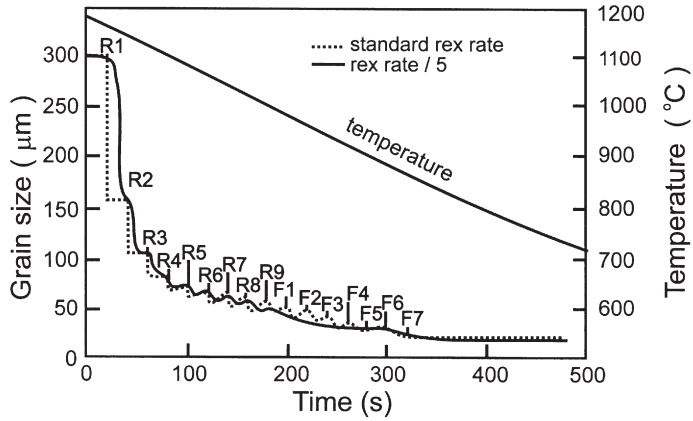

Fig. 16.14. The predicted evolution of microstructure during the hot rolling of 20 mm C–Mn steel plate, (Sellars and Whiteman 1979).

16.3.3.3 Application to aluminium alloys

Although there has been substantial activity in modelling the hot rolling of aluminium alloys as discussed in §13.2.5 (e.g. Sellars 1992a, Sellars et al. 1994, Vatne et al. 1996c), the models are less well developed than for steels. There are several reasons for this including:

- Accumulation of strain over several passes occurs before recrystallization takes place.
- The microstructure and texture are very dependent on the history of the specimen, more so than in steels, where the austenite/ferrite transformation may wipe out much of the previous processing history by changing the grain size and orientation.
- The development of microstructure and texture is critically dependent on the influence of second-phase particles, whose size and distribution may alter during the processing.

These aluminium process models do not generally make use of the micro-models discussed in §16.2, but make extensive use of the various analytical and empirical models for evolution of microstructure and texture which are discussed elsewhere in this book.

Appendix 1

TEXTURE

The crystallographic orientation or texture is an important parameter describing the microstructure of a crystalline material. Traditionally, textures have been determined by x-ray **diffraction** and represented by **pole figures,** but in recent years, new methods of texture representation and determination have also become widely used. The purpose of this appendix is to provide the non-specialist with sufficient information to understand the discussions of texture in the book.

In this appendix we examine how textures are obtained experimentally and displayed. Some of the experimental methods used, such as EBSD, are also important methods of quantitative microstructural characterisation, and these aspects are considered in appendix 2.

A1.1 REPRESENTATION OF TEXTURE

A simple treatment of texture representation is given in this section, and further details may be found in Hatherly and Hutchinson (1979), Cahn (1991b) and Randle and Engler (2000). Detailed accounts of texture representation with particular reference to orientation distribution functions (**ODF**) may be found in the works of Bunge (e.g. Bunge 1982), and Randle (2003) discusses texture representation with particular reference to microtextures.

A1.1.1 Pole figures

A pole figure is a stereographic projection which shows the distribution of a particular crystallographic direction in the assembly of grains that constitutes the specimen. If it is to have meaning it must also contain some reference directions that relate to the material itself. Traditionally these directions refer to the forming process, e.g. the drawing direction in wires or the rolling direction etc. in rolled sheets. Idealized pole figures for a drawn wire and a rolled sheet are given in figure A1.1.

In figure A1.1a, the drawing direction of a wire specimen is shown at the top and the distribution of $<100>$ directions indicates that the grains have these directions at 45° and 90° to the wire axis. This axis, is therefore, parallel to a $<110>$ direction and the texture is described as a $<110>$ fibre texture. Figure A1.1b refers to a rolled sheet. The orthogonal specimen axes, rolling direction (RD), transverse direction (TD) and sheet normal direction (ND) are plotted with ND at the centre and RD at the top. Once again the distribution of the $<100>$ directions is shown. There is a concentration of these directions at RD and in the plane defined by ND and TD at 45° to ND. Such a texture is described by the notation $\{110\}<001>$ which states that planes of the form $\{110\}$ are parallel to the surface of the sheet and directions of the form $<001>$ are parallel to the rolling direction.

The distribution of intensity in real pole figures is much more diffuse than shown above. The intensity distribution is usually represented by contour lines with values 1 to n times **R** where **R** is the value associated with a specimen of completely random orientation. The texture of heavily rolled copper (fig. 3.1) shows the typical spread observed.

A1.1.2 Inverse pole figures

The inverse pole figure is particularly useful for deformation processes such as wire drawing or extrusion, which require the specification of only a single axis. The

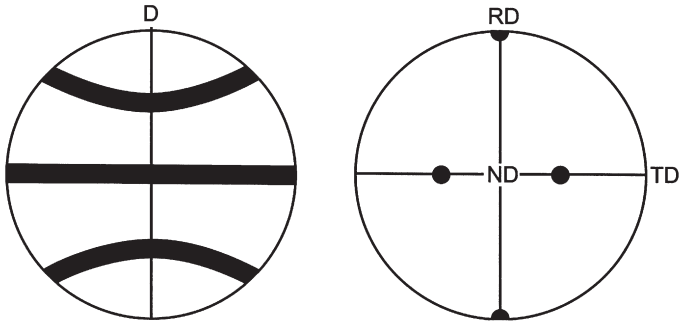

Fig. A1.1. Idealized 100 pole figures for: (a) drawn wire, showing $<110>$ fibre texture, (b) rolled sheet, showing $\{110\}<001>$ rolling texture.

frequency with which a particular crystallographic direction coincides with the specimen axis is plotted in a single triangle of a stereographic projection (fig. 3.14). Rolling textures can also be described by inverse pole figures but in this case two or sometimes three separate plots are presented, one being used for each of the principal strain axes ND, RD (and TD if required). This method is used much more frequently for bcc steels than for fcc materials.

A1.1.3 Orientation distribution functions and Euler space

The description of texture by pole figures is incomplete. The information provided refers only to the statistical distribution of a single direction and there is no way of using this to obtain the complete orientation of individual grains or volume elements. A better description is given by the ODF which describes the orientation of all the discrete volumes in the aggregate. ODF analysis was developed originally for materials with cubic crystallography and orthorhombic sample symmetry, i.e. for sheet products. There have been a few studies of hexagonal metals but most of the literature and most of what follows refer to rolled materials with fcc or bcc structures. Some explanation of the formalism used to describe the ODF is necessary but no description of the mathematics involved in generating the ODF will be given. The interested reader is referred instead to the definitive work of Bunge (1982).

Consider the case of a rolled sheet in which a particular volume element has the orientation (hkl)[uvw]. The orientation of this element can be described in terms of three Euler angles. Several different notations have been used to define these angles, but that of Bunge is most common and will be used here. The crystallographic axes are represented in the normal way in a standard projection (fig. A1.2) and the specimen orientation is specified by the reference directions ND and RD. The angles Φ and φ_2 completely specify the direction ND. RD lies in the plane normal to ND and the angle φ_1 completely specifies the direction RD. Because three variables have been used to define (hkl)[uvw], the ODF can only be displayed as a three dimensional plot with the

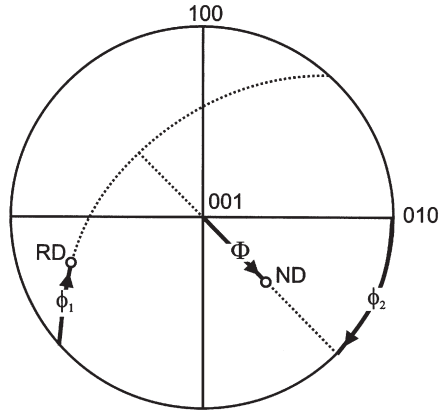

Fig. A1.2. Definition of Euler angles used for rolled sheet.

three Euler angles as axes as shown in fig. A1.3a. For rolled fcc materials the data are normally shown as a series of slices taken through the three dimensional ODF space at $\varphi_2 = 0, 5, 10 \ldots 90^\circ$; as shown in fig. A1.3b.

Equations A1–A9 define the relationship between Euler angles and Miller indices for cubic materials. In order to obtain consistent results, equations A1.1 to A1.6 should be used to obtain Miller indices from Euler angles, and equations A1.7 to A1.9 to obtain Euler angles from Miller indices.

$$h = \sin\Phi \sin\varphi_2 \tag{A1.1}$$

$$k = \sin\Phi \cos\varphi_2 \tag{A1.2}$$

$$l = \cos\Phi \tag{A1.3}$$

$$u = \cos\varphi_1 \cos\varphi_2 - \sin\varphi_1 \sin\varphi_2 \cos\Phi \tag{A1.4}$$

$$v = -\cos\varphi_1 \sin\varphi_2 - \sin\varphi_1 \cos\varphi_2 \cos\Phi \tag{A1.5}$$

$$w = \sin\varphi_1 \sin\Phi \tag{A1.6}$$

$$\tan\Phi \cos\varphi_2 = \frac{k}{l} \tag{A1.7}$$

$$\tan\varphi_2 = \frac{h}{k} \tag{A1.8}$$

$$\cos\Phi \tan\varphi_1 = \frac{lw}{ku - hv} \tag{A1.9}$$

Table A1.1 gives the Euler angles for $\{110\}<112>$ and $\{110\}<001>$, two of the orientations that are commonly used to describe the textures of fcc metals, and fig. A1.3b indicates where these occur in ODF space. It should be noted that the general

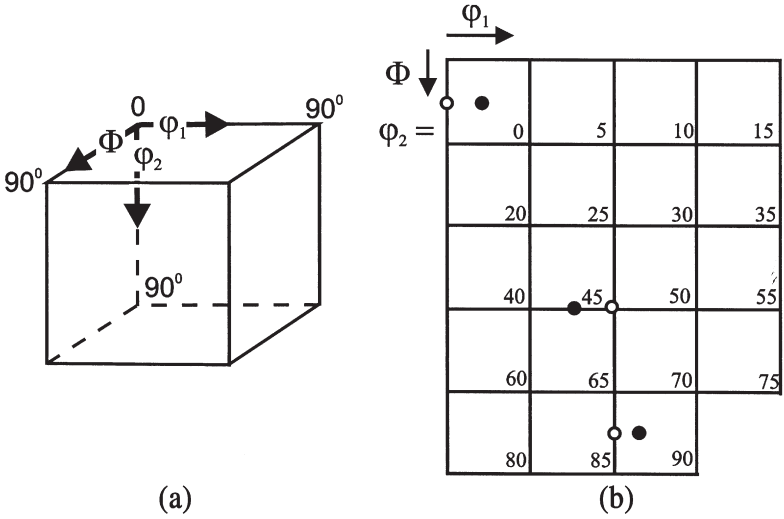

Fig. A1.3. (a) Location of Euler angles in ODF space, (b) ODF sections showing location of $\{110\}<112>$ (filled circles), and $\{110\}<001>$ (open circles) orientations.

Table A1.1
Euler angles for some texture components.

Component	φ_1	Φ	φ_2
{110} < 112 >	35	45	0
	55	90	45
	35	45	90
{110} < 001 >	90	90	45
	0	45	0
	0	45	90

orientation {hkl} < uvw > appears more than once in the customary $90^\circ \times 90^\circ \times 90^\circ$ cube of Euler space.

The use of ODFs allows a more quantitative description of textures than is possible with pole figures. Although the interpretation of a full ODF (e.g. fig. 3.3) is not immediately apparent to the non-specialist, there are, in any material only a relatively few important orientations (e.g. tables 3.1 and 3.3) and these are readily identified in the ODF sections (e.g. fig. A1.3b).

More importantly, the ODF allows the identification of **texture fibres** as shown in figure 3.4, and quantitative plots of intensity along these fibres (e.g. fig. 3.5) provide very detailed information. The volume fractions of any texture components (often defined as orientations within 10° or 15° of the ideal) may also be readily calculated from the ODF data. Such simple yet quantitative representations of the data (e.g. table 3.2, figures 12.17–12.19) may be compared directly with theoretical predictions or may form part of the specification of an industrial product.

Despite the benefits derived from the use of ODFs and their general acceptance, there are a number of disadvantages associated with the use of Euler space (e.g. Randle 2003).

- Each orientation appears three times in the conventional $90^\circ \times 90^\circ \times 90^\circ$ cube (table A1.1 and fig. A1.3b).
- The population of Euler space by a random array of orientations is very distorted. If $\Phi = 0$ the orientation is determined by $(\varphi_1 + \varphi_2)$ and all points in the plane $\Phi = 0$ and having the same value of $(\varphi_1 + \varphi_2)$ represent the same orientation. This is particularly confusing with respect to orientations of the form {001} < hk0 > .
- Significant fibres in the texture often lie on curves in Euler space (fig. 3.4) and may be difficult to recognise.

A1.1.4 Rodrigues-Frank space

Some of the problems discussed above can be overcome by the use of other three-dimensional representations and of these the most suitable appears to be that advocated by Frank (1988), and based on the analysis of Rodrigues (1840). A brief description

follows, but for more detailed accounts the reader is referred to the text by Randle (2003) or to Frank's paper.

The concept of an angle/axis of rotation is widely used to describe the misorientation relationship between neighbouring grains (§4.2). In order to express the absolute orientation of a crystal, the reference crystal is taken to be the standard cube crystal orientation. If the axis is defined by a vector **L** and the rotation angle by θ the required relationship is given by the so-called **Rodrigues vector**

$$\underline{R} = L \tan(\theta/2) \tag{A1.10}$$

The three orthogonal axes $\mathbf{R_1}$, $\mathbf{R_2}$, $\mathbf{R_3}$ define a **Rodrigues-Frank** (**R-F**) space in which all possible angle/axis combinations are found. There are 24 possible R vectors and in practice that with the smallest rotation angle is used. By definition this has the smallest R vector and it follows that all such R vectors lie close to the origin of **R-F** space. A full set of equivalent orientations lies in a fundamental zone of **R-F** space but in the case of high symmetry crystals only a small part of this zone is needed. Figure A1.4 shows the form of the fundamental zone for cubic crystals and details of the reduced volumes that suffice for high symmetry. The major advantages of this method of representation have been summarized by Randle (2003):

- Each orientation appears only once in the fundamental zone.
- Rotations about a common axis fall on a straight line. This means that the identification of fibre components is simple.
- The volume element of **R-F** space is much more homogeneous than is the case for Euler space.
- The axes of **R-F** space coincide with those of the specimen.

It is important to remember that **R-F** space is three dimensional and although there has been some use of sections taken through the reduced zones, these are much more

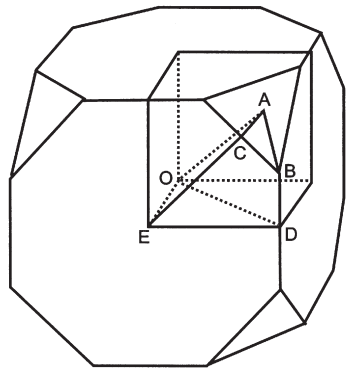

Fig. A1.4. The fundamental zone of Rodrigues-Frank space for holosymmetric cubic crystals. Internal volumes define 1/8th and 1/48th of the fundamental zone, (after Randle 2003).

difficult to comprehend than the sections of Euler space shown in fig. A1.3b, and this has limited the use of R-F space for the representation of bulk textures. In addition, unlike the methods discussed above the data cannot be directly extracted from bulk x-ray data (Becker and Panchanadeeswaran 1989). However, it does have some potential advantages for the representation of **misorientation** data (Randle 2003).

A1.1.5 Misorientations

The increasing availability and sophistication of equipment for measuring single orientations (§A1.3) has led to a considerable interest in the misorientations that exist across grain boundaries and the association of these misorientations with textures. The difference between a normal texture orientation and a misorientation is simply that in the former case the external axes of the specimen provide the frame of reference, whilst in the latter the axes of one of the grains serves this purpose. The misorientation parameters can be expressed in a number of ways.

- Misorientations may be expressed as Euler angles and displayed in Euler space as misorientation distribution functions (MODF).
- The axes of misorientation may be represented on inverse pole figures. In this case the angle of misorientation (θ) is conveniently plotted on an axis orthogonal to the inverse pole figure, and the data presented as sections of constant θ.
- The misorientations may be represented in R-F space.

A1.2 MEASUREMENT OF MACROTEXTURE

A1.2.1 X-ray diffraction

The most commonly used X-ray techniques are those developed by Schulz (1949). Most measurements involve materials that have been rolled or annealed and originally two separate methods of examination, involving back reflection and transmission techniques, were required to obtain a complete pole figure. Nowadays the transmission method is rarely used and useful pole figures (covering an area of up to 85° from the centre) are obtained by the back reflection technique. If complete pole figures are required these can be recalculated from an ODF which has been obtained from a number of partial pole figures.

A typical specimen is some 25 mm square with a flat surface, and the specimen must be thick enough (>0.2 mm) to prevent penetration of the incident X-ray beam. The specimen is mounted in a two-circle goniometer (fig. A1.5) which permits simultaneously, a rotation through an angle, δ, about its normal and a rotation, α, about an orthogonal axis that lies in the plane defined by that normal and the incident and diffracted beams. These beams which are restricted by a series of slits are set at the appropriate Bragg angles for diffraction from the required plane. The intensity of the diffracted beam is measured by normal counting methods and normalised to that obtained from a randomly oriented standard specimen. Because of the absorption effects that develop as α approaches 90° this technique provides a partial pole figure that

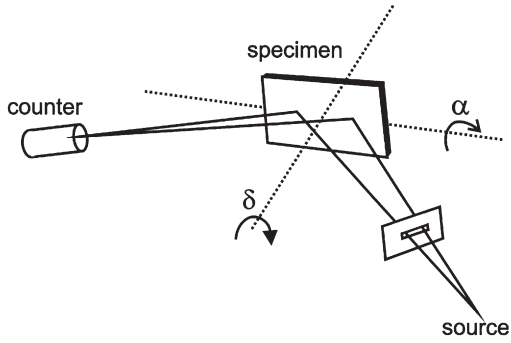

Fig. A1.5. The reflection method for pole figure determination.

extends only some 70–85° from the centre. For a full account of a modern, computer controlled goniometer see Hirsch et al. (1984).

Although most texture determinations are made with X-ray equipment and the Schulz back reflection method, there are some severe limitations involved. The most important of these is the small volume of material actually examined. The depth to which the incident beam penetrates (and from which the diffracted beams emerge) is governed principally by the wavelength of the X-rays used and the absorption coefficient of the specimen material and is rarely greater than 0.1 mm. It has been pointed out many times in this book that the most prominent feature of a deformed metal is the heterogeneity of the microstructure and it will be clear that there must always be some doubt as to whether or not an X-ray based texture result is truly representative of a rolled specimen. In many rolled products the texture varies through the thickness of the sheet, and in most cases texture studies are made on mid-plane sections. Because recrystallization does not necessarily occur homogeneously in such a material similar doubts must also apply to annealed specimens.

The time to acquire the data depends on the material, the resolution required, and the strength of the texture, but typically a single partial pole figure is collected in ~1 hr. The very high intensities of X-rays emitted by synchrotrons enable rapid data collection (Szpunar and Davies 1984), and it is possible to investigate changes taking place during the annealing of deformed materials.

If an ODF is required, this is calculated by deconvoluting the data of 3–4 separate pole figures from a sample. These need not be complete and modern practice uses only the Schulz back reflection method. The separate pole figures are determined sequentially and in some cases the goniometer head is capable of holding several specimens so that continuous overnight data collection is possible. The raw data are used to derive an orientation distribution function, **f,** for a particular orientation, usually by a series expansion method, and the combination of all possible **f** values gives the ODF.

There are a number of problems arising in the calculation of ODFs from pole figures. One of these is the so-called 'ghost' problem which affected all of the early ODFs and manifests itself by the generation of components that are known not to be present in the

texture (Matthies 1979, Lücke et al. 1981). In addition the peak intensities may be reduced by as much as 10–30%. This difficulty has its origin in the use of the series expansion technique to calculate the ODF from the experimental pole figures. Such expansions have both odd and even terms but assumptions made about symmetry led initially to the use of only the even coefficients and the appearance of the non-existent ghost peaks in the ODF. Ghosts in bcc textures are less significant than in fcc and the nature of the texture components is such that the ghosts appear only in high intensity regions. Because of this they cannot usually be recognised. Exceptions occur only for the $\{112\}<110>$ and $\{001\}<110>$ components. These problems do not exist if the ODFs are constructed from individual orientation measurements, such as from EBSD, as discussed in §A1.3.4.

A1.2.2 Neutron diffraction

The availability of thermal neutrons with a wavelength of $\sim$1Å provides an opportunity for the use of neutron diffraction in texture studies. Because the absorption of neutrons in most metals is low it is then possible to use large specimens. A steel specimen of thickness 10 mm will absorb about 20% of a typical neutron beam whereas a 0.1 mm specimen will absorb $>90\%$ of a similar X-ray beam. Neutron beam techniques are therefore useful for the examination of coarse grained materials and for gathering information from the full thickness of an inhomogeneous material. In some cases it is possible to examine directly the texture changes occurring during annealing (see, for example, Juul Jensen et al. 1984).

A1.3 MEASUREMENT OF MICROTEXTURE

There are many occasions when it is desirable to obtain data about the local array of orientations present in particular parts of the specimen, and the textures within small specified volumes are generally referred to as microtextures. By linking the orientation and spatial parameters this approach provides a more complete description of the specimen, and, as outlined in appendix 2 can also provide detailed quantitative microstructural data.

There is a range of methods available, each with its own particular application, and further details may be found in the reviews of Humphreys (1988b), Randle (2003), Schwarzer (1993) and Randle and Engler (2000).

A1.3.1 Optical methods

The optical techniques used by geologists and mineralogists and applied to transparent non-cubic minerals are described in standard mineralogical texts. Using plane polarised light in a transmission optical microscope equipped with a universal stage (goniometer), the specimen is manipulated until extinction of a grain or subgrain is achieved, and hence the crystallographic direction parallel to the optic axis of the microscope is determined.

Surface films such as anodic films, whose thickness or surface topography are dependent on the orientation of the underlying crystalline material may sometimes be used to obtain information about orientations. In the case of cubic metals, such as aluminium, the high symmetry of the material makes it difficult to obtain unambiguous data from an anodised specimen (Saetre et al. 1986b). However for hexagonal metals such as magnesium or titanium, the orientation of the basal plane may be obtained with the use of a polarising reflection microscope (Couling and Pearsall 1957).

A1.3.2 Deep etching

This etching technique (Köhlhoff et al. 1988b) has been used with considerable success by Duggan, Köhlhoff and their collaborators (e.g. Duggan et al. 1993) to study copper and copper alloys. The heavily etched surface is examined at a magnification in the range 500–2000X in an optical or scanning electron microscope, and a typical example is seen in figure 12.14. The basis of the technique is that the {111} planes are attacked more slowly than others so that a relief structure of tilted {111} planes is developed. The lines of the internal structure within the grains define the intersections of the {111} planes and are therefore $<110>$ directions. The various etched patterns are characteristic of the crystallographic orientation and may be readily identified to an accuracy of $\sim 5^\circ$ and with a spatial resolution of ~ 10 μm.

A1.3.3 Transmission electron microscopy (TEM)

Techniques for the determination of the orientation of small regions of a specimen in the transmission electron microscope from **spot** or **Kikuchi line** diffraction patterns have been well established for many years and are fully discussed in textbooks on electron microscopy. However, their use for the determination of local textures, which requires the acquisition and solution of many diffraction patterns has increased with the availability of computer based on-line techniques for the rapid solution of the patterns (e.g. Schwarzer and Weiland 1984).

A1.3.3.1 Single orientations

Transmission electron diffraction is particularly suited to applications requiring high spatial resolution, as electron microscopes can produce beams of less than 10 nm diameter. Thus the technique is suitable for the examination of very small cell or subgrain sizes in deformed materials. The crystallographic orientation may be determined from the diffraction spots, but because of relaxation of the Bragg diffracting conditions in thin specimens, the angular resolution is usually in the range 2–5° (Duggan and Jones 1977). The orientation may be determined to a much higher accuracy ($<0.1^\circ$) using the Kikuchi line patterns in a convergent beam diffraction pattern. The Kikuchi patterns are normally analysed according to the method of Heimendahl et al. (1964), a similar technique to that used for EBSD patterns (A1.3.4). However, because fully automatic indexing of TEM Kikuchi patterns is unreliable because of the large non-systematic intensity variations in the patterns (see e.g. Randle and Engler 2000), the analysis is normally carried out semi-automatically on-line, and thus the number of measurements obtainable may be small.

A1.3.3.2 Pole figures

A microtexture method which does not require the measurement of individual diffraction patterns has been developed by Humphreys (1983) and Weiland and Schwarzer (1984). Using this method, which is implemented on a TEM, a pole figure is obtained from a selected area, typically 5–10 μm in diameter, of a thin specimen. A eucentrically-mounted specimen is tilted through an angle of $\pm 50^\circ$ in steps of $\sim 2^\circ$, and at each tilt the intensity around a low index Debye ring is measured by scanning the beam over a transmission electron detector. The technique is fully automated and has a similar geometry to the transmission x-ray method. Using this method, partial pole figures are obtained from the selected areas in a few minutes. The technique is ideally suited to the study of highly deformed materials in which the number of cells or subgrains is too large for the acquisition of individual TEM patterns to be feasible. It has been used to study the orientations near second-phase particles and the texture of shear bands.

A1.3.4 Electron Backscatter Diffraction (EBSD)

As discussed above, the disadvantage of obtaining complete texture data (e.g. ODFs) from pole figures is that errors are introduced when the pole figures are deconvoluted to obtain the orientation distribution functions. However, if individual orientations are measured, then the ODFs can be obtained directly from a sufficient number of measurements. Methods based on TEM can only provide data from small volumes of material, whereas individual orientation measurements from EBSD in the SEM can be obtained rapidly from either small areas of interest or over the whole surface of a sample. With the improved spatial resolution for EBSD now possible in Field Emission Gun SEMs (FEGSEM), EBSD is likely to become the standard method of texture measurement in the near future.

A1.3.4.1 The EBSD technique

Electron backscattered diffraction (EBSD) is based on the acquisition of diffraction patterns from bulk samples in the scanning electron microscope, and although such patterns were first obtained over 40 years ago, it was the work of Dingley (e.g. Dingley and Randle 1992), who pioneered the use of low light TV cameras for pattern acquisition and on-line pattern solution, which stimulated widespread interest in the technique, leading to the development of commercially available systems; recent reviews include those of Randle and Engler (2000) and Humphreys (2001). A more recent innovation has been the use of EBSD in conjunction with Field Emission Gun Scanning Electron Microscopes (FEGSEM) (Humphreys and Brough 1999), and the consequent increase in spatial resolution has further extended the range of applications of EBSD.

The EBSD acquisition hardware generally comprises a sensitive CCD camera, and an image processing system for pattern averaging and background subtraction. Figure A1.6 is a schematic diagram showing the main components of an EBSD system. The EBSD acquisition software will control the data acquisition, solve the diffraction patterns and store the data. Further software is required to analyse, manipulate and display the data.

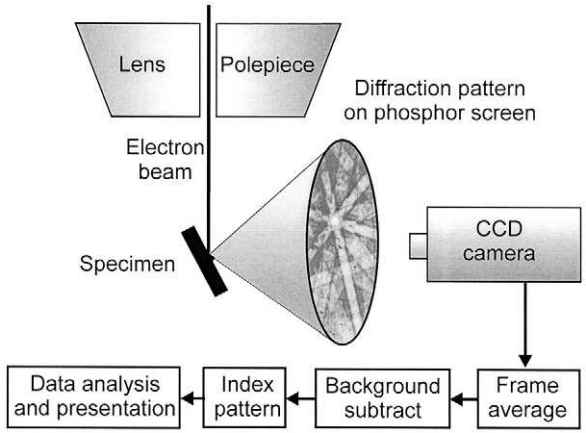

Fig. A1.6. Schematic diagram of a typical EBSD installation in an SEM.

EBSD is carried out on a specimen which is tilted between 60° and 70° from the horizontal, and a series of data points are obtained by rastering the beam across the sample. These data points may be plotted as pixels to form an **orientation map,** and several examples of this are presented in this book. Because the beam moves off the optic axis during such a scan, errors in the absolute orientation are introduced at very low magnifications and beam defocussing due to the highly tilted sample may lead to a loss of spatial resolution (Humphreys 1999b). For these reasons, beam scanning is generally limited to areas of less than $\sim 500 \times 500$ μm. In order to avoid these errors when measuring larger areas, a stationary electron beam is used and the specimen is moved relative to the beam with stage stepping motors controlled by the EBSD software. The disadvantage of stage scanning is that it is much slower than beam scanning, and the time for stage movement is typically ~1 second. In addition, the positional accuracy of stage scanning using a normal SEM stage is not high, and stage scanning is most suitable for scan steps larger than ~1 μm.

There are a number of factors which must be taken into account when deciding if EBSD can be successfully used for a particular investigation.

The specimen – The backscattered electron signal increases with the atomic number (**z**) of the material. The quality of the diffraction pattern increases with **z** and the spatial resolution may also improve with increasing **z**. The specimen surface must be carefully prepared (e.g. electropolished) so as to eliminate any artefacts introduced by sample preparation.

The speed of data acquisition – The time to acquire a data point during a scan depends on the **slowest** of three operations:

- The time required to obtain an analysable diffraction pattern. This depends primarily on the material and microscope operating conditions.
- The time required to analyse the pattern. This depends on the processing speed of the computer, the speed of the pattern-solving algorithm and the number of lines in

the pattern required for a solution. Software which recognises that subsequent similar patterns do not require analysis may lead to significant increases in speed.
- The time to reposition the beam or stage, which as discussed above is negligible for beam scanning but may be greater than 1s for stage scanning.

Spatial resolution – If the area of the sample contributing to a diffraction pattern contains more than one crystallographic orientation, e.g. a grain boundary region, a single crystal diffraction pattern is not obtained, the automated pattern solving routines may fail and the pattern will not be indexed. The spatial resolution therefore depends on the size of the electron probe and the nature of the material. Due to the tilt of the sample, the spatial resolution parallel to the axis of tilt (Λ_A) is typically around three times better than that perpendicular to the tilt axis (Λ_P). The small intense beam produced in a FEGSEM gives a significant advantage over the conventional W-filament electron gun.

Angular resolution – The **absolute orientation** of a crystallite, is typically obtained with an accuracy of $\sim 2^\circ$, depending on the sample alignment and EBSD operating conditions. However, the **relative orientation** between adjacent data points is related to the precision with which the orientations of data points within the same crystallite can be measured. The corresponding angular resolution is $\sim 1^\circ$, but this can be significantly improved by data averaging methods (Humphreys et al. 2001a).

The current status of EBSD – When routinely acquiring data for quantitative metallography in a standard SEM and using commercially available EBSD equipment, the most relevant parameters which affect the quantity and quality of the data are **material, pattern acquisition time, effective spatial resolution and relative angular precision,** and the current values of these parameters are summarised in table A1.2 for W-filament and FEG microscopes.

Table A1.2
Summary of typical EBSD performance for various metals in W-filament and FEG microscopes.

Sample and microscope type		Spatial resolution (nm)		Angular precision (degrees)		Time/pattern (s)	
		Λ_A	Λ_P	Raw data	Data averaging	Beam scan	Stage scan
Al	W	60	180	1	0.5	0.03	1
	FEG	20	60	1	0.5	0.03	1
Brass	W	25	75	1	0.5	0.02	1
	FEG	9	27	1	0.5	0.02	1
α-iron	W	30	90	1	0.5	0.02	1
	FEG	10	30	1	0.5	0.02	1

A1.3.4.2 Obtaining textures by EBSD

EBSD is most commonly used to obtain local crystallographic or microstructural information (see also appendix 2). However, it is being increasingly used to obtain the 'bulk' texture from a sample. The sample, which should be representative of the bulk material, is often polished on the RD-ND plane because in rolled material this section samples the microstructure better than the rolling plane. A specimen which is 15 mm in the rolling direction, cut from 3 mm sheet in a material of grain size 50 μm would reveal ~20000 grains on its surface. Diffraction patterns are obtained from a grid of points covering the entire specimen or a selected region. From these data the orientation distributions are obtained and these can be displayed as pole figures or ODFs, or alternatively the volume fraction of material approximating to selected ideal texture components may be calculated. If a texture representative of the bulk material is to be obtained then it is important that data are obtainable from all parts of the microstructure. A heavily deformed material may contain cells or subgrains which are below the resolution of a W-filament SEM, and this may result in an unacceptably low fraction of indexed diffraction patterns. In addition, if the cell size depends on grain orientation, certain orientations will be sampled more efficiently than others and measured texture will be incorrect. For such materials, it may be necessary to use a FEGSEM to achieve an acceptable level of pattern solution.

If the technique described above is to be used to determine the 'bulk' texture of a specimen then the number of data points required to produce a statistically significant orientation distribution function needs consideration. Experiments have indicated that the number of orientation determinations required is in the range 2000–10000 (Wright and Kocks 1996, Hutchinson et al. 1999a). If these individual orientations are used directly, then the pole figures or orientation distribution functions may be noisy, and the data may be smoothed by convolution with a Gaussian of half width 1–5°. Such a texture determination using 2000 points and carried out by stage scanning will take only ~30 min, which should be compared with the 4–5 hrs required for the multiple pole-figure x-ray analysis discussed in §A1.2.1. **We therefore conclude that for suitable materials, bulk texture determination by EBSD, in addition to being more accurate, may offer a significant time saving over conventional x-ray analysis.**

In many rolled materials the deformation or recrystallization textures vary through the sheet thickness. In such circumstances, suitable data grids on a single ND-RD section specimen may be analysed by EBSD to provide through-thickness texture data at a fraction of the time which would be required for conventional x-ray analysis of several specimens sectioned parallel to the rolling plane and ground to the required depths.

Appendix 2

THE MEASUREMENT OF RECRYSTALLIZATION

In this appendix we provide a brief overview of some quantitative aspects of recrystallization, including the experimental techniques used to measure recrystallization, the determination of some of the parameters associated with the annealing processes, and the quantification of some important features of the associated microstructures. We do not attempt to cover the subject matter in detail, but aim to highlight important and new aspects of the subject and indicate key references where further information may be obtained. Because the use of EBSD for quantitative metallography is relatively new, the use of this technique will be covered in rather more detail than other methods. As will be discussed below, EBSD enables important microstructural parameters which were hitherto unobtainable, to be determined.

A2.1 TECHNIQUES FOR MEASURING RECRYSTALLIZATION

Recrystallization and the other annealing phenomena discussed in this book are all processes of microstructural evolution, and most techniques available for studying the microstructure of crystalline materials may be used to measure some aspect of recrystallization. Brief comments on the main techniques which have been employed are given below, and some further details of their applications in specific areas are given in subsequent sections.

A2.1.1 Optical microscopy

As the earliest metallographic technique, optical microscopy is too well known to require further explanation here. With a spatial resolution of ~0.5 μm, it is frequently used for both opaque and transparent materials and has the advantages that it is simple, rapid and inexpensive and can be used to examine large areas. Because of this, it should always be the first method employed to examine an annealed material. However, the amount and accuracy of the information which may be obtained is often limited by the contrast mechanism employed (e.g. surface contrast from etching or contrast from anodic films, and in many cases only partial microstructural information is obtainable.

A2.1.2 Transmission electron microscopy (TEM)

Diffraction contrast in the TEM allows the study of individual dislocations at a spatial resolution of ~5 nm, and the evolution of dislocation structures during recovery. Quantitative measurements of dislocation densities and particle content can be made, although their accuracy depends critically on measurement of the thickness of the thin foil specimens. Recovery, and the early stages of recrystallization may be studied, although the limited area of the sample makes quantitative analysis difficult. In-situ annealing experiments (e.g. fig. 9.10) provide some clues as to the nature of the annealing processes, but the strong effects of the surfaces in samples which are often less than 1 μm thick, may lead to microstructural changes which would not occur in bulk samples.

A2.1.3 Scanning electron microscopy (SEM)

Although the SEM may be used on etched samples as a 'high resolution optical microscope', its main advantage is the availability of diffraction or 'channelling' contrast when using backscattered electrons. This is a similar contrast mechanism to that of the TEM, and although individual dislocations cannot generally be detected (Wilkinson and Hirsch 1997), small changes in orientation across low angle boundaries enable them to be readily imaged (e.g. fig. 7.1). With a FEGSEM operating at ~10 keV, substructures can be revealed with a spatial resolution of ~25 nm in aluminium, and even better resolution is obtainable in heavier metals. As the sample is only polished on one surface, large areas may be examined, and the technique is ideal for measuring the progress of recrystallization and the determination of grain and subgrain sizes. In-situ annealing experiments in the SEM are readily undertaken, and provide valuable information (e.g. fig. 7.2). The presence of only one free surface makes such experiments more reliable than those carried out in the TEM, although great caution must still be used in their interpretation.

A2.1.4 Electron backscatter diffraction (EBSD)

The principles of EBSD are discussed in appendix 1, with particular relevance to the determination of textures. However, the use of EBSD as a technique for quantitative

metallography is now widely recognised, and is discussed by Humphreys (2001). Using EBSD maps, both the size and orientation of grains and subgrains may be determined, and detailed metallography of partly recrystallized samples carried out. The current limitations of the technique for studying deformed materials are primarily the spatial and angular resolutions (see table A1.2). Nevertheless, even highly deformed samples of a subgrain-forming material such as aluminium may be successfully studied as shown in figure 14.4.

A2.1.5 X-ray diffraction

In addition to its use for texture determination, x-ray diffraction may be used to investigate the deformed state and the annealing of materials in a number of ways including stored energy measurement. (§A2.2.1), and boundary migration during grain growth (§A2.7.2). Changes in texture during dynamic heating experiments may be followed by x-ray or neutron diffraction (Hansen et al. 1981), and with care, interpreted in terms of microstructural evolution. There is currently an interest in developing x-ray microscopy based on synchrotron radiation for investigating recrystallization and grain growth (Juul Jensen and Poulson 2000). This would have the benefits of providing 3-D information and enabling 3-D in situ annealing experiments to be carried out. However, it is too early to ascertain if sufficient spatial resolution will be obtainable by this technique for the measurement of recrystallization.

A2.1.6 Ultrasonics

A relatively new technique for studying microstructure, which is particularly suitable for dynamic measurements is laser-ultrasonics (Lindh–Ulmgren et al. 2001). Laser light is pulsed onto the surface of a sample, where it generates an ultrasonic signal. The signal is complex, and may be analysed to reveal changes in elastic modulus, which are related to texture, and also grain structure. As the technique can readily be applied to hot samples and is remote and non-intrusive, it offers the potential for directly monitoring the progress of recrystallization.

A2.1.7 Property measurements

Changes in microstructure during annealing are often reflected in changes in the mechanical properties, and changes in hardness or yield stress can be used to follow recovery or recrystallization (e.g. figs. 6.3–6.6). However, because of the complex relationships between strength and microstructure it is often difficult to unambiguously interpret mechanical property changes in terms of microstructural events.

Physical properties, such as resistivity or density are strongly dependent on defect content, and may be used to follow annealing (e.g. fig. 6.3). However, detailed interpretation of the data in terms of microstructural changes is again difficult.

A2.2 DRIVING PRESSURE FOR RECRYSTALLIZATION

The driving pressure for recrystallization arises from the crystal defects stored in the deformed material. These include high angle grain boundaries, dislocations and dislocation boundaries such as cell or subgrain walls. Unfortunately, this important parameter is very difficult to measure accurately. Brief reviews of methods of measuring the stored energy of deformed metals are given by Borbely and Driver (2001) and Bacroix et al. (2000).

A2.2.1 Calorimetry

A sensitive calorimeter may be used to determine the release of stored energy (Schmidt 1989, Haessner 1990, Scholz et al. 1999), and some of the measurements are discussed in §2.2.2.

However, because of the small amount of stored energy in a deformed material, reliable calorimetric measurements of recovery and recrystallization can only be made on materials in which no phase transformations such as precipitation (e.g.Verdier et al. 1997) or surface reaction (Scholz et al. 1999) occur over the temperature range of the experiment. For example, the stored energy of deformed aluminium is $\sim$20 J/mol (§2.2), and the latent heat released by precipitating a volume fraction of only 0.01 of $CuAl_2$ in aluminium is also $\sim$20 J/mol. It is now thought that some early measurements of stored energy are unreliable because of the occurrence of small amounts of phase transformation during the experiments.

A2.2.2 X-ray diffraction

The lattice distortions due to dislocations can be detected as a broadening of x-ray diffraction peaks, and this has been used to measure stored energies for many years (§2.2). The shape and symmetry of the peaks depend on a number of factors including the overall dislocation density, the long-range stress fields, cell size and grain orientation effects. By measuring the profiles of several diffraction peaks, it is possible to deconvolute the data so as to determine the dislocation arrangements in some detail, and many models for this have been proposed (e.g. Williamson and Hall 1953, Wilkens 1965, Groma et al. 1988). The stored energies of grains of different orientations may be estimated (e.g. fig. 2.7) and the edge or screw character of the dislocations determined (Schaffler et al. 2001).

The use of high intensity x-ray synchrotron sources enables very small volumes containing a few or even single small grains to be investigated, and the high beam intensity and resolution enables further parameters such as cell misorientations to be measured (Borbely and Driver 2001, Bacroix et al. 2000).

A2.2.3 Electron microscopy and diffraction

The stored energy may also be determined from microstructural measurements, the method depending on the dislocation distribution, and we consider three cases.

The dislocations are relatively **uniformly distributed.** In this situation, which is rather unusual (e.g. Al–5%Mg), the stored energy may be estimated from a measurement by TEM of the dislocation density. The stored energy is then calculated from relationships such as equation 2.4.

Well-defined subgrains are formed (e.g. recovered aluminium or metals deformed at high temperatures). In this case, measurements of subgrain size (D) and subgrain misorientation (θ) are best made by EBSD. A relationship between boundary misorientation and boundary energy such as the Read–Shockley relationship of equation 4.5 must be assumed, and the stored energy is then calculated from D and θ, using equations 2.7 or 2.8. However, boundary energies are not well known, and the accuracy and general applicability of equation 4.5 is not well established. In some cases both a subgrain structure and unbound dislocations are formed (§13.2.3), and these terms must both be included.

A **dislocation cell structure** is formed (e.g. deformed copper). This is a very difficult case because the high dislocation density in the cell walls is difficult to measure and the dislocation density is inhomogeneous, making the application of equation 2.4 doubtful.

More detailed reviews of measurements of stored energy by TEM are given by Bacroix et al. (2000) and Borbely and Driver (2001). If the defect structure is more complex, such as in a material which undergoes both slip and deformation twinning (e.g. α-brass or magnesium) there are no established methods for estimating the stored energy from microscopic measurements.

A2.3 FRACTION RECRYSTALLIZED

Measurement of the amount of recrystallization is an essential part of the determination of recrystallization kinetics. Although some indication of this parameter may be obtained from indirect measurements of e.g. hardness or resistivity (e.g. fig. 7.18), accurate measurements can only be obtained by studying the microstructure.

A2.3.1 Microscopical methods

Optical microscopy is traditionally used to measure the progress of recrystallization, and similar results may be obtained by SEM imaging. If the recrystallized and unrecrystallized regions can be distinguished by e.g. etching, then standard methods of quantitative metallography using areal, lineal or point counting methods may be employed (Orsetti Rossi and Sellars 1997). Point counting is the most efficient, and this may be carried out using a standard point-counting microscope. If $\mathbf{n_r}$ is the number of the measured points which are recrystallized in a sample whose recrystallized fraction is $\mathbf{X_V}$, the confidence limits (σ) are given (Gladman and Woodhead 1960) as

$$\left(\frac{\sigma}{X_V}\right)^2 = \frac{1 - X_V}{n_r} \qquad \text{(A2.1)}$$

For a sample which is ~50% recrystallized, the number of measurements required is typically ~500, but for $X_V < 0.1$ the number of points required is unrealistically large for such a manual technique (Orsetti Rossi and Sellars 1997).

A2.3.2 EBSD methods

There are several ways in which EBSD may be used to determine the fraction recrystallized (Humphreys 2001).

- **Point counting**

If it is possible to distinguish between the diffraction patterns from recrystallized and unrecrystallized material, then point counting methods may be used. Such techniques rely on the quality of the diffraction pattern being lower in an unrecrystallized region than in a recrystallized grain due to dislocation debris. Several approaches have been proposed (e.g. Black and Higginson 1999, Tarasiuk et al. 2001), but although such methods are very rapid, careful calibration is required. In most aluminium alloys deformed at room temperature and many metals deformed at elevated temperatures, the subgrain structures are relatively clean, and of an area larger than the EBSD resolution (table A1.2). Therefore the diffraction patterns obtained from within subgrains in the deformed regions will be of similar quality to those for recrystallized regions, and in this case, point counting techniques based on pattern quality do not work reliably.

- **Lineal analysis**

In a subgrain-forming material (e.g. aluminium), lineal EBSD analysis may be used. One method is to identify high or low angle boundaries during a scan and to assume that the region between two adjacent boundaries which are high angle, is a recrystallized grain (Humphreys 2001). Alternatively, the fraction of boundaries which are high angle can be measured from a linescan, and this provides an indirect measure of the fraction recrystallized (see fig. 14.6).

- **Areal analysis**

The fraction recrystallized may be obtained from analysis of EBSD maps (Humphreys 2001). Although the technique is considerably slower than point counting methods, it is particularly suitable for studying the early stages of recrystallization, and can be used to identify the orientation distributions of the recrystallizing grains. The recrystallized regions may be identified on the basis of pre-defined size, pattern quality, size and boundary character criteria, and although very detailed measurements may be made in this way, there are rather few cases when such a time-consuming method is justified.

A2.4 NUCLEATION AND GROWTH RATES

The overall rate of recrystallization during isothermal annealing may be found from the increase in the volume recrystallized (§A2.3) as a function of time. However, a more detailed interpretation of the recrystallization behaviour is often obtained by determining the rates of nucleation and growth of the new grains. Recent reviews include those of Orsetti Rossi and Sellars (1997) and Juul Jensen (2001).

A2.4.1 Nucleation of recrystallization

The nucleation of recrystallization is discussed in chapter 7, where it was pointed out that the rate of nucleation (dN/dt) was a complex parameter. For simplicity, two

possibilities are usually considered, **site-saturated nucleation,** where all nuclei are present at $t = 0$ or a **constant nucleation rate.**

The most common method of distinguishing between these possibilities is by counting the grains per unit area (N_p) on a 2-D section from microscopic or EBSD data, and using standard quantitative metallographic analyses (e.g. Fullman 1953). As the nuclei grow, then N_p increases, and if it is assumed that the nuclei are spheres of radius **r,** the number of nuclei per unit volume (N) is given by

$$N = \frac{N_p}{2r} \tag{A2.2}$$

This analysis can be extended to allow for nuclei of different sizes and shapes (Fullman 1953).

Alternatively, the microstructural path analysis of Vandermeer and Rath (1989a) based on the work of Gokhale and DeHoff (1985), which is discussed in §7.3.2 may be used. This is based on the variation with time of the extended recrystallized volume fraction (X_{VEX}) and extended interfacial area per unit volume between recrystallized and unrecrystallized material (S_{VEX}), which are given by equations 7.25 and 7.26 respectively. From the term δ, obtained via equation 7.30 from the exponents **n** and **m** in these equations, it is possible to determine the type of nucleation. If $\delta = 0$ then nucleation is site saturated and if $\delta = 1$ then the nucleation rate is constant. The analysis is strictly valid only for a random spatial distribution of nuclei, although it can be modified to allow for non-random distributions (see e.g. Orsetti Rossi and Sellars 1997).

A2.4.2 Growth rates

The simplest method of determining the growth rates of recrystallizing grains is to measure the sizes of the largest grains visible on 2-D sections as a function of annealing time (Anderson and Mehl 1945). However, this method is only applicable in the early stages of recrystallization, before impingement of the grains occurs.

A better method of measuring growth rates is that suggested by Cahn and Hagel (1960) and given by equation 7.18. This requires measurement from 2-D sections of the fraction recrystallized ($\mathbf{X_V}$) and the area per unit volume between recrystallized and unrecrystallized material ($\mathbf{S_V}$). Both these parameters can be readily measured by standard microscopical methods or by EBSD. From EBSD data, it is possible to extend this analysis to measure the growth rates of recrystallizing grains of particular orientations (e.g. Juul Jensen 1995a). More detailed information as to whether growth rates are anisotropic may be obtained from methods such as those proposed by Vandermeer and Rath (1989a), and outlined in §7.3.2.

A2.5 GRAIN AND SUBGRAIN SIZE

The grain size has traditionally been measured by optical microscopy, and the methods of determining grain size and related parameters have been well

documented (e.g. DeHoff and Rhines 1968, Underwood 1970. Scanning electron microscopy is increasingly being used, although, as with any scanning technique, particular care must be taken with instrument calibration (Dyson and Quested 2001). For the smallest grain sizes and for subgrain structures, transmission electron microscopy (TEM) may be required, although the problems of preparing and working with the thin specimens required for TEM make it difficult to measure representative microstructures, and the subtleties of the image contrast make automated analysis of TEM images very difficult. EBSD is increasingly being used to characterise grain and subgrain structures, and this has the additional advantage that dimensional information may readily be correlated with the grain or subgrain orientations (Humphreys 2001). Because the sample is typically tilted by 70° to the optic axis, great care must be taken with calibration and sample alignment if accurate measurements are required.

A2.5.1 EBSD measurements

The grain or subgrain size may be determined by EBSD using rather similar methods to those developed for microscopy (Humphreys 2001), and the recent improvements in the speed of EBSD pattern acquisition (table A1.2) enable sufficient data to be obtained in reasonable times.

A significant advantage of EBSD determination over microscopic methods is that EBSD determines all boundaries (above the noise level), whereas metallographic methods only reveal some of the boundaries. Thus optical etching may not reveal low-Σ boundaries or low angle boundaries, and SEM channelling contrast images will only reveal boundaries if the backscattered electron intensity differs between the adjacent grains. Comparison between grain sizes determined by optical imaging, SEM imaging and EBSD (Humphreys 2001), shows significant differences, particularly in recrystallized material with a strong texture.

EBSD **linescans** may be used to obtain values of the mean linear intercept (MLI). By noting orientation changes between successive measurements, the intercept size can be determined for high angle or low angle boundaries, or for any specified angular range. In order to avoid oversampling, the spacing between successive linescans should not be significantly less than the grain/subgrain size. Linear intercepts may either be obtained directly from linescans or from subsequent analysis of an EBSD map, the formed being much faster. The method of determining MLI from analysis of a linescan is given in §A2.5.2.1.

If an EBSD map is obtained, the grains or subgrains may be **reconstructed** by identifying areas whose pixels have orientations within a specified range. This is equivalent to the image analysis methods used for reconstructing metallographic images, and has the advantage that complete information on size, area and shape is obtained. The grain or subgrain size is subsequently determined as an equivalent circle diameter (ECD) as discussed in §A2.5.2.2. The real power of this method is that it enables a significant amount of extra information to be obtained such as the misorientations of all the boundaries of a subgrain and the size and misorientation of subgrains of specific orientations (Humphreys 2001).

When using either linear intercepts or grain reconstruction methods, the size of the steps between adjacent data points is important, because if the step size is too large, small grains or intercepts will be missed and the measured grain/subgrain size will be too large. For an accuracy of ~5%, approximately 10 pixels per grain/subgrain are required (Humphreys 2001). For small grain or subgrain sizes, the EBSD pattern solving efficiency is reduced (A1.3.4.1), and it has been shown that when less than ~50% of patterns are solved, significant errors in the size measurements occur (Humphreys 2001). The step size and pattern solving factors therefore set a lower limit on the grain or subgrain size which can accurately be measured by EBSD, and for aluminium, these are currently ~0.15 μm and 0.4 μm for FEGSEM and W-filament microscopes respectively (Humphreys 2001).

A2.5.2 Calculation of size

If intercept or area measurements of grains or subgrains are made, the following analyses, based on the work of Fullman (1953) and Underwood (1970) may be used to obtain the grain sizes.

A2.5.2.1 Mean linear intercept

For a single-phase material of uniform grain size the grain size may be related to $\overline{L}$, the mean linear intercept distance (MLI) across a grain as measured on a plane section. $\overline{L}$ is determined by measuring the average number of boundary intercepts (N_L) with a line of unit length so that

$$\overline{L} = 1/N_L \tag{A2.3}$$

The boundary surface area per unit volume (S_V) is given by

$$SV = 2N_L \tag{A2.4}$$

$\overline{L}$ will be less than the true grain size because of sectioning effects. If it is assumed that the grain shapes approximate to spheres of diameter $\overline{D}$ then

$$\overline{D} = 1.5\overline{L} \tag{A2.5}$$

$\overline{L}$ is a simple unambiguous parameter which is often used to characterise a grain structure. If the grains are not equiaxed then they can be characterised by mean linear intercepts in the x, y and z directions. However, these cannot readily be converted to a mean diameter.

A2.5.2.2 Equivalent circle diameter

If spherical grains of diameter $\overline{D}$ intersect a random plane, the mean area of intersection is

$$\overline{S} = \pi D^2/6 \tag{A2.6}$$

If these areas are circular, the mean diameter is the **Equivalent Circle Diameter** (ECD) which is given by

$$\mathrm{ECD} = (2/3)^{1/2}\overline{D} = 0.816\overline{D} \tag{A2.7}$$

Note that the ECD is not the same as the MLI, and for uniform spherical grains

$$\mathrm{ECD} = 1.224\overline{L} \tag{A2.8}$$

If the grains are not equiaxed, an ECD is less valid and alternative parameters such as the mean grain area $\overline{S}$ or the mean grain dimensions in orthogonal directions can be used.

A2.5.3 Precision of measurement

If the data set comprises N measurements (e.g. intersections) of a parameter X, then the **mean is** $\mathrm{X} = \sum \mathrm{X_i}/\mathrm{n}$. The **standard deviation** (σ) is

$$\sigma = \sqrt{\frac{(\mathrm{X_i} - \overline{\mathrm{X}})^2}{\mathrm{n}-1}} = \sqrt{\frac{\mathrm{X_i^2} - (\mathrm{X_i})^2/\mathrm{n}}{\mathrm{n}-1}} \tag{A2.9}$$

The standard error of the mean (SE) is

$$\mathrm{SE} = \frac{\sigma}{\sqrt{\mathrm{n}}} = \sqrt{\frac{(\mathrm{X} - \overline{\mathrm{X}})^2}{\mathrm{n}(\mathrm{n}-1)}} \tag{A2.10}$$

The 95% confidence limit is $\overline{\mathrm{X}} \pm 2\,\mathrm{SE}$, and it is recommended that grain/subgrain sizes are presented in this form.

It is usually found that ~300–400 grain or intersection measurements are required to give sufficient precision.

A2.6 GRAIN BOUNDARY CHARACTER DISTRIBUTION

The development of EBSD has made the characterisation of grain boundary misorientations relatively simple, and parameters such as the distribution of grain boundary character (GBCD) in a sample may be rapidly obtained. The three parameters which are of particular significance are the **angle** and **axis** of misorientation and the **boundary plane.**

A2.6.1 Misorientation angle

The misorientation distribution, which was first discussed by McKenzie (1958), is shown for an ideal random polycrystalline assembly in figure 4.2. However, it is sensitive to the

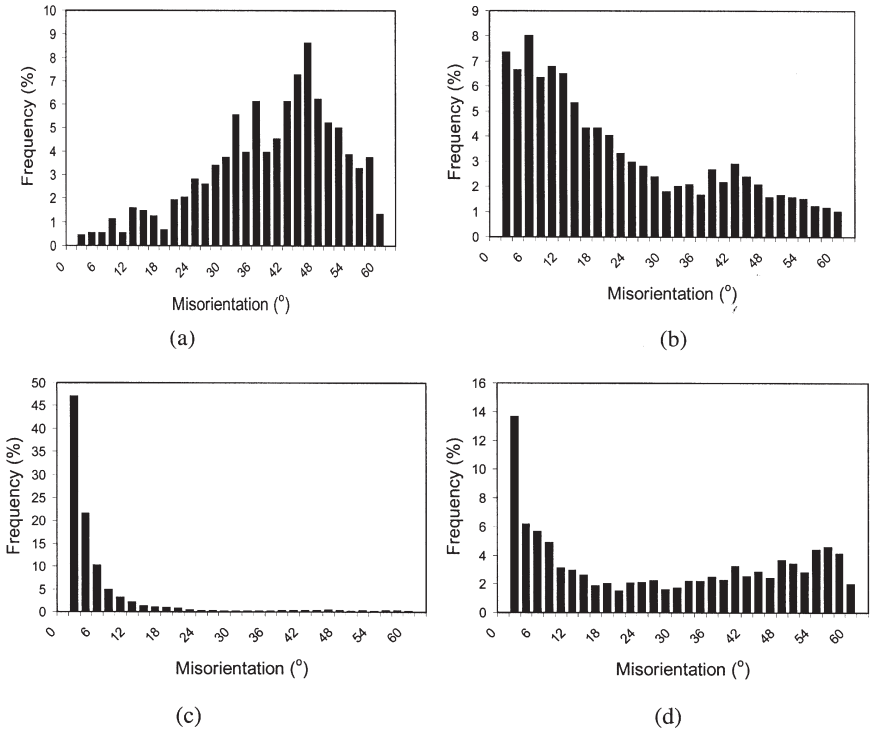

Fig. A2.1. Examples of grain boundary misorientation distributions (McKenzie plots), obtained by EBSD, in commercial purity aluminium. (a) Recrystallized, with random texture, showing a distribution close to that of figure 4.2. (mean misorientation 39.6°, %HAGB = 95), (b) Recrystallized to strong cube texture (mean misorientation 21.9°, %HAGB = 55), (c) Cold rolled 20% (mean misorientation 7.4°, %HAGB = 9.8), (d) Cold rolled 98% (mean misorientation 28°, %HAGB = 63).

texture of the material, and is also altered by plastic deformation and annealing, and examples are shown in figure A2.1. Subsets of the data such as the fraction of high angle and low angle boundaries (e.g. fig. 14.6) or the fractions of low-Σ boundaries, are now becoming commonly used parameters of a thermomechanically processed material and many examples are given in this book.

The frequencies of boundaries of particular types may be obtained as **length** fractions or **number** fractions depending on the method of data analysis (Humphreys 2001). The data are normally obtained from measuring the misorientations of adjacent grains, but the **uncorrelated misorientation distribution** (e.g. table 2.7), can also be determined by comparing the misorientations between all pixels or subgrains in a measured area. This parameter gives a measure of the orientation spread within the area and is thus an indication of long range orientation gradients.

The accuracy of the misorientation data are limited by the precision with which the diffraction patterns are analysed. In high speed EBSD acquisition, which is normally

used for microstructural investigations (table A1.2), the misorientations are typically accurate to within ~1°, although this may be considerably reduced by data averaging and filtering (Humphreys et al. 2001a). The relative angular resolution may be improved by a factor of up to ~10 if techniques involving direct comparison of successive diffraction patterns are used (e.g. Wilkinson 2001). However, such procedures are comparatively slow and are not yet widely used.

A2.6.2 Misorientation axis

In addition to the angles, the axes of misorientation and their distributions may also be of interest, and these are readily obtained when the misorientations are determined. The errors in determining the angle of misorientation limit the accuracy with which the misorientation axis can be determined, and this is particularly important for small misorientations (Prior 1999, Wilkinson 2001).

A2.6.3 Boundary plane

The two degrees of freedom describing the boundary plane are less readily determined experimentally. Trace analysis has long been used to obtain partial information, and when combined with EBSD, this enables one of the boundary plane parameters to be determined. The other parameter, which is the inclination of the boundary to the surface of the sample, is not directly obtainable, and is discussed by Randle and Engler (2000). For large grains, the boundary plane may be determined by sectioning and examining the sample in two orthogonal planes, or in the more general case, by serial sectioning in which the sample is measured after controlled etching.

A2.7 GRAIN BOUNDARY PROPERTIES

The energies and mobilities of boundaries are important during recovery, recrystallization and grain growth. However, measurements of both parameters are very difficult, and additionally there are a large number of important variables including the 5 grain boundary degrees of freedom (§4.1), and the effects of solute, temperature and driving pressure. It is therefore not surprising that a coherent and comprehensive picture of grain boundary properties has not yet been obtained.

A2.7.1 Boundary energy

Measurement of the absolute energies of boundaries is difficult and in most cases the measurements are made relative to a reference interface or surface (see e.g. Hondros 1969, Gottstein and Shvindlerman 1999). If torque terms can be neglected, the geometry of a triple point or groove is given by equation 4.10, and the results shown in figure 4.12 were obtained in this manner. In a variation on this method, the equilibrium shapes of amorphous silica particles at grain boundaries in copper are measured (Mori et al. 1988,

Goukon et al. 2000). This method is very sensitive and avoids the inevitable problems associated with tri-crystals or grooving experiments at free surfaces.

In a novel large-scale investigation of boundary properties, Rollett and colleagues (e.g. Yang et al. 2001) have determined the boundary properties of aluminium from detailed measurements of triple junctions in thick foils. The boundary geometry is simplified by the columnar grain structure which develops in the foils. If it is assumed that the migration rate is proportional to the driving pressure which arises from capillarity (equation 7.1) it is possible from detailed measurements of triple point angles, boundary shapes and grain orientations, together with detailed theoretical analysis, to ascertain boundary energies and mobilities. The measurements of the effect of misorientation on boundary energy are in good agreement with the Read–Shockley relationship of equation 4.5, although a small effect of the misorientation axis is found (fig. 4.7).

A2.7.2 Boundary mobility

Information about boundary mobilities may be made from measurements of individual boundaries or from the growth of a subgrain or grain assembly. Reviews of the techniques used are given by Gleiter and Chalmers (1972), Masteller and Bauer (1978) and Gottstein and Shvindlerman (1999).

A2.7.2.1 Measurements of individual boundaries

- **Curvature or capillary induced migration**

Many early measurements of boundary mobility were made on bicrystals, where the boundary is driven by the shape of the sample, such as a wedge bicrystal (e.g. fig. 5.4). More recently, Shvindlerman and colleagues have made extensive use of an x-ray tracking method to measure boundary velocities dynamically under a constant driving pressure provided by the boundary curvature in a bicrystal (e.g. Gottstein and Shvindlerman 1999). The sample is oriented so that diffraction is obtained from one grain, and a detector monitors the diffracted intensity at the boundary, the sample being automatically moved so as to maintain a constant diffracted intensity. The sample velocity is thus equal to the boundary velocity, and the method has the advantage that the driving pressure remains constant. Several examples of the results of this type of experiment are given in chapter 5, e.g. figures 5.9 and 5.12.

These experiments are very suitable for obtaining fundamental information about the migration of specific types of boundary, and can be used to investigate the effects of small orientation changes or solute additions. The main disadvantage is that the driving pressures are low, and therefore experiments cannot be carried out on very low angle boundaries nor at low temperatures. The boundary migration occurs under grain growth conditions and it is not yet clear if the boundary behaviour is identical to that during recrystallization.

- **Defect induced migration**

The migration of individual recrystallizing boundaries in single crystals which have either been deformed to produce a substructure, or which have lineage structure formed

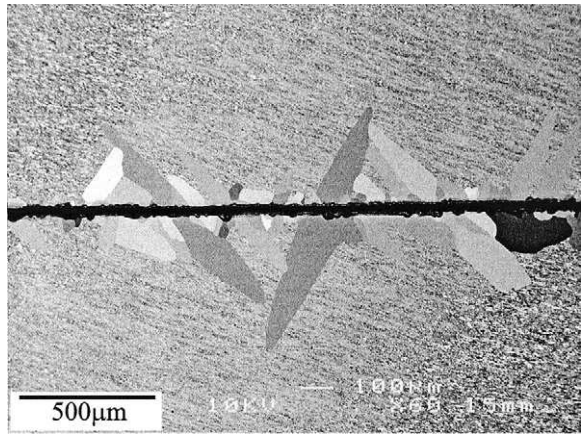

Fig. A2.2. SEM backscattered electron image from an in-situ annealing experiment to determine the growth rate of grains nucleated at the horizontal scratch, and growing into the recovered matrix, (Huang and Humphreys 1999b).

during solidification, has been extensively studied. The well known experiments of Liebmann et al. (1956) on the orientation dependence of mobility were made on deformed single crystals, and those of Aust and Rutter (1959a,b), on the effect of impurities on mobility (fig. 5.21) were made on crystals containing lineage substructures.

Huang and Humphreys (1999a) used a related technique for in-situ SEM measurements of boundary migration in deformed single crystals. The crystal was scratched to provide nucleation sites for the recrystallization which occurred on heating the sample (fig. A2.2). EBSD was used to measure the subgrain sizes and misorientations in the recovered crystals, so that the driving pressure could be calculated (equation 2.8) and also to determine the orientations of the recrystallizing grains and the recovered matrix. The variation of mobility with misorientation obtained in this way is shown in figure 5.11.

Although experiments in which boundaries migrate into a deformed or recovered substructure do not provide the detailed physical insight that can be provided by the curvature driven experiments, they provide valuable data relevant to the recrystallization of metals and can provide the required input for annealing models.

A2.7.2.2 Mean values from subgrain or grain assemblies

Many experiments in which the growth rates of polycrystalline assemblies have been measured have been carried out. If these can be analysed correctly, they provide mean values of the boundary mobility. However, as discussed in §11.1.4, many of these experiments do not obey the simple growth law of equation 11.5, and therefore analysis is difficult. It is likely that in many cases the samples are not 'ideal' because of the presence of second-phase particles or textures.

Measurements of the growth of subgrain assemblies in which the range of misorientations is small, have been made by Huang and Humphreys (2000) (figs. 5.5 and 5.6). Although these only provide mean values, the method is one of the few available for obtaining the mobilities of low angle boundaries.

The project by Rollett and colleagues in which the geometry of triple junctions was measured (see A2.7.1), has also provided information about boundary mobilities (e.g. Yang et al. 2001). Results to date indicate a similar effect of misorientation on mobility to that shown in figures 5.5 and 5.6.

A2.8 PARAMETERS OF TWO-PHASE ALLOYS

In order to quantify the annealing behaviour of two-phase alloys, it is necessary to define the various parameters which describe a distribution of second-phase particles. Experimental measurements are carried out using standard methods of optical, scanning or transmission electron microscopy as appropriate and will not be discussed further. From such measurements a number of parameters may be obtained, and in the following sections we consider only the simplest cases; for more detailed discussion the reader is referred to Underwood (1970), Exner (1972) or Martin (1980).

A2.8.1 Particle size

All multi-phase materials contain particles of a spectrum of sizes and shapes. In modelling the effect of particles it is often necessary to simplify the situation and to assume that the dispersion is of uniform spheres of radius **r.** In comparing experimental data with such a model, a mean value of particle diameter is often used, and for the case of non-spherical but equiaxed particles, an equivalent radius is usually calculated. For particles which are not equiaxed, it is necessary to use more than one parameter to define the particle size and shape.

A2.8.2 Volume fraction

The volume fraction F_V of particles may be measured experimentally or calculated from a knowledge of the phase diagram. For a random distribution of particles, F_V is also equal to the fractional area occupied by particles on a plane section, and the fractional length occupied by the particles on a random straight line.

A2.8.3 Interparticle spacing

For a dispersion of uniform spheres of radius **r,** the **number of particles per unit volume** (N_V) is related to the volume fraction by

$$N_V = \frac{3F_V}{4\pi r^3} \tag{A2.11}$$

The **number of particles intersecting unit area** (N_S) of a plane surface is $N_V.2r$ and hence

$$N_S = \frac{3F_V}{2\pi r^2} \tag{A2.12}$$

If the particles are arranged on a square lattice, then the centre to centre **nearest neighbour spacing on a plane** is

$$\lambda = N_S^{-1/2} \tag{A2.13}$$

For randomly distributed particles, the centre to centre **nearest neighbour spacing on a plane** is

$$\Delta_2 = 0.5N_S^{-1/2} \tag{A2.14}$$

and the centre to centre **nearest neighbour spacing in the volume** is

$$\Delta_3 = 0.554N_V^{-1/3} \tag{A2.15}$$

A2.8.4 Particle distribution

The spatial distribution of the particles, i.e. whether it is uniform, random or clustered may be important. However, there is as yet no simple method of quantitative classification (Fridy et al. 1992).

REFERENCES

Aaronson, H.I., Laird, C. and Kinsman, K.R. (1962), in **Phase Transformations,** ASM, Metals Park, Ohio, 313.

Abbruzzese, G. and Brozzo, P. (1992), (eds.) **Grain Growth in Polycrystalline Materials,** Trans Tech Publns, Switzerland.

Abbruzzese, G. and Lücke, K. (1986), Acta Metall. 34, 905.

Abbruzzese, G. and Lücke, K. (1992), in **Grain Growth in Polycrystalline Materials,** eds. Abbruzzese and Brozzo, Trans Tech Publns, 597.

Abbruzzese, G., Heckelmann, I. and Lücke, K. (1992), Acta Metall. 40, 519.

Abbruzzese, G., Lücke, K. and Eichelkraut, H. (1988), Proc. ICOTOM 8, eds. Kallend and Gottstein, TMS, Warrendale, 693.

Abe, H. and Satoh, S. (1990), Kawasaki Steel Tech. Rep. 22, 48.

Abe, H., Suzuki, T. and Okada, S. (1983), Tetsu-to-Hagané, 69, S1415.

Abe, H., Nagashima, S., Hayami, S. and Nakaoka, K. (1978), Proc. ICOTOM 5, eds. Gottstein and Lücke, Springer-Verlag, 2, 21.

Abe, H., Suzuki, T. and Takagi, K. (1980), Trans. ISIJ, 20, 100.

Aboav, D.A. and Langdon, T.G. (1969), Metallography, 2, 171.

Abrahamson, E.P. and Blakeny, B.S. (1960), Trans. Metall. Soc. A.I.M.E. 218, 1101.

Adam, C.M. and Wolfenden, A. (1978), Acta Metall. 26, 1307.

Adcock, F. (1922), J. Inst. Met. 27, 73.

Ahlborn, H., Hornbogen, E. and Köster, U. (1969), J. Mats. Sci. 4, 944.

Akef, A. and Driver, J.H. (1991), Mat. Sci. and Eng. A132, 245.

Alexander, B. and Balluffi, R.W. (1957), Acta Metall. 5, 666.

Altherthum, H. (1922), Z. Metallk. 14, 417.

Amelinckx, S. and Strumane, R. (1960), Acta Metall. 8, 312.

Anand, L. and Gurland, J. (1975), Metall. Trans. 6A, 928.

Anand, L. and Gurland, J. (1976), Acta Metall. 24, 901.

Anderson, l., Grong, O. and Ryum, N. (1995), Acta Metall. 43, 2689.

Anderson, M.P. (1986), Proc. 7th Int. Risø Symposium, ed. Hansen, Risø, Denmark, 15.

Anderson, M.P., Srolovitz, D.J., Grest, G.A. and Sahni, P.S. (1984), Acta Metall. 32, 783.

Anderson, M.P., Grest, G.S. and Srolovitz, D.J. (1985), Scripta Metall. 19, 225.

Anderson, M.P., Grest, G.S. and Srolovitz, D.J. (1989a), Phil. Mag. B59, 293.

Anderson, M.P., Grest, G.S., Doherty, R.D., Li, K. and Srolovitz, D.J. (1989b), Scripta Metall. 23, 753.

Anderson, W.A. and Mehl, R.F. (1945), Trans. Metall. Soc. A.I.M.E. 161, 140.

Ando, H., Sugita, J., Onaka, S. and Miura, S. (1990), J. Mats. Sci. 9, 314.

Arai, K.J. and Yamashiro, Y. (1989), in MRS Int. Mtg. on Advanced Materials, 11, 187.

Ardakani, M.G. and Humphreys, F.J. (1992), in **Recrystallization'92,** eds. Fuentes and Gil Sevillano, Trans. Tech. Publications, 213.

Ardakani, M.G. and Humphreys, F.J. (1994), Acta Metall. 42, 763.

Ardell, A.J. (1972), Acta Metall. 20, 601.

Ardell, A.J. (1985), Metall. Trans. 16A, 2131.

Aretz, W., Ponger, D. and Gottstein, G. (1992), Scripta Metall. 27, 1593.

Argon, A.S. and Moffatt, W.C. (1981), Acta Metall. 29, 293.

Argon, A.S., Im, J. and Safoglu, R. (1975), Metall. Trans. 6A, 825.

Ashby, M.F. (1966), Phil. Mag. 14, 1157.

Ashby, M.F. (1970), Phil. Mag. 21, 399.

Ashby, M.F. (1980), Proc. 1st Int. Risø Symp., ed. N. Hansen, Risø, Denmark, 325.

Ashby, M.F. and Centamore, R.M.A. (1968), Acta Metall. 16, 1081.

Ashby, M.F. and Palmer, I.G. (1967), Acta Metall. 15, 420.

Ashby, M.F., Harper, J. and Lewis, J. (1969), Trans. Metall. Soc. A.I.M.E. 245, 413.

Assmus, F., Boll, R., Ganz, D. and Pfeifer, F. (1957), Z. Metallk. 48, 341.

Atkinson, H.V. (1988), Acta Metall. 36, 469.

Atwater, H.A., Thompson, C.V. and Smith, H.I. (1988), J. Appl. Phys. 64, 2337.

Aust, K.T. (1969), Can. Met. Quart. 8, 173.

Aust, K.T. and Rutter, J.W. (1959a), Trans. Metall. Soc. A.I.M.E. 215, 119.

Aust, K.T. and Rutter, J.W. (1959b), Trans. Metall. Soc. A.I.M.E. 215, 820.

Aust, K.T. and Rutter, J.W. (1963), in **Recovery and Recrystallization of Metals,** ed. Himmel, Interscience, 131.

Aust, K.T., Ferran, G. and Cizeron, G. (1963), C.R. Acad. Sci. Paris, 257, 3595.

Aust, K.T., Erb, U. and Palumbo, G. (1993), in **Interfaces, Structure and Propoerties.** Kluwer Academic, (Netherlands), 107.

Avrami, M. (1939), J. Chem. Phys. 7, 1103.

Babcock, S.E. and Balluffi, R.W. (1989a), Acta Metall. 37, 2357.

Babcock, S.E. and Balluffi, R.W. (1989b), Acta Metall. 37, 2367.

Bacroix, B. and Jonas, J.J. (1988), Text. Microstruct. 8/9, 267.

Bacroix, B., Castelnau, O., Miroux, A. and Reglé, H. (2000), Proc. 21st Int. Risø Symposium, eds. N. Hansen et al., Risø, Denmark, 1.

Baczynski, G.J., Guzzo, R., Ball, M.D. and Lloyd, D.J. (2000), Acta Mater. 48, 3361.

Bahk, S. and Ashby, M.F. (1975), Scr. Met. 9, 129.

Bailey, J.E. and Hirsch, P.B. (1960), Phil. Mag. 5, 485.

Bailey, J.E. and Hirsch, P.B. (1962), Proc. R. Soc. Lond. A267, 11.

Bainbridge, D.W., Li, C.H. and Edwards, E.H. (1954), Acta Metall. 2, 322.

Baker, I. (1991), in **Structure and Property Relationships for Interfaces,** eds. Walter et al. ASM, 67.

Baker, I. (2000), Intermetallics, 8, 1183.

Baker, I. and Gaydosh, D.J. (1987), Metallography, 20, 347.

Baker, I. and Martin, J.W. (1980), J. Mater. Sci. 15, 1533.

Baker, I. and Martin, J.W. (1983a), Metal Sci. 17, 459.

Baker, I. and Martin, J.W. (1983b), Metal Sci. 17, 469.

Baker, I. and Munroe, P.R. (1990), in **High Temperature Aluminides and Intermetallics,** eds. Whang et al. TMMMS, 425.

Baker, I. and Munroe, P.R. (1997), Int. Mater. Rev. 42, 181.

Baker, I., Viens, D.V. and Schulson, E.M. (1984), J. Mats. Sci. 19, 1799.

Ball, E. and Humphreys, F.J. (1996), in **Thermomechanical Processing (TMP^2)**, eds. W.B. Hutchinson et al., ASM, Ohio, 184.

Ball, J. and Gottstein, G. (1993a), Intermetallics, 1, 171.

Ball, J. and Gottstein, G. (1993b), Intermetallics, 1, 191.

Ball, J., Mitteau, J. and Gottstein, G. (1992), in **Ordering and Disordering in Alloys,** ed. Yavari, 138.

Balluffi, R.W. (1980), (ed.) **Grain Boundary Structure and Kinetics,** ASM, Ohio.

Balluffi, R.W. (1982), Metall. Trans. A. 13, 2069.

Balluffi, R.W., Koehler, J.S. and Simmons, R.O. (1963), in **Recovery and Recrystallization of Metals,** ed. Himmel, Interscience, 1.

Bampton, C.C., Wert, J.A. and Mahoney, M.W. (1982), Met. Trans. 13A, 193.

Bardal, A., Lindseth, I., Vatne, H. and Nes, E. (1995). Proc. 16th Int. Risø Symp., eds, Hansen et al., 262.

Barioz, C., Brechet, Y., Legresy, J.M., Cheynet, M.C., Courbon, J., Guyot, P. and Ratnaud, G.M. (1992), Proc. 3rd Int. Conf. on Aluminium, Trondheim., 347.

Barnett, M.R. (1998), ISIJ Int. 38, 78.

Barnett, M.R. and Jonas, J.J. (1997), ISIJ Int. 37, 697.

Barrett, C.R., Nix, W.D. and Sherby, O.D. (1966), Trans. ASM. 59, 3.

Barrett, C.S. (1939), Trans. Metall. Soc. A.I.M.E. 135, 296.

Barrett, C.S. (1940), Trans. Metall. Soc. A.I.M.E. 137, 128.

Barrett, C.S. and Massalski, T. (1980), **Structure of Metals,** 3rd edn., Pergamon Press, Oxford.

Barto, R.L. and Ebert, L.J. (1971), Metall. Trans. 2, 1643.

Bassani, J.L. (2001), J. Mech. Phys. Solids. 49, 1983.

Basson, F., Chenal, B., Necker, C., Embury, J.D. and Driver, J.H. (1998), Proc. 6th Int. Al. Conf. ICAA6, eds. Sato et al., 1167.

Basson, J.A., Knutsen, R.D. and Lang, C.I. (2000), Proc 21st Int. Risø Symposium, eds. N. Hansen et al., Risø, Denmark, 243.

Bate, P.S. (1989), Technical Report, CRC/TR/89/4C, Comalco Research Centre.

Bate, P.S. (1999), Phil. Trans. Royal Soc. Lond. A357, 1589.

Bate, P.S. (2001a), Proc. Int. Conf. on Recrystallization and Grain Growth, Aachen, eds. G. Gottstein and D. Molodov, Springer-Verlag, Berlin, 39.

Bate, P.S. (2001b), Acta Mater. 49, 1453.

Bate, P.S. (2003), Private communication.

Bate, P.S. and Hutchinson, W.B. (1997), Scr. Mater. 36, 199.

Bate, P.S. and Oscarrson, A. (1990), Mats Sci. and Tech. 6, 520.

Baudin, T., Julliard, F., Paillard, P. and Penelle, R. (2000), Scripta Mater. 43, 63.

Bauer, C.L. (1974), Canad. Met. Q. 13, 303.

Bauer, C.L. and Lanxner, M. (1986), in **Grain Boundary Structure and Related Phenomena. Proc. JIMIS-4,** Suppl. to Trans. Jap. Inst. Met. 27, 411.

Baxter, G.J., Furu, T., Zhu, Q., Whiteman, J.A. and Sellars, C.M. (1999), Acta Mater. 47, 2367.

Bay, B. and Hansen, N. (1979), Metall. Trans. A10, 279.

Bay, B., Hansen, N., Hughes, D.A. and Kuhlmann-Wilsdorf, D. (1992), Acta Metall. 40, 205.

Beck, P.A., (1953), Acta Metall. 1, 230.

Beck, P.A. (1954), Adv. Phys. 3, 245.

Beck, P.A. (1963), in Sorby Centennial Symposium on the History of Metallurgy. Met. Soc. Conf. No. 27. ed. Smith, Gordon and Breach, New York, 313.

Beck, P.A. and Hu, H. (1952), Trans. Metall. Soc. A.I.M.E. 194, 83.

Beck, P.A. and Hu, H. (1966), in **Recrystallization, Grain Growth and Textures,** ed. Margolin, ASM, 393.

Beck, P.A. and Sperry, P.R. (1949), Trans. Metall. Soc. A.I.M.E. 180, 240.

Beck, P.A. and Sperry, P.R. (1950), J. Appl. Phys. 21, 150.

Beck, P.A., Holdsworth, M.L. and Sperry, P.R. (1949), Trans. Metall. Soc. A.I.M.E. 180, 163.

Beck, P.A., Sperry, P.R. and Hu, H. (1950), J. Appl. Phys. 21, 420.

Beck, P.A., Ricketts, B.G. and Kelly, A. (1959), Trans. Metall. Soc. A.I.M.E. 215, 949.

Becker, R. and Panchanadeeswaran, S. (1989), Text. Microstruct. 10, 167.

Bellier, S.P. and Doherty, R.D. (1977), Acta Metall. 25, 521.

Benford, J.G. and Stanley, E.B. (1969), J. App. Phys. 40, 1583.

Benjamin, J.S. (1970), Metall. Trans. 1, 2943.

Benum, S., Engler, O. and Nes, E. (1994), Mats. Sci. Forum, 157–162, 913.

Berger, A., Wilbrandt, P.J. and Haasen, P. (1983), Acta Metall. 31, 1433.

Berger, A., Wilbrandt, P.J., Ernst, F., Klement, U. and Haasen, P. (1988), Prog. Mater. Sci. 32, 1.

Bever, M.B. (1957), in **Creep and Recovery,** ASM, Cleveland, 14.

Bever, M.B., Holt, D.L. and Titchener, A.L. (1973), Prog. Mater. Sci. 17, 1.

Beynon, J.H. (1999), Phil. Trans. R. Soc. Lond. A357, 1573.

Beynon, J.H. and Sellars, C.M. (1992), ISIJ, 32, 359.

Bhadeshia, H.K.D.H. (1997), Mats. Sci. and Eng. A233, 64.

Bhatia, M.L. and Cahn, R.W. (1978), Proc. R. Soc. Lond. A. 362, 341.

Biberger, M. and Blum, W. (1992), Phil. Mag. 66, 27.

Bishop, G.H., Harrison, R.J., Kwok, T. and Yip, S. (1980), in **Grain boundary Structure and Kinetics,** ed. Balluffi, ASM Metals Park, Ohio, 373.

Black, M.P. and Higginson, R.L. (1999), Scripta Mater. 41, 125.

Blade, J.C. and Morris, P.L. (1975), Proc. 4th Int. Conf. on Textures, Cambridge, 171.

Blicharski, M., Nourbaksh, S. and Nutting, J. (1979), Met. Sci. 13, 516.

Blum, W. (1993). in **Materials Science and Technology,** eds. Cahn, Haasen and Kramer, VCH, Weinheim, 6, 360.

Bockstein, B.S., Kopetsky, C.V. and Shvindlerman, L.S. (1986), **Metallurgia,** Moscow, 224.

Bolingbroke, R.K., Creed, E., Marshall, G.J. and Ricks, R.A. (1993), in **Aluminium Alloys for Packaging,** eds. Morris et al., TMS, Warrendale, USA, 215.

Bolingbroke, R.K., Marshall, G.J. and Ricks, R.A. (1994), Materials Science Forum, 157–162, 1145.

Bolingbroke, R.K., Marshall, G.J. and Ricks, R.A. (1995), Proc. 16th Int. Risø Symp, eds. Hansen et al., 281.

Bolling, G.F. and Winegard, W.C. (1958), Acta Metall. 6, 283.

Bölling, F., Günther, K., Böttcher, A. and Hammer, B. (1992), Steel, 63, 405.

Bollmann, W. (1970), in **Crystal Defects and Crystalline Interfaces,** Springer-Verlag, Berlin.

Borbely, A. and Driver, J.H. (2001), Proc. Int. Conf. on Recrystallization and Grain Growth, Aachen. eds. G. Gottstein and D. Molodov, Springer-Verlag, Berlin, 635.

Böttcher, A., Gerber, T. and Lücke, K. (1992), Mats. Sci. Tech. 8, 16.

Bourelier, F. and Le Hericy, J. (1963), in **Ecrouissage, Restauration, Recristallisation,** Presses Univ. de France, Paris, 33.

Bowen, A.W. (1990), Mats. Sci. and Tech. 6, 1058.

Bowen, A.W. and Humphreys, F.J. (1991), Proc. ICOTOM 9, ed. Bunge, Avignon. 715.

Bowen, A.W., Ardakani, M. and Humphreys, F.J. (1991), Proc. 12th Risø Int. Symp. eds. Hansen et al., Risø, Denmark, 241.

Bowen, A.W., Ardakani, M. and Humphreys, F.J. (1993), in Proc. ICOTOM 10, ed. Bunge, Clausthal, Trans. Tech. Pubs., 919.

Bowles, J.S. and Boas, W. (1948), J. Inst. Met. 74, 501.

Bragg, L. and Nye, J.F. (1947), Proc. R. Soc. Lond. A190, 474.

Brandon, D.G. (1966), Acta Metall. 14, 1479.

Brandon, D.G., Ralph, B., Ranganathan, S. and Wald, M.S. (1964), Acta Metall. 12, 813.

Brigeman, P.W. (1950), **Studies in Large Plastic Flow and Fracture,** McGraw-Hill.

Brimhall, J.L., Klein, M.J. and Huggins, R.A. (1966), Acta Metall. 14, 459.

Brook, R.J. (1976), in **Ceramic Fabrication Processes,** ed. Wang, Academic Press, New York, 331.

Brown, A.F. (1952), Advan. Phys. 1, 427.

Brown, K. (1972), J. Inst. Met. 100, 341.

Brown, K. and Hatherly, M. (1970), J. Inst. Met. 98, 317.

Brown, L.M. (1985), Proc. 5th Int. Conf. on Strength of Metals and Alloys, 3, 1551.

Brown, L.M. (1997), Phil. Trans. Royal Soc. Lond. A355, 1979.

Buckley, R.A. (1979), Met. Sci. 13, 67.

Bunge, H. (1982), **Texture Analysis in Materials Science,** Butterworth, London.

Bunge, H.-J. and Dahlem-Klein, E. (1988), in **ICOTOM 8,** eds. Kallend and Gottstein, TMS, Warrendale, 705.

Burger, G.B., Gupta, A.K., Jeffrey, P.W. and Lloyd, D.J. (1995), Mats. Characterisation, 35, 23.

Burgers, J.M. (1940), Proc. Phys. Soc. (London), 52, 23.

Burgers, W.G. (1941), **Rekristallisation, Verformter Zustand und Erholung,** Leipzig.

Burgers, W.G. and Louwerse, P.C. (1931), Z. Phys. 67, 605.

Burgers, W.G. and Snoek, J.L. (1935), Z. Metallk. 27, 158.

Burke, J.E. (1949), Trans. Metall. Soc. A.I.M.E. 180, 73.

Burke, J.E. (1950), Trans. Metall. Soc. A.I.M.E. 188, 1324.

Burke, J.E. and Turnbull, D. (1952), Prog. Metal Phys. 3, 220.

Byrne, J.G. (1965), **Recovery, Recrystallization and Grain Growth,** McMillan, New York.

Cahn, J.W. (1956), Acta Metall. 4, 449.

Cahn, J.W. (1962), Acta Metall. 10, 789.

Cahn, J.W. and Hagel, W. (1960), in **Decomposition of Austenite by Diffusional Processes,** eds. Zackey and Aaronson, Interscience, Publ., New York, 131.

Cahn, R.W. (1949), J. Inst. Metals, 76, 121.

Cahn, R.W. (1983), in **Physical Metallurgy,** 3rd edn., eds. Cahn and Haasen, Elsevier Science Publishers, 1595.

Cahn, R.W. (1990), in **High Temperature Aluminides and Intermetallics,** eds. Whang et al., TMS, 245.

Cahn, R.W. (1991a), in **Intermetallic Compounds,** ed. Izumi, Jap. Inst. Met, 771.

Cahn, R.W. (1991b), in **Processing of Metals and Alloys,** ed. Cahn, VCH, Heinheim, 429.

Cahn, R.W. and Westmacott, K.H. (1990), cited in Cahn (1991a).

Cahn, R.W., Takeyama, M., Horton, J.A. and Liu, C.T. (1991), J. Mat. Res. 6, 57.

Caleyo, F., Baudin, T. and Penelle, R. (2002), Scripta Mater. 46, 829.

Carmichael, C., Malin, A.S. and Hatherly, M. (1982), Proc. 6th Int. Conf. on Strength of Metals and Alloys, ed. Gifkins, Melbourne, 381.

Carpenter, H.C.H. and Elam, C.F. (1920). J. Inst. Met. 24.2, 83.

Carrington, W., Hale, K.F. and McLean, D. (1960), Proc. Royal. Soc. Lond. 259A, 303.

Castro-Fernandez, F.R. and Sellars, C.M. (1988), Mats. Sci. and Tech. 4, 621.

Castro-Fernandes, F.R., Sellars, C.M. and Whiteman, J.A. (1990), Mats. Sci. and Tech. 6, 453.

Ceppi, E.A. and Nasello, O.B. (1984), Scr. Met. 18, 1221.

Chadwick, G.A. and Smith, D.A. (1976), **Grain Boundary Structure and Properties,** Academic Press, New York.

Chan, H.M. and Humphreys, F.J. (1984a), Proc. El. Mic. Soc. America, 476.

Chan, H.M. and Humphreys, F.J. (1984b), Acta Metall. 32, 235.

Chan, H.M. and Humphreys, F.J. (1984c), Metal Science, 18, 527.

Charpy, G. (1910)., Rev. Met. 7.1, 655.

Chin, G.Y. (1969), in **Textures in Research and Practice,** eds. Grewen and Wassermann, Berlin, 236.

Chin, L.I.J. and Grant, N.J. (1967), Powder Metall. 10, 344.

Chowdhury, S.G., Ray, R.K. and Jena, A.K. (1998), Mats. Sci. and Eng. A246, 289.

Christian, J.W. (2002), **The Theory of Transformations in Metals and Alloys,** Pergamon, Oxford.

Chung, C.Y., Duggan, B.J., Bingley, M.S. and Hutchinson, W.B. (1988), Proc. 8th Int. Conf. on Strength of Metals and Alloys, 1, 319.

Clareborough, L.M. (1950), Aust. J. Sci. Res. 3A, 72.

Clareborough, L.M., Hargreaves, M.E. and West, G.W. (1955), Proc. R. Soc. Lond. A232, 252.

Clareborough, L.M., Hargreaves, M.E. and West, G.W. (1956), Phil. Mag. 1, 528.

Clareborough, L.M., Hargreaves, M.E. and Loretto, M.H. (1963), in **Recovery and Recrystallization of Metals,** ed. Himmel, Interscience, 43.

Cline, R.S. and Hu, H. (1978), unpublished research, quoted by Hu (1978).

Coble, R.L. and Burke, J.E. (1963), in **Progress in Ceramic Science,** Pergamon Press.

Cooke, B.A. and Ralph, B. (1980), Proc. 1st Int. Risø Symp, eds. Hansen et al., Risø, Denmark, 211.

Cooke, B.A., Jones, A.R. and Ralph, B. (1979), Met. Sci. 13, 179.

Cook, M. and Richards, T.L. (1940), J. Inst. Met. 66, 1.

Cook, M. and Richards, T.L. (1946), J. Inst. Met. 73, 1.

Cotterill, P. and Mould, P.R. (1976), **Recrystallization and Grain Growth in Metals,** Surrey Univ. Press, London.

Cottrell, A.H. (1953), **Dislocations and Plastic Flow in Crystals,** OUP, Oxford.

Cottrell, A.H. and Aytekin, V. (1950), J. Inst. Metals. 77, 389.

Couling, S.L. and Pearsall, G.W. (1957), Trans. Metall. Soc. A.I.M.E. 209, 939.

Courbon, J. (2000), Mats. Sci. Forum, 331–337, 17.

Czubayco, U., Sursaeva, V.G., Gottstein, G. and Shvindlerman, L.S. (1998), Acta Mater. 46, 5863.

Daaland, O. and Nes, E. (1995), Acta Mater. 43, 1389.

Daaland, O. and Nes, E. (1996), Acta Mater. 44, 1413.

Dadras, M.M. and Morris, D.G. (1993), Scr. Met. et Mat. 28, 1245.

Dahl, O. and Pawlek, F. (1936), Z. Metallk. 28, 320.

Davenport, S.B., Higginson, R.L. and Sellars, C.M. (1999), Phil. Trans. R. Soc. Lond. A357, 1645.

Davenport, S.B., Silk, N.J., Sparks, C.N. and Sellars, C.M. (2000), Mats. Sci. and Tech. 16, 539.

Davies, R.G. and Stoloff, N.S. (1966), Trans. Metall. Soc. A.I.M.E. 236, 1905.

Dawson, P.R., Mika, D.P. and Barton, N.R. (2002), Scripta Mater. 47, 713.

De Hoff, R.T. and Rhines, F.N. (1968), **Quantitative Microscopy,** McGraw Hill, New York.

Demianczuc, D.W. and Aust, K.T. (1975), Acta Metall. 23, 1149.

Derby, B. (1991), Acta Metall. 39, 955.

Derby, B. and Ashby, M.F. (1987), Scripta Metall. 21, 879.

Detert, K. (1959), Acta Metall. 7, 589.

Detert, K. (1978), in **Recrystallization of Metallic Materials,** ed. F. Haessner, Dr. Riederer-Verlag GmbH, Stuttgart, 97.

Dillamore, I.L. (1978a), in Proc. ICOTOM 5, eds. Gottstein and Lücke, Springer-Verlag, Berlin, 67.

Dillamore, I.L. (1978b), in **Recrystallization of Metallic Materials,** ed. F. Haessner, Springer, 223.

Dillamore, I.L. and Katoh, H. (1974), Met. Sci. 8, 73.

Dillamore, I.L. and Roberts, W.T. (1965), Met. Rev. 10 (39), 271.

Dillamore, I.L., Smith, C.J.E. and Watson, T.W. (1967), Met. Sci. J. 1, 49.

Dillamore, I.L., Morris, P.L., Smith, C.J.E. and Hutchinson, W.B. (1972), Proc. R. Soc. Lond. A. 329, 405.

Dillamore, I.L., Katoh, H. and Haslam, K. (1974), Texture, 1, 151.

Dillamore, I.L., Roberts, J.G. and Busch, A.C. (1979), Met. Sci. 13, 73.

Dimitrov, O., Fromageau, R. and Dimitrov, C. (1978), in **Recrystallization of Metallic Materials,** ed. Haessner, Dr. Riederer-Verlag GMBH, Stuttgart, 137.

Dingley, D.J. (1984), Scan. Elec. Mic. 11, 74.

Dingley, D.J. and Pond, R.C. (1979), Acta Metall. 28, 667.

Dingley, D.J. and Randle, V. (1992), J. Mats. Sci. 27, 4545.

Distl, J.S., Welch, P.I. and Bunge, H.J. (1982), Scripta Metall. 17, 975.

Djaic, R.A.P. and Jonas, J.J. (1972), J. Iron and Steel Inst. 210, 256.

Doherty, R.D. (1975), Metall. Trans. 6A, 588.

Doherty, R.D. (1978), in **Recrystallization of Metallic Materials,** ed. F. Haessner, Dr. Riederer-Verlag GmbH, Stuttgart, 23.

Doherty, R.D. (1982), Metal Sci. 16, 1.

Doherty, R.D. and Cahn, R.W. (1972), J. Less Common Metals, 28, 279.

Doherty, R.D. and Martin, J.W. (1962), J. Inst. Metals, 91, 332.

Doherty, R.D. and Martin, J.W. (1964), Trans. ASM, 57, 874.

Doherty, R.D. and Szpunar, J.A. (1984), Acta Metall. 32, 1789.

Doherty, R.D., Rollett, A.R. and Srolovitz, D.J. (1986), Proc. 7th Risø Symp., eds. Hansen et al., Risø, Denmark, 53.

Doherty, R.D., Li, K., Kashyap, K., Rollett, A.R. and Srolovitz, D.J. (1989), Proc. 10th Risø Symp., eds. Bilde-Sorensen et al., Risø, Denmark, 31.

Doherty, R.D., Li, K., Anderson, M.P., Rollett, A.R. and Srolovitz, D.J. (1990), in **Recrystallization'90,** ed. Chandra, TMS, 122.

Doherty, R.D., Kashyap, K. and Panchanadeeswaran, S. (1993), Acta Met. 41, 3029.

Driver, J.H. (1995). Proc. 16th Int. Risø Symp. Eds. Hansen et al. 25.

Driver, J.H., Theyssier, M. and Maurice, C. (1996), Mats. Sci. and Tech. 12, 851.

Driver, J.H., Paul, H., Glez, J.C. and Maurice, C. (2000). Proc 21st Int. Risø Symposium, Eds. N. Hansen et al. Risø, Denmark. 35.

Drolet, J.P. and Galibois, A. (1968), Acta Metall. 16, 1387.

Drouard, R., Washburn, J. and Parker, E.R. (1953), Trans. Metall. Soc. A.I.M.E. 197, 1226.

Drury, M.D. and Humphreys, F.J. (1986), Acta Metall. 34, 2259.

Drury, M.D., Humphreys, F.J. and White, S.H. (1989), J. Mater. Sci. 24, 154.

Duckham, A., Knutsen, R.D. and Engler, O. (2001), Acta Mater. 49, 2739.

Duggan, B.J. and Jones, I.P. (1977), Texture, 2, 205.

Duggan, B.J. and Lee, W.B. (1988), in **ICOTOM 8,** eds. Kallend and Gottstein, TMS, Warrendale, 625.

Duggan, B.J., Hatherly, M., Hutchinson, W.B. and Wakefield, P.T. (1978a), Met. Sci. 12, 343.

Duggan, B.J., Hutchinson, W.B. and Hatherly, M. (1978b), Scr. Met. 12, 1293.

Duggan, B.J., Lücke, K., Köhlhoff, G. and Lee, C.S. (1993), Acta Metall. 41, 1921.

Duly, D., Baxter, G.J., Shercliff, H.R., Whiteman, J.A., Sellars, C.M. and Ashby, M.F. (1996), Acta Mater. 44, 2947.

Dunn, C.G. (1966), Acta Metall. 14, 221.

Dunn, C.G. and Koh, P.K. (1956), Trans. Metall. Soc. A.I.M.E. 206, 1017.

Dunn, C.G. and Walter, J.L. (1959), Trans. Metall. Soc. A.I.M.E. 218, 448.

Dunn, C.G. and Walter, J.L. (1966), in **Recrystallization, Grain Growth and Textures,** ASM, Ohio, 461.

Dutta, S.K. and Spriggs, R.M. (1970), J. Am. Ceram. Soc. 53, 61.

Dyson, D.J. and Quested, P.N. (2001). in **Quantitative Microscopy of High Temperature Materials,** eds. Strang and Crawley, IOM Communications, 98.

Eastwood, L.W., Bousu, A.E. and Eddy, C.T. (1935), Trans. Metall. Soc. A.I.M.E. 117, 246.

Edward, G.H., Etheridge, M.A. and Hobbs, B.E. (1988), Text. Microstruct. 5, 127.

Eichelkraut, H., Abbruzzese, G. and Lücke, K. (1988), Acta Metall. 36, 55.

Ekstrom, H.E., Hagstrom, J. and Hutchinson, W.B. (1999), Proc. 4th Int. Conf. on Recrystallization. Tsukuba, eds. T. Sakai and H. Suzuki, Japan Inst. Metals, 809.

Ells, C.E. (1963), Acta Metall. 11, 87.

Embury, J.D., Poole, W.J. and Koken, E. (1992), Scripta Metall. 27, 1465.

Emren, F., von Schlippenback, U. and Lücke, K. (1986), Acta. Met. 34, 2105.

Engler, O. (1997), Proc. Rex'96, Recrystallization and Related Phenomena, ed. T. McNelley, Monterey Institute of Advanced Studies, Monterey, California, 503.

Engler, O. (1998), Proc. 19th Risø Int. Symp. eds. Carstensen et al., Risø, Denmark, 253.

Engler, O. (2000), Acta Mater. 48, 4827.

Engler, O. (2001a), Acta Mater. 49, 1237.

Engler, O. (2001b), Scripta Mater. 44, 229.

Engler, O. and Hirsch, J. (2002), Mats. Sci. Eng. A336, 249.

Engler, O. and Huh, M. (1999), Mats. Sci. and Eng. A271, 371.

Engler, O. and Yang, P. (1995), Proc. 16th Int. Risø Symp, eds. Hansen et al., 335.

Engler, O., Hirsch, J. and Lucke, K. (1995), Acta Mater. 43, 121.

Engler, O., Kong, X.W. and Lucke, K. (1999), Scripta Mater. 41, 493.

Engler, O., Kong, X.W. and Lucke, K. (2001), Philos. Mag. 81, 543.

English, A.T., Backofen, W.A. (1964), Trans. Metall. Soc. A.I.M.E. 230, 396.

Escher, C., Neves, S. and Gottstein, G. (1998), Acta Mater. 46, 441.

Estrin, Y., Gottstein, G. and Shvindlerman, L.S. (1999), Acta Mater. 47, 3541.

Estrin, Y., Gottstein, G., Rabkin, E. and Shvindlerman, L.S. (2000), Scripta Mater. 43, 147.

Every, R.L. and Hatherly, M. (1974), Texture, 1, 183.

Ewing, J.A. and Rosenhain, W. (1900), Phil. Trans. Royal Soc. 193A, 353.

Exell, S.F. and Warrington, D. (1972), Phil. Mag. 26, 1121.

Exner, H.E. (1972), Int. Met. Reviews, 17, 25.

Faivre, P. and Doherty, R.D. (1979), J. Mats. Sci. 14, 897.

Farag, M.M., Sellars, C.M. and Tegart, W.McG. (1968), in **Deformation under Hot Working Conditions,** ed. Moore, Iron & Steel Inst., London, 103.

Farrell, K., Schauffhauser, A.C. and Houston, J.T. (1970), Metall. Trans. 1, 2899.

Feltham, P. (1957), Acta Metall. 5, 97.

Feltner, P.K. and Loughhunn, D.J. (1962), Acta Metall. 10, 685.

Feppon, J.M. and Hutchinson, W.B. (2002). Acta Mater. 50, 3293.

Ference, T.G. and Balluffi, R.W. (1988), Scripta Metall. 22, 1929.

Ferran, G., Cizeron, G. and Aust, K.T. (1967), Mem. Sci. 64, 1064.

Ferry, M. and Humphreys, F.J. (1996a), Acta Mater. 44, 1293.

Ferry, M. and Humphreys, F.J. (1996b), Acta Mater. 44, 3089.

Ferry, M. and Humphreys, F.J. (1996c), Mats. Sci. Forum, 217–222, 493.

Ferry, M., Munroe, P., Crosky, A. and Chandra, T. (1992), Mats. Sci. and Tech. 8, 43.

Fleck, N.A. and Hutchnison, J.W. (1994), J. Mech. Phys. Solids. 41, 1825.

Flower, H.M. (1990), Mats. Sci. and Tech. 6, 1082.

Forbord, B., Holmestad, R., Daaland, O. and Nes, E. (1997), Proc. Rex'96, ed. T. McNelley, Monterey Institute of Advanced Studies, Monterey, California, 247.

Form, W., Gindreaux, G. and Mlyncar, V. (1980), Metal Sci. 14, 16.

Foster, K., Kramer, J.J. and Weiner, G.W. (1963), Trans. Metall. Soc. A.I.M.E. 227, 185.

Frank, F.C. (1988), Metall. Trans. 19A, 403.

Fridman, E.M., Kopezky, C.V. and Shvindlerman, L.S. (1975), Z. Metallk. 66, 533.

Fridy, J.M., Marthinsen, K., Rouns, T.N., Lippert, K.B., Nes, E. and Richmond, O. (1992), Proc. 3rd Int. Conf. on Aluminium, Trondheim, 333.

Friedel, J. (1964), **Dislocations,** Addison-Wesley, London.

Frois, C. and Dimitrov, O. (1966), Ann. Chim. Paris, 1, 113.

Frost, H.J. (1992), in **Grain Growth in Polycrystalline Materials,** eds. Abbruzzese and Brozzo, Trans. Tech. Publns., 903.

Frost, H.J. and Ashby, M.F. (1982), **Deformation-Mechanism Maps,** Pergamon Press.

Frost, H.J. and Thompson, C.V. (1988), J. Electronic Mats. 17, 447.

Frost, H.J. Whang, J. and Thompson, C.V. (1986), Pro. 7th Risø Int. Symp., eds. Hansen et al., Risø, Denmark, 315.

Frost, H.J., Thompson, C.V. and Walton, D.T. (1990), Acta Metall. 38, 1455.

Frost, H.J., Thompson, C.V. and Walton, D.T. (1992), in **Grain Growth in Polycrystalline Materials,** eds. Abbruzzese and Brozzo, Trans. Tech. Publns., 543.

Fuchizaki, K., Kusaba, T. and Kawasaki, K. (1995), Phil. Mag. B71, 333.

Fudaba, K., Akisue, O. and Tokunaga Y. (1988), in 27th CIM Conf. (Montreal), 290.

Fuentes, M. and Sevillano, J.G. (1992), (eds) **Recrystallization'92,** Trans. Tech. Publications. San Sebastian, Spain.

Fukuda, F. and Sadayori, T. (1989), Steel Times Int. July, 38.

Fukuda, N. and Shimizu, M. (1972), Sosei-to-Kako, 13, 841.

Fullman, R.E. and Fisher, J.C. (1951), J. Appl. Phys. 22, 1350.

Fullman, R.L. (1953), Trans. AIME. 197, 447.

Fullman, R.L. (1952), in **Metal Interfaces,** ASM, Cleveland, Ohio, 179.

Furley, J. and Randle, V. (1991), Mats. Sci. and Tech. 7, 12.

Furu, T. (1992), Doctoral Thesis. NTH, Trondheim.

Furu, T. and Nes, E. (1992), in **Recrystallization'92,** eds. Fuentes and Sevillano, San Sebastian, Spain, 311.

Furu, T., Marthinsen, K. and Nes, E. (1990), Mats. Sci. and Tech. 6, 1093.

Furu, T., Marthinsen, K. and Nes, E. (1992), in **Recrystallization'92,** eds. Fuentes and Sevillano, San Sebastian, Spain, 41.

Furu, T., Orsund, R. and Nes, E. (1995). Acta Metall. Mater. 43, 2209.

Furu, T., Shercliff, H.R., Sellars, C.M. and Ashby, M.F. (1996), Proc. ICAA5, Grenoble, 453.

Galina, A.V., Fradkov, V.Y. and Shvindlerman, L.S. (1987), Fiz. Metal. Metalloved. 63.6, 1220.

Galiyev, A., Kaibyshev, R. and Gottstein, G. (2001), Acta Mater. 49, 1199.

Gardner, K.J. and Grimes, R. (1979), Metal Sci. 13, 216.

Gastaldi, J., Jourdan, C. and Grange, G. (1992). Materials Science Forum, 94–96, 17.

Gawne, D.T. and Higgins, R.A. (1969), in **Textures in Research and Practice,** eds. Grewen and Wasserman, Springer, New York, 319.

Gawne, D.T. and Higgins, R.A. (1971), J. Mats. Sci. 6, 403.

Gholinia, A., Prangnell, P.B. and Markuchev, M.V. (2000), Acta Mater. 48, 1115.

Gholinia, A., Humphreys, F.J. and Prangnell, P.B. (2002a), Materials Forum, 408–412, 1519.

Gholinia, A., Humphreys, F.J. and Prangnell, P.B. (2002b), Acta Mater. 50, 4461.

Ghosh, A.K. and Ghandi, C. (1986), in **Strength of Metals and Alloys. Proc. 7th Int. Conf. on Strength of Metals and Alloys,** eds. McQueen et al., Pergamon Press, 3, 2065.

Gialanella, S., Cahn, R.W., Malagelada, J., Surinach, S. and Barò, M.D. (1992), in **Kinetics of Ordering Transformations in Metals,** eds. Chang et al., 161.

Gifkins, R.C. (1952), J. Inst. Metals, 81, 417.

Gil Sevillano, J., van Houtte, P. and Aernoudt, E. (1980), Prog. Mater. Science, 25, 69.

Gilman, J.J. (1955), Acta Metall. 3, 277.

Gjostein, N.A. and Rhines, F.N. (1959), Acta Metall. 7, 319.

Gladman, T. (1966), Proc. R. Soc. Lond. A294, 298.

Gladman, T. (1980), Proc. 1st Int. Risø Symposium, ed. Hansen, Risø, Denmark, 183.

Gladman, T. (1990), Mats. Sci. and Tech. 6, 1131.

Gladman, T. (1992), in **Grain Growth in Polycrystalline Materials,** eds. Abbruzzese and Brozzo, Trans. Tech. Publns., 113.

Gladman, T. and Woodhead, J.H. (1960), J. Iron and Steel Inst. 194, 189.

Gleiter, H. (1969a), Acta Metall. 17, 565.

Gleiter, H. (1969b), Acta Metall. 17, 853.

Gleiter, H. (1969c), Acta Metall. 17, 1421.

Gleiter, H. (1970a), Acta Metall. 18, 117.

Gleiter, H. (1970b), Acta Metall. 18, 23.

Gleiter, H. (1970c), Z. Metallk. 61, 282.

Gleiter, H. (1971), Phys. Stat. Solidi (b), 45, 9.

Gleiter, H. (1980), in **Grain Boundary Structure and Kinetics,** ASM, Ohio, 427.

Gleiter, H. (2000), Acta Mater. 48, 1.